

**Imperial College  
London**



**“Synthesis of Aromatic and Heterocyclic Platform Chemicals  
from Bio-derived Furans”**

**Paraskevi Filippousi**

Supervised by: Dr. Jason Hallett, Dr. James Wilton-Ely and Prof. Paul Fennell

Department of Chemical Engineering  
Imperial College London of Science Technology and Medicine

Thesis submitted for the degree of Doctor of Philosophy (PhD) to Imperial  
College London of Science, Technology and Medicine

February 2018

**To my father and my mother**

## **“Ithaka” – P. Cavafy**

**Translated by Edmund Keeley and Philip Sherrard**

As you set out for Ithaka, hope the voyage is a long one, full of adventure, full of discovery.

Laistrygonians and Cyclops, angry Poseidon; don't be afraid of them: you'll never find things like that on your way as long as you keep your thoughts raised high, as long as a rare excitement stirs your spirit and your body. Laistrygonians and Cyclops, wild Poseidon—you won't encounter them unless you bring them along inside your soul, unless your soul sets them up in front of you.

May there be many summer mornings when, with what pleasure, what joy, you come into harbours seen for the first time. May you stop at Phoenician trading stations to buy fine things, mother of pearl and coral, amber and ebony, sensual perfume of every kind—as many sensual perfumes as you can; and may you visit many Egyptian cities to gather stores of knowledge from their scholars.

Keep Ithaka always in your mind. Arriving there is what you are destined for. But do not hurry the journey at all. Better if it lasts for years, so you are old by the time you reach the island, wealthy with all you have gained on the way, not expecting Ithaka to make you rich.

Ithaka gave you the marvellous journey. Without her you would not have set out. She has nothing left to give you now. And if you find her poor, Ithaka won't have fooled you. Wise as you will become, full of experience, you will have understood by then what these Ithakas mean.

## **Declaration of Originality**

I certify, as the author of this thesis, that I was the person primarily involved in the design, implementation and data analysis for the experimental work that is described in this manuscript. I declare that the work presented in the thesis is to the best of my knowledge and belief, original and otherwise properly referenced.

## **Copyright Declaration**

The copyright of this thesis rests with the author and is made available under a Creative Commons Attribution Non-Commercial No Derivatives licence. Researchers are free to copy, distribute or transmit the thesis on the condition that they attribute it, that they do not use it for commercial purposes and that they do not alter, transform or build upon it. For any reuse or redistribution, researchers must make clear to others the licence terms of this work.

## Abstract

### “Synthesis of Aromatic and Heterocyclic Platform Chemicals from Bio-derived Furans”

The environmental impact of the extensive use of fossil fuels to produce fuels and chemicals as well as the cost sensitivity of platform chemicals to oil prices remain major concerns. Sustainable biomass processing is the only viable solution for the large-scale production of bio-based products with a projected average of 30 % of the production of chemicals to derive from biomass within the EU (Joint European Biorefinery Vision for 2030). The co-production of fuels and high-value bio-derived chemicals would contribute to the environmental sustainability, as well as the economic viability, of the future biorefineries. Lignocellulosic biomass is relatively inexpensive and abundant, without competing with food sources, and thus it can be considered as the most suitable feedstock for a full-scale biorefinery. The production of highly functionalized intermediates such as 5-(hydroxymethyl)furfural (5-HMF) and 2,5-dimethylfuran (2,5-DMF) from lignocellulose has been established. The conversion of such platform chemicals into other high-value products remains a challenge. A plethora of published studies focused on the transformations of the functional groups rather than using the furan ring chemistry. The overall project objective was the study of novel reaction protocols to produce heterocyclic and aromatic platform chemicals from established biomass intermediates by using ionic liquids as catalysts or co-catalysts. Thiophene synthesis from bio-derived furanics, such as 2,5-DMF, was studied under acidic conditions, focusing on Lewis acidic ionic liquids that promoted the recyclization of bio-derived 2,5-DMF into its thiophene analogue. Moisture-stable chlorometallate ILs were synthesised and characterised separately to elucidate speciation, acidity and thermal stability prior to being applied towards thiophene synthesis in liquid-liquid biphasic reactions. Lewis acidic chlorozincate(II) ionic liquids were also supported on an inexpensive, high surface area silica support, affording supported ionic liquids (SILPs) that were studied for their surface properties and IL/support interactions. The SILP materials were successfully tested as catalysts for the novel, gas-phase synthesis of 2,5-dimethylthiophene (2,5-DMT) in a pressurised fluidised bed reactor that was constructed in-house. The latter experiments aimed for process control where parameters such as temperature and substrate/H<sub>2</sub>S ratios were controlled with the overall process economics improving as a thin layer of ionic liquid was used instead of a biphasic system. 2,5-DMF was also investigated as an activated diene in acid-catalysed Diels-Alder reactions in the presence of maleic anhydride towards the synthesis of phthalic anhydride derivatives. The domino reactions for the formation of 3,6-dimethylphthalic anhydride (3,6-DMPA), a potential precursor for polymer synthesis, was studied in binary IL/acid systems of different acidity profiles, indicating the potential towards the direct synthesis of 3,6-DMPA from bio-based furanic compounds.

## Acknowledgments

First and foremost, I would like to express my gratitude to my supervisory team: Dr. Jason Hallett, Dr. James Wilton-Ely and Prof. Paul Fennell. My PhD has been a challenging “path” and without their consistent support, it would not have been possible to reach the point of its completion. I would like to say a big thank you to Dr. Jason Hallett for his relentless support. Thank you for your daily motivation, your insights and for believing in me, even at times when I would doubt myself or lose motivation. It has been a bumpy ride that involved many personal and technical challenges, a few lab moves, department changes, project changes, building reactors and working with toxic gases. However, I am glad that I took this challenge. I did learn a lot from whilst enjoying a big part of it all. I would also like to thank Dr. James Wilton-Ely for contributing in getting this project successfully funded as well as for his guidance, supervision as well as his kind support throughout my PhD. Special thanks also go to Prof. Paul Fennell who became part of the supervisory team amid important project changes that required many new skills to be learned; his technical expertise and genuine interest have been invaluable for the continuation of my project. I am also grateful to become part of the Fennell group who has welcomed me and helped me, to a great extent, during the final two years of my PhD.

I received significant assistance from many members of the Chemical Engineering support staff without whom the continuation of my PhD would have not been as smooth as it was or maybe not even possible. A sincere thank you goes to Richard Wallington, Tony Meredith and Paul Mayer of the workshop team; Chin Lang of the electrical workshop; Patricia Carry and Andrew Macey of analytical services; Keith Walker and Ben Kitnash of the Chemical Engineering stores; as well as Sarah McCallum and Susi Underwood for their administrative support. Thanks also go to Dr. Lisa Haigh (Department of Chemistry) who has helped me a lot with running several GC(MS) and LSIMS experiments. Additionally, I would like to mention and thank Lisa Weigand for her kind assistance with setting up the GC(FID)/(MS) equipment (Hallett group). I am also grateful to Peter Haycock (Department of Chemistry) for all the support that he has provided over the years with NMR spectroscopy. I would also like to thank Dr. Kevin Lovelock and Dr. Nacho Villar-Garcia for their help with the preliminary LEIS and XPS experiments. I am also very grateful to Oliver Levers and Dr. Rob Law who assisted with performing and interpreting solid state NMR spectroscopy experiments (Department of Chemistry). Many thanks also go to Kai Ni Teh and Linqian (Michelle) Li for their contributions on the study of the aromatic compounds synthesis from bio-derived furans as part of their “MRes in Green Chemistry” project. My thanks also go to Climate-KIC for funding my PhD and making it possible for me to be at Imperial College and complete my research. I would also like to acknowledge Imperial College Trust and the Royal Society of Chemistry (RSC) for the additional

funding that I received, allowing me to attend both Pacifichem 2015 and IUPAC 2016 where I could present my research work and attend several useful sessions related with my PhD.

Big thanks go to many members of the “Hallett Empire” for all the support and good company over the years: Oliver Levers, Dr. Coby Clarke, Lisa Weigand, Wei-Chien Tu, Dr. Mayte Mota Martinez, Francisco Malaret, Amir Al Ghatta, Dr. Alex Brogan, Dr. Paul Corbett, Shaochen Huang, Bing Tian, Angela Chen, Dr. Agi Brandt-Talbot, Florence Gschwend and Clementine Chambon. Thank you, Alex and Ollie, for proofreading part of my thesis as well. To the Fennell group, thank you for all your tremendous help as well as for all the good times in and outside of the lab; I am greatly indebted to all of you: Dr. Zili Zhang, Dr. Matthew Boot-Handford, Peter Clough, Dr. Joseph Yao, Dr. Thomas Hills, Dr. Liya Zheng, Dr. Salman Masoudi Soltani, Dr. John Blamey and the fellow 222-labmate Lorena dos Santos de Souza. To Zhili, your patience, your technical expertise and most importantly your friendship have been invaluable. They helped me to move forward during my PhD. Special thanks also go to my friend Anita Toscani (JWE group) for her friendship, moral support and even for beating the 20 km walk with me whilst fundraising for Cancer Research UK. I would also like to say thank you to another friend and colleague, Dr. Saif Al Ghafri, for all his motivation, mentoring and kind interest on my progress. I would like to thank Tom Welton’s research group for helping me start off on the right foot during my first year at the Department of Chemistry. I would especially like to thank Dr. Gilbert de Gregorio, Dr. Liyana Ismail, Hanim Mohd Saupi, Eduards Bakis, Dr. Alastair McIntosh, Rafiq Mohamed Sulaiman, Dr. Raquel Prado-Garcia and John Graskvik. Thanks also go to Piotr but also Mark and Dom, part of DSV, for all their support during the ‘crazy’ attempt to write up my thesis and participate in a start-up accelerator. To my childhood friends, Athena and Sofia, thank you for putting up with me throughout these years and for being there in good and bad times. To my dear friends at Imperial College: Ollie, Anita, Coby, Zhili, Gilly, Matt, Peter, Lisa, Wei-Chien, Joe, Liya, Lorena, Saif, Mayte, Salman, Liyana, Eduards, Hanim and Rafiq: thank you for your motivation, your advice and the good memories.

Finally, I would like to thank my family. To my brother, Fragkiskos, I look up to you. Your presence always reminds how important it is to cherish the people whom we have the privilege to call our family. To my nephew, Stamatis, you are the “light” and joy that came into our lives almost 3 years ago and you just made everything more beautiful. Mom, thank you for all your sacrifices, for teaching me all that I would ever need to be here today and for your unconditional love. To my father, you have always been a great example with a strong but very kind heart. Your belief in me have always given me the courage that I needed to keep moving forward. Thank you for always reminding me that “tomorrow is another day”, for making me laugh even on the “darkest” days and for being next to me when I needed you the most.

# Table of Contents

<b>List of Figures</b>	12
<b>List of Tables</b>	21
<b>Abbreviations</b>	23
<b>Nomenclature</b>	27
<b>Chapter 1: Introduction</b>	
<b>1.1 Biorefining as an alternative to oil refining</b>	29
1.1.1 The Petroleum refinery	30
1.1.2 Biorefinery challenges; establishing a sustainable bioeconomy	31
1.1.3 Lignocellulose as a promising feedstock for the future integrated biorefinery	32
1.1.4 Lignocellulose pretreatment; a key processing step to produce biofuels and bio-derived chemicals	34
<b>1.2 Bio-derived chemicals development</b>	36
1.2.1 Bio-derived chemicals from polysaccharides	36
1.2.2 Bio-derived chemicals from lignin	38
<b>1.3 Ionic liquids and their application in the development of the future biorefinery</b>	39
1.3.1 Ionic Liquids and lignocellulosic biomass pretreatment	41
1.3.2 Ionic Liquids and 5-HMF synthesis	43
<b>1.4 5-(Hydroxymethyl)furfural (5-HMF) as a platform chemical</b>	46
1.4.1 5-HMF functional group transformations	46
1.4.2 5-HMF furan ring transformations; heterocyclic and aromatic compounds synthesis	50
<b>1.5 2,5-dimethylfuran (2,5-DMF) as a platform chemical</b>	56
<b>1.6 Project aims and objectives</b>	66
<b>1.7 Thesis outline</b>	67
<b>1.8 References</b>	70
<b>Chapter 2: Ionic liquids as catalysts for the small-scale synthesis of bio-derived thiophenes</b>	
<b>2.1 Acidic ionic liquids</b>	79
2.1.1 Chlorometallate Lewis acidic ionic liquids overview	79
2.1.1.1 General properties and applications of halometallate ILs	79
2.1.1.2 Anionic speciation of halometallate ILs	80
2.1.1.3 Acidity determination and intramolecular interactions in chlorometallate ILs	82
2.1.2 Brønsted acidic ionic liquids (BAILs) overview	84
2.1.2.1 General properties and applications of Brønsted acidic ionic liquids (BAILs)	84
2.1.2.2 Acidity determination of Brønsted acidic ionic liquids (BAILs)	86
<b>2.2 Thiophene chemistry and the application of thiophene analogues</b>	88



2.2.1 Preparation of thiophene derivatives from non-heterocyclic precursors	89
2.2.2 Thiophene formation from heterocyclic precursors (Furan, 2,5-dimethylfuran)	93
2.2.3 Ionic liquids and thiophene synthesis	97
<b>2.3 Results &amp; Discussion</b>	98
2.3.1 Ionic liquids synthesis	98
2.3.2 Determination of anionic speciation by Mass Spectrometry	100
2.3.3 Thermal degradation behaviour of [C <sub>4</sub> C <sub>1</sub> im]Cl·MCl <sub>x</sub> (ZnCl <sub>2</sub> , FeCl <sub>3</sub> , InCl <sub>3</sub> ; X <sub>MCl<sub>x</sub></sub> = 0.67) Dynamic Scans	101
2.3.4 Thermal stability of [C <sub>4</sub> C <sub>1</sub> im]Cl·ZnCl <sub>2</sub> as a function of composition; Dynamic Scans	104
2.3.5 Chemical shift as a function of composition; chlorometallate ILs	106
2.3.5.1 Complex intramolecular interactions in 1,3-dialkylimidazolium-based ionic liquids	106
2.3.5.2 NMR spectroscopy as a tool for studying Intramolecular interactions in ionic liquids	108
2.3.5.3 Intramolecular interactions in chlorometallate ionic liquids (Results & Discussion)	109
2.3.6 Long-term thermal stability and decomposition kinetics of [C <sub>4</sub> C <sub>1</sub> im]Cl·ZnCl <sub>2</sub> (X <sub>ZnCl<sub>2</sub></sub> = 0.67)	112
2.3.7 Synthesis of thiophene-derivatives from bio-derived furans in ionic liquids	115
2.3.7.1 Synthesis of 5-Hydroxymethyl-2-furaldehyde and 2,5-DMT in ionic liquids	116
<b>2.4 Experimental</b>	124
2.4.1 Synthesis and characterisation of ionic liquids and intermediates	126
2.4.1.1 1-butyl-3-methylimidazolium chloride ([C <sub>4</sub> C <sub>1</sub> im]Cl)	126
2.4.1.2 Chlorozincates(II): [C <sub>4</sub> C <sub>1</sub> im]Cl·ZnCl <sub>2</sub> (0.10 ≤ X <sub>ZnCl<sub>2</sub></sub> ≤ 0.75)	127
2.4.1.3 Chloroindates(III) ([C <sub>4</sub> C <sub>1</sub> im]Cl·InCl <sub>3</sub> , X <sub>InCl<sub>3</sub></sub> = 0.67)	129
2.4.1.4 Chloroferrates(III) ([C <sub>4</sub> C <sub>1</sub> im]Cl·FeCl <sub>3</sub> , X <sub>FeCl<sub>3</sub></sub> = 0.67)	130
2.4.1.5 1-butyl-3-methylimidazolium Hydrogen Sulfate ([C <sub>4</sub> C <sub>1</sub> im][HSO <sub>4</sub> ])	131
2.4.2 Small-scale synthesis of bio-derived thiophene analogues in ionic liquids	132
2.4.2.1 Reference compounds	132
2.4.2.2 Reaction of 5-HMF and H <sub>2</sub> S in a Lewis acid ionic liquid ([C <sub>4</sub> C <sub>1</sub> im]Cl·ZnCl <sub>2</sub> , X <sub>ZnCl<sub>2</sub></sub> = 0.67)	133
2.4.2.3 Control reaction of 5-HMF and H <sub>2</sub> S in [C <sub>4</sub> C <sub>1</sub> im]Cl	133
2.4.2.4 Reaction of 2,5-DMF and H <sub>2</sub> S in a Lewis acidic IL ([C <sub>4</sub> C <sub>1</sub> im]Cl·ZnCl <sub>2</sub> , X <sub>ZnCl<sub>2</sub></sub> = 0.67).	134
2.4.2.4 a) Characterisation of the crude reaction mixture (IL layer) by <sup>1</sup> H NMR spectroscopy	135
2.4.2.4 b) Characterisation of the Kugelrohr distillate (top layer) by <sup>1</sup> H NMR spectroscopy	137
2.4.2.4 c) Characterisation of the Kugelrohr distillate (bottom layer) by <sup>1</sup> H NMR spectroscopy	138
2.4.2.5 Reference compounds (2,5-DMF, 2,5-DMT) - Kugelrohr studies	138
2.4.2.6 GC(EI) protocol – Qualitative characterisation of the Kugelrohr distillation products; Reaction of 2,5-DMF and H <sub>2</sub> S in Lewis acidic ionic liquids ([C <sub>4</sub> C <sub>1</sub> im]Cl·ZnCl <sub>2</sub> , X <sub>ZnCl<sub>2</sub></sub> = 0.67).	139
2.4.2.7 Reaction of 2,5-DMF and H <sub>2</sub> S in Lewis basic ionic liquids ([C <sub>4</sub> C <sub>1</sub> im]Cl·ZnCl <sub>2</sub> , X <sub>ZnCl<sub>2</sub></sub> = 0.25)	140
2.4.2.8 Reaction of 2,5-DMF and H <sub>2</sub> S in Lewis acidic ionic liquids ([C <sub>4</sub> C <sub>1</sub> im]Cl·ZnCl <sub>2</sub> , X <sub>ZnCl<sub>2</sub></sub> = 0.50)	140
2.4.2.9 Reaction of 2,5-DMF and H <sub>2</sub> S in a Brønsted acid ionic liquid ([C <sub>4</sub> C <sub>1</sub> im][HSO <sub>4</sub> ])	140
<b>2.5 References</b>	142
<b>2.6 Appendix</b>	149

2.6.1 Sample mass spectra of [C <sub>4</sub> C <sub>1</sub> im]Cl·ZnCl <sub>2</sub> (X <sub>ZnCl<sub>2</sub></sub> = 0.67) (FB <sup>-</sup> /FB <sup>+</sup> )	149
2.6.2 <sup>13</sup> C chemical shift progression (δ / ppm) as a function of X <sub>ZnCl<sub>2</sub></sub> ; [C <sub>4</sub> C <sub>1</sub> im]Cl·ZnCl <sub>2</sub>	150
2.6.3 Isothermal TGA scans; [C <sub>4</sub> C <sub>1</sub> im][NTf <sub>2</sub> ], [C <sub>4</sub> C <sub>1</sub> im]Cl and [C <sub>4</sub> C <sub>1</sub> im]Cl·ZnCl <sub>2</sub> (X <sub>ZnCl<sub>2</sub></sub> = 0.67)	152
2.6.4 Arrhenius plots (ln(dw/dt) = f(1/T)) for the determination of Arrhenius parameters: E <sub>a</sub> and A; thermal decomposition of [C <sub>4</sub> C <sub>1</sub> im][NTf <sub>2</sub> ], [C <sub>4</sub> C <sub>1</sub> im]Cl and [C <sub>4</sub> C <sub>1</sub> im]Cl·ZnCl <sub>2</sub> (X <sub>ZnCl<sub>2</sub></sub> = 0.67).	153
2.6.5 Exponential decay plots for [C <sub>4</sub> C <sub>1</sub> im][NTf <sub>2</sub> ], [C <sub>4</sub> C <sub>1</sub> im]Cl and [C <sub>4</sub> C <sub>1</sub> im]Cl·ZnCl <sub>2</sub> (X <sub>ZnCl<sub>2</sub></sub> = 0.67).	154
<b>Chapter 3: Lewis acidic Supported Ionic Liquid Phases (SILPs) as catalysts for the synthesis of bio-derived thiophenes in a fluidised bed reactor (FBR)</b>	
<b>3.1 Supported Ionic Liquid Phase systems (SILP)</b>	155
3.1.1 SILP synthetic protocols overview	155
3.1.2 Selected examples of applications of Supported Ionic Liquid Phases; Acidic SILPs	158
3.1.3 Ionic liquids and continuous flow processes; SILP applications	159
<b>3.2 Results &amp; Discussion</b>	163
3.2.1 Preparation of Lewis acidic supported ionic liquids (SILP) - [C <sub>4</sub> C <sub>1</sub> im]Cl·ZnCl <sub>2</sub> , X <sub>ZnCl<sub>2</sub></sub> = 0.67	163
3.2.2 Surface area and pore structure analysis of Supported Ionic Liquid phases by gas adsorption	164
3.2.2.1 [C <sub>4</sub> C <sub>1</sub> im]Cl·ZnCl <sub>2</sub> (X <sub>ZnCl<sub>2</sub></sub> = 0.67)-based SILPs; characterisation by gas adsorption	166
3.2.3 Solid-state NMR spectroscopy investigations on Supported Ionic Liquid Phases (SILPs). Pore filling and the orientation of ionic liquids at the solid-liquid interface	172
3.2.3.1 [C <sub>4</sub> C <sub>1</sub> im]Cl·ZnCl <sub>2</sub> (X <sub>ZnCl<sub>2</sub></sub> = 0.67)-based SILPs, IL - silica gel (60 Å and 150 Å) support interactions	175
3.2.4 Lewis acidic [C <sub>4</sub> C <sub>1</sub> im]Cl·ZnCl <sub>2</sub> (X <sub>ZnCl<sub>2</sub></sub> = 0.67)-based SILPs; Thermal stability	196
3.2.5 Study of the fluidisation behaviour of [C <sub>4</sub> C <sub>1</sub> im]Cl·ZnCl <sub>2</sub> (X <sub>ZnCl<sub>2</sub></sub> = 0.67)/SiO <sub>2</sub> 60 Å-based SILPs	196
3.2.6 Experimental apparatus design	192
3.2.6.1 Main reactor body description	193
3.2.6.2 Temperature, pressure and gas flow control – equipment description	194
3.2.6.3 Vapour delivery system (2,5-dimethylfuran (2,5-DMF)/N <sub>2</sub> )	195
3.2.6.4 Solid SILP catalyst feeding assembly	196
3.2.6.5 Process control and data collection	196
3.2.6.6 Liquid sampling system (LSS) development – Gas/liquid separation	197
3.2.7 Study of the gas-phase recyclization of 2,5-dimethylfuran (2,5-DMF) to form 2,5-dimethylthiophene (2,5-DMT), catalysed by Lewis acidic chlorozincate(II) SILPs.	198
3.2.7.1 Preliminary testing (blanks); H <sub>2</sub> S/bed interactions and 2,5-DMF recovery	198
3.2.7.2 Gas-phase recyclization of 2,5-DMF to 2,5-DMT; summary of attempted reactions	200
3.2.7.3 Summary and outlook on future work	205
<b>3.3 Experimental</b>	207
3.3.1 Synthesis of Lewis acidic, silica-supported ILs ([C <sub>4</sub> C <sub>1</sub> im]Cl·ZnCl <sub>2</sub> , X <sub>ZnCl<sub>2</sub></sub> = 0.67)	209
3.3.2 Liquid sampling system (LSS) development	211

3.3.3 Operating protocol for the gas-phase synthesis of bio-derived thiophenes, catalysed by Lewis acidic supported ionic liquids (SILP) in a spouted bed reactor	214
<b>3.4 References</b>	218
<b>3.5 Appendix</b>	221
3.5.1 IUPAC classification of N <sub>2</sub> -physisorption isotherms	221
3.5.2 Pore area distribution graphs of SiO <sub>2</sub> -150 Å-based SILPs as a function of ε <sub>IL</sub> – BJH theory	222
3.5.3 Effect of n <sub>IL</sub> (mmol g <sup>-1</sup> ) on the surface characteristics of Lewis acidic SILPs with varying amounts of [C <sub>4</sub> C <sub>1</sub> im]Cl·ZnCl <sub>2</sub> (X <sub>ZnCl<sub>2</sub></sub> = 0.67)	223
3.5.4 Static and <sup>1</sup> H MAS ssNMR spectra of SiO <sub>2</sub> -150 Å-based SILPs as a function of composition; [C <sub>4</sub> C <sub>1</sub> im]Cl·ZnCl <sub>2</sub> (X <sub>ZnCl<sub>2</sub></sub> = 0.67)	224
3.5.5 T <sub>1</sub> relaxation time calculations for SiO <sub>2</sub> -150 Å-based SILPs as a function of composition; [C <sub>4</sub> C <sub>1</sub> im]Cl·ZnCl <sub>2</sub> (X <sub>ZnCl<sub>2</sub></sub> = 0.67) – Inversion recovery pulse sequence	225
3.5.6 Thermal stability of SiO <sub>2</sub> -150 Å-based SILPs as a function of ε <sub>IL</sub> ([C <sub>4</sub> C <sub>1</sub> im]Cl·ZnCl <sub>2</sub> (X <sub>ZnCl<sub>2</sub></sub> = 0.67)); Dynamic Scans	226
3.5.7 Thermal stability of the bulk ionic liquid: ([C <sub>4</sub> C <sub>1</sub> im]Cl·ZnCl <sub>2</sub> (X <sub>ZnCl<sub>2</sub></sub> = 0.67))	227
3.5.8 Nitrogen density and viscosity correlations with T and P; NIST Chemistry webbook data	228
3.5.9 Standards GC(EI) – Mass spectra (2,5-DMF, 2,5-DMT, 2,5-hxd)	229
3.5.10 Sample GC chromatographs; study of the gas-phase synthesis of 2,5-DMT, catalysed by Lewis acidic chlorozincate(II) SILPs.	231
3.5.11 Calibration curves (2,5-DMF, 2,5-DMT, 2,5-hxd) – Quantitative analysis GC(FID)	233

## Chapter 4: Ionic liquids for the synthesis of bio-derived 3,6-dimethylphthalic anhydride

<b>4.1 Introduction</b>	234
<b>4.2 Results &amp; Discussion</b>	237
4.2.1 Diels-Alder cycloaddition between 2,5-dimethylfuran (2,5-DMF) and maleic anhydride (MA)	237
4.2.2 Dehydrative aromatization of the cycloadduct intermediate: 1,7-dimethyl-4,10-dioxatricyclo[5.2.1.0 <sup>2,6</sup> ]dec-8-ene-3,5-dione	240
4.2.3 Direct synthesis of 3,6-DMPA in binary acidic systems	242
4.2.3.1 3,6-DMPA synthesis in [C <sub>4</sub> C <sub>1</sub> im][NTf <sub>2</sub> ]/TFA (20 mol%); preliminary observations	243
4.2.3.2 3,6-DMPA synthesis; reaction metrics calculations	244
4.2.3.3 The direct synthesis of 3,6-DMPA in [C <sub>4</sub> C <sub>1</sub> im][NTf <sub>2</sub> ]/TFA (20 mol%); reaction temperature	245
4.2.3.4 The direct synthesis of 3,6-DMPA in [C <sub>4</sub> C <sub>1</sub> im][NTf <sub>2</sub> ]/TFA; TFA loading effect (rt)	246
4.2.3.5 The direct synthesis of 3,6-DMPA synthesis in [C <sub>4</sub> C <sub>1</sub> im][NTf <sub>2</sub> ]/H <sub>2</sub> SO <sub>4</sub> (rt)	248
4.2.3.6 Summary and outlook on future work	250
<b>4.3 Experimental</b>	251
4.3.1 Synthesis of 1-butyl-3-methylimidazolium bis(trifluoromethanesulfonyl)imide ([C <sub>4</sub> C <sub>1</sub> im][NTf <sub>2</sub> ])	251

4.3.2 General protocol for the reaction between 2,5-dimethylfuran (2,5-DMF) and maleic anhydride (MA); synthesis of 1,7- dimethyl-4,10-dioxa-tricyclo[5.2.1.0 <sup>2,6</sup> ]dec-8-ene-3,5-dione	252
4.3.3 General protocol for the dehydrative aromatization of 1,7- dimethyl-4,10-dioxa-tricyclo[5.2.1.0 <sup>2,6</sup> ]dec-8-ene-3,5-dione by using binary IL/H <sub>2</sub> SO <sub>4</sub> mixtures	253
4.3.4 General protocol for the direct synthesis of 3,6-DMPA in [C <sub>4</sub> C <sub>1</sub> im][NTf <sub>2</sub> ]/TFA mixtures.	253
<b>4.4 References</b>	254

## List of Figures

<b>Figure 1.1</b>	Global proven oil reserves and reserves-to-production ratio (R/P) in 2015	29
<b>Figure 1.2</b>	Platform chemicals and key derivatives in the petroleum refinery	30
<b>Figure 1.3</b>	The competing impacts for the delivery of a sustainable bio-based economy	32
<b>Figure 1.4</b>	The structure and chemical composition of lignocellulose. Cellulose, a biopolymer of $\beta$ -1,4-linked glucose (G) monomers, is the main component of lignocellulose. Hemicellulose is composed of C5 and C6-carbon sugars such as galactose (Gal), glucose (G), mannose (Man) and xylose (X). Lignin is composed of three major phenolic components: p-coumaryl alcohol, coniferyl alcohol and sinapyl alcohol, polymerising at ratios that vary between different plants. Cellulose, hemicellulose and lignin form microfibrils, organized into macrofibrils, promoting the structural stability in the plant cell wall.	33
<b>Figure 1.5</b>	Simplified representation of biomass pretreatment and the disruption of lignocellulose	35
<b>Figure 1.6</b>	Generic representation of the biomass pretreatment processing	35
<b>Figure 1.7</b>	Saccharides-derived platform chemicals; 5-HMF and furfural as key dehydration products	37
<b>Figure 1.8</b>	Heterocyclic compounds obtained from N- and S-containing polysaccharides	37
<b>Figure 1.9</b>	Lignin-derived chemicals produced by pyrolysis, hydrolysis, hydrogenolysis or gasification	38
<b>Figure 1.10</b>	Common IL cations and anions	39
<b>Figure 1.11</b>	Cellulose dissolution mechanism. Electron donor-acceptor complex formation	42
<b>Figure 1.12</b>	Putative mechanism for the formation of 5-HMF from glucose in $[\text{C}_2\text{C}_1\text{im}]\text{Cl}/\text{CrCl}_2$ via the isomerisation of glucose into fructose, catalysed by $[\text{CrCl}_3]^-$	44
<b>Figure 1.13</b>	5-HMF oxidation products	47
<b>Figure 1.14</b>	5-HMF reduction products	48
<b>Figure 1.15</b>	Illustration of the conversion of fructose into furanics via 5-HMF in an integrated multi-step microreactor	49
<b>Figure 1.16</b>	Brønsted acid-catalysed mechanism of levulinic acid synthesis from 5-HMF	50
<b>Figure 1.17</b>	3-MCO and 2,5-hexanedione production via the reductive ring-opening of 5-HMF	51
<b>Figure 1.18</b>	Polysubstituted benzenes synthesis from bio-based furfural building blocks	54

<b>Figure 1.19</b>	Characteristic examples of heterocyclic fragments in pharmaceutical compounds	54
<b>Figure 1.20</b>	Multi-step synthesis of pyridinols from fructose	55
<b>Figure 1.21</b>	Conversion of 5-HMF into pyrroles (A), thiophenes (B) and pyridazines (C)	55
<b>Figure 1.22</b>	Catalytic condensation of equimolar amounts of 2,5-DMF with <i>m</i> -methylaniline	56
<b>Figure 1.23</b>	Multi-step synthesis of renewable <i>p</i> -xylene; a) Isomerization of glucose to fructose b) fructose dehydration to 5-HMF c) 5-HMF hydrogenolysis to 2,5-DMF d) tandem 2,5-DMF cycloaddition to ethylene and dehydrative aromatisation to <i>p</i> -xylene, followed by e) <i>p</i> -xylene oxidation to terephthalic acid	57
<b>Figure 1.24</b>	Mechanism elucidation of the 1,4-dimethyl-7-oxabicyclo[2.2.1]hept-2-ene dehydrative aromatization, promoted by a Brønsted acidic (HY)-(A) or Lewis acidic (MY)-(B) catalyst	58
<b>Figure 1.25</b>	Aromatics synthesis from furan or 2,5-DMF and ethylene and key by-products; R <sup>1</sup> =R <sup>2</sup> =H or CH <sub>3</sub>	59
<b>Figure 1.26</b>	Reaction mechanisms for the Brønsted acid-catalysed hydrolysis of 2,5-DMF by A) α-protonation B) β-protonation mechanisms based on NBO analysis	60
<b>Figure 1.27</b>	Formation of <i>p</i> -xylene and from the cycloaddition/dehydrative aromatisation of 2,5-DMF and acrolein	61
<b>Figure 1.28</b>	Reaction pathway for the conversion of 2,5-DMF into <i>p</i> -xylene and 2,5-DMBA	61
<b>Figure 1.29</b>	Cycloaddition of phenyl vinyl sulfonate (PVSO <sub>3</sub> ) (a) and phenyl vinyl sulfone (PVSO <sub>2</sub> ) (b) to 2,5-DMF	62
<b>Figure 1.30</b>	Synthesis of bio-derived phthalic anhydride derivatives from furanics and maleic anhydride (MA), followed by dehydrative aromatization and possible side-reactions under acidic conditions	63
<b>Figure 1.31</b>	Alternative catalytic route to renewable aromatics from maleic anhydride (MA) and furanics via a solution or solid-phase conversion of the hydrogenated cycloadduct	64
<b>Figure 2.1</b>	Examples of cations and anions of Lewis acidic, Brønsted acidic and dual acidic ionic liquids	79
<b>Figure 2.2</b>	Series of equilibria upon mixing quaternary halide salts with varying X <sub>MCl<sub>x</sub></sub> (MCl <sub>x</sub> : AlCl <sub>3</sub> , ZnCl <sub>2</sub> ), forming Lewis basic, neutral, acidic or highly acidic chlorozincates(II) and chloroaluminates(III)	81
<b>Figure 2.3</b>	Chemical structure of the 1-butyl-3-methylimidazolium cation, [C <sub>4</sub> C <sub>1</sub> im] <sup>+</sup>	82
<b>Figure 2.4</b>	Schematic diagram for the synthesis of [HC <sub>1</sub> im][HSO <sub>4</sub> ] and [N <sub>2220</sub> ][HSO <sub>4</sub> ] by acid-base neutralisation	84

<b>Figure 2.5</b>	Schematic representation of the preparation of SO <sub>3</sub> H-functionalised BAILs ([HSO <sub>3</sub> ) <sup>n</sup> C <sub>n</sub> C <sub>1</sub> im][HSO <sub>4</sub> ) or bifunctional acidic ionic liquids ([HSO <sub>3</sub> ) <sup>n</sup> C <sub>n</sub> C <sub>1</sub> im]Cl·ZnCl <sub>2</sub> )	85
<b>Figure 2.6</b>	Examples of Hammett acidity dye indicators (I)	86
<b>Figure 2.7</b>	Protonated and unprotonated forms of mesityl oxide	87
<b>Figure 2.8</b>	Electrophilic substitution of thiophene and positional selectivity (α:β)	88
<b>Figure 2.9</b>	Paal-Knorr thiophene synthesis from 1,4-dicarbonyl compounds and a source of sulfur	89
<b>Figure 2.10</b>	Thiol pathways for the Paal-Knorr synthesis of 2,5-dimethylthiophene (2,5-DMF) in the absence of H <sub>2</sub> O (A1), with H <sub>2</sub> O (B1) and in the presence of H <sub>3</sub> O <sup>+</sup> (C1)	90
<b>Figure 2.11</b>	Hemithioketal pathways for the Paal-Knorr synthesis of 2,5-dimethylthiophene (2,5-DMF) in the absence of explicit H <sub>2</sub> O (A2), with explicit H <sub>2</sub> O (B2) and under proton catalysis (C2)	90
<b>Figure 2.12</b>	Example of Fiesselmann thiophene synthesis from thioglycolic acid methyl ester and acetylenedicarboxylic acid	91
<b>Figure 2.13</b>	Example of the base-catalysed Gewald 2-aminothiophene synthesis from a β-ketonitrile and a ketone	92
<b>Figure 2.14</b>	Example of the base-catalysed Hinsberg thiophene synthesis from a 1,2-dicarbonyl and thiodiacetates	93
<b>Figure 2.15</b>	Putative mechanism of the furan recyclization into thiophene on the surface of Al <sub>2</sub> O <sub>3</sub> via the dissociative adsorption of H <sub>2</sub> S and the chemisorption of furan onto the catalyst surface	94
<b>Figure 2.16</b>	Brønsted acid-catalysed recyclization of 2,5-dimethylfuran to 2,5-dimethylthiophene under anhydrous conditions (A) or with water as a competing nucleophile (B)	95
<b>Figure 2.17</b>	Reaction mechanisms for the Brønsted acid-catalysed hydrolysis of 2,5-DMF by A) α-protonation B) β-protonation mechanisms based on NBO analysis	96
<b>Figure 2.18</b>	Lewis acid-catalysed Paal-Knorr thiophene synthesis in [C <sub>4</sub> C <sub>1</sub> im][BF <sub>4</sub> ]/Bi(OTf) <sub>3</sub>	97
<b>Figure 2.19</b>	Base-catalysed Gewald synthesis of 4,5-dialkyl-2-aminothiophenes in [C <sub>4</sub> C <sub>1</sub> im][OH]	97
<b>Figure 2.20</b>	Chemical structures of the studied [C <sub>4</sub> C <sub>1</sub> im] <sup>+</sup> -based ionic liquids, incorporating chloride (1), bis(trifluoromethanesulfonyl)imide (2), hydrogen sulfate (6) and metal chloride (3a-3e, 4, 5) anions. [Zn <sub>x</sub> Cl <sub>y</sub> ] <sup>-</sup> , [In <sub>x</sub> Cl <sub>y</sub> ] <sup>-</sup> and [Fe <sub>x</sub> Cl <sub>y</sub> ] <sup>-</sup> represent the complex anions formed at different compositions (0.10 ≤ X <sub>MCl<sub>x</sub></sub> ≤ 0.75)	98
<b>Figure 2.21</b>	Reaction scheme for the synthesis of [C <sub>4</sub> C <sub>1</sub> im]Cl	99
<b>Figure 2.22</b>	Synthesis of [C <sub>4</sub> C <sub>1</sub> im]Cl·ZnCl <sub>2</sub> (0.10 ≤ X <sub>ZnCl<sub>2</sub></sub> ≤ 0.75) from [C <sub>4</sub> C <sub>1</sub> im]Cl with a varying anionic composition [Zn <sub>x</sub> Cl <sub>y</sub> ] <sup>-</sup>	99

<b>Figure 2.23</b>	(a) Temperature-ramped (TG) (a) and derivative (DTG) (b) curves for $[C_4C_{1im}]^+$ -based ILs and a series of anions: chloride (1), bis(trifluoromethanesulfonyl)imide (2) and metal chloride-based anions (3d, 4 and 5, $X_{MClx} = 0.67$ ). All thermographs were obtained with a heating rate of $10\text{ K min}^{-1}$	103
<b>Figure 2.24</b>	a) TG (a) and DTG (b) curves of $[C_4C_{1im}]Cl \cdot ZnCl_2$ with $X_{ZnCl_2} = 0.10, 0.25, 0.50, 0.67$ and $0.75$ (3a-e). Thermographs were obtained with a heating rate of $10\text{ }^\circ\text{C min}^{-1}$	105
<b>Figure 2.25</b>	Schematic representation of the $^1H$ NMR spectra of $[C_4C_{1im}]Cl \cdot ZnCl_2$ and $[C_4C_{1im}]Cl \cdot InCl_3$ at $X_{MClx} = 0.67$ , recorded neat at $80\text{ }^\circ\text{C}$ with a DMSO capillary (500 MHz). The aromatic protons at the $C^2$ and $C^4/C^5$ positions on the imidazolium ring are labelled for each compound	110
<b>Figure 2.26</b>	Observed $^1H$ chemical shift $\delta$ (ppm) for $C_2 - C_{10}$ protons as a function of composition ( $X_{ZnCl_2}$ ) for $[C_4C_{1im}]Cl \cdot ZnCl_2$ ( $0.10 < X_{ZnCl_2} < 0.75$ ). $^1H$ NMR spectra were recorded neat at $80\text{ }^\circ\text{C}$ with a DMSO capillary (500 MHz).	110
<b>Figure 2.27</b>	Thiophene analogues of bio-based furans: 5-(hydroxymethyl)furfural (5-HMF) and 2,5-dimethylfuran (2,5-DMF)	115
<b>Figure 2.28</b>	Schematic representation of the recyclization of 2,5-DMF into 2,5-DMT in $[C_4C_{1im}]Cl \cdot ZnCl_2$ ( $X_{ZnCl_2} = 0.67$ )	117
<b>Figure 2.29</b>	$^1H$ NMR spectrum of the Kugelrohr distillation product [2,5-DMF + $H_2S$ in $[C_4C_{1im}]Cl \cdot ZnCl_2$ ( $X_{ZnCl_2} = 0.67$ )	118
<b>Figure 2.30</b>	LEIS spectra ( $^4He^+$ , $E_0 = 3\text{ keV}$ ) for a series of Lewis acidic $[C_4C_{1im}]Cl \cdot ZnCl_2$ compositions ( $0.50 \leq X_{ZnCl_2} \leq 0.75$ )	119
<b>Figure 2.31</b>	IR spectra ( $1350 - 1600\text{ cm}^{-1}$ ) of pyridine/IL mixtures ( $[C_4C_{1im}]Cl \cdot ZnCl_2$ ( $0.25 \leq X_{ZnCl_2} \leq 0.67$ ))	120
<b>Figure 2.32</b>	Lewis acid-assisted Brønsted acid-catalysed 2,5-DMT synthesis in chlorozincates(II), accounting for the contribution of the Lewis acidic anions on the activation of the 2,5-DMF furan ring and/or 2,5-hexadione.	123
<b>Figure 2.33</b>	Small-scale experimental apparatus; bio-derived thiophene synthesis	124
<b>Figure 2.34</b>	Chemical structure of $[C_4C_{1im}]Cl$	126
<b>Figure 2.35</b>	Chemical structure of $[C_4C_{1im}]Cl \cdot ZnCl_2$ ; $[Zn_xCl_y]^{2-}$ indicates the formation of polyanions	127
<b>Figure 2.36</b>	Chemical structure of $[C_4C_{1im}]Cl \cdot InCl_3$ , $X_{InCl_3} = 0.67$ ; $[In_xCl_y]^{2-}$ indicates the formation of complex polyanions	129
<b>Figure 2.37</b>	Chemical structure of $[C_4C_{1im}]Cl \cdot FeCl_3$ ; $[Fe_xCl_y]^{2-}$ indicates the formation of complex polyanions	130
<b>Figure 2.38</b>	Chemical structure of $[C_4C_{1im}][HSO_4]$	131



<b>Figure 2.39</b>	Chemical structure and ring numbering of 2,5-DMF (I), 2,5-DMT (II), 5-HMF (III), 5-(hydroxymethyl)-2-thiophenecarboxaldehyde (IV) and 2,5-hexanedione (V): a key intermediate	132
<b>Figure 2.40</b>	Kugelrohr distillation set-up; products separation from the ionic liquid layer	135
<b>Figure 2.41</b>	Small-scale 2,5-DMT synthesis in $[C_4C_{1im}]Cl \cdot ZnCl_2$ , $X_{ZnCl_2} = 0.67$ . Crude reaction mixture; $^1H$ NMR spectrum	136
<b>Figure 2.42</b>	Small-scale 2,5-DMT synthesis in $[C_4C_{1im}]Cl \cdot ZnCl_2$ , $X_{ZnCl_2} = 0.67$ . Kugelrohr distillate (Top Layer); $^1H$ NMR spectrum	137
<b>Figure 2.43</b>	Small-scale 2,5-DMT synthesis in $[C_4C_{1im}]Cl \cdot ZnCl_2$ , $X_{ZnCl_2} = 0.67$ . Kugelrohr distillate (Bottom Layer); $^1H$ NMR spectrum	138
<b>Figure 2.44</b>	Reaction of 2,5-DMF + $H_2S$ in $[C_4C_{1im}][HSO_4]$ ; $^1H$ NMR spectrum of the neat IL and the crude reaction mixture	141
<b>Figure 2.45</b>	Mass spectra of $[C_4C_{1im}]Cl \cdot ZnCl_2$ ( $X_{ZnCl_2} = 0.67$ ) in the positive ( $FB^+$ ) and negative ( $FB^-$ ) mode	149
<b>Figure 2.46</b>	Observed $^{13}C$ chemical shift $\delta$ (ppm) for A) $C^2 - C^5$ , $C^8 - C^{10}$ , B) $C^6$ and C) $C^7$ carbons as a function of $X_{ZnCl_2}$ in $[C_4C_{1im}]Cl \cdot ZnCl_2$ ( $0.10 < X_{ZnCl_2} < 0.75$ ). $^{13}C$ NMR spectra were recorded neat at 80 °C with a DMSO capillary (500 MHz)	150
<b>Figure 2.47</b>	Isothermal TGA scans a) $[C_4C_{1im}][NTf_2]$ (200 – 300 °C), b) $[C_4C_{1im}]Cl$ (100 – 200 °C), c) $[C_4C_{1im}]Cl \cdot ZnCl_2$ ; $X_{ZnCl_2} = 0.67$ (200 – 300 °C)	152
<b>Figure 2.48</b>	Determination of the Arrhenius parameters relating to the thermal decomposition of ionic liquids (a) $[C_4C_{1im}][NTf_2]$ , $E_a = 111 \text{ kJ mol}^{-1}$ , $A = 8.3 \times 10^8$ ; (b) $[C_4C_{1im}]Cl$ , $E_a = 138 \text{ kJ mol}^{-1}$ , $A = 3.1 \times 10^{14}$ and (c) $[C_4C_{1im}]Cl \cdot ZnCl_2$ ( $X_{ZnCl_2} = 0.67$ ), $E_a = 134 \text{ kJ mol}^{-1}$ , $A = 2.6 \times 10^{10}$	153
<b>Figure 2.49</b>	Determination of $T_{1\%/10h}$ from the exponential plot of $t_{0.99}$ , the time taken for 1 % mass loss to occur, as a function of temperature. $T_{1\%/10h}$ was determined as 143 °C for $[C_4C_{1im}]Cl$ , 221 °C for $[C_4C_{1im}][NTf_2]$ and 270 °C for $[C_4C_{1im}]Cl \cdot ZnCl_2$ ( $X_{ZnCl_2} = 0.67$ )	154
<b>Figure 3.1</b>	Schematic representation of the incorporation of ionic liquids into the porous structure of a solid support by: (A) covalent grafting of the ionic liquid on the pore wall and (B) physical confinement of multilayers of the IL into the nanopores	155
<b>Figure 3.2</b>	Immobilisation of a chloroaluminate(III) ionic liquid via (i) the anion or (ii) the cation (grafting)	156
<b>Figure 3.3</b>	Illustration of the production of SILP materials production by spray coating in a fluidised-bed reactor	157
<b>Figure 3.4</b>	The transition from the lab-scale preparation of chlorocuprate(II) SILPs through to a pilot-scale production, using 100 $cm^3$ of SILPs, and finally the large-scale mercury removal where 20 $m^3$ of SILP was applied	159

<b>Figure 3.5</b>	Continuous flow isopropylation of toluene and cumene catalysed by $\{C_2C_{1im}\}Cl \cdot AlCl_3/SiO_2$ ( $\alpha_{IL} = 0.1 - 0.3$ ).	160
<b>Figure 3.6</b>	Continuous flow, gas-phase hydroformylation catalysed by $[C_2C_{1im}][NTf_2]--Rh[(CO)_2(acac)]/SiO_2$ ( $\epsilon_{IL} = 0.15$ )	160
<b>Figure 3.7</b>	Continuous gas-phase hydroaminomethylation of ethylene, catalysed by $[C_1C_1C_{1im}][NTf_2]-[RhH(CO)_2(L)_2]/SiO_2$ ( $\alpha_{IL} = 0.1$ ). The hydroformylation of ethylene is followed by a reaction with diethylamine to form N,N-diethylpropan-1-amine (DEPA) through an enamine intermediate	161
<b>Figure 3.8</b>	Schematic representation of the SILP/Ni-catalysed ( $\alpha_{IL} = 0.3 - 0.9$ ) ethylene to propylene reaction via the formation of 1-butene, the subsequent isomerization of 1-butene and the metathesis of 2-butene with ethylene	161
<b>Figure 3.9</b>	Experimental set-up for the SILPs-catalysed dimerization of ethene in a fluidised bed or a fixed bed reactor. The flow rates of purified ethene/Ar were adjusted by mass flow controllers and the gas stream was analysed online via GC	162
<b>Figure 3.10</b>	Schematic representation of the SILP catalyst particle containing $[C_4C_{1im}Cl \cdot ZnCl_2]$ , $X_{ZnCl_2} = 0.67$	163
<b>Figure 3.11</b>	Adsorption/desorption isotherms of a) $SiO_2$ -60 Å-based and b) $SiO_2$ -150 Å-based SILP catalysts, both impregnated with increasing amounts of $[C_4C_{1im}Cl \cdot ZnCl_2]$ ( $X_{ZnCl_2} = 0.67$ ). ( $\epsilon_{IL} = 10 - 100\%$ )	167
<b>Figure 3.12</b>	Characteristic BET surface area plot; $SiO_2$ -60 Å-based SILPs with variable loadings of $[C_4C_{1im}Cl \cdot ZnCl_2]$ ( $X_{ZnCl_2} = 0.67$ ) ( $\epsilon_{IL} = 10 - 100\%$ )	168
<b>Figure 3.13</b>	Pore diameter distribution for 1.7 - 50 nm (mesoporous region) as determined by BJH $N_2$ adsorption analysis for a) $SiO_2$ 60 Å-based SILP catalysts with varying loadings of $[C_4C_{1im}Cl \cdot ZnCl_2]$ ( $X_{ZnCl_2} = 0.67$ ) - ( $\epsilon_{IL} = 10 - 100\%$ ) and b) $SiO_2$ 150 Å-based SILP catalysts ( $\epsilon_{IL} = 10 - 60\%$ )	171
<b>Figure 3.14</b>	Schematic representation of Magic Angle Spinning (MAS). The spinning axis of the sample is at an angle of $54.74^\circ$ with respect to the static magnetic field $B_0$	172
<b>Figure 3.15</b>	Schematic representation of the pore filling mode for ionic liquids confined in MCM-41 or amorphous silica (MB): A) $[C_6C_{1im}][NTf_2]$ , B) $[C_6C_{1im}][OTf]$ and C) $[C_6C_{1im}][OAc]$	173
<b>Figure 3.16</b>	Schematic representation of the pore filling mode for ionic liquids confined in amorphous silica (MB).	174
<b>Figure 3.17</b>	Static $^1H$ NMR spectra of $SiO_2$ -60 Å-based SILPs as a function of $\epsilon_{IL}$ ; $[C_4C_{1im}Cl \cdot ZnCl_2]$ ( $X_2 = 0.67$ ) a) Parent support ( $SiO_2$ -60 Å), b) $\epsilon_{IL} = 10\%$ , c) $\epsilon_{IL} = 30\%$ , d) $\epsilon_{IL} = 60\%$ and d) $\epsilon_{IL} = 100\%$	176
<b>Figure 3.18</b>	Composition dependence of the full width at half maximum (FWHM, Hz) of the static $^1H$ NMR spectra of $SiO_2$ -60 Å- and $SiO_2$ -150 Å-based SILPs as a function of $\epsilon_{IL}$ ( $[C_4C_{1im}Cl \cdot ZnCl_2]$ ( $X_{ZnCl_2} = 0.67$ )). The fitted curves serve as a visual guide.	176

<b>Figure 3.19</b>	$^1\text{H}$ MAS NMR spectra of $\text{SiO}_2$ -60 Å-based SILPs with variable loadings of $[\text{C}_4\text{C}_{1\text{im}}]\text{Cl}\cdot\text{ZnCl}_2$ ( $X_{\text{ZnCl}_2} = 0.67$ ). $\epsilon_{\text{IL}}$ : A1: 0 %, B1: 10 %, C1: 30 %, D1: 60 % and E1: 100 %	177
<b>Figure 3.20</b>	Schematic representation of the Inversion recovery pulse sequence	179
<b>Figure 3.21</b>	Estimated $^1\text{H}$ $T_1$ (s) relaxation times across the imidazolium cation ( $\text{C}^2 - \text{C}^{10}$ ) for the $\text{SiO}_2$ -60 Å-based SILP catalysts as a function of composition/ $\epsilon_{\text{IL}}$ ( $[\text{C}_4\text{C}_{1\text{im}}]\text{Cl}\cdot\text{ZnCl}_2$ ( $X_{\text{ZnCl}_2} = 0.67$ ))	180
<b>Figure 3.22</b>	Comparison of the estimated $^1\text{H}$ $T_1$ relaxation times across the imidazolium cation for the Lewis acidic, $\text{SiO}_2$ -60 Å-based SILPs as a function of composition ( $[\text{C}_4\text{C}_{1\text{im}}]\text{Cl}\cdot\text{ZnCl}_2$ ( $X_{\text{ZnCl}_2} = 0.67$ )).	180
<b>Figure 3.23</b>	a) Temperature-ramped (TG) and b) derivative (DTG) curves for $\text{SiO}_2$ -60 Å-based SILPs with variable loadings of $[\text{C}_4\text{C}_{1\text{im}}]\text{Cl}\cdot\text{ZnCl}_2$ ( $X_{\text{ZnCl}_2} = 0.67$ ) - ( $\epsilon_{\text{IL}} = 10\% - 60\%$ )	184
<b>Figure 3.24</b>	Fluidisation behaviour as a function of gas velocity ( $u$ )	185
<b>Figure 3.25</b>	a) Schematic diagram of the spouted bed reactor configuration and b) cold modelling fluidisation experiments with 20 g silica gel inorganic support ( $\text{SiO}_2$ -60 Å) at ambient temperature ( $(\text{N}_2, \text{rt}, V = 0.5 \text{ L min}^{-1})$ ).	186
<b>Figure 3.26</b>	Temperature gradient across the bed as a function of $V_{\text{N}_2}$ ( $\text{L min}^{-1}$ ) – ( $\text{SiO}_2$ 60 Å, 250 °C, $h_{\text{bed}} = 10 \text{ cm}$ ). The fitted curves serve as a visual guide.	187
<b>Figure 3.27</b>	Temperature gradient across the bed as a function of $V_{\text{N}_2}$ ( $\text{L min}^{-1}$ ) – (SILP30 (60A), 250 °C, $h_{\text{bed}} = 10 \text{ cm}$ ). The fitted curves serve as a visual guide.	188
<b>Figure 3.28</b>	Temperature gradient across the bed as a function of $V_{\text{N}_2}$ ( $\text{L min}^{-1}$ ) – (SILP60 (60A), 250 °C, $h_{\text{bed}} = 10 \text{ cm}$ ). The fitted curves serve as a visual guide.	189
<b>Figure 3.29</b>	Process flow diagram for the gas-phase synthesis of bio-derived thiophenes in a spouted-bed reactor	192
<b>Figure 3.30</b>	Schematic diagram of the main reactor body	193
<b>Figure 3.31</b>	Reactor internals; quartz-liner set-up	194
<b>Figure 3.32</b>	Characteristic example of the temperature gradient across the SILP-based bed ( $h_{\text{bed}} = 10 \text{ cm}$ ); R01	201
<b>Figure 3.33</b>	Online Mass spectrometry data (R01); evolution of the peak intensity corresponding to 2,5-DMF ( $m/z$ : 96)	201
<b>Figure 3.34</b>	Online Mass spectrometry data (R02); evolution of the peak intensity corresponding to 2,5-DMF ( $m/z$ : 96) and $\text{H}_2\text{S}$ ( $m/z$ : 34)	202
<b>Figure 3.35</b>	Schematic representation of the SILP synthesis protocol and the pore filling mode for ILs confined in silica gel.	209

<b>Figure 3.36</b>	Design of the first prototype of a low-temperature vapour trap	211
<b>Figure 3.37</b>	Modifications of the liquid sampling system (LSS) - preliminary testing, by-passing the reactor [(coolant mixtures: (A)& (B): = ethylene glycol/water, (C): dry ice/acetone	212
<b>Figure 3.38</b>	Final design of the two-stage liquid sampling system (A), and the detachable Swagelok sample cylinder (B).	213
<b>Figure 3.39</b>	Experimental set-up for the gas-phase synthesis of bio-derived thiophenes in a spouted-bed reactor	214
<b>Figure 3.40</b>	Chemical structure and ring numbering of 2,5-DMF, 2,5-DMT and 2,5-hexanedione: a key reaction intermediate	217
<b>Figure 3.41</b>	Physisorption isotherms and hysteresis loops; IUPAC classification; Type I: characteristic for microporous materials; Type II and IV: indicative of either non-porous materials or materials with very large pores; Types III and V: characteristic of conditions where the adsorptive molecules have a greater affinity to one another than they do for the solid; Type VI: indicative of a non-porous material and a rarely uniform surface	221
<b>Figure 3.42</b>	Pore area distribution for 1.7 - 50 nm (mesoporous region) as determined by BJH N <sub>2</sub> adsorption analysis for a) SiO <sub>2</sub> 60 Å-based SILPs with varying loadings of [C <sub>4</sub> C <sub>1</sub> im]Cl·ZnCl <sub>2</sub> (X <sub>ZnCl<sub>2</sub></sub> = 0.67) - (ε <sub>IL</sub> = 10 - 100 %) and b) SiO <sub>2</sub> 150 Å-based SILPs with varying loadings of [C <sub>4</sub> C <sub>1</sub> im]Cl·ZnCl <sub>2</sub> (X <sub>ZnCl<sub>2</sub></sub> = 0.67) - (ε <sub>IL</sub> = 10 - 60 %).	222
<b>Figure 3.43</b>	Effect of the ionic loading (n / mmol g <sup>-1</sup> ) on the surface characteristics of [C <sub>4</sub> C <sub>1</sub> im]Cl·ZnCl <sub>2</sub> (X <sub>ZnCl<sub>2</sub></sub> = 0.67) - based SILPs: i) surface area (A <sub>BET</sub> ; m <sup>2</sup> g <sup>-1</sup> ), single point adsorption total pore volume (V <sub>pore</sub> ; cm <sup>3</sup> g <sup>-1</sup> ) and average pore size (D <sub>p</sub> , nm).	223
<b>Figure 3.44</b>	Static <sup>1</sup> H NMR spectra of SiO <sub>2</sub> -150 Å-based SILPs as a function of ε <sub>IL</sub> ; [C <sub>4</sub> C <sub>1</sub> im]Cl·ZnCl <sub>2</sub> (X <sub>ZnCl<sub>2</sub></sub> = 0.67) a) Parent support (SiO <sub>2</sub> -150 Å), b) ε <sub>IL</sub> = 10 %, c) ε <sub>IL</sub> = 30 % and d) ε <sub>IL</sub> = 60 %	224
<b>Figure 3.45</b>	<sup>1</sup> H MAS NMR spectra of SiO <sub>2</sub> -150 Å-based SILPs with variable loadings of [C <sub>4</sub> C <sub>1</sub> im]Cl·ZnCl <sub>2</sub> (X <sub>ZnCl<sub>2</sub></sub> = 0.67). Ionic liquid loading (ε <sub>IL</sub> ): A2: 0 %, B2: 10 %, C2: 30 % and D2: 60 %	224
<b>Figure 3.46</b>	Estimated <sup>1</sup> H T <sub>1</sub> relaxation times across the imidazolium cation for SiO <sub>2</sub> -150 Å-based SILP catalysts as a function of ε <sub>IL</sub> (10 % - 60 %) - (IL: [C <sub>4</sub> C <sub>1</sub> im]Cl·ZnCl <sub>2</sub> (X <sub>ZnCl<sub>2</sub></sub> = 0.67)).	225
<b>Figure 3.47</b>	a) Temperature-ramped (TG) and b) derivative (DTG) curves for SiO <sub>2</sub> -150 Å-based SILPs with variable loadings of [C <sub>4</sub> C <sub>1</sub> im]Cl·ZnCl <sub>2</sub> (X <sub>ZnCl<sub>2</sub></sub> = 0.67) - (ε <sub>IL</sub> = 10 % - 60 %)	226
<b>Figure 3.48</b>	a) Temperature-ramped (TG) and b) derivative (DTG) curves of the bulk [C <sub>4</sub> C <sub>1</sub> im]Cl·ZnCl <sub>2</sub> (X <sub>ZnCl<sub>2</sub></sub> = 0.67). [T <sub>onset</sub> = 431 °C, T <sub>peak</sub> = 476 °C]	227
<b>Figure 3.49</b>	NIST Chemistry Webbook data for N <sub>2</sub> as a function of T or P: a) density (Kg/m <sup>3</sup> ) and b) viscosity (Pa s)	228
<b>Figure 3.50</b>	GC(EI) spectrum - 2,5-dimethylfuran (2,5-DMF) standard	229
<b>Figure 3.51</b>	GC(EI) spectrum - 2,5-dimethylthiophene (2,5-DMT) standard	229

<b>Figure 3.52</b>	GC(EI) spectrum – 2,5-hexanedione (2,5-hxd) standard	230
<b>Figure 3.53</b>	GC(EI) (R01); [200 °C, SILP30(60A), H <sub>2</sub> S (6.7E-06 mol s <sup>-1</sup> )/2,5-DMF (2.6E-05 mol s <sup>-1</sup> )]	231
<b>Figure 3.54</b>	GC(EI) (R02); [200 °C, SILP30(60A), H <sub>2</sub> S (2.1E-05 mol s <sup>-1</sup> )/2,5-DMF (2.1E-05 mol s <sup>-1</sup> )]	231
<b>Figure 3.55</b>	GC(EI) (R04/Soxhlet);[200 °C, SILP60(60A), 1:1 H <sub>2</sub> S)/2,5-DMF	232
<b>Figure 3.56</b>	GC(FID) calibration curves: i) 2,5-DMF (1.82 min), ii) 2,5-DMT (3.82 min) and iii) 2,5-hxd (6.20 min)	233
<b>Figure 4.1</b>	Synthesis of bio-derived 3,6-dimethylphthalic anhydride (3,6-DMPA) from 2,5-DMF and maleic anhydride (MA), followed by dehydrative aromatization	234
<b>Figure 4.2</b>	MA + 2,5-DMF cycloadduct dehydration mechanisms: (a) uncatalyzed; (b) Lewis acid catalysed and c) Brønsted acid catalysed (gas phase)	235
<b>Figure 4.3</b>	<sup>1</sup> H NMR of the crude reaction mixture; ([C <sub>4</sub> C <sub>1</sub> im][NTf <sub>2</sub> ]/20 mol% TFA, RT, 30 min).	243
<b>Figure 4.4</b>	<sup>1</sup> H NMR spectrum of the crude reaction mixture; ([C <sub>4</sub> C <sub>1</sub> im][NTf <sub>2</sub> ]/20 mol% TFA, RT, 24 h).	243
<b>Figure 4.5</b>	The effect of temperature (rt, 0 °C, -8 °C) on 3,6-DMPA synthesis from 2,5-DMF and MA ([C <sub>4</sub> C <sub>1</sub> im][NTf <sub>2</sub> ]/TFA (20 mol%))	245
<b>Figure 4.6</b>	The effect of TFA loading (mol%) on 3,6-DMPA synthesis from 2,5-DMF and MA ([C <sub>4</sub> C <sub>1</sub> im][NTf <sub>2</sub> ]/TFA (room temperature)	247
<b>Figure 4.7</b>	The effect of acidity on 3,6-DMPA synthesis in [C <sub>4</sub> C <sub>1</sub> im][NTf <sub>2</sub> ]/20 mol% TFA (left), H <sub>2</sub> SO <sub>4</sub> (right), RT, 24 h.	240
<b>Figure 4.8</b>	Direct 3,6-DMPA synthesis from 2,5-DMF and MA in [C <sub>4</sub> C <sub>1</sub> im][NTf <sub>2</sub> ]/H <sub>2</sub> SO <sub>4</sub> (H <sub>2</sub> SO <sub>4</sub> : 30 mol% & 40 mol%) in comparison with [C <sub>4</sub> C <sub>1</sub> im][NTf <sub>2</sub> ]/TFA (TFA: 30 mol% & 40 mol%)	249
<b>Figure 4.9</b>	Chemical structure of 1-butyl-3-methylimidazolium bis(trifluoromethanesulfonyl)imide	251
<b>Figure 4.10</b>	Chemical structure of 1,7- dimethyl-4,10-dioxo-tricyclo[5.2.1.0 <sup>2,6</sup> ]dec-8-ene-3,5-dione	252
<b>Figure 4.11</b>	Chemical structure of 3,6-dimethylphthalic anhydride	253

## List of Tables

<b>Table 1.1</b>	Projected bio-based chemicals global market penetration	30
<b>Table 1.2</b>	Global annual production of key fossil-derived bulk organic chemicals (2011)	31
<b>Table 1.3</b>	Composition (% wt) of different lignocellulosic biomass feedstocks	34
<b>Table 1.4</b>	Comparison of ionic liquids (ILs) with organic solvents	40
<b>Table 1.5</b>	Diels-Alder dehydration of oxygenated furans with ethylene	53
<b>Table 2.1</b>	Examples of Hammett acidity functions of BAILs and binary IL/acids mixtures determined by UV-vis spectroscopy	87
<b>Table 2.2</b>	Paal-Knorr thiophene synthesis: reaction of 1,2-di-bromobenzoyl ethane with H <sub>2</sub> S/HCl	91
<b>Table 2.3</b>	Comparison of T <sub>onset</sub> and T <sub>peak</sub> for Lewis acidic chlorometallates, [C <sub>4</sub> C <sub>1</sub> im]Cl and [C <sub>4</sub> C <sub>1</sub> im][NTf <sub>2</sub> ]	102
<b>Table 2.4</b>	Comparison of T <sub>onset</sub> and T <sub>peak</sub> for Lewis acidic chlorozincate(II) compositions	104
<b>Table 2.5</b>	Linear fit coefficients for <sup>1</sup> H NMR δ(ppm) as a function of X <sub>ZnCl<sub>2</sub></sub> ; [C <sub>4</sub> C <sub>1</sub> im]Cl·ZnCl <sub>2</sub> (0.10 < X <sub>ZnCl<sub>2</sub></sub> < 0.75)	111
<b>Table 2.6</b>	Thermal decomposition kinetic parameters of [C <sub>4</sub> C <sub>1</sub> im]Cl·ZnCl <sub>2</sub> (X <sub>ZnCl<sub>2</sub></sub> = 0.67), [C <sub>4</sub> C <sub>1</sub> im]Cl, and [C <sub>4</sub> C <sub>1</sub> im][NTf <sub>2</sub> ].	114
<b>Table 2.7</b>	Composition of [C <sub>4</sub> C <sub>1</sub> im]Cl·ZnCl <sub>2</sub> ionic liquids	127
<b>Table 2.8</b>	Chemical shift changes in [C <sub>4</sub> C <sub>1</sub> im][HSO <sub>4</sub> ] upon reaction between 2,5-DMF and H <sub>2</sub> S.	141
<b>Table 2.9</b>	Linear fit coefficients for <sup>13</sup> C NMR δ(ppm) as a function of X <sub>ZnCl<sub>2</sub></sub> ; [C <sub>4</sub> C <sub>1</sub> im]Cl·ZnCl <sub>2</sub> (0.10 < X <sub>ZnCl<sub>2</sub></sub> < 0.75)	151
<b>Table 2.10</b>	Fitting parameters of the Arrhenius plots (ln(dw/dt) = f(1/T))	153
<b>Table 2.11</b>	Fitting parameters for exponential decay (1% degradation)	154
<b>Table 3.1</b>	Surface characteristics of uncoated SiO <sub>2</sub> -60 Å, SiO <sub>2</sub> -150 Å and silica gel-based SILPs with varying loadings (ε <sub>IL</sub> = 10 – 100 %) of [C <sub>4</sub> C <sub>1</sub> im]Cl·ZnCl <sub>2</sub> (X <sub>ZnCl<sub>2</sub></sub> = 0.67); BET theory calculations	169
<b>Table 3.2</b>	Average pore diameter calculations for uncoated SiO <sub>2</sub> -60 Å, SiO <sub>2</sub> -150 Å and silica gel-based SILPs with varying loadings (ε <sub>IL</sub> = 10 – 100 %) of [C <sub>4</sub> C <sub>1</sub> im]Cl·ZnCl <sub>2</sub> (X <sub>ZnCl<sub>2</sub></sub> = 0.67); BET and BJH theories.	170
<b>Table 3.3</b>	Comparison of the T <sub>onset</sub> and T <sub>peak</sub> values for SiO <sub>2</sub> -60 Å-based chlorozincate(II) SILPs	183
<b>Table 3.4</b>	Fluidisation testing of SiO <sub>2</sub> 60 Å (250 °C, h <sub>bed</sub> = 10 cm); P (mbar) and T (°C) as a function of V <sub>N<sub>2</sub></sub> (L min <sup>-1</sup> )	187

<b>Table 3.5</b>	Fluidisation testing of SILP10(60A) ( $[\text{C}_4\text{C}_{1\text{im}}]\text{Cl}\cdot\text{ZnCl}_2$ , $X_{\text{ZnCl}_2} = 0.67$ , $\epsilon_{\text{IL}} = 30\%$ ) - (250 °C, $h_{\text{bed}} = 10\text{ cm}$ ); P (mbar) and T (°C) as a function of $V_{\text{N}_2}$ ( $\text{L min}^{-1}$ )	188
<b>Table 3.6</b>	Fluidisation testing of SILP60(60A) ( $[\text{C}_4\text{C}_{1\text{im}}]\text{Cl}\cdot\text{ZnCl}_2$ , $X_{\text{ZnCl}_2} = 0.67$ , $\epsilon_{\text{IL}} = 60\%$ ) - (250 °C, $h_{\text{bed}} = 10\text{ cm}$ ); P (mbar) and T (°C) as a function of $V_{\text{N}_2}$ ( $\text{L min}^{-1}$ ).	189
<b>Table 3.7</b>	Theoretical $u_{\text{mf}}$ ( $\text{cm s}^{-1}$ ) ( $P_{\text{abs}} = 2\text{ bar}$ , $T = 120 - 250\text{ °C}$ ) of $[\text{C}_4\text{C}_{1\text{im}}]\text{Cl}\cdot\text{ZnCl}_2$ ( $X_{\text{ZnCl}_2} = 0.67$ )/ $\text{SiO}_2$ 60 Å - based SILPs	191
<b>Table 3.8</b>	Summary of the gas-phase experiments examining the synthesis of 2,5-DMT in the spouted bed reactor	200
<b>Table 3.9</b>	Summary of the composition of the isolated product mixtures; gas-phase synthesis of bio-derived 2,5-DMT	204
<b>Table 3.10</b>	Composition of the synthesized Lewis acidic SILPs ( $[\text{C}_4\text{C}_{1\text{im}}]\text{Cl}\cdot\text{ZnCl}_2$ ( $X_{\text{ZnCl}_2} = 0.67$ )).	210
<b>Table 3.11</b>	Inversion recovery pulse sequence – $^1\text{H}$ $T_1$ estimation; RSS for the regression with 1 or 2 components for the $\text{SiO}_2$ -150 Å-based SILP catalyst at $\epsilon_{\text{IL}} = 10\%$ and the $\text{SiO}_2$ -60 Å-based SILPs at $\epsilon_{\text{IL}} = 10\%$ or $30\%$ ( $[\text{C}_4\text{C}_{1\text{im}}]\text{Cl}\cdot\text{ZnCl}_2$ ( $X_{\text{ZnCl}_2} = 0.67$ )).	225
<b>Table 3.12</b>	Comparison of the $T_{\text{onset}}$ and $T_{\text{peak}}$ values for $\text{SiO}_2$ -150 Å-based chlorozincate(II) SILPs.	226
<b>Table 4.1</b>	Literature Kamlet-Taft parameters ( $\alpha$ , $\beta$ and $\pi^*$ ) for sample organic solvents and imidazolium-based ionic liquids	238
<b>Table 4.2</b>	Diels-Alder cycloaddition of 2,5-DMF and MA, using ionic liquids or organic solvents	239
<b>Table 4.3</b>	Dehydrative aromatisation of ,7- dimethyl-4,10-dioxo-tricyclo[5.2.1.0 <sup>2,6</sup> ]dec-8-ene-3,5-dione using binary IL/ $\text{H}_2\text{SO}_4$ systems combinations of ionic liquids and $\text{H}_2\text{SO}_4$ .(0 °C)	241
<b>Table 4.4</b>	Summary of the key reactions towards the direct 3,6-DMPA synthesis in $[\text{C}_4\text{C}_{1\text{im}}][\text{NTf}_2]/\text{TFA}$ , $[\text{C}_4\text{C}_{1\text{im}}][\text{NTf}_2]/\text{H}_2\text{SO}_4$ and $[\text{C}_4\text{C}_{1\text{im}}\text{-SO}_3\text{H}][\text{NTf}_2]$ (24 h, MA: 2,5-DMF: 1:1)	242
<b>Table 4.5</b>	The effect of TFA loading (mol%) on 3,6-DMPA synthesis from 2,5-DMF and MA ( $[\text{C}_4\text{C}_{1\text{im}}][\text{NTf}_2]/\text{TFA}$ (0 °C, 24 h)	248

## Abbreviations

AFM	atomic force microscopy
AILs	acidic ionic liquids
AN	Gutmann Acceptor Number
BAILs	Brønsted acidic ionic liquids
BE	Binding energy
BET	Brunauer, Emmett and Teller theory
BHMF	2,5-bis(hydroxymethyl)furan
BJH	Barrett-Joyner-Halenda
BSPP	British Standard Pipe Parallel
BSPT	British Standard Pipe Thread
CEM	controlled evaporator mixer
CSA	chemical shift anisotropy
CSTR	continuous stirred tank reactors
D-A	Diels-Alder
DAQ	data acquisition interface
DCM	Dichloromethane
DFF	2,5-diformylfuran
DFT	Density functional theory
DMFDC	2,5-furandicarboxylate ester
DMSO	Dimethyl sulfoxide
DMTHF	2,5-dimethyltetrahydrofuran
DSC	differential scanning calorimetry
EA	Elemental analysis
EDG	electron-donating group
EMF	5-ethoxymethylfurfural
ESI	Electrospray ionization
EWG	electron-withdrawing group
EXAFS	Extended X-Ray Absorption Fine Structure



FBR	fluidised bed reactor
FDCAM	2,5-furandicarboxylic acid methyl ester
FFA	furfuryl alcohol
FFCA	2,5-formylfurancarboxylic acid
FID	flame ionization detector
FTIR	Fourier-transform infrared spectroscopy
FWHM	full width at half maximum
GC	Gas chromatography
HBA	hydrogen bond accepting
HBD	hydrogen bond donating
HKPA	5-hydroxy-4-keto-pentenoic acid
HMFCFA	5-hydroxymethyl-2-furancarboxylic acid
HOMO	highest energy occupied molecular orbital
ILs	ionic liquids
IUPAC	The International Union of Pure and Applied Chemistry
KF	Karl Fischer
LEIS	low-energy ion scattering spectroscopy
LSS	liquid sampling system
LUMO	lowest unoccupied molecular orbital
MA	maleic anhydride
MALDI-TOF	matrix-assisted laser desorption/ionization
MAS	Magic angle spinning
MCPBA	3-chloroperbenzoic acid
MCO	3-methyl-2-cyclopenten-1-one
MD	molecular dynamics
MF	5-methylfurfural
MFA	5-methylfurfuryl alcohol
mfc	mass flow controller

MIBK	methyl isobutyl ketone
MMFC	methyl 5-(methoxymethyl)-furan-2-carboxylate
MS	mass spectrometry
MTHFA	5-methyltetrahydrofurfuryl alcohol
NIST	National Institute of Standards and Technology
NMR	Nuclear magnetic resonance spectroscopy
PET	polyethylene terephthalate
PID	proportional–integral–derivative
PILs	protic ionic liquids
QMS	quadrupole mass spectrometer
QSAR	quantitative structure–activity relationship
R/P	Reserves-to-Production ratio
rt	room temperature
SFVS	sum-frequency vibrational spectroscopy
SILP	Supported Ionic Liquid Phase
ssNMR	solid-state NMR spectroscopy
STP	standard temperature and pressure
TEOS	tetraethyl orthosilicate
TFA	trifluoromethane sulphonic acid
TGA	thermogravimetric analysis
USDA	The United States Department of Agriculture
UV-vis	Ultraviolet–visible
XPS	X-ray photoelectron spectroscopy
2,5-FDCA	2,5-furandicarboxylic acid
5-HMF	5-(hydroxymethyl)furfural
5-CMF	5-(chloromethyl)furfural
2,5-DMF	2,5-dimethylfuran
2,5-DMT	2,5-dimethylthiophene

2,5-hxd	2,5-hexanedione
3,6-DMPA	3,6-dimethylphthalic anhydride
[NTf <sub>2</sub> ] <sup>-</sup>	bis(trifluoromethanesulfonyl)imide
[BF <sub>4</sub> ] <sup>-</sup>	Tetrafluoroborate
[PF <sub>6</sub> ] <sup>-</sup>	Hexafluorophosphate
[NO <sub>3</sub> ] <sup>-</sup>	Nitrate
[HSO <sub>4</sub> ] <sup>-</sup>	hydrogen sulfate
[CH <sub>3</sub> COO] <sup>-</sup>	Acetate
[C <sub>2</sub> C <sub>1</sub> im]	1-ethyl-3-methylimidazolium
[C <sub>4</sub> C <sub>1</sub> im]	1-butyl-3-methylimidazolium
[HNEt <sub>3</sub> ]	Triethylammonium

## Nomenclature

A	Pre-exponential factor	
Ar	Archimedes number	
bp <sub>760</sub>	boiling point at atmospheric pressure (760 mmHg)	°C
D <sub>p</sub>	pore diameter	nm
E <sub>a</sub>	activation energy	kcal mol <sup>-1</sup> / kJ mol <sup>-1</sup>
E <sub>F</sub>	energy of the backscattered ions	eV
F <sub>x</sub>	flow rate	ml s <sup>-1</sup> / g min <sup>-1</sup> / mol s <sup>-1</sup>
FWHM	full width at half maximum	Hz
H <sub>o</sub>	Hammett acidity	
<sup>3</sup> J <sub>HH</sub>	spin–spin coupling constant	Hz
k	rate constant	% min <sup>-1</sup>
m/z	mass divided by charge number	
n <sub>IL</sub>	ionic liquid loading (mmol) by mass of support	mmol g <sup>-1</sup>
N <sub>A</sub>	Avogadro constant	mol <sup>-1</sup>
P <sub>abs</sub>	absolute pressure	bar
P <sub>gauge</sub>	gauge pressure	bar
pK <sub>b</sub>	logarithmic base dissociation constant	
P/P <sub>o</sub>	relative pressure	
Re <sub>mf</sub>	Reynold's number	
s	specific surface area	
s <sub>IL</sub>	thickness of the ionic liquid layer	nm
TOF	turnover frequency	mol <sub>product</sub> mol <sub>catayst</sub> <sup>-1</sup> h <sup>-1</sup>
TON	turnover number	mol <sub>product</sub> mol <sub>catayst</sub> <sup>-1</sup>
TOS	time on stream	h
T <sub>bed</sub>	temperature across the catalyst bed	°C
T <sub>onset</sub>	onset decomposition temperature	°C
T <sub>peak</sub>	temperature of maximum sample degradation	°C

$T_{\text{wall}}$	Temperature of the external wall of the reactor	$^{\circ}\text{C}$
$t_{0.99}$	time required for 1 % sample decomposition	min
$T_{z/x}$	temperature of z (%) decomposition time x ( min)	$^{\circ}\text{C}$
$T_1$	spin-lattice relaxation time	s
$T_2$	spin-spin relaxation time	s
$u_{\text{mf}}$	minimum fluidisation velocity	$\text{m s}^{-1}$
$u_t$	terminal velocity	$\text{m s}^{-1}$
$V_a$	volume of absorbed gas	$\text{cm}^3$
$V_{\text{mf}}$	minimum fluidisation volumetric flow rates	$\text{L min}^{-1}$
$V_{\text{pore}}$	pore volume	$\text{cm}^3$
$X_{\text{MCl}_x}$	molar ratio of a metal chloride	
$\alpha_{\text{IL}}$	pore filling degree	%
$\delta$	chemical shift	ppm
$\epsilon_{\text{IL}}$	ionic liquid loading by mass	%
$\mu_f$	fluid viscosity	$\text{kg/m s}$
$\rho_f$	fluid density	$\text{kg/m}^3$
$\rho_p$	particle density	$\text{kg/m}^3$
$\rho_{\text{skel}}$	skeletal density	$\text{kg/m}^3$
$\rho_{\text{bulk}}$	bulk density	$\text{kg/m}^3$
$\phi$	porosity	
$\chi_{50}$	mean particle size	$\mu\text{m}$

## CHAPTER 1: Introduction

### 1.1 Biorefining as an alternative to oil refining

Petroleum refining remains the primary source of fuels and platform chemicals. More than 80 % of the global production of energy and chemicals is derived from fossil fuels.<sup>1</sup> Fossil feedstocks are non-renewable natural resources and their depletion is imminent as indicated by the estimated reserves-to-production ratio (R/P) for 2015 with an average R/P of 50 years for crude oil (Figure 1.1), 53 years for natural gas and 100 years for coal, with geographical variations.<sup>2</sup> Additionally, the environmental impact of the extensive use of fossil fuels, energy security risks associated with the oil supply chain, and the cost sensitivity of platform chemicals to oil prices are all major concerns.<sup>3</sup>

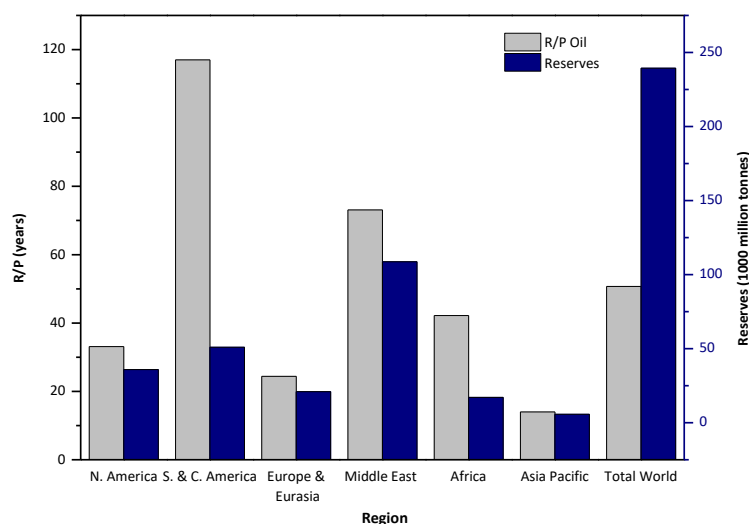


**Figure 1.1:** Global proven oil reserves and reserves-to-production ratio (R/P) in 2015 (source: BP 2016)

Solar and wind power have been used for the production of renewable energy and heat but sustainable biomass processing is the only viable solution for the large-scale production of bio-based products.<sup>4,5</sup> Research by the US Department of Agriculture (USDA) suggests that there will be a significant growth in bio-based chemicals, particularly with respect to specialty chemicals with an estimated 50 % market share by 2025 (Table 1.1).<sup>6</sup> Similarly, the “Joint European Biorefinery Vision for 2030” has also indicated that a notable proportion of the European demand in chemicals, materials and energy will be met by utilising biorefinery-based processes.<sup>7</sup> More specifically, an average of 30 % of the production of chemicals is expected to derive from biomass in addition to 25 % of transport energy needs being covered by biofuels within the EU by 2030. The aim is for biorefineries to produce low-value but high-volume products such as ethanol together with high-value products such as specialty chemicals and

materials.<sup>8</sup> The pathway to commercialisation of a number of bio-based chemicals, including succinic acid, 2,5-furandicarboxylic acid (2,5-FDCA) and 5-(hydroxymethyl)furfural (5-HMF), has been recently reviewed, underlining the active interest of the industry for a transition towards a bio-based economy.<sup>9</sup>

**Table 1.1:** Projected bio-based chemicals global market penetration (values calculated from Ref. [6])

Chemical sector	2010 (%)	2025 (%)
Commodity Chemicals	1 – 2 %	6 – 10 %
Specialty Chemicals	20 – 25 %	45 – 50%
Fine Chemicals	20 – 25 %	45 – 50%
Polymers	5 – 10 %	10 – 20 %

### 1.1.1 The Petroleum refinery

The distillation of crude oil produces various fractions: naphtha, gasoline, kerosene, petrol and diesel oil.<sup>8</sup> Naphtha, a liquid mixture of hydrocarbons, is converted into intermediates which are functionalised to obtain high-value chemicals (Figure 1.2).<sup>8,10</sup> A mixture of olefins and aromatics are either used directly or undergo further transformations for the synthesis of commodity chemicals.<sup>10</sup> Currently, the fossil-derived bulk chemicals represent the fundamental building blocks of the chemical industry.<sup>11</sup>

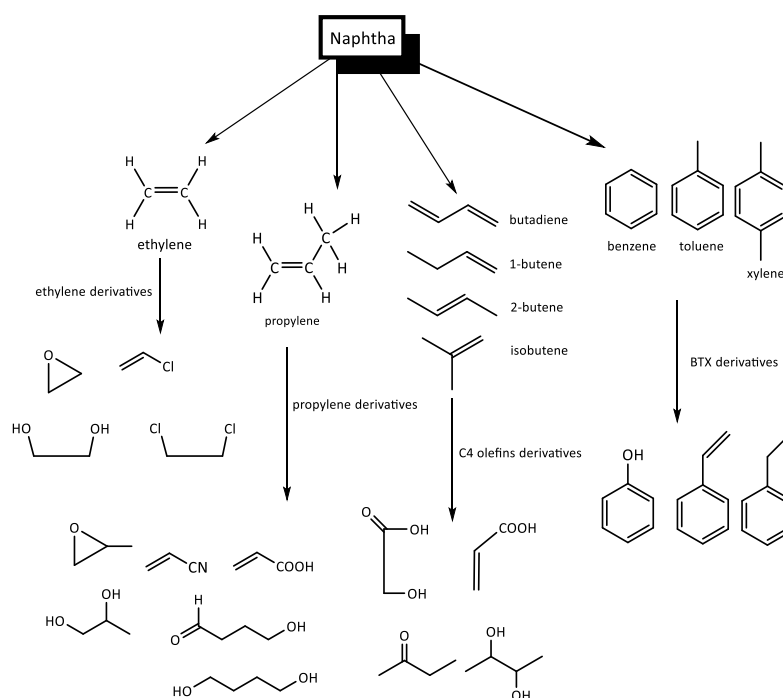


**Figure 1.2:** Platform chemicals and key derivatives in the petroleum refinery

C2 C3 and C4 olefins, aromatics (benzene, toluene and xylenes) and methanol account for more than 300 million tonnes on a global annual scale with ethylene being produced at more than 100 million tonnes per annum (Table 1.2). It is remarkable that there has been a consistent growth in the global production of these key fossil-derived chemicals with rates that exceed a 60 % increase in production over the past two decades. It is also evident that the majority of petrochemicals do not contain heteroatoms and therefore a number of costly and energy-intensive chemical transformations are required for further functionalization and the production of a diverse array of commodity chemicals.<sup>12</sup>

**Table 1.2:** Global annual production of key fossil-derived bulk organic chemicals (2011)<sup>11</sup>

Category	Platform chemical	Predominant Feedstock	Annual production (10 <sup>6</sup> t a <sup>-1</sup> )	% increase in global production (1990 - 2010)
<b>Olefins</b>	Ethylene	Oil, gas	123.3	<b>117 %</b>
	Propylene	Oil, gas	74.9	<b>154 %</b>
	Butadiene	Oil, gas	10.2	<b>62 %</b>
<b>Aromatics</b>	Benzene	Oil	40.2	<b>80 %</b>
	Toluene	Oil	19.8	<b>85 %</b>
	Xylenes (o-, m-, p-)	Oil	42.5	<b>199 %</b>
	Methanol	Syngas	49.1	<b>143 %</b>

### 1.1.2 Biorefinery challenges; establishing a sustainable bioeconomy

The development of biorefining as an analogue of oil refining, regarding the diversity and quantity of produced chemicals, has intensified over the last decades.<sup>5</sup> The successful development of a sustainable biobased economy requires the consideration of economic, environmental and social criteria in addition to technical innovation (Figure 1.3). A number of challenges have been identified for the development of an integrated biorefinery, accounting for the life-cycle of biofuels and bio-derived chemicals.<sup>5,13</sup> The cost with regards to the collection and transportation of biomass can be significant which will have an effect on the biorefinery logistics. The delivery cost of switchgrass to a biorefinery with a capacity of 2000 dry t/day has been estimated to be: 44 – 47 \$/t for baling, 37 \$/t for loafing, 40 \$/t for chopping and piling and 48 \$/t for chopping and ensiling.<sup>14</sup> Consequently, the development of decentralised biorefineries and/or the transportation of biomass that has undergone densification have been proposed as an approach for tackling some of these logistical challenges.<sup>15</sup>



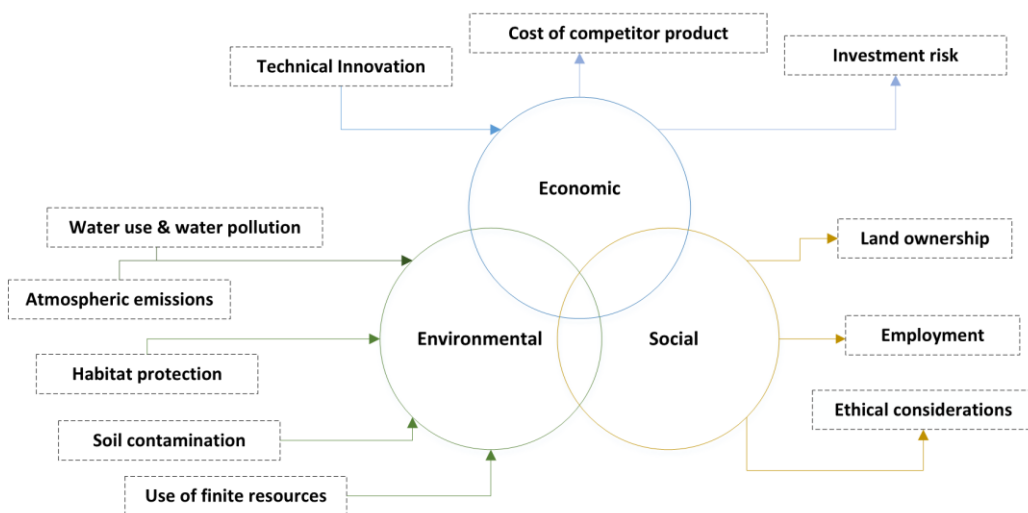


**Figure 1.3:** The competing impacts for the delivery of a sustainable bio-based economy

High volumes of biomass would be required to meet the annual demand for fuels and chemicals in a scenario where the biorefinery products fully replace their petroleum-derived analogues.<sup>5</sup> The use of agricultural residues and highly productive lignocellulosic energy crops has been encouraged in order to avoid the extensive use of arable land.<sup>16–18</sup> Overall, the transition towards a bio-based economy requires investment in combination with political strategies that will effectively drive the shift from oil refining to biorefining. In 2012, the EU developed an action plan promoting the sustainable use of renewable resources: *“Innovating for Sustainable growth: a Bioeconomy for Europe”*.<sup>19</sup> Reducing the dependence on non-renewable feedstocks, maintaining the competitiveness of the European market via the bioeconomy development and creating a coherent policy framework stimulating the collaboration between policy-makers and stakeholders are at the core of the strategy.

### 1.1.3 Lignocellulose as a promising feedstock for the future integrated biorefinery

It is essential that biorefining efficiently integrates the production of power, fuels, and chemicals from biomass. The co-production of fuels and high-value bio-derived chemicals would contribute to the environmental sustainability, as well as the economic viability, of the future biorefineries.<sup>12,20</sup> The development of the first-generation biorefineries, based on food crops such as sugarcane, corn and palm oil, raised major ethical and political concerns regarding food security and fluctuating crop prices.<sup>21</sup> Current scientific research has focused on the development of second generation biofuels and bio-derived chemicals from non-food biomass feedstocks such as lignocellulose.<sup>5,18,22,23</sup> Lignocellulosic

biomass is relatively inexpensive and abundant and thus a suitable feedstock for a full-scale biorefinery.<sup>24</sup> It can be categorised into wood and non-wood lignocellulosic biomass. Hardwood and softwood are common types of wood lignocellulosic biomass whereas non-wood lignocellulosic biomass usually refers to agricultural residues and non-wood plant fibres such as sugarcane bagasse and different types of perennial grass.<sup>24,25</sup> Perennial grasses such as *Miscanthus* and switchgrass can reach up to 144 million tons of annual cellulose yields; hence they are promising feedstocks with regards to bioethanol production.<sup>24</sup> As an example, *Miscanthus x giganteus* exhibits excellent photosynthetic and growth efficiency, even with limited water and nutrient resources.<sup>16</sup> Wood and non-wood lignocellulosic biomass differ in composition with non-wood fibres having additional benefits towards the production of bioethanol due to their lower lignin content that enhances the enzyme digestibility of cellulose.<sup>26</sup>

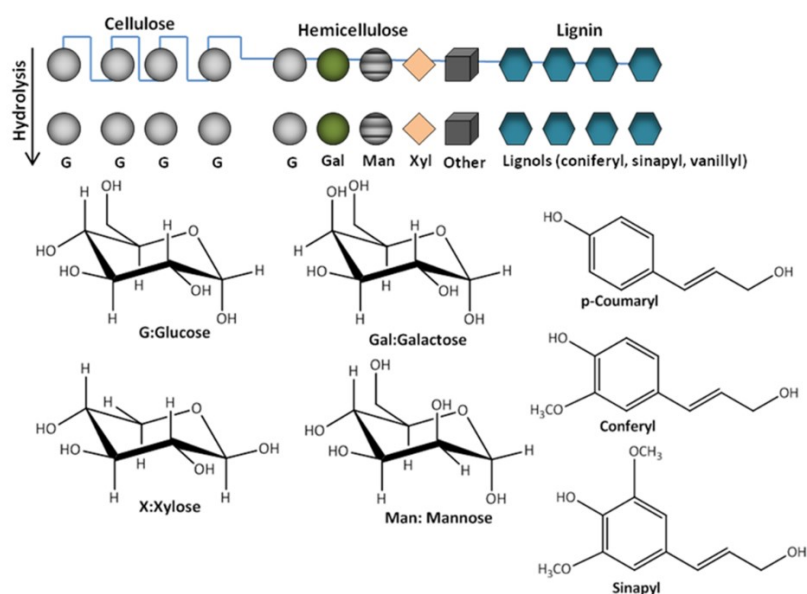


**Figure 1.4:** The structure and chemical composition of lignocellulose. Cellulose, a biopolymer of  $\beta$ -1,4-linked glucose (G) monomers, is the main component of lignocellulose. Hemicellulose is composed of C5 and C6-carbon sugars such as galactose (Gal), glucose (G), mannose (Man) and xylose (X). Lignin is composed of three major phenolic components: p-coumaryl alcohol, coniferyl alcohol and sinapyl alcohol, polymerising at ratios that vary between different plants. Cellulose, hemicellulose and lignin form microfibrils, organized into macrofibrils, promoting the structural stability in the plant cell wall.

Lignocellulose is found in the cell wall of plants where it provides mechanical strength and rigidity. It is composed of highly oxygenated bio-polymers, cellulose, hemicellulose and lignin (Figure 1.4).<sup>12</sup> Cellulose is based on D-glucose monomers that are connected by  $\beta$ -1,4 glycosidic bonds whereas hemicellulose is a low molecular weight, amorphous polysaccharide containing pentoses (xylose, arabinose) and hexoses (glucose, mannose, galactose) connected via varying glycosidic bonds. Lignin, a high molecular weight, crosslinked polymer, contributes to the robustness of the cell wall and the protection of the plant against oxidative stress and infections. Its complex structure is composed of

phenyl propanolic aromatic compounds that are chemically bonded by ether and carbon-carbon bonds. The composition of lignocellulosic biomass and the distribution of polysaccharides and lignin vary depending on the plant species (Table 1.3) with cellulose being a major constituent.<sup>17</sup>

**Table 1.3:** Composition (% wt) of lignocellulosic biomass feedstocks<sup>17</sup>

<b>Plant material</b>	<b>Cellulose (wt%)</b>	<b>Hemicellulose (wt%)</b>	<b>Lignin (wt %)</b>
Hardwood stem	40 – 55	24 - 40	18 - 25
Softwood stem	45 – 50	25 - 35	25 - 35
Silver grass	37	29	19
Switchgrass	31 – 45	24 - 31	12 - 23
Rice straw	35 – 38	25 - 26	13 - 25
Wheat straw	35 – 40	21 - 27	15 - 25
Bagasse	41 – 50	25 - 30	18 - 25
Corn stover	27 – 48	13 - 27	14 - 31
Corn cob	34	34	18
Beet pulp	23	36	1
Coconut husk	44	12	33

#### **1.1.4 Lignocellulose pretreatment; a key processing step to produce biofuels and bio-derived chemicals**

The aim of biorefining is to convert biomass into biofuels and chemicals. This can be achieved by the thermochemical (gasification, pyrolysis), biological (enzymes treatment), or chemical conversion of biomass into fuels and/or platform chemicals.<sup>5,8,13</sup> The deconstruction of the complex biomass structure upon pretreatment is necessary prior to cellulose hydrolysis, followed by the fermentation of sugars into bioethanol or the chemical conversion of sugars into chemicals. Pretreatment involves the disruption of the network between the lignocellulose components by reducing the degree of cellulose crystallinity and polymerisation as well as achieving delignification; hence the available specific area increases and the overall biomass digestability is enhanced (Figure 1.5).<sup>27,28</sup> A large number of pretreatment methods have been explored including the use of physical, chemical and physicochemical pretreatment protocols.<sup>29</sup>

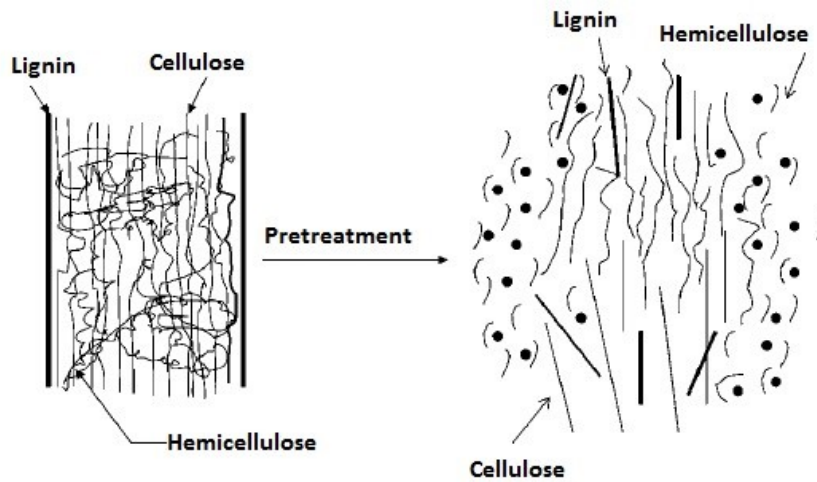


**Figure 1.5:** Simplified representation of biomass pretreatment and the disruption of lignocellulose<sup>27</sup>

In contrast with the crude oil constituents, the non-volatile lignocellulose components cannot be separated by distillation; hence the use of additives is required for physical or chemical pretreatment and the separation of the final products.<sup>27</sup> The ideal method would employ low-toxicity additives offering good separation efficiency with a minimum energy input. Pretreatment requires high energy input in the form of heat and mechanical energy.<sup>27</sup> Consequently, it is considered as one of the most cost and energy-intensive steps of the processing of lignocellulose (Figure 1.6).<sup>29</sup> Increasing the yield of fermentable carbohydrates, inhibiting the formation of sugar degradation by-products and reducing the energy input have been the key areas of focus in regards with research on biomass pretreatment.<sup>28,29</sup>

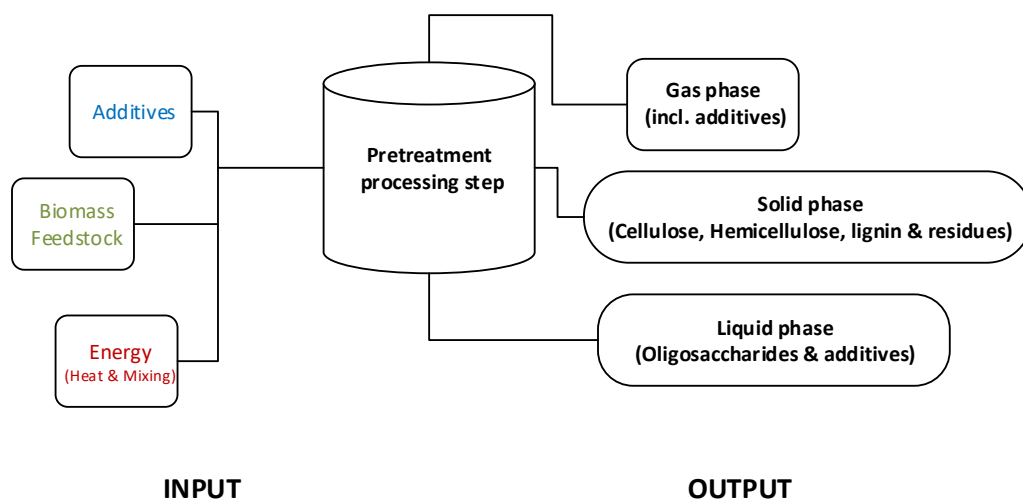


**Figure 1.6:** Generic representation of the biomass pretreatment processing

## 1.2 Bio-derived chemicals development

Bio-derived chemicals must have the necessary physicochemical properties allowing them to replace petroleum-based products.<sup>30</sup> Two strategies have been considered for this purpose: synthesising products of the exact same chemical structure as their petroleum-derived analogues, or producing molecules of different structure but with the potential of deploying the functional groups found in the biomass components.<sup>30,31</sup> Cellulose-derived organic acids as well as functionalised furanics have been recognised as some of the most promising biorefinery building blocks.<sup>32</sup> The use of a renewable feedstock for the production of bio-derived chemicals is in line with the 12 Principles of Green Chemistry.<sup>33</sup> However, the sustainable development of the future biorefinery will also depend on the chemistry behind the transformations of biomass into chemicals, utilising more Green Chemistry principles such as the use of safer solvents and selective catalysis. The design of chemical reactions with optimum green chemistry metrics such as atom economy and E-factor (e.g. pericyclic reactions) must also be considered as part of the design of second generation biofuels and bio-based chemicals. It is critical to assess the environmental impact associated with all stages of obtaining any given biorefining product, determining the real societal and environmental advantages in comparison with its crude oil-derived analogue.<sup>34,35</sup> The conversion of biomass into versatile intermediates and their subsequent conversion into high-value chemicals are discussed in the following **Sections 1.3, 1.4** and **1.5** with an additional focus on the application of ionic liquids as co-catalysts in these chemical transformations.

### 1.2.1 Bio-derived chemicals from polysaccharides

Once the biomass has been pretreated, the newly accessible polysaccharides can be converted to monomeric sugars that can be subsequently transformed to bioethanol via fermentation, or chemically converted to useful platform chemicals such as 5-(hydroxymethyl)furfural (5-HMF) and furfural (Figure 1.7).<sup>29,31,32,36</sup> Establishing efficient processes for the formation of such platform chemicals is of vital importance for the financial viability of the biorefinery concept.<sup>5,32</sup> Both 5-HMF and furfural have been recognised as very important bio-based building blocks towards the successful development of sustainable biorefining.<sup>32</sup> 5-HMF, a product of the dehydration of hexoses, is highly functionalised, consisting of a furan ring, an aldehyde as well as an alcohol functional group.<sup>31</sup> The synthetic production processes to 5-HMF in ionic liquids and other conventional reaction media have been recently reviewed and a focus on ionic liquids is provided in **Section 1.3.2**.<sup>31,37–39</sup> The formation of polymeric side-products, humins<sup>40</sup> or the formation of other by-products (e.g. organic acids, aromatics)<sup>31</sup> has been an important obstacle for optimising 5-HMF yields. Both the furan ring and functional side-groups can be utilised to obtain high-value platform chemicals from 5-HMF (**Section 1.4**). Hemicellulose-derived furfural is

prepared from the dehydration of pentoses mainly via homogeneous Brønsted acid catalysis at high temperatures (150 °C – 250 °C).<sup>36</sup> Similarly to 5-HMF, acid-catalysed furfural synthesis suffers from the formation of solid degradation products, suppressing the reaction yields.<sup>41</sup>

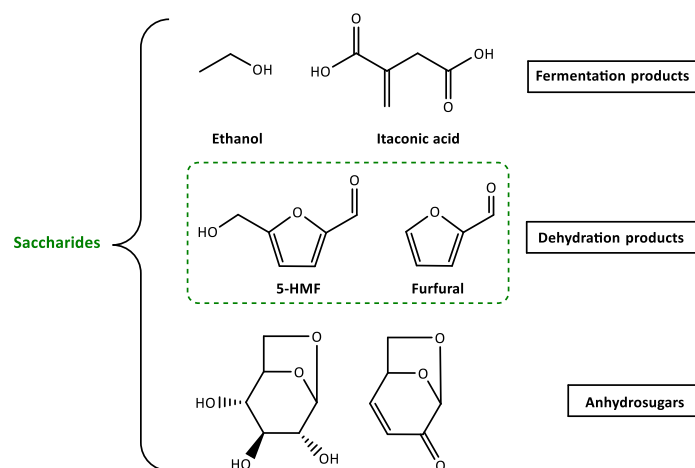


**Figure 1.7:** Saccharides-derived platform chemicals; 5-HMF and furfural as key sugars-dehydration products

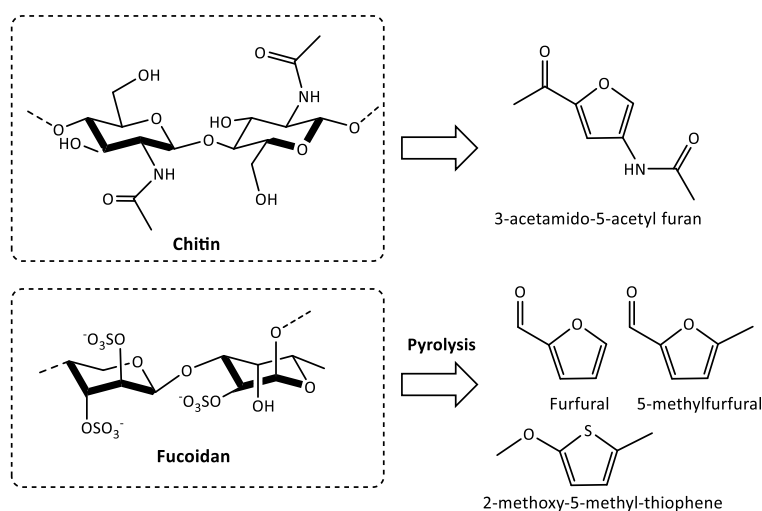


**Figure 1.8:** Heterocyclic compounds obtained from N- and S-containing polysaccharides<sup>42,43</sup>

In addition to cellulose and hemicellulose, there are other natural polysaccharides containing heteroatoms other than oxygen. Chitin, a by-product of the seafood industry, has been previously tested for the production of a number of nitrogen-containing platform chemicals such as the synthesis of 3-acetamido-5-acetyl furan in relatively low yields (Figure 1.8).<sup>42</sup> Sulphated polysaccharides, present in seaweed, have also been tested for the preparation of 5-methylfurfural and furfural, but also some thiophene derivatives such as 2-methoxy-5-methyl-thiophene (Figure 1.8).<sup>43</sup>

## 1.2.2 Bio-derived chemicals from lignin

Lignin is an important constituent of lignocellulosic biomass (10 – 30 wt%) and its valorisation for the production of bio-based aromatics, energy and materials has been researched intensively.<sup>44,45</sup> The Borregaard biorefinery in Norway already utilises lignocellulosic biomass as a feedstock for the production of bioethanol from cellulose (capacity: 20,000 m<sup>3</sup>) whereas lignin is also one of the main product lines.<sup>46</sup> Several aromatic compounds, such as vanillin, catechol, syringol can be isolated through chemical transformations of lignin (Figure 1.9).<sup>45,47</sup>

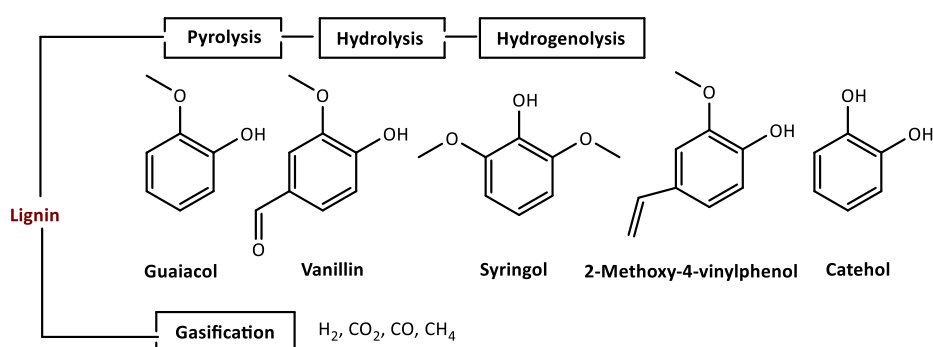


**Figure 1.9:** Lignin-derived chemicals produced by pyrolysis, hydrolysis, hydrogenolysis or gasification

Lignin is typically transformed to useful building blocks by pyrolysis or chemical depolymerisation (Figure 1.9). Lignin pyrolysis and hydrolysis processes are energy-intensive, requiring the application of high temperatures (> 300 °C) and pressures (> 50 bar).<sup>44</sup> A number of publications have presented the successful use of milder reaction conditions for the catalytic conversion of lignin to aromatic platform chemicals.<sup>48–50</sup> The effective deployment of lignin as a chemical feedstock is critical for the development of second generation lignocellulose biorefineries.<sup>5,13,47,51</sup> Converting lignin into high-value aromatics is favoured over its use as a fuel<sup>47</sup> accounting for an existing market of fossil-derived aromatics (BTX) with a volume of 102 Mtpa and a value of €73 bn, (2012).<sup>10,47</sup> Nonetheless, the use of lignin as a chemical feedstock presents unresolved challenges due its complex structure with various functional groups and linkages between monomers, affecting the reactivity of lignin.<sup>44</sup> The selective synthesis of lignin-derived aromatics and the subsequent isolation of the products are complex processes and therefore the use of lignin as a source of mixed aromatics or the valorisation of lignin into polymers or materials are considered as more feasible short-term options.<sup>47</sup>

### 1.3 Ionic liquids and their application in the development of the future biorefinery

Ionic liquids (ILs) are salts having a melting point below 100 °C whereas room temperature ionic liquids (RTILs) are in the liquid state under ambient conditions.<sup>52</sup> They are composed of large organic cations of low symmetry and weakly coordinating inorganic or organic anions.<sup>52</sup> The choice of the anion and/or cation can influence all of the physicochemical properties.<sup>53,54</sup> Some of the most common cations and anions are illustrated in Figure 1.10.

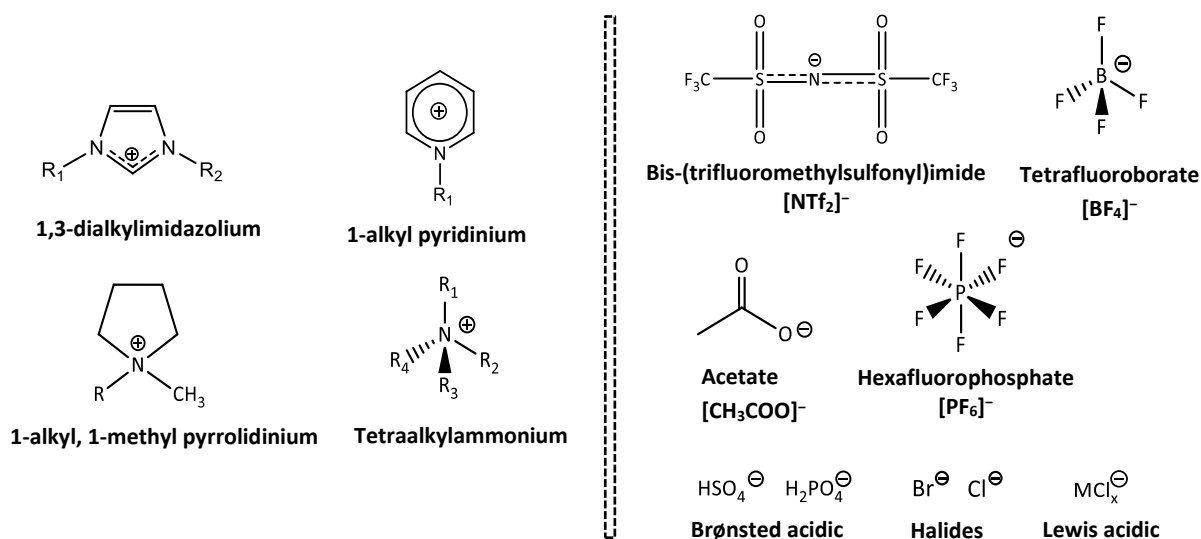


Figure 1.10: Common IL cations and anions

Ammonium, imidazolium, pyridinium and pyrrolidinium-based cations have been used in several applications where ionic liquids are applied either as solvents or catalysts.<sup>52,55</sup> Following the design of oxophilic chloroaluminate(III) ionic liquids,<sup>56,57</sup> the development of a second generation of ionic liquids with non-metallic anions, such as [NTf<sub>2</sub>]<sup>-</sup>, [BF<sub>4</sub>]<sup>-</sup> and [PF<sub>6</sub>]<sup>-</sup>, was combined with the development of moisture-stable halometallate ionic liquids.<sup>58,59</sup> Significant scientific progress has been made after the late 1990s in regards to ILs research, as reflected by the rise of publications and patents in the area.<sup>52,55,60</sup> This exponential growth was driven by the remarkable properties offered by ionic liquids and their potential advantages over conventional organic solvents. An overall comparison between traditional organic solvents and ionic liquids is summarised in Table 1.4. The tuneability of the physicochemical properties of ionic liquids by the large number of possible combinations of anions and cations as well as their application as both catalysts/co-catalysts and solvents are considered as key advantages. The applications of ionic liquids range from biomass pretreatment and cellulose dissolution to organic synthesis and separation of platform chemicals.<sup>22,31,61</sup> However, the high price and viscosity of ionic liquids are often a challenge towards their large-scale implementation.



**Table 1.4:** Comparison of ionic liquids (ILs) with organic solvents

Properties	Organic solvents	Ionic Liquids
<b>Number</b>	> 10 <sup>3</sup>	> 10 <sup>6</sup> (estimate)
<b>Catalytic activity</b>	Rare	Common and tuneable
<b>Chirality</b>	Rare	Common and tuneable
<b>Vapour pressure</b>	Clausius-Clapeyron equation applies	Negligible
<b>Flammability</b>	Usually flammable	Usually non-flammable
<b>Tunability</b>	Limited	Tuneable
<b>Polarity</b>	Conventional polarity principles	Medium Polarity (Kamlet-Taft parameters implementation) <sup>62</sup>
<b>Cost</b>	Inexpensive (x)	2x - 100x
<b>Viscosity (cP)</b>	0.2 - 100	22 - 40,000
<b>Stability</b>	Usually stable	High thermal stability structure-dependant stability
<b>Toxicity</b>	High volatility/ high exposure toxicity	Reduced air contamination structure-dependant toxicity

In general, ionic liquids can be several orders of magnitude more viscous compared to conventional organic solvents.<sup>63,64</sup> The absolute viscosity of ionic liquids,  $\eta$ (cP), ranges from 10 cP to values that are higher than 1000 cP, with a clear temperature and pressure dependence.<sup>64</sup> An additional effect of any impurities has also been shown. For example, viscosity measurements for [C<sub>2</sub>C<sub>1</sub>im][BF<sub>4</sub>] and [C<sub>2</sub>C<sub>1</sub>im][NO<sub>3</sub>] confirmed the positive correlation between the increase or decrease of the dynamic viscosity upon increasing the concentration of Cl<sup>-</sup> or the one of residual water, respectively.<sup>65</sup> The cost of ionic liquids has been estimated to be 5 to 20 times higher when compared to traditional solvents.<sup>60</sup> However, a recent techno-economic analysis on the production of protic ionic liquids showed that the bulk price of ionic liquids could be competitive to the one of conventional organic solvents.<sup>66</sup> More specifically, the cost was estimated at 1.24 \$ kg<sup>-1</sup> and 2.96 - 5.88 \$ kg<sup>-1</sup> for [HNEt<sub>3</sub>][HSO<sub>4</sub>] and [HC<sub>1</sub>im][HSO<sub>4</sub>] respectively. Ionic liquids exhibit excellent thermal stability and onset decomposition temperatures that often exceed 300 °C with a large dependence on the nucleophilicity of the anion.<sup>67</sup> However, protic ionic liquids may start decomposing at lower temperatures (120 °C < T<sub>onset</sub> < 360 °C), before even reaching their boiling point.<sup>68</sup> Both endothermic and exothermic mechanisms have been recently reviewed for the decomposition of ionic liquids.<sup>69</sup> One of the principal mechanisms is the elimination of the side-chain of the cation, yielding neutral species. Transalkylation and retroalkylation are also possible depending on the nucleophilicity of the anion. The vaporization of [NTf<sub>2</sub>]-based ionic liquids is also known to occur together with decomposition that dominates at temperatures over 350 °C.<sup>70</sup> The decomposition of [NTf<sub>2</sub>]<sup>-</sup> to more nucleophilic moieties is followed by Hoffman elimination or

the nucleophilic attack on the alkyl groups of the cation. In addition to thermal stability considerations, ionic liquids must be examined for their chemical stability. The hydrolytic instability of fluorine-containing anions (e.g.  $[\text{BF}_4]^-$  and  $[\text{PF}_6]^-$ ) may lead to the formation of toxic and corrosive HF.<sup>71,72</sup> Moreover, imidazolium-based cations, non-substituted at the C2 position, can be reactive in the presence of strong bases and nucleophiles.<sup>71,72</sup> The overall low vapour pressure of ionic liquids minimises any risks of flammability and exposure toxicity; albeit their environmental fate must be assessed separately.<sup>73</sup> The interaction between ionic liquids and cellular membranes affects their toxicity profile with a drastic effect of the alkyl chain length, the cation type as well as the lipophilicity and stability of the anion.<sup>74,75</sup> For example, comparing ionic liquids with the same side chain on the cation, without modifying the anion, higher toxicity was observed for the ILs bearing an imidazolium cation when compared to piperidinium or pyrrolidinium-based ILs.<sup>75</sup> More lipophilic and hydrolytically unstable ions, such as fluoroorganic and cyano-based anions, have also shown a significant contribution to the toxic effects of ionic liquids.<sup>76</sup> Overall, most of the above parameters (Table 1.4) should be considered when opting to use an ionic liquid over a conventional organic solvent/catalyst whereas more emphasis should be given in developing more quantitative structure–activity relationship (QSAR) models for predicting the toxicity of ionic liquids.

### **1.3.1 Ionic Liquids and lignocellulosic biomass pretreatment**

Ionic liquids have been a subject of research as pretreatment agents that can dissolve both lignin and cellulose.<sup>22,23,77–79</sup> Their ionic composition makes them a superior choice in comparison to water or organic solvents with the anion having a pivotal role in lignocellulose dissolution.<sup>78</sup> Ionic liquids have also been tested as lubrication agents, providing the benefit of reducing the cost and energy requirements for raw biomass grinding.<sup>79</sup> Overall, they improve the pretreatment conditions but heat input is still required to enhance the dissolution rate and yield.<sup>22</sup> In order to establish them as biomass solvents, their stability, recovery and recyclability profile has to be optimised so that pretreatment with ILs becomes a financially viable and sustainable option.<sup>23</sup> Recycling without any loss of activity for more than one cycle has been reported.<sup>80</sup> Nonetheless, the build-up of degradation products in the ionic liquid phase affects the conversion of sugars and the extraction of lignin.<sup>22,80</sup> The long-term formation of degradation products due to the thermal decomposition of ionic liquids also affects their applicability as pretreatment agents and the maximum stable operating temperature conditions.<sup>22,27</sup> However, modifying the cation and/or anion of the IL as well as adjusting the sugar concentration and pretreatment temperature can improve the stability of ionic liquids in biomass pretreatment.<sup>81</sup> Cellulose dissolution in ionic liquids has been found to be strongly correlated to the hydrogen-bond basicity of

the anion.<sup>77,78</sup> Anions such as hydrogen sulfate ( $[\text{HSO}_4]^-$ )<sup>23</sup> and acetate ( $[\text{CH}_3\text{COO}]^-$ )<sup>80</sup> have shown high performance for biomass swelling and dissolution.<sup>22,29</sup> Ionic liquids containing basic anions, such as  $\text{Cl}^-$ , disrupt the hydrogen-bond network in cellulose by creating strong hydrogen-bonds with the hydroxyl groups of the glucose monomers.<sup>77,82</sup> Additional mechanistic studies indicate the formation of electron donor-acceptor complexes between the ions composing the IL and the hydroxyl functional groups of the cellulose monomers (Figure 1.11).<sup>83</sup>

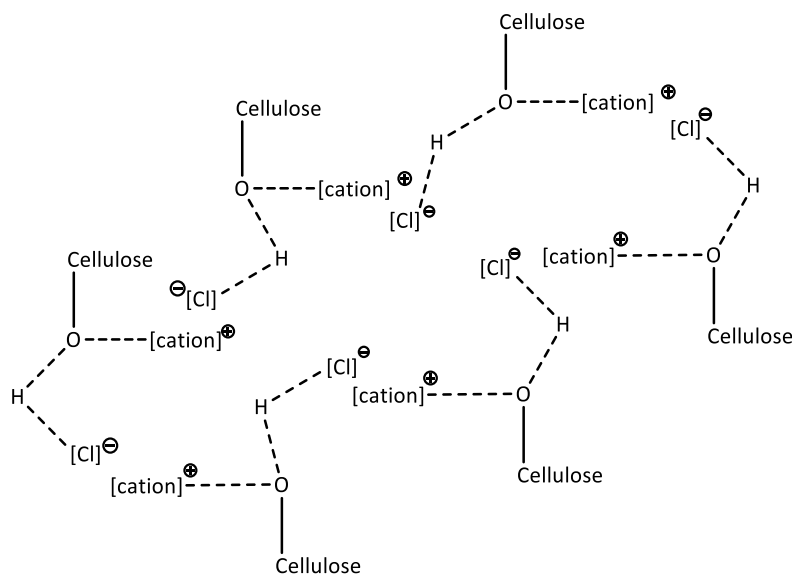


**Figure 1.11:** Cellulose dissolution mechanism. Electron donor-acceptor complex formation

Lignocellulosic biomass pretreatment is followed by saccharification in order to obtain sugar monomers upon hydrolysis of the glycosidic linkages in cellulose.<sup>24</sup> Enzymatic hydrolysis is a more attractive option compared to acid hydrolysis due to the high selectivity provided through biocatalysis.<sup>84</sup> Biomass pretreatment with ionic liquids reduces the crystallinity index of the cellulose in the pulp and therefore increases the substrate surface area.<sup>85</sup> Consequently, the enzyme access has proven to be facilitated with improvements in the saccharification kinetics.<sup>86,87</sup> However, enzyme deactivation and inhibition is promoted even in the presence of ionic liquid residues, impacting negatively on the saccharification yields with a previously reported cellulase activity decreasing by 70 - 85 % in the presence of ILs.<sup>87,88</sup> Nevertheless, the modification of the IL properties or the enzyme structure have been reviewed as promising methods for the stabilisation and activation of enzymes in ionic media.<sup>89</sup>

### 1.3.2 Ionic Liquids and 5-HMF synthesis

A breakthrough in the large-scale production of 5-HMF was accomplished by AVA Biochem in early 2014.<sup>90</sup> A continuous hydrothermal carbonisation process is employed where biomass is hydrolysed and dehydrated with HMF being produced and directly extracted during the biomass carbonization step.<sup>90</sup> The use of polar solvents (e.g. DMSO), supercritical solvents and homogeneous or heterogeneous acid catalysis for the small-scale synthesis of 5-HMF in single-phase or biphasic systems has been recently reviewed.<sup>31,38</sup> The first study of 5-HMF synthesis in ionic liquid media was reported in 1983, where moderate yields were obtained via the dehydration of fructose in pyridinium chloride.<sup>91</sup> Despite this, it was not until later that ionic liquids gained momentum as solvents and co-catalysts for the production of 5-HMF. In 2003, 5-HMF was prepared from fructose with a strongly acidic polymeric resin and a neutral ionic liquid ( $[\text{C}_4\text{C}_1\text{im}][\text{PF}_6]$ ,  $[\text{C}_4\text{C}_1\text{im}][\text{BF}_4]$ ).<sup>92</sup> DMSO was added as a co-solvent in the hydrophobic ionic liquid in order to increase the solubility of fructose.<sup>92</sup> Lewis and Brønsted acidic IL/DMSO systems were also studied to establish a relationship between acidity and the activity towards fructose dehydration to 5-HMF.<sup>93</sup> A positive correlation was found between the HMF yield and the Hammett acidity ( $H_0$ ) of the IL media with an additional impact of the IL/fructose ratio as well as the reaction time and temperature.<sup>93</sup> Superior performance was observed for the Lewis acidic medium in comparison with the Brønsted acidic IL; a lower IL loading was required in order to achieve the same performance of fructose dehydration to 5-HMF.<sup>93</sup> A near-quantitative conversion of fructose to 5-HMF (96 %, 3h) has also been reported for a dual Brønsted/Lewis acidic system combining  $[\text{C}_4\text{C}_1\text{im}][\text{HSO}_4]$  and a Cr(III) hydrated salt:  $\text{CrCl}_3 \cdot 6\text{H}_2\text{O}$ .<sup>94</sup> The typical operating temperature conditions for the conversion of hexoses into 5-HMF range from approximately 80 °C to 200 °C,<sup>31</sup> but temperatures as low as 50 °C have also been successfully tested in  $[\text{C}_4\text{C}_1\text{im}]\text{Cl}/\text{WCl}_6$ .<sup>95</sup>

The reactivity differences between aldoses and ketoses as well as the impact of different Lewis acidic metal chlorides has also been investigated.<sup>96</sup> The use of fructose as a substrate in  $[\text{C}_2\text{C}_1\text{im}]\text{Cl}$  resulted in good 5-HMF yields (70 %) even in the absence of an additional catalyst.<sup>96</sup> However, a transition metal chloride catalyst was required for the successful conversion of glucose into 5-HMF. A 5-HMF yield of approximately 70 % was achieved when catalytic amounts of  $\text{CrCl}_2$  were added to the IL with the catalyst promoting the isomerisation of glucose to fructose and more specifically  $[\text{CrCl}_3]^-$  catalysing the proton transfer steps (Figure 1.12).<sup>96</sup> Both  $\text{Cr}^{2+}$  and  $\text{Cr}^{3+}$  salts can coordinate to glucose and thus they have both been selective in the catalysis of glucose dehydration to 5-HMF.<sup>97</sup> Brønsted acid catalysis has also been studied as an alternative reaction pathway for the synthesis of 5-HMF from glucose.<sup>41</sup> Fast kinetics were observed for the conversion of fructose into 5-HMF in a catalytic system composed of  $\text{H}_2\text{SO}_4$  and  $[\text{C}_4\text{C}_1\text{im}]\text{Cl}$ .<sup>41</sup> However, the conversion of glucose or mannose into 5-HMF was problematic under

Brønsted acidic conditions, with the latter also promoting the formation of humins and suppressing 5-HMF yields (< 20 %).<sup>41</sup> The Lewis-acid catalysed (e.g.  $[\text{CrCl}_4]^-$ ) isomerization of glucose to fructose is necessary to enhance the formation of 5-HMF with resulting optimised yields such as 90 % at 7 mol% loading of  $\text{CrCl}_3 \cdot 6\text{H}_2\text{O}$  (120 °C, 30 min).<sup>98</sup> The selective glucose to fructose isomerisation has also been conducted in aqueous systems containing an Sn-Beta catalyst, with promising applications in isomerisation/dehydration reactions.<sup>99</sup>

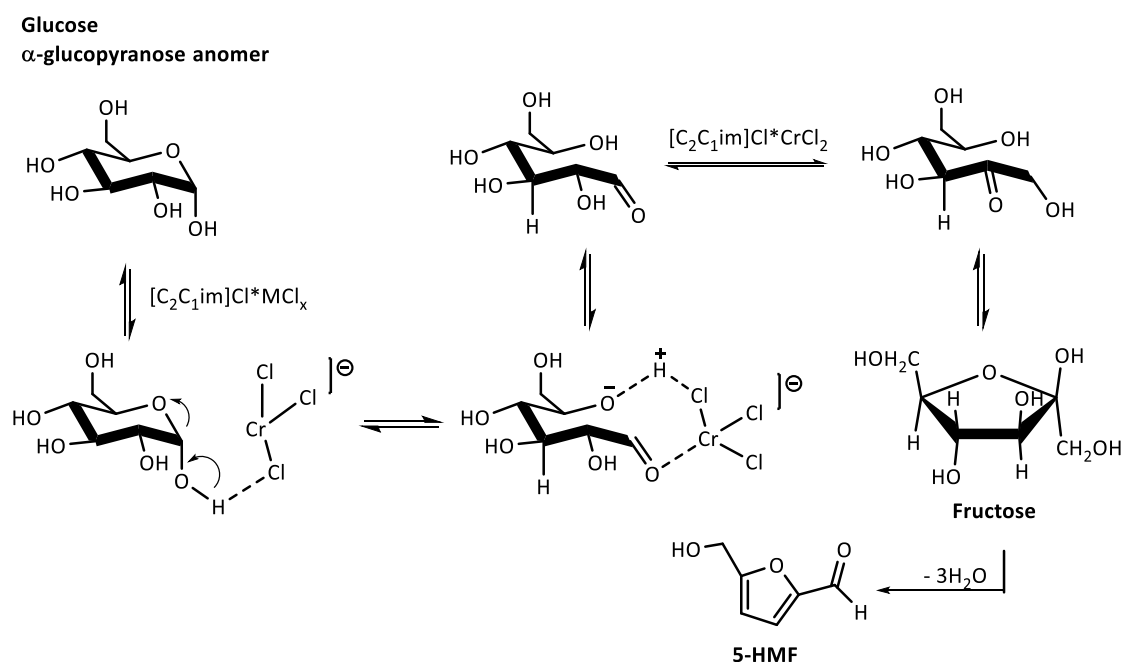


**Figure 2.12:** Putative mechanism for the formation of 5-HMF from glucose in  $[\text{C}_2\text{C}_1\text{im}]\text{Cl}/\text{CrCl}_2$  via the isomerisation of glucose into fructose, catalysed by  $[\text{CrCl}_3]^-$

The direct conversion of lignocellulose-derived polysaccharides would greatly benefit the viability of large-scale HMF synthesis.<sup>100</sup> Microwave irradiation has been used with  $[\text{C}_4\text{C}_1\text{im}]\text{Cl} \cdot \text{CrCl}_3$  to achieve the synthesis of HMF (60 %) from cellulose.<sup>101</sup> The use of microwave irradiation has also allowed the direct catalytic conversion of lignocellulose into 5-HMF in yields up to 52 %.<sup>102</sup> It was suggested that  $\text{CrCl}_3$  catalyses both the polysaccharide hydrolysis via the weakening of the glycosidic bonds, and the isomerisation of glucose to fructose prior to dehydration to 5-HMF.<sup>102</sup> A thorough investigation of the cellulose conversion into HMF with  $[\text{C}_4\text{C}_1\text{im}]^+$ -based ILs, bearing  $\text{Cl}^-$  or  $[\text{HSO}_4]^-$  anions and a range of added metal chlorides, has been performed as an alternative to microwave irradiation.<sup>103</sup> Lowering the cellulose loading and optimising the temperature and reaction time achieved a 58 % HMF yield after one hour at 150 °C with a 7 mol% loading of the  $\text{CrCl}_3 \cdot 6\text{H}_2\text{O}$  catalyst.<sup>103</sup>

Overall, a catalytic system composed of 1,3-dialkylimidazolium ionic liquids and Cr(II) or Cr(III) salts is highly effective for the production of bio-derived 5-HMF with high non-isolated yields.<sup>96–98</sup> However, the separation and purification of 5-HMF from the ionic liquid is a technical challenge. The interaction of 5-HMF with [C<sub>4</sub>C<sub>1</sub>im]<sup>+</sup>-based ionic liquids bearing anions with varying hydrogen-bonding basicity has been investigated using FTIR and NMR spectroscopy.<sup>104</sup> FTIR indicated the disruption of the intramolecular hydrogen-bonding network between 5-HMF molecules upon the addition of an ionic liquid, due to strong interactions between the anion and the OH moiety of 5-HMF, with negligible contribution from the C=O group.<sup>104</sup> An upfield chemical shift was observed for the protons of [C<sub>4</sub>C<sub>1</sub>im]<sup>+</sup> whereas a less pronounced effect was found for the alkyl chain protons of the imidazolium cation with the latter being driven by modified π-π interactions between the IL imidazolium rings in the presence of HMF.<sup>104,105</sup> A limited number of promising studies have been published on 5-HMF isolation from ionic liquids, mainly describing the application of large volumes of organic solvents. Nevertheless, the use of less volatile organic solvents can also render the final HMF isolation by distillation challenging due to the reduced stability of 5-HMF at higher temperatures.<sup>106,107</sup> A biphasic continuous process of fructose dehydration in [C<sub>4</sub>C<sub>1</sub>im]Cl·WCl<sub>6</sub> resulted in high 5-HMF yields (average: 80 %).<sup>95</sup> Both 5-HMF and water were extracted *in situ* from the IL into THF (bp<sub>760</sub> = 66 °C); promoting HMF synthesis and the separation of the ionic liquid upon the evaporation of the organic phase.<sup>95</sup> Ethyl acetate has also been used as a less effective extraction solvent for 5-HMF recovery in the presence of [C<sub>4</sub>C<sub>1</sub>im]Cl·CrCl<sub>3</sub>.<sup>40</sup> A novel process based on entrainer-intensified vacuum reactive distillation has also been explored for the separation of 5-HMF from a mixture of metal chloride and [C<sub>8</sub>C<sub>1</sub>im]Cl.<sup>108</sup> Fructose or glucose were transformed into 5-HMF, followed by reactive distillation under high vacuum (3 mbar) and temperatures above 120 °C, yielding high 5-HMF recoveries (> 85 %).<sup>108</sup> Recently, compressed CO<sub>2</sub> has been tested as an 5-HMF extractant (> 70 %), improving the purity of the final product that was obtained by the dehydration of glucose in [C<sub>4</sub>C<sub>1</sub>im]Cl·CrCl<sub>2</sub> whereas IL/catalyst recycling was achieved without using organic solvents.<sup>109</sup>

Lignocellulose-derived halogenated furfurals such as of 5-(chloromethyl)furfural (5-CMF) have been considered as a viable alternative to 5-HMF due to their higher stability under acidic conditions whilst their hydrophobic nature facilitates their isolation.<sup>110,111</sup> The application of deep eutectic solvents and metal chlorides in a biphasic system for the conversion of sugars into 5-CMF at moderate yields has been reported (50.3 %, 120 °C, 5 h).<sup>112</sup> AlCl<sub>3</sub>·6H<sub>2</sub>O-catalysed fructose dehydration in choline chloride was followed by extraction and halogenation due to the *in situ* HCl generation from AlCl<sub>3</sub>·6H<sub>2</sub>O.<sup>112</sup> The chlorine atom in 5-CMF enhances the reactivity of the molecule towards nucleophilic substitution whereas a number of CMF-derivatives have been prepared such as levulinic acid, 2,5-furandicarboxylic acid (2,5-FDCA), 2,5-dimethylfuran (2,5-DMF) and high-value pharmaceutical chemicals.<sup>110,113,114</sup> Future

research needs to concentrate on improving the 5-HMF isolated yields and controlling the formation of solid by-products.<sup>100</sup> Alternatively, successive 5-HMF transformations to other, more stable chemicals has to be considered to avoid the need to separate HMF from the crude reaction mixture prior to its conversion to high-value chemicals.

## **1.4 5-(Hydroxymethyl)furfural (5-HMF) as a platform chemical**

### **1.4.1 5-HMF functional group transformations**

A plethora of 5-HMF transformations have been studied by converting the functional groups of HMF or the furan ring itself.<sup>115–117</sup> For example, the reactive aldehyde group has participated in reductive amination,<sup>118</sup> acetal formation<sup>119</sup> reactions whilst the hydroxyl functional group has been successfully tested under halogenation,<sup>110–112</sup> or etherification<sup>120</sup> reactions. Overall, the conversion of biomass into chemicals requires multiple steps and cascade catalysis, rendering catalyst development a major challenge.<sup>115,121</sup> The significant role of metal catalysts for the conversion of biomass into chemicals has been recently reviewed, focusing on the hydrogenation and oxidation of sugars or 5-HMF.<sup>115</sup> Improving the robustness, selectivity and activity of the chosen catalyst could be addressed by bifunctional catalysts; hence allowing for process intensification.<sup>121</sup>

The oxidation of either the aldehyde group and/or the alcohol group of HMF has been thoroughly studied with a focus on optimising the reaction conditions and the respective metrics (Figure 1.13).<sup>31</sup> FDCA (2,5-furandicarboxylic acid) has been recognised as a leading value-added chemical that could replace terephthalic acid in the production of polyesters or other polymers containing an aromatic moiety.<sup>32</sup> The oxidation of 5-HMF to FDCA has been attempted with a range of inorganic oxidants, homogeneous or heterogeneous catalysts, electrochemical oxidation, and biocatalytic transformations.<sup>122,123</sup> The prospect of the direct the conversion of carbohydrates to FDCA is considered as a challenging but attractive option due to the higher availability and lower cost of carbohydrates in comparison to HMF.<sup>123</sup> A biphasic system based on water and methyl isobutyl ketone (MIBK), separated by a membrane, was used for the HMF oxidation into FDCA whilst preventing the oxidation of fructose.<sup>124</sup> More specifically, a Brønsted acidic solid catalyst promoted the fructose dehydration to HMF, followed by the HMF extraction of into the MIBK phase containing a metal oxidation catalyst, finally only yielding a maximum of 25 % FDCA.<sup>124</sup>

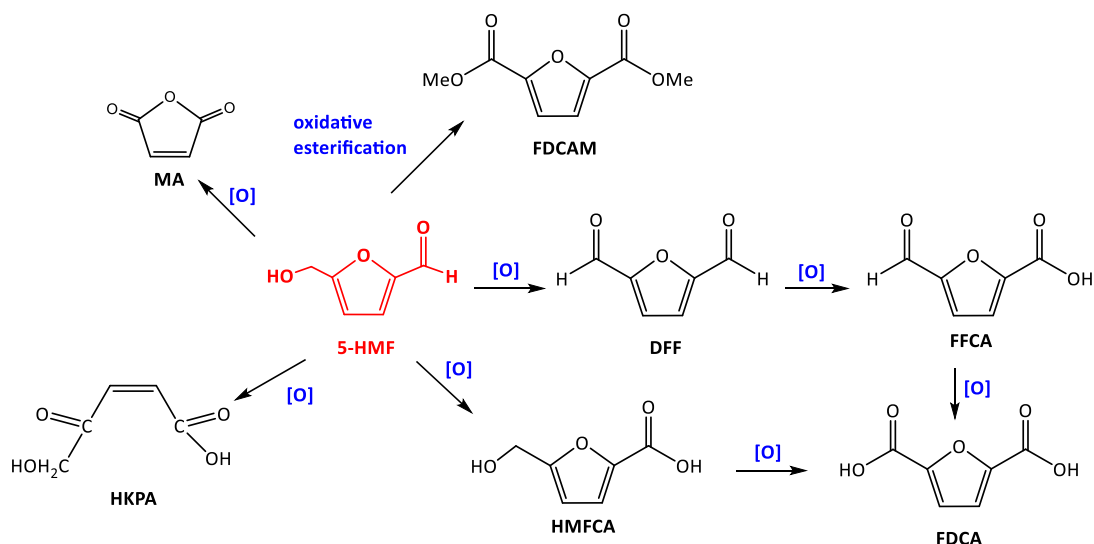
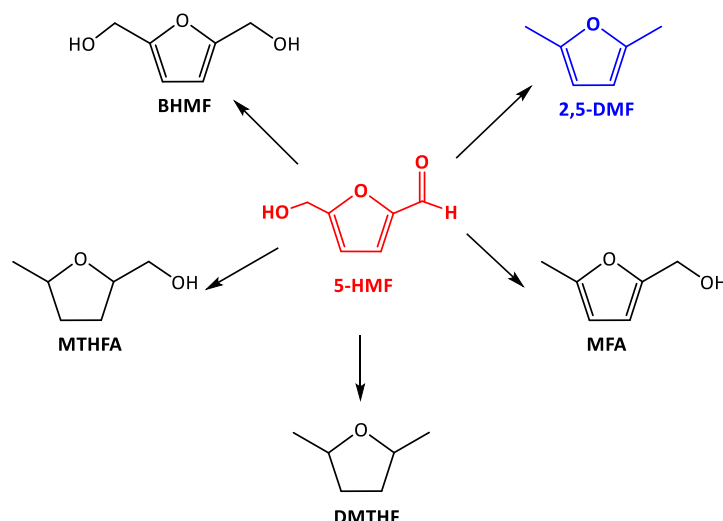


Figure 1.13: 5-HMF oxidation products

The oxidative esterification of 5-HMF produces 2,5-furandicarboxylic acid methyl ester (FDCAM) that benefits from a simpler purification via vacuum distillation, allowing FDCA to be obtained via a subsequent hydrolysis step.<sup>125</sup> The partially oxidised intermediate, 2,5-diformylfuran (DFF), has also been obtained by selective oxidation.<sup>126</sup> This symmetrical dialdehyde is a great building block for the production of polymers or pharmaceuticals.<sup>127,128</sup> Alternatively, the selective oxidation of the aldehyde functional group of HMF produces 5-hydroxymethyl-2-furancarboxylic acid (HMFCFA) with a tuneable HMFCFA/FDCA selectivity.<sup>129</sup> Maleic anhydride (MA) is an important precursor in the production of polyester resins or copolymers via the conversion of the reactive anhydride moieties.<sup>130,131</sup> The synthesis of MA via the oxidative C-C bond cleavage of 5-HMF has been achieved, albeit with a clear effect of the solvent, the catalyst and the oxygen concentration on the MA/DFF selectivity.<sup>132</sup> Additional mechanistic investigations suggested that the aerobic oxidation of 5-HMF to MA proceeds via the C-C bond cleavage between the hydroxymethyl group and the furan ring of HMF without the formation of DFF, FDCA and HMFCFA as intermediates.<sup>133</sup> Carrying out oxidation reactions in ionic liquids is a promising field where ILs are mainly used as a phase transfer catalyst in IL/organic solvent mixtures.<sup>134,135</sup> One example was found where the HMF oxidation in ionic liquids was accomplished over solid ruthenium hydroxide catalysts in ionic liquids at high temperatures and pressures.<sup>136</sup> The best performance was obtained in [C<sub>2</sub>C<sub>1</sub>im][OAc] over Ru(OH)<sub>x</sub>/La<sub>2</sub>O<sub>3</sub> (100 °C, P<sub>O<sub>2</sub></sub> = 30 bar), affording relatively low yields of 2,5-FDCA (48 %) and HMFCFA (12 %).<sup>136</sup>





**Figure 1.14:** 5-HMF reduction products

Reduction chemistry has also been extensively studied for obtaining platform chemicals from 5-HMF due to the high oxygen content of the biomass-derived compounds (Figure 1.14).<sup>31,38</sup> The selective reduction of the formyl group via its adsorption on a catalyst surface leads to the synthesis of 2,5-bis(hydroxymethyl)furan (BHMF).<sup>137</sup> The reduction of both the aldehyde and hydroxyl groups is the pathway to 2,5-dimethylfuran (2,5-DMF).<sup>138</sup> Recent evidence suggested an excellent 5-HMF conversion to 2,5-DMF (93 %) over Ru/Co<sub>3</sub>O<sub>4</sub> at relatively low temperatures and H<sub>2</sub> pressures (130 °C, 0.7 MPa).<sup>139</sup> The application of a bimetallic catalyst, ZnCl<sub>2</sub>–Pd/C, has also been investigated for the hydrodeoxygenation of 5-HMF, showing a significant contribution from ZnCl<sub>2</sub> to promote the hydrogenolysis of BHMF to 2,5-DMF.<sup>140</sup> Replacing the Lewis acid catalyst with a Brønsted acidic system promoted the hydrogenation of the furan ring; hence products such as DMTHF and MTHFA were formed in excess (Figure 1.14).<sup>140</sup> Furthermore, it has been shown that 2,5-DMF can be synthesised in a biphasic process combining the dehydration of fructose and the hydrogenolysis of 5-HMF over a (CuRu/C) catalyst.<sup>141</sup> The dehydration of fructose to 5-HMF takes place in the aqueous phase of a biphasic reactor (3 min, 180 °C) containing an inorganic salt and HCl with the product being extracted into an organic phase (75 % conversion).<sup>141</sup> Recycling of the aqueous phase is followed by the hydrogenation of 5-HMF over a Ru-Cu catalyst (76 – 79 % yield).<sup>141</sup> Ionic liquids have also been studied as co-catalysts for the production of 2,5-DMF from 5-HMF.<sup>142</sup> More specifically, the acid-catalysed glucose dehydration by 12-molybdophosphoric acid has been accomplished in a mixture of [C<sub>2</sub>C<sub>1</sub>im]Cl/acetonitrile before 5-HMF was converted to 2,5 DMF over a Pd/C catalyst.<sup>142</sup>

2,5-DMF has excellent properties as an alternative liquid fuel such as high energy density (30 kJ cm<sup>-3</sup>) and high octane rating.<sup>143</sup> Its hydrophobicity increases its chemical stability in the presence of water,

and its lower volatility compared to ethanol (bp<sub>760</sub>: 92-94 °C) minimises fuel losses, allowing optimum storage.<sup>143</sup> Moreover, the relatively low boiling point enables easy product separation from the crude reaction mixture by distillation.<sup>144</sup> Consequently, the hydrogenation of 5-HMF to 2,5-DMF could also resolve the product separation challenges of the thermally unstable 5-HMF (**Section 1.3.2**). Integrating the synthesis of 5-HMF with a subsequent oxidation or hydrogenation step to produce FDCA or 2,5-DMF is in fact considered as a way of upgrading 5-HMF.<sup>144</sup>

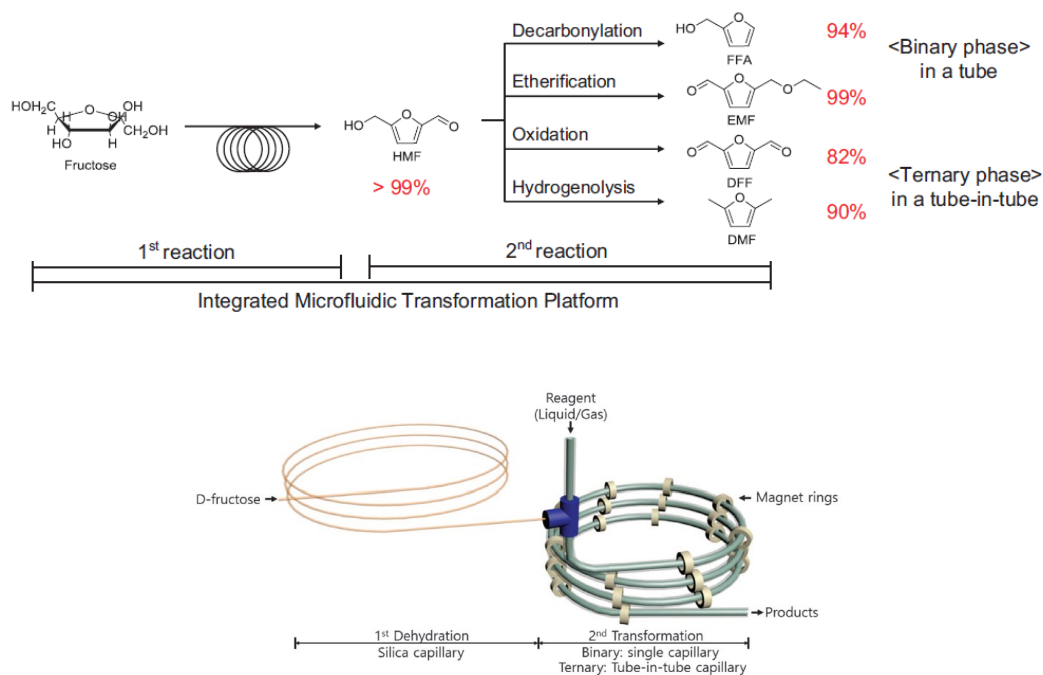


**Figure 1.15:** Illustration of the conversion of fructose into furanics via 5-HMF in an integrated multi-step microreactor<sup>145</sup>

There are very few examples of the direct synthesis of furanics from carbohydrates without the isolation and purification of 5-HMF. The application of a continuous-flow microfluidic system for the dehydration of fructose and the subsequent decarbonylation, etherification, oxidation, or hydrogenolysis of HMF has been reported in good yields.<sup>145</sup> Excellent heat transfer due to a high surface area to volume ratio and a good control of retention time by finetuning the flow rates were achieved with the microreactor assembly (Figure 1.15). Additionally, catalyst recycling was facilitated by immobilizing the heterogeneous catalyst within the microchannels.<sup>145</sup> A tandem process was used to accomplish the dehydration of fructose into HMF over a sulfonic acid-based catalyst (150 °C, 6 min), followed by the conversion of HMF into other furanics over mixed-phase catalysts, supported on magnetic Fe<sub>3</sub>O<sub>4</sub> particles.<sup>145</sup> More specifically, the decarbonylation or esterification of HMF afforded furfuryl alcohol (94 %, Pd/Fe<sub>3</sub>O<sub>4</sub>/SiO<sub>2</sub>, 150 °C, 12 min) and 5-ethoxymethylfurfural (99 %, Fe<sub>3</sub>O<sub>4</sub>/N-doped graphene oxide,

70 °C, 6 min) whereas the oxidation and hydrogenolysis of HMF yielded 2,5-diformylfuran (82 %,  $\text{Fe}_3\text{O}_4/\text{SiO}_2/\text{Mn}$ , 150 °C, 70 min) and 2,5-dimethylfuran (90 %,  $\text{Ru}/\text{Cu}/\text{Fe}_3\text{O}_4/\text{N-doped graphene oxide}$ , 150 °C, 26 min). This approach appears to be promising towards the intensification of downstream lignocellulose transformations. Microreactors have received a great amount of interest regarding their benefits in multiphase reactions.<sup>146</sup> However, the use of cascade microreactors presents several challenges such as pressure-drop and clogging upon the formation of solid products along the walls of the reactor as well as enhanced corrosion challenges due to the high surface area to volume ratio.<sup>147</sup>

### 1.4.2 5-HMF furan ring transformations; heterocyclic and aromatic compounds synthesis

A relatively limited number of studies have focused on the transformations of the furan ring of HMF. The photo-oxidation of the ring under acidic conditions leads to the formation of 5-hydroxy-4-keto-2-pentenoic acid (HKPA).<sup>148</sup> HKPA contains four different functional groups: hydroxyl, carbonyl, carboxylic and a C=C bond; hence it can be considered a very versatile intermediate (Figure 1.13).

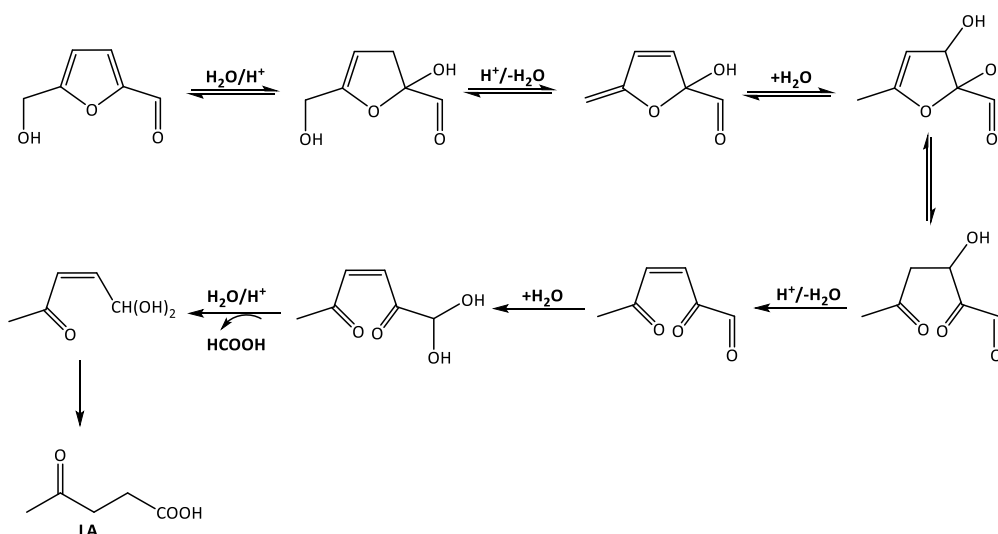


**Figure 1.16:** Brønsted acid-catalysed mechanism of levulinic acid synthesis from 5-HMF<sup>149</sup>

The acid-catalysed ring opening can also lead to the formation of formic acid and levulinic acid, a key bio-based platform chemical<sup>32</sup> and a building block for specialty chemicals such as  $\gamma$ -valerolactone and acrylic acid.<sup>150,151</sup> A proposed mechanism for the formation of levulinic acid from 5-HMF, under Brønsted acidic conditions, is illustrated in Figure 1.16.<sup>149</sup> The addition of water to the furan ring, catalysed by the

Brønsted acid, and the subsequent water elimination have been calculated as endothermic whereas the subsequent hydrolysis and dehydration steps are estimated to be exothermic.<sup>152</sup>

The co-production of 2,5-hexanedione ( $\leq 27.3\%$ ) and 3-methyl-2-cyclopenten-1-one (3-MCO) ( $\leq 30.5\%$ ) via the reductive ring-opening of HMF has also been reported as a green synthetic strategy.<sup>153,154</sup> 5-HMF is converted into 5-methylfurfural (MF) that is further reduced to 5-methyl-2-furanmethanol (MFM) with the  $H_2$  generated *in situ* upon oxidation of Zn in high-temperature water ( $250\text{ }^\circ\text{C}$ ) (Figure 1.17). MFM becomes the substrate for the formation of 2,5-hexanedione upon acid-catalysed rehydration of the molecule, followed by ring opening and a reduction step, finally yielding 2,5-hexanedione (Figure 1.17).<sup>154</sup> 2,5-hexanedione can be further transformed into 3-MCO via an aldol condensation in the presence of ZnO (Figure 1.17). Alternatively, the transformation MF into 3-MCO occurs via a protonation–dehydration sequence, a nucleophilic attack by water, ring opening and subsequent recyclisation steps prior to a final hydrogenation–dehydration to afford 3-MCO (Figure 1.17).

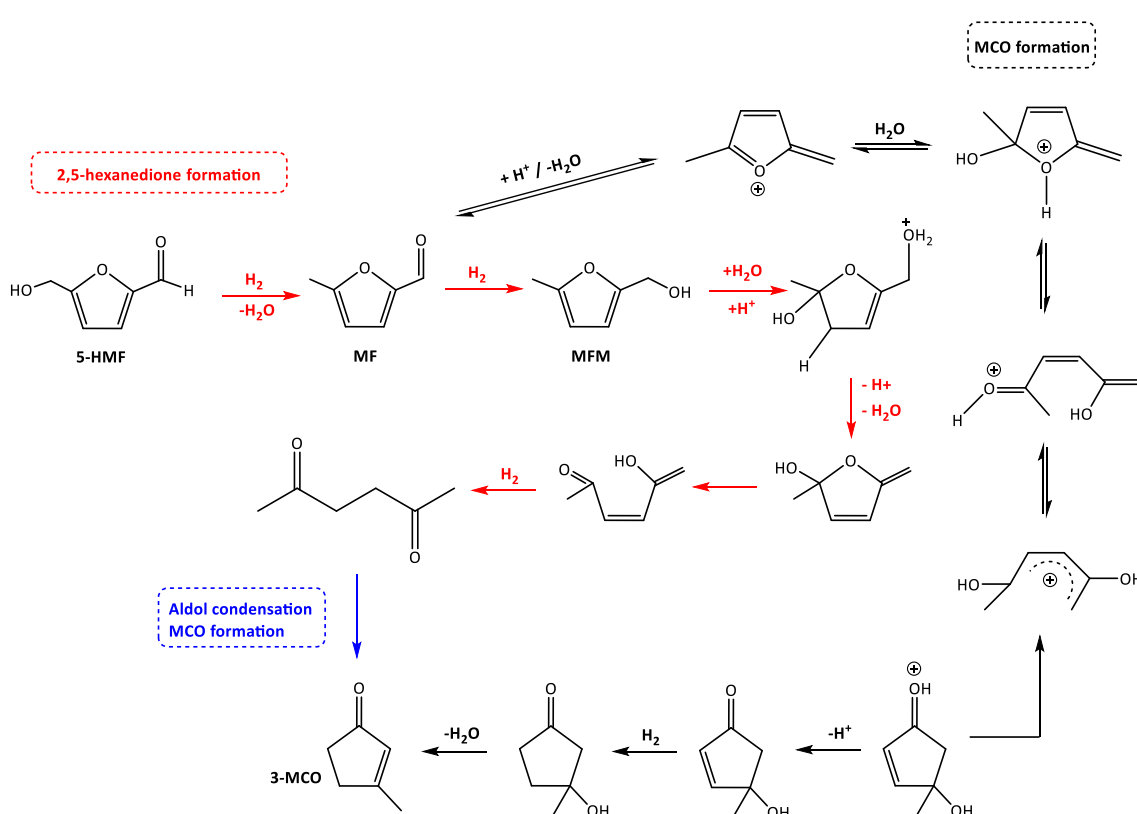


**Figure 1.17:** 3-MCO and 2,5-hexanedione production via the reductive ring-opening of 5-HMF<sup>154</sup>

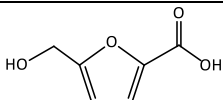
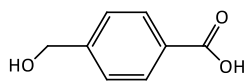
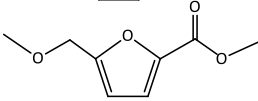
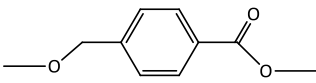
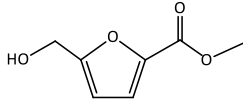
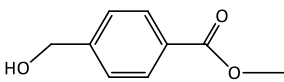
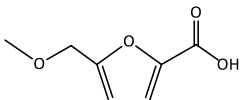
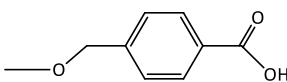
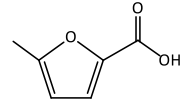
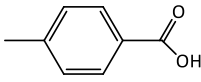
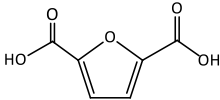
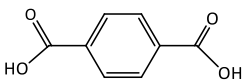
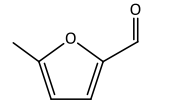
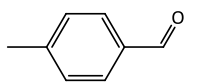
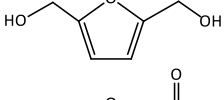
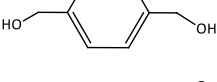
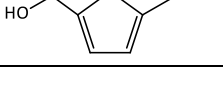
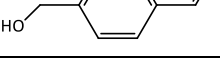
Interestingly, the direct electrochemical reduction of 5-HMF to 2,5-hexanedione has also been demonstrated on the surface of a zinc electrode in acidic aqueous media at high Faradaic efficiencies

(pH 2.0, FE > 70 %).<sup>153</sup> Zinc catalyses the Clemmensen reduction of the aldehyde group to the corresponding hydrocarbon whereas the hydrogenolysis and the Clemmensen reduction steps occur simultaneously, affording 2,5-hexanedione from HMF at ambient pressure and temperature.<sup>153</sup>

The production and application of “green” plastics from bio-based aromatics has already attracted a wide industrial interest. A number of leading companies, Procter & Gamble, Coca-Cola, Heinz and Ford, have already created the Plant PET Technology Collaborative agreement regarding their commitment to replace petroleum-based poly(ethylene terephthalate) with bio-based PET.<sup>155</sup> PET is produced by the condensation of *p*-xylene-derived terephthalic acid and ethylene glycol; with a market value for terephthalic acid of \$65 million by 2018.<sup>155</sup> A revealing techno-economic analysis has been published on the production of *p*-xylene from 5-HMF.<sup>156</sup> This analysis considered some of the best known protocols for the hydrogenation of 5-HMF into 2,5-DMF over a Cu:Ru/C catalyst (76 - 79 %).<sup>141</sup> It also included the subsequent conversion of 2,5-DMF into *p*-xylene in a two-step reaction that requires cycloaddition of ethylene to 2,5-DMF and dehydration of the DA adduct in the presence of a HY zeolite and *n*-heptane (75 %, 300 °C).<sup>143,144</sup> The formation of 2,5-hexanedione upon ring-opening of 2,5-DMF as well as the polymerisation of 2,5-hexanedione were highlighted as challenges for the acid-catalysed *p*-xylene production.<sup>157</sup> The estimated cost for *p*-xylene deriving from 5-HMF was estimated as \$3,962 t<sup>-1</sup> with a competing market price for petroleum-derived *p*-xylene at \$1,630 t<sup>-1</sup> with a considerable impact being the 5-HMF cost.<sup>156</sup> The direct use of 5-HMF as a diene without proceeding with the hydrogenation of HMF into 2,5-DMF would be a step towards optimising the cost of sugar-derived aromatics such as *p*-xylene. The tandem Diels-Alder and dehydrative aromatisation between 5-HMF or its oxidised derivatives and ethylene gas has therefore been investigated to produce terephthalic acid and other aromatic compounds (Table 1.5).<sup>158</sup> The Lewis acidity of the catalyst and the absence of strong Brønsted acidic sites was crucial for obtaining appreciable selectivity at high temperatures (190 °C) and pressures (70 bar).<sup>158</sup> Lewis acids can form complexes to the carbonyl groups of biomass intermediates and enhance reactivity.<sup>159</sup> It is apparent from the reaction metrics summarised in Table 1.5 that 5-HMF (**entry 9**) is not reactive towards ethylene to form of its 6-membered aromatic analogue. Coke formation was reported for all the furan derivatives containing an aldehyde and/or hydroxyl moiety (**entries 7-9**).<sup>158</sup> FDCA (**entry 6**) was also found to be inactive towards the cycloaddition reaction with ethylene, suggesting the deactivation of the diene due to the presence of the electron withdrawing carboxylic acid groups. Low yield and moderate selectivity were obtained for the partial 5-HMF oxidation product, HMFCA (**entry 1**) as well as its ester and ether derivatives (**entries 2-4**). Protecting the carboxylic acid moiety resulted in an increase in selectivity whereas the protection of the hydroxyl group resulted in an increase of the overall diene conversion but a reduced selectivity towards the formation of the aromatic

product (**entries 2-4**). The best reaction metrics were achieved for **entry 2**, methyl 5-(methoxymethyl)-furan-2-carboxylate (MMFC), where both functional groups were protected by the addition of methanol. Maximum selectivity (100 %) but low conversion (12 %) was reported when the hydroxyl moiety was replaced by an electron donating CH<sub>3</sub> group and the carboxylic acid functionality was converted to the corresponding ester.<sup>158</sup> A further investigation of the Lewis acid-catalysed Diels-Alder dehydration between ethylene and MMFC has also been carried out with silica molecular sieves containing Lewis acid centres.<sup>160</sup> A complex system of tandem reaction steps was implicated, including the reversible adsorption of reactants and intermediates onto the catalyst surface, the Diels-Alder cycloaddition, the dehydrative aromatization as well as the reversible Diels-Alder reaction.<sup>160</sup>

**Table 1.5:** Diels-Alder dehydration of oxygenated furans with ethylene<sup>158</sup>

Diene	Product	Conversion (%)	Yield (%)	Selectivity (%)	Entry
		61	19	31	<u>1</u>
		50	24	48	<u>2</u>
		12	5.0	42	<u>3</u>
		52	9.0	17	<u>4</u>
		45	12	27	<u>5</u>
		0	0	0	<u>6</u>
		2	0	0	<u>7</u>
		100	< 1	< 1	<u>8</u>
		16	0	0	<u>9</u>

Lewis acidic Zn sites in a beta-zeolite framework have been found to be effective in catalysing the direct synthesis of dimethylterephthalate ester (yield: 3.4 %, selectivity: 5.1 %) via the tandem Diels-Alder cycloaddition/dehydration of 2,5-furandicarboxylate (DMFDC), the dimethyl ester of FDCA,<sup>119</sup> and

ethylene at high pressures (60 - 80 bar) and temperatures (190 °C). Methyl 2-furoate (50.5 %), methyl benzoate (5.3 %), and 2-cyclohexenone (2.8 %) were detected as key by-products, mainly driven by decarboxylation<sup>161</sup> reactions and subsequent Diels-Alder reactions.

The synthesis of polysubstituted benzenes with pharmacological properties is another example of how aromatics from bio-based furans bearing an aldehyde moiety can be applied. Furfural derivatives were used together with maleimide and dimethylhydrazine in a three-step cascade reaction that involved the formation of a hydrazone derivative prior to a Diels-Alder/aromatisation reaction sequence in water, affording moderate to high isolated yields of polysubstituted phthalimides (41 – 97 %) (**Figure 1.18**).<sup>162</sup>

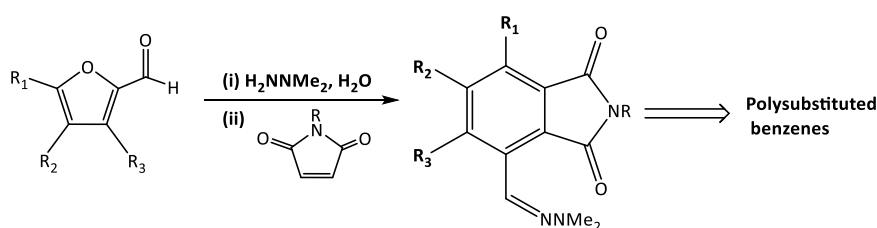


**Figure 1.18:** Polysubstituted benzenes synthesis from bio-based furfural building blocks<sup>162</sup>

A small number of studies have described the conversion of 5-HMF to other heterocyclic compounds.<sup>31,38</sup> Heterocycles can be considered platform chemicals with pharmacological properties, constituting fragments of drug compounds mainly due to bioisosterism and other properties such as their unique electron configuration, hydrogen-bonding and  $\pi$ - $\pi$  stacking.<sup>163,164</sup> Figure 1.19 shows a few well-known drug compounds, incorporating a furan, a pyrrole, or a thiophene ring. Other applications include electronics, supramolecular chemistry, and agrochemicals.<sup>165,166</sup>

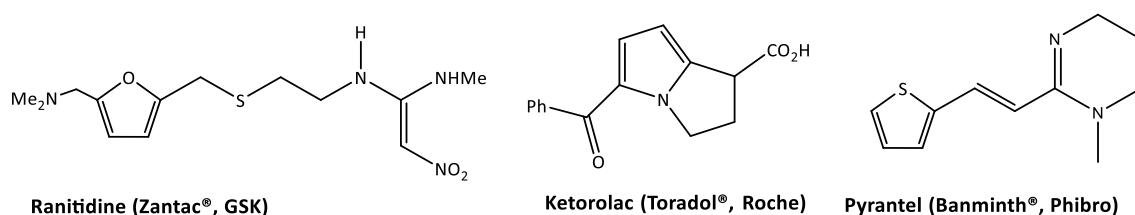


**Figure 1.19:** Characteristic examples of heterocyclic fragments in pharmaceutical compounds

The synthesis of pyridinols with a hydroxymethyl moiety is another example of bio-derived heterocyclic compounds from fructose.<sup>167</sup> However, the conversion of fructose into 6-hydroxymethyl-3-pyridinol is a multi-step process; the acid-catalysed dehydration of fructose into HMF is followed by reductive amination and *N*- and *O*- protection prior to oxidation.<sup>167</sup> The oxidation was accomplished

electrochemically in methanol whereas deacetylation and acetal hydrolysis preceded the furan ring recyclization into pyridine (Figure 1.20).<sup>167</sup>

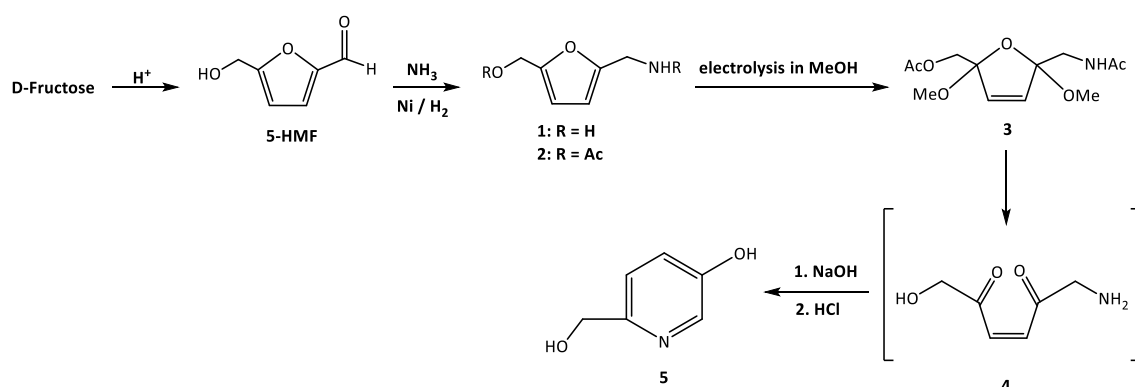


Figure 1.20: Multi-step synthesis of pyridinols from fructose<sup>167</sup>

The conversion of 5-HMF into substituted pyrroles, pyridazines and thiophenes has also been achieved in good yields (> 70 %) in conventional solvents and catalysts (Figure 1.21).<sup>168</sup> The oxidation of 5-HMF derivatives resulted in opening the furan ring and the formation of both 1,6-dioxy-3-hexene-2,5-dione stereoisomers.

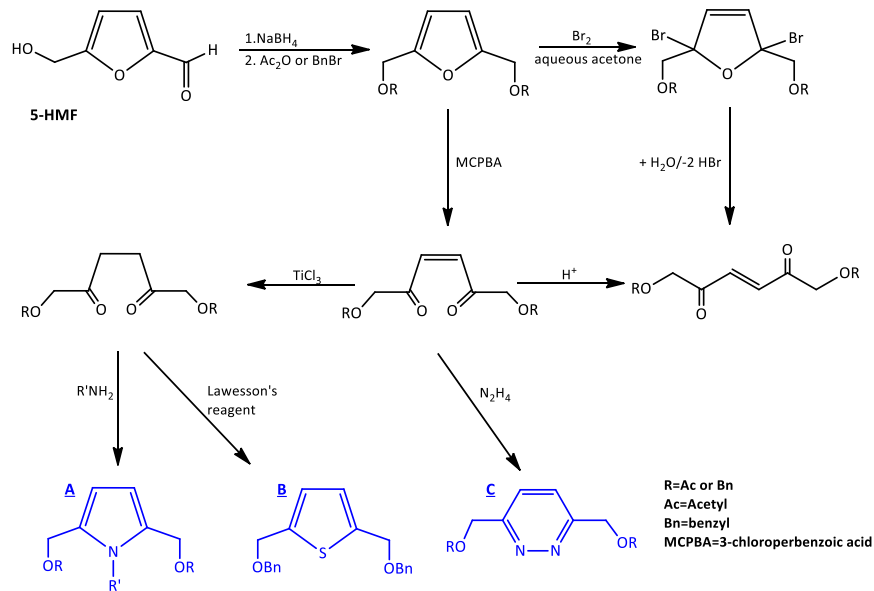


Figure 1.21: Conversion of 5-HMF into pyrroles (A), thiophenes (B) and pyridazines (C)<sup>168</sup>

Selective oxidation was possible when 3-chloroperbenzoic acid (MCPBA) was employed, yielding the cis-isomer of the 1,4-dicarbonyl compound.<sup>168</sup> The reduction of the unsaturated 1,4-diketone was followed



by the addition of primary amines or Lawesson's reagent, forming the corresponding pyrrole, pyridazine and thiophene derivatives, respectively. The direct synthesis of pyrroles, pyridines, or indoles from biomass has also been attempted via the thermo-catalytic conversion and ammonization of biomass over HZSM-5 catalysts.<sup>169</sup>

There is a considerable range of chemicals that have already been obtained through 5-HMF transformations but there are still opportunities to develop reactions of the furan moiety. Additionally, the investigation of ionic liquids as solvents and/or catalysts for the synthesis of platform chemicals should also be further investigated in an ongoing effort to improve metrics such as rates, selectivity and yield. 2,5-DMF could also be thoroughly studied as an intermediate given its chemical stability and easier separation by distillation from the reaction mixture.

### 1.5 2,5-dimethylfuran (2,5-DMF) as a platform chemical

A recent study described the heterogeneous condensation of anilines with bio-derived furanoids towards the synthesis of pyrrole derivatives under relatively mild conditions (Figure 1.22).<sup>170</sup> The fine-tuning of the acidity strength of the catalyst as well as the Brønsted/Lewis acid sites ratio was crucial. A strong acidic character was linked to pronounced binding interactions between the N-containing intermediates and the active sites of the catalyst, suppressing the condensation reaction.<sup>170</sup> A significant role of Brønsted acidity over Lewis acidity was underlined with the H-Y zeolite showing an optimum performance for 2,5-DMF (99 %, 0.7 h), whereas 2,5-hexanedione was detected as a reactive intermediate that undergoes a fast conversion to *N*-substituted pyrroles in a similar way to the Paal-Knorr reaction of 2,5-hexanedione with a variety of amines.<sup>170,171</sup>

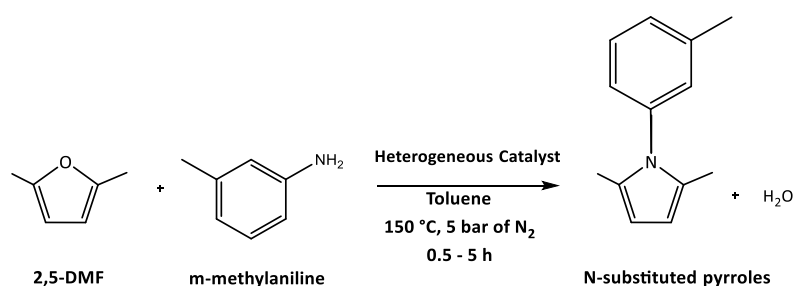
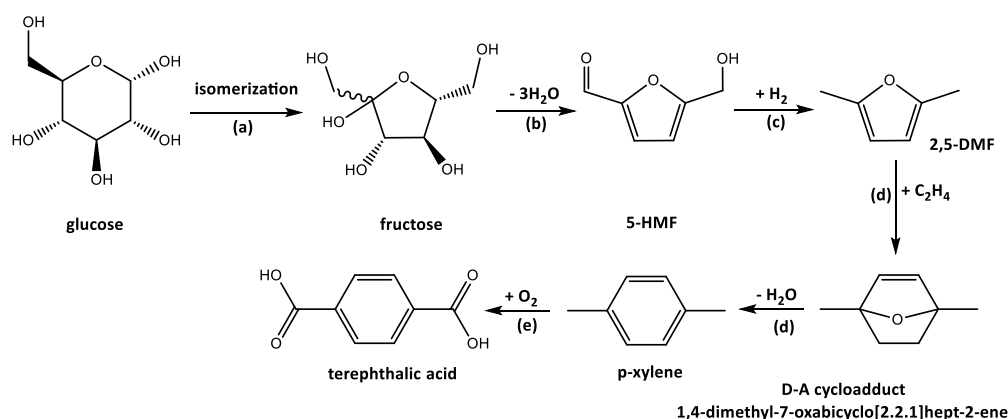


Figure 1.22: Catalytic condensation of equimolar amounts of 2,5-DMF with m-methylaniline<sup>170</sup>

2,5-DMF has been widely studied as a platform chemical but mainly as a diene in cycloadditions, given that it contains a furan moiety and two electron-donating methyl groups that promote the formation of

a [4 + 2] cycloadduct.<sup>172,173</sup> Furans undergo Diels-Alder cycloadditions with a variety of dienophiles whereas the substitution of the furan ring and/or the dienophile impact the reaction metrics as well as the experimental conditions.<sup>174</sup> As discussed in **Section 1.4.2**, the electron-withdrawing nature of the aldehyde group makes 5-HMF a less suitable diene for Diels-Alder reactions.<sup>158</sup> Reducing 5-HMF into 2,5-DMF has therefore been a more desirable option for the synthesis of bio-based aromatics. Moreover, the presence of methyl groups in 2,5-DMF facilitates the dehydration step by stabilizing charged intermediates upon the dehydrative aromatization of the bicyclic adduct.<sup>175</sup>



**Figure 1.23:** Multi-step synthesis of renewable *p*-xylene; a) isomerization of glucose to fructose b) fructose dehydration to 5-HMF c) 5-HMF hydrogenolysis to 2,5-DMF d) tandem 2,5-DMF cycloaddition to ethylene and dehydrative aromatisation to *p*-xylene, followed by e) *p*-xylene oxidation to terephthalic acid

**Sections 1.4.1** and **1.4.2** have already outlined two possible pathways for the replacement of the petroleum-derived *p*-xylene and terephthalic acid: 1) by using the glucose-derived FDCA as a terephthalic acid analogue or 2) through deployment of bio-derived furanics in tandem cycloaddition/dehydrative aromatization reactions to produce *p*-xylene or other aromatic compounds. More than 40 million tonnes of *p*-xylene are produced every year (Table 1.2) and the vast majority of the production volume is used for the synthesis of terephthalic acid.<sup>176</sup> There are already many publications summarising the attempt to produce bio-based *p*-xylene from sugar-derived furanics (Figure 1.23).<sup>157,173,176–178</sup> The synthesis of *p*-xylene from 2,5-DMF and ethylene usually requires the use of high pressures (> 50 bar) and temperatures (200–300 °C) due to the large HOMO–LUMO gap present in reactants.<sup>157,176,179</sup> However, the use of a Lewis acid catalyst decreases the HOMO–LUMO gap, promoting the 2,5-DMF-ethylene cycloaddition whilst the second step of the dehydrative aromatisation proceeds effectively in the presence of Brønsted acidic sites.<sup>179,180</sup> The cycloaddition of 2,5-DMF and ethylene becomes the rate-limiting step in the presence of a Brønsted acid, whereas the subsequent dehydration reaction becomes the slower step when a Lewis acid is used instead.<sup>179</sup> The dehydrative aromatisation requires the opening of the oxygen-bridge of the cycloadduct with a calculated activation

energy value of more than 60 kcal.mol<sup>-1</sup>, as determined by gas-phase DFT.<sup>179</sup> The Brønsted-acid catalysed dehydration of 1,4-dimethyl-7-oxabicyclo[2.2.1]hept-2-ene is combined with a significant reduction in the activation energy from 60 kcal.mol<sup>-1</sup> to 12.2 kcal.mol<sup>-1</sup> for breaking the oxanorbornene oxygen bridge.<sup>180</sup> In the presence of a Brønsted acid (Figure 1.24A), the protonation of the oxygen-bridge is followed by water formation upon an intramolecular proton transfer to the oxygen of the protonated intermediate (E<sub>a</sub> = 7.8 kcal.mol<sup>-1</sup>) and a concomitant proton transfer from the C5 carbon to an oxygen catalytic site, affording *p*-xylene and water, regenerating the catalyst. The Lewis acid-catalysed reaction mechanism (Figure 1.24B) takes place via the coordination of a Lewis acid catalytic centre to the heteroatom of the cycloadduct but a smaller efficiency is observed in comparison with Brønsted acidic catalysts.<sup>180</sup> The effect of the actual concentration of Brønsted acidic sites on the tandem cycloaddition/dehydration kinetics has also been attempted, using an H-Y zeolite-based catalyst.<sup>181</sup> A linear relationship was established between the formation of *p*-xylene and the density of Brønsted acid sites at low catalyst loadings with the kinetics being controlled by the dehydrative aromatization step.<sup>181</sup> A second regime was described for high catalyst loadings where the cycloaddition between 2,5-DMF and ethylene becomes rate-limiting, being the most energetically demanding step of the tandem reaction scheme.<sup>181</sup> Overall, promoting the cycloaddition step is critical given that the overall maximum rate is controlled by the cycloaddition of 2,5-DMF and ethylene.<sup>181</sup>

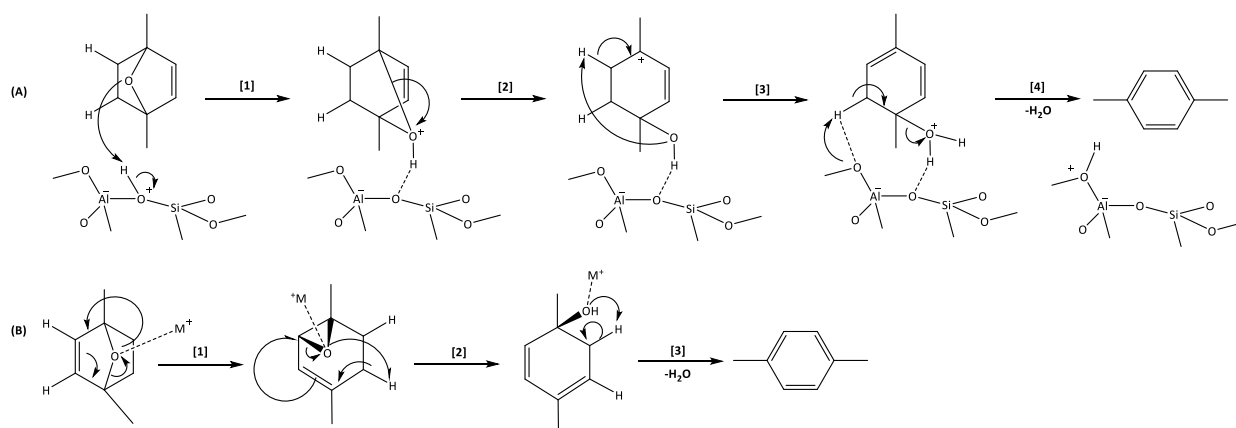


**Figure 1.24:** Mechanism of the 1,4-dimethyl-7-oxabicyclo[2.2.1]hept-2-ene dehydrative aromatization, promoted by a Brønsted acidic (HY)-(A) or Lewis acidic (MY)-(B) catalyst<sup>180</sup>

Competing reactions alongside the formation of *p*-xylene include the acid-catalysed hydrolysis of 2,5-DMF to 2,5-hexanedione, the alkylation of *p*-xylene as well as the oligomerization of 2,5-hexanedione (Figure 1.25).<sup>157</sup> A study of the 2,5-DMF/ethylene reaction mechanism by NMR/GC-MS has also confirmed the aforementioned competing side-reactions over HY zeolites.<sup>178</sup> The intramolecular aldol reaction of 2,5-hexanedione may also yield 3-methyl-2-cyclopentenone in small quantities (Figure

1.25).<sup>173</sup> 3,6-dimethyl-2-cyclohexenone (Figure 1.25) has also been assigned as a by-product in the presence of predominantly Lewis acidic catalysts that promote the rearrangement of the adduct over the dehydrative aromatisation in comparison with Brønsted acid catalysts.<sup>173</sup> Furthermore, the formation of  $\gamma$ -dicarbonyl compounds and their oligomerisation has been found to be enhanced upon removing one or both methyl substituents of the diene when methylfuran or furan were used instead of 2,5-DMF.<sup>173</sup> Using furan as a substrate may also lead to the formation of benzofuran in the presence of solid acid catalysts due to the cycloaddition of two furan molecules (Figure 1.25).<sup>182</sup> The 2,5-hexanedione can strongly adsorb on the surface of acidic zeolites, competing with the oxanorborene intermediate, whereas desorption is possible upon the reversible conversion of 2,5-hexanedione into 2,5-DMF.<sup>181</sup> The addition of a hydrophobic solvent has previously improved the overall selectivity towards *p*-xylene by suppressing water adsorption on the catalyst surface, increasing the adsorption of ethylene and controlling most of the aforementioned water-induced side-reactions.<sup>183</sup>

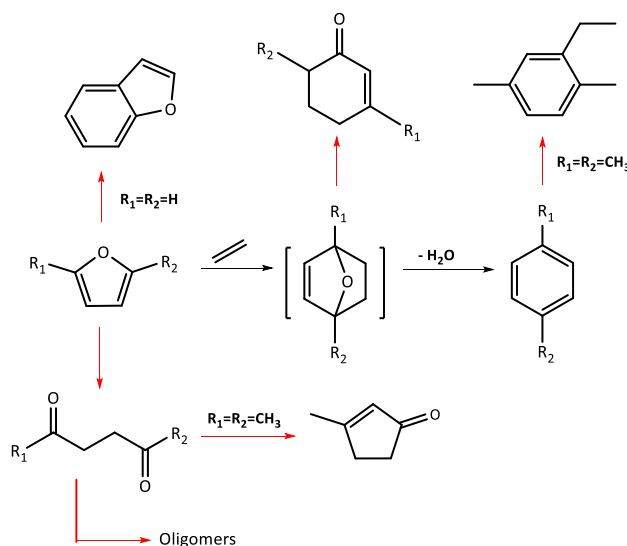


**Figure 1.25:** Aromatics synthesis from furan or 2,5-DMF and ethylene and key by-products; R<sub>1</sub> = R<sub>2</sub> = H or CH<sub>3</sub>

The susceptibility of furanic compounds towards hydrolysis in the presence of a Brønsted acid catalyst has been investigated via quantum-chemical calculations.<sup>184</sup> The hydrolysis of 2,5-DMF is estimated as an endothermic process with the primary proton transfer between H<sub>3</sub>O<sup>+</sup> and the C<sub>3</sub> carbon being the rate-limiting step ( $E_a = 20 \text{ kcal mol}^{-1}$ ) (Figure 1.26B).<sup>184</sup> An alternative pathway (Figure 1.26A) involves an initial  $\alpha$ -protonation with the water-binding step being the slowest ( $E_a = 27 \text{ Kcal mol}^{-1}$ ). However, it is the  $\beta$ -C protonation pathway that has been proposed as the one behind the 2,5-hexanedione synthesis. This occurs by the hydrolytic cleavage of the furan ring of 2,5-DMF with a pronounced effect by electron-donating substituents, in agreement with earlier experimental studies.<sup>185</sup> Turning now to the calculations on the hydrolysis of furanics with an electron withdrawing carbonyl moiety, the

rehydration of 5-HMF to afford levulinic acid (**Section 1.4.2**) has been reported in contrast to the ring-opening via the protonation at the  $\beta$ -position of the furan moiety of 2,5-DMF.<sup>184,186</sup>

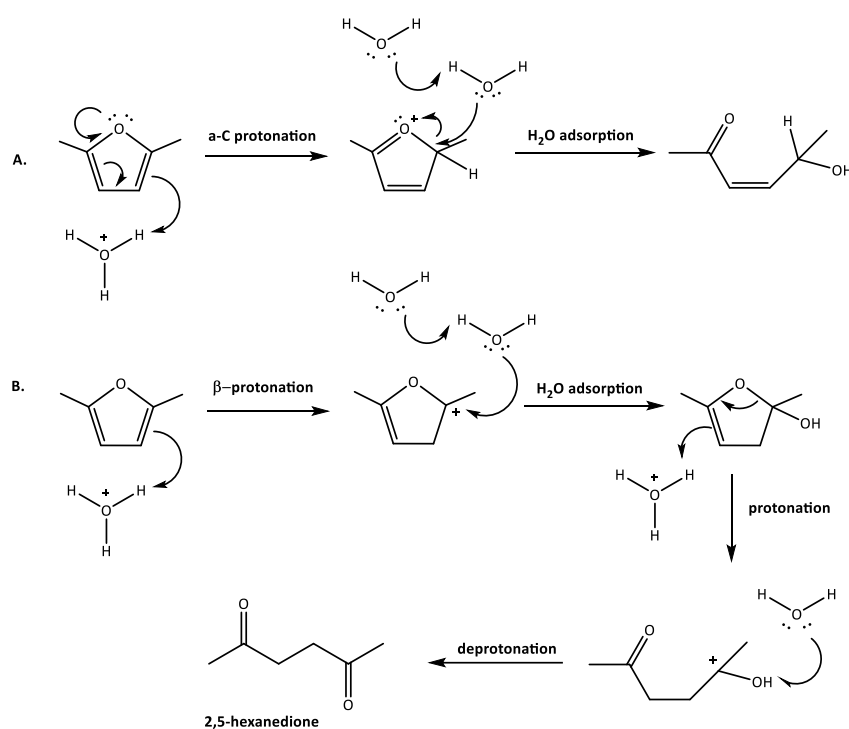


**Figure 1.26:** Reaction mechanisms for the Brønsted acid-catalysed hydrolysis of 2,5-DMF by A)  $\alpha$ -protonation B)  $\beta$ -protonation mechanisms based on NBO analysis.<sup>184</sup>

Acrolein, acrylic acid, and maleic anhydride have been investigated as more activated dienophiles in comparison with ethylene. Acrolein has been used in a Lewis acid-catalysed reaction with 2,5-DMF with the aim of forming *p*-xylene ( $-55\text{ }^{\circ}\text{C}$ , 0.1 %  $\text{Sc}(\text{OTf})_3$ ).<sup>187</sup> The cycloaddition of 2,5-DMF and acrolein is followed by the oxidation of the carbonyl group to produce a more stable intermediate prior to its dehydrative aromatisation under homogeneous Brønsted acidic conditions (15 min,  $0\text{ }^{\circ}\text{C}$ ) and a final decarboxylation step ( $210\text{ }^{\circ}\text{C}$ , 4 h) so that *p*-xylene is obtained in a 34 % yield (Figure 1.27). The addition of more than 0.5 % of  $\text{Sc}(\text{OTf})_3$  or higher loadings of other Lewis acid catalysts (e.g.  $\text{AlCl}_3$  and  $\text{ZnCl}_2$ ) resulted into a considerable decomposition of acrolein, even at low temperatures.<sup>187</sup> The use of molecular sieves was also required in order to avoid the decomposition of acrolein as well as for preventing the deactivation of the catalyst in the presence of water. Acrolein is a more activated dienophile in comparison with ethylene due to the electron-withdrawing carbonyl group. However, there are significant cooling requirements for the thermodynamically controlled DA reaction of 2,5-DMF and acrolein, independent of the catalytic conditions. In contrast, there is a requirement for heating to achieve the dehydration and decarboxylation steps required to finally afford *p*-xylene (Figure 1.27).<sup>176,187</sup>

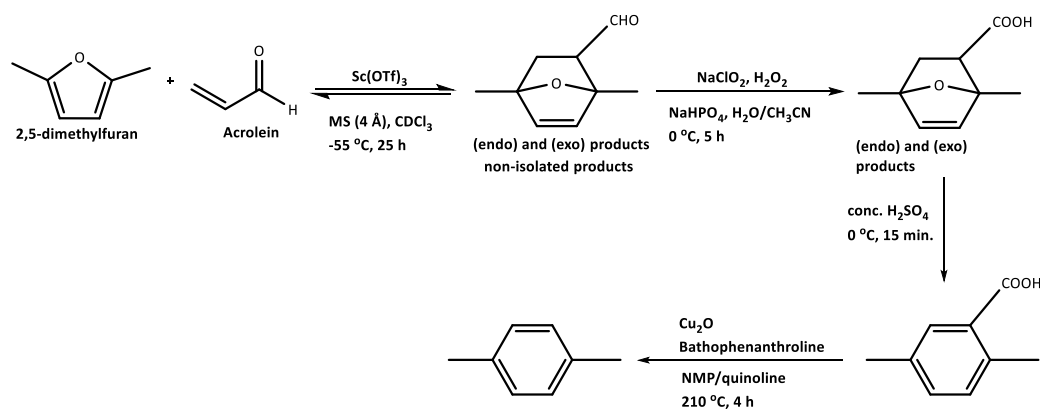


**Figure 1.27:** Formation of *p*-xylene and from the cycloaddition/dehydrative aromatisation of 2,5-DMF and acrolein <sup>187</sup>

Ionic liquids have also been tested, in combination with metal triflates, as alternative media for the tandem Diels-Alder/dehydration reaction of 2,5-DMF and acrylic acid.<sup>188</sup> ILs are known for enhancing the rate and selectivity of DA reactions, mainly via hydrogen-bonding between the IL components and a dienophile.<sup>189</sup> Such interactions can be rationalised by measuring the Kamlet-Taft parameters ( $\alpha$ ,  $\beta$ ,  $\pi^*$ ) of the applied IL and thus estimating its hydrogen bond acidity and polarity properties.<sup>189</sup>

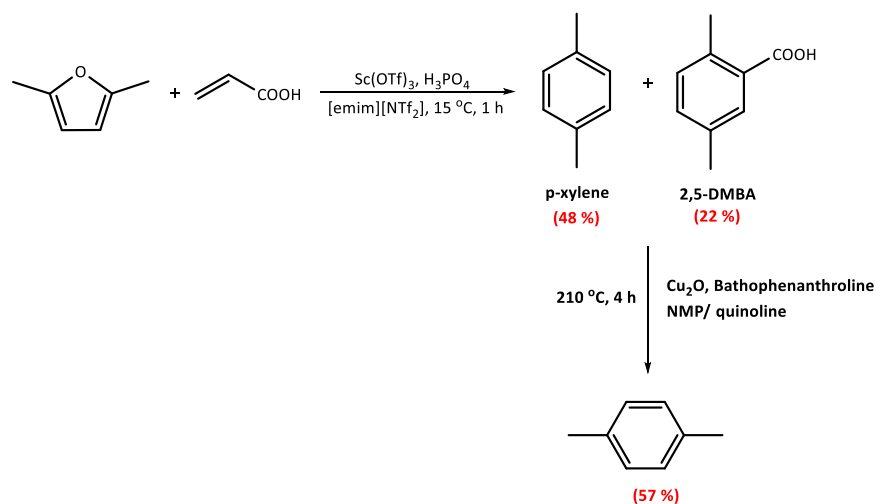


**Figure 1.28:** Reaction pathway for the conversion of 2,5-DMF into *p*-xylene and 2,5-DMBA<sup>188</sup>

The ionic liquid and Lewis acid combination,  $[\text{C}_2\text{C}_1\text{im}][\text{NTf}_2]/\text{Sc}(\text{OTf})_3$ , proved to be a good catalytic system for the synthesis of aromatics (*p*-xylene and 2,5-DMBA) from acrylic acid and 2,5-DMF with the IL stabilising the active reaction intermediates (**Figure 1.28**).<sup>188</sup> Additionally, the hydrophobic properties of  $[\text{NTf}_2]^-$  suppressed water-induced side-reactions and the deactivation of  $\text{Sc}(\text{OTf})_3$  by water. This water, is formed as a by-product of the dehydrative aromatization, forming a separate aqueous layer in the presence of  $[\text{C}_2\text{C}_1\text{im}][\text{NTf}_2]$ .<sup>188</sup> Increasing the reaction temperature from 15 °C to 90 °C enhanced side-

reactions such as the formation of 2,5-hexanedione.<sup>188</sup> The addition of a Brønsted acid promoted the dehydration step and increased the selectivity towards aromatics from 68 % for [C<sub>2</sub>C<sub>1</sub>im][NTf<sub>2</sub>]/Sc(OTf)<sub>3</sub> to 80 - 92 % upon addition of H<sub>3</sub>PO<sub>4</sub> (**Figure 1.28**). Obtaining pure *p*-xylene required a separate decarboxylation of 2,5-DMBA at 210 °C.<sup>188</sup> Both dehydration and decarboxylation are enhanced by higher temperatures whilst low-temperatures favour the cycloaddition and prevent the decomposition of the starting materials.<sup>161,188</sup>

Bifunctional catalysts containing both Brønsted and Lewis acid sites have been more efficient for the conversion of furan, 2-methylfuran, and 2,5-DMF over Lewis acidic solid catalysts, highlighting the significance of Brønsted acidity for the production of aromatics.<sup>173</sup> H-BEA zeolites proved to be more than an order of magnitude more active than other heterogeneous catalysts such as H-ZSM-5 and γ-Al<sub>2</sub>O<sub>3</sub>, exhibiting 90 % conversion for 2,5-DMF in 10 h over 50 – 60 % conversion in 30 h under similar reaction conditions.<sup>177</sup> Other furanic compounds such as 2-methylfuran, furfuryl alcohol and furfural have been tested in combination with ethylene or propylene, over a ZSM-5 zeolite in a fixed-bed reactor, furnishing a mixture of aromatics at high temperatures (450 – 600 °C).<sup>190</sup>

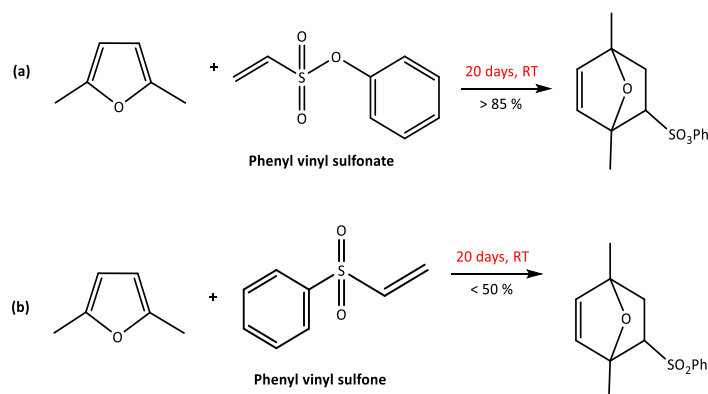


**Figure 1.29:** Cycloaddition of phenyl vinyl sulfonate (PVS(O)<sub>3</sub>) (a) and phenyl vinyl sulfone (PVS(O)<sub>2</sub>) (b) to 2,5-DMF.<sup>174,191</sup>

Phenyl vinyl sulfonate and phenyl vinyl sulfone have been previously tested as highly activated alkenes in the presence of furan or 2,5-DMF.<sup>174,191</sup> Long reaction times (20 h, rt) led to very good yields at room temperature even in the absence of a Lewis acid catalyst or a solvent that could promote further the cycloaddition reactions (Figure 1.29).<sup>191</sup> The activation of olefins by the addition of sulphur functionalities is controlled by the oxidation state of the sulphur atom; sulfoxides and sulfones induce electrophilicity and enhance the reactivity of the dienophile in the presence of electron-rich dienes.<sup>192</sup> The potential of an additional synthetic step involving reductive desulfonylation<sup>193</sup> or the removal of RSO<sub>2</sub>O- as a good leaving group would be an interesting option for the synthesis of aromatic compounds from furanics and phenyl vinyl sulfone or phenyl vinyl sulfonate (PVS(O)<sub>3</sub>) respectively.

Phthalic anhydride (PA) is a valuable building block for the production of plasticizers and unsaturated polyesters.<sup>194</sup> It is currently produced from the oxidation of petroleum-derived *o*-xylene whereas its irritant nature necessitates a replacement; the synthesis of bio-derived PA analogues is therefore a promising path towards the production of renewable polyesters and polycarbonates.<sup>195,196</sup> Similarly to the synthesis of bio-derived *p*-xylene, the use of bio-derived furanics towards the synthesis of phthalic anhydride derivatives is a tandem reaction: a cycloaddition to maleic anhydride (MA), followed by an acid-catalysed cycloadduct dehydration (Figure 1.30).<sup>197,198</sup>

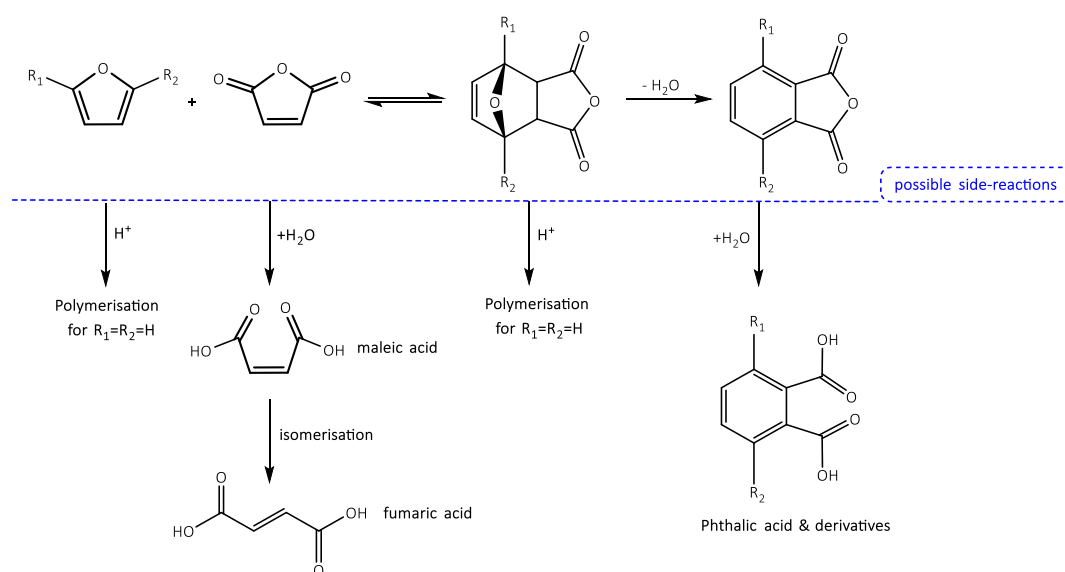


**Figure 1.30:** Synthesis of bio-derived phthalic anhydride (PA) derivatives from furanics and maleic anhydride (MA), followed by dehydrative aromatization and possible side-reactions under acidic conditions.

The *endo* cycloadduct is the predicted kinetic product whilst the *exo*-isomer is the thermodynamic product for the reaction of MA with furanics.<sup>172</sup> The inherent difficulties behind the stability of the adduct and the competition between the retro-DA reaction and the desired dehydrative aromatisation step have also been highlighted for the cycloaddition of furanoids and MA.<sup>198</sup> Additionally, phthalic acid derivatives, fumaric acid and maleic acid have been detected as reaction by-products upon hydrolysis of phthalic anhydride and maleic anhydride respectively whereas the overall selectivity is enhanced upon increasing the substitution of the diene (Figure 1.30).<sup>198</sup> The acid-catalysed hydrolysis of phthalic anhydride has been estimated as being eight times faster than that of 3,6-dimethylphthalic anhydride (3,6-DMPA), mainly due to differences in the entropy of the respective hydrolysis reaction, with the methyl groups driving the cyclisation of the diacid into 3,6-DMPA.<sup>199</sup> Maleic acid and fumaric acid correspond to the different configurations of butenedioic acid with the former being the *cis* isomer and the latter being the *trans* isomer. Fumaric acid is obtained from the acid-catalysed *cis-trans* isomerisation of maleic acid, enhanced by thermal treatment or even the addition of a polar solvent.<sup>200</sup>



The formation of fumaric acid upon the nonconcerted retro-DA cycloaddition of furanics and MA has also been proposed in addition to the direct isomerisation of maleic acid into fumaric acid.<sup>201</sup>

An early example of 3,6-dimethylphthalic anhydride (3,6-DMPA) synthesis was reported in 1944, proceeding with the cycloaddition of 2,5-DMF and MA in diethyl ether (rt, 4h; 85 %) prior to the dehydration of the isolated adduct with the latter reaction requiring temperature control (0 – 10 °C) and strong Brønsted acidity, affording moderate yields of pure phthalic anhydride (< 30 %).<sup>202</sup> Yields were improved by using concentrated H<sub>2</sub>SO<sub>4</sub> in sulfolane for the synthesis of 3-methylphthalic anhydride (66 %). However, for this to be achieved, the reaction temperature was maintained at -55 °C in order to control the unfavourable retro-DA reaction and such low temperatures render this approach industrially irrelevant.<sup>197,203</sup> Nearly quantitative yields (96 %) were obtained for the cycloaddition of MA and furan even under solvent and catalyst-free conditions (rt, 4 h).<sup>198</sup> However, the dehydration of the oxanorborene intermediate to phthalic anhydride (selectivity: 80 %) was achieved with mixed sulfonic carboxylic anhydrides such as acetyl methanesulfonate.<sup>198</sup>

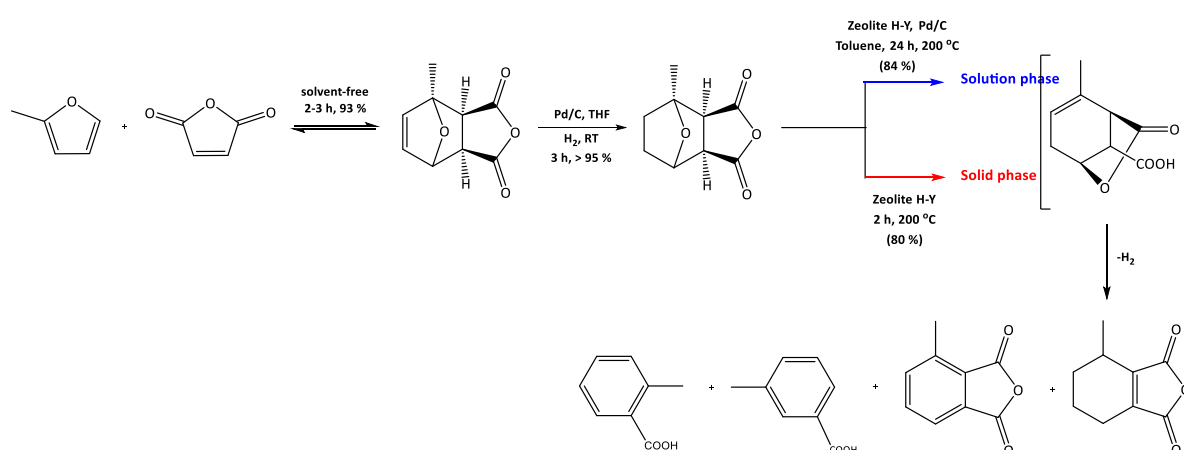


**Figure 1.31:** Alternative catalytic route to renewable aromatics from maleic anhydride (MA) and furanics via a solution or solid-phase conversion of the hydrogenated cycloadduct<sup>204</sup>

The use of an alternative three-step process has been proposed for addressing the reversible nature of the cycloaddition of furanics to maleic anhydride, affording a combined selectivity of 84 % for all aromatics.<sup>197</sup> This synthetic strategy involved the hydrogenation of the cycloadduct to a thermally stable hydrogenated DA adduct prior to the final aromatisation (Figure 1.31).<sup>197,204,205</sup> Nonetheless, such an approach requires additional reaction steps and tandem catalysis for the dehydrative aromatisation where both a metal-based dehydrogenation catalyst and a solid acid dehydration catalyst were used.<sup>197</sup> The optimisation of HY zeolites with strong Brønsted acid sites and mesoporosity led to a successful tandem dehydration/dehydrogenation in the solid phase, omitting the addition of a transition metal

dehydrogenation catalyst yet still obtaining a combined yield of 80 % for all aromatics (Figure 1.31).<sup>204</sup> DFT calculations on the acid-catalysed cycloaddition between 2,5-DMF and MA and the subsequent dehydrative aromatisation suggested that a single Brønsted acid could potentially catalyse both reaction steps with solvent effects becoming prominent mainly for a Lewis acid-catalysed dehydration step.<sup>206,207</sup>

In conclusion, the synthesis of aromatics from bio-derived furans and appropriate dienophiles may benefit from the efficient combination of the cycloaddition step with the dehydrative aromatization due to the lack of stability of the cycloadduct intermediate that is often prone to the retro-Diels-Alder reaction. The different reaction conditions required for the steps of the Diels-Alder/dehydration scheme remain the main challenge. Brønsted acidity promotes the dehydration reaction whereas Lewis acidic catalysts can better reduce the activation energy for the Diels-Alder reaction especially when less activated dienophiles are employed. Nevertheless, controlling the selectivity, especially under Brønsted acidic conditions, must be considered. Low-temperature conditions effectively control the retro-Diels-Alder reactions, reducing the decomposition of starting materials and enhancing the metrics of the cycloaddition reaction. However, high temperatures promote the dehydration and/or decarboxylation reactions, decreasing the yield of aromatics due to the formation of side-products.

## 1.6 Project aims and objectives

The transition from an economy that is heavily reliant on oil to a bio-based economy clearly requires the development of sustainable processes for producing both fuels and a wide range of platform chemicals. Bio-based furanics, such as 5-(hydroxymethyl)furfural (5-HMF) and 2,5-dimethylfuran (2,5-DMF), are obtained from lignocellulosic biomass via the acid-catalysed dehydration of sugars. From this literature review, it became apparent that a great number of chemical transformations have been attempted for the functional groups of 5-HMF, mainly focusing on oxidation and reduction reactions. It was also deduced that 2,5-DMF has been predominantly used as a diene for the formation of bio-based aromatics; albeit with relatively low selectivity and variable catalyst requirements for the tandem cycloaddition and the dehydrative aromatization reactions. However, to date, limited research has been dedicated on converting bio-based furanics to other high-value heterocyclic compounds. The overarching project objective was therefore to study novel reaction protocols for synthesizing heterocyclics and aromatics from established biomass intermediates, using ionic liquids as catalysts/ co-catalysts. Ionic liquids have proved to be excellent solvents and catalysts with applications ranging from biomass pretreatment to the synthesis of bio-derived platform chemicals; hence showing a promise for a holistic implementation in biorefining. In the context of producing high-value heterocyclic compounds, the synthesis of thiophene analogues was attempted by using acidic ionic liquids to promote the recyclization of bio-derived furans under mild conditions, when compared to current protocols of thiophene synthesis from heterocyclic or non-heterocyclic precursors (Chapter 2). A separate study of chlorometallate ionic liquids was conducted to elucidate several physicochemical properties of the IL-based catalysts that were employed in both batch and continuous gas-phase reactions. Finally, the cascade reaction between 2,5-DMF and maleic anhydride (MA) towards the formation of 3,6-dimethylphthalic anhydride (3,6-DMPA), a versatile precursor for polymer synthesis, was also chosen to be studied. The literature review clearly indicated that 5-HMF is not an activated diene whereas the synthesis of 3,6-DMPA, or other aromatics, from 2,5-DMF requires strategies of multiple synthetic steps with low to moderate yields for the dehydrative aromatization of the isolated cycloadduct. Ionic liquids and binary systems of ionic liquids and Brønsted acids were opted as acidic media to promote the tandem Diels-Alder/dehydrative aromatization reaction between 2,5-DMF and MA.

## 1.7 Thesis outline

**Chapter 1** provides a literature review of biorefining as an alternative to oil refining. The chapter begins by introducing the motivations behind the transition from the current oil-based economy to a bio-economy where fuels and chemicals are produced in an integrated biorefinery. The multifaceted challenges of the bioeconomy development are highlighted, followed by a discussion of the application of lignocellulose as a promising second generation biorefinery feedstock. A focus on the holistic application of ionic liquids as sustainable solvents and catalysts/co-catalysts, from biomass pretreatment to the preparation of platform chemicals, is also provided. The final sections give an overview on how bio-based furanoids, 5-HMF and 2,5-DMF, have been used as platform chemicals for the preparation of high-value commodity chemicals via the transformation of their functional groups and/or the furan moiety. Attention is paid to the reported research on the 5-HMF conversion into other heterocyclic compounds and its application as a diene in tandem cycloaddition/dehydrative aromatization reactions (in comparison to 2,5-DMF) as a platform chemical to produce aromatics.

**Chapter 2** discusses the investigation of acidic ionic liquids as homogeneous catalysts for the synthesis of thiophene derivatives upon the recyclization of bio-based furanics, concentrating on the liquid/liquid interfacial synthesis of 2,5-dimethylthiophene (2,5-DMT). The Chapter begins by providing a brief description of acidic ionic liquids with Brønsted acidic and/or Lewis acidic properties. A summary of their key physicochemical properties and applications is presented, discussing on how those are affected mainly by anionic speciation and the resulting modifications in the existing intramolecular interactions. The second part of this Chapter reviews the current synthetic protocols of thiophenes from heterocyclic or non-heterocyclic precursors by either homogeneous or heterogeneous catalysis, assessing the respective challenges and opportunities. The application of ionic liquids as alternative catalysts/co-catalysts for the preparation of thiophene derivatives is also reviewed. The synthesis of thiophenes in ionic liquids has not been widely researched and only a few examples are available, mainly on their application on the cyclization of open-chain precursors. The synthesis of thiophenes from heterocyclic precursors in ionic liquids, used as catalysts, has not been previously reported. In this work, chlorometallate ionic liquids, based on  $\text{ZnCl}_2$ ,  $\text{FeCl}_3$  and  $\text{InCl}_3$ , are first synthesized and studied against their thermal stability and their interionic interactions as a function of their composition ( $X_{\text{MCl}_x}$ ). The Lewis acidity of these ionic liquids is largely attributed to the formation of polynuclear anions when the metal chloride molar fraction is over the stoichiometric neutral point. Confirming the anionic speciation and the acidity of the chlorometallate ionic liquids is achieved by mass spectrometry and IR spectroscopy, respectively. Dynamic and isothermal thermogravimetric analysis (TGA) is used to examine the superior short-term and long-term thermal stability of the studied ionic liquids. Capillary

NMR spectroscopy ( $^1\text{H}$ ,  $^{13}\text{C}$ ) is applied to obtain further information on the modification of the interionic interactions in the chlorometallate ILs as a function of  $X_{\text{MCl}_x}$ , attempting to understand how those could affect the thermal stability of chlorozincates(II). Lewis basic and Lewis acidic chlorozincates(II) are finally examined as catalysts towards the synthesis of thiophene derivatives from 5-HMF and 2,5-DMF. The Lewis acidic composition of  $[\text{C}_4\text{C}_1\text{im}]\text{Cl}\cdot\text{ZnCl}_2$  ( $X_{\text{ZnCl}_2} = 0.67$ ) successfully catalyses the recyclization of 2,5-DMF into 2,5-DMT with a clear effect of the anionic speciation ( $X_{\text{ZnCl}_2}$ ) on promoting the reaction. The outer atomic surface of the Lewis acidic compositions of the chlorozincate(II) ionic liquids ( $0.50 \leq X_{\text{ZnCl}_2} \leq 0.75$ ) is also briefly studied by low-energy scattering spectroscopy (LEIS), indicating the availability of zinc for catalysis on the surface of the IL while being in the form of oligomeric species ( $[\text{Zn}_x\text{Cl}_{2x+2}]^{2-}$ ).

**Chapter 3** focuses on the application of Lewis acidic Supported Ionic Liquid Phases (SILPs) as catalysts for the synthesis of bio-derived thiophenes in a fluidised bed reactor (FBR). The Chapter provides a review on Supported Ionic Liquid Phase systems (SILP), focusing on their application continuous flow processes. The preparation of SILPs is presented. The SILP catalysts were prepared by the physisorption of  $[\text{C}_4\text{C}_1\text{im}]\text{Cl}\cdot\text{ZnCl}_2$  ( $X_{\text{ZnCl}_2} = 0.67$ ) onto silica supports of two different pore sizes: 60 Å and 150 Å. The surface characteristics of the parent supports and the acidic SILP catalysts are reviewed. The impregnation of the porous material with increasing loadings of  $[\text{C}_4\text{C}_1\text{im}]\text{Cl}\cdot\text{ZnCl}_2$  ( $X_{\text{ZnCl}_2} = 0.67$ ) resulted to a reduction of both the pore volume and the surface area, accompanied by an increase in the mean pore diameter; hence it is suggested that the smaller pores must be filled first upon increasing the loading of the ionic liquid. The narrowing of the BJH pore size distributions ( $dV/d\log D_p$ ) of the mesoporous region and the similar trend for the pore area distributions ( $dA/d\log D_p$ ) are provided as additional evidence. The application of solid-state NMR spectroscopy (ssNMR) is summarized, investigating the interactions between the Lewis acidic composition of  $[\text{C}_4\text{C}_1\text{im}]\text{Cl}\cdot\text{ZnCl}_2$  ( $X_{\text{ZnCl}_2} = 0.67$ ) and mesoporous silica gel as a function of the loading of the ionic liquid ( $\epsilon_{\text{IL}}$ ). The static spectra suggested that a transition towards a state of lower viscosity occurs at higher loadings, albeit the dynamics of bulk IL are not attained.  $^1\text{H}$  MAS NMR spectroscopy is used to provide evidence of IL/silanol interactions. Additionally, the determination of the  $^1\text{H}$   $T_1$  relaxation times across the imidazolium cation for the Lewis acidic ionic liquid is presented, proving that the dynamics of the ionic liquid were affected by pore wall/IL interactions. The impact of the IL/support interactions is discussed further in regards with their effect on the short-term thermal stability of the SILP catalysts. The fluidization behaviour of the Lewis acidic SILPs and the theoretical calculation of the fluidization velocity is also provided in this section, indicating excellent fluidization and heat transfer properties of the SILP materials. The design and construction of a spouted bed reactor, as a modified fluidised bed reactor, is described in detail given that it was used for studying the synthesis of bio-derived thiophenes with Lewis acidic SILPs. The experiments towards

the gas phase recyclization of bio-derived 2,5-dimethylfuran (2,5-DMF) into its thiophene analogue is described as a continuous process ( $P_{\text{abs}} = 2 \text{ bar}$ ,  $120 - 250 \text{ }^\circ\text{C}$ ) where gaseous mixtures of  $\text{H}_2\text{S}$  (1 – 5 %  $\text{H}_2\text{S}$ ,  $\text{H}_2\text{S}/\text{N}_2$ ) were applied. 2,5-DMF was introduced into the reactor in the vapour phase whereas optimizations in the design of the two-stage liquid sampling system allowed for a maximum recovery of the product mixtures that were qualitatively and quantitatively assessed. The preliminary experiments demonstrate a significant promise with the Lewis acidic SILP catalyst promoting the recyclization of 2,5-DMF to 2,5-DMT whilst 2,5-hexanedione was formed as one of the main intermediates. The opportunities and challenges of this process are discussed, providing an outlook for future work.

**Chapter 4** presents the application of ionic liquid-based catalytic systems for the direct synthesis of bio-derived 3,6-dimethylphthalic anhydride (3,6-DMPA), a potential monomer to produce renewable polyesters and polycarbonates. The current challenges of producing 3,6-DMPA are discussed. The current protocols require strategies of multiple synthetic steps, providing good yields for the cycloaddition reaction but low to moderate yields for the dehydrative aromatization of the isolated intermediate. The application of ionic liquids and binary systems of ionic liquids and Brønsted acids are presented for testing the tandem Diels-Alder/dehydrative aromatization reaction between 2,5-DMF and MA. The novel direct synthesis of 3,6-DMPA from 2,5-DMF and MA was achieved in acidic media based on  $[\text{C}_4\text{C}_1\text{im}][\text{NTf}_2]$  and trifluoromethane sulphonic acid (TFA) with a superior performance of TFA over  $\text{H}_2\text{SO}_4$ . The effect of both the catalytic loading and the reaction temperature are discussed together the challenge of controlling the formation of maleic acid and fumaric acid as the main by-products. The potential of further optimizing the system performance by finetuning the acidity and the viscosity of the reaction medium at lower temperatures is suggested.

## 1.8 References

- 1 S. Fernando, S. Adhikari, C. Chandrapal and N. Murali, *Energy & Fuels*, 2006, **20**, 1727–1737.
- 2 British Petroleum, *BP Statistical Review of World Energy*, 2016.
- 3 D. Gielen, F. Boshell and D. Saygin, *Nat. Mater.*, 2016, **15**, 117–120.
- 4 O. Ellabban, H. Abu-Rub and F. Blaabjerg, *Renew. Sustain. Energy Rev.*, 2014, **39**, 748–764.
- 5 S. K. Maity, *Renew. Sustain. Energy Rev.*, 2015, **43**, 1446–1466.
- 6 US Department of Agriculture (USDA), *U.S. Biobased Products Market Potential and Projections Through 2025, OCE-2008-01.*, .
- 7 Star-Colibri, *Star-COLIBRI (2011) Joint European Biorefinery Vision for 2030*, 2011.
- 8 F. Cherubini, *Energy Convers. Manag.*, 2010, **51**, 1412–1421.
- 9 S. Choi, C. W. Song, J. H. Shin and S. Y. Lee, *Metab. Eng.*, 2015, **28**, 223–239.
- 10 J. van Haveren, E. L. Scott and J. Sanders, *Biofuels, Bioprod. Biorefining*, 2008, **2**, 41–57.
- 11 UNEP, *Global Chemicals Outlook: Towards Sound Management of Chemicals*, 2013.
- 12 A. J. Ragauskas, C. K. Williams, B. H. Davison, G. Britovsek, J. Cairney, C. A. Eckert, W. J. Frederick, J. P. Hallett, D. J. Leak, C. L. Liotta, J. R. Mielenz, R. Murphy, R. Templer and T. Tschaplinski, *Science*, 2006, **311**, 484–9.
- 13 S. K. Maity, *Renew. Sustain. Energy Rev.*, 2015, **43**, 1427–1445.
- 14 A. Kumar and S. Sokhansanj, *Bioresour. Technol.*, 2007, **98**, 1033–1044.
- 15 T. L. Richard, *Science*, 2010, **329**, 793–796.
- 16 S. L. Naidu, *PLANT Physiol.*, 2003, **132**, 1688–1697.
- 17 H. Kobayashi and A. Fukuoka, *Green Chem.*, 2013, **15**, 1740–1763.
- 18 V. Menon and M. Rao, *Prog. Energy Combust. Sci.*, 2012, **38**, 522–550.
- 19 European Commission, *Communication from the commission to the European Parliament, the council, the European Economic and Social Committee and the Committee of the Regions.*, 2012.
- 20 IEA Bioenergy, *Bio-based Chemicals Value Added Products from Biorefineries (Task 42 Biorefinery)*, 2011.
- 21 D. J. Tenenbaum, *Environ. Health Perspect.*, 2008, **116**, A254–A257.
- 22 A. Brandt, J. Gräsvik, J. P. Hallett and T. Welton, *Green Chem.*, 2013, **15**, 550–583.
- 23 A. George, A. Brandt, K. Tran, S. M. S. N. S. Zahari, D. Klein-Marcuschamer, N. Sun, N. Sathitsuksanoh, J. Shi, V. Stavila, R. Parthasarathi, S. Singh, B. M. Holmes, T. Welton, B. a. Simmons and J. P. Hallett, *Green Chem.*, 2015, **17**, 1728–1734.
- 24 Y. Y. Tye, K. T. Lee, W. N. Wan Abdullah and C. P. Leh, *Renew. Sustain. Energy Rev.*, 2016, **60**, 155–172.
- 25 J. Y. Zhu and X. J. Pan, *Bioresour. Technol.*, 2010, **101**, 4992–5002.
- 26 P. Alvira, E. Tomás-Pejó, M. Ballesteros and M. J. Negro, *Bioresour. Technol.*, 2010, **101**, 4851–

- 4861.
- 27 N. MOSIER, *Bioresour. Technol.*, 2005, **96**, 673–686.
- 28 A. Brandt, J. Gräsvik, J. P. Hallett and T. Welton, *Green Chem.*, 2013, **15**, 550.
- 29 S. Haghighi Mood, A. Hossein Golfeshan, M. Tabatabaei, G. Salehi Jouzani, G. H. Najafi, M. Gholami and M. Ardjmand, *Renew. Sustain. Energy Rev.*, 2013, **27**, 77–93.
- 30 G. Fiorentino, M. Ripa and S. Ulgiati, *Biofuels, Bioprod. Biorefining*, 2017, **11**, 195–214.
- 31 R.-J. van Putten, J. C. van der Waal, E. de Jong, C. B. Rasrendra, H. J. Heeres and J. G. de Vries, *Chem. Rev.*, 2013, **113**, 1499–1597.
- 32 J. J. Bozell and G. R. Petersen, *Green Chem.*, 2010, **12**, 539–554.
- 33 P. Anastas and N. Eghbali, *Chem. Soc. Rev.*, 2009, **39**, 301–312.
- 34 A. Singh, D. Pant, N. E. Korres, A.-S. Nizami, S. Prasad and J. D. Murphy, *Bioresour. Technol.*, 2010, **101**, 5003–5012.
- 35 T. M. Lammens, J. Potting, J. P. M. Sanders and I. J. M. De Boer, *Environ. Sci. Technol.*, 2011, **45**, 8521–8528.
- 36 C. M. Cai, T. Zhang, R. Kumar and C. E. Wyman, *J. Chem. Technol. Biotechnol.*, 2014, **89**, 2–10.
- 37 M. E. Zakrzewska, E. Bogel-Lukasik and R. Bogel-Lukasik, *Chem. Rev.*, 2011, **111**, 397–417.
- 38 A. a. Rosatella, S. P. Simeonov, R. F. M. Frade and C. a. M. Afonso, *Green Chem.*, 2011, **13**, 754.
- 39 T. Ståhlberg, W. Fu, J. M. Woodley and A. Riisager, *ChemSusChem*, 2011, **4**, 451–458.
- 40 X. Qi, M. Watanabe, T. M. Aida and R. L. Smith, *ChemSusChem*, 2010, **3**, 1071–1077.
- 41 C. Sievers, I. Musin, T. Marzaletti, M. B. Valenzuela Olarte, P. K. Agrawal and C. W. Jones, *ChemSusChem*, 2009, **2**, 665–671.
- 42 X. Chen, S. L. Chew, F. M. Kerton and N. Yan, *Green Chem.*, 2014, 2204–2212.
- 43 K. Anastasakis, A. B. Ross and J. M. Jones, *Fuel*, 2011, **90**, 598–607.
- 44 P. Azadi, O. R. Inderwildi, R. Farnood and D. A. King, *Renew. Sustain. Energy Rev.*, 2013, **21**, 506–523.
- 45 A. J. Ragauskas, G. T. Beckham, M. J. Bidy, R. Chandra, F. Chen, M. F. Davis, B. H. Davison, R. a Dixon, P. Gilna, M. Keller, P. Langan, A. K. Naskar, J. N. Saddler, T. J. Tschaplinski, G. a Tuskan and C. E. Wyman, *Science (80-. )*, 2014, **344**, 1246843–1246843.
- 46 G. Rødsrud, M. Lersch and A. Sjöde, *Biomass and Bioenergy*, 2012, **46**, 46–59.
- 47 Z. Strassberger, S. Tanase and G. Rothenberg, *RSC Adv.*, 2014, **4**, 25310–25318.
- 48 A. Rahimi, A. Ulbrich, J. J. Coon and S. S. Stahl, *Nature*, 2014, **515**, 249–252.
- 49 A. K. Deepa and P. L. Dhepe, *ACS Catal.*, 2015, **5**, 365–379.
- 50 K. Barta, G. R. Warner, E. S. Beach and P. T. Anastas, *Green Chem.*, 2014, **16**, 191–196.
- 51 A. J. Ragauskas, *Science (80-. )*, 2006, **311**, 484–489.



- 52 J. P. Hallett and T. Welton, *Chem. Rev.*, 2011, **111**, 3508–3576.
- 53 H. Tokuda, K. Hayamizu, K. Ishii, M. A. B. H. Susan and M. Watanabe, *J. Phys. Chem. B*, 2004, **108**, 16593–16600.
- 54 H. Tokuda, K. Hayamizu, K. Ishii, M. A. B. H. Susan and M. Watanabe, *J. Phys. Chem. B*, 2005, **109**, 6103–6110.
- 55 T. Welton, *Chem. Rev.*, 1999, **99**, 2071–2084.
- 56 F. H. Hurley and T. P. Wier, *J. Electrochem. Soc.*, 1951, **98**, 203–206.
- 57 J. S. Wilkes, J. A. Levisky, R. A. Wilson and C. L. Hussey, *Inorg. Chem.*, 1982, **21**, 1263–1264.
- 58 P. Bonhôte, A.-P. Dias, N. Papageorgiou, K. Kalyanasundaram and M. Grätzel, *Inorg. Chem.*, 1996, **35**, 1168–1178.
- 59 A. P. Abbott, G. Capper, D. L. Davies, H. L. Munro, R. K. Rasheed and V. Tambyrajah, *Chem. Commun.*, 2001, 2010–2011.
- 60 N. V. Plechkova and K. R. Seddon, *Chem Soc Rev*, 2008, **37**, 123–150.
- 61 A. Stark, *Energy Environ. Sci.*, 2011, **4**, 19–32.
- 62 L. Crowhurst, P. R. Mawdsley, J. M. Perez-Arlandis, P. A. Salter and T. Welton, *Phys. Chem. Chem. Phys.*, 2003, **5**, 2790–2794.
- 63 P. Wasserscheid and T. Welton, *Ionic liquids in synthesis*, John Wiley & Sons Ltd., 2008.
- 64 G. Yu, D. Zhao, L. Wen, S. Yang and X. Chen, *AIChE J.*, 2012, **58**, 2885–2899.
- 65 K. R. Seddon, A. Stark and M. J. Torres, *Pure Appl. Chem.*, 2000, **72**, 2275–2287.
- 66 L. Chen, M. Sharifzadeh, N. Mac Dowell, T. Welton, N. Shah and J. P. Hallett, *Green Chem.*, 2014, **16**, 3098.
- 67 Y. Cao and T. Mu, *Ind. Eng. Chem. Res.*, 2014, **53**, 8651–8664.
- 68 T. L. Greaves and C. J. Drummond, *Chem. Rev.*, 2008, **108**, 206–237.
- 69 C. Maton, N. De Vos and C. V Stevens, *Chem. Soc. Rev.*, 2013, **42**, 5963–5977.
- 70 Y. Chen, Y. Cao, Y. Shi, Z. Xue and T. Mu, *Ind. Eng. Chem. Res.*, 2012, **51**, 7418–7427.
- 71 S. Sowmiah, V. Srinivasadesikan, M.-C. Tseng and Y.-H. Chu, *Molecules*, 2009, **14**, 3780–3813.
- 72 B. Wang, L. Qin, T. Mu, Z. Xue and G. Gao, *Chem. Rev.*, 2017, **117**, 7113–7131.
- 73 M. Amde, J.-F. Liu and L. Pang, *Environ. Sci. Technol.*, 2015, **49**, 12611–12627.
- 74 R. Biczak, B. Pawłowska, P. Bałczewski and P. Rychter, *J. Hazard. Mater.*, 2014, **274**, 181–190.
- 75 Y. Zhao, J. Zhao, Y. Huang, Q. Zhou, X. Zhang and S. Zhang, *J. Hazard. Mater.*, 2014, **278**, 320–329.
- 76 S. Steudte, J. Neumann, U. Bottin-Weber, M. Diedenhofen, J. J. J. Arning, P. Stepnowski and S. Stolte, *Green Chem.*, 2012, **14**, 2474–2483.
- 77 A. Pinkert, K. N. Marsh, S. Pang and M. P. Staiger, *Chem. Rev.*, 2009, **109**, 6712–6728.

- 78 A. Brandt, J. P. Hallett, D. J. Leak, R. J. Murphy and T. Welton, *Green Chem.*, 2010, **12**, 672.
- 79 A. Brandt, J. K. Erickson, J. P. Hallett, R. J. Murphy, A. Potthast, M. J. Ray, T. Rosenau, M. Schrems and T. Welton, *Green Chem.*, 2012, **14**, 1079–1085.
- 80 P. Weerachanchai and J.-M. Lee, *Bioresour. Technol.*, 2014, **169**, 336–343.
- 81 M. T. Clough, K. Geyer, P. A. Hunt, S. Son, U. Vagt and T. Welton, *Green Chem.*, 2015, **17**, 231–243.
- 82 L. Feng and Z. Chen, *J. Mol. Liq.*, 2008, **142**, 1–5.
- 83 R. C. Remsing, R. P. Swatloski, R. D. Rogers and G. Moyna, *Chem. Commun.*, 2006, 1271–1273.
- 84 H. Jørgensen, J. B. Kristensen and C. Felby, *Biofuels, Bioprod. Biorefining*, 2007, **1**, 119–134.
- 85 X. Tian, Z. Fang, D. Jiang, X. Sun, K. Gray, L. Zhao, M. Emptage, N. Mosier, C. Wyman, B. Dale, R. Elander, Y. Lee, M. Holtzapple, M. Gharpuray, Y. Lee, L. Fan, T. Heinze, T. Liebert, M. Galbe, G. Zacchi, R. Swatloski, S. Spear, J. Holbrey, R. Rogers, J. Wu, J. Zhang, H. Zhang, J. He, Q. Ren, M. Guo, D. Phillips, L. Drummy, D. Conrady, D. Fox, R. Naik, M. Stone, A. Dadi, S. Varanasi, C. Schall, Q. Li, Y. He, M. Xian, G. Jun, X. Xu, J. Yang, Q. Li, X. Jiang, Y. He, L. Li, M. Xian, J. Yang, M. Mora-Pale, L. Meli, T. Doherty, R. Linhardt, J. Dordick, M. Zavrel, D. Bross, M. Funke, J. Buchs, A. Spiess, S. Zhu, R. Rinaldi, A. Pinkert, K. Marsh, S. Pang, M. Staiger, B. Kosan, C. Michels, F. Meister, X. Sui, J. Yuan, W. Yuan, M. Zhou, M. Luo, A. Neogi, H. West, C. Han, S. Ha, L. Ngoc, G. An, Y. Koo, H. Zhang, J. Wu, J. Zhang, J. He, R. Lungwitz, S. Spange, T. Doherty, M. Mora-Pale, S. Foley, R. Linhardt, J. Dordick, C. Kuo, C. Lee, J. Hong, X. Ye, Y. Zhang, L. Rahkamo, L. Viikari, J. Buchert, T. Paakkari, T. Suortti, I. Kilpelainen, H. Xie, A. King, M. Granstrom, S. Heikkinen, D. Argyropoulos, J. Zhang, J. Luo, D. Tong, L. Zhu, L. Dong, C. Hu, A. Hendriks, G. Zeeman, Y. Zhang, L. Lynd, C. Wyman, C. Liu, K. Ohmine, H. Ooshima, Y. Harano, S. Abu-Eishah, K. Haerens, S. Van Deuren, E. Matthijs, B. Van der Bruggen, K. Shill, S. Padmanabhan, Q. Xin, J. Prausnitz, D. Clark, H. Blanch, G. Singh, A. Kumar, C. Seeton, C. Boned, C. Zeberg-Mikkelsen, A. Baylaucq, P. Daug, M. Dubois, K. Gilles, J. Hamilton, P. Rebers, F. Smith, M. Selig, N. Weiss and Y. Ji, *Biotechnol. Biofuels*, 2011, **4**, 53.
- 86 A. P. Dadi, S. Varanasi and C. A. Schall, *Biotechnol. Bioeng.*, 2006, **95**, 904–910.
- 87 H. Zhao, C. L. Jones, G. A. Baker, S. Xia, O. Olubajo and V. N. Person, *J. Biotechnol.*, 2009, **139**, 47–54.
- 88 P. Engel, R. Mladenov, H. Wulfhorst, G. Jäger and A. C. Spiess, *Green Chem.*, 2010, **12**, 1959–1966.
- 89 H. Zhao, *J. Chem. Technol. Biotechnol.*, 2010, **85**, 891–907.
- 90 S. Krawielitzki and T. M. Kläusli, *Ind. Biotechnol.*, 2015, **11**, 6–8.
- 91 C. Fayet and J. Gelas, *Carbohydr. Res.*, 1983, **122**, 59–68.
- 92 C. Lansalot-Matras and C. Moreau, *Catal. Commun.*, 2003, **4**, 517–520.

- 93 Q. Bao, K. Qiao, D. Tomida and C. Yokoyama, *Catal. Commun.*, 2008, **9**, 1383–1388.
- 94 S. Eminov, J. D. E. T. Wilton-Ely and J. P. Hallett, *ACS Sustain. Chem. Eng.*, 2014, **2**, 978–981.
- 95 J. Y. G. Chan and Y. Zhang, *ChemSusChem*, 2009, **2**, 731–734.
- 96 H. Zhao, J. E. Holladay, H. Brown and Z. C. Zhang, *Science (80-. )*, 2007, **316**, 1597–1600.
- 97 Y. Zhang, E. A. Pidko and E. J. M. Hensen, *Chem. - A Eur. J.*, 2011, **17**, 5281–5288.
- 98 S. Eminov, A. Brandt, J. D. E. T. Wilton-Ely and J. P. Hallett, *PLoS One*, 2016, **11**, e0163835.
- 99 M. Moliner, Y. Roman-Leshkov and M. E. Davis, *Proc. Natl. Acad. Sci.*, 2010, **107**, 6164–6168.
- 100 A. Mukherjee, M.-J. Dumont and V. Raghavan, *Biomass and Bioenergy*, 2015, **72**, 143–183.
- 101 C. Li, Z. Zhang and Z. K. Zhao, *Tetrahedron Lett.*, 2009, **50**, 5403–5405.
- 102 Z. Zhang and Z. K. Zhao, *Bioresour. Technol.*, 2010, **101**, 1111–1114.
- 103 S. Eminov, P. Filippousi, A. Brandt, J. Wilton-Ely and J. Hallett, *Inorganics*, 2016, **4**, 32.
- 104 H. Wang, S. Liu, Y. Zhao, H. Zhang and J. Wang, *ACS Sustain. Chem. Eng.*, 2016, **4**, 6712–6721.
- 105 T. Singh and A. Kumar, *J. Phys. Chem. B*, 2007, **111**, 7843–7851.
- 106 P. Y. Nikolov and V. A. Yaylayan, *J. Agric. Food Chem.*, 2011, **59**, 10104–10113.
- 107 P. Chambel, M. . Oliveira, P. . Andrade, J. . Fernandes, R. . Seabra and M. . Ferreira, *Food Chem.*, 1998, **63**, 473–477.
- 108 Z. Wei, Y. Liu, D. Thushara and Q. Ren, *Green Chem.*, 2012, **14**, 1220.
- 109 X. Sun, Z. Liu, Z. Xue, Y. Zhang and T. Mu, *Green Chem.*, 2015, **17**, 2719–2722.
- 110 M. Mascal and E. B. Nikitin, *Angew. Chemie Int. Ed.*, 2008, **47**, 7924–7926.
- 111 E. Meller, A. Aviv, Z. Aizenshtat and Y. Sasson, *RSC Adv.*, 2016, **6**, 36069–36076.
- 112 M. Zuo, Z. Li, Y. Jiang, X. Tang, X. Zeng, Y. Sun and L. Lin, *RSC Adv.*, 2016, **6**, 27004–27007.
- 113 M. Mascal, *ChemSusChem*, 2015, **8**, 3391–3395.
- 114 M. Mascal and S. Dutta, *Green Chem.*, 2011, **13**, 3101.
- 115 M. Besson, P. Gallezot and C. Pinel, *Chem. Rev.*, 2014, **114**, 1827–1870.
- 116 D. Zhang and M.-J. Dumont, *J. Polym. Sci. Part A Polym. Chem.*, , DOI:10.1002/pola.28527.
- 117 L. Hu, L. Lin, Z. Wu, S. Zhou and S. Liu, *Renew. Sustain. Energy Rev.*, 2017, **74**, 230–257.
- 118 Z. Xu, P. Yan, W. Xu, S. Jia, Z. Xia, B. Chung and Z. C. Zhang, *RSC Adv.*, 2014, **4**, 59083–59087.
- 119 O. Casanova, S. Iborra and A. Corma, *J. Catal.*, 2009, **265**, 109–116.
- 120 P. Lanzafame, D. M. Temi, S. Perathoner, G. Centi, A. Macario, A. Aloise and G. Giordano, *Catal. Today*, 2011, **175**, 435–441.
- 121 H. Li, Z. Fang, R. L. Smith and S. Yang, *Prog. Energy Combust. Sci.*, 2016, **55**, 98–194.
- 122 A. F. Sousa, C. Vilela, A. C. Fonseca, M. Matos, C. S. R. Freire, G.-J. M. Gruter, J. F. J. Coelho and A. J. D. Silvestre, *Polym. Chem.*, 2015, **6**, 5961–5983.
- 123 Z. Zhang and K. Deng, *ACS Catal.*, 2015, **5**, 6529–6544.

- 124 M. Kröger, U. Prüße and K. Vorlop, *Top. Catal.*, 2000, **13**, 237–242.
- 125 J. Deng, H.-J. Song, M.-S. Cui, Y.-P. Du and Y. Fu, *ChemSusChem*, 2014, **7**, 3334–3340.
- 126 Y.-Z. Qin, Y.-M. Li, M.-H. Zong, H. Wu and N. Li, *Green Chem.*, 2015, **17**, 3718–3722.
- 127 K. T. Hopkins, W. D. Wilson, B. C. Bender, D. R. McCurdy, J. E. Hall, R. R. Tidwell, A. Kumar, M. Bajic and D. W. Boykin, *J. Med. Chem.*, 1998, **41**, 3872–3878.
- 128 A. S. Amarasekara, D. Green and L. D. Williams, *Eur. Polym. J.*, 2009, **45**, 595–598.
- 129 S. E. Davis, L. R. Houk, E. C. Tamargo, A. K. Datye and R. J. Davis, *Catal. Today*, 2011, **160**, 55–60.
- 130 T. Pompe, S. Zschoche, N. Herold, K. Salchert, M.-F. Gouzy, C. Sperling and C. Werner, *Biomacromolecules*, 2003, **4**, 1072–1079.
- 131 J. M. Sadler, F. R. Toulan, G. R. Palmese and J. J. La Scala, *J. Appl. Polym. Sci.*, 2015, **132**, n/a-n/a.
- 132 Z. Du, J. Ma, F. Wang, J. Liu and J. Xu, *Green Chem.*, 2011, **13**, 554.
- 133 J. Lan, J. Lin, Z. Chen and G. Yin, *ACS Catal.*, 2015, **5**, 2035–2041.
- 134 N. Gunasekaran, *Adv. Synth. Catal.*, 2015, **357**, 1990–2010.
- 135 J. Muzart, *Adv. Synth. Catal.*, 2006, **348**, 275–295.
- 136 T. Ståhlberg, E. Eyjólfsdóttir, Y. Y. Gorbanev, I. Sádaba and A. Riisager, *Catal. Letters*, 2012, **142**, 1089–1097.
- 137 J. Ohyama, A. Esaki, Y. Yamamoto, S. Arai and A. Satsuma, *RSC Adv.*, 2013, **3**, 1033–1036.
- 138 Y. Qian, L. Zhu, Y. Wang and X. Lu, *Renew. Sustain. Energy Rev.*, 2015, **41**, 633–646.
- 139 Y. Zu, P. Yang, J. Wang, X. Liu, J. Ren, G. Lu and Y. Wang, *Appl. Catal. B Environ.*, 2014, **146**, 244–248.
- 140 B. Saha, C. M. Bohn and M. M. Abu-Omar, *ChemSusChem*, 2014, **7**, 3095–3101.
- 141 Y. Román-Leshkov, C. J. Barrett, Z. Y. Liu and J. A. Dumesic, *Nature*, 2007, **447**, 982–985.
- 142 M. Chidambaram and A. T. Bell, *Green Chem.*, 2010, **12**, 1253.
- 143 J. M. Simmie and J. Würmel, *ChemSusChem*, 2013, **6**, 36–41.
- 144 J. M. R. Gallo, D. M. Alonso, M. A. Mellmer and J. A. Dumesic, *Green Chem.*, 2013, **15**, 85–90.
- 145 G.-Y. Jeong, A. K. Singh, S. Sharma, K. W. Gyak, R. A. Maurya and D.-P. Kim, *NPG Asia Mater.*, 2015, **7**, e173.
- 146 R. P. Utikar and V. V. Ranade, *ACS Sustain. Chem. Eng.*, 2017, **5**, 3607–3622.
- 147 K. F. Jensen, *AIChE J.*, 2017, **63**, 858–869.
- 148 C. Marisa, D. S. Ilaria, R. Marotta, A. Roberto and C. Vincenzo, *J. Photochem. Photobiol. A Chem.*, 2010, **210**, 69–76.
- 149 J. Horvat, B. Klaić, B. Metelko and V. Šunjić, *Tetrahedron Lett.*, 1985, **26**, 2111–2114.
- 150 K. Yan, C. Jarvis, J. Gu and Y. Yan, *Renew. Sustain. Energy Rev.*, 2015, **51**, 986–997.
- 151 V. Choudhary, S. H. Mushrif, C. Ho, A. Anderko, V. Nikolakis, N. S. Marinkovic, A. I. Frenkel, S. I.

- Sandler and D. G. Vlachos, *J. Am. Chem. Soc.*, 2013, **135**, 3997–4006.
- 152 R. S. Assary, P. C. Redfern, J. R. Hammond, J. Greeley and L. A. Curtiss, *J. Phys. Chem. B*, 2010, **114**, 9002–9009.
- 153 J. J. Roylance and K.-S. Choi, *Green Chem.*, 2016, **18**, 2956–2960.
- 154 D. Ren, Z. Song, L. Li, Y. Liu, F. Jin and Z. Huo, *Green Chem.*, 2016, **18**, 3075–3081.
- 155 D. I. Collias, A. M. Harris, V. Nagpal, I. W. Cottrell and M. W. Schultheis, *Ind. Biotechnol.*, 2014, **10**, 91–105.
- 156 Z. Lin, M. Ierapetritou and V. Nikolakis, *AIChE J.*, 2013, **59**, 2079–2087.
- 157 C. L. Williams, C.-C. Chang, P. Do, N. Nikbin, S. Caratzoulas, D. G. Vlachos, R. F. Lobo, W. Fan and P. J. Dauenhauer, *ACS Catal.*, 2012, **2**, 935–939.
- 158 J. J. Pacheco and M. E. Davis, *Proc. Natl. Acad. Sci.*, 2014, **111**, 8363–8367.
- 159 Y. Román-Leshkov and M. E. Davis, *ACS Catal.*, 2011, **1**, 1566–1580.
- 160 J. J. Pacheco, J. A. Labinger, A. L. Sessions and M. E. Davis, *ACS Catal.*, 2015, **5**, 5904–5913.
- 161 G. J. S. Dawes, E. L. Scott, J. Le Nôtre, J. P. M. Sanders and J. H. Bitter, *Green Chem.*, 2015, **17**, 3231–3250.
- 162 S. Higson, F. Subrizi, T. D. Sheppard and H. C. Hailes, *Green Chem.*, 2016, **18**, 1855–1858.
- 163 K. Joule, John A.; Mills, *Heterocyclic Chemistry*, Wiley-Blackwell, 2010.
- 164 P. Martins, J. Jesus, S. Santos, L. Raposo, C. Roma-Rodrigues, P. Baptista and A. Fernandes, *Molecules*, 2015, **20**, 16852–16891.
- 165 W. Wu, Y. Liu and D. Zhu, *Chem. Soc. Rev.*, 2010, **39**, 1489–1502.
- 166 A. F. Pozharskii, A. T. Soldatenkov and A. R. Katritzky, *Heterocycles in Life and Society*, John Wiley & Sons, Ltd, Chichester, UK, 2011.
- 167 C. Müller, V. Diehl and F. W. Lichtenthaler, *Tetrahedron*, 1998, **54**, 10703–10712.
- 168 F. W. Lichtenthaler, A. Brust and E. Cuny, *Green Chem.*, 2001, **3**, 201–209.
- 169 L. Xu, Q. Yao, J. Deng, Z. Han, Y. Zhang, Y. Fu, G. W. Huber and Q. Guo, *ACS Sustain. Chem. Eng.*, 2015, **3**, 2890–2899.
- 170 L. Tao, Z.-J. Wang, T.-H. Yan, Y.-M. Liu, H.-Y. He and Y. Cao, *ACS Catal.*, 2017, **7**, 959–964.
- 171 H. Cho, R. Madden, B. Nisanci and B. Török, *Green Chem.*, 2015, **17**, 1088–1099.
- 172 J. Sauer, *Angew. Chemie Int. Ed. English*, 1967, **6**, 16–33.
- 173 D. Wang, C. M. Osmundsen, E. Taarning and J. A. Dumesic, *ChemCatChem*, 2013, **5**, 2044–2050.
- 174 C. Oliver Kappe, S. Shaun Murphree and A. Padwa, *Tetrahedron*, 1997, **53**, 14179–14233.
- 175 J. M. Fraile, J. I. García, M. A. Gómez, A. de la Hoz, J. A. Mayoral, A. Moreno, P. Prieto, L. Salvatella and E. Vázquez, *European J. Org. Chem.*, 2001, **2001**, 2891.
- 176 A. Maneffa, P. Priecel and J. A. Lopez-Sanchez, *ChemSusChem*, 2016, **9**, 2736–2748.

- 177 C.-C. Chang, S. K. Green, C. L. Williams, P. J. Dauenhauer and W. Fan, *Green Chem.*, 2014, **16**, 585–588.
- 178 P. T. M. Do, J. R. McAtee, D. A. Watson and R. F. Lobo, *ACS Catal.*, 2013, **3**, 41–46.
- 179 N. Nikbin, P. T. Do, S. Caratzoulas, R. F. Lobo, P. J. Dauenhauer and D. G. Vlachos, *J. Catal.*, 2013, **297**, 35–43.
- 180 N. Nikbin, S. Feng, S. Caratzoulas and D. G. Vlachos, *J. Phys. Chem. C*, 2014, **118**, 24415–24424.
- 181 R. E. Patet, N. Nikbin, C. L. Williams, S. K. Green, C.-C. Chang, W. Fan, S. Caratzoulas, P. J. Dauenhauer and D. G. Vlachos, *ACS Catal.*, 2015, **5**, 2367–2375.
- 182 Y.-T. Cheng and G. W. Huber, *ACS Catal.*, 2011, **1**, 611–628.
- 183 R. Xiong, S. I. Sandler, D. G. Vlachos and P. J. Dauenhauer, *Green Chem.*, 2014, **16**, 4086.
- 184 N. Nikbin, S. Caratzoulas and D. G. Vlachos, *ChemSusChem*, 2013, **6**, 2066–2068.
- 185 A. and R. A. Kankaanpera, *Acta Chem. Scand*, 1972, **26**, 2537–2540.
- 186 G. Yang, E. A. Pidko and E. J. M. Hensen, *J. Catal.*, 2012, **295**, 122–132.
- 187 M. Shiramizu and F. D. Toste, *Chem. - A Eur. J.*, 2011, **17**, 12452–12457.
- 188 L. Ni, J. Xin, H. Dong, X. Lu, X. Liu and S. Zhang, *ChemSusChem*, , DOI:10.1002/cssc.201700020.
- 189 C. Chiappe, M. Malvaldi and C. S. Pomelli, *Green Chem.*, 2010, **12**, 1330.
- 190 Y.-T. Cheng and G. W. Huber, *Green Chem.*, 2012, **14**, 3114.
- 191 L. L. Klein and T. M. Deeb, *Tetrahedron Lett.*, 1985, **26**, 3935–3938.
- 192 O. de Lucchi and L. Pasquato, *Tetrahedron*, 1988, **44**, 6755–6794.
- 193 N. S. Simpkins, *Tetrahedron*, 1990, **46**, 6951–6984.
- 194 R. F. Fischer, *J. Polym. Sci.*, 1960, **44**, 155–172.
- 195 C. R. Dias, M. F. Portela and G. C. Bond, *J. Catal.*, 1995, **157**, 353–358.
- 196 S. Giarola, C. Romain, C. K. Williams, J. P. Hallett and N. Shah, *Chem. Eng. Res. Des.*, 2016, **107**, 181–194.
- 197 S. Thiyagarajan, H. C. Genuino, M. Śliwa, J. C. van der Waal, E. de Jong, J. van Haveren, B. M. Weckhuysen, P. C. A. Bruijninx and D. S. van Es, *ChemSusChem*, 2015, **8**, 3052–3056.
- 198 E. Mahmoud, D. A. Watson and R. F. Lobo, *Green Chem.*, 2014, **16**, 167–175.
- 199 M. D. Hawkins, *J. Chem. Soc. Perkin Trans. 2*, 1975, 282.
- 200 S. Chatterjee, V. R. Pedireddi and C. N. R. Rao, *Tetrahedron Lett.*, 1998, **39**, 2843–2846.
- 201 W. Shih, N. Lau and S. Seltzer, *J. Org. Chem.*, 1975, **40**, 1269–1274.
- 202 M. S. Newman and B. T. Lord, *J. Am. Chem. Soc.*, 1944, **66**, 733–735.
- 203 M. S. Newman and V. Lee, *J. Org. Chem.*, 1977, **42**, 1478–1479.
- 204 S. Thiyagarajan, H. C. Genuino, J. C. van der Waal, E. de Jong, B. M. Weckhuysen, J. van Haveren, P. C. A. Bruijninx and D. S. van Es, *Angew. Chemie Int. Ed.*, 2016, **55**, 1368–1371.

- 205 H. C. Genuino, S. Thiyagarajan, J. C. van der Waal, E. de Jong, J. van Haveren, D. S. van Es, B. M. Weckhuysen and P. C. A. Bruijninx, *ChemSusChem*, 2017, **10**, 277–286.
- 206 T. Salavati-fard, S. Caratzoulas and D. J. Doren, *Chem. Phys.*, 2017, **485–486**, 118–124.
- 207 T. Salavati-fard, S. Caratzoulas and D. J. Doren, *J. Phys. Chem. A*, 2015, **119**, 9834–9843.

## CHAPTER 2

### Ionic liquids as catalysts for the small-scale synthesis of bio-derived thiophenes

#### 2.1 Acidic ionic liquids

Acidic ionic liquids (ALLs) can have a Brønsted, Lewis or dual Brønsted/Lewis acidic character with the acidity deriving from the cation, the anion or both ionic species (Figure 2.1).<sup>1-4</sup> Lewis acidity usually arises from the presence of an anion with electron-accepting properties whereas Brønsted acidic ILs are composed of anions and/or cations with proton donor properties, forming protic or aprotic ILs.<sup>3,5,6</sup> An example of a Brønsted-Lewis acidic ionic liquid is illustrated in Figure 2.1 where an alkyl sulfonate functionalized cation is combined with a metal chloride-based anion with interesting catalytic properties. As an example, a synergistic effect has been observed for  $[\text{HO}_3\text{SC}_3\text{NET}]\text{Cl}\cdot\text{ZnCl}_2$  regarding selectivity improvements in alkylation reactions with the metal chloride exerting a great influence.<sup>7</sup>

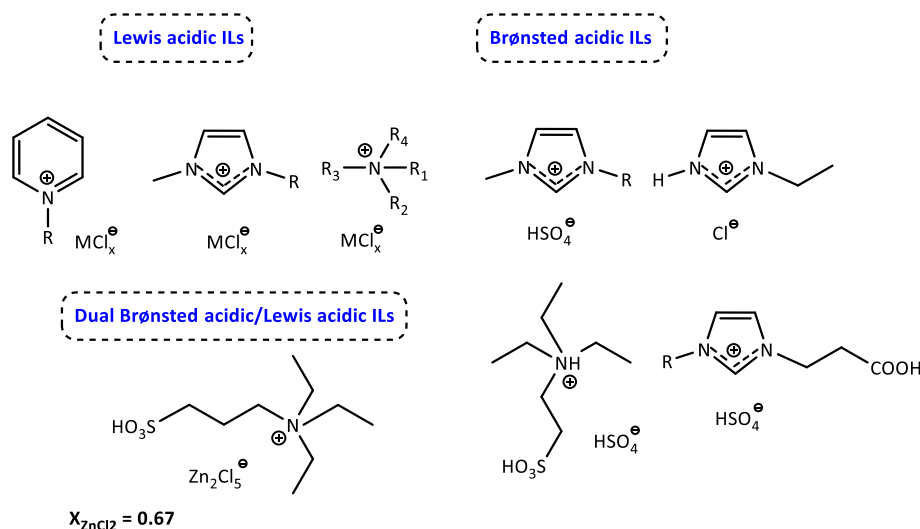


Figure 2.1: Examples of cations and anions of Lewis acidic, Brønsted acidic and dual acidic ionic liquids.

#### 2.1.1 Chlorometallate Lewis acidic ionic liquids overview

##### 2.1.1.1 General properties and applications of halometallate ILs

Lewis acidic ionic liquids are typically formed by mixing quaternary halide salts with a given molar ratio of a metal halide ( $X_{\text{MCl}_x}$ ) under anhydrous conditions so that monomeric and/or polynuclear anionic species are afforded in a dynamic equilibrium.<sup>2,3,8</sup> The enhanced conductivity properties, wide electrochemical window and tuneable acidity make halometallate ILs excellent electrolytes and

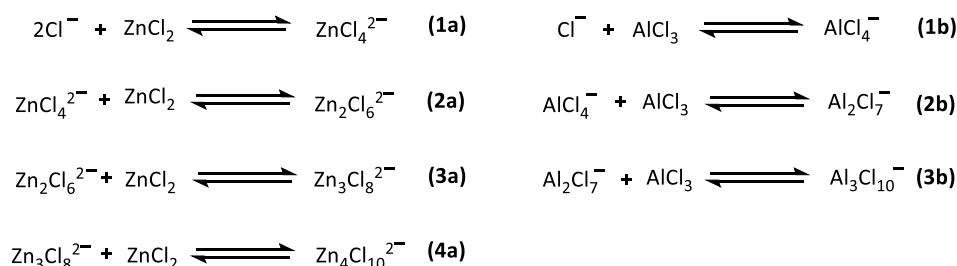


catalysts.<sup>3,9</sup> There is a plethora of published studies where Lewis acidic ILs were tested as catalysts for Friedel-Crafts alkylations,<sup>10</sup> acylations<sup>10</sup> and isomerization<sup>11</sup> reactions or even as separation media for the extraction of aromatics<sup>12</sup> and fuels desulfurisation<sup>13</sup>, as well as electrochemistry applications.<sup>14</sup> Chloroaluminate(III) ionic liquids with pyridinium or imidazolium cations were studied as part of the first generation of ILs.<sup>15,16</sup> However, chloroaluminates(III) are oxophilic and prone to hydrolysis in the presence of atmospheric moisture; making their handling challenging.<sup>8,17</sup> Infrared spectroscopy with pyridine as the basic probe has previously suggested a dual Lewis/Brønsted acidic character for chloroaluminates(III) with the Brønsted acidity arising from  $[\text{Al}_2\text{Cl}_6\text{OH}]^-$  combined with the release of HCl in the presence of moisture,<sup>3</sup> whereas Lewis acidity is induced by the formation of polynuclear anions.<sup>17</sup> A second generation of moisture-stable Lewis acidic ILs has been developed by using metal chlorides other than  $\text{AlCl}_3$  (e.g.  $\text{SnCl}_2$ ,  $\text{ZnCl}_2$ ).<sup>18,19</sup> Reversible stoichiometric hydration may still occur when water molecules coordinate to the metal centre of the anion, affecting the speciation but without a reported concomitant release of HCl.<sup>3</sup> Moisture-stable chlorozincates(II) have been tested as recyclable catalysts as well as media for Zn electrodeposition with a positive effect of increasing  $X_{\text{ZnCl}_2}$ .<sup>20,21</sup> Dialkylimidazolium chloroferrates(III)<sup>22</sup> exhibit hydrophobicity and a unique thermomorphic behaviour, forming biphasic mixtures with water at elevated temperatures.<sup>23</sup>  $[\text{FeCl}_4]^-$  ions were found to be in equilibrium with polynuclear ionic species as well as soluble iron(III) hydroxide hydrates such as  $[\text{Fe}(\text{OH})_x]^{3-}$  ( $x = 1$  or  $2$ ).<sup>23</sup> The magnetic characterization of imidazolium and phosphonium-based chloroferrate(III) ILs has confirmed their paramagnetic properties with a magnetic moment associated with the presence of the  $\text{Fe}^{3+}$  ion.<sup>24</sup> Magnetic ILs containing different transition metals have therefore attracted an increasing interest in catalysis<sup>25</sup> and separation<sup>26</sup> processes with chemical processing control benefits due to the facile solvent/catalyst separation.

### 2.1.1.2 Anionic speciation of halometallate ILs

Speciation is a key parameter affecting most physicochemical properties of chlorometallate ILs; it is significantly influenced by the metal chloride molar ratio ( $X_{\text{MCl}_x}$ ) as well as the coordination chemistry and the oxidation state of the metal.<sup>3,19,27,28</sup> Vibrational spectroscopy (Raman, IR), mass spectrometry (ESI, FAB), NMR spectroscopy and XPS are some of the techniques that have been applied for the determination of speciation in ILs in the liquid state.<sup>3,19,21,22,29–31</sup> The speciation in chloroaluminate(III) ionic liquids is well established; basic compositions ( $X_{\text{AlCl}_3} \leq 0.50$ ) contain  $\text{Cl}^-$  and  $[\text{AlCl}_4]^-$  with  $[\text{AlCl}_4]^-$  dominating neutral chloroaluminates(III) whereas  $[\text{Al}_2\text{Cl}_7]^-$  arises in Lewis acidic compositions and the complex  $[\text{Al}_3\text{Cl}_{10}]^-$  is found at  $X_{\text{AlCl}_3} > 0.67$  (Figure 2.2).<sup>32</sup> The characterisation of variable compositions of  $[\text{C}_4\text{C}_1\text{im}]\text{Cl}\cdot\text{ZnCl}_2$  by Raman Spectroscopy has indicated the presence of mononuclear  $[\text{ZnCl}_4]^{2-}$  at  $X_{\text{ZnCl}_2} < 0.33$  whereas both  $[\text{ZnCl}_4]^{2-}$  and  $[\text{Zn}_2\text{Cl}_6]^{2-}$  were detected for  $0.30 < X_{\text{ZnCl}_2} < 0.60$  and measurable amounts

of more complex clusters,  $[\text{Zn}_3\text{Cl}_8]^{2-}$  and  $[\text{Zn}_4\text{Cl}_{10}]^{2-}$ , were found at  $X_{\text{ZnCl}_2} = 0.75$  (Figure 2.2).<sup>33</sup> Raman spectroscopy mainly monitors the M-Cl bond vibrations ( $600 - 650 \text{ cm}^{-1}$ ) but further information is obtained by monitoring the C-H stretching frequencies related to the cation due to the anionic speciation changes that induce changes in the interactions between the ionic species.<sup>3</sup>



	Basic	Neutral	Acidic	Highly acidic
<b>chloroaluminates(III)</b>	$X_{\text{AlCl}_3} < 0.50$	$X_{\text{AlCl}_3} = 0.50$	$X_{\text{AlCl}_3} > 0.50$	$X_{\text{AlCl}_3} > 0.75$
	<div style="border: 1px dashed blue; border-radius: 10px; padding: 5px; display: inline-block;"> <math>\text{Cl}^- \quad [\text{AlCl}_4]^-</math> </div>		$[\text{AlCl}_4]^-$ $[\text{Al}_2\text{Cl}_7]^-$	$[\text{Al}_2\text{Cl}_7]^-$ $[\text{Al}_3\text{Cl}_{10}]^-$
<b>chlorozincates(II)</b>	$X_{\text{ZnCl}_2} < 0.33$	$X_{\text{ZnCl}_2} = 0.33$	$X_{\text{ZnCl}_2} = 0.50$ $[\text{Zn}_2\text{Cl}_6]^{2-}$ $0.50 < X_{\text{ZnCl}_2} < 0.67$ $[\text{Zn}_2\text{Cl}_6]^{2-} \quad [\text{Zn}_3\text{Cl}_8]^{2-}$	$X_{\text{ZnCl}_2} = 0.67$ $[\text{Zn}_3\text{Cl}_8]^{2-}$ $X_{\text{ZnCl}_2} = 0.75$ $[\text{Zn}_4\text{Cl}_{10}]^{2-}$
	$\text{Cl}^-$	$[\text{ZnCl}_4]^{2-}$	$[\text{ZnCl}_4]^{2-}$	

**Figure 2.2:** Series of equilibria established upon mixing quaternary halide salts with varying  $X_{\text{MCl}_x}$  ( $\text{MCl}_x$ :  $\text{AlCl}_3$ ,  $\text{ZnCl}_2$ ), forming Lewis basic, neutral, acidic or highly acidic chlorozincates(II) and chloroaluminates(III).

The XPS analysis of several compositions of  $[\text{C}_8\text{C}_1\text{im}]\text{Cl}\text{-ZnCl}_2$  was in agreement with what has been previously reported using Raman spectroscopy with regards to speciation.<sup>31</sup> Nonetheless, contrasting ESI-MS and FAB-MS speciation data have been published.<sup>19,34</sup> More specifically,  $[\text{ZnCl}_3]^-$  was detected for  $X_{\text{ZnCl}_2} < 0.5$ ,  $[\text{ZnCl}_3]^-$  and  $[\text{Zn}_2\text{Cl}_5]^-$  for  $X_{\text{ZnCl}_2} = 0.5$  whereas  $[\text{ZnCl}_3]^-$ ,  $[\text{Zn}_2\text{Cl}_5]^-$  and  $[\text{Zn}_3\text{Cl}_7]^-$  were found for the Lewis acidic chlorozincates(II).<sup>31,47</sup> For the moisture-stable chloroferrates(III),  $[\text{FeCl}_4]^-$  anions of a tetrahedral geometry have been observed when an excess of  $[\text{C}_4\text{C}_1\text{im}]\text{Cl}$  was mixed with  $\text{FeCl}_3$  whereas  $[\text{Fe}_2\text{Cl}_7]^-$  with a C2 configuration appears for  $X_{\text{FeCl}_3} > 0.5$ .<sup>22,23,35</sup> Indium-115 NMR spectroscopy has previously indicated the sole presence of monomeric species ( $[\text{InCl}_4]^-$ ) for a large range of compositions ( $0.25 < X_{\text{InCl}_3} < 0.75$ ).<sup>30</sup> Similarly, speciation studies performed by XPS, EXAFS and solid-state NMR spectroscopy did not indicate the appearance of  $[\text{In}_2\text{Cl}_7]^-$  at  $X_{\text{InCl}_3} > 0.5$ .<sup>30</sup> Basic chloroindates(III) contain

hexa-, penta- and tetra-coordinate anions ( $[\text{InCl}_6]^{3-}$ ,  $[\text{InCl}_5]^{2-}$ ,  $[\text{InCl}_4]^{-}$ ) in a dynamic equilibrium with  $\text{InCl}_3$  precipitation occurring at  $X_{\text{InCl}_3} > 0.5$ .<sup>30,36</sup> Despite the absence of polynuclear anions, chloroindate(III) ILs have also been successfully used as acidic catalysts in organic reactions such as the alkylation of aromatic compounds<sup>37</sup> or Friedel-Crafts acylation reactions<sup>38</sup>.

### 2.1.1.3 Acidity determination and intramolecular interactions in chlorometallate ILs

The Lewis acidity of ionic liquids increases with an enhanced electrophilicity of the metal incorporated in the anion and it is highly dependent on the complexity of the anionic speciation.<sup>3</sup> This type of acidity of chlorometallates has been described quantitatively by  $-\log[\text{Cl}^-]$  with the acid being the  $\text{Cl}^-$  acceptor.<sup>39</sup> Acidic anions in chlorometallate ILs are strongly non-coordinating compared with the basic anions of the quaternary halide salts.<sup>40</sup> As an example,  $[\text{AlCl}_4]^-$  anions have been categorised as weakly coordinating whereas  $[\text{Al}_2\text{Cl}_7]^-$  and  $[\text{Al}_3\text{Cl}_{10}]^-$  are considered acidic and non-coordinating.<sup>40</sup>

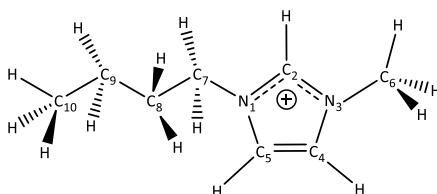


**Figure 2.3:** Chemical structure of the 1-butyl-3-methylimidazolium cation,  $[\text{C}_4\text{C}_{1\text{im}}]^+$ .

$^1\text{H}$  NMR spectroscopy, using the IL as a probe, has been explored for estimating the coordination properties of the anion and the strength of hydrogen-bonding in imidazolium-based ILs.<sup>41,42</sup> In the case of chloroaluminates(III), the chemical shift of the acidic  $\text{C}^2$  ring proton (Figure 2.3) has been successfully expressed as a function of the hydrogen bond accepting (HBA) and donating (HBD) properties of the IL.<sup>42</sup> A strong correlation was observed between the upfield chemical shift of the  $\text{C}^2$  proton peak and  $X_{\text{AlCl}_3}$  ( $X_{\text{AlCl}_3} \leq 0.50$ ), attributed to the complexation of free  $\text{Cl}^-$  and the formation of weakly coordinating anions in combination with cation charge modifications.<sup>32</sup> The application of  $^1\text{H}$  NMR spectroscopy for monitoring the chemical shifts of the most acidic ring protons ( $\text{C}^2$  &  $\text{C}^4/\text{C}^5$ ; Figure 2.3) of imidazolium-based halometallates, can be therefore considered for assessing the Lewis basicity of the anion.<sup>43</sup> The crystal structure of 1,3-dialkylimidazolium-based halometallate ILs has also indicated the formation of a hydrogen-bonding network between the protons of the imidazolium cation (Figure 2.3) and the chlorine atoms of  $[\text{MCl}_4]^{2-}$  whereas the formation of oligomeric anions results in the disruption of the hydrogen-bonding network due to their less-pronounced hydrogen-bond acceptor properties.<sup>44</sup> The interionic interaction energy for chlorometallate ionic liquids,  $[\text{C}_4\text{C}_{1\text{im}}]\text{Cl}\cdot\text{ZnCl}_2$  and  $[\text{C}_4\text{C}_{1\text{im}}]\text{Cl}\cdot\text{AlCl}_3$ ,

has been calculated to be significantly less negative than for the ion pair of [C<sub>4</sub>C<sub>1</sub>im]Cl where shorter and stronger interactions are found between the most acidic C<sup>2</sup> proton of the imidazolium ring and the chloride.<sup>45</sup> Surface electrostatic potential calculations have confirmed the increase in Lewis acidity upon increasing the metal chloride molar ratio and therefore the complexity of the anion.<sup>3,45</sup> XPS spectroscopy has been investigated for the acidity determination of imidazolium-based halometallate systems with a varying metal chloride composition ( $X_{\text{MCl}_x} = \text{FeCl}_3, \text{FeCl}_2, \text{CoCl}_2, \text{NiCl}_2$  and  $\text{ZnCl}_2$ ).<sup>31</sup> More specifically, the XPS binding energies (BEs) of the metal, nitrogen, carbon and chlorine photoelectron peaks were used for predicting trends in the hydrogen-bonding basicity and Lewis acidity properties of the ionic liquids.<sup>31</sup> The increase in the binding energies of nitrogen, carbon and chlorine photoelectron peaks of [C<sub>n</sub>C<sub>1</sub>im]Cl·ZnCl<sub>2</sub> as a function of  $X_{\text{ZnCl}_2}$  confirmed the weaker coordinating strength of higher order complex anions ( $[\text{Zn}_x\text{Cl}_{2x+2}]^{2-}$ ,  $X_{\text{ZnCl}_2} > 0.33$ ) and therefore the less pronounced interionic charge-transfer effects as well as lower hydrogen-bond anion basicity in the presence of Lewis acidic polynuclear anions.<sup>31</sup> IR spectroscopy has also been tested as a more generic method for determining the Lewis acidity of ionic liquids based on the changes in the IR frequencies of basic probes interacting with the IL.<sup>46,47</sup> Specific wavenumber (cm<sup>-1</sup>) bands were monitored for mixtures of pyridine (1400 - 1700 cm<sup>-1</sup>) or acetonitrile (2250 - 2340 cm<sup>-1</sup>) and chlorometallate ILs, in order to detect the coordination of Lewis acidic anions to the basic probe and/or the protonation of the probe in the presence of Brønsted acid sites.<sup>47</sup> Similarly, acetonitrile has also been used as a basic probe for the determination of Lewis acidity.<sup>46</sup> Lewis acid-base interactions between acetonitrile and the ionic liquid led to the appearance of an IR band near 2312 cm<sup>-1</sup> (CN stretching vibrations).<sup>48</sup> Measuring the Gutmann Acceptor Number (AN)<sup>48</sup> has also been explored as a quantitative measure of Lewis acidity for chloroaluminates(III), chloroindates(III) and chlorogallates(III) based on the electrophilic properties of the anion.<sup>36</sup> A strongly basic probe, triethylphosphine oxide, is used in the presence of the ionic liquid and the strength of interaction is determined by <sup>31</sup>P NMR spectroscopy.<sup>36,48</sup> The AN number is a function of the measured <sup>31</sup>P NMR chemical shift ( $\text{AN} = 2.348 * \delta_{\text{inf}}$ ) and these values are used for comparing the acidity profile of ionic liquids with other reference Lewis and Brønsted acids.<sup>51</sup> Both IR spectrometry and the Gutmann Acceptor Number methods are useful for estimating the acidity as a function of speciation of halometallate, albeit providing acidity orders that are highly-dependant on the basicity of the probe. NMR and XPS spectroscopy provide a great insight on the acidity in addition to the coordinating strength of the anionic species that are formed in the melt.

## 2.1.2 Brønsted acidic ionic liquids (BAILs) overview

### 2.1.2.1 General properties and applications of Brønsted acidic ionic liquids (BAILs)

Brønsted acidic ionic liquids (BAILs) contain acidic protons that reside on the cation and/or the anion and they are usually prepared by an exothermic neutralisation reaction between a Brønsted acid and a Brønsted base, yielding protic ionic liquids (Figure 2.4).<sup>2,6</sup>

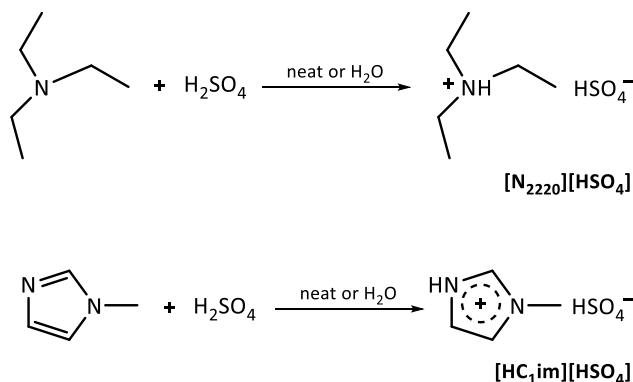


**Figure 2.4:** Schematic diagram for the synthesis of [HC<sub>1im</sub>][HSO<sub>4</sub>] and [N<sub>2220</sub>][HSO<sub>4</sub>] by acid-base neutralisation.

Assessing the ionic character of protic ionic liquids (PILs) has been attempted as a way of evaluating the extent of proton transfer in the final product.<sup>49,50</sup> Plotting the respective molar conductivity,  $\log\Lambda$ , as a function of fluidity ( $\phi$ ), ( $\log(\eta^{-1})$ ), known as the Walden plot, has been used for qualitatively estimating the degree of ionicity in ionic liquids.<sup>49</sup> The determination of ionicity has also been attempted by <sup>1</sup>H NMR spectroscopy for several PILs, accounting for a direct relationship of ionicity and the formation of interionic hydrogen-bonded complexes.<sup>51</sup> In addition to PILs with the acidic hydrogen residing on the cation and/or the anion,<sup>52,53</sup> BAILs may also contain acidic protons on a functional group such as in SO<sub>3</sub>H-functionalised ILs.<sup>54</sup> Sulfonic acid functionalized ILs are typically prepared by the 'sultone method' that involves the reaction between an 1-alkylimidazole and a sultone to give a zwitterionic precursor that is converted into the desired BAIL upon the addition of a Brønsted acid (Figure 2.5).<sup>54</sup> Alternatively, a bifunctional acidic ionic liquid can be obtained upon the further addition of a metal chloride, resulting in the formation of oligomeric Lewis acidic anions (Figure 2.5).<sup>55</sup>

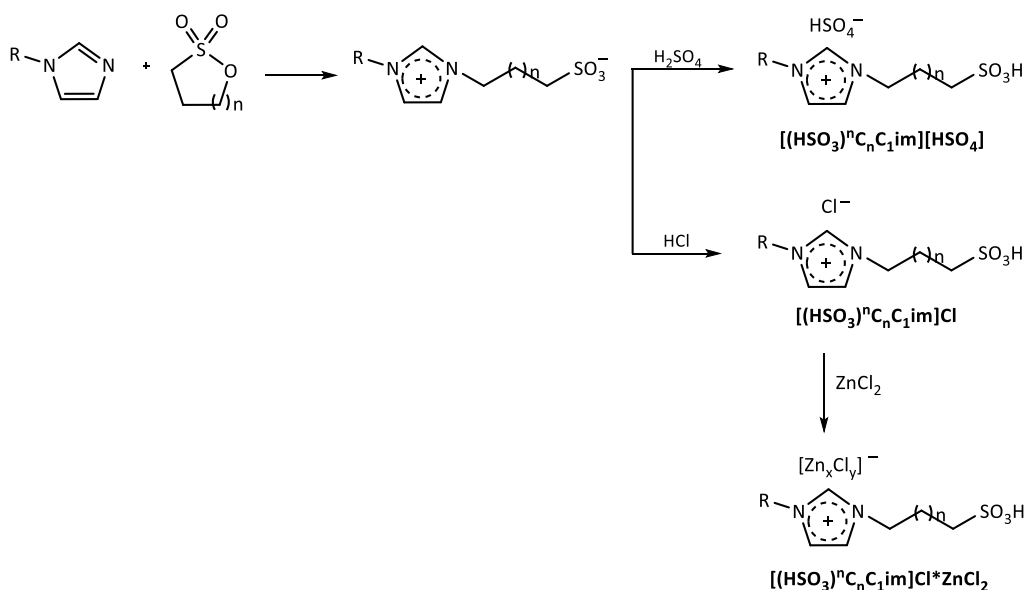


**Figure 2.5:** Schematic representation of the preparation of SO<sub>3</sub>H-functionalised BAILs ( $[(\text{HSO}_3)^n\text{C}_n\text{C}_1\text{im}][\text{HSO}_4]$ ) or bifunctional acidic ionic liquids ( $[(\text{HSO}_3)^n\text{C}_n\text{C}_1\text{im}]\text{Cl} \cdot \text{ZnCl}_2$ ).

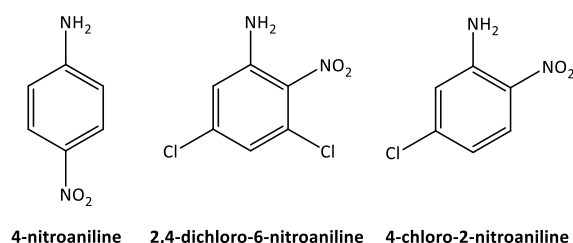
Brønsted acidic ionic liquids have been tested as catalysts in esterification reactions as an alternative to conventional homogeneous Brønsted acids that are often unsustainable due to their corrosive properties and their lack of recyclability.<sup>56,57</sup> Other examples of catalytic applications include acetalization<sup>58</sup> and dehydration<sup>59</sup> reactions such as the application of  $[\text{C}_4\text{C}_1\text{im}][\text{HSO}_4]$  for the conversion of glycerol into acrolein (50 - 58 % yield, 270 °C). Other interesting applications of BAILs include their use as battery electrolytes, electrophoresis and electroplating media with a significant impact of the anion on their electroconductivity properties.<sup>60</sup> The extraction and recovery of metals is another recent application for BAILs.<sup>61</sup> Treating brass waste with  $[\text{C}_4\text{C}_1\text{im}][\text{HSO}_4]$  under mild conditions (60 – 100 °C) results in the complete dissolution of all zinc that is then recovered by electrowinning, followed by the recycling and reuse of the ionic liquid.<sup>61</sup> The hydrolysis of lignocellulose and its conversion into chemicals have also been important research areas involving the application of BAILs.<sup>62</sup> As an example,  $[\text{C}_4\text{C}_1\text{im}][\text{HSO}_4]$  has shown great hydrolysis and depolymerisation efficiency for microcrystalline cellulose under mildly acidic conditions.<sup>63</sup> The combined dissolution and hydrolysis of cellulose has also been successful in -SO<sub>3</sub>H functionalised ILs bearing basic anions such as chloride.<sup>64</sup> Furthermore, the tuneable acidic properties of BAILs have been studied in the dehydration of carbohydrates in furan derivatives, 5-HMF or furfural, albeit with the catalytic contribution of Lewis acids needed for the *in situ* isomerization of glucose to fructose and the enhancement of HMF yields.<sup>65</sup> Replacing metal catalysts with SO<sub>3</sub>H-functionalised ILs for the direct conversion of glucose into 5-HMF has also proved to be feasible with the functionalised cation of the BAIL promoting the reaction with the SO<sub>3</sub>H group, which acts as both a proton acceptor and a proton donor whilst the chloride stabilises the reaction intermediates and transition states.<sup>66</sup>

### 2.1.2.2 Acidity determination of Brønsted acidic ionic liquids (BAILs)

The application of BAILs as catalysts makes the determination of their acidity crucial for explaining their activity in various acid-catalysed reactions. The Hammett acidity scale ( $H_0$ ) has been used for the direct comparison of different BAILs or binary mixtures of acids and ILs in regards to their acidity profile in non-aqueous media.<sup>67–69</sup> As an example, a positive relationship has been previously established between the Hammett acidity of  $SO_3H$ -functionalised ionic liquids and their catalytic activity towards the alkolysis of furfuryl alcohol to produce alkyl levulinates.<sup>70</sup>

$$H_0 = pK(I)_{aq} + \log([I]_s/[IH^+]_s) \quad (2.1)$$

The  $H_0$  values, equivalent to the pH scale in aqueous systems, are obtained by measuring the extent of protonation of an uncharged indicator (I), expressed as  $[I]/[IH^+]$ . The absorbance, and therefore the concentration, of the protonated and unprotonated forms of the indicator is determined by UV-vis spectroscopy, before and after the addition of the solvent, to determine the respective  $H_0$  value (2.1).



4-nitroaniline    2,4-dichloro-6-nitroaniline    4-chloro-2-nitroaniline

**Figure 2.6:** Examples of Hammett acidity dye indicators (I)

Hammett dyes (Figure 2.6) can be partially protonated by strong acids whereas their structure allows for the monitoring of their concentration by UV-vis spectroscopy. The indicators are typically derivatives of aniline such as 4-nitroaniline ( $pK_{BH^+} = 1.00$ ), 2,4-dichloro-6-nitroaniline ( $pK_{BH^+} = -3.01$ ) and 4-dichloro-2-nitroaniline ( $pK_{BH^+} = -0.97$ ) with the choice of the probe depending on the range of acidity of the studied ionic liquid. The addition of highly electron-withdrawing nitro groups makes the lone pair of  $-NH_2$  of nitroaniline-based dyes less basic whilst other ring substituents are typically used for fine-tuning the  $pK_{BH^+}$  values of the indicator. A few examples of estimated  $H_0$  values for different ILs is summarised in Table 2.1. The Brønsted acidity of  $HNTf_2$  in  $[C_4C_1im][NTf_2]$  and  $[C_4C_1im][BF_4]$  has been determined on the basis of the Hammett acidity function by UV/Vis spectroscopy, indicating a significantly higher acidity for the tetrafluoroborate-based IL, potentially due to the different solvation properties of  $[BF_4]^-$  in

comparison with  $[\text{NTf}_2]^-$ . Additionally, sulfonic acid-functionalised ILs bearing the same anion show a stronger acidity profile and thus lower  $H_o$  values.

**Table 2.2:** Examples of Hammett acidity functions of BAILs and binary IL/acids mixtures determined by UV-vis spectroscopy

Ionic liquid	Added acid	Indicator	$H_o$
$[\text{C}_4\text{C}_1\text{im}][\text{NTf}_2]$		2,4-dinitroaniline	- 4.55 <sup>67</sup>
$[\text{C}_4\text{C}_1\text{im}][\text{BF}_4]$	$\text{HNTf}_2^{\text{a}}$	6-bromo-2,4-dinitroaniline	- 7.00 <sup>67</sup>
		3-nitroaniline	1.48 <sup>69</sup>
$[\text{HC}_1\text{im}]\text{Cl}$		4-nitroaniline	1.93 <sup>71</sup>
$[\text{C}_4\text{C}_1\text{im}][\text{HSO}_4]$		3-nitroaniline	2.08 <sup>69</sup>
$[\text{HC}_1\text{im}][\text{HSO}_4]$	NA	4-nitroaniline	1.59 <sup>71</sup>
$([\text{HSO}_3]^-\text{C}_4\text{C}_1\text{im})[\text{HSO}_4]$		4-nitroaniline	1.18 <sup>71</sup>

a:  $[\text{H}^+] = 105 \text{ mmol L}^{-1}$

The use of UV-vis spectroscopy for the acidity determination of BAILs can be problematic, often suffering from overlapping peaks of the IL with those of the Hammett acidity probe whereas the presence of water and/or impurities affects the accuracy of the measurement due to the low concentration of the indicator.<sup>72</sup> Capillary  $^{13}\text{C}$  NMR spectroscopy has therefore been proposed as an alternative method for studying the acidity of ILs with mesityl oxide used as the probe together with the neat ionic liquid.<sup>72</sup>

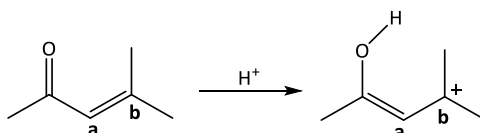


**Figure 2.7:** Protonated and unprotonated forms of mesityl oxide.

The acidity is assessed by monitoring the change in chemical shift ( $\Delta\delta$  ppm) between the  $\alpha$  and  $\beta$  carbon of mesityl oxide by  $^{13}\text{C}$  NMR spectroscopy in the presence of different concentrations of the probe (Figure 2.7). A model correlating Hammett acidity ( $H_o$ ) and the  $\Delta\delta$  (ppm) values for mesityl oxide has been previously studied for  $[\text{HSO}_4]^-$ -based BAILs and their respective mixtures with  $\text{H}_2\text{SO}_4$ . Acidity corresponding to  $H_o$  values of -1 to -9 can be measured using this technique, allowing for a wider range of acidity measurements that are not possible by using a single UV-vis probe.



## 2.2 Thiophene chemistry and the application of thiophene analogues

Thiophene derivatives are heterocyclic compounds consisting of a flat five membered ring and a sulfur heteroatom that contributes to the aromatic sextet by providing 2  $\pi$  electrons. The aromaticity is indicated by the ability of thiophene to participate in a series of electrophilic substitution reactions.<sup>73</sup> Thiophene can be obtained by the reactive distillation of petroleum but it is the functionalisation of the aromatic ring that leads to the formation of high-value building blocks. The delocalisation of the charge usually favours electrophilic attack at the  $\alpha$ -position compared to the  $\beta$ -position (Figure 2.8). The reduction in stability of the complexes with the positive charge distributed between the heteroatom and one  $\alpha$  carbon ( $N^+ > S^+ > O^+$ ) correlates well with the ability of pyrrole, thiophene and furan to form  $\beta$ -substituted products.<sup>73</sup> The addition of an electron-withdrawing group on the  $\alpha$ -carbons has an additional effect on the reactivity of the  $\beta$ -position of the aromatic ring.<sup>73</sup>

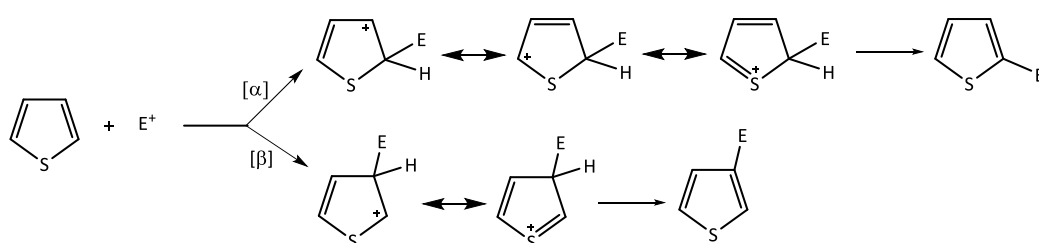


**Figure 2.8:** Electrophilic substitution of thiophene and positional selectivity ( $\alpha$ : $\beta$ ).

Thiophene derivatives possess promising pharmacological characteristics and thus they have been used for the manufacturing of compounds with applications in pharmaceuticals<sup>74</sup> and agrochemicals<sup>75</sup>. Thiophene has been used as part of a fused ring system in, or as a replacement for, aromatic rings in biologically active molecules.<sup>76</sup> In addition to the bioisosterism between benzene and thiophene analogues, the presence of the heteroatom and the lower resonance energy in thiophene affect the toxicity and therapeutic properties of the final product.<sup>76</sup> Additionally, polymerised thiophenes form conducting polymers whereas the self-assembly and self-organization properties of thiophene-based materials result in the spontaneous formation of supramolecular structures.<sup>77</sup> A linear arrangement of the oligothiophene backbone is obtained upon a 2,5- or 2,4-ligation of the thiophene monomers.<sup>78</sup>

### 2.2.1 Preparation of thiophene derivatives from non-heterocyclic precursors

Thiophene analogues can be derived from the functionalisation of a pre-constructed ring or the synthesis of the thiophene units from open chain precursors. The vapour-phase synthesis of thiophene from butane, butadiene, or butene at high temperatures ( $> 400\text{ }^{\circ}\text{C}$ ) was already established by Socony-Vacuum Oil Company in the early 1940s. However, Paal-Knorr synthesis is one of the most important methods for obtaining substituted thiophenes via the acid-catalysed dehydrative cyclisation of 1,4-diketones in the presence of a sulfur source (Figure 2.9). Phosphorus sulfides ( $\text{P}_x\text{S}_y$ ),  $\text{H}_2\text{S}$  and Lawesson's reagent are common sulfur sources in Paal-Knorr thiophene synthesis.

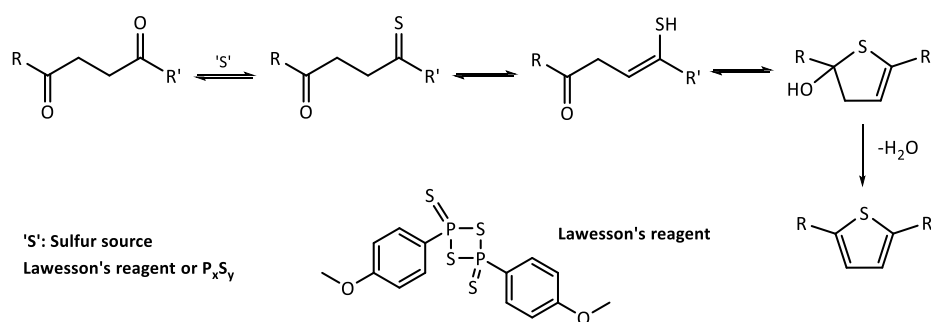
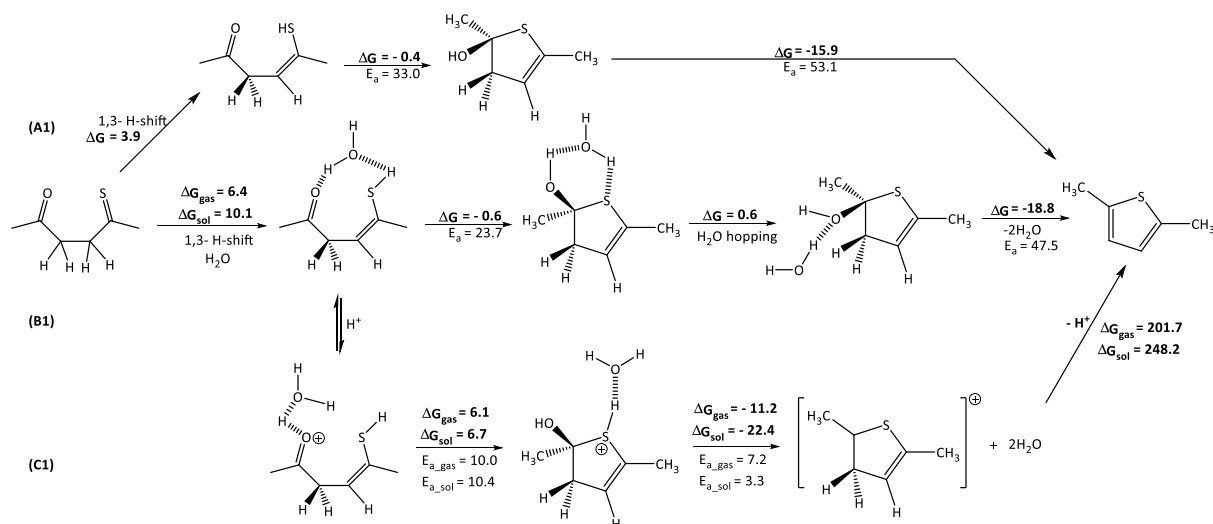


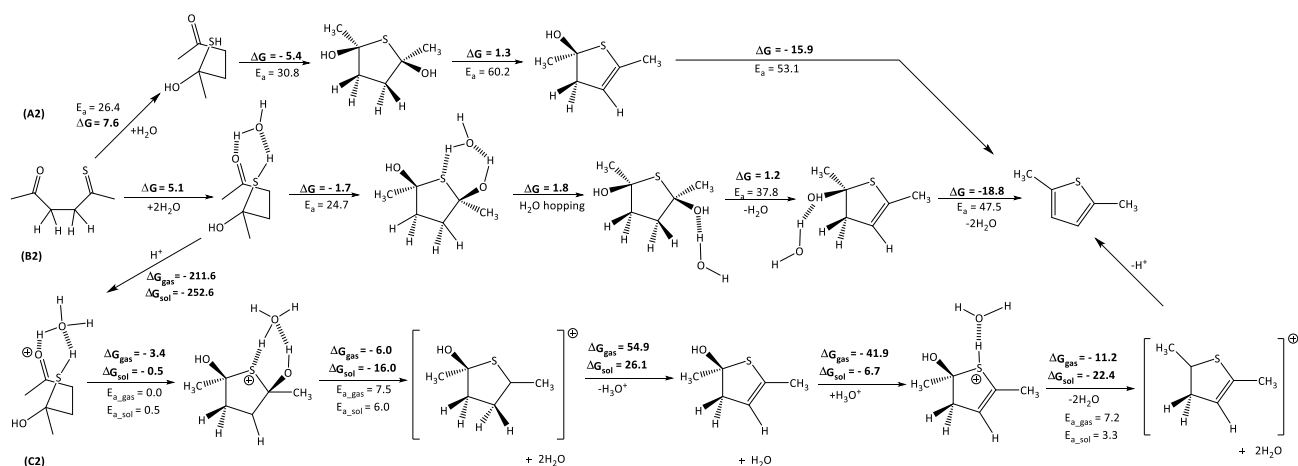
Figure 2.9: Paal-Knorr thiophene synthesis from 1,4-dicarbonyl compounds and a source of sulfur.

There is only one available study on the mechanistic investigation of thiophene synthesis from 1,4-diketones, suggesting that this reaction is an exergonic process with a high energy barrier for the cyclization and water elimination steps for both the thiol and the hemithioketal pathways (Figures 2.10 & 2.11).<sup>79</sup> The reaction of a 1,4-diketone with a sulfur source can form a 1-keto-4-thioiketone that undergoes tautomerisation (Figure 2.10). The simultaneous proton transfer from the thiol group to the carbonyl oxygen and the attack of sulfur at the carbonyl carbon leads to the cyclization of the intermediate with a high energy barrier ( $E_a = 33.0\text{ kcal mol}^{-1}$ ). The participation of water results in conformational changes, facilitating the proton transfer and reducing the cyclization barrier from 33 to  $23.7\text{ kcal mol}^{-1}$  (Figure 2.10; B1).<sup>79</sup> The lower activation energy of the Brønsted-acid catalysed cyclization step was estimated at approximately  $10\text{ kcal mol}^{-1}$  (Figure 2.10; C1). Additionally, both the water-assisted dehydration (B1) and the participation of  $\text{H}_3\text{O}^+$  (C1) proved to be energetically favourable for the final water elimination step with significantly reduced  $E_a$  values, especially for the Brønsted acid-catalysed pathway (Figure 2.10; C1).



**Figure 2.10:** Thiol pathways for the Paal-Knorr synthesis of 2,5-dimethylthiophene (2,5-DMF) in the absence of H<sub>2</sub>O (A1), with H<sub>2</sub>O (B1) and in the presence of H<sub>3</sub>O<sup>+</sup> (C1).<sup>79</sup>

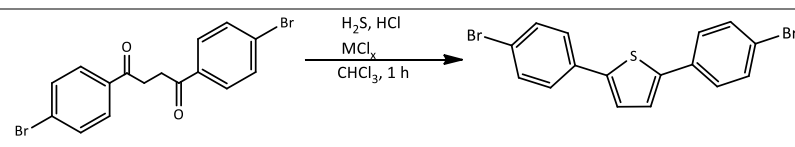
The hemithioketal pathway has also been investigated as an alternative mechanism for the Paal-Knorr thiophene synthesis (Figure 2.11). The addition of a molecule of water to the 1-keto-4-thioketone affords a hemithioketal with an energy barrier of 26.4 kcal mol<sup>-1</sup>, whereas the following cyclisation step has a barrier of 30 kcal mol<sup>-1</sup>. It was demonstrated that water participation facilitates the cyclization process in the hemithioketal pathway as well, whereas proton catalysis reduces the cyclization energy barrier further ( $E_a = 0$ -0.5 kcal mol<sup>-1</sup>) and promotes the final water elimination step.



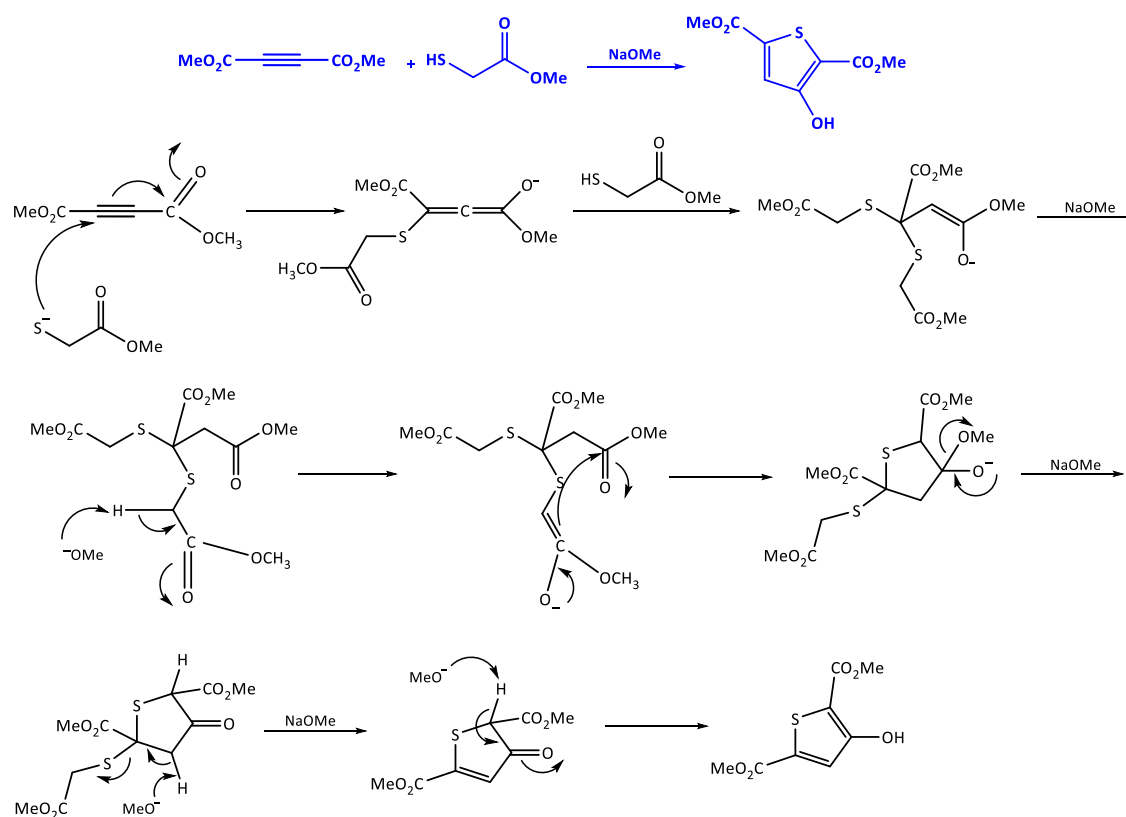
**Figure 2.11:** Hemithioketal pathways for the Paal-Knorr synthesis of 2,5-dimethylthiophene (2,5-DMF) in the absence of explicit H<sub>2</sub>O (A2), with explicit H<sub>2</sub>O (B2) and under proton catalysis (C2).

**Table 2.2:** Paal-Knorr thiophene synthesis: reaction of 1,2-di-bromobenzoyl ethane with H<sub>2</sub>S/HCl.<sup>80</sup>

Dehydrating agent	Yield (%)	Recovered diketone (%)
None	0	80
(CH <sub>3</sub> CO) <sub>2</sub> O	5	66
ZnCl <sub>2</sub>	56	38
SnCl <sub>4</sub>	73	17

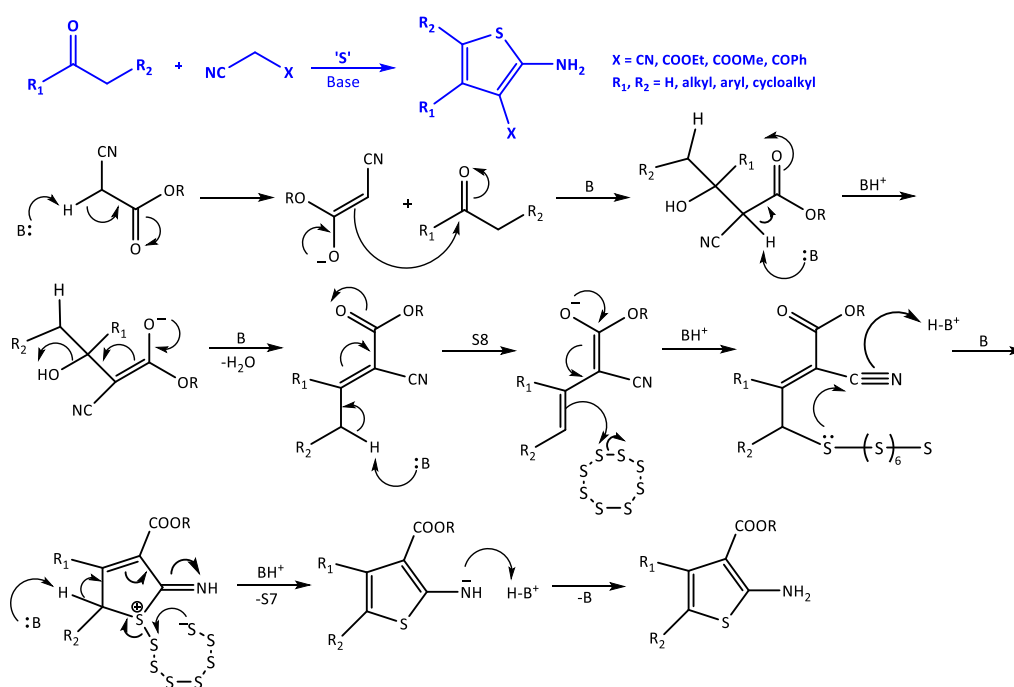
  


The addition of a Lewis acid such as SnCl<sub>4</sub> or ZnCl<sub>2</sub> has also been shown to promote the cyclisation of 1,4-diketones in the presence of H<sub>2</sub>S/HCl for the synthesis of 2,5-diarylthiophenes.<sup>80</sup> The addition of metal chlorides improved the reaction yields due to their dehydrating properties with a superior performance of the Lewis acids over acetic anhydride (Table 2.2).<sup>80</sup> There are several limitations in Paal-Knorr synthesis; harsh conditions such as prolonged heating in acidic media are usually applied whereas the availability of substituted 1,4-diketones can be an obstacle for large-scale applications.

**Figure 2.12:** Example of Fiessemann thiophene synthesis from thioacetic acid methyl ester and acetylenedicarboxylic acid.

The Fiesselmann thiophene synthesis is a common synthetic protocol for the base-catalysed formation of substituted thiophenes via the condensation between thioglycolic acid derivatives with  $\alpha,\beta$ -acetylenic esters to form 3-hydroxy-2-thiophenecarboxylic acid derivatives (Figure 2.12).<sup>81</sup> However, strongly basic conditions and long reaction times are usually required. Recyclable solid-supported catalysts such as  $\text{KF}/\text{Al}_2\text{O}_3$  have therefore been explored as a replacement for organic and inorganic bases for Fiesselmann-type synthesis of steroidal and non-steroidal thiophene derivatives.<sup>82</sup>

The Gewald synthesis is a major synthetic pathway for the preparation of functionalised 2-aminothiophenes using the base-catalysed condensation of a ketone with a  $\beta$ -ketonitrile to form an olefin prior to the cyclization step with elemental sulfur to afford a 2-aminothiophene (Figure 2.13).<sup>83</sup> Most methods based on the Gewald synthesis suffer from high catalyst loadings (> 50 mol%) and long reaction times required for the condensation step.<sup>84</sup> Consequently, the use of microwave irradiation over conventional heating and the application of solid base catalysts have been attempted to improve the reaction time and the catalyst recyclability, leading to good yields (55 – 92 %, 3 – 8 min).<sup>85</sup>



**Figure 2.13:** Example of the base-catalysed Gewald 2-aminothiophene synthesis from a  $\beta$ -ketonitrile and a ketone.

The Hinsberg reaction between 1,2-dicarbonyl compounds and diethyl thiodiacetates is another established synthetic method for the preparation of 3,4-dialkyl- or 3,4-diarylthiophene-2,5-dicarboxylic acids (Figure 2.14). The base-catalysed condensation between a 1,2-dicarbonyl compound and dialkyl

thiodiacetate can be then followed by the acid-catalysed hydrolysis of the ester functional groups to afford a 2,5-dicarboxylic acid.<sup>86</sup>

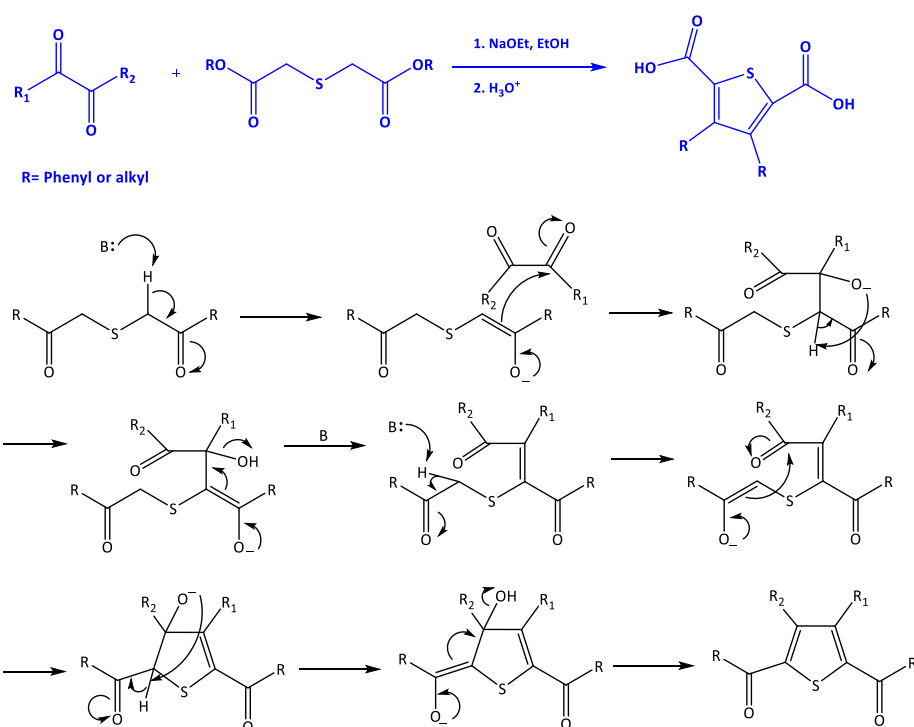


**Figure 2.14:** Example of the base-catalysed Hinsberg thiophene synthesis from a 1,2-dicarbonyl and thiodiacetates.

### 2.2.2 Thiophene formation from heterocyclic precursors (Furan, 2,5-dimethylfuran)

The synthesis of thiophene derivatives from heterocyclic precursors has been reported to a lesser extent. In 1935, Yur'ev discovered that furan can be converted into thiophene in the presence of a highly active heterogeneous catalysts and H<sub>2</sub>S, in a gas-phase reaction.<sup>87</sup> Nevertheless, the yield of the desired product did not exceed 40 % at 300 - 600 °C with carbon monoxide and hydrocarbons being reported as the main by-products.<sup>87</sup> More recent studies attempted to investigate the recyclization of furan into thiophene over calcined Al<sub>2</sub>O<sub>3</sub> in a fixed-bed reactor.<sup>88</sup> The reaction was performed from 260 °C to 500 °C with an H<sub>2</sub>S : furan molar ratio ranging from 2 to 10 with both parameters showing a positive correlation with the yield of thiophene (30 % - 90 %).<sup>88</sup> Additionally, it was observed that the catalyst performance was highly dependent to the surface area and the concentration of the Lewis acid sites.<sup>88</sup> Increasing the specific area (> 330 m<sup>2</sup> g<sup>-1</sup>) and the pore volume (> 0.08 cm<sup>3</sup> g<sup>-1</sup>) of γ-Al<sub>2</sub>O<sub>3</sub> enhanced the reaction rate between furan and H<sub>2</sub>S given that heterogeneous reactions are dominated by diffusion phenomena.<sup>89</sup> Promoted γ-Al<sub>2</sub>O<sub>3</sub> with strong Lewis acid sites (Al<sup>3+</sup>) has shown a better catalytic

performance over SiO<sub>2</sub>-supported acids and aluminosilicate zeolites with a reported thiophene yield of 95 - 98 mol% when an excess was used of H<sub>2</sub>S over furan.<sup>90,91</sup> It was found that there was a significant effect of the H<sub>2</sub>S/furan molar ratio (M) on the thiophene yield with an increase from 42 % for M = 3 to 86 % for M = 11 for W/Al<sub>2</sub>O<sub>3</sub> at 400 °C.<sup>90</sup> The reaction of furan with H<sub>2</sub>S over  $\gamma$ -Al<sub>2</sub>O<sub>3</sub> is described by first order kinetics with respect to both reactants.<sup>89</sup> The strength and the concentration of the Lewis basic sites was also considered critical for the activation of H<sub>2</sub>S.<sup>90</sup> Catalysts with Brønsted acidic sites showed low activity towards the formation of thiophene (< 34 %) whilst the decomposition and polymerization of furan was promoted.<sup>90</sup>

One of the proposed mechanisms for the recyclization of furan into thiophene involves the dissociative adsorption of H<sub>2</sub>S onto the acidic and basic centres of Al<sub>2</sub>O<sub>3</sub>, followed by the adsorption of furan on the catalyst surface upon the interaction of the heteroatom with Al<sup>3+</sup> (Figure 2.15). The chemisorption of furan results in the furan ring opening at the C-O bond followed by the subsequent C-S bond formation, yielding thiophene upon recyclization of the acyclic intermediate (Figure 2.15). DFT calculations have also indicated that the dissociative chemisorption of H<sub>2</sub>S on Al<sub>2</sub>O<sub>3</sub> occurs with SH<sup>-</sup> being adsorbed on Al<sup>3+</sup>, followed by a dehydration reaction between OH<sup>-</sup> and SH<sup>-</sup>.<sup>92</sup> These theoretical calculations also suggested the adsorption of furan via its heteroatom and the formation of Al-O and C-S bonds with the highest energy barrier assigned to the primary dehydration step (242.1 kJ mol<sup>-1</sup>).<sup>92</sup>

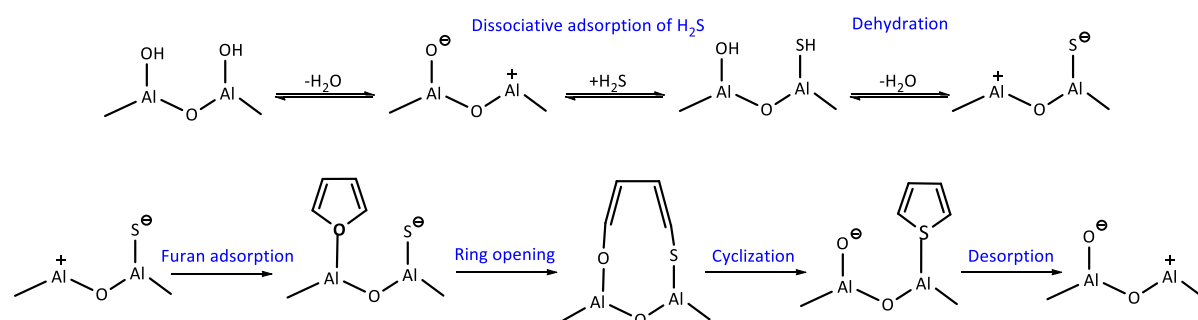


**Figure 2.15:** Putative mechanism of the furan recyclization into thiophene on the surface of Al<sub>2</sub>O<sub>3</sub> via the dissociative adsorption of H<sub>2</sub>S and the chemisorption of furan onto the catalyst surface.<sup>88</sup>

Overall, the determination of the exact mechanism for the gas-phase recyclization of furan into thiophene does not appear to be well-established due to contradictory evidence. Monitoring the interactions between H<sub>2</sub>S and  $\gamma$ -Al<sub>2</sub>O<sub>3</sub> by IR spectroscopy has also suggested the dissociative chemisorption of H<sub>2</sub>S on the catalyst surface until a monolayer is formed.<sup>91</sup> However, the recyclization of furan was still enhanced at H<sub>2</sub>S concentrations exceeding the amounts required for the formation of a monolayer; hence the participation of molecular H<sub>2</sub>S was implied.<sup>91</sup> Furthermore, the interaction of

the furan oxygen with the L-sites of the catalyst seems unlikely since oxygen contributes two  $\pi$  electrons to the aromatic sextet and therefore its ability to form complexes with Lewis acidic centres is reduced.<sup>91</sup> Therefore, it has been proposed instead that it is the electron rich  $\alpha$ -carbons of the furan ring that could interact with the acceptor sites of the catalyst.<sup>90,91</sup>

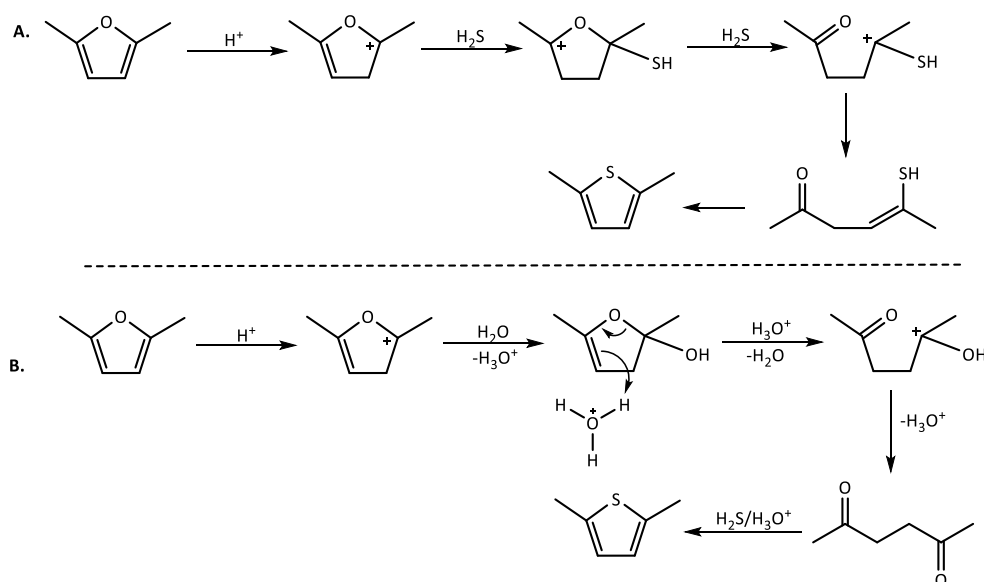


**Figure 2.16:** Brønsted acid-catalysed recyclization of 2,5-dimethylfuran to 2,5-dimethylthiophene under anhydrous conditions (A) or with water as a competing nucleophile (B).

The recyclization of functionalised furans has been explored under homogeneous Brønsted acid catalysis conditions. The use of acidified ethanol (EtOH/HCl, 30 – 60 °C) as the reaction medium has been thoroughly studied; indicating the need for an excess of H<sub>2</sub>S and high loadings of the Brønsted acid catalyst.<sup>87,93–96</sup> The recyclization of 2,5-dialkylfurans may proceed via the formation of a 1,4-dicarbonyl compound, followed by a Brønsted acid-catalysed Paal Knorr thiophene synthesis (thiol or hemithioketal pathways; **Section 2.2.1**). Alternatively, furanics undergo a direct recyclization into their thiophene analogues under anhydrous conditions via the formation of hemithioketal as an intermediate (Figure 2.16).<sup>95</sup> The protonation of the furan was suggested to be the rate-determining step for both pathways with water acting as a competing nucleophile.<sup>95,96</sup> The direct conversion of 2,5-dimethylfuran (2,5-DMF) to 2,5-dimethylthiophene (2,5-DMT) was estimated as the kinetically preferred pathway ( $1.68 \cdot 10^{-4} \text{ s}^{-1}$ ) with the hydrolysis of 2,5-DMF being a slower process ( $0.58 \cdot 10^{-4} \text{ s}^{-1}$ ) under homogeneous Brønsted acid catalysis conditions.<sup>95</sup> These preliminary studies on the acid-catalysed recyclization of furans into thiophenes did not exclude the protonation of the  $\beta$ -carbons whereas a protonated oxygen intermediate was not considered to be thermodynamically stable.<sup>97</sup> More recent quantum-chemical calculations on the hydrolysis of 2,5-DMF in the presence of a Brønsted acid catalyst has estimated that



the primary proton transfer between  $\text{H}_3\text{O}^+$  and the  $\text{C}_3$  carbon was the rate-limiting step ( $E_a = 20 \text{ kcal mol}^{-1}$ ) (Figure 2.17B).<sup>98</sup> An alternative pathway for the formation of 2,5-hexanedione (Figure 2.17A) involves an initial  $\alpha$ -protonation with the water-binding step being the slowest, having an  $E_a$  value of  $27 \text{ Kcal mol}^{-1}$ . The  $\beta$ -C protonation pathway was therefore proposed for the hydrolysis of 2,5-DMF into 2,5-hexanedione, which is also an intermediate of the recyclization of 2,5-DMF into 2,5-DMT.<sup>95,98</sup>

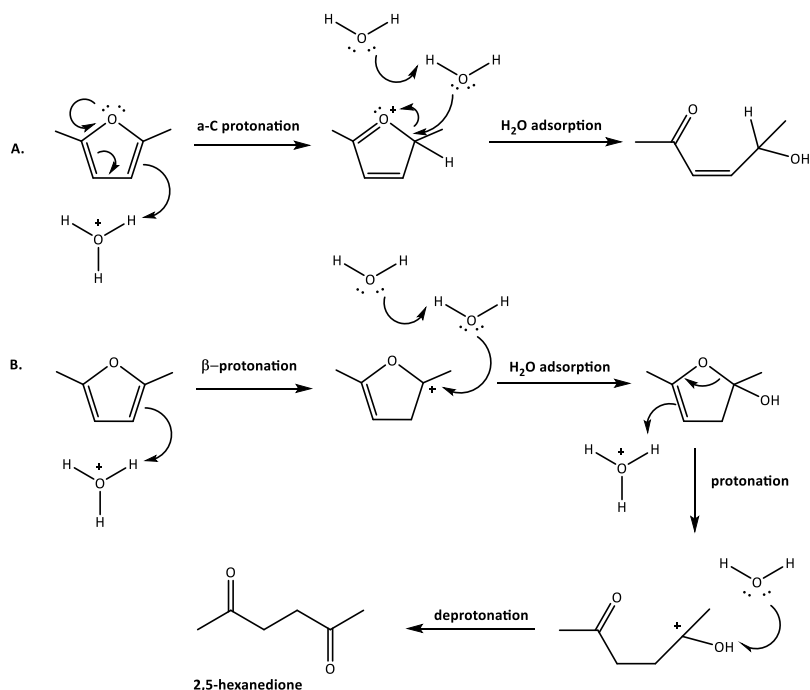


**Figure 2.17:** Reaction mechanisms for the Brønsted acid-catalysed hydrolysis of 2,5-DMF by A)  $\alpha$ -protonation B)  $\beta$ -protonation mechanisms based on NBO analysis.<sup>98</sup>

The recyclization of 2,5-DMF into 2,5-DMT proceeds via acid-catalysis in anhydrous media, common for conditions for strong acids in polar solvents, with the rate constant being directly proportional on the acidity of the reaction medium as expressed by the Hammett acidity function ( $H_0$ ).<sup>96</sup> Carbonyl and carboxyl groups at the  $\alpha$  position of the furan ring exhibit an inhibitory effect for the recyclization of the furan derivatives by reducing the electron density of the ring.<sup>87,93,94</sup> A decrease of the recyclization rate was observed upon the introduction of alkyl substituents at the  $\beta$  position of the ring and a similar effect was observed on the rate of hydrolysis towards the formation of 1,4-diketones, with tetraalkylfurans failing to not hydrolyse under the same experimental conditions.<sup>94</sup>

### 2.2.3 Ionic liquids and thiophene synthesis

The synthesis of thiophenes in ionic liquids has not been widely researched and only a few examples have been reported, mainly involving the cyclization of open-chain precursors. To the best of our knowledge, there have been no reports of the synthesis of thiophenes from heterocyclic precursors using ionic liquids as solvents and/or catalysts. Substituted thiophenes have been prepared from 1,4-dicarbonyl compounds and Lawesson's reagent (resulting in very poor atom economy) in  $[\text{C}_4\text{C}_1\text{im}][\text{BF}_4]/\text{Bi}(\text{OTf})_3$  (5 h, 90 °C, 80 - 87 % yield) (Figure 2.18).<sup>99</sup> Nevertheless, the cyclization of 1,4-diketones did not occur in the absence of the added Lewis acid catalyst (5 mol %  $\text{Bi}(\text{OTf})_3$ ).<sup>99</sup> Recyclability was therefore reported as the main benefit of the IL-based catalyst with the products being isolated by extraction with diethyl ether.<sup>99</sup>

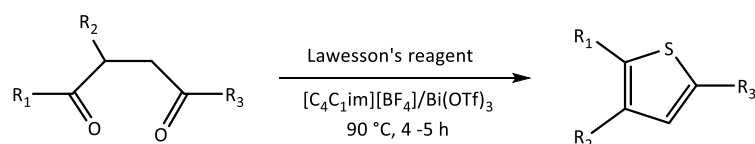


Figure 2.18: Lewis acid-catalysed Paal-Knorr thiophene synthesis in  $[\text{C}_4\text{C}_1\text{im}][\text{BF}_4]/\text{Bi}(\text{OTf})_3$ .

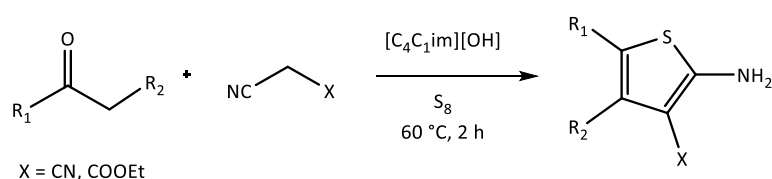
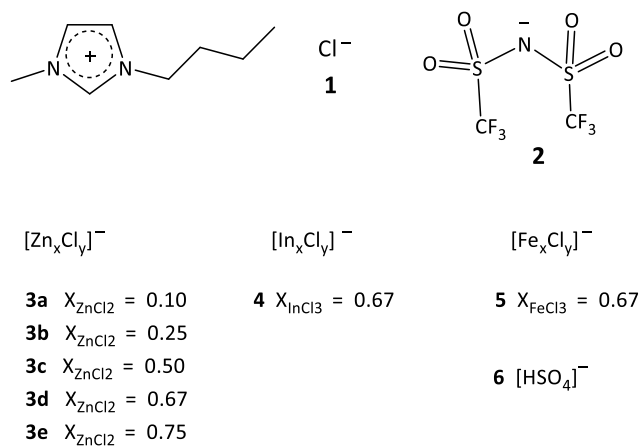


Figure 2.19: Base-catalysed Gewald synthesis of 4,5-dialkyl-2-aminothiophenes in  $[\text{C}_4\text{C}_1\text{im}][\text{OH}]$ .

4,5-dialkyl-2-aminothiophenes have been synthesized in basic  $[\text{C}_4\text{C}_1\text{im}][\text{OH}]$ , used as a solvent and a catalyst, in yields up to 92 % (60 °C, 2 h) (Figure 2.19).<sup>100</sup> Gewald synthesis involves condensation, base-promoted activation of the intermediates, sulfur-addition and cyclization (**Section 2.2.1**). It was suggested that  $[\text{C}_4\text{C}_1\text{im}][\text{OH}]$  catalysed both the condensation of the ketone with the activated nitrile and the sulfur addition step with an enhanced product selectivity (> 90 %).<sup>100</sup> However,  $[\text{C}_4\text{C}_1\text{im}][\text{OH}]$  is the subject of questions over its composition and stability.<sup>101,102</sup> DFT calculations indicated that  $[\text{C}_2\text{C}_1\text{im}][\text{OH}]$  does not exist in the form of ion pairs but as water and an imidazole carbene upon the complete dissociation of the  $\text{C}^2$ -proton from the cation.<sup>101</sup> The dilution of 1,3-disubstituted imidazolium hydroxides in water or polar organic solvents improves their stability, albeit through deviation from the properties associated with neat ionic liquids.<sup>102,103</sup> The addition of water has shown to favour the formation of ion pairs with the negative charge of the anion being dispersed over the hydrogen-bonded  $\text{OH}^-/\text{H}_2\text{O}$  cluster.<sup>101</sup>

## 2.3 Results & Discussion

### 2.3.1 Ionic liquids synthesis



**Figure 2.20:** Chemical structures of the studied  $[C_4C_1im]^+$ -based ionic liquids, incorporating chloride (1), bis(trifluoromethanesulfonyl)imide (2), hydrogen sulfate (6) and metal chloride (3a-3e, 4, 5) anions.  $[Zn_xCl_y]^-$ ,  $[In_xCl_y]^-$  and  $[Fe_xCl_y]^-$  represent the complex anions formed at different compositions ( $0.10 \leq X_{MCl_x} \leq 0.75$ ).

A series of moisture-stable halometallate ionic liquids were prepared upon mixing  $[C_4C_1im]Cl$  with varying molar concentrations of anhydrous metal chlorides:  $ZnCl_2$ ,  $FeCl_3$  and  $InCl_3$ . In the context of testing the effect of Brønsted acidity on the recyclization of furanics with  $H_2S$ ,  $[C_4C_1im][HSO_4]$  was prepared via an acid-base neutralisation between  $[C_4C_1im]Cl$  and concentrated  $H_2SO_4$  (DCM, 0 °C). Additionally,  $[C_4C_1im][NTf_2]$  was synthesised via a metathesis reaction between  $[C_4C_1im]Cl$  and  $LiNTf_2$  (48 h, DCM, rt) and this was used as a benchmark for the thermal stability study of the halometallate ILs. The detailed synthetic protocols are provided in **Section 2.4**. Ionic liquids based on 1,4-dialkylimidazolium cations have been broadly studied as biomass deconstruction solvents<sup>104</sup> as well as stable solvents and catalysts for the formation of 5-HMF from sugars.<sup>105,106</sup> The precursor salt,  $[C_4C_1im]Cl$ , was prepared by the alkylation of 1-methylimidazole in ethyl acetate at 65 - 70 °C (Figure 2.21). Ethyl acetate dissolved the starting materials but not the desired halide salt, allowing better mass transport and easier product separation. The relatively high activation energy of the nucleophilic substitution led to prolonged reaction times (> 4 days) before high yields (> 70 %) were ultimately achieved. The product was a solid compound at room temperature and thus it was purified by recrystallization from a mixture of dry ethyl acetate and acetonitrile (5:1), affording white crystals. The purification of ionic liquids is crucial in order to exclude the possibility of impurities modifying their activity as catalysts as well as for preventing any changes in their nature as solvents.<sup>107</sup>  $[C_4C_1im]Cl$  is highly hygroscopic; hence water was removed by overnight heating under vacuum. Nonetheless, a

complete removal of residual water must be considered challenging given the enhanced intermolecular interactions between the ions of the IL and water.<sup>107</sup>

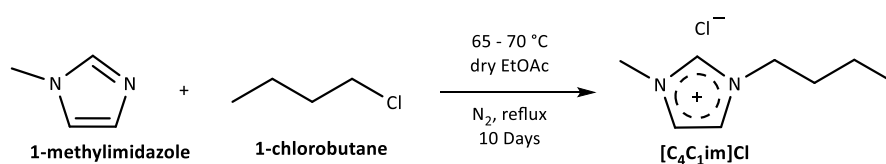


**Figure 2.21:** Reaction scheme for the synthesis of [C<sub>4</sub>C<sub>1</sub>im]Cl.

The metal chloride molar ratio used for the synthesis of the halometallate ILs is defined by equation 2.2 and an exothermic reaction was observed upon the addition of the metal chloride to [C<sub>4</sub>C<sub>1</sub>im]Cl. Overnight heating (105 °C, 12 h) was still required to obtain a transparent viscous liquid. All chlorozincate(II) compositions ( $0.10 \leq X_{\text{ZnCl}_2} \leq 0.75$ ) were highly viscous, homogeneous compounds, and were found to be liquid at room temperature. They were therefore applied to the acid-catalysed synthesis of bio-derived thiophenes (**Section 2.3.7**). However, the Lewis acidic compositions of [C<sub>4</sub>C<sub>1</sub>]Cl·InCl<sub>3</sub> and [C<sub>4</sub>C<sub>1</sub>]Cl·FeCl<sub>3</sub> were found to exist as suspensions even after prolonged mixing with undissolved InCl<sub>3</sub> and FeCl<sub>3</sub> at  $X_{\text{MCl}_x} = 0.67$ .

$$X_{\text{MCl}_x} = \frac{n_{\text{MCl}_x}}{n_{\text{MCl}_x} + n_{[\text{C}_4\text{C}_1\text{im}]\text{Cl}}} \quad (2.2)$$

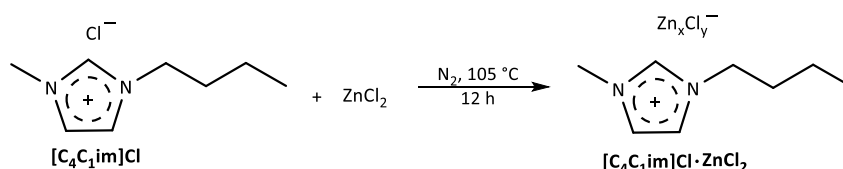


**Figure 2.22:** Synthesis of [C<sub>4</sub>C<sub>1</sub>im]Cl·ZnCl<sub>2</sub> ( $0.10 \leq X_{\text{ZnCl}_2} \leq 0.75$ ) from [C<sub>4</sub>C<sub>1</sub>im]Cl with a varying anionic composition [Zn<sub>x</sub>Cl<sub>y</sub>].

The purity of all ionic liquids was tested by NMR spectroscopy (<sup>1</sup>H, <sup>13</sup>C), elemental analysis and mass spectrometry. Water content, as determined by coulometric Karl Fischer (KF) titration, was less than 100 ppm. The confirmation of the anionic speciation and the acidity of the chlorometallate ionic liquids were achieved by Mass Spectrometry and IR spectroscopy, respectively. Thermogravimetric analysis (TGA) was used to examine the short-term and long-term thermal stability of the chlorometallate ionic liquids whereas capillary NMR spectroscopy (<sup>1</sup>H, <sup>13</sup>C) was applied to obtain further information on the interionic interactions in the chlorometallate ionic liquids as a function of their composition.

### 2.3.2 Determination of anionic speciation by Mass Spectrometry

The compositions of  $[\text{C}_4\text{C}_1\text{im}]\text{Cl}\cdot\text{ZnCl}_2$  ( $X_{\text{ZnCl}_2} = 0.10, 0.25, 0.50, 0.67$  and  $0.75$ ) as well as the Lewis acidic suspensions of  $[\text{C}_4\text{C}_1\text{im}]\text{Cl}\cdot\text{FeCl}_3$  and  $[\text{C}_4\text{C}_1\text{im}]\text{Cl}\cdot\text{InCl}_3$  ( $X_{\text{FeCl}_3} = X_{\text{InCl}_3} = 0.67$ ) were probed by MALDI-TOF and FAB mass spectrometry. The MALDI-TOF spectra contained much heavier clusters in comparison with the respective FAB spectra. FAB was therefore used to confirm the anionic speciation of the synthesised ILs containing varying amounts of  $\text{ZnCl}_2$ ,  $\text{FeCl}_3$  or  $\text{InCl}_3$ . The peak corresponding to  $[\text{C}_4\text{C}_1\text{im}]^+$  ( $m/z$  139) was the one of highest intensity for all chlorometallate ILs. In the negative mode ( $\text{FB}^-$ ), a peak at  $m/z$  172, assigned to  $[\text{ZnCl}_3]^-$ , was detected in all chlorozincate(II) compositions whereas the expected peak of  $[\text{ZnCl}_4]^{2-}$  ( $m/z$  104) was not observed. The binuclear anion ( $m/z$  309),  $[\text{Zn}_2\text{Cl}_5]^-$ , was present in both basic and acidic compositions whereas  $[\text{Zn}_3\text{Cl}_7]^-$  ( $m/z$  444) was only detected for  $X_{\text{ZnCl}_2} = 0.67$ , with a low intensity ( $< 10\%$ ). Similar speciation studies based on FAB-MS and ESI-MS have also previously suggested the presence of  $[\text{ZnCl}_3]^-$  and  $[\text{Zn}_2\text{Cl}_5]^-$  in the melt instead of the doubly-charged anions:  $[\text{ZnCl}_4]^{2-}$  and  $[\text{Zn}_2\text{Cl}_6]^{2-}$ .<sup>19,21,108</sup> The absence of double charged anions can be attributed to the fragmentation of  $[\text{ZnCl}_4]^{2-}$  to  $[\text{ZnCl}_3]^-$  that reacts with  $\text{ZnCl}_2$  further, forming bulkier anions:  $[\text{Zn}_2\text{Cl}_5]^-$  and  $[\text{Zn}_3\text{Cl}_7]^-$ .<sup>3</sup> Overall, the application of mass spectrometry allows the different compositions of halometallate ionic liquids to be distinguished but a precise determination of anionic speciation can be challenging given that gas-phase reactions and/or the thermal decomposition of the anionic species may affect speciation in ways that are not always easy to predict.<sup>3,108</sup> A cluster comprising the cation and chloride,  $[(\text{C}_4\text{C}_1\text{im})\text{Cl}_2]^-$  ( $m/z$  210), was also observed in all compositions with a variable intensity. Additional peaks, belonging to unidentified clusters, were consistently present at  $m/z$  267 and 282. Negative ion mass spectrometry of  $[\text{C}_4\text{C}_1\text{im}]\text{Cl}\cdot\text{InCl}_3$  ( $X_{\text{InCl}_3} = 0.67$ ) was indicative of  $[\text{InCl}_4]^-$  ( $m/z$  258, 100%) whereas a low intensity peak at  $m/z$  482 was assigned to  $[\text{In}_2\text{Cl}_7]^-$ . The presence of  $[\text{In}_2\text{Cl}_7]^-$  has been reported before when mass spectrometry was applied as a speciation determination tool.<sup>3</sup> In this work, the dominant presence of  $[\text{FeCl}_4]^-$  ( $m/z$  199) and the appearance of undissolved  $\text{FeCl}_3$  were also confirmed by ( $\text{FB}^-$ ). Clusters with  $m/z$  values of 290, 326 and 417 were assigned to  $[\text{Fe}_2\text{Cl}_5]^-$ ,  $[\text{Fe}_2\text{Cl}_6]^-$  and  $[\text{Fe}_2\text{Cl}_7]^-$  respectively, with a very low intensity ( $< 5\%$ ) peak for the latter. Speciation determination in the liquid state have previously shown that  $[\text{Fe}_2\text{Cl}_7]^-$  coexists with  $[\text{FeCl}_4]^-$  at  $X_{\text{FeCl}_3} > 0.60$  whereas higher  $\text{FeCl}_3$  concentrations do not result into the existence of pure  $[\text{Fe}_2\text{Cl}_7]^-$ .<sup>22,23,35</sup> The sample FAB-MS spectra, in positive and negative mode, are provided for  $[\text{C}_4\text{C}_1\text{im}]\text{Cl}\cdot\text{ZnCl}_2$  ( $X_{\text{ZnCl}_2} = 0.67$ ) (**Appendix 2.6.1**).

### 2.3.3 Thermal degradation behaviour of [C<sub>4</sub>C<sub>1</sub>im]Cl·MCl<sub>x</sub> (MCl<sub>x</sub>: ZnCl<sub>2</sub>, FeCl<sub>3</sub>, InCl<sub>3</sub>; X<sub>MCl<sub>x</sub></sub> = 0.67); Dynamic Scans

The thermal stability of ionic liquids is crucial as the formation of degradation products has an impact on their suitability for high-temperature applications and their recycling efficiency due to alterations in the physicochemical properties of the melt.<sup>109</sup> Additionally, the accumulation of toxic and volatile degradation products can be a safety hazard upon prolonged operation times. Temperature-ramped thermogravimetric analysis (TGA) is an efficient method for the rapid comparison of the thermal stability of ionic liquids by determining their onset decomposition temperature ( $T_{\text{onset}}$ ), under comparable experimental conditions.<sup>110–112</sup> The effect of the anion on thermal stability is known to be prominent with a reported increase of the  $T_{\text{onset}}$  by more than 100 °C upon performing anion metathesis in imidazolium-based ILs, such as replacing halide ions with perfluorinated anions that are associated with superior thermal stability.<sup>110,112–117</sup> However, the formation of impurities without mass losses has been detected for pyrrolidinium and imidazolium bistriflimide-based ILs at temperatures as low as 150 °C, as determined by UV-vis and fluorescence spectroscopy.<sup>111</sup> In contrast to the endothermic decomposition in the presence of inorganic anions, an exothermic thermal breakdown occurs for salts comprising organic anions such as [NTf<sub>2</sub>]<sup>-</sup>.<sup>110</sup> Anion degradation has been proposed as the primary step of the thermal breakdown of [C<sub>4</sub>C<sub>1</sub>im][NTf<sub>2</sub>], combined with SO<sub>2</sub> gas release.<sup>118</sup> The decomposition of [NTf<sub>2</sub>]<sup>-</sup> and the formation of strongly nucleophilic groups, NH<sub>2</sub><sup>-</sup> and F<sup>-</sup>, is followed by a nucleophilic attack on the alkyl groups of the imidazolium cation or elimination, over 350 °C.<sup>119</sup> Ionic liquids, based on non-coordinating anions such as [NTf<sub>2</sub>]<sup>-</sup>, are generally dominated by Hoffman-type elimination reactions over the S<sub>N</sub>1/S<sub>N</sub>2 decomposition mechanisms.<sup>119</sup> The reverse Menshutkin dealkylation reaction is the main mechanism for the decomposition of 1,3-dialkylimidazolium halide salts, yielding neutral species with the degradation of the cation occurring above 500 °C.<sup>120,121</sup> Even though the thermal decomposition of ionic liquids has been thoroughly reviewed,<sup>112,121</sup> there has been little emphasis on the thermal stability of acidic ionic liquids. Sulfonic acid-functionalized, Brønsted acidic ILs, have been found to be less thermally stable (213 °C <  $T_{\text{onset}}$  < 353 °C) than their corresponding neutral ILs (282 °C <  $T_{\text{onset}}$  < 470 °C) whereas the nucleophilicity of the anion had a similar effect between neutral and acidic ILs.<sup>122</sup> The thermal stability of the Lewis acidic, [C<sub>4</sub>C<sub>1</sub>im]<sup>+</sup>-based, chlorohafnates(IV) and chlorozirconates(IV) (X<sub>MCl<sub>x</sub></sub> = 0.33) has proven to be higher than that of [C<sub>4</sub>C<sub>1</sub>im]Cl with a  $T_{\text{onset}}$  of more than 30 degrees higher for the chlorometallate ILs.<sup>123</sup> Nevertheless, the effect of speciation and metal chloride ratio on the thermal stability has not been discussed. Furthermore, a study on the thermophysical properties of chloroferrates(III) has estimated a  $T_{\text{onset}}$  of 371 °C for [C<sub>4</sub>C<sub>1</sub>im]Cl·FeCl<sub>3</sub> (X<sub>FeCl<sub>3</sub></sub> = 0.50) and the need to investigate the long-term thermal stability of these ionic liquids was highlighted.<sup>24</sup> Phase transition studies have been completed for several chlorometallate ionic liquids such as [C<sub>8</sub>C<sub>1</sub>im]Cl·ZnCl<sub>2</sub>,

indicating more than one glass transition due to the presence of dynamic equilibria between multiple anions.<sup>19,108</sup> Differential scanning calorimetry (DSC) analysis of the C2-substituted [C<sub>4</sub>C<sub>1</sub>im]Cl·ZnCl<sub>2</sub> with variation of X<sub>ZnCl<sub>2</sub></sub> yielding a relative trend of increasing the decomposition temperature upon increasing the X<sub>ZnCl<sub>2</sub></sub>.<sup>19</sup> DSC studies have been mainly performed on 1,3-dialkylimidazolium-based halometallate ionic liquids to study the phase behaviour, as an indirect tool for examining the anionic speciation.<sup>19,30,108,123–125</sup> In this work, the short-term thermal stability of chlorometallate ILs was assessed via TGA in order to examine the relationship between the anionic composition of the ionic liquid and its short-term thermal stability. The temperature-ramped experiments monitored the weight loss (%) as a function of temperature, at a constant heating rate (10 K min<sup>-1</sup>). The T<sub>onset</sub> was extrapolated as the intersection of the baseline and the tangent of the weight dependence on the temperature curve as decomposition occurs. Additionally, the derivative curves were used to obtain the respective first derivative peak temperature (T<sub>peak</sub>), indicating the point at which the sample undergoes maximum decomposition. Plotting the first derivative of weight loss (dw/dt) allows the distinction between subtle, overlapping weight loss processes that might not be evident by solely examining the TG curves. The T<sub>peak</sub> value is therefore an additional parameter of the short-term thermal stability of the ionic liquids tested.<sup>112,126</sup> Figure 2.23 shows both the TG and DTG curves of the Lewis acidic compositions of [C<sub>4</sub>C<sub>1</sub>im]Cl·ZnCl<sub>2</sub>, [C<sub>4</sub>C<sub>1</sub>im]Cl·InCl<sub>3</sub> and [C<sub>4</sub>C<sub>1</sub>im]Cl·FeCl<sub>3</sub> (X<sub>MCl<sub>x</sub></sub> = 0.67), obtained under a nitrogen atmosphere. [C<sub>4</sub>C<sub>1</sub>im][NTf<sub>2</sub>] and [C<sub>4</sub>C<sub>1</sub>im]Cl were also screened as reference compounds.

**Table 2.3:** Comparison of T<sub>onset</sub> and T<sub>peak</sub> for Lewis acidic chlorometallates, [C<sub>4</sub>C<sub>1</sub>im]Cl and [C<sub>4</sub>C<sub>1</sub>im][NTf<sub>2</sub>].

Ionic liquid	X <sub>MCl<sub>x</sub></sub>	T <sub>onset</sub> / °C	T <sub>peak</sub> / °C
[C <sub>4</sub> C <sub>1</sub> im]Cl	0	259	284
[C <sub>4</sub> C <sub>1</sub> im][NTf <sub>2</sub> ]	0	418	456
[C <sub>4</sub> C <sub>1</sub> im]Cl·FeCl <sub>3</sub>	0.67	355	409 <sup>a</sup>
[C <sub>4</sub> C <sub>1</sub> im]Cl·InCl <sub>3</sub>	0.67	428	462 <sup>b</sup>
[C <sub>4</sub> C <sub>1</sub> im]Cl·ZnCl <sub>2</sub>	0.67	398	530 <sup>c</sup>

\*Note: a, b: shoulders appear at T > T<sub>peak</sub> c: broad shoulder observed at T > 400 °C (T < T<sub>peak</sub>)

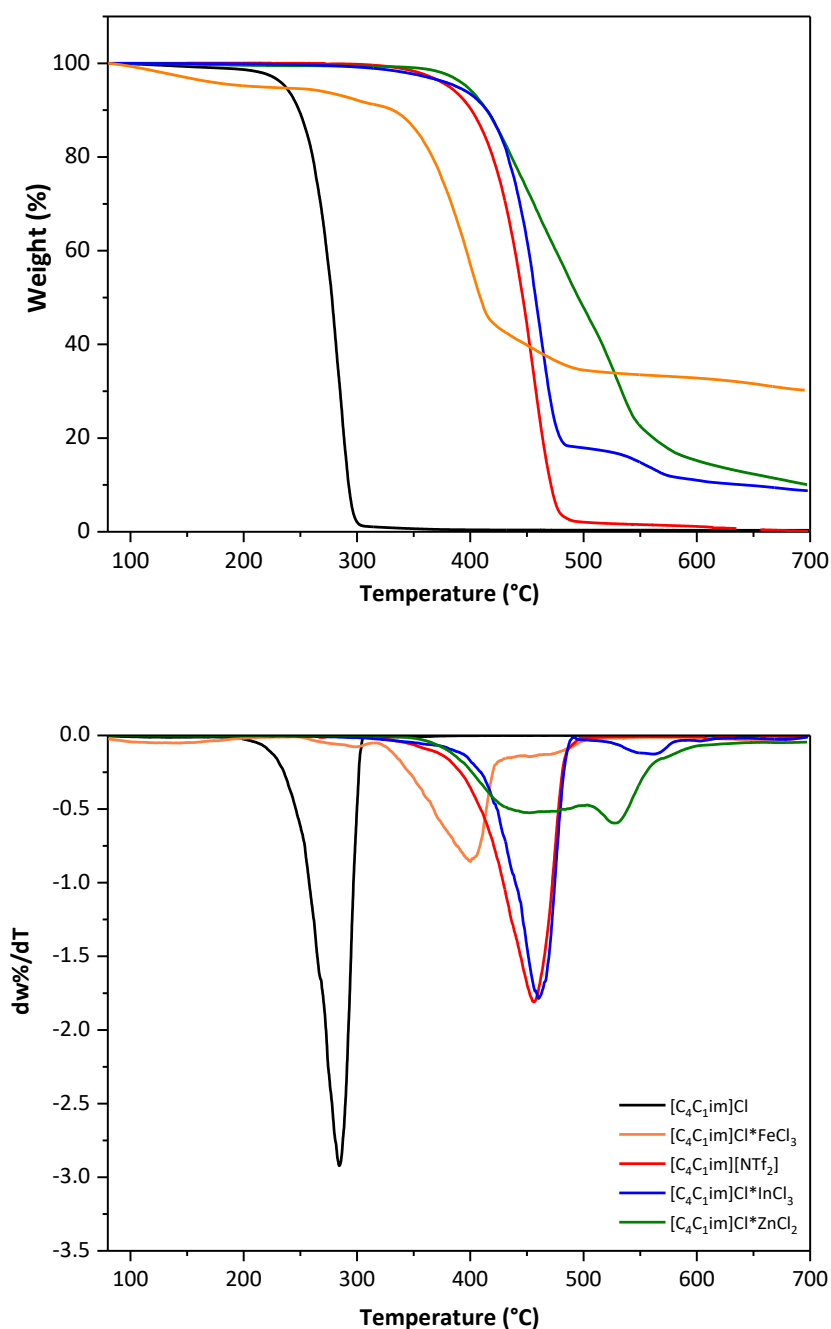


**Figure 2.23:** a) Temperature-ramped (TG) and b) derivative (DTG) curves for  $[\text{C}_4\text{C}_1\text{im}]^+$ -based ILs and a series of anions: chloride (1), bis(trifluoromethanesulfonyl)imide (2) and metal chloride-based anions (3d, 4 and 5,  $X_{\text{MClx}} = 0.67$ ). All thermographs were obtained with a heating rate of  $10 \text{ K min}^{-1}$ .

The  $T_{\text{onset}}$  value of  $[\text{C}_4\text{C}_1\text{im}]\text{Cl}$  was estimated at  $259 \text{ }^\circ\text{C}$ , in agreement with literature values ( $254 \text{ }^\circ\text{C}$ ).<sup>116</sup> Furthermore, the  $T_{\text{onset}}$  of  $[\text{C}_4\text{C}_1\text{im}][\text{NTf}_2]$  was estimated at  $418 \text{ }^\circ\text{C}$ , in line with previously reported  $T_{\text{onset}}$  values, exceeding  $400 \text{ }^\circ\text{C}$  for  $[\text{C}_4\text{C}_1\text{im}][\text{NTf}_2]$ .<sup>126</sup> Herein, the introduction of Lewis acidic chlorometallate anions led to significant improvements in the thermal stability of  $[\text{C}_4\text{C}_1\text{im}]^+$ , with a  $T_{\text{onset}}$  comparable to



that of  $[\text{C}_4\text{C}_1\text{im}][\text{NTf}_2]$ . The thermal stability trend followed for the anions was  $[\text{In}_x\text{Cl}_y]^- > [\text{Zn}_x\text{Cl}_y]^- > [\text{Fe}_x\text{Cl}_y]^-$  with the following  $T_{\text{onset}}$ : 428 °C, 398 °C and 355 °C, respectively. The first derivative plot (DTG) revealed one single peak for  $[\text{C}_4\text{C}_1\text{im}]\text{Cl}$  and  $[\text{C}_4\text{C}_1\text{im}][\text{NTf}_2]$ . The peak temperature for  $[\text{C}_4\text{C}_1\text{im}]\text{Cl}$  appears at approximately 284 °C whilst the  $T_{\text{peak}}$  of  $[\text{C}_4\text{C}_1\text{im}][\text{NTf}_2]$  was estimated at 456 °C, in agreement with literature values.<sup>112</sup> The presence of more than one broad shoulder was found in the DTG curves of the Lewis acidic compositions ( $X_{\text{MCl}_x} = 0.67$ ) of  $[\text{C}_4\text{C}_1\text{im}]\text{Cl}\cdot\text{FeCl}_3$  and  $[\text{C}_4\text{C}_1\text{im}]\text{Cl}\cdot\text{ZnCl}_2$ , highlighting decomposition mechanisms that are highly dependent on the nature of the anionic species. An additional DTG peak also arised above 500 °C for the  $\text{InCl}_3$ -based suspension ( $X_{\text{InCl}_3} = 0.67$ ). Assigning a single  $T_{\text{peak}}$  is challenging and the values summarised in Table 2.3 indicate the temperature corresponding to the highest peak. Solely  $[\text{InCl}_4]^-$  is expected to be found in the melt at  $X_{\text{InCl}_3} = 0.67$  together with undissolved  $\text{InCl}_3$ , whereas the acidic chlorozincates(II) and chloroferrates(III) contain polynuclear anions, potentially affecting the steps of the thermal degradation process.

### 2.3.4 Thermal stability of $[\text{C}_4\text{C}_1\text{im}]\text{Cl}\cdot\text{ZnCl}_2$ as a function of composition; Dynamic Scans

Five compositions of  $[\text{C}_4\text{C}_1\text{im}]\text{Cl}\cdot\text{ZnCl}_2$  ( $0.10 \leq X_{\text{ZnCl}_2} \leq 0.75$ ) were tested for their thermal decomposition with the aim of confirming the dependence of the thermal stability on the formation of oligomeric anions. Figure 2.24 illustrates the thermogravimetric analysis for each composition and the derivative of the mass loss curve. The TG curves reveal a gradual increase of the  $T_{\text{onset}}$  as the  $X_{\text{ZnCl}_2}$  was augmented with the acidic melts ( $X_{\text{ZnCl}_2} > 0.33$ ) exhibiting the highest  $T_{\text{onset}}$  and  $T_{\text{peak}}$  values (Table 2.4).

**Table 2.4:** Comparison of  $T_{\text{onset}}$  and  $T_{\text{peak}}$  for Lewis acidic chlorozincate(II) compositions.

Ionic liquid	$X_{\text{MCl}_x}$	$T_{\text{onset}} / ^\circ\text{C}$	$T_{\text{peak}} / ^\circ\text{C}$
	0.10	255	283 <sup>a</sup>
	0.25	253	280, 337, 458 <sup>b</sup>
$[\text{C}_4\text{C}_1\text{im}]\text{Cl}\cdot\text{ZnCl}_2$	0.50	362	444, 507 <sup>c</sup>
	0.67	398	532 <sup>d</sup>
	0.75	422	501 <sup>e</sup>

b – e: an approximate  $T_{\text{peak}}$  value being provided due to the presence of broad shoulders near the DTG peaks

The Lewis acidity in halometallate ionic liquids has been linked to the presence of polynuclear anions and  $X_{\text{MCl}_x} = 0.50$  has often been determined as the neutral point.<sup>3,27</sup> Nevertheless, free chloride anions are only found in chlorozincate(II) melts at  $X_{\text{ZnCl}_2} < 0.33$  whereas polynuclear anions are detected at  $X_{\text{ZnCl}_2} \geq 0.33$ .<sup>31,33,108</sup> The recognition that chlorozincate(II) ionic liquids were acidic at  $X_{\text{ZnCl}_2} = 0.50$  was

confirmed by means of IR spectroscopy (Section 2.3.7.1), in line with reported results obtained by the Gutmann Acceptor Number (AN) or similar screening tests by IR spectroscopy.<sup>27,108</sup> An investigation on how the modifications in interionic interactions, upon varying the anionic composition, may be associated with the thermal stability of the studied halometallate ILs is described in Section 2.3.5.

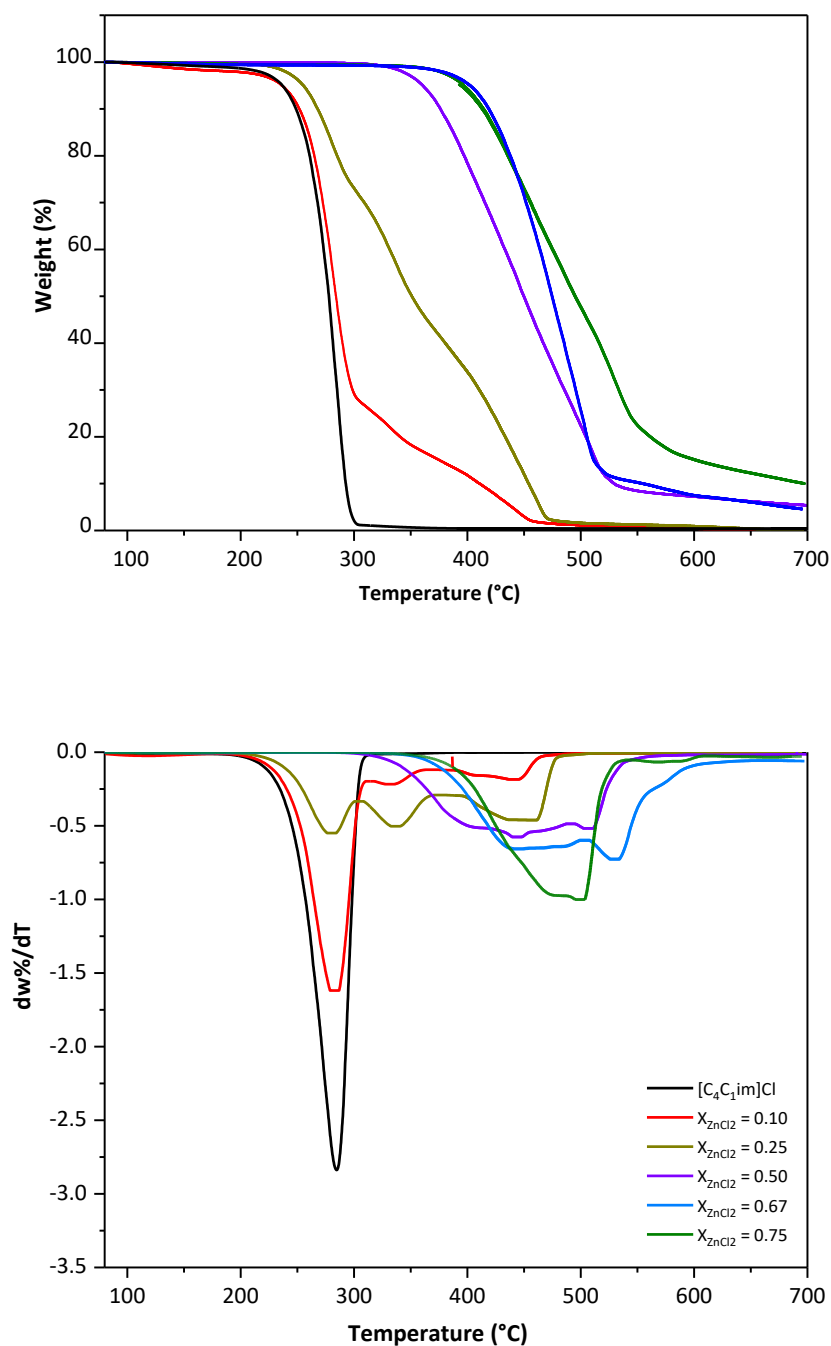


**Figure 2.24:** a) TG and b) DTG curves of [C<sub>4</sub>C<sub>1</sub>im]Cl·ZnCl<sub>2</sub> with X<sub>ZnCl<sub>2</sub></sub> = 0.10, 0.25, 0.50, 0.67 and 0.75 (3a-e). Thermographs were obtained with a heating rate of 10 °C min<sup>-1</sup>.

## 2.3.5 Chemical shift progression as a function of composition; chlorometallate ILs

### 2.3.5.1 Complex intramolecular interactions in 1,3-dialkylimidazolium-based ionic liquids

Ionic liquids are characterised by a complex combination of Coulombic, Lewis acid/base, hydrogen bonding, dipole-dipole, dispersion and Van-Der-Waals interactions between their ions.<sup>127</sup> Electrostatic interactions dominate the ion pair and therefore contribute to the relative arrangements of the ions in both aprotic and protic ionic liquids.<sup>128</sup> Nonetheless, a strong directionality has been deduced for the intramolecular interactions within protic ionic liquids with the anions preferably interacting with the N-H bonds of the cation.<sup>128</sup> Amongst the different types of ionic liquids, 1,3-dialkylimidazolium-based salts have a unique electronic structure comprising a weak charge delocalization in the central region of the aromatic ring.<sup>127,129</sup> The concept of 1,3-dialkylimidazolium-based ionic liquids being polymeric supramolecules, partially due to an extended three-dimensional H-bonding network, has been proposed for both the solid and liquid state.<sup>130,131</sup> However, Coulombic and solvophobic interactions as well as the relative dimensions of polar and non-polar moieties of the ions have been considered as additional factors impacting the self-assembly process.<sup>132</sup> Additionally, the competitive relationship between  $\pi^+$ - $\pi^+$  stacking,  $\pi^+$ -anion interactions and hydrogen-bonding creates a complex interplay of structural features in imidazolium-based ionic liquids.<sup>133</sup> In the case of  $[\text{C}_4\text{C}_1\text{im}]\text{Cl}$ ,  $\text{Cl}^-$  interacts with the hydrogen atoms of the cation via H-bonding, with charge-transfer effects influencing the charge of the  $\text{C}_{\text{ring}}$  and  $\text{C}_{\text{alkyl}}$  carbon atoms.<sup>129</sup> Crystal structure analysis has also confirmed the presence of an extended hydrogen-bonding network between  $\text{Cl}^-$  and  $[\text{C}_4\text{C}_1\text{im}]^+$ , in addition to hydrophobic interactions between the n-butyl chains attached to the cation.<sup>134</sup> The formation of charged hydrogen-bonded complexes between  $\text{Cl}^-$  and the cation of imidazolium-based ionic liquids has also been confirmed by more recent *ab initio* calculations.<sup>135</sup> Hydrogen-bonding in ionic liquids deviates from the ideal arrangement found in molecular liquids.<sup>132,135,136</sup> This is reflected in the exaggerated elongation of each C-H bond and the total attractive energy values, given the stronger electrostatic and induction forces in such charged complexes.<sup>135</sup> Ion-ion interactions where  $\text{Cl}^-$  is found either above or below the plane of the imidazolium ring, are stabilised by Coulombic interactions, whereas the location of the anion in the plane of the imidazolium ring, is promoted by the relatively weaker hydrogen bonding interactions.<sup>135</sup> Distinguishing between the net effect of the Coulombic interactions between the ions and the Coulomb electrostatic energy contribution to the hydrogen-bonding motif in the ionic liquid is challenging.<sup>137</sup> Molecular dynamics investigations have confirmed four different interactions between  $\text{Cl}^-$  and  $[\text{C}_4\text{C}_1\text{im}]^+$  with the strongest being the H-bonding between  $\text{Cl}^-$  and the ring protons ( $\text{C}^2$ ,  $\text{C}^4/\text{C}^5$ ), whereas weaker, mostly electrostatic in nature, hydrogen-bonds appear between the hydrogens of the alkyl chains and  $\text{Cl}^-$ .<sup>130,137</sup> The protons on the  $\text{C}^6$  and  $\text{C}^7$  carbon atoms do show a higher coordination number towards  $\text{Cl}^-$ , resulting in a stabilisation of the H-bonding network within the ionic liquid.<sup>136,137</sup> Interestingly, the out-of-plane

conformers, driven by anion- $\pi$  interactions, are also stabilised by these interactions and additional contributions from the alkyl chain hydrogen atoms of the n-butyl chain.<sup>137</sup> Quantum chemical calculations on imidazolium-based ionic liquids with multiatomic perfluorinated anions have also been applied to the investigation of non-covalent interionic interactions and their effect on the electron density distribution within the IL.<sup>138</sup> These investigations confirmed the contribution of diverse non-covalent, intramolecular interactions. A trend similar to that found for [C<sub>4</sub>C<sub>1</sub>im]Cl was discovered in terms of varying strength of hydrogen-bonding between the anion and the different cationic C-H sites, albeit with a lack of strong directional hydrogen bonds when less basic anions are present.<sup>138</sup> The study of [C<sub>8</sub>C<sub>1</sub>im]<sup>+</sup>-based ILs with basic or perfluorinated anions by XPS and NMR spectroscopy indicated cation-anion charge-transfer phenomena, mainly driven by the coordinating properties of the anion.<sup>139</sup> Charge-transfer and hydrogen bonding between an imidazolium-based cation and a given anion can be mutually independent, although, the strength of both interactions is significantly reduced for large, weakly coordinating anions.<sup>139</sup> The increasing binding energies of the nitrogen, carbon and chlorine photoelectron peaks of [C<sub>n</sub>C<sub>1</sub>im]Cl·ZnCl<sub>2</sub> as a function of X<sub>ZnCl<sub>2</sub></sub> revealed the weaker coordinating strength of high-order anions ([Zn<sub>x</sub>Cl<sub>2x+2</sub>]<sup>2-</sup>, X<sub>ZnCl<sub>2</sub></sub> > 0.33) with less pronounced interionic charge-transfer effects and a lower hydrogen-bond anion basicity ( $\beta$ ) for the Lewis acidic anions.<sup>31</sup> A few early publications studied the hydrogen-bonding interactions in halometallate 1,3-dialkylimidazolium-based ionic liquids.<sup>44,140</sup> Crystal structure analysis indicated the involvement of the imidazolium-ring protons in the formation of a hydrogen-bonding network with the [MCl<sub>4</sub>]<sup>2-</sup> anions, found in Lewis basic compositions.<sup>44</sup> The intramolecular network is the result of the interactions between the chlorine atoms of the chlorometallate anion and the protons of the imidazolium ring.<sup>44</sup> Accounting for the charge density of each halide atom within the complex anion, it was suggested that hydrogen-bonding interactions are still present in Lewis basic compositions but an excess of the metal chloride and the formation of oligomeric anions affect the H-bonding network negatively.<sup>44</sup> A significant hydrogen-bonding contribution has been suggested by the crystallographic determination of basic chloroaluminates(III) where [AlX<sub>4</sub>]<sup>-</sup> anions are found in equilibrium with X<sup>-</sup> (X = Cl or Br).<sup>140</sup> Nonetheless, Lewis acidic chloroaluminates(III) are characterised by the successive formation of [Al<sub>2</sub>X<sub>7</sub>]<sup>-</sup> with these anions having weak hydrogen-bond acceptor properties.<sup>140</sup> Chlorometallate anions are found above the imidazolium ring of [C<sub>4</sub>C<sub>1</sub>im]<sup>+</sup>-based ionic liquids, interacting via hydrogen bonding with the C<sup>2</sup> proton as well as the protons of the alkyl chains.<sup>45</sup> The cation-anion interaction energy for chlorometallate ionic liquids, [C<sub>4</sub>C<sub>1</sub>im]Cl·ZnCl<sub>2</sub> and [C<sub>4</sub>C<sub>1</sub>im]Cl·AlCl<sub>3</sub>, has been calculated as being significantly less negative than for [C<sub>4</sub>C<sub>1</sub>im]Cl, where shorter and stronger hydrogen-bonding interactions are found between C<sup>2</sup>-H and Cl<sup>-</sup>.<sup>45</sup> The surface electrostatic potential calculations have also confirmed a stronger Lewis acidity upon increasing the metal chloride molar ratio and therefore the complexity of the

anion.<sup>3,45</sup> Overall, the control of H-bonding network formation can be crucial for applications where ILs are used as solvents/co-catalysts<sup>141</sup> or even as electrolytes,<sup>142</sup> where proton mobility is key.

### 2.3.5.2 NMR spectroscopy as a tool for studying intramolecular interactions in ionic liquids

NMR spectroscopy has proved a powerful tool for studying changes in the intramolecular interactions of ionic liquids as well as mixtures of ILs with molecular solvents. This is due to the ability of the technique to detect even subtle changes in the electronic environment of the nuclei of the constituent atoms.<sup>32,143–145</sup> <sup>1</sup>H NMR spectroscopy, where the IL is used as a probe, has therefore been used for estimating the strength of hydrogen-bonding in imidazolium-based ILs.<sup>41,42</sup> Both conductivity measurements and NMR spectroscopy have been employed for approaching experimentally the concept of hydrogen-bonding in imidazolium-based ionic liquids with halide anions.<sup>146</sup> The composition of Lewis basic, [C<sub>2</sub>C<sub>1</sub>im]<sup>+</sup>-based, chloroaluminates(III) has been determined via NMR spectroscopy, showing an upfield chemical shift progression as a function of composition ( $X_{\text{AlCl}_3}$ ).<sup>143</sup> The chemical shift of the acidic C<sup>2</sup> and C<sup>4</sup>/C<sup>5</sup> protons has shown a composition-dependence as a function of  $X_{\text{AlCl}_3}$ , albeit not upon further increasing the complexity of the anions at  $X_{\text{AlCl}_3} > 0.50$ .<sup>32,143,146</sup> This was attributed to the significant effect of the initial complexation of free Cl<sup>-</sup> upon the formation of weakly coordinating anions: [AlCl<sub>4</sub>]<sup>-</sup> and [Al<sub>2</sub>Cl<sub>7</sub>]<sup>-</sup>.<sup>32</sup> Similarly, an upfield chemical shift progression for the resonance of the C<sup>2</sup>-carbon as a function of  $X_{\text{AlCl}_3}$  has been attributed to the formation of complex anions, affecting the interionic interactions and the charge of the imidazolium ring.<sup>144</sup> Monitoring the progression of the C<sup>2</sup>-proton chemical shift in chlorostannates(II) has also indicated that the proton signal depended heavily on the basicity of the anion.<sup>43</sup> The progressive addition of SnCl<sub>2</sub> led to a decrease of the chemical shift of the C<sup>2</sup>-proton resonance from approximately 10 ppm to 8.3 ppm when Cl<sup>-</sup> was replaced by [SnCl<sub>3</sub>]<sup>-</sup> or [SnCl<sub>4</sub>]<sup>2-</sup> until  $X_{\text{SnCl}_2} = 0.50$  was reached. Smaller changes are noted when the even less basic [Sn<sub>2</sub>Cl<sub>5</sub>]<sup>-</sup> is formed and the chemical shift of this peak was reduced from 8.3 ppm to 7.7 ppm at  $0.60 < X_{\text{SnCl}_2} < 0.75$ .<sup>43</sup> Less pronounced anion concentration-dependant effects have been observed on the chemical shift of the imidazolium ring protons of [C<sub>4</sub>C<sub>1</sub>im]<sup>+</sup>-based ILs bearing non-coordinating anions, [OTf]<sup>-</sup> and [NTf<sub>2</sub>]<sup>-</sup>, mainly attributed to randomised aggregation in place of the organised stacking, which occurs in the presence of basic anions.<sup>147</sup> A positive correlation has also been found between the <sup>1</sup>H chemical shift of the C<sup>2</sup> proton of the imidazolium ring and the empirical Kamlet-Taft parameters of a wide range of anions, suggesting NMR spectroscopy as an alternative way of assessing the Hydrogen Bond Accepting (HBA) properties of ILs.<sup>41,42</sup> The HBA of different anions has been evaluated as the experimental and/or predictive hydrogen bond basicity ( $\beta$ ) following the order of decreasing basicity: [OAc]<sup>-</sup> > [Me<sub>2</sub>PO<sub>4</sub>]<sup>-</sup> > Cl<sup>-</sup> > [MeSO<sub>3</sub>]<sup>-</sup> > [MeSO<sub>4</sub>]<sup>-</sup> > [N(CN)<sub>2</sub>]<sup>-</sup> > [OTf]<sup>-</sup> > [BF<sub>4</sub>]<sup>-</sup> > [NTf<sub>2</sub>]<sup>-</sup> > [PF<sub>6</sub>]<sup>-</sup> > [SbF<sub>6</sub>]<sup>-</sup>.<sup>148,149</sup> The structural complexity of the anion of the IL results in weaker H-bonding interactions but potentially a greater

number of such interactions.<sup>136</sup> The presence of electron withdrawing or electron donating groups in the anion also affects its HBA strength.<sup>150</sup> Weak H-bonding between the alkyl hydrogens and the anions has been observed in IL/solvent mixtures of imidazolium-based ILs comprising perfluorinated anions.<sup>145</sup> An upfield chemical shift for the alkyl chain protons in aqueous mixtures of ILs has been attributed to a changeover from trans to gauche conformations in the alkyl chain, combined with aggregation phenomena.<sup>151</sup> Overall, interpreting the progression of the <sup>13</sup>C NMR chemical shifts is challenging since any variations mainly occur due to changes in the environment of the carbon nuclei such as the H-bonding of the attached protons or the electron density redistribution of the cation.<sup>152</sup>

### 2.3.5.3 Intramolecular interactions in chlorometallate ionic liquids (Results & Discussion)

The intramolecular interactions of the studied chlorometallate ILs were investigated by examining the progression of both the proton and carbon 13 chemical shifts in the presence of Lewis basic and acidic anions. A capillary, containing DMSO, was inserted into the NMR tube with the neat ionic liquid. Performing NMR spectroscopy with an external reference avoids internal referencing challenges and any dilution effects due to sample concentration differences. Nonetheless, this method may result in differences between the real chemical shift and the observed values due to variations in the volume magnetic susceptibilities of the sample and the reference solvent with an additional influence of the geometric properties of the capillary.<sup>145</sup> Referencing the chemical shifts to one of the signals of the IL, such as the terminal methyl group of the alkyl chain attached to the cation, can eliminate the need for a magnetic susceptibility correction in mixtures of molecular solvents and imidazolium-based ILs.<sup>145,153</sup> The preliminary comparison of the <sup>1</sup>H NMR chemical shifts for [C<sub>4</sub>C<sub>1</sub>im]Cl and those of two Lewis acidic ionic liquids, [C<sub>4</sub>C<sub>1</sub>im]Cl·ZnCl<sub>2</sub> and [C<sub>4</sub>C<sub>1</sub>im]Cl·InCl<sub>3</sub> ( $X_{\text{MCl}_x} = 0.67$ ), revealed an upfield chemical shift of the imidazolium protons for both chlorozincates(II) and chloroindates(III) (Figure 2.25). Consequently, the intramolecular interactions between Cl<sup>-</sup> and [C<sub>4</sub>C<sub>1</sub>im]<sup>+</sup> are expected to be interrupted upon formation of [Zn<sub>3</sub>Cl<sub>8</sub>]<sup>2-</sup> and [InCl<sub>4</sub>]<sup>-</sup>, inducing a substantial upfield chemical shift. A further study was therefore performed of the impact of anionic speciation on the chemical shift progression for the different compositions of [C<sub>4</sub>C<sub>1</sub>im]Cl·ZnCl<sub>2</sub> ( $0.10 < X_{\text{ZnCl}_2} < 0.75$ ). A linear decrease of the chemical shift of the C<sup>2</sup> and C<sup>4</sup>/C<sup>5</sup> protons of the imidazolium moiety was exhibited across the whole range of compositions ( $\Delta\delta > 2$  ppm) whereas a linear correlation of decreasing strength was also found for the C<sup>6</sup>-C<sup>10</sup> protons of the cation (Figure 2.26). The value of the negative slope indicates the degree to which the chemical shift reduces as a function of  $X_{\text{ZnCl}_2}$  (Table 2.5).

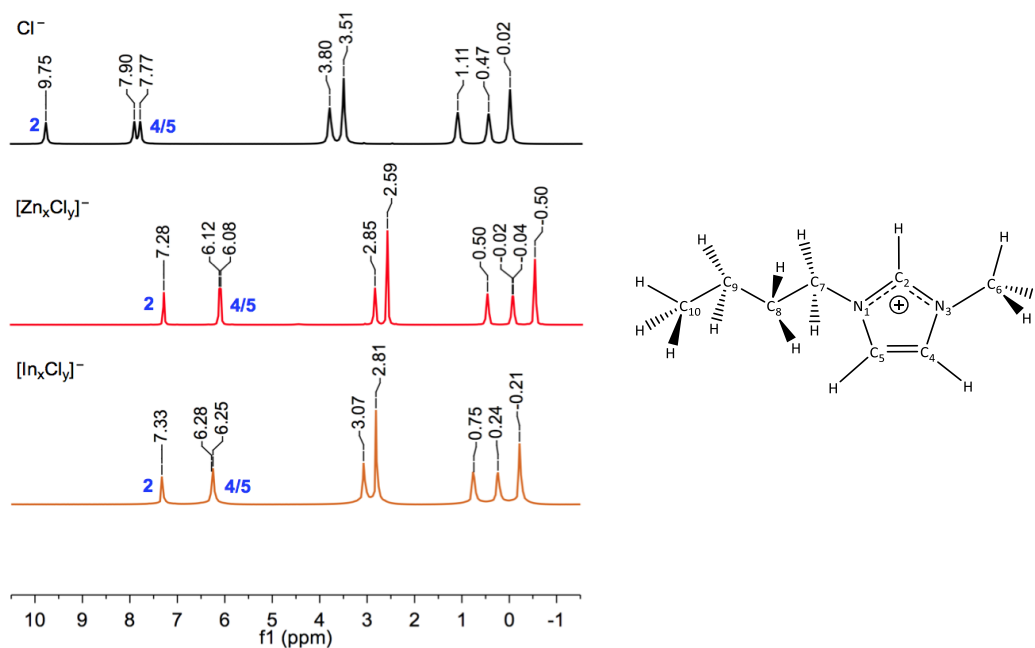


**Figure 2.25:** Schematic representation of the  $^1\text{H}$  NMR spectra of  $[\text{C}_4\text{C}_1\text{im}]\text{Cl}\cdot\text{ZnCl}_2$  and  $[\text{C}_4\text{C}_1\text{im}]\text{Cl}\cdot\text{InCl}_3$  at  $X_{\text{MCl}_x} = 0.67$ , recorded neat at  $80^\circ\text{C}$  with a DMSO capillary (500 MHz). The aromatic protons at the C2 and C4/C5 positions on the imidazolium ring are labelled for each compound.

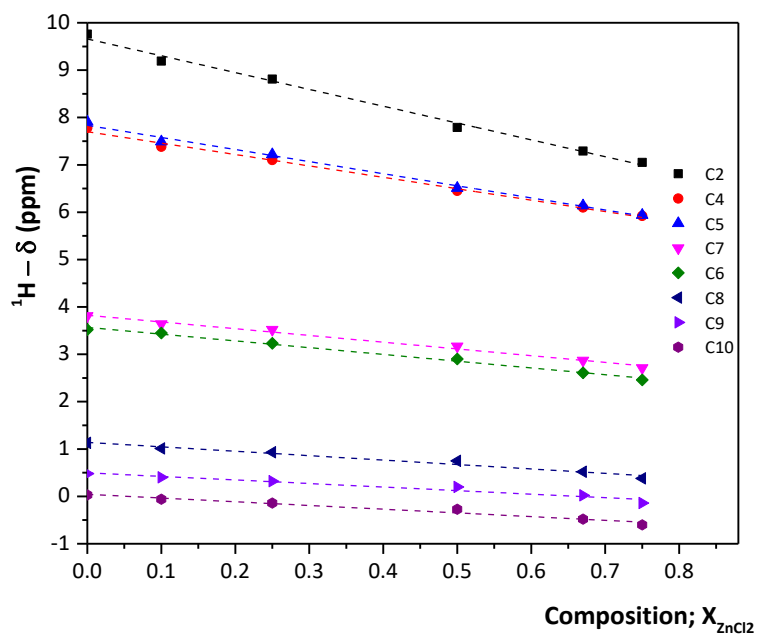


**Figure 2.26:** Observed  $^1\text{H}$  chemical shift  $\delta(\text{ppm})$  for  $\text{C}_2 - \text{C}_{10}$  protons as a function of composition ( $X_{\text{ZnCl}_2}$ ) for  $[\text{C}_4\text{C}_1\text{im}]\text{Cl}\cdot\text{ZnCl}_2$  ( $0.10 < X_{\text{ZnCl}_2} < 0.75$ ).  $^1\text{H}$  NMR spectra were recorded neat at  $80^\circ\text{C}$  with a DMSO capillary (500 MHz).

**Table 2.5** Linear fit coefficients for  $^1\text{H}$  NMR  $\delta(\text{ppm})$  as a function of  $X_{\text{ZnCl}_2}$ ;  $[\text{C}_4\text{C}_1\text{im}]\text{Cl}\cdot\text{ZnCl}_2$  ( $0.10 < X_{\text{ZnCl}_2} < 0.75$ )

$[\text{C}_4\text{C}_1\text{im}]^+$ proton	Slope	Intercept	Adj. R-square
C2	-3.55	9.66	0.992
C5	-2.55	7.83	0.993
C4	-2.41	7.70	0.993
C7	-1.42	3.82	0.987
C6	-1.43	3.57	0.991
C8	-0.93	1.14	0.966
C9	-0.74	0.50	0.941
C10	-0.78	0.04	0.958

The capillary  $^{13}\text{C}$  NMR spectra show a similar, yet less dramatic, trend regarding the upfield chemical shift progression upon transitioning from Lewis basic ( $X_{\text{ZnCl}_2} < 0.33$ ) to acidic compositions (**Appendix: 2.6.2**). The progression of the chemical shift appears significant for the  $\text{C}^2$ -carbon ( $\Delta\delta > 3$  ppm) whereas the reduction in the observed chemical shift for the  $\text{C}^4/\text{C}^5$  and  $\text{C}^8 - \text{C}^{10}$  carbons does not exceed 1 ppm across the tested compositions ( $0.10 < X_{\text{ZnCl}_2} < 0.75$ ). The data do not indicate a clear chemical shift progression for the  $\text{C}^6$  and  $\text{C}^7$  carbons that are adjacent to the imidazolium ring. A consistent downfield chemical shift was observed up to  $X_{\text{ZnCl}_2} = 0.50$  for both  $\text{C}^6$  and  $\text{C}^7$  carbons whereas a steady decrease of the chemical shift was observed at  $X_{\text{ZnCl}_2} > 0.50$ . The  $\text{C}^2$ -carbon is expected to be affected by the adjacent  $\text{C}^2$  hydrogen that strongly interacts with the anion present in the melt. Any chemical shift variations of the other alkyl carbons of the cation are probably the result of an electron density redistribution<sup>145</sup> upon weakening the existing interionic interactions. The chlorozincate anions are expected to coordinate through the chlorine atoms that become less electron rich when the negative charge is delocalised over complex and less basic anions. There is a clear indication that the formation of high-order anions upon increasing  $X_{\text{ZnCl}_2}$  is combined with less pronounced interionic charge transfer effects as well as lower hydrogen-bond anion basicity ( $\beta$ ) for the Lewis acidic polynuclear anions. The continuous decrease in the basicity of the anion could therefore be correlated with the consistent enhancement in the thermal stability of the tested chlorozincates(II) upon increasing the Lewis acidity and the complexity of the anions (**Section 2.3.4**).



### 2.3.6 Long-term thermal stability and decomposition kinetics of [C<sub>4</sub>C<sub>1</sub>im]Cl·ZnCl<sub>2</sub> (X<sub>ZnCl<sub>2</sub></sub> = 0.67)

Isothermal TGA measurements were performed on [C<sub>4</sub>C<sub>1</sub>im]Cl·ZnCl<sub>2</sub> (X<sub>ZnCl<sub>2</sub></sub> = 0.67) to investigate on its superior thermal stability (Section 2.3.4). Overall, there is a limited amount of long-term thermal stability studies of ionic liquids, focusing mainly on halide and perfluorinated anions.<sup>112,113,117,126,154–159</sup> An overestimation of thermal stability occurs upon simply comparing the onset temperature values. For example, 1,3-dialkylimidazolium ILs, composed of anions with strong hydrogen-bonding basicity, have been reported as effective agents for biomass pretreatment<sup>160</sup> with T<sub>onset</sub> exceeding 200 °C; yet their long-term thermal stability is problematic with appreciable decomposition at temperatures that are below their reported T<sub>onset</sub> values (120 °C < T < 170 °C).<sup>158</sup> Isothermal TGA experiments record the change in weight (%) as a function of time, at a constant temperature, offering perspective on the long-term stability and the decomposition kinetics of the tested IL. After measuring the isothermal decomposition, a pseudo zero-order rate expression is used for determining the kinetic parameters of the studied thermal degradation.<sup>112,126,161</sup> The rate constant is then determined at different temperatures as the slope of the decomposition curves. The temperature dependence of the pseudo-zero-order rate constant is expressed by the Arrhenius equation (2.3) where E<sub>a</sub> (kJ mol<sup>-1</sup>) is the activation energy and A is the pre-exponential coefficient. The activation energy is equivalent to the slope of the Arrhenius plot (lnk vs. 1/T) and the pre-exponential factor A is estimated from the intercept of the fitted curve. The time required for 1 % sample decomposition (t<sub>0.99</sub>) can also be calculated at different temperatures from the respective k (% min<sup>-1</sup>) values (2.4). Plotting the t<sub>0.99</sub> values as a function of temperature obeys a first-order exponential fit from which the T<sub>z/x</sub> parameter is obtained (2.5). T<sub>z/x</sub> indicates the temperature at which z % decomposition occurs over a certain amount of experimental time (x / min), representing a better estimation of the maximum operating temperature over T<sub>onset</sub> or T<sub>peak</sub>.<sup>162,163</sup> The thermal stability criteria (z %, x) are dictated by the intended application of the IL.<sup>126</sup> Positive correlations have been observed between T<sub>onset</sub> and T<sub>1%/10h</sub> whereas a correlation between E<sub>a</sub> and T<sub>onset</sub> is not always obvious.<sup>112</sup> The comparison of T<sub>1%/10h</sub> with the T<sub>onset</sub> values of a large number of ILs has suggested differences ranging from 100 °C to 270 °C.<sup>112</sup>

$$k = A \exp\left(\frac{-E_a}{RT}\right) \quad (2.3)$$

$$t_{0.99} = \frac{1}{k} \quad (2.4)$$

$$t_d = a + b e^{-cT} \quad (2.5)$$

In this work, the temperatures of the isothermal scans were chosen to be lower than the  $T_{\text{onset}}$  values of the tested ILs, as determined through dynamic scans under  $N_2$  ( $10\text{ }^\circ\text{C min}^{-1}$ ) (**Section 2.3.3& 2.3.4**). The isothermal measurements were performed with intervals of  $20 - 40\text{ }^\circ\text{C}$ , in the range  $100 - 200\text{ }^\circ\text{C}$  for  $[\text{C}_4\text{C}_1\text{im}]\text{Cl}$  and  $200 - 300\text{ }^\circ\text{C}$  for  $[\text{C}_4\text{C}_1\text{im}]\text{Cl}\cdot\text{ZnCl}_2$  ( $X_{\text{ZnCl}_2} = 0.67$ ) or  $[\text{C}_4\text{C}_1\text{im}][\text{NTf}_2]$ . A linear weight change regime was not observed for the entire duration of the isothermal scans (720 min) (**Appendix 2.6.3**). Five and three distinct regions of linear weight change were detected for  $[\text{C}_4\text{C}_1\text{im}]\text{Cl}\cdot\text{ZnCl}_2$  ( $X_{\text{ZnCl}_2} = 0.67$ ), at  $200\text{ }^\circ\text{C}$  and  $220\text{ }^\circ\text{C}$  respectively, indicating varying mechanisms of decomposition. The timeframe of  $100 - 300\text{ min}$  was chosen to estimate all of the kinetic and long-term thermal stability parameters for the decomposition of  $[\text{C}_4\text{C}_1\text{im}]\text{Cl}\cdot\text{ZnCl}_2$  ( $X_{\text{ZnCl}_2} = 0.67$ ) (Table 2.6). Deviations from linearity were also observed for  $[\text{C}_4\text{C}_1\text{im}]\text{Cl}$  and  $[\text{C}_4\text{C}_1\text{im}][\text{NTf}_2]$  at  $200\text{ }^\circ\text{C}$  and  $300\text{ }^\circ\text{C}$ , respectively. Two discrete regions were observed at  $300\text{ }^\circ\text{C}$  for the weight loss of  $[\text{C}_4\text{C}_1\text{im}][\text{NTf}_2]$  as a function of time and an average  $k$  ( $\% \text{ min}^{-1}$ ) was calculated to estimate  $E_a$  and  $A$  (Table 2.6). The weight losses of  $[\text{C}_4\text{C}_1\text{im}]\text{Cl}$  increased gradually at  $100 - 160\text{ }^\circ\text{C}$  with a rapid decomposition at  $200\text{ }^\circ\text{C}$ . A gradually decreasing thermal stability was observed for  $[\text{C}_4\text{C}_1\text{im}][\text{NTf}_2]$  at  $200 - 260\text{ }^\circ\text{C}$  and substantial weight losses were observed at  $300\text{ }^\circ\text{C}$ . Interestingly, the Lewis acidic chlorozincate(II) IL exhibited substantial long-term thermal stability with 82 % of the IL mass remaining upon testing for 720 h at  $300\text{ }^\circ\text{C}$  in comparison with 47 % and 5 % for  $[\text{C}_4\text{C}_1\text{im}][\text{NTf}_2]$  ( $300\text{ }^\circ\text{C}$ , 720 h) and  $[\text{C}_4\text{C}_1\text{im}]\text{Cl}$  ( $200\text{ }^\circ\text{C}$ , 720 min) (**Appendix 2.6.3**). The Arrhenius parameters,  $E_a$  and  $A$ , were determined from the isothermal TGA analysis (**Appendix 2.6.4**). It must be noted that the quality of the linear correlation of  $\ln k$  against  $1/T$  was greater for  $[\text{C}_4\text{C}_1\text{im}][\text{NTf}_2]$  ( $R^2 > 0.99$ ) and  $[\text{C}_4\text{C}_1\text{im}]\text{Cl}$  ( $R^2 > 0.99$ ) compared to the Lewis acidic chlorozincate(II) IL ( $R^2 > 0.87$ ). The decreased strength of intramolecular hydrogen-bonding and electrostatic interactions (**Section 2.3.5.3**) might therefore lead to improvements in the observed short-term and long-term thermal stability of  $[\text{C}_4\text{C}_1\text{im}]\text{Cl}\cdot\text{ZnCl}_2$  ( $X_{\text{ZnCl}_2} = 0.67$ ). However, any differences in the temperature ranges of the isothermals could translate into differences in the  $E_a$  and  $A$  values and thus a direct comparison of  $[\text{C}_4\text{C}_1\text{im}][\text{NTf}_2]$  and  $[\text{C}_4\text{C}_1\text{im}]\text{Cl}\cdot\text{ZnCl}_2$  ( $X_{\text{ZnCl}_2} = 0.67$ ) might be more realistic ( $200 - 300\text{ }^\circ\text{C}$ ). A higher  $E_a$  value for  $[\text{C}_4\text{C}_1\text{im}]\text{Cl}\cdot\text{ZnCl}_2$  ( $X_{\text{ZnCl}_2} = 0.67$ ) ( $134\text{ kJ mol}^{-1}$ ) over  $[\text{C}_4\text{C}_1\text{im}][\text{NTf}_2]$  ( $111\text{ kJ mol}^{-1}$ ) indicates a slower decomposition for the chlorozincate(II) IL. From each of the linear isotherms, a  $t_{0.99}$  value was extracted and the  $T_{1\%/10\text{h}}$  values were estimated from a first-order exponential, generated upon plotting  $t_{0.99}$  against temperature (**Appendix 2.6.5**). The estimated  $t_{0.99}$  and  $T_{1\%/10\text{h}}$  (Table 2.6) confirmed the improved long-term thermal stability of  $[\text{C}_4\text{C}_1\text{im}]\text{Cl}\cdot\text{ZnCl}_2$  ( $X_{\text{ZnCl}_2} = 0.67$ ) even if the  $T_{\text{onset}}$  value of  $[\text{C}_4\text{C}_1\text{im}][\text{NTf}_2]$  ( $T_{\text{onset}} = 418\text{ }^\circ\text{C}$ ) was estimated to be higher over Lewis acidic chlorozincate(II) IL ( $T_{\text{onset}} = 398\text{ }^\circ\text{C}$ ) (**Section 2.3.3**). Smaller temperature differences were also calculated between  $T_{1\%/10\text{h}}$  and  $T_{\text{onset}}$  for  $[\text{C}_4\text{C}_1\text{im}]\text{Cl}\cdot\text{ZnCl}_2$  ( $X_{\text{ZnCl}_2} = 0.67$ ) ( $\Delta T = 127\text{ }^\circ\text{C}$ ) as to  $[\text{C}_4\text{C}_1\text{im}][\text{NTf}_2]$  ( $\Delta T = 196\text{ }^\circ\text{C}$ ) with this ionic liquid having the highest  $T_{1\%/10\text{h}}$  value ( $270\text{ }^\circ\text{C}$ ) (Table 2.6).

**Table 3.6:** Thermal decomposition kinetic parameters of [C<sub>4</sub>C<sub>1</sub>im]Cl·ZnCl<sub>2</sub> (X<sub>ZnCl<sub>2</sub></sub> = 0.67), [C<sub>4</sub>C<sub>1</sub>im]Cl, and [C<sub>4</sub>C<sub>1</sub>im][NTf<sub>2</sub>].

Ionic liquid	T (°C)	k* (% min <sup>-1</sup> )	E <sub>a</sub> (kJ mol <sup>-1</sup> )	A	t <sub>0.99</sub> (min)	T <sub>1%/10h</sub> (°C)
[C <sub>4</sub> C <sub>1</sub> im][NTf <sub>2</sub> ]	200	<b>4.72E-4</b> [4.33E-4] <sup>112</sup>			<b>2309.47</b> [2303.5] <sup>112</sup>	
	220	<b>1.64E-3</b> [1.18E-3] <sup>112</sup>			<b>609.76</b> [851.06] <sup>112</sup>	
	260	<b>1.04E-2</b> [9.03E-3] <sup>112</sup>	<b>111.03</b> [126.4] <sup>112</sup>	<b>8.27E<sup>8</sup></b> [3.06E <sup>10</sup> ] <sup>112</sup>	<b>96.15</b> [110.71] <sup>112</sup>	<b>221.37</b> [227] <sup>112</sup>
	300	<b>5.18E-2<sup>a</sup></b> <b>8.50E-2<sup>b</sup></b> [0.109] <sup>112</sup>	[113] <sup>161</sup>		<b>14.62</b> [9.17] <sup>112</sup>	
	100	<b>1.98E-5</b>			<b>50556</b>	
[C <sub>4</sub> C <sub>1</sub> im]Cl	120	<b>1.59E-4</b> [2.85E-4] <sup>112</sup>			<b>6289.31</b> [6706.9] <sup>112</sup>	
	160	<b>1.09E-2</b> [1.15E-2] <sup>112</sup>	<b>137.55</b> [132.2] <sup>112</sup>	<b>3.09E<sup>14</sup></b> [9.65E <sup>13</sup> ] <sup>112</sup>	<b>91.74</b> [168.78] <sup>112</sup>	<b>143.57</b> [140.4] <sup>112</sup>
	200	<b>0.1933</b> [0.233] <sup>112</sup>	[121] <sup>154</sup> [129] <sup>157</sup>	[3.8E <sup>10</sup> ] <sup>154</sup> [2.8E <sup>13</sup> ] <sup>157</sup>	<b>5.17</b> [9] <sup>112</sup>	
	200	<b>7.71E-4<sup>c</sup></b> <b>5.61E-4<sup>d</sup></b> <b>2.94E-4<sup>e</sup></b> <b>1.72E-4<sup>f</sup></b> <b>8.36E-5<sup>g</sup></b>			X	
[C <sub>4</sub> C <sub>1</sub> im]Cl·ZnCl <sub>2</sub> X <sub>ZnCl<sub>2</sub></sub> = 0.67	220	<b>4.84E-4<sup>h</sup></b> <b>2.44E-4<sup>i</sup></b> <b>1.44E-4<sup>k</sup></b>	<b>134.05<sup>i</sup></b>	<b>2.62E<sup>10</sup></b>	<b>4098.36<sup>i</sup></b>	<b>270.23</b>
	260	<b>1.12E-3<sup>l</sup></b> <b>1.10E-3<sup>m</sup></b>			<b>909.09<sup>m</sup></b>	
	300	<b>2.66E-2<sup>n</sup></b> <b>2.42E-2<sup>o</sup></b>			<b>41.32<sup>o</sup></b>	

\*k (% min<sup>-1</sup>) values for R<sup>2</sup> > 0.9 [w % = f(t)]

\*\* a: < 280 min, b: > 280 min, c: < 100 min, d: 100 – 300 min, e: 300 – 400 min, f: 400 – 580 min, g: > 580 min, h: < 100 min i: 100 – 300 min, k: >300 min, l & n: full t (min) range, m & o: 100 – 300 min.

\*\*\*data: c – g (200 °C) were not taken into consideration in any further investigations of kinetics and long-term thermal stability, given their lack of fit in any of the models that were used to calculate E<sub>a</sub>, A, t<sub>0.99</sub> and T<sub>0.01/10h</sub>.

### 2.3.7 Synthesis of thiophene-derivatives from bio-derived furans in ionic liquids.

The acid-catalysed synthesis of thiophene analogues from furan-based and non-heterocyclic precursors, as well as the contribution of Brønsted and Lewis acid catalytic sites, have been reviewed earlier (Section 2.2). Herein, the conversion of bio-based furanic compounds into their thiophene analogues was investigated by using acidic ionic liquids as recyclable reaction media. Using ionic liquids as solvents and catalysts creates an excellent opportunity for their complete integration in biorefining. Brønsted and Lewis acidic or basic ionic liquids such as  $[C_4C_{1im}][HSO_4]$  and several compositions of  $[C_4C_{1im}]Cl \cdot ZnCl_2$  were studied as catalysts for the reaction of  $H_2S$  with 2,5-DMF or 5-HMF (Figure 2.27). The conclusions from the thiophene synthesis experiments were combined with the physicochemical characterisation of the ILs to deduce any structure-catalytic activity relationship.

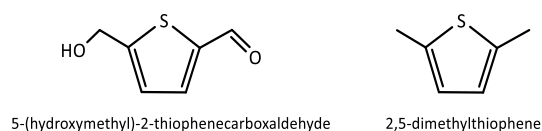


**Figure 2.27:** Thiophene analogues of bio-based furans: 5-(hydroxymethyl)furfural (5-HMF) and 2,5-dimethylfuran (2,5-DMF).

The experimental conditions had to be established given the absence of an available protocol for the recyclization of furan derivatives into thiophenes in ionic liquids. All preliminary experiments on the conversion of 5-HMF into its thiophene analogue were completed in the range of 80 - 120 °C because of the low thermal stability of 5-HMF at prolonged high reaction temperatures.<sup>164</sup> Additionally, such reaction conditions are similar to those applied to the selective conversion of carbohydrates into 5-HMF in ionic liquids.<sup>160</sup> The reactions between  $H_2S$  and 2,5-DMF were performed below 80 °C in order to reduce reactant-losses due to the volatility of 2,5-DMF (bp<sub>760</sub>: 92 - 94 °C). Heating the ionic liquid medium led to decreased viscosity, enhancing the dissolution of 5-HMF in the ionic liquid phase and the diffusion of 2,5-DMF in the interphase between the IL layer and the less polar phase of the substrate. The enhancement of the reaction yields and rates upon heating cannot be excluded.

Hydrogen sulfide gas was chosen as a sulfur source over other  $H_2S$ -releasing compounds such as Lawesson's reagent or the highly toxic and carcinogenic thioacetamide ( $CH_3CSNH_2$ ).<sup>165</sup> Lawesson's reagent contains a four-membered ring comprised of sulfur and phosphorus atoms; it produces two reactive dithiophosphine ylides ( $R-PS_2$ ) upon heating, followed by the release of  $H_2S$  in the presence of water. Therefore, it is expected that using the Lawesson's reagent or even thioacetamide would impact the green credentials of thiophene synthesis by reducing the atom economy due to the formation of additional by-products. The oxidation-prone sodium hydrosulfide (NaHS) and sodium sulfide ( $Na_2S$ ) were also excluded due to their variable purity.<sup>165</sup> On the contrary,  $H_2S$  gas is a high purity sulfur-source

and therefore it was chosen over other reagents containing traces of impurities or variable amounts of water. A limited number of experimental studies have been conducted on the solubility of H<sub>2</sub>S in ionic liquids due to the apparent safety concerns linked with the direct use of H<sub>2</sub>S gas. The first experimental results were reported for the solubility of H<sub>2</sub>S in [C<sub>4</sub>C<sub>1</sub>im][PF<sub>6</sub>]; a strong relationship was found between solubility and temperature at isobaric conditions (20 bar) with the H<sub>2</sub>S:[C<sub>4</sub>C<sub>1</sub>im][PF<sub>6</sub>] molar ratio decreasing from 0.84 at 298 K to 0.20 at 403 K.<sup>166</sup> The solubility of H<sub>2</sub>S in [C<sub>4</sub>C<sub>1</sub>im]<sup>+</sup>-based ionic liquids, comprising of anions of variable hydrogen-bond basicity properties, (Cl<sup>-</sup>, [OTf]<sup>-</sup>, [BF<sub>4</sub>]<sup>-</sup>, [NTf<sub>2</sub>]<sup>-</sup> and [PF<sub>6</sub>]<sup>-</sup>), has also been studied by NMR spectroscopy and computational analysis.<sup>167</sup> Overall, the reported solubility of H<sub>2</sub>S was very high in all tested ionic liquids without any indication of chemical instability of the tested ILs that interact with H<sub>2</sub>S via physical absorption (25 °C, 14 bar).<sup>167</sup> Molecular simulation studies (333 - 453K, < 20 bar) on the physical solubility of H<sub>2</sub>S in ILs have shown an important contribution of H<sub>2</sub>S-anion interactions for [C<sub>4</sub>C<sub>1</sub>im][BF<sub>4</sub>], [C<sub>4</sub>C<sub>1</sub>im][NTf<sub>2</sub>] and [C<sub>4</sub>C<sub>1</sub>im][PF<sub>6</sub>].<sup>168</sup> The structure of the ionic liquids upon H<sub>2</sub>S absorption remains unchanged with H<sub>2</sub>S molecules found in the cavities formed between the ions.<sup>168</sup> It has been deduced that van der Waals forces dominate the cation-H<sub>2</sub>S interactions whereas both electrostatic energy contributions and van der Waals forces influence the anion-H<sub>2</sub>S interactions.<sup>168</sup>

The solubility of bio-derived furans in the tested ionic liquids varied depending on the polarity and the functional groups present in the reaction substrate. It was observed that 5-HMF was soluble in [C<sub>4</sub>C<sub>1</sub>im]Cl·ZnCl<sub>2</sub> (X<sub>ZnCl<sub>2</sub></sub> = 0.67) whereas 2,5-DMF formed a biphasic mixture upon its addition to any chlorozincate(II) composition (0.25 ≤ X<sub>ZnCl<sub>2</sub></sub> ≤ 0.67). The details of the experimental set-up for the small-scale synthesis of bio-derived thiophenes in ionic liquids is illustrated and described in **Section 2.4**.

### 2.3.7.1 Synthesis of 5-hydroxymethyl-2-furaldehyde and 2,5-DMT in ionic liquids.

The direct conversion of 5-HMF into 5-(hydroxymethyl)-2-thiophenecarboxaldehyde was attempted. However, the reactivity of the functional groups of 5-HMF in the presence of H<sub>2</sub>S was a great complication regarding selectivity. Additionally, Lewis acid catalysts coordinate to carbonyl-containing molecules such as 5-HMF, enhancing the electrophilicity of the carbonyl carbon atom, rendering it more susceptible to nucleophilic attack.<sup>169,170</sup> Moreover, furanics, containing one or more electron-withdrawing carbonyl groups in the α-position, show reduced reactivity towards ring opening and recyclization due to the decrease in the electron density of the ring.<sup>93</sup> In this work, the reaction between 5-HMF and H<sub>2</sub>S was tested in an excess (10:1) of the Lewis acidic ionic liquid, [C<sub>4</sub>C<sub>1</sub>im]Cl·ZnCl<sub>2</sub> (X<sub>ZnCl<sub>2</sub></sub> = 0.67), that was used both as a solvent and catalyst (100 °C, 1 h). The reaction yielded a dark brown solid

that was insoluble in conventional organic solvents. The acid-catalysed polymerisation of 5-HMF is potentially driven by the enhanced reactivity of the exocyclic functional groups, given the substitution of the  $\alpha$ -carbons.<sup>164</sup> Consequently, it becomes apparent that the acid-catalysed reaction between 5-HMF and  $\text{H}_2\text{S}$  would require the protection of one or both functional groups, increasing the complexity of the process and the formation of waste products. 2,5-DMF, another promising biorefinery intermediate (**Section 1.5**), was subsequently studied as a more reactive bio-based substrate towards recyclization due to the presence of two electron-donating methyl groups. It was also considered as a better model compound due to the lack of additional reactive functional groups, reducing the risk of side reactions in the presence of  $\text{H}_2\text{S}$ . To evaluate the impact of acid catalysis, a control reaction was performed between 2,5-DMF and  $\text{H}_2\text{S}$  in an excess of the non-acidic  $[\text{C}_4\text{C}_1\text{im}]\text{Cl}$  (5:1, 80 °C, 1 h).  $^1\text{H}$  NMR spectroscopy proved that there was no formation of 2,5-DMT under these experimental conditions.

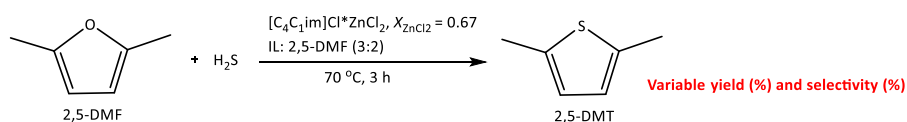


**Figure 2.28:** Schematic representation of the recyclization of 2,5-DMF into 2,5-DMT in  $[\text{C}_4\text{C}_1\text{im}]\text{Cl}\cdot\text{ZnCl}_2$  ( $X_{\text{ZnCl}_2} = 0.67$ ).

The reaction was repeated with a slight excess of the Lewis acidic  $[\text{C}_4\text{C}_1\text{im}]\text{Cl}\cdot\text{ZnCl}_2$  ( $X_{\text{ZnCl}_2} = 0.67$ ) (Figure 2.28). The addition of a cold-finger condenser aimed to control any losses of 2,5-DMF that otherwise would have evaporated from the reaction mixture, even at temperatures below its boiling point. Furthermore,  $\text{H}_2\text{S}$  was finally directly added into the reaction mixture under these modified experimental conditions since it boils at  $-77$  °C. A biphasic mixture was formed due to the immiscibility of 2,5-DMF in the tested ionic liquid, whereas a highly viscous product was obtained at the end of the reaction. Subsequently, short-path Kugelrohr distillation was used for the isolation of the unreacted 2,5-DMF and the reaction product(s). Negligible vapour pressure and low volatility are defining characteristics of ionic liquids and thus distillation was used for the facile separation of the reaction products. The distillate corresponded to 38 % of the mass input of the reactant: 2,5-DMF. The distillation product was analysed by  $^1\text{H}$  NMR spectroscopy and gas chromatography/electron ionisation-mass spectrometry (GC/EI-MS). Both techniques provided qualitative information on the structure of the yielded products. Additionally,  $^1\text{H}$  NMR spectroscopy was used for the quantification of 2,5-DMT (peaks: C, D) by comparing its peak integrals to the ones corresponding to 2,5-DMF (peaks: A, B) (Figure 2.29). It was confirmed that the reaction was successful towards the formation of 2,5-DMT. Clearly distinguishable proton resonances for 2,5-DMT were found in the distilled product alongside peaks assigned to unreacted 2,5-DMF. Both NMR spectroscopy and GC/EI-MS indicated the additional

formation of 2,5-hexadione as a by-product (peaks: E & F). The other signals illustrated in Figure 2.29 were assigned to DMSO (2.55 ppm) and residual water (3.33 ppm).

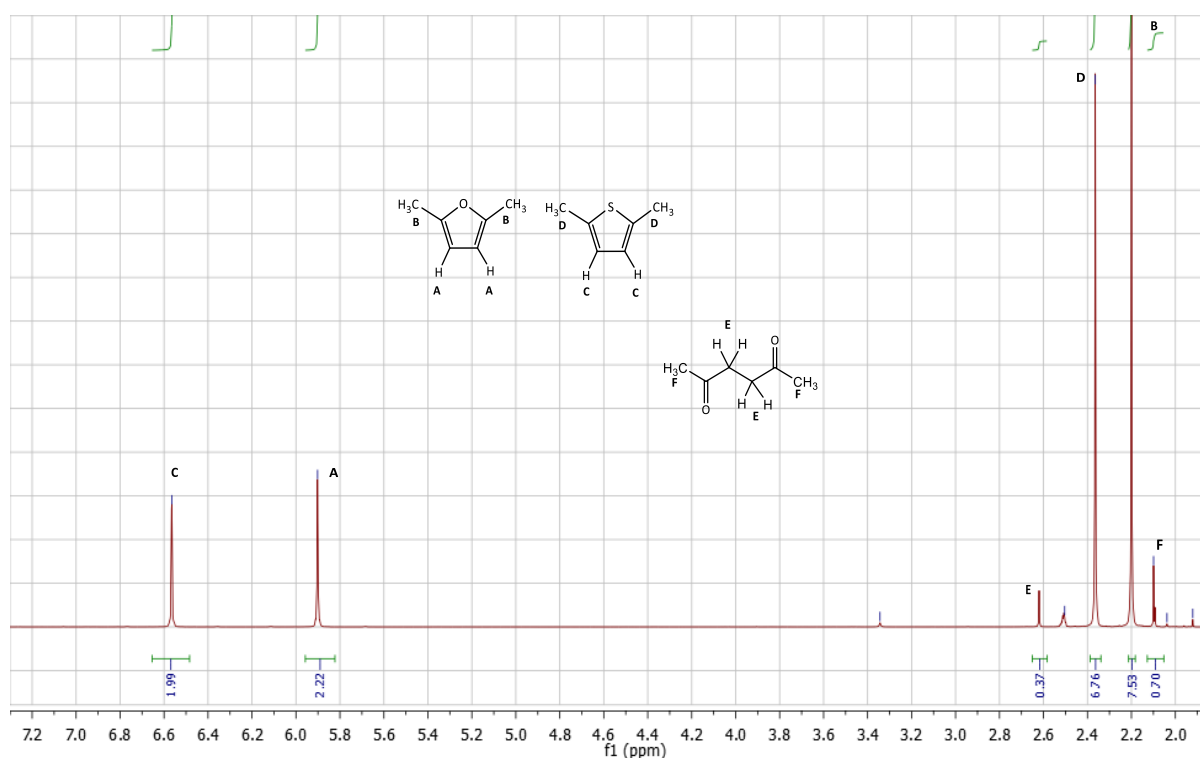


**Figure 2.29:** <sup>1</sup>H NMR spectrum of the Kugelrohr distillation product [2,5-DMF + H<sub>2</sub>S in [C<sub>4</sub>C<sub>1</sub>im]Cl·ZnCl<sub>2</sub> (X<sub>ZnCl<sub>2</sub></sub> = 0.67)].

The reaction was repeated several times but the mass of the distillate over the mass input of 2,5-DMF (38 % - 59 %) as well as the selectivity towards 2,5-DMT (48 % - 90 %) varied greatly. This could indicate chemical interactions between the heterocyclic compounds and the Lewis acidic IL, affecting the separation by distillation. However, the effect of a reduced mixing efficiency, due to diffusion limitations of the viscous medium, on the variability of reaction metrics cannot be excluded. 2,5-DMF and chlorozincates(II) formed a biphasic mixture and thus any reaction, catalysed by the anionic species, is likely to have occurred in the IL/2,5-DMF interphase. Improving the surface area of the catalyst and the mass transport properties would allow better diffusion of the acidic catalytic species within the IL layer and the enhanced mass transfer of 2,5-DMF within the IL/2,5-DMF interphase.

Given the positive correlation between the surface reactivity and the atoms present on the outer atomic surface, Lewis acidic chlorozincate(II) ionic liquids ( $0.50 \leq X_{\text{ZnCl}_2} \leq 0.75$ ) were studied by low-energy scattering spectroscopy (LEIS). It was attempted to identify the presence of characteristic surface peaks for both Zn and Cl to confirm that zinc was available for catalysis on the outer atomic surface of the chlorozincates(II). The properties of ionic liquids in the bulk can be very different from those in the

region close to the IL-vacuum surface, due to differences in atom composition and orientation.<sup>171,172</sup> Thanks to their negligible vapour pressure, several ionic liquids have been previously investigated by ultra-high vacuum techniques such as X-ray photoelectron spectroscopy (XPS).<sup>173</sup> Low-energy ion scattering spectroscopy (LEIS), one of the most sensitive surface analysis techniques, has been seldom used for compositional analysis of the outermost layer of neat ILs or IL mixtures.<sup>171,172,174</sup> Previous studies have mainly focused on ionic liquids with perfluorinated or halide anions, concluding that both the cation and multiple orientations of the anion are present at the IL-vacuum outer atomic surface, even for cations bearing long alkyl chains.<sup>171</sup> Fine-tuning of the size of the cation and, even more importantly, the cation-anion intermolecular interactions, appear to be crucial for the IL–vacuum surface composition.<sup>171,172</sup> For example, the addition of  $[\text{C}_4\text{C}_1\text{im}][\text{NTf}_2]$  to  $[\text{C}_4\text{C}_1\text{im}]\text{I}$  reduced the number of hydrogen-bond acceptor adsorption sites at the IL–vacuum outer atomic surface with the non-coordinating  $[\text{NTf}_2]^-$  dominating the outer atomic surface.<sup>172</sup> The experimental protocol involves the bombardment of the sample with  $\text{He}^+$ , followed by measuring the energy of the backscattered ions ( $E_F$  / eV). The energy for each surface peak is characteristic of an element and the peak area is proportional to the concentration of this element.

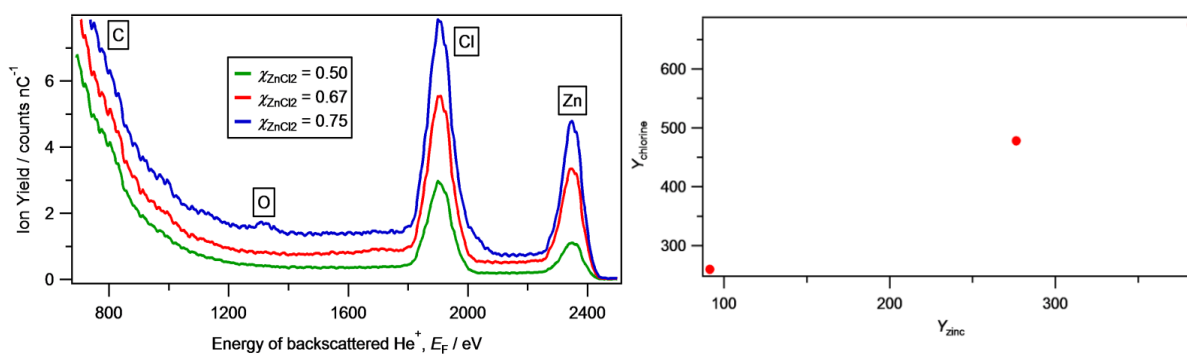


**Figure 2.30:** LEIS spectra ( $^4\text{He}^+$ ,  $E_0 = 3$  keV) for a series of Lewis acidic  $[\text{C}_4\text{C}_1\text{im}]\text{Cl}\cdot\text{ZnCl}_2$  compositions ( $0.50 \leq X_{\text{ZnCl}_2} \leq 0.75$ ).

In Figure 2.30, both the LEIS spectra of the selected chlorozincates(II) and a graph of the functional relationship between the scattered ion yields ( $Y_i$ ) for Zn and Cl are presented. The exposure of the ionic liquid to  $^4\text{He}^+$  ions leads to sputtering of the sample.<sup>174</sup> Consequently, the LEIS signal was affected for energies below 1000 eV due to the background contribution from sputtered ions (Figure 2.30). The relatively high noise/signal ratio in this region can be an obstacle for the accurate determination of lighter elements such as carbon, oxygen and nitrogen. Nonetheless, sharp peaks were observed for zinc ( $Y_{\text{zinc}}$ ) and chlorine ( $Y_{\text{chlorine}}$ ) between 1800 eV and 2400 eV. It can be safely deduced that Zn was available on the outer atomic surface of the tested ILs even for the highly acidic compositions that contain bulky polynuclear anions. The results of this study confirm that the zinc metal centre is not completely



sterically hindered by the chlorine atoms or the alkyl chains of the cation. Plotting the scattered ion yield for Zn ( $Y_{zinc}$ ) and Cl ( $Y_{chlorine}$ ), it becomes apparent that there is a growth of Cl as the outer atomic surface becomes enriched in zinc. The reduction in the strength of interionic interactions as a function of the anionic composition ( $X_{ZnCl_2}$ ), confirmed by  $^1H$  and  $^{13}C$  NMR spectroscopy (Section 2.3.5.3), may also explain the increasing availability of the anions on the outer atomic surface upon increasing their complexity. In conclusion, zinc is available for catalysis on the surface of the studied Lewis acid ILs while still being in the form of oligomeric species ( $[Zn_xCl_{2x+2}]^{2-}$ ).

Furthermore, the acidity of  $[C_4C_1im]Cl \cdot ZnCl_2$  ( $0.25 \leq X_{ZnCl_2} \leq 0.67$ ) was determined by IR spectroscopy given their application as catalysts. Pyridine ( $pK_b = 9$ ) was mixed with each of the tested ILs at a given IL/pyridine ratio (5:1 by weight) before further analysis. Pyridine has been previously used as a probe to distinguish between Brønsted and Lewis acid sites in solid acids as well as ionic liquids.<sup>27</sup> Monitoring the IR bands in the  $1400 - 1700 \text{ cm}^{-1}$  region provides information on whether pyridine coordinates to Lewis acid sites and/or is bonded to Brønsted acid sites. The formation of pyridinium ions due to interactions with Brønsted acid sites leads to the appearance of a band near  $1540 \text{ cm}^{-1}$ , assigned to  $N^+ - H$  stretching vibrations.<sup>27</sup> Changes in the ring vibration modes due to coordination of pyridine to Lewis acid sites are reflected by the presence of a band near  $1450 \text{ cm}^{-1}$ .<sup>27</sup>

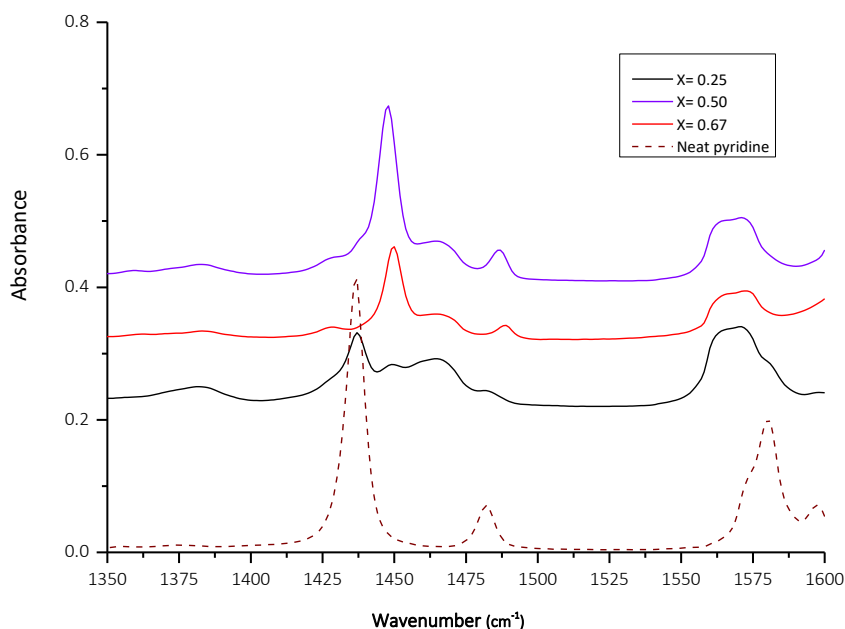


**Figure 2.31:** IR spectra ( $1350 - 1600 \text{ cm}^{-1}$ ) of pyridine/IL mixtures ( $[C_4C_1im]Cl \cdot ZnCl_2$  ( $0.25 \leq X_{ZnCl_2} \leq 0.67$ )).

In the absence of Lewis acidic ionic liquids, a well-resolved band near  $1437 \text{ cm}^{-1}$  was observed for neat pyridine. This band was still present when pyridine was mixed with the basic chlorozincate(II) ionic liquid

( $X_{\text{ZnCl}_2} = 0.25$ ) but it disappeared at  $X_{\text{ZnCl}_2} = 0.50$ . In addition, a band near  $1450 \text{ cm}^{-1}$  appeared at  $X_{\text{ZnCl}_2} = 0.50$  and  $X_{\text{ZnCl}_2} = 0.67$ , indicating Lewis acidic properties for both compositions. It has been shown that neutral chlorozincate(II) anions ( $[\text{ZnCl}_4]^{2-}$ ) and  $\text{Cl}^-$  are present at  $X_{\text{ZnCl}_2} < 0.35$  but oligomeric anions ( $[\text{Zn}_x\text{Cl}_{2x+2}]^{2-}$ ) are detected at  $X_{\text{ZnCl}_2} > 0.35$ .<sup>31</sup> Defining the neutral composition requirements is impacted by the coordination properties of the metal present in the anionic species and  $X_{\text{MCl}_x} = 0.50$  is not the neutral point for all chlorometallate ionic liquids.<sup>3</sup> Pyridine was found to be strongly coordinated to acidic polynuclear anions formed at  $X_{\text{ZnCl}_2} > 0.33$  but the basic probe possibly could not clearly distinguish between  $X_{\text{ZnCl}_2} = 0.50$  and  $X_{\text{ZnCl}_2} = 0.67$ . Nonetheless, the wavenumber of the band corresponding to the coordination of pyridine to Lewis acidic species increased from  $1448 \text{ cm}^{-1}$  for  $X_{\text{ZnCl}_2} = 0.50$  to  $1450 \text{ cm}^{-1}$  for  $X_{\text{ZnCl}_2} = 0.67$ , indicating a potential rise in Lewis acidity. There was no indication of a band arising near  $1540 \text{ cm}^{-1}$ , corresponding to the protonated form of pyridine, for any of the tested compositions; hence the absence of Brønsted acidity was implied.

Two additional compositions,  $X_{\text{ZnCl}_2} = 0.25$  and  $X_{\text{ZnCl}_2} = 0.50$ , were therefore tested as catalysts towards the recyclization of 2,5-DMF into 2,5-DMT. The close inspection of the  $^1\text{H}$  NMR spectrum of the distilled product also confirmed that there were no distinguishable proton signals for 2,5-DMT and/or 2,5-hexanedione when the latter composition was used as a catalyst. It is likely that the lack of acidic polynuclear anions prevented the ring-opening and the recyclization of 2,5-DMF. In the case of  $[\text{C}_4\text{C}_1\text{im}]\text{Cl}\cdot\text{ZnCl}_2$  ( $X_{\text{ZnCl}_2} = 0.50$ ), it has already been highlighted that it is not a neutral composition but rather Lewis acidic due to the presence of polynuclear anions. The product of the reaction between 2,5-DMF and  $\text{H}_2\text{S}$  in this ionic liquid provided 2,5-DMT at a low selectivity (10 %) with 2,5-hexanedione also being detected in the reaction mixture.

In the context of studying the effect of Brønsted acidity,  $[\text{C}_4\text{C}_1\text{im}][\text{HSO}_4]$  was screened as a strong Brønsted acidic IL and a potential catalyst for the synthesis of 2,5-DMT. However, the peak that was initially assigned to  $[\text{HSO}_4]^-$  was not detected upon the completion of the reaction, indicating a possible redox side-reaction between the anion and  $\text{H}_2\text{S}$  to produce elemental sulfur,  $\text{SO}_2$  and water. Therefore, no clear conclusion could be drawn on the effect of Brønsted acidity in ionic liquids since  $[\text{C}_4\text{C}_1\text{im}][\text{HSO}_4]$  was not chemically stable in the presence of  $\text{H}_2\text{S}$ . However, the quantitative conversion of 2,5-DMF into 2,5-DMT proved to be feasible when an excess of a homogeneous Brønsted acid catalyst,  $\text{EtOH}/\text{HCl}$ , was used under experimental conditions similar to those employed for ILs. At this point, the  $^1\text{H}$  NMR spectrum of the crude reaction mixture did not contain any clearly discernible signals that could be assigned to the product of 2,5-DMF hydrolysis: 2,5-hexanedione. The investigation of the recyclization of 2,5-DMF by homogeneous Brønsted acid catalysts has been reported before with a slightly different

experimental set-up.<sup>95,96</sup> In the presence of water, 2,5-DMF is converted to its thiophene analogue via the formation of 2,5-hexadione. The respective mechanism under anhydrous conditions involves the protonation of the  $\alpha$ -carbons of the furan ring, a subsequent nucleophilic attack by  $\text{H}_2\text{S}$ , ring opening, E1 water elimination and recyclization into 2,5-DMT. The absence of 2,5-hexadione from the reaction mixture in the presence of acidified ethanol (3 h, 70 °C) could be explained by the anhydrous conditions and/or the fast cyclisation of the intermediate 2,5-dicarbonyl compound into 2,5-DMT. However, 2,5-hexadione was isolated as a by-product when Lewis acidic chlorozincates(II) were applied in the tested biphasic system. As summarized in **Section 2.2.2**, 2,5-DMF is susceptible to specific acid-catalysed hydrolysis with a contribution from the functional groups present, as reported for many bio-based furanics<sup>175</sup>. Lewis acidic metal chlorides such as  $\text{AlCl}_3$  and  $\text{FeCl}_2$  have been successful in catalysing the ring-opening of functionalised furanics (80 °C, 24 h), albeit with reduced yields in comparison with strong homogeneous Brønsted acids (e.g.  $\text{HCl}$  and  $\text{H}_2\text{SO}_4$ ).<sup>175</sup>

Several hypotheses could be made regarding the mechanism of the recyclization of 2,5-DMF into 2,5-DMT in the presence of Zn-containing polynuclear anions (IL-based biphasic system). It was assumed that there was a lack of free Brønsted acid protons in the melt, as indicated by IR spectroscopy. All reactions were performed under anhydrous conditions but water is a by-product of the recyclization of 2,5-DMF into 2,5-DMT. In general, it is quite challenging to identify the exact contribution of Lewis and Brønsted acid sites on the yield and selectivity of a reaction.<sup>169</sup> Brønsted acid sites can be produced by Lewis acid sites upon hydrolysis in the presence of residual amounts of water. However, the use of moisture-stable chlorozincate(II) ILs and air-free techniques were some of the control measures applied.  $\text{ZnCl}_2$ -based ionic liquids are hygroscopic but they are moisture-stable and non-oxophilic; hence they do not react irreversibly with water.<sup>3</sup> The interactions between  $\text{Zn}^{2+}$  and water are weaker compared with the ones between  $\text{Zn}^{2+}$  and the chloride ligands (bond exchange rate ( $\text{Zn-OH}_2$ ) =  $2 \times 10^7 \text{ s}^{-1}$ ).<sup>176</sup> Chlorozincates(II) are prone to stoichiometric hydration instead of hydrolysis with water molecules coordinating to the metal centre of the anionic species.<sup>3</sup> A Lewis acid-assisted Brønsted acid-catalysed reaction by chlorozincates(II) ( $X_{\text{ZnCl}_2} \geq 0.50$ ) is proposed here (Figure 2.32). The coordination of Zn(II)-based species,  $[\text{Zn}_x\text{Cl}_{2x+2}]^{2-}$ , to the oxygen atom of the furan ring cannot be supported. The electrons from the furan oxygen atom participate in the aromatic conjugation of the molecule and thus the heteroatom must lose the ability for complex formation with the electron-withdrawing Lewis acid. However, the coordination of the Zn(II)-sites to water molecules, a reaction by-product or an impurity of the initial reaction mixture, could invoke Brønsted acidity in the melt. Generally, there is an additional contribution of hydrogen bond donors in polarising the O-H bond of water molecules when Lewis acidic zinc(II)-sites are present.<sup>177</sup> Brønsted acidity in the melt could result in the protonation and activation

of the furan ring whereas 2,5-hexanedione could be produced as an intermediate in the presence of water. Additionally, it is known that the formation of carbonyl-Lewis acid complexes increases the electrophilicity and reactivity of carbonyl-containing molecules.<sup>170</sup> Consequently, Lewis acidic species could also activate 2,5-hexanedione towards the nucleophilic attack by H<sub>2</sub>S and the subsequent recyclization into 2,5-DMT. Any additional dehydration properties of Lewis acidic species might contribute to the synthesis of 2,5-DMT via the formation and activation of 2,5-hexadione.

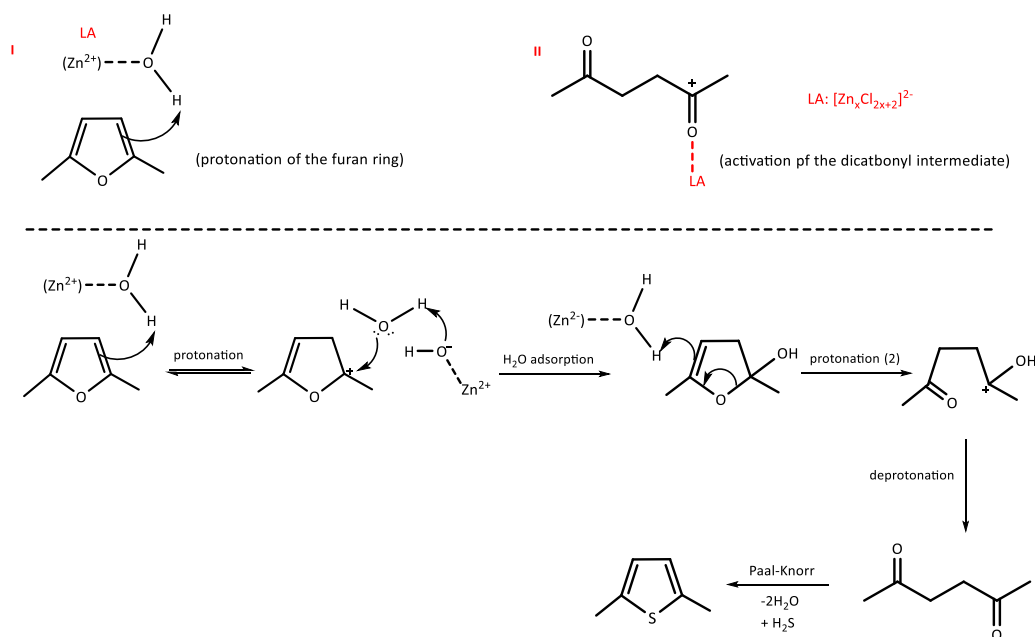


**Figure 2.32:** Lewis acid-assisted Brønsted acid-catalysed 2,5-DMT synthesis in chlorozincates(II), accounting for the contribution of the Lewis acidic anions on the activation of the 2,5-DMF furan ring and/or 2,5-hexadione.

These preliminary experiments focused on thiophene synthesis in a biphasic liquid-liquid system, composed of an excess of a highly viscous ionic liquid. Process control limitations regarding the supply of H<sub>2</sub>S were also a factor. Consequently, it was decided to examine the reactivity of the successful Lewis acidic chlorozincate(II) ILs under conditions where mixing and diffusion are improved, aiming for fewer performance limitations. More specifically, the development of silica-supported [C<sub>4</sub>C<sub>1</sub>im]Cl·ZnCl<sub>2</sub> (X<sub>ZnCl<sub>2</sub></sub> = 0.67) (SILPs) (Chapter 3) was followed by screening the reaction between 2,5-DMF and H<sub>2</sub>S in the gas phase, aiming to improve the reaction mass transfer properties, the economic utilization of the IL-based catalyst and process control.

## 2.4 Experimental

All reagents were purchased from Sigma-Aldrich, Fluka, VWR and Acros Organics. The precursor of the chlorometallate ionic liquids,  $[C_4C_{1im}]Cl$ , as well as all anhydrous metal chlorides ( $> 98\%$ ;  $InCl_3$ ,  $ZnCl_2$  and  $FeCl_3$ ) were handled in a glovebox ( $H_2O$ ,  $O_2 < 5$  ppm) whilst synthesis was performed under nitrogen, using standard Schlenk line techniques. All organic solvents were used dry, unless stated otherwise. The resulting ionic liquids were dried under vacuum (2.1 mbar,  $45\text{ }^\circ\text{C}$ ,  $> 12$  h) due to their hygroscopic nature. A series of halometallate ILs was prepared upon mixing the quaternary halide salt with the corresponding metal halide (3a - 5, Figure 2.20). The purity of the synthesised ionic liquids was confirmed by NMR spectroscopy, elemental analysis and mass spectroscopy. Water content, as determined by Kamlet-Taft, was less than 10 ppm.



**Figure 2.33:** Small-scale experimental apparatus; bio-derived thiophene synthesis.

A lecture bottle of  $H_2S$  (99.5%, 225 g liquefied gas) and a single-stage stainless steel regulator (outlet: 0 - 50 psi) were obtained from CK Special Gases Ltd. The lecture bottle was equipped with a stainless-steel regulator, adequate for primary pressure control of corrosive gases. A three-necked round-bottom flask was connected to the cylinder, a cold finger condenser and an  $H_2S$  trap via acid-resistant Tygon tubing (Figure 2.33). The trap was filled with sodium hypochlorite (500mL NaOCl, 12% w/w) so that any unreacted  $H_2S$  was oxidised to  $H_2SO_4$ . NaOH (500 mL, 2.4 M) was used as a chemical scrubber in the presence of acidified ethanol (EtOH/HCl). An empty Dreschel bottle was placed between the cylinder and the reaction flask for better control of back pressure. 5-HMF was stored at low temperatures ( $1\text{ }^\circ\text{C}$ -

5 °C) and handled under oxygen-free conditions due to its instability. The small-scale thiophene synthesis reactions were repeated at least twice at each condition and IL composition.

<sup>1</sup>H NMR and <sup>13</sup>C NMR spectra were recorded using a Bruker Avance III HD (400 Hz) spectrometer in dimethyl sulfoxide (DMSO). Chemical shifts ( $\delta$ ) are reported in ppm, the DMSO signal at 2.50 ppm (<sup>1</sup>H dimension) and 39.52 ppm (<sup>13</sup>C dimension). The coupling constants are given in Hertz. Capillary <sup>1</sup>H-NMR and <sup>13</sup>C-NMR spectra were recorded on a Bruker Avance III HD (500 Hz) at 80 °C to decrease the effects of the high viscosity on the spectral resolution. The capillary insert was flame-sealed upon the addition of DMSO-d<sub>6</sub> and placed into a standard 5 mm NMR tube. The residual signal of the lock solvent did not interfere with the IL resonances. High sample viscosities have been previously linked with broader NMR signals due to long reorientational correlation times.<sup>3,43</sup> An increasing viscosity was observed for the chlorozincates(II) upon augmenting X<sub>ZnCl<sub>2</sub></sub>. Viscosity is typically lower in the acidic regime where complex anions, with a more dispersed charge, dominate the melt. Nevertheless, a decrease in the strength of interionic H-bonding, combined with losses of configurational variation could also result into counter-intuitive increasing viscosities.<sup>178</sup> Dynamic and isothermal TGA scans were performed on a TA Instruments 'TGA-Q500' thermogravimetric analyzer, using platinum sample pans of 6 mm diameter. Nitrogen was used as the carrier gas at a flow rate of 20 mL min<sup>-1</sup> for all TGA experiments. The temperature-ramped experiments were performed on 5 – 10 mg of neat IL in a range of 30 – 700 °C (10 °C min<sup>-1</sup>). Isothermal TGA experiments were conducted on 17 - 26 mg of sample that was tested at a range of temperatures for 720 min. Isothermal heating at 80 °C for 30 min preceded both dynamic and isothermal scans to remove any residual moisture. Infrared (IR) spectra were obtained with a Perkin Elmer Spectrum 100 FTIR spectrometer with a universal ATR sampling accessory. Liquid secondary ion mass spectrometry (20 - 2500 Da) was performed in both positive and negative modes by Dr. Lisa Haigh (Department of Chemistry, Imperial College London) on a Micromass Autopsec Premier mass spectrometer. MALDI mass spectra were recorded with Micromass MALDI TOF, equipped with a 337 nm nitrogen laser. GC(EI) chromatograms were obtained with a Micromass Autospec Premier/Agilent HP6890 GC chromatography instrument. LEIS spectra were recorded by Dr. Kevin Lovelock (University of Oxford) and they were obtained by using a Qtac 100 instrument (ION-TOF). The tests were performed at a pressure of 3×10<sup>-10</sup> mbar that increased to 10<sup>-8</sup> mbar due to the flow of helium gas during the experiment. The samples were analysed with a 3000 eV <sup>4</sup>He<sup>+</sup> ion beam that was directed perpendicularly to the sample. The instrument was equipped with a double toroidal energy analyser collecting the backscattered ions at an angle of 145° from all azimuth angles.

## 2.4.1 Synthesis and characterisation of ionic liquids and intermediates

### 2.4.1.1 1-butyl-3-methylimidazolium chloride ([C<sub>4</sub>C<sub>1</sub>im]Cl) – (1)

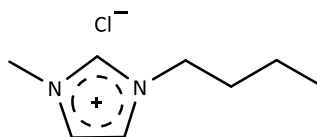


Figure 2.34: Chemical structure of [C<sub>4</sub>C<sub>1</sub>im]Cl.

1-methylimidazole (190 mL 2.31 mol) and 1-chlorobutane (255 mL, 2.76 mol) were vigorously stirred under N<sub>2</sub> and dried over KOH and P<sub>2</sub>O<sub>5</sub>, respectively (24 h, rt). Subsequently, 1-chlorobutane was distilled by atmospheric distillation whereas 1-methylimidazole was distilled under vacuum. Ethyl acetate was dried over CaH<sub>2</sub> and used as a reaction and purification solvent. A 1 L two-necked flask, equipped with a magnetic stirrer and a nitrogen inlet adapter, was used as a reaction vessel. Ethyl acetate (116 mL) and 1-methylimidazole (97 g, 1.18 mol, 1 eq.) were mixed together prior to the drop-wise addition of 1-butylimidazole (120 g, 1.30 mol, 1.1 eq.). The resulting mixture was heated under reflux up to 70 °C and N<sub>2</sub> was supplied during the reaction (10 d, 65 – 70 °C). A biphasic mixture was formed as the reaction progressed and the conversion was monitored by <sup>1</sup>H-NMR spectroscopy. The top layer, containing ethyl acetate and unreacted starting materials, was removed by cannula. The product was washed with ethyl acetate (9x40 mL) and it was purified further by recrystallization from a mixture of dry acetonitrile and ethyl acetate (1:5) until spectroscopically pure [C<sub>4</sub>C<sub>1</sub>im]Cl was obtained. The product was dried under vacuum, affording [C<sub>4</sub>C<sub>1</sub>im]Cl as a white crystalline solid (171.04 g, 0.98 mol, 83 %). This ionic liquid was used for the synthesis of the chlorometallate ILs.

<sup>1</sup>H NMR: δ<sub>H</sub> (400 MHz, DMSO-d<sub>6</sub>) ppm: 9.15 (1H, s, N<sub>2</sub>CH), 7.80 and 7.71 (2H, m, 2NCH), 4.17 (2H, t, <sup>3</sup>J<sub>HH</sub> = 7.2 Hz, NCH<sub>2</sub>CH<sub>2</sub>CH<sub>2</sub>CH<sub>3</sub>), 3.85 (3H, s, NCH<sub>3</sub>), 1.77 (2H, quintet, <sup>3</sup>J<sub>HH</sub> = 7.6 Hz, NCH<sub>2</sub>CH<sub>2</sub>CH<sub>2</sub>CH<sub>3</sub>), 1.26 (2H, sextet, <sup>3</sup>J<sub>HH</sub> = 7.2 Hz, NCH<sub>2</sub>CH<sub>2</sub>CH<sub>2</sub>CH<sub>3</sub>) and 0.91 (3H, t, <sup>3</sup>J<sub>HH</sub> = 7.2 Hz, NCH<sub>2</sub>CH<sub>2</sub>CH<sub>2</sub>CH<sub>3</sub>).

<sup>13</sup>C NMR: δ<sub>C</sub> (100 MHz, DMSO-d<sub>6</sub>) ppm: 137.01 (s, N<sub>2</sub>C), 124.10 and 122.75 (s, 2NCH), 48.96 (s, NCH<sub>2</sub>CH<sub>2</sub>CH<sub>2</sub>CH<sub>3</sub>), 36.23 (s, NCH<sub>3</sub>), 31.82 (s, NCH<sub>2</sub>CH<sub>2</sub>CH<sub>2</sub>CH<sub>3</sub>), 19.25 (s, NCH<sub>2</sub>CH<sub>2</sub>CH<sub>2</sub>CH<sub>3</sub>) and 13.74 (s, NCH<sub>2</sub>CH<sub>2</sub>CH<sub>2</sub>CH<sub>3</sub>).

<sup>1</sup>H NMR (capillary, neat compound): δ<sub>H</sub> (500 MHz, DMSO-d<sub>6</sub>) ppm: 9.76 (1H, s, N<sub>2</sub>CH), 7.91 and 7.78 (2H, m, 2NCH), 3.81 (2H, t, <sup>3</sup>J<sub>HH</sub> = 7.2 Hz, NCH<sub>2</sub>CH<sub>2</sub>CH<sub>2</sub>CH<sub>3</sub>), 3.52 (3H, s, NCH<sub>3</sub>), 1.13 (2H, quintet, <sup>3</sup>J<sub>HH</sub> = 7.6 Hz, NCH<sub>2</sub>CH<sub>2</sub>CH<sub>2</sub>CH<sub>3</sub>), 0.48 (2H, sextet, <sup>3</sup>J<sub>HH</sub> = 7.2 Hz, NCH<sub>2</sub>CH<sub>2</sub>CH<sub>2</sub>CH<sub>3</sub>) and 0.03 (3H, t, <sup>3</sup>J<sub>HH</sub> = 7.2 Hz, NCH<sub>2</sub>CH<sub>2</sub>CH<sub>2</sub>CH<sub>3</sub>).

$^{13}\text{C}$  NMR (**capillary, neat compound**):  $\delta_c$  (125 MHz, DMSO- $d_6$ ) ppm: 136.23 (s,  $\text{N}_2\text{C}$ ), 122.46 and 121.46 (s,  $2\text{NCH}$ ), 47.43 (s,  $\text{NCH}_2\text{CH}_2\text{CH}_2\text{CH}_3$ ), 34.97 (s,  $\text{NCH}_3$ ), 30.50 (s,  $\text{NCH}_2\text{CH}_2\text{CH}_2\text{CH}_3$ ), 17.62 (s,  $\text{NCH}_2\text{CH}_2\text{CH}_2\text{CH}_3$ ) and 11.82 (s,  $\text{NCH}_2\text{CH}_2\text{CH}_2\text{CH}_3$ ).

MS ( $\text{FB}^+$ )  $m/z$ : 142 ( $[\text{C}_4\text{C}_1\text{im}]^+$ , 100 %), ( $\text{FB}^-$ )  $m/z$ : 35 ( $\text{Cl}^-$ , 100 %).

EA (calc.): %C = 54.86 (55.01), %H = 8.75 (8.66), %N = 14.23 (16.04).

#### 2.4.1.2 Chlorozincates(II): $[\text{C}_4\text{C}_1\text{im}]\text{Cl}\cdot\text{ZnCl}_2$ ( $0.10 \leq X_{\text{ZnCl}_2} \leq 0.75$ ) – (3a – 3e)<sup>19</sup>

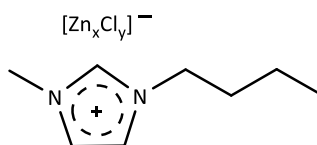


**Figure 2.35:** Chemical structure of  $[\text{C}_4\text{C}_1\text{im}]\text{Cl}\cdot\text{ZnCl}_2$ ;  $[\text{Zn}_x\text{Cl}_y]^{2-}$  indicates the formation of complex polyanions.

A range of compositions of chlorozincate(II) ILs, based on  $[\text{C}_4\text{C}_1\text{im}]\text{Cl}$ , were prepared on a 6 - 7 g scale (Table 2.7). In a glovebox, the desired amount of crystalline  $[\text{C}_4\text{C}_1\text{im}]\text{Cl}$  was weighted into a round bottomed flask. An appropriate amount of anhydrous  $\text{ZnCl}_2$  was added slowly to achieve the desired composition ( $X_{\text{ZnCl}_2}$ ). When the addition of both reagents was completed, the flask was sealed and the mixture was stirred overnight at 105 °C until a transparent and highly viscous liquid was obtained.

**Table 2.7:** Composition of  $[\text{C}_4\text{C}_1\text{im}]\text{Cl}\cdot\text{ZnCl}_2$  ionic liquids.

$X_{\text{ZnCl}_2}$	$[\text{C}_4\text{C}_1\text{im}]\text{Cl}$	$\text{ZnCl}_2$
	m (g) / n (mmol)	m (g) / n (mmol)
0.10	5.5 / 31.49	0.48 / 3.42
0.25	5.1 / 29.20	1.33 / 9.76
0.50	3.6 / 20.61	2.81 / 20.61
0.67	2.5 / 14.31	3.96 / 29.05
0.75	1.9 / 10.88	4.5 / 33.02



- $X_{ZnCl_2} = 0.67$  composition (3d)

$^1H$  NMR (**capillary, neat compound**):  $\delta_H$  (500 MHz, DMSO- $d_6$ ) ppm: 7.29 (1H, s,  $N_2CH$ ), 6.12 (2H, d,  $^3J_{HH} = 16.5$  Hz, 2NCH), 2.87 (2H, s,  $NCH_2CH_2CH_2CH_3$ ), 2.61 (3H, s,  $NCH_3$ ), 0.52 (2H, s,  $NCH_2CH_2CH_2CH_3$ ), -0.01 (2H, s,  $NCH_2CH_2CH_2CH_3$ ) and -0.048 (3H, s,  $NCH_2CH_2CH_2CH_3$ ).

$^{13}C$  NMR (**capillary, neat compound**):  $\delta_C$  (125 MHz, DMSO- $d_6$ ) ppm: 133.30 (s,  $N_2C$ ), 121.90 and 120.62 (s, 2NCH), 47.94 (s,  $NCH_2CH_2CH_2CH_3$ ), 35.06 (s,  $NCH_3$ ), 29.61 (s,  $NCH_2CH_2CH_2CH_3$ ), 17.23 (s,  $NCH_2CH_2CH_2CH_3$ ) and 11.48 (s,  $NCH_2CH_2CH_2CH_3$ ).

EA (calc.): %C = 20.56 (21.28), %H = 3.86 (3.34), %N = 6.24 (6.20).

- $X_{ZnCl_2} = 0.10$  composition (3a)

$^1H$  NMR (**capillary, neat compound**):  $\delta_H$  (500 MHz, DMSO- $d_6$ ) ppm: 9.19 ( $^1H$ , s,  $N_2CH$ ), 7.49 and 7.38 (2H, d,  $^3J_{HH} = 55.0$  Hz, 2NCH), 3.64 (2H, s,  $NCH_2CH_2CH_2CH_3$ ), 3.45 (3H, s,  $NCH_3$ ), 1.01 (2H, s,  $NCH_2CH_2CH_2CH_3$ ), 0.40 (2H, s,  $NCH_2CH_2CH_2CH_3$ ) and -0.06 (3H, s,  $NCH_2CH_2CH_2CH_3$ ).

$^{13}C$  NMR (**capillary, neat compound**):  $\delta_C$  (125 MHz, DMSO- $d_6$ ) ppm: 135.68 (s,  $N_2C$ ), 122.27 and 121.26 (s, 2NCH), 47.50 (s,  $NCH_2CH_2CH_2CH_3$ ), 34.96 (s,  $NCH_3$ ), 30.41 (s,  $NCH_2CH_2CH_2CH_3$ ), 17.51 (s,  $NCH_2CH_2CH_2CH_3$ ) and 11.71 (s,  $NCH_2CH_2CH_2CH_3$ ).

EA (calc.): %C = 48.85 (50.62), %H = 9.42 (7.96), %N = 13.69 (14.76)

- $X_{ZnCl_2} = 0.25$  composition (3b)

$^1H$  NMR (**capillary, neat compound**):  $\delta_H$  (500 MHz, DMSO- $d_6$ ) ppm: 8.81 ( $^1H$ , s,  $N_2CH$ ), 7.22 and 7.16 (2H, d,  $^3J_{HH} = 30.0$  Hz, 2NCH), 3.52 (2H, s,  $NCH_2CH_2CH_2CH_3$ ), 3.26 (3H, s,  $NCH_3$ ), 0.93 (2H, s,  $NCH_2CH_2CH_2CH_3$ ), 0.32 (2H, s,  $NCH_2CH_2CH_2CH_3$ ) and -0.14 (3H, s,  $NCH_2CH_2CH_2CH_3$ ).

$^{13}C$  NMR (**capillary, neat compound**):  $\delta_C$  (125 MHz, DMSO- $d_6$ ) ppm: 135.32 (s,  $N_2C$ ), 122.08 and 121.09 (s, 2NCH), 47.57 (s,  $NCH_2CH_2CH_2CH_3$ ), 35.10 (s,  $NCH_3$ ), 30.30 (s,  $NCH_2CH_2CH_2CH_3$ ), 17.45 (s,  $NCH_2CH_2CH_2CH_3$ ) and 11.66 (s,  $NCH_2CH_2CH_2CH_3$ ).

EA (calc.): %C = 45.75 (43.66), %H = 7.01 (6.87), %N = 12.59 (12.73).

- $X_{\text{ZnCl}_2} = 0.50$  composition (3c)

$^1\text{H}$  NMR (**capillary, neat compound**):  $\delta_{\text{H}}$  (500 MHz, DMSO- $d_6$ ) ppm: 7.79 (1H, s,  $\text{N}_2\text{CH}$ ), 6.51 and 6.45 (2H, s, 2NCH), 3.17 (2H, s,  $\text{NCH}_2\text{CH}_2\text{CH}_2\text{CH}_3$ ), 2.90 (3H, s,  $\text{NCH}_3$ ), 0.75 (2H, s,  $\text{NCH}_2\text{CH}_2\text{CH}_2\text{CH}_3$ ), 0.20 (2H, s,  $\text{NCH}_2\text{CH}_2\text{CH}_2\text{CH}_3$ ) and -0.26 (3H, s,  $\text{NCH}_2\text{CH}_2\text{CH}_2\text{CH}_3$ ).

$^{13}\text{C}$  NMR (**capillary, neat compound**):  $\delta_{\text{C}}$  (125 MHz, DMSO- $d_6$ ) ppm: 134.12 (s,  $\text{N}_2\text{C}$ ), 121.95 and 120.75 (s, 2NCH), 47.91 (s,  $\text{NCH}_2\text{CH}_2\text{CH}_2\text{CH}_3$ ), 35.22 (s,  $\text{NCH}_3$ ), 29.93 (s,  $\text{NCH}_2\text{CH}_2\text{CH}_2\text{CH}_3$ ), 17.36 (s,  $\text{NCH}_2\text{CH}_2\text{CH}_2\text{CH}_3$ ) and 11.58 (s,  $\text{NCH}_2\text{CH}_2\text{CH}_2\text{CH}_3$ ).

EA (calc.): %C = 31.07 (30.90), %H = 4.99 (4.86), %N = 8.89 (9.01).

- $X_{\text{ZnCl}_2} = 0.75$  composition (3e)

$^1\text{H}$  NMR (**capillary, neat compound**):  $\delta_{\text{H}}$  (500 MHz, DMSO- $d_6$ ) ppm: 7.05 (1H, s,  $\text{N}_2\text{CH}$ ), 5.94 and 5.92 (2H, s, 2NCH), 2.71 (2H, s,  $\text{NCH}_2\text{CH}_2\text{CH}_2\text{CH}_3$ ), 2.46 (3H, s,  $\text{NCH}_3$ ), 0.38 (2H, s,  $\text{NCH}_2\text{CH}_2\text{CH}_2\text{CH}_3$ ), -0.14 (2H, s,  $\text{NCH}_2\text{CH}_2\text{CH}_2\text{CH}_3$ ) and -0.60 (3H, s,  $\text{NCH}_2\text{CH}_2\text{CH}_2\text{CH}_3$ ).

$^{13}\text{C}$  NMR (**capillary, neat compound**):  $\delta_{\text{C}}$  (125 MHz, DMSO- $d_6$ ) ppm: 132.89 (s,  $\text{N}_2\text{C}$ ), 121.81 and 120.53 (s, 2NCH), 47.89 (s,  $\text{NCH}_2\text{CH}_2\text{CH}_2\text{CH}_3$ ), 34.95 (s,  $\text{NCH}_3$ ), 29.43 (s,  $\text{NCH}_2\text{CH}_2\text{CH}_2\text{CH}_3$ ), 17.13 (s,  $\text{NCH}_2\text{CH}_2\text{CH}_2\text{CH}_3$ ) and 11.41 (s,  $\text{NCH}_2\text{CH}_2\text{CH}_2\text{CH}_3$ ).

EA (calc.): %C = 16.60 (16.46), %H = 3.25 (2.59), %N = 5.21 (4.81).

#### 2.4.1.3 Chloroindates(III) ( $[\text{C}_4\text{C}_1\text{im}]\text{Cl}\cdot\text{InCl}_3$ , $X_{\text{InCl}_3} = 0.67$ )<sup>38</sup> (4)

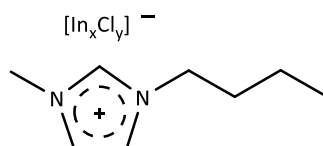


**Figure 2.36:** Chemical structure of  $[\text{C}_4\text{C}_1\text{im}]\text{Cl}\cdot\text{InCl}_3$ ,  $X_{\text{InCl}_3} = 0.67$ ;  $[\text{In}_x\text{Cl}_y]^{2-}$  indicates the formation of complex polyanions.

$[\text{C}_4\text{C}_1\text{im}]\text{Cl}$  (0.99 g, 5.65 mmol) was heated above its melting point (70 °C). An excess of  $\text{InCl}_3$  (2.5 g, 11.3 mmol,  $X_{\text{InCl}_3} = 0.67$ ) was slowly added into molten  $[\text{C}_4\text{C}_1\text{im}]\text{Cl}$  under nitrogen. The reaction mixture was left stirring overnight at 80 °C. A white liquid suspension was obtained and it is believed that the white

solid is unreacted  $\text{InCl}_3$ . The resulting compound is relatively hygroscopic, hence it was handled and stored in a glovebox.

$^1\text{H}$  NMR (**capillary, neat compound**):  $\delta_{\text{H}}$  (500 MHz,  $\text{DMSO-d}_6$ ) ppm: 7.33 (1H, s, br,  $\text{N}_2\text{CH}$ ), 6.25 (2H, s, br,  $2\text{NCH}$ ), 3.07 (2H, s, br,  $\text{NCH}_2\text{CH}_2\text{CH}_2\text{CH}_3$ ), 2.82 (3H, s, br,  $\text{NCH}_3$ ), 0.77 (2H, s, br,  $\text{NCH}_2\text{CH}_2\text{CH}_2\text{CH}_3$ ), 0.24 (2H, s, br,  $\text{NCH}_2\text{CH}_2\text{CH}_2\text{CH}_3$ ) and -0.22 (3H, s, br,  $\text{NCH}_2\text{CH}_2\text{CH}_2\text{CH}_3$ ).

$^{13}\text{C}$  NMR (**capillary, neat compound**):  $\delta_{\text{C}}$  (125 MHz,  $\text{DMSO-d}_6$ ) ppm: 133.16 (s,  $\text{N}_2\text{C}$ ), 122.02 and 120.78 (s,  $2\text{NCH}$ ), 48.24 (s,  $\text{NCH}_2\text{CH}_2\text{CH}_2\text{CH}_3$ ), 35.13 (s,  $\text{NCH}_3$ ), 29.73 (s,  $\text{NCH}_2\text{CH}_2\text{CH}_2\text{CH}_3$ ), 17.43 (s,  $\text{NCH}_2\text{CH}_2\text{CH}_2\text{CH}_3$ ) and 11.54 (s,  $\text{NCH}_2\text{CH}_2\text{CH}_2\text{CH}_3$ ).

#### 2.4.1.4 Chloroferrates(III) ( $[\text{C}_4\text{C}_1\text{im}]\text{Cl}\cdot\text{FeCl}_3$ , $X_{\text{FeCl}_3} = 0.67$ )<sup>112</sup> (5)

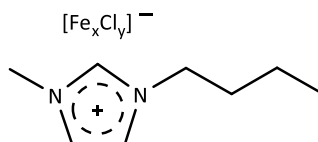


**Figure 2.37:** Chemical structure of  $[\text{C}_4\text{C}_1\text{im}]\text{Cl}\cdot\text{FeCl}_3$ ;  $[\text{Fe}_x\text{Cl}_y]^{2-}$  indicates the formation of complex polyanions.

$[\text{C}_4\text{C}_1\text{im}]\text{Cl}$  (1.50 g, 8.59 mmol) was heated above its melting point ( $70^\circ\text{C}$ ). An excess of  $\text{FeCl}_3$  (2.83 g, 17.44 mmol,  $X_{\text{FeCl}_3}=0.67$ ) was slowly added into molten  $[\text{C}_4\text{C}_1\text{im}]\text{Cl}$  under nitrogen. The reaction mixture was left stirring overnight at room temperature. Nevertheless, a homogeneous solution could not be obtained, and the mixture was heated at  $50^\circ\text{C}$  for achieving homogenization. The final product was still a suspension and it is believed that the black suspension was unreacted  $\text{FeCl}_3$ . The resulting compound is relatively hygroscopic and thus it was stored in a glovebox for later use. The NMR spectra of  $[\text{C}_4\text{C}_1\text{im}]\text{Cl}\cdot\text{FeCl}_3$  could not be obtained since ionic liquids, composed of tetrachloroferrate(III) anions, have paramagnetic properties.

### 2.4.1.5 1-butyl-3-methylimidazolium Hydrogen Sulfate ([C<sub>4</sub>C<sub>1</sub>im][HSO<sub>4</sub>])<sup>179</sup>

(6)

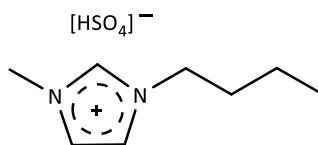


**Figure 2.38** Chemical structure of [C<sub>4</sub>C<sub>1</sub>im][HSO<sub>4</sub>].

1-butyl-3-methylimidazolium hydrogen sulfate, [C<sub>4</sub>C<sub>1</sub>im][HSO<sub>4</sub>], was prepared from its chloride salt via an acid-base reaction. A three-necked, 500 mL round-bottom flask was connected with two Dreschel bottles filled with NaOH aqueous solution (5% w/w) via acid-resistant Tygon tubing. [C<sub>4</sub>C<sub>1</sub>im]Cl (73.92 g, 0.423 mol, 1 eq.) was mixed with anhydrous CH<sub>2</sub>Cl<sub>2</sub> (130 mL) and the mixture was cooled at 0 °C. Concentrated H<sub>2</sub>SO<sub>4</sub> (95-98% v/v, 43.02 g, 0.423 mol, 1 eq.) was added drop wise via a dropping funnel with pressure equalisation. A reflux condenser was added onto the round bottom flask and the reaction mixture was stirred for 48 h at room temperature. HCl gas evolved during the reaction. HCl (g) was distilled out of the condenser under the stream of dry N<sub>2</sub> and it was neutralised by the solution of NaOH (aq). Upon the reaction completion, CH<sub>2</sub>Cl<sub>2</sub> (bp<sub>760</sub>: 39.6 °C) was removed by rotary evaporation and the ionic liquid was dried under vacuum (35 °C, 1.4 mbar). The product is relatively hygroscopic transparent liquid and it was stored under nitrogen.

<sup>1</sup>H NMR: δ<sub>H</sub> (400 MHz, DMSO-d<sub>6</sub>) ppm: 9.70 (1H, s, br, HSO<sub>4</sub><sup>-</sup>), 9.15 (1H, s, N<sub>2</sub>CH), 7.78 and 7.72 (2H, m, 2NCH), 4.17 (2H, t, <sup>3</sup>J<sub>HH</sub> = 7.2 Hz, NCH<sub>2</sub>CH<sub>2</sub>CH<sub>2</sub>CH<sub>3</sub>), 3.86 (3H, s, NCH<sub>3</sub>), 1.77 (2H, quintet, <sup>3</sup>J<sub>HH</sub> = 7.6 Hz, NCH<sub>2</sub>CH<sub>2</sub>CH<sub>2</sub>CH<sub>3</sub>), 1.26 (2H, sextet, <sup>3</sup>J<sub>HH</sub> = 7.2 Hz, NCH<sub>2</sub>CH<sub>2</sub>CH<sub>2</sub>CH<sub>3</sub>) and 0.90 (3H, t, <sup>3</sup>J<sub>HH</sub> = 7.6 Hz, NCH<sub>2</sub>CH<sub>2</sub>CH<sub>2</sub>CH<sub>3</sub>).

<sup>13</sup>C NMR: δ<sub>C</sub> (100 MHz, DMSO-d<sub>6</sub>) ppm: 137.07 (s, N<sub>2</sub>C), 124.10 and 122.75 (s, 2NCH), 48.95 (s, NCH<sub>2</sub>CH<sub>2</sub>CH<sub>2</sub>CH<sub>3</sub>), 36.20 (s, NCH<sub>3</sub>), 31.84 (s, NCH<sub>2</sub>CH<sub>2</sub>CH<sub>2</sub>CH<sub>3</sub>), 19.25 (s, NCH<sub>2</sub>CH<sub>2</sub>CH<sub>2</sub>CH<sub>3</sub>) and 13.75 (s, NCH<sub>2</sub>CH<sub>2</sub>CH<sub>2</sub>CH<sub>3</sub>).

MS (FAB<sup>+</sup>) *m/z*: 142 ([C<sub>4</sub>C<sub>1</sub>im]<sup>+</sup>, 100 %), (FAB<sup>-</sup>) *m/z*: 97 ([HSO<sub>4</sub>]<sup>-</sup>, 100%).

## 2.4.2 Small-scale synthesis of bio-derived thiophene analogues in ionic liquids

### 2.4.2.1 Reference compounds

2,5-dimethylfuran (2,5-DMF, 99%), 2,5-dimethylthiophene (2,5-DMT, 98.5%) and 2,5-hexanedione (98 %) were purchased by Sigma-Aldrich as standards. The crude reaction mixtures, distillation product(s) and reference compounds were characterised by  $^1\text{H}$  and  $^{13}\text{C}$  NMR spectroscopy. GC-EI-MS was also employed for further characterisation of the isolated products.

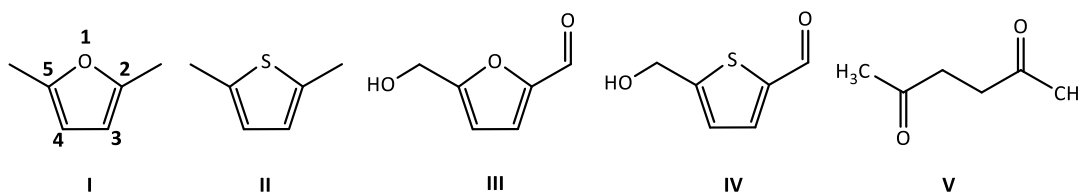


**Figure 2.39:** Chemical structure and ring numbering of 2,5-DMF (I), 2,5-DMT (II), 5-HMF (III), 5-(hydroxymethyl)-2-thiophenecarboxaldehyde (IV) and 2,5-hexanedione (V): a key intermediate.

#### (I) 2,5-dimethylfuran (2,5-DMF)

$^1\text{H}$  NMR:  $\delta_{\text{H}}$  (400 MHz, DMSO- $d_6$ ) ppm: 5.89 (2H, s, ring 2CH), 2.19 (6H, s, 2CH<sub>3</sub>).

$^{13}\text{C}$  NMR:  $\delta_{\text{C}}$  (100 MHz, DMSO- $d_6$ ) ppm: 149.95 (2C, s, ring C<sup>2,5</sup>), 106.64 (2C, s, ring C<sup>3,4</sup>), 13.56 (2C, s, 2CH<sub>3</sub>).

MS(EI<sup>+</sup>)  $m/z$ : 95 (100 %), 84 (58 %). Accurate mass (major ion): 95.05 (C<sub>6</sub>H<sub>7</sub>O).

#### (II) 2,5-dimethylthiophene (2,5-DMT)

$^1\text{H}$  NMR:  $\delta_{\text{H}}$  (400 MHz, DMSO- $d_6$ ) ppm: 6.56 (2H, s, ring 2CH), 2.36 (6H, s, 2CH<sub>3</sub>).

$^{13}\text{C}$  NMR:  $\delta_{\text{C}}$  (100 MHz, DMSO- $d_6$ ) ppm: 137.07 (2C, s, ring C<sup>2,5</sup>), 125.49 (2C, s, ring C<sup>3,4</sup>), 15.33 (2C, s, 2CH<sub>3</sub>).

MS(EI<sup>+</sup>)  $m/z$ : 111 (100%), 97 (84%), 84 (83%). Accurate mass (major ion): 111.03 (C<sub>6</sub>H<sub>7</sub>S).

#### (III) 5-(hydroxymethyl)furfural (5-HMF)

$^1\text{H}$  NMR:  $\delta_{\text{H}}$  (400 MHz, DMSO- $d_6$ ) ppm: 9.55 (1H, s, CHO), 7.50 (1H, d,  $^3J_{\text{HH}} = 4.0$  Hz, ring C<sup>3</sup>H), 6.60 (1H, d,  $^3J_{\text{HH}} = 3.6$  Hz, ring C<sup>4</sup>H), 5.56 (1H, t,  $^3J_{\text{HH}} = 6.0$  Hz, OH) and 4.50 (2H, d,  $^3J_{\text{HH}} = 6.0$  Hz, CH<sub>2</sub>OH).

$^{13}\text{C}$  NMR:  $\delta_{\text{C}}$  (100 MHz, DMSO- $d_6$ ) ppm: 178.44 (s, CHO), 162.66 (s, ring C<sup>5</sup>), 152.21 (s, ring C<sup>2</sup>), 124.88 (s, ring C<sup>3</sup>H), 110.14 (s, ring C<sup>4</sup>H) and 56.40 (s, CH<sub>2</sub>OH).

MS(EI<sup>+</sup>)  $m/z$ : 126 (100 %), 109 (72 %). Accurate mass (major ion): 95.05 (C<sub>6</sub> H<sub>7</sub> O).

#### (IV) 5-(hydroxymethyl)-2-thiophenecarboxaldehyde

$^1\text{H}$  NMR:  $\delta_{\text{H}}$  (400 MHz, DMSO- $d_6$ ) ppm: 9.86 (1H, s, CHO), 7.90 (1H, d,  $^3J_{\text{HH}} = 3.6$  Hz, ring C<sup>3</sup>H), 7.16 (1H, m, ring C<sup>4</sup>H), 5.82 (1H, m, OH) and 4.72 (2H, d,  $^3J_{\text{HH}} = 5.2$  Hz, CH<sub>2</sub>OH).

$^{13}\text{C}$  NMR:  $\delta_{\text{C}}$  (100 MHz, DMSO- $d_6$ ) ppm: 184.48 (s, CHO), 158.68 (s, ring C<sup>5</sup>), 142.07 (s, ring C<sup>2</sup>), 138.69 (s, ring C<sup>3</sup>H), 125.37 (s, ring C<sup>4</sup>H) and 59.16 (s, CH<sub>2</sub>OH).

MS(EI<sup>+</sup>)  $m/z$ : 142 (42 %), 113 (94 %), 85 (100 %).

#### (V) 2,5-hexanedione (2,5-hxd)

$^1\text{H}$  NMR:  $\delta_{\text{H}}$  (400 MHz, DMSO- $d_6$ ) ppm: 2.62 (4H, s, -O=CCH<sub>2</sub>CH<sub>2</sub>C=O-), 2.10 (6H, s, 2CH<sub>3</sub>C=O-).

#### 2.4.2.2 Reaction of 5-HMF and H<sub>2</sub>S in a Lewis acid ionic liquid ([C<sub>4</sub>C<sub>1</sub>im]Cl·ZnCl<sub>2</sub>, X<sub>ZnCl<sub>2</sub></sub> = 0.67)

[C<sub>4</sub>C<sub>1</sub>im]Cl·ZnCl<sub>2</sub> (X<sub>ZnCl<sub>2</sub></sub> = 0.67) (10.00 g, 0.022 mol) was weighed in a 150 mL three-necked round-bottom flask. The flask was connected to an H<sub>2</sub>S gas lecture bottle (99.5%) and a trap containing NaOCl (500 mL, 12 % w/w). The flask was equipped with two adapters with GP Rotaflo PTFE stopcock that provided a relative gas flow control and positive closure. The ionic liquid was heated to 100 °C so that its viscosity was decreased prior to addition of 5-HMF. 5-HMF (1.00 g, 0.008 mol) was weighed in a glovebox and added to the ionic liquid under nitrogen. The IL/5-HMF mixture was stirred vigorously under nitrogen until a homogenous solution was formed. The flow of nitrogen gas was stopped and an excess of H<sub>2</sub>S gas (approx. 30.75 g, 0.90 mol) was bubbled into the solution for 1 hour. The amount of H<sub>2</sub>S was approximately calculated by measuring the volume and number of bubbles h<sup>-1</sup> that were generated in a trap containing 500 mL of NaOCl (90 bubbles min<sup>-1</sup>, 4.19 cm<sup>3</sup> bubble<sup>-1</sup>, 60 min). The colour of the reaction mixture changed rapidly from light yellow to dark brown upon the addition of H<sub>2</sub>S. The final product was a dark brown solid that could not be completely dissolved in any conventional organic solvent. As a result, the product was not further characterized by NMR spectroscopy or MS spectrometry.

#### 2.4.2.3 Control reaction of 5-HMF and H<sub>2</sub>S in [C<sub>4</sub>C<sub>1</sub>im]Cl

[C<sub>4</sub>C<sub>1</sub>im]Cl (10.00 g, 0.057 mol) was weighed in a 150 mL three-necked round-bottom flask with an experimental set-up similar to has been described in **Section 2.4.2.2**. [C<sub>4</sub>C<sub>1</sub>im]Cl, solid at room temperature, was heated up to 100 °C until it became a transparent viscous liquid. Subsequently, 5-HMF (1.00 g, 0.008 mol) was weighed in a glovebox and added to the ionic liquid under nitrogen. The IL/5-HMF mixture was then stirred vigorously under nitrogen until a homogenous solution was formed. The flow of nitrogen was stopped and an excess of H<sub>2</sub>S (approx. 30.75 g, 0.90 mol) was bubbled into the solution for 1 hour. The amount of H<sub>2</sub>S gas was approximately calculated as described in **Section 2.4.2.2**.

The colour of the reaction mixture changed rapidly from light yellow to dark red upon the addition of H<sub>2</sub>S. The final product was a dark red viscous liquid that was characterized by <sup>1</sup>H NMR, looking for the peaks of [C<sub>4</sub>C<sub>1</sub>im]Cl, 5-HMF and 5-(hydroxymethyl)-2-thiophenecarboxaldehyde.

<sup>1</sup>H NMR for [C<sub>4</sub>C<sub>1</sub>im]Cl: δ<sub>H</sub> (400 MHz, DMSO-d<sub>6</sub>) ppm: 9.27 (1H, s, N<sub>2</sub>CH), 7.80 and 7.73 (2H, m, 2NCH), 4.17 (2H, t, <sup>3</sup>J<sub>HH</sub> = 7.2 Hz, NCH<sub>2</sub>CH<sub>2</sub>CH<sub>2</sub>CH<sub>3</sub>), 3.86 (3H, s, NCH<sub>3</sub>), 1.76 (2H, quintet, <sup>3</sup>J<sub>HH</sub> = 7.2 Hz, NCH<sub>2</sub>CH<sub>2</sub>CH<sub>2</sub>CH<sub>3</sub>), 1.26 (2H, sextet, <sup>3</sup>J<sub>HH</sub> = 7.2 Hz, NCH<sub>2</sub>CH<sub>2</sub>CH<sub>2</sub>CH<sub>3</sub>) and 0.90 (3H, t, <sup>3</sup>J<sub>HH</sub> = 7.2 Hz, NCH<sub>2</sub>CH<sub>2</sub>CH<sub>2</sub>CH<sub>3</sub>).

<sup>1</sup>H NMR for 5-HMF: δ<sub>H</sub> (400 MHz, DMSO-d<sub>6</sub>) ppm: 9.54 (1H, s, CHO), 7.49 (1H, d, <sup>3</sup>J<sub>HH</sub> = 4.0 Hz, ring C<sup>3</sup>H), 6.60 (1H, d, <sup>3</sup>J<sub>HH</sub> = 3.6 Hz, ring C<sup>4</sup>H) and 4.50 (2H, d, <sup>3</sup>J<sub>HH</sub> = 6.0 Hz, CH<sub>2</sub>OH).

The peak that could be assigned to the hydroxyl proton (-OH) of 5-HMF could not be detected. There was no spectroscopic evidence for the formation of 5-(hydroxymethyl)-2-thiophenecarboxaldehyde.

#### 2.4.2.4 Reaction of 2,5-DMF and H<sub>2</sub>S in a Lewis acidic ionic liquid ([C<sub>4</sub>C<sub>1</sub>im]Cl·ZnCl<sub>2</sub>, X<sub>ZnCl<sub>2</sub></sub> = 0.67).

[C<sub>4</sub>C<sub>1</sub>im]Cl·ZnCl<sub>2</sub>, X<sub>ZnCl<sub>2</sub></sub> = 0.67 (6 g, 0.019 mol) was weighed in a single-neck, 50 mL Rbf. The flask was connected to an H<sub>2</sub>S gas lecture bottle (99.5%) via a straight adapter with quick disconnect and acid-resistant Tygon tubing; the overall experimental set-up was as described in **Section 2.4** (Figure 2.33). The ionic liquid was heated up to 70 °C so that its viscosity was well decreased prior to the addition of 2,5-DMF. 2,5-DMF (4.50 mL, 4.0 g, 0.042 mol) was added into the ionic liquid under nitrogen with the condenser already in place and a biphasic mixture was formed. The mixture was then stirred under nitrogen for 2-3 min at 70 °C. The flow of nitrogen gas was stopped and an excess of H<sub>2</sub>S gas was bubbled into the solution for approximately 1 hour. The cold-finger condenser was used both during the stage of mixing 2,5-DMF with the ionic liquid and during the total reaction time in order to condense any vapours. The H<sub>2</sub>S gas flow was stopped and the reaction was continued for 2 additional hours (total reaction time: 3h, 70 °C). During this time, H<sub>2</sub>S was cooled below its boiling point (bp<sub>760</sub>: -60 °C), therefore it was continuously condensing and adding directly to the reaction mixture instead of bubbling on the surface. At the end of the reaction, the oil bath was removed and the flask was left to cool down. The acetone/CO<sub>2</sub> mixture was removed from the cold-finger condenser. Subsequently, the flask was placed into an ice water bath (0 °C) so that H<sub>2</sub>S was released and oxidised in the trap whilst the losses of any unreacted 2,5-DMF and/or 2,5-DMT (bp<sub>760</sub>: 135 °C) were minimised.

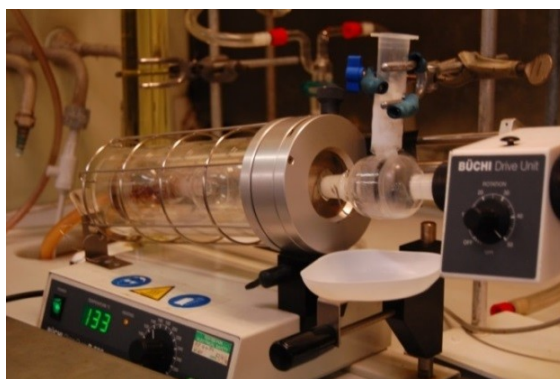


**Figure 2.40:** Kugelrohr distillation set-up; products separation from the ionic liquid layer.

The reaction afforded a brown viscous liquid that was distilled under atmospheric pressure by using a Kugelrohr apparatus (B-580 Buchi) from 25 °C to 170 °C. The 50 mL rbf containing the crude reaction mixture and an empty flask were placed inside the Kugelrohr glass oven (Figure 2.40). A receiving flask was placed outside of the oven and the products were collected upon condensation. A transparent biphasic mixture was obtained (1.76 g: 42.18 % and 37.69 %, accounting for the 2,5-DMF input and 100 % conversion of 2,5-DMF into 2,5-DMT respectively). The top layer of the distillation product accounted for approximately 90 % of the total volume. Both product layers were characterised by <sup>1</sup>H NMR spectroscopy and GC(EI), identifying for the peaks of [C<sub>4</sub>C<sub>1</sub>im]<sup>+</sup>, 2,5-DMF and 2,5-DMT. The determination of the 2,5-DMT/2,5-DMF selectivity in the distillate was done by <sup>1</sup>H NMR spectroscopy. The reaction spectra and the distillation data are summarised in the following sections.

#### **2.4.2.4 a) Characterisation of the crude reaction mixture (ionic liquid layer) by <sup>1</sup>H NMR spectroscopy**

There is evidence that 2,5-hexanedione (bp<sub>760</sub>: 191.4 °C) (Figure 2.41) was formed as the 2,5-DMF hydrolysis by-product during the reaction. The proton chemical shifts data agree with the values obtained for the reference compound (Section 2.4.2.1). A large water peak was also detected at 3.33 ppm. Residual water is a by-product of the 2,5-DMF recyclization into 2,5-DMT. Additionally, the baseline of the <sup>1</sup>H NMR spectrum indicates the presence of other impurities. The unidentified by-products could be attributed to the formation of polymerisation products under strongly acidic conditions.<sup>180</sup> The hydrolysis of 2,5-DMF to 2,5-hexanedione could therefore compete with the polymerization of 2,5-hexanedione via an acid-catalysed aldol condensation.<sup>181,182</sup> The latter may explain the darkening of the reaction media during the course of the reaction. Eliminating the hydrolytic decomposition of 2,5-DMF may be very challenging unless constant water removal is achieved. Water molecules are generated in the final recyclization step and water has also proved to have a catalytic effect towards the reduction of the recyclization activation energy; hence controlling all side-products formation is a complex endeavour.<sup>79</sup>



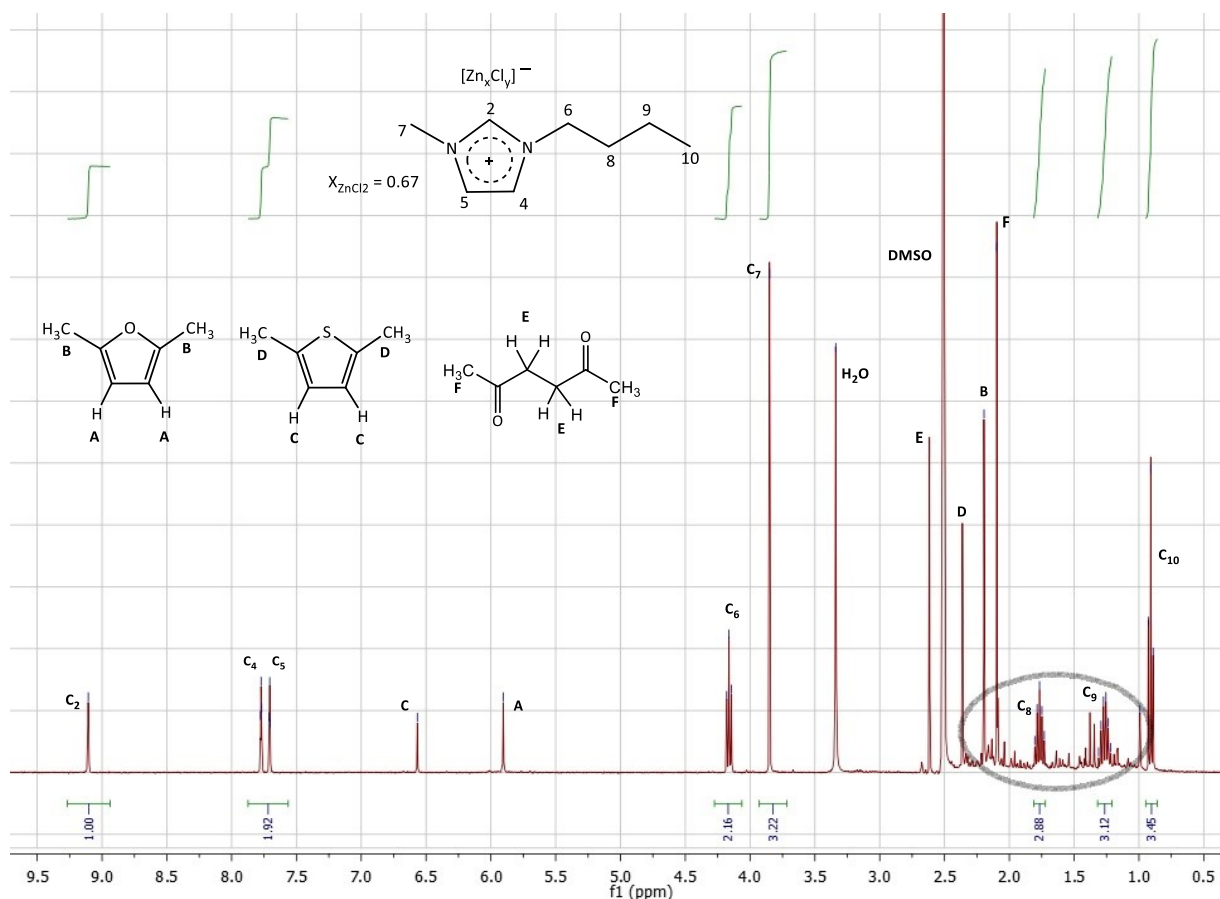


**Figure 2.41:** Small-scale 2,5-DMT synthesis in  $[C_4C_{1im}]Cl \cdot ZnCl_2$ ,  $X_{ZnCl_2} = 0.67$ . Crude reaction mixture;  $^1H$  NMR spectrum.

$^1H$  NMR for  $[C_4C_{1im}]Cl \cdot ZnCl_2$  ( $X_{ZnCl_2} = 0.67$ ):  $\delta_H$  (400 MHz, DMSO- $d_6$ ) ppm: 9.11 (1H, s,  $N_2CH$ ), 7.77 and 7.71 (2H, m,  $2NCH$ ), 4.16 (2H, t,  $^3J_{HH} = 7.2$  Hz,  $NCH_2CH_2CH_2CH_3$ ), 3.85 (3H, s,  $NCH_3$ ), 1.77 (2H, quintet,  $^3J_{HH} = 7.2$  Hz,  $NCH_2CH_2CH_2CH_3$ ), 1.25 (2H, sextet,  $^3J_{HH} = 7.6$  Hz,  $NCH_2CH_2CH_2CH_3$ ) and 0.91 (3H, t,  $^3J_{HH} = 7.2$  Hz,  $NCH_2CH_2CH_2CH_3$ ).

$^1H$  NMR for 2,5-DMF:  $\delta_H$  (400 MHz, DMSO- $d_6$ ) ppm: 5.90 (2H, s, ring  $2CH$ ), 2.20 (6H, s,  $2CH_3$ ).

$^1H$  NMR for 2,5-DMT:  $\delta_H$  (400 MHz, DMSO- $d_6$ ) ppm: 6.57 (2H, s, ring  $2CH$ ), 2.35 (6H, s,  $2CH_3$ ).

$^1H$  NMR for 2,5-hexanedione:  $\delta_H$  (400 MHz, DMSO- $d_6$ ) ppm: 2.62 (4H, s,  $-O=CCH_2CH_2C=O-$ ), 2.10 (6H, s,  $2CH_3C=O-$ ).

The crude reaction mixture was subjected to Kugelrohr distillation and the  $^1H$  NMR spectroscopy analysis of the biphasic mixture is summarised in the following sections.

### 2.4.2.4 b) Characterisation of the Kugelrohr distillation product (top layer) by $^1\text{H}$ NMR spectroscopy

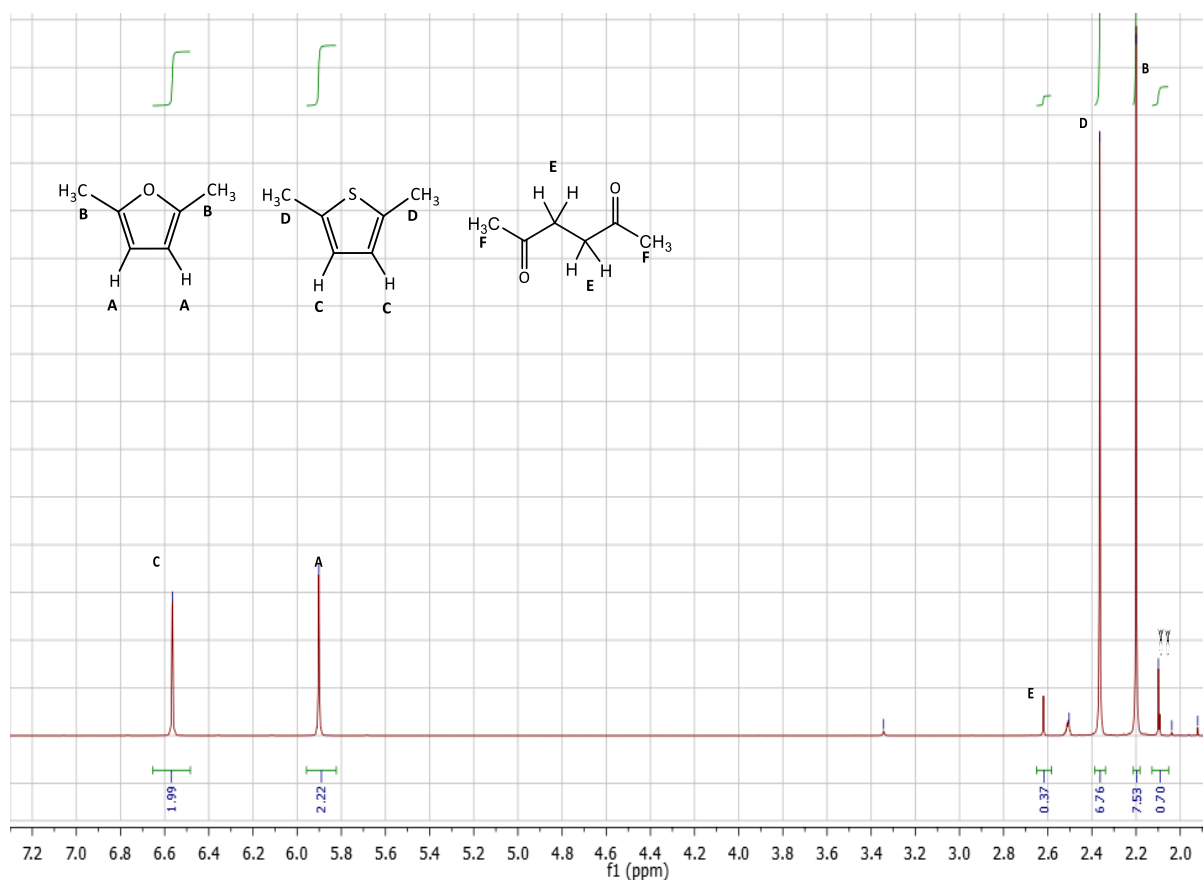


**Figure 2.42:** Small-scale 2,5-DMT synthesis in  $[\text{C}_4\text{C}_{1\text{im}}]\text{Cl}\cdot\text{ZnCl}_2$ ,  $X_{\text{ZnCl}_2} = 0.67$ . Kugelrohr distillate (Top Layer):  $^1\text{H}$  NMR spectrum.

$^1\text{H}$  NMR for 2,5-DMF:  $\delta_{\text{H}}$  (400 MHz,  $\text{DMSO-d}_6$ ) ppm: 5.90 (2H, s, ring 2CH), 2.20 (6H, s, 2CH<sub>3</sub>).

$^1\text{H}$  NMR for 2,5-DMT:  $\delta_{\text{H}}$  (400 MHz,  $\text{DMSO-d}_6$ ) ppm: 6.56 (2H, s, ring 2CH), 2.36 (6H, s, 2CH<sub>3</sub>).

$^1\text{H}$  NMR for 2,5-hexanedione:  $\delta_{\text{H}}$  (400 MHz,  $\text{DMSO-d}_6$ ) ppm: 2.62 (4H, s,  $-\text{O}=\text{CCH}_2\text{CH}_2\text{C}=\text{O}-$ ), 2.10 (6H, s, 2CH<sub>3</sub>C=O-).

Theoretical yield (100% conversion of 2,5-DMF into 2,5-DMT) = 4.67 g.

Isolated product = 1.76 g, **37.67 %**.

Comparing the peak integrals of the desired product (2,5-DMT) and those corresponding to the starting material (2,5-DMF) and the known by-product (2,5-hxd), an approximate calculation of 2,5-DMT selectivity (%) was calculated (**46.25 %**). Variability in the reaction selectivity was observed upon repeating the reaction under the same experimental conditions as discussed in **Section 2.3.7.1**.

### 2.4.2.4 c) Characterisation of the distillation product (bottom layer) by $^1\text{H}$ NMR spectroscopy

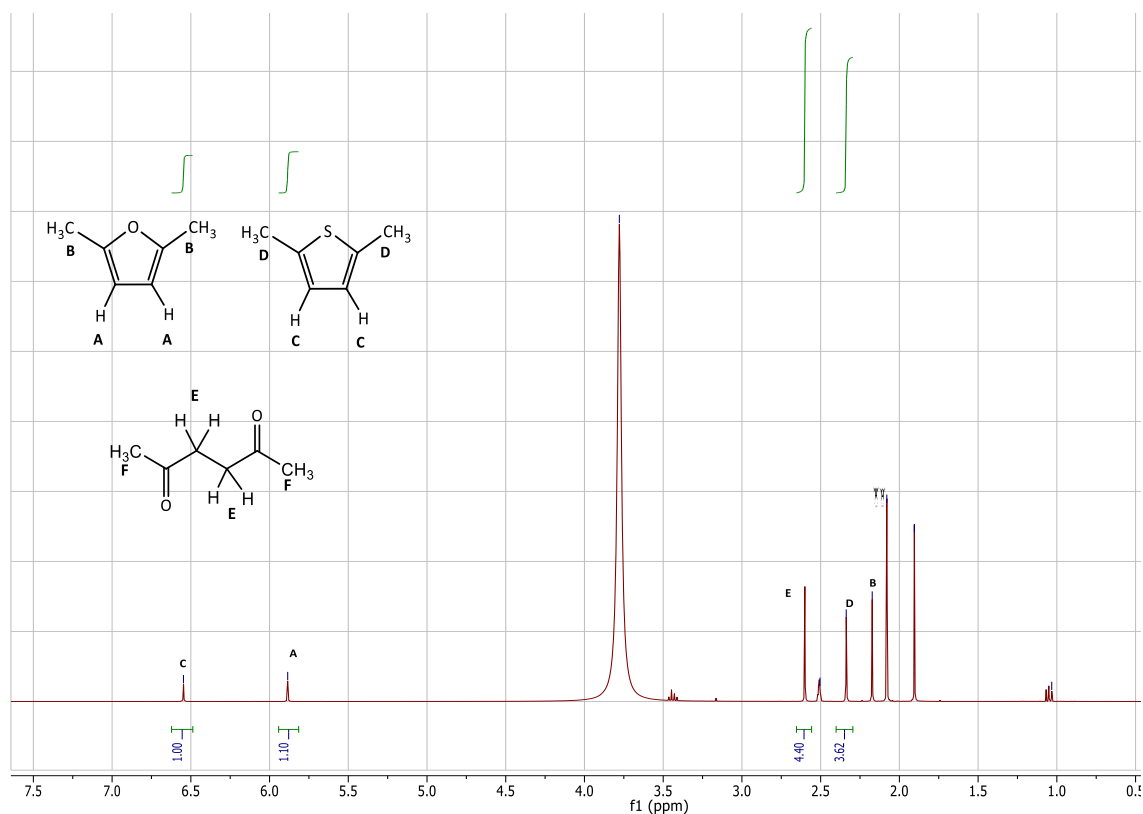


**Figure 2.43:** Small-scale 2,5-DMT synthesis in  $[\text{C}_4\text{C}_1\text{im}]\text{Cl}\cdot\text{ZnCl}_2$ ,  $X_{\text{ZnCl}_2} = 0.67$ . Kugelrohr distillate (Bottom Layer):  $^1\text{H}$  NMR spectrum.

Smaller peaks that could be assigned to 2,5-DMF, 2,5-DMT and 2,5-hexanedione were also observed in the bottom/aqueous layer (ca. 10 % v/v of the distillate volume). Integrating the area under the peaks of the protons corresponding to 2,5-DMF, 2,5-DMT and 2,5-hexanedione indicates that larger amounts of the more polar 2,5-hexanedione (34.4 %) are found in the aqueous layer compared to the top layer of the biphasic mixture (2,5-hxd: < 1 %). Additionally, a very broad peak appears at 3.78 ppm and it is assigned to water (reaction by-product), underlining the fact that the formation of the separate aqueous layer was mainly driven due to low solubility of 2,5-DMF and 2,5-DMT in water.

### 2.4.2.5 Reference compounds (2,5-DMF, 2,5-DMT) - Kugelrohr studies

Kugelrohr distillation studies were also performed by using reference compounds that have been purchased by Sigma-Aldrich. A 50:50 % w/w mixture of 2,5-DMF:2,5-DMT (4 g) was added to  $[\text{C}_4\text{C}_1\text{im}]\text{Cl}\cdot\text{ZnCl}_2$  ( $X_{\text{ZnCl}_2} = 0.67$ ) (6 g, 0.019 mol) and the mixture was heated up to 70 °C in the absence of adding  $\text{H}_2\text{S}$  prior to the distillation. The distillation conditions for this experiment were the same as those applied for the distillation of the crude reaction mixtures. The  $^1\text{H}$  NMR spectrum of the distillate did not

show any indication for the formation of 2,5-hexanedione under the tested conditions whereas a 58.7 % distillation efficiency was recorded, accounting for the mass input. The latter could be explained by evaporation losses during the distillation process but also due to potentially strong interactions between the Lewis acidic ionic liquid and aromatic compounds (2,5-DMF, 2,5-DMT).

#### **2.4.2.6 GC(EI) protocol – Qualitative characterisation of the Kugelrohr distillation products; Reaction of 2,5-DMF and H<sub>2</sub>S in Lewis acidic ionic liquids ([C<sub>4</sub>C<sub>1</sub>im]Cl·ZnCl<sub>2</sub>, X<sub>ZnCl<sub>2</sub></sub> = 0.67).**

In addition to using <sup>1</sup>H NMR spectroscopy as a qualitative and quantitative tool, GC(EI) was also performed on the following samples: 2,5-DMF, 2,5-DMT and 50 : 50 mixture of 2,5-DMF and 2,5-DMT. The retention times (min) were used as a reference for the analysis of the Kugelrohr distillates. All the samples were dissolved in CH<sub>2</sub>Cl<sub>2</sub> (50 µl/mL). GC-MS was carried out using a BPX 5 column (30 m × 0.32 mm) at a carrier gas flow of 1 mL/min helium. The initial oven temperature of 50 °C was maintained for 5 min and then raised to 100 °C at 10 °C/min and held at 100 °C for 1 min before reaching 300 °C at a heating rate of 35 °C/min.

##### **a) Reference compounds (GC(EI))**

GC (retention time / min) – Reference compounds: 2,5-DMF (0.80) and 2,5-DMT (1.81).

2,5-DMF: MS (EI<sup>+</sup>) (*m/z*): 96 (100 %); 2,5-DMT: MS (EI<sup>+</sup>) (*m/z*): 111 (100 %).

##### **b) Distillation products analysis (GC(EI))- Kugelrohr distillation product (Top layer)**

GC (retention time / min): 2,5-DMF (0.78) and 2,5-DMT (1.74).

Another peak was detected at 3.08 min. Further analysis with MS (EI<sup>+</sup>) confirmed the presence of 2,5-hexanedione (*m/z*: 114 (15 %)). 2,5-DMF (*m/z*: 95 (87 %)) and 2,5-DMT (*m/z*: 95 (100 %)) were also detected.

##### **c) Distillation products analysis (GC(EI))- Kugelrohr distillation product (Bottom layer)**

GC (retention time): 2,5-DMF (0.78) and 2,5-DMT (1.74).

Similarly to the top layer of the biphasic distilled product, a peak was found at 3.08 min. (*m/z*: 114 (15 %)) and 1.02 min (*m/z*: 91 (100 %)) that have been assigned to 2,5-hexanedione and an unknown by-product. 2,5-DMF (*m/z*: 96 (78 %)) and 2,5-DMT (*m/z*: 95 (100 %)) were detected as well.

#### 2.4.2.7 Reaction of 2,5-DMF and H<sub>2</sub>S in Lewis basic ionic liquids ([C<sub>4</sub>C<sub>1</sub>im]Cl·ZnCl<sub>2</sub>, X<sub>ZnCl<sub>2</sub></sub> = 0.25)

As for the reaction of 2,5-DMF with H<sub>2</sub>S in the Lewis acidic [C<sub>4</sub>C<sub>1</sub>im]Cl·ZnCl<sub>2</sub> (X<sub>ZnCl<sub>2</sub></sub> = 0.67) (Section 2.4.2.4) but in this case, [C<sub>4</sub>C<sub>1</sub>im]Cl·ZnCl<sub>2</sub> (X<sub>ZnCl<sub>2</sub></sub> = 0.25) (4.27 g, 0.014 mol) or [C<sub>4</sub>C<sub>1</sub>im]Cl·ZnCl<sub>2</sub> (X<sub>ZnCl<sub>2</sub></sub> = 0.25) (6.12 g, 0.020 mol) were mixed with 2,5-DMF in the following concentrations: (2.85 g, 0.030 mol) and (4 g, 0.041 mol). The reaction afforded a light orange viscous liquid and a transparent layer was formed on top of the IL. Both layers were analysed by <sup>1</sup>H NMR spectroscopy, identifying for the peaks of the IL and 2,5-DMF. Neither 2,5-DMT nor 2,5-hexanedione were detected.

#### 2.4.2.8 Reaction of 2,5-DMF and H<sub>2</sub>S in Lewis acidic ionic liquids ([C<sub>4</sub>C<sub>1</sub>im]Cl·ZnCl<sub>2</sub>, X<sub>ZnCl<sub>2</sub></sub> = 0.50)

As for the reaction of 2,5-DMF with H<sub>2</sub>S in the Lewis acidic [C<sub>4</sub>C<sub>1</sub>im]Cl·ZnCl<sub>2</sub> (X<sub>ZnCl<sub>2</sub></sub> = 0.67) but in this case, [C<sub>4</sub>C<sub>1</sub>im]Cl·ZnCl<sub>2</sub> (X<sub>ZnCl<sub>2</sub></sub> = 0.50) (6.67 g, 0.021 mol) or [C<sub>4</sub>C<sub>1</sub>im]Cl·ZnCl<sub>2</sub> (X<sub>ZnCl<sub>2</sub></sub> = 0.50) (5.78 g, 0.0186 mol) were mixed with 2,5-DMF in the following concentrations: (4.45 g, 0.046 mol) and (3.85 g, 0.040 mol). This reaction afforded a dark orange viscous liquid whereas a transparent layer was still present on top of the IL layer. Both layers were characterised by <sup>1</sup>H NMR spectroscopy. There was an inconsistency between the results of the two repeat experiments. The first experiment did not yield any spectroscopically detectable 2,5-DMT. However, when the experiment was repeated with a stronger magnet and better mixing, the spectroscopic analysis indicated that the top layer contained small amounts of 2,5-DMT together with unreacted 2,5-DMF and traces of impurities. The crude reaction mixture was washed with diethyl ether (3x20 mL) and atmospheric distillation afforded 1.70 g of product. The theoretical yield, accounting for a 100 % 2,5-DMF conversion into 2,5-DMT, was 4.48 g. Integration of the 2,5-DMF and 2,5-DMT peaks shows that there was a maximum of 10 % of 2,5-DMT in the distillate. Weak <sup>1</sup>H NMR signals were found for 2,5-DMF, 2,5-DMT and 2,5-hexanedione even after washing the IL with diethyl ether. The presence of 2,5-DMT and 2,5-hexanedione in the distillate was also confirmed by GC(EI) (2,5-DMF (1.02), 2,5-DMT (1.69), 2,5-hexanedione (3.02)).

#### 2.4.2.9 Reaction of 2,5-DMF and H<sub>2</sub>S in a Brønsted acid ionic liquid ([C<sub>4</sub>C<sub>1</sub>im][HSO<sub>4</sub>])

As for the reaction of 2,5-DMF with H<sub>2</sub>S in the Lewis acidic [C<sub>4</sub>C<sub>1</sub>im]Cl·ZnCl<sub>2</sub> (X<sub>ZnCl<sub>2</sub></sub> = 0.67) (Section 2.4.2.4) but in this case, [C<sub>4</sub>C<sub>1</sub>im][HSO<sub>4</sub>] (4.56 g, 0.019 mol) was mixed with 2,5-DMF (4.50 mL, 4.0 g, 0.042 mol), forming a biphasic mixture (70 °C, 3 h). The reaction afforded a solidified product with a dark brown colour. Both layers were analysed by <sup>1</sup>H NMR spectroscopy. The formation of 2,5-DMT was not spectroscopically detected. Furthermore, there was no peak indicative of the presence of the [HSO<sub>4</sub>]<sup>-</sup> anion upon the completion of the reaction between 2,5-DMF and H<sub>2</sub>S. An upfield chemical shift for the all of the imidazolium ring protons was also observed. Both facts could demonstrate a chemical

interaction between H<sub>2</sub>S and [HSO<sub>4</sub>]<sup>-</sup>. The values in Table 2.8 represent the δ (ppm) of the protons of the neat ionic liquid and the ones post-reaction with H<sub>2</sub>S.

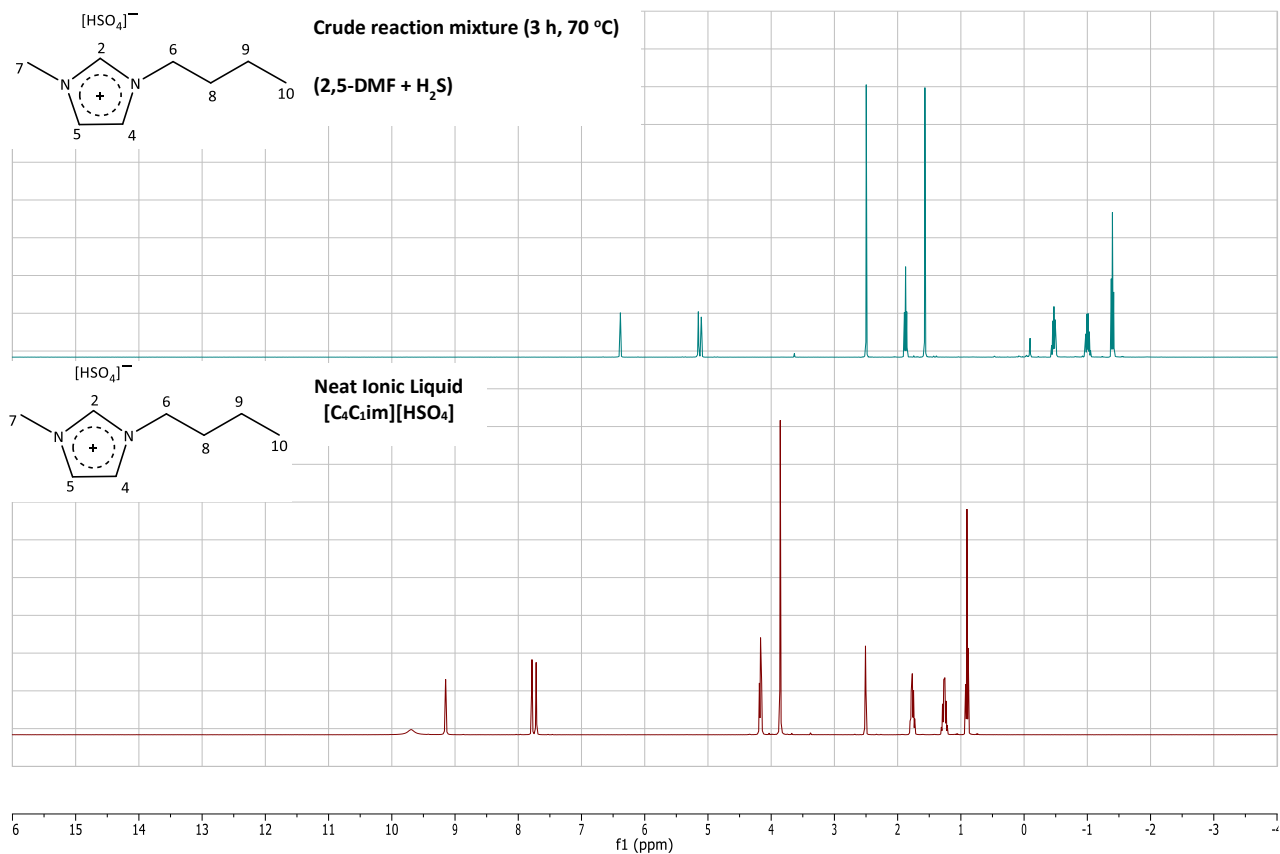


**Figure 2.44:** Reaction of 2,5-DMF + H<sub>2</sub>S in [C<sub>4</sub>C<sub>1</sub>im][HSO<sub>4</sub>]; <sup>1</sup>H NMR spectrum of the neat IL and the crude reaction mixture

**Table 2.8:** Chemical shift changes in [C<sub>4</sub>C<sub>1</sub>im][HSO<sub>4</sub>] upon reaction between 2,5-DMF and H<sub>2</sub>S (70 °C, 3h).

NMR Spectral Assignment (400 MHz, DMSO-d <sup>6</sup> )	Post-reaction	Neat
	[C <sub>4</sub> C <sub>1</sub> im][HSO <sub>4</sub> ] Crude reaction mixture	[C <sub>4</sub> C <sub>1</sub> im][HSO <sub>4</sub> ]
(1H, s, br, HSO <sub>4</sub> <sup>-</sup> )	NA	9.69
(1H, s, N <sub>2</sub> CH)	8.68	9.15
(2H, m, 2NCH)	7.45, 7.41	7.78, 7.72
Unknown	5.93	/
(2H, t, <sup>3</sup> J <sub>HH</sub> =7.2 Hz, NCH <sub>2</sub> CH <sub>2</sub> CH <sub>2</sub> CH <sub>3</sub> )	4.19, 4.17, 4.16	4.19, 4.17, 4.15
(3H, s, NCH <sub>3</sub> )	3.87	3.86
DMSO	2.21	2.5 (q) solvent
(2H, quintet, <sup>3</sup> J <sub>HH</sub> = 7.2 Hz, NCH <sub>2</sub> CH <sub>2</sub> CH <sub>2</sub> CH <sub>3</sub> )	1.83	1.76
(2H, sextet, <sup>3</sup> J <sub>HH</sub> = 7.6 Hz, NCH <sub>2</sub> CH <sub>2</sub> CH <sub>2</sub> CH <sub>3</sub> )	1.31	1.29
(3H, t, <sup>3</sup> J <sub>HH</sub> = 7.2 Hz, NCH <sub>2</sub> CH <sub>2</sub> CH <sub>2</sub> CH <sub>3</sub> ).	0.50	0.90

## 2.5 References

- 1 C. Chiappe and S. Rajamani, *European J. Org. Chem.*, 2011, 5517–5539.
- 2 A. S. Amarasekara, *Chem. Rev.*, 2016, **116**, 6133–6183.
- 3 J. Estager, J. D. Holbrey and M. Swadźba-Kwaśny, *Chem. Soc. Rev.*, 2014, **43**, 847–886.
- 4 A. R. Hajipour and F. Rafiee, *Org. Prep. Proced. Int.*, 2010, **42**, 285–362.
- 5 J. M. S. S. Esperança, J. N. Canongia Lopes, M. Tariq, L. M. N. B. F. Santos, J. W. Magee and L. P. N. Rebelo, *J. Chem. Eng. Data*, 2010, **55**, 3–12.
- 6 T. L. Greaves and C. J. Drummond, *Chem. Rev.*, 2008, **108**, 206–237.
- 7 S. Liu, C. Chen, F. Yu, L. Li, Z. Liu, S. Yu, C. Xie and F. Liu, *Fuel*, 2015, **159**, 803–809.
- 8 T. Welton, *Chem. Rev.*, 1999, **99**, 2071–2084.
- 9 J. P. Hallett and T. Welton, *Chem. Rev.*, 2011, **111**, 3508–3576.
- 10 J. A. Boon, J. A. Levisky, J. L. Pflug and J. S. Wilkes, *J. Org. Chem.*, 1986, **51**, 480–483.
- 11 R. Zhang, X. Meng, Z. Liu, J. Meng and C. Xu, *Ind. Eng. Chem. Res.*, 2008, **47**, 8205–8210.
- 12 J. Zhang, C. Huang, B. Chen, P. Ren and Z. Lei, *Energy and Fuels*, 2007, **21**, 1724–1730.
- 13 X. Chen, D. Song, C. Asumana and G. Yu, *J. Mol. Catal. A Chem.*, 2012, **359**, 8–13.
- 14 A. P. Abbott, C. A. Eardley, N. R. S. Farley, G. A. Griffith and A. Pratt, *J. Appl. Electrochem.*, 2001, **31**, 1345–1350.
- 15 J. Robinson and R. a Osteryoung, *J. Am. Chem. Soc.*, 1979, **101**, 323–327.
- 16 J. S. Wilkes, J. A. Levisky, R. A. Wilson and C. L. Hussey, *Inorg. Chem.*, 1982, **21**, 1263–1264.
- 17 J. Cui, J. de With, P. A. A. Klusener, X. Su, X. Meng, R. Zhang, Z. Liu, C. Xu and H. Liu, *J. Catal.*, 2014, **320**, 26–32.
- 18 A. P. Abbott, G. Capper, D. L. Davies, H. L. Munro, R. K. Rasheed and V. Tambyrajah, *Chem. Commun.*, 2001, 2010–2011.
- 19 V. Lecocq, A. Graille, C. C. Santini, A. Baudouin, Y. Chauvin, J. M. Basset, L. Arzel, D. Bouchu and B. Fenet, *New J. Chem.*, 2005, **29**, 700–706.
- 20 A. P. Abbott, G. Capper, D. L. Davies, R. K. Rasheed and V. Tambyrajah, *Green Chem.*, 2002, **4**, 24–26.
- 21 S.-I. Hsiu, J.-F. Huang, I.-W. Sun, C.-H. Yuan and J. Shiea, *Electrochim. Acta*, 2002, **47**, 4367–4372.
- 22 M. S. Sitze, E. R. Schreiter, E. V. Patterson and R. G. Freeman, *Inorg. Chem.*, 2001, **40**, 2298–2304.
- 23 Z.-L. Xie and A. Taubert, *ChemPhysChem*, 2011, **12**, 364–368.
- 24 M. M. Cruz, R. P. Borges, M. Godinho, C. S. Marques, E. Langa, A. P. C. Ribeiro, M. J. V. Lourenço, F. J. V. Santos, C. A. Nieto de Castro, M. Macatrão, M. Tariq, J. M. S. S. Esperança, J. N. Canongia Lopes, C. A. M. Afonso and L. P. N. Rebelo, *Fluid Phase Equilib.*, 2013, **350**, 43–50.
- 25 V. Misuk, D. Breuch and H. Löwe, *Chem. Eng. J.*, 2011, **173**, 536–540.
- 26 E. Santos, J. Albo, A. Rosatella, C. A. M. Afonso and Á. Irabien, *J. Chem. Technol. Biotechnol.*, 2014, **89**, 866–871.
- 27 Y.-L. Yang and Y. Kou, *Chem. Commun.*, 2004, 226.
- 28 F. H. Hurley and T. P. Wler, *J. Electrochem. Soc.*, 1951, **98**, 203–206.
- 29 C. Hardacre, R. W. Murphy, K. R. Seddon, G. Srinivasan and M. Swadźba-Kwaśny, *Aust. J. Chem.*, 2010, **63**, 845–848.

- 30 D. C. Apperley, C. Hardacre, P. Licence, R. W. Murphy, N. V Plechkova, K. R. Seddon, G. Srinivasan, M. Swadźba-Kwaśny and I. J. Villar-Garcia, *Dalt. Trans.*, 2010, **39**, 8679–8687.
- 31 A. W. Taylor, S. Men, C. J. Clarke and P. Licence, *RSC Adv.*, 2013, **3**, 9436–9445.
- 32 A. A. Fannin, L. A. King, J. A. Levisky and J. S. Wilkes, *J. Phys. Chem.*, 1984, **88**, 2609–2614.
- 33 M. B. Alves, V. O. Santos jr., V. C. D. Soares, P. A. Z. Suarez and J. C. Rubim, *J. Raman Spectrosc.*, 2008, **39**, 1388–1395.
- 34 S.-I. Hsiu, J.-F. Huang, I.-W. Sun, C.-H. Yuan and J. Shiea, *Electrochim. Acta*, 2002, **47**, 4367–4372.
- 35 A. W. Taylor, F. Qiu, I. J. Villar-Garcia and P. Licence, *Chem. Commun.*, 2009, 5817–5819.
- 36 J. Estager, A. A. Oliferenko, K. R. Seddon and M. Swadźba-Kwaśny, *Dalt. Trans.*, 2010, **39**, 11375.
- 37 H. Q. N. Gunaratne, T. J. Lotz and K. R. Seddon, *New J. Chem.*, 2010, **34**, 1821–1824.
- 38 M. J. Earle, U. Hakala, C. Hardacre, J. Karkkainen, B. J. McAuley, D. W. Rooney, K. R. Seddon, J. M. Thompson and K. Wähälä, *Chem. Commun.*, 2005, 903–905.
- 39 T. A. Zawodzinski and R. A. Osteryoung, *Inorg. Chem.*, 1989, **28**, 1710–1715.
- 40 P. Wasserscheid and W. Keim, *Angew. Chemie*, 2000, **39**, 3772–3789.
- 41 R. Lungwitz and S. Spange, *New J. Chem.*, 2008, **32**, 392–394.
- 42 R. Lungwitz and S. Spange, *ChemPhysChem*, 2012, **13**, 1910–1916.
- 43 M. Currie, J. Estager, P. Licence, S. Men, P. Nockemann, K. R. Seddon, M. Swadźba-Kwaśny and C. Terrade, *Inorg. Chem.*, 2013, **52**, 1710–1721.
- 44 P. B. Hitchcock, K. R. Seddon and T. Welton, *J. Chem. Soc. Dalt. Trans.*, 1993, 2639–2643.
- 45 W. Wu, Y. Lu, H. Ding, C. Peng and H. Liu, *Phys. Chem. Chem. Phys.*, 2015, **17**, 1339–1346.
- 46 D. Yin, C. Li, L. Tao, N. Yu, S. Hu and D. Yin, *J. Mol. Catal. A Chem.*, 2006, **245**, 260–265.
- 47 Y. Yang and Y. Kou, *Chem. Commun.*, 2004, 226.
- 48 V. Gutmann, *Electrochim. Acta*, 1976, **21**, 661–670.
- 49 D. R. MacFarlane, M. Forsyth, E. I. Izgorodina, A. P. Abbott, G. Annat and K. Fraser, *Phys. Chem. Chem. Phys.*, 2009, **11**, 4962.
- 50 M. Yoshizawa, W. Xu and C. A. Angell, *J. Am. Chem. Soc.*, 2003, **125**, 15411–15419.
- 51 D. N. Moreira, N. Fresno, R. Pérez-Fernández, C. P. Frizzo, P. Goya, C. Marco, M. A. P. Martins and J. Elguero, *Tetrahedron*, 2015, **71**, 676–685.
- 52 M. S. Miran, T. Yasuda, M. A. B. H. Susan, K. Dokko and M. Watanabe, *J. Phys. Chem. C*, 2014, **118**, 27631–27639.
- 53 V. SINGH, S. KAUR, V. SAPEHIYIA, J. SINGH and G. KAD, *Catal. Commun.*, 2005, **6**, 57–60.
- 54 J. Gui, X. Cong, D. Liu, X. Zhang, Z. Hu and Z. Sun, *Catal. Commun.*, 2004, **5**, 473–477.
- 55 R. Kore and R. Srivastava, *J. Mol. Catal. A Chem.*, 2013, **376**, 90–97.
- 56 Y. Li, S. Hu, J. Cheng and W. Lou, *Chinese J. Catal.*, 2014, **35**, 396–406.
- 57 J. H. Clark, T. J. Farmer, D. J. Macquarrie and J. Sherwood, *Sustain. Chem. Process.*, 2013, **1**, 23.
- 58 B. Wang, Y. Shen, J. Sun, F. Xu and R. Sun, *RSC Adv.*, 2014, **4**, 18917.
- 59 L. Shen, H. Yin, A. Wang, X. Lu, C. Zhang, F. Chen, Y. Wang and H. Chen, *J. Ind. Eng. Chem.*, 2014, **20**, 759–766.
- 60 L. Lasmane, E. Ausekle, G. Vaivars and A. Priksane, *IOP Conf. Ser. Mater. Sci. Eng.*, 2013, **49**, 12039.



- 61 A. Kilicarslan and M. N. Saridede, *JOM*, 2015, **67**, 2739–2746.
- 62 A. M. da Costa Lopes and R. Bogel-Lukasik, *ChemSusChem*, 2015, **8**, 947–965.
- 63 J. Mao, A. Osorio-Madrado and M.-P. Laborie, *Cellulose*, 2013, **20**, 1829–1840.
- 64 A. S. Amarasekara and P. Shanbhag, *BioEnergy Res.*, 2013, **6**, 719–724.
- 65 S. Lima, P. Neves, M. M. Antunes, M. Pillinger, N. Ignatyev and A. A. Valente, *Appl. Catal. A Gen.*, 2009, **363**, 93–99.
- 66 J. Li, J. Li, D. Zhang and C. Liu, *J. Phys. Chem. B*, 2015, **119**, 13398–13406.
- 67 C. Thomazeau, H. Olivier-Bourbigou, L. Magna, S. Luts and B. Gilbert, *J. Am. Chem. Soc.*, 2003, **125**, 5264–5265.
- 68 T. Robert, L. Magna, H. Olivier-Bourbigou and B. Gilbert, *J. Electrochem. Soc.*, 2009, **156**, F115.
- 69 B. J. Cox, S. Jia, Z. C. Zhang and J. G. Ekerdt, *Polym. Degrad. Stab.*, 2011, **96**, 426–431.
- 70 G. Wang, Z. Zhang and L. Song, *Green Chem.*, 2014, **16**, 1436–1443.
- 71 P. Lu, Z.-P. Zhao, X.-Y. Wang, G.-J. Lan and X.-L. Wang, *Mol. Catal.*, 2017, **435**, 24–32.
- 72 J. Gr̆svik, J. P. Hallett, T. Q. To and T. Welton, *Chem. Commun.*, 2014, **50**, 7258.
- 73 L. I. Belen'kii, I. A. Suslov and N. D. Chuvylkin, *Chem. Heterocycl. Compd.*, 2003, **39**, 36–48.
- 74 F. C. Meotti, D. O. Silva, A. R. . dos Santos, G. Zeni, J. B. T. Rocha and C. W. Nogueira, *Environ. Toxicol. Pharmacol.*, 2003, **15**, 37–44.
- 75 P. Caboni, G. Sarais, N. Aissani, G. Tocco, N. Sasanelli, B. Liori, A. Carta and A. Angioni, *J. Agric. Food Chem.*, 2012, **60**, 7345–7351.
- 76 S. Gronowitz, Ed., *Chemistry of Heterocyclic Compounds*, John Wiley & Sons, Inc., Hoboken, NJ, USA, 1985, vol. 44.
- 77 G. Barbarella, M. Melucci and G. Sotgiu, *Adv. Mater.*, 2005, **17**, 1581–1593.
- 78 M. Teiber and T. J. J. M̆ller, *Chem. Commun.*, 2012, **48**, 2080.
- 79 S. Abbat, D. Dhaked, M. Arfeen and P. V. Bharatam, *RSC Adv.*, 2015, **5**, 88353–88366.
- 80 E. Campaigne and W. O. Foye, *J. Org. Chem.*, 1952, **17**, 1405–1412.
- 81 J. J. Li, in *Name Reactions*, Springer Berlin Heidelberg, Berlin, Heidelberg, pp. 230–232.
- 82 P. Bezboruah, P. Gogoi, J. Gogoi and R. Boruah, *Synthesis (Stuttg.)*, 2013, **45**, 1341–1348.
- 83 J. J. Li, in *Name Reactions: A Collection of Detailed Mechanisms and Synthetic Applications*, Springer Berlin Heidelberg, Berlin, Heidelberg, 2009, pp. 254–256.
- 84 A. El-Mekabaty, *Synth. Commun.*, 2014, **44**, 1–31.
- 85 M. Sridhar, R. M. Rao, N. H. K. Baba and R. M. Kumbhare, *Tetrahedron Lett.*, 2007, **48**, 3171–3172.
- 86 H. Wynberg and H. J. Kooreman, *J. Am. Chem. Soc.*, 1965, **87**, 1739–1742.
- 87 T. I. Gubina and V. G. Kharchenko, *Chem. Heterocycl. Compd.*, 1995, **31**, 900–916.
- 88 Q. Li, Y. Xu, C. Liu and J. Kim, *Catal. Letters*, 2008, **122**, 354–358.
- 89 A. V. Mashkina, *Russ. J. Appl. Chem.*, 2011, **84**, 1223–1228.
- 90 A. V. Mashkina and L. N. Khairulina, *Kinet. Catal.*, 2008, **49**, 245–252.
- 91 A. V. Mashkina, *Chem. Heterocycl. Compd.*, 2010, **46**, 1063–1067.
- 92 H. Song-Qing, Y. Jian-Ye, S. Xin, G. Ai-Ling and H. Jian-Chun, *Brazilian J. Chem. Eng.*, 2011, **28**, 95–99.

- 93 V. G. Kharchenko, T. I. Gubina, S. P. Voronin and I. A. Markushina, *Chem. Heterocycl. Compd.*, 1986, **22**, 1170–1173.
- 94 T. I. Gubina, V. I. Labunskaya, A. N. Pankratov, S. A. Trushin and V. G. Kharchenko, *Chem. Heterocycl. Compd.*, 1993, **29**, 1393–1398.
- 95 S. P. Voronin, T. I. Gubina, I. A. Markushina and V. G. Kharchenko, *Chem. Heterocycl. Compd.*, 1989, **25**, 1113–1117.
- 96 S. P. Voronin, T. I. Gubina, S. A. Trushin, I. A. Markushina and V. G. Kharchenko, *Chem. Heterocycl. Compd.*, 1989, **25**, 1216–1220.
- 97 T. I. Gubina, V. I. Labunskaya, A. N. Pankratov, S. P. Voronin and V. G. Kharchenko, *Chem. Heterocycl. Compd.*, 1997, **33**, 898–902.
- 98 N. Nikbin, S. Caratzoulas and D. G. Vlachos, *ChemSusChem*, 2013, **6**, 2066–2068.
- 99 J. . Yadav, B. V. . Reddy, B. Eeshwaraiah and M. K. Gupta, *Tetrahedron Lett.*, 2004, **45**, 5873–5876.
- 100 V. R. Kaki, R. R. Akkinepalli, P. K. Deb and M. R. Pichika, *Synth. Commun.*, 2015, **45**, 119–126.
- 101 Z. Song, H. Wang and L. Xing, *J. Solution Chem.*, 2009, **38**, 1139–1154.
- 102 A. K. L. Yuen, A. F. Masters and T. Maschmeyer, *Catal. Today*, 2013, **200**, 9–16.
- 103 S. Himmler, A. König and P. Wasserscheid, *Green Chem.*, 2007, **9**, 935.
- 104 A. Brandt, J. Gräsvik, J. P. Hallett and T. Welton, *Green Chem.*, 2013, **15**, 550–583.
- 105 H. Zhao, J. E. Holladay, H. Brown and Z. C. Zhang, *Science (80-. )*, 2007, **316**, 1597–1600.
- 106 S. Eminov, J. D. E. T. Wilton-Ely and J. P. Hallett, *ACS Sustain. Chem. Eng.*, 2014, **2**, 978–981.
- 107 K. R. Seddon, A. Stark and M. J. Torres, *Pure Appl. Chem.*, 2000, **72**, 2275–2287.
- 108 J. Estager, P. Nockemann, K. R. Seddon, M. Swadźba-Kwaśny and S. Tyrrell, *Inorg. Chem.*, 2011, **50**, 5258–5271.
- 109 P. Keil, M. Kick and A. König, *Chemie Ing. Tech.*, 2012, **84**, 859–866.
- 110 H. L. Ngo, K. LeCompte, L. Hargens and A. B. McEwen, *Thermochim. Acta*, 2000, **357–358**, 97–102.
- 111 R. E. Del Sesto, T. M. McCleskey, C. Macomber, K. C. Ott, A. T. Koppisch, G. A. Baker and A. K. Burrell, *Thermochim. Acta*, 2009, **491**, 118–120.
- 112 Y. Cao and T. Mu, *Ind. Eng. Chem. Res.*, 2014, **53**, 8651–8664.
- 113 M. Götz, R. Reimert, S. Bajohr, H. Schnetzer, J. Wimberg and T. J. S. Schubert, *Thermochim. Acta*, 2015, **600**, 82–88.
- 114 H. Liu, E. Maginn, A. E. Visser, N. J. Bridges and E. B. Fox, *Ind. Eng. Chem. Res.*, 2012, **51**, 7242–7254.
- 115 P. Liu, M. Wang and Z.-M. Cheng, *J. Chem. Eng. Data*, 2015, **60**, 836–844.
- 116 J. G. Huddleston, A. E. Visser, W. M. Reichert, H. D. Willauer, G. a. Broker and R. D. Rogers, *Green Chem.*, 2001, **3**, 156–164.
- 117 M. Lorenzo, M. Vilas, P. Verdía, M. Villanueva, J. Salgado and E. Tojo, *RSC Adv.*, 2015, **5**, 41278–41284.
- 118 M. C. Kroon, W. Buijs, C. J. Peters and G.-J. Witkamp, *Thermochim. Acta*, 2007, **465**, 40–47.
- 119 Y. Chen, Y. Cao, Y. Shi, Z. Xue and T. Mu, *Ind. Eng. Chem. Res.*, 2012, **51**, 7418–7427.
- 120 H. Ohtani, S. Ishimura and M. Kumai, *Anal. Sci.*, 2008, **24**, 1335–1340.
- 121 C. Maton, N. De Vos and C. V Stevens, *Chem. Soc. Rev.*, 2013, **42**, 5963–5977.

- 122 A. S. Amarasekara and O. S. Owereh, *J. Therm. Anal. Calorim.*, 2011, **103**, 1027–1030.
- 123 P. S. Campbell, C. C. Santini, D. Bouchu, B. Fenet, L. Rycerz, Y. Chauvin, M. Gaune-Escard, C. Bessada and A. Rollet, *Dalt. Trans.*, 2010, **39**, 1379–1388.
- 124 A. A. Fannin, D. A. Floreani, L. A. King, J. S. Landers, B. J. Piersma, D. J. Stech, R. L. Vaughn, J. S. Wilkes and J. L. Williams, *J. Phys. Chem.*, 1984, **88**, 2614–2621.
- 125 Y. Yoshida and G. Saito, *J. Mater. Chem.*, 2006, **16**, 1254.
- 126 M. Villanueva, A. Coronas, J. García and J. Salgado, *Ind. Eng. Chem. Res.*, 2013, **52**, 15718–15727.
- 127 H. Weingärtner, *Angew. Chemie Int. Ed.*, 2008, **47**, 654–670.
- 128 S. Tsuzuki, W. Shinoda, M. S. Miran, H. Kinoshita, T. Yasuda and M. Watanabe, *J. Chem. Phys.*, 2013, **139**, 174504.
- 129 P. a. Hunt, B. Kirchner and T. Welton, *Chem. - A Eur. J.*, 2006, **12**, 6762–6775.
- 130 J. Dupont, *J. Braz. Chem. Soc.*, 2004, **15**, 341–350.
- 131 S. Chen, S. Zhang, X. Liu, J. Wang, J. Wang, K. Dong, J. Sun and B. Xu, *Phys. Chem. Chem. Phys.*, 2014, **16**, 5893–5906.
- 132 R. Hayes, G. G. Warr and R. Atkin, *Chem. Rev.*, 2015, **115**, 6357–6426.
- 133 R. P. Matthews, T. Welton and P. A. Hunt, *Phys. Chem. Chem. Phys.*, 2014, **16**, 3238.
- 134 S. Saha, S. Hayashi, A. Kobayashi and H. Hamaguchi, *Chem. Lett.*, 2003, **32**, 740–741.
- 135 E. I. Izgorodina and D. R. MacFarlane, *J. Phys. Chem. B*, 2011, **115**, 14659–14667.
- 136 P. A. Hunt, C. R. Ashworth and R. P. Matthews, *Chem. Soc. Rev.*, 2015, **44**, 1257–1288.
- 137 I. Skarmoutsos, D. Dellis, R. P. Matthews, T. Welton and P. A. Hunt, *J. Phys. Chem. B*, 2012, **116**, 4921–4933.
- 138 B. a. Marekha, O. N. Kalugin and A. Idrissi, *Phys. Chem. Chem. Phys.*, 2015, **17**, 16846–16857.
- 139 T. Cremer, C. Kolbeck, K. R. J. Lovelock, N. Paape, R. Wölfel, P. S. Schulz, P. Wasserscheid, H. Weber, J. Thar, B. Kirchner, F. Maier and H.-P. Steinrück, *Chem. - A Eur. J.*, 2010, **16**, 9018–9033.
- 140 A. Elaiwi, P. B. Hitchcock, K. R. Seddon, N. Srinivasan, Y.-M. Tan, T. Welton and J. A. Zora, *J. Chem. Soc. Dalt. Trans.*, 1995, 3467–3472.
- 141 A. Aggarwal, N. L. Lancaster, A. R. Sethi and T. Welton, *Green Chem.*, 2002, **4**, 517–520.
- 142 M. Galiński, A. Lewandowski and I. Stępnia, *Electrochim. Acta*, 2006, **51**, 5567–5580.
- 143 J. S. Wilkes, J. A. Levisky, J. L. Pflug, C. L. Hussey and T. B. Scheffler, *Anal. Chem.*, 1982, **54**, 2378–2379.
- 144 J. S. Wilkes, J. S. Frye and G. F. Reynolds, *Inorg. Chem.*, 1983, **22**, 3870–3872.
- 145 B. a Marekha, O. N. Kalugin, M. Bria and A. Idrissi, *Phys. Chem. Chem. Phys.*, 2015, **17**, 23183–23194.
- 146 A. G. Avent, P. a. Chaloner, M. P. Day, K. R. Seddon and T. Welton, *J. Chem. Soc. Dalt. Trans.*, 1994, 3405–3413.
- 147 P. Bonhôte, A.-P. Dias, N. Papageorgiou, K. Kalyanasundaram and M. Grätzel, *Inorg. Chem.*, 1996, **35**, 1168–1178.
- 148 L. Crowhurst, P. R. Mawdsley, J. M. Perez-Arlandis, P. A. Salter and T. Welton, *Phys. Chem. Chem. Phys.*, 2003, **5**, 2790–2794.
- 149 H. Niedermeyer, C. Ashworth, A. Brandt, T. Welton and P. a Hunt, *Phys. Chem. Chem. Phys.*, 2013, **15**, 11566–11578.

- 150 T. Steiner, *Angew. Chemie Int. Ed.*, 2002, **41**, 48–76.
- 151 T. Singh and A. Kumar, *J. Phys. Chem. B*, 2007, **111**, 7843–7851.
- 152 T. Takamuku, H. Hoke, A. Idrissi, B. a Marekha, M. Moreau, Y. Honda, T. Umecky and T. Shimomura, *Phys. Chem. Chem. Phys.*, 2014, **16**, 23627–23638.
- 153 A. Stark, A. W. Zidell, J. W. Russo and M. M. Hoffmann, *J. Chem. Eng. Data*, 2012, **57**, 3330–3339.
- 154 V. Kamavaram and R. G. Reddy, *Int. J. Therm. Sci.*, 2008, **47**, 773–777.
- 155 D. H. Zaitsau, Y. U. Paulechka and G. J. Kabo, *J. Phys. Chem. A*, 2006, **110**, 11602–11604.
- 156 D. M. Fox, J. W. Gilman, H. C. De Long and P. C. Trulove, *J. Chem. Thermodyn.*, 2005, **37**, 900–905.
- 157 Y. Hao, J. Peng, S. Hu, J. Li and M. Zhai, *Thermochim. Acta*, 2010, **501**, 78–83.
- 158 M. T. Clough, K. Geyer, P. a Hunt, J. Mertes and T. Welton, *Phys. Chem. Chem. Phys.*, 2013, **15**, 20480–95.
- 159 I. H. J. Arellano, J. G. Guarino, F. U. Paredes and S. D. Arco, *J. Therm. Anal. Calorim.*, 2011, **103**, 725–730.
- 160 A. Brandt, J. Gräsvik, J. P. Hallett and T. Welton, *Green Chem.*, 2013, **15**, 550.
- 161 J. Salgado, M. Villanueva, J. J. Parajó and J. Fernández, *J. Chem. Thermodyn.*, 2013, **65**, 184–190.
- 162 T. J. Wooster, K. M. Johanson, K. J. Fraser, D. R. MacFarlane and J. L. Scott, *Green Chem.*, 2006, **8**, 691.
- 163 K. J. Baranyai, G. B. Deacon, D. R. MacFarlane, J. M. Pringle and J. L. Scott, *Aust. J. Chem.*, 2004, **57**, 145–147.
- 164 P. Y. Nikolov and V. A. Yaylayan, *J. Agric. Food Chem.*, 2011, **59**, 10104–10113.
- 165 M. N. Hughes, M. N. Centelles and K. P. Moore, *Free Radic. Biol. Med.*, 2009, **47**, 1346–1353.
- 166 F.-Y. Jou and A. E. Mather, *Int. J. Thermophys.*, 2007, **28**, 490–495.
- 167 C. S. Pomelli, C. Chiappe, A. Vidis, G. Laurenczy and P. J. Dyson, *J. Phys. Chem. B*, 2007, **111**, 13014–13019.
- 168 R. Singh, *Mol. Simul.*, 2017, **43**, 291–297.
- 169 A. Corma and H. García, *Chem. Rev.*, 2003, **103**, 4307–4366.
- 170 Y. Román-Leshkov and M. E. Davis, *ACS Catal.*, 2011, **1**, 1566–1580.
- 171 I. J. Villar-Garcia, S. Fearn, G. F. De Gregorio, N. L. Ismail, F. J. V. Gschwend, A. J. S. McIntosh and K. R. J. Lovelock, *Chem. Sci.*, 2014, **5**, 4404–4418.
- 172 I. J. Villar-Garcia, S. Fearn, N. L. Ismail, A. J. S. McIntosh and K. R. J. Lovelock, *Chem. Commun.*, 2015, **51**, 5367–5370.
- 173 H.-P. Steinrück, *Phys. Chem. Chem. Phys.*, 2012, **14**, 5010.
- 174 A. Kauling, G. Ebeling, J. Morais, A. Pádua, T. Grehl, H. H. Brongersma and J. Dupont, *Langmuir*, 2013, **29**, 14301–14306.
- 175 C. R. Waidmann, A. W. Pierpont, E. R. Batista, J. C. Gordon, R. L. Martin, L. A. ‘Pete’ Silks, R. M. West and R. Wu, *Catal. Sci. Technol.*, 2013, **3**, 106–115.
- 176 K. S. Lovejoy, C. A. Corley, E. K. Cope, M. C. Valentine, J. G. Leid, G. M. Purdy, J. S. Wilkes, A. T. Koppisch and R. E. Del Sesto, *Cryst. Growth Des.*, 2012, **12**, 5357–5364.
- 177 J. C. Mareque-Rivas, R. Prabaharan and R. T. Martín de Rosales, *Chem. Commun.*, 2004, 76–77.
- 178 P. A. Hunt, *J. Phys. Chem. B*, 2007, **111**, 4844–4853.

- 179 J. Fraga-Dubreuil, K. Bourahla, M. Rahmouni, J. P. Bazureau and J. Hamelin, *Catal. Commun.*, 2002, **3**, 185–190.
- 180 P. T. M. Do, J. R. McAtee, D. A. Watson and R. F. Lobo, *ACS Catal.*, 2013, **3**, 41–46.
- 181 J. P. Guthrie and J. Guo, *J. Am. Chem. Soc.*, 1996, **118**, 11472–11487.
- 182 S. Song, G. Wu, W. Dai, N. Guan and L. Li, *J. Mol. Catal. A Chem.*, 2016, **420**, 134–141.

## 2.6 Appendix

### 2.6.1 Sample mass spectra of $[C_4C_1im]Cl \cdot ZnCl_2$ ( $X_{ZnCl_2} = 0.67$ ) ( $FB^-/FB^+$ )

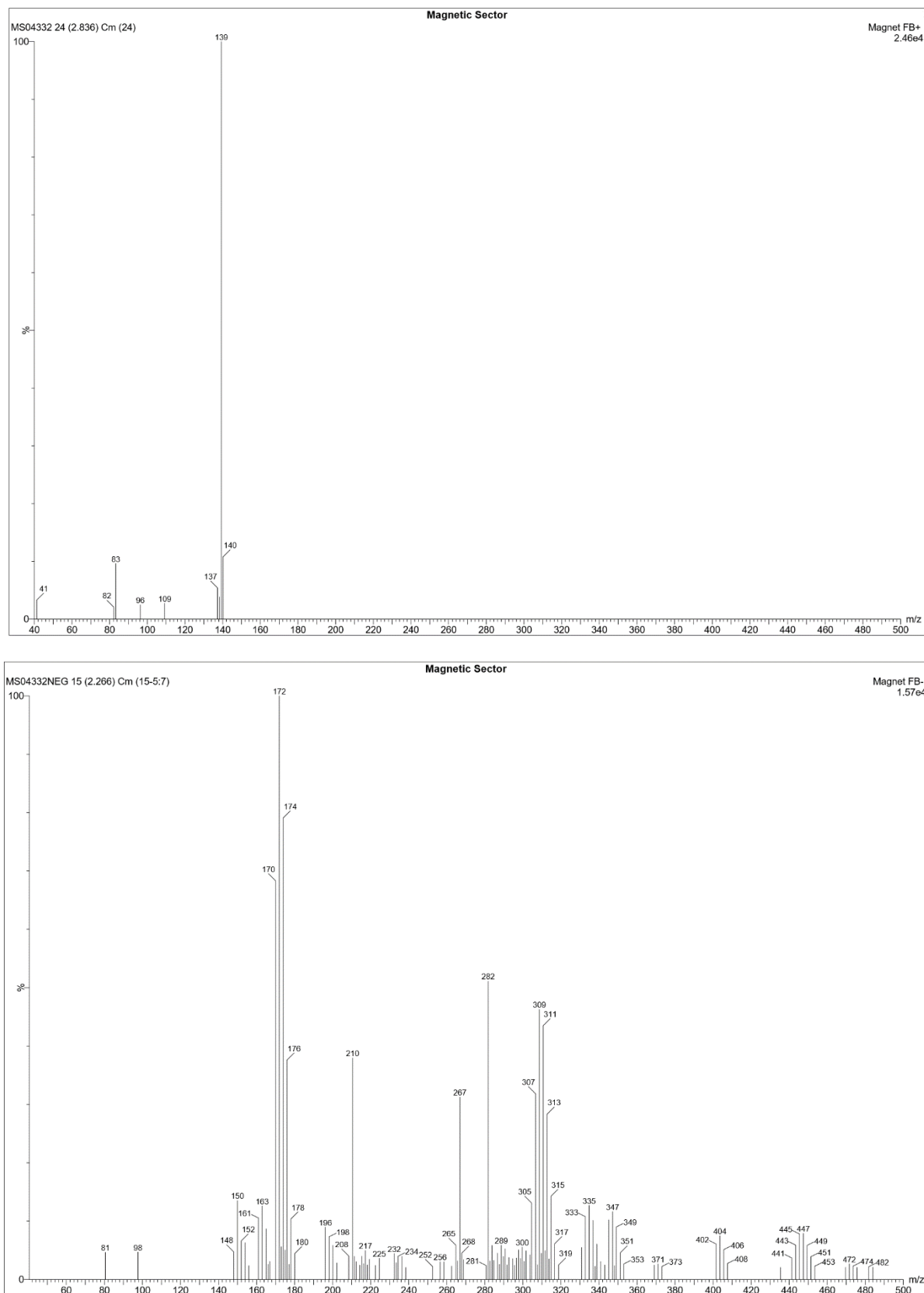
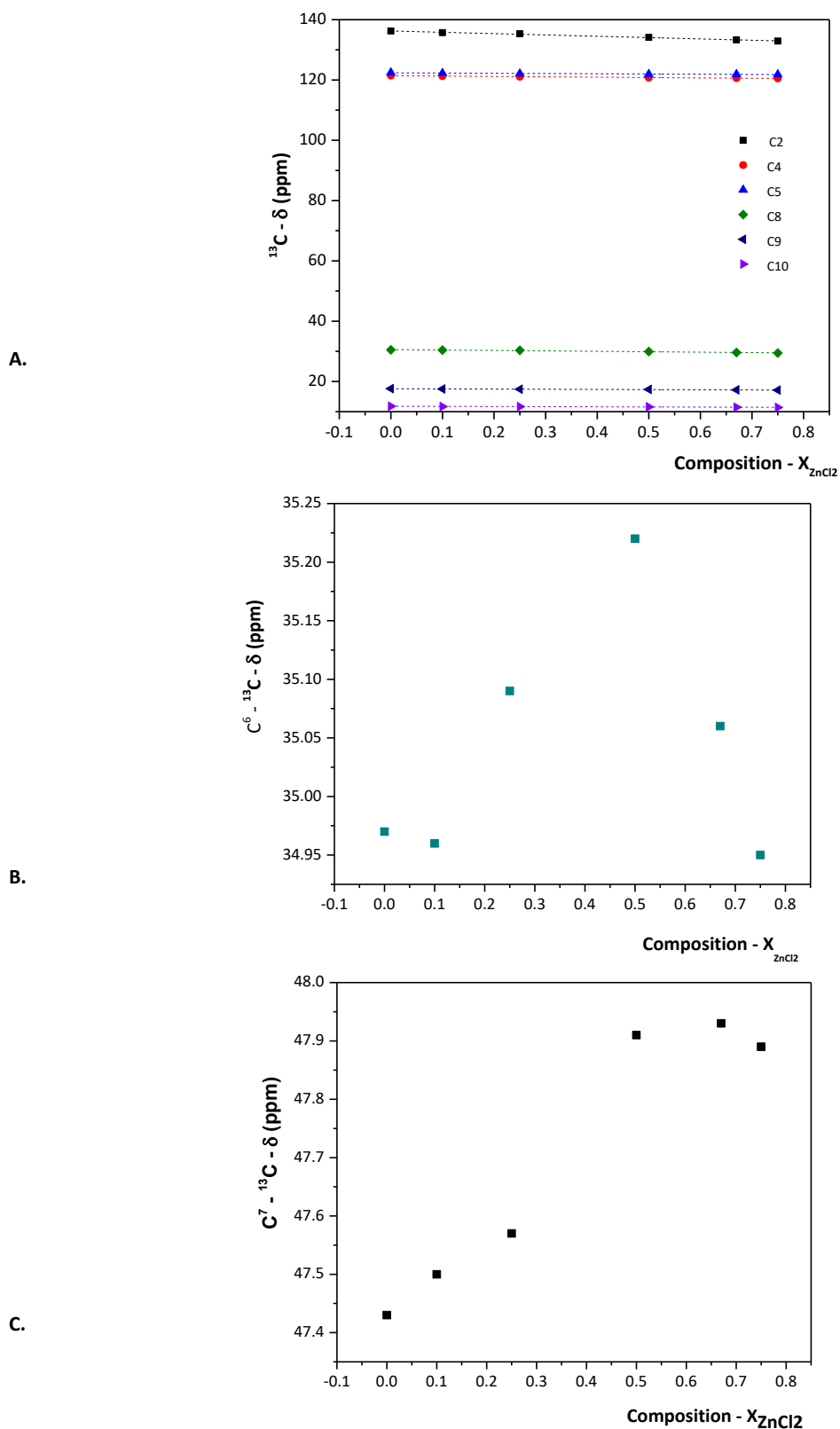


Figure 2.45: Mass spectra of  $[C_4C_1im]Cl \cdot ZnCl_2$  ( $X_{ZnCl_2} = 0.67$ ) in the positive ( $FB^+$ ) and negative ( $FB^-$ ) mode.

2.6.2  $^{13}\text{C}$  chemical shift progression ( $\delta$  / ppm) as a function of  $X_{\text{ZnCl}_2}$ ;  $[\text{C}_4\text{C}_{1\text{im}}]\text{Cl}\cdot\text{ZnCl}_2$ .



**Figure 2.46:** Observed  $^{13}\text{C}$  chemical shift  $\delta$ (ppm) for A)  $\text{C}^2 - \text{C}^5$ ,  $\text{C}^8 - \text{C}^{10}$ , B)  $\text{C}^6$  and C)  $\text{C}^7$  carbons as a function of  $X_{\text{ZnCl}_2}$  in  $[\text{C}_4\text{C}_{1\text{im}}]\text{Cl}\cdot\text{ZnCl}_2$  ( $0.10 < X_{\text{ZnCl}_2} < 0.75$ ).  $^{13}\text{C}$  NMR spectra were recorded neat at  $80^\circ\text{C}$  with a DMSO capillary (500 MHz).

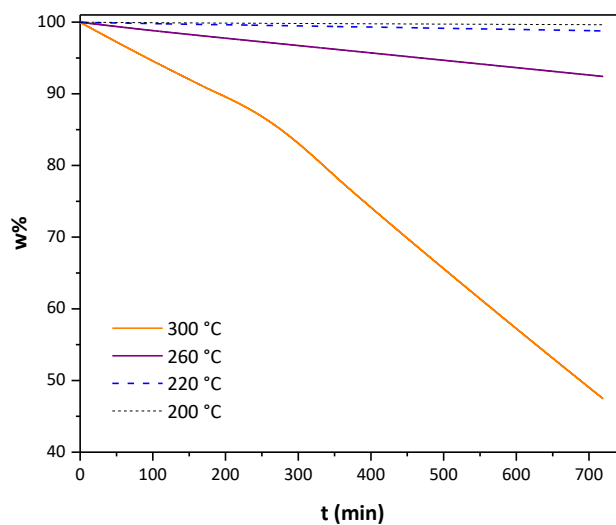
**Table 2.9:** Linear fit coefficients for  $^{13}\text{C}$  NMR  $\delta(\text{ppm})$  as a function of  $X_{\text{ZnCl}_2}$ ;  $[\text{C}_4\text{C}_1\text{im}]\text{Cl}\cdot\text{ZnCl}_2$  ( $0.10 < X_{\text{ZnCl}_2} < 0.75$ )

<b><math>[\text{C}_4\text{C}_1\text{im}]^+</math> proton</b>	<b>Slope</b>	<b>Intercept</b>	<b>Adj. R-square</b>
C2	-4.38	136.25	0.992
C4	-1.21	121.41	0.986
C5	-0.77	122.37	0.910
C8	-1.43	30.58	0.955
C9	-0.58	17.60	0.958
C10	-0.48	11.79	0.962

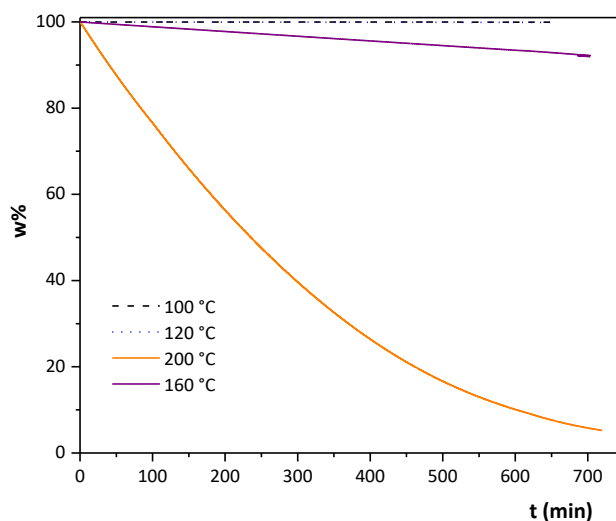


2.6.3 Isothermal TGA scans;  $[C_4C_1im][NTf_2]$ ,  $[C_4C_1im]Cl$  and  $[C_4C_1im]Cl \cdot ZnCl_2$  ( $X_{ZnCl_2} = 0.67$ )

a.



b.



c.

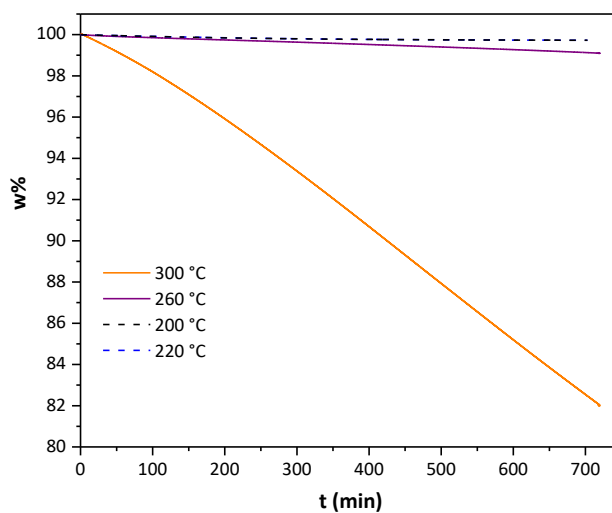
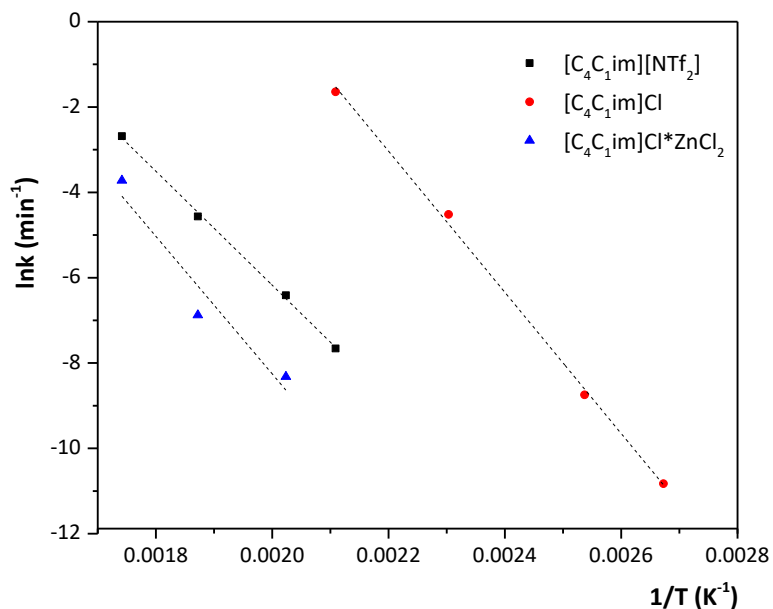


Figure 2.47: Isothermal TGA scans: a)  $[C_4C_1im][NTf_2]$  (200 – 300 °C), b)  $[C_4C_1im]Cl$  (100 – 200 °C), c)  $[C_4C_1im]Cl \cdot ZnCl_2$ ;  $X_{ZnCl_2} = 0.67$  (200 – 300 °C).

**2.6.4 Arrhenius plots ( $\ln(dw/dt) = f(1/T)$ ) for the determination of Arrhenius parameters:  $E_a$  and  $A$ ; thermal decomposition of  $[C_4C_1im][NTf_2]$ ,  $[C_4C_1im]Cl$  and  $[C_4C_1im]Cl \cdot ZnCl_2$  ( $X_{ZnCl_2} = 0.67$ ).**



**Figure 3.48:** Determination of the Arrhenius parameters relating to the thermal decomposition of ionic liquids (a)  $[C_4C_1im][NTf_2]$ ,  $E_a = 111 \text{ kJ mol}^{-1}$ ,  $A = 8.3 \times 10^8$ ; (b)  $[C_4C_1im]Cl$ ,  $E_a = 138 \text{ kJ mol}^{-1}$ ,  $A = 3.1 \times 10^{14}$  and (c)  $[C_4C_1im]Cl \cdot ZnCl_2$  ( $X_{ZnCl_2} = 0.67$ ),  $E_a = 134 \text{ kJ mol}^{-1}$ ,  $A = 2.6 \times 10^{10}$ .

**Table 2.10:** Fitting parameters of the Arrhenius plots ( $\ln(dw/dt) = f(1/T)$ )

Ionic liquid	Equation: $y = a + b \cdot x$		
	a	b	R <sup>2</sup>
$[C_4C_1im][NTf_2]$	33.37	-16545.22	0.99
$[C_4C_1im]Cl \cdot ZnCl_2$ ( $X_{ZnCl_2} = 0.67$ )	23.99	-16123	0.87
$[C_4C_1im]Cl$	20.53	-13354	0.99

### 2.6.5 Exponential decay plots for [C<sub>4</sub>C<sub>1</sub>im][NTf<sub>2</sub>], [C<sub>4</sub>C<sub>1</sub>im]Cl and [C<sub>4</sub>C<sub>1</sub>im]Cl·ZnCl<sub>2</sub> (X<sub>ZnCl<sub>2</sub></sub> = 0.67).

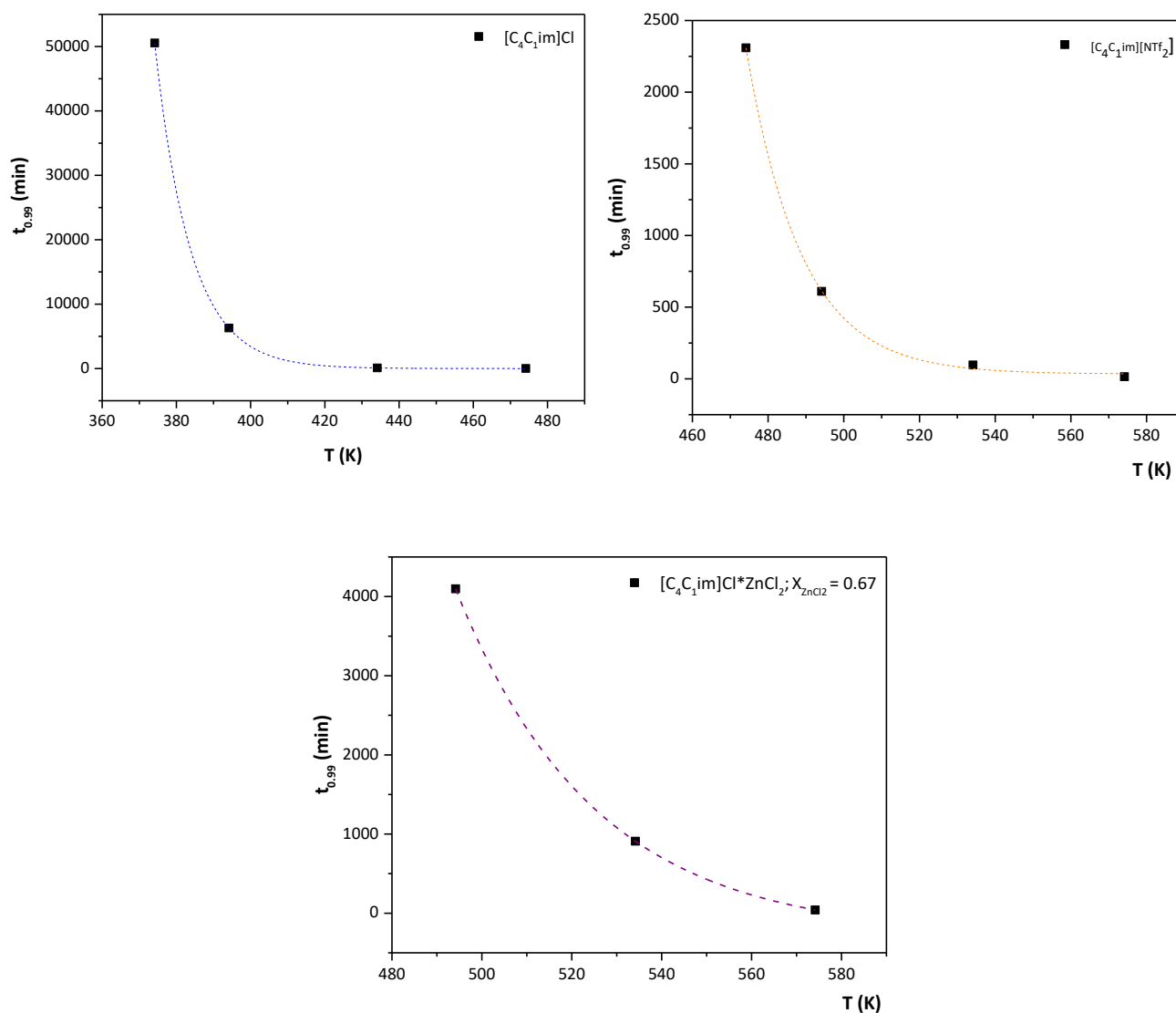


**Figure 2.49:** Determination of  $T_{1\%/10h}$  from the exponential plot of  $t_{0.99}$ , the time taken for 1% mass loss to occur, as a function of temperature.  $T_{1\%/10h}$  was determined as 143 °C for [C<sub>4</sub>C<sub>1</sub>im]Cl, 221 °C for [C<sub>4</sub>C<sub>1</sub>im][NTf<sub>2</sub>] and 270 °C for [C<sub>4</sub>C<sub>1</sub>im]Cl·ZnCl<sub>2</sub> (X<sub>ZnCl<sub>2</sub></sub>=0.67)..

**Table 2.11:** Fitting parameters for exponential decay (1% degradation)

Ionic liquid	Equation: $y = A_1 \cdot \exp(-x/T_1) + y_0$			
	A <sub>1</sub>	y <sub>0</sub>	T <sub>1</sub>	R <sup>2</sup>
[C <sub>4</sub> C <sub>1</sub> im][NTf <sub>2</sub> ]	2.61E <sup>17</sup>	33.390	14.647	0.99
[C <sub>4</sub> C <sub>1</sub> im]Cl·ZnCl <sub>2</sub> (X <sub>ZnCl<sub>2</sub></sub> = 0.67)	4.22E <sup>10</sup>	-283.05	30.731	0.96
[C <sub>4</sub> C <sub>1</sub> im]Cl	4.33E <sup>21</sup>	-0.881	9.596	0.99

## CHAPTER 3

### Lewis acidic Supported Ionic Liquid Phases (SILPs) as catalysts for the synthesis of bio-derived thiophenes in a fluidised bed reactor (FBR)

#### 3.1 Supported Ionic Liquid Phase systems (SILP)

During the last decade, a concept that involves the immobilisation of an ionic liquid onto a highly porous solid support has been developed (supported ionic liquid phase; SILP).<sup>1-3</sup> Ionic liquids provide a great advantage over conventional solvents due to their negligible vapour pressure. Therefore, there is a reduced risk of evaporation and catalyst leaching from the support, even at elevated temperatures. The preparation of SILPs is accomplished by the physisorption or chemisorption of the ionic liquid onto the support, whereas homogeneous catalysts can also be immobilized in the IL phase.<sup>4</sup> Amorphous silica gel, composed of random spheroidal aggregates of SiO<sub>2</sub> particles, is the most common support in SILP applications, providing high surface areas (300 – 1000 m<sup>2</sup> g<sup>-1</sup>).<sup>1,2,4</sup> The surface of silica gel contains polar silanol (Si–OH) groups as well as hydrophobic siloxane (Si–O–Si) bonds. Other inorganic oxides, Al<sub>2</sub>O<sub>3</sub>,<sup>5</sup> TiO<sub>2</sub><sup>6</sup> and ZrO<sub>2</sub>,<sup>6</sup> have also been tested for SILP catalysis but they provide much lower pore volumes and surface areas compared to SiO<sub>2</sub>. Low pore volume and small surface area supports has been linked with poor catalytic performance.<sup>2</sup> Materials with pore diameters larger than 50 nm are considered macroporous while mesoporous solids have pore widths between 2 nm and 50 nm (IUPAC). Microporous materials ( $D_p < 2$  nm) are not often used for SILP applications.

##### 3.1.1 SILP synthetic protocols overview

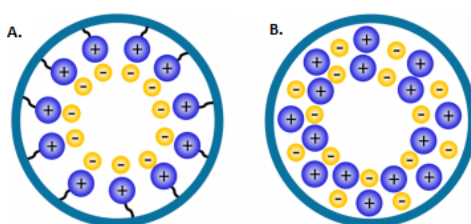


**Figure 3.1:** Schematic representation of the incorporation of ionic liquids into the porous structure of a solid support by: (A) covalent grafting of the ionic liquid on the pore wall and (B) physical confinement of multilayers of the IL into the nanopores.<sup>7</sup>

The thermal or chemical pretreatment of silica is necessary in order to eliminate residual water and the surface –OH groups prior to the physisorption or chemisorption of the ionic liquid.<sup>2,8</sup> The reported calcination protocols involve prolonged treatment under high temperatures but the exact conditions

vary (e.g. 400 °C for 12 h, 500 °C for 3 h or 15 h).<sup>2,8</sup> The elimination of surface –OH groups can be crucial, especially for SILPs containing Lewis acidic ILs, the acidity profile of which can be impacted by the presence of silanols.<sup>6,8,9</sup> Silanol groups may interact with the catalytic species of the IL or the ligands of an added catalyst.<sup>2</sup> The chemical pre-treatment of silica gel has also been tested for chloroaluminate(III)-based SILPs by using an excess of the acidic ionic liquid ([C<sub>2</sub>C<sub>1</sub>im]Cl·AlCl<sub>3</sub>), leading to the dehydroxylation of the inorganic support.<sup>8</sup> There are a few methods that have been explored for the preparation of SILPs such as physisorption or the covalent anchoring of the IL via the anion or the cation (chemisorption) (Figure 3.1).<sup>1,10</sup> However, chemisorption may result in the modification of important bulk properties such as acidity, viscosity and conductivity.<sup>3,7</sup> One of the first examples of a covalently grafted Lewis acidic IL onto silica gel was reported in 2002.<sup>10</sup> The immobilisation of the IL via the anion resulted in the formation of HCl as a by-product with additional effects on the stability of the structured support. An alternative immobilisation pathway, involving the grafting of the cation via one or two Si-O-Si bonds was followed by the addition of the metal chloride so that Lewis acidic anionic species were formed (Figure 3.2). Sol-gel synthesis has also been applied for the immobilization of [(CH<sub>2</sub>)<sub>3</sub>SO<sub>3</sub>H-Him][HSO<sub>4</sub>] using tetraethyl orthosilicate (TEOS) as the silica source.<sup>11</sup>

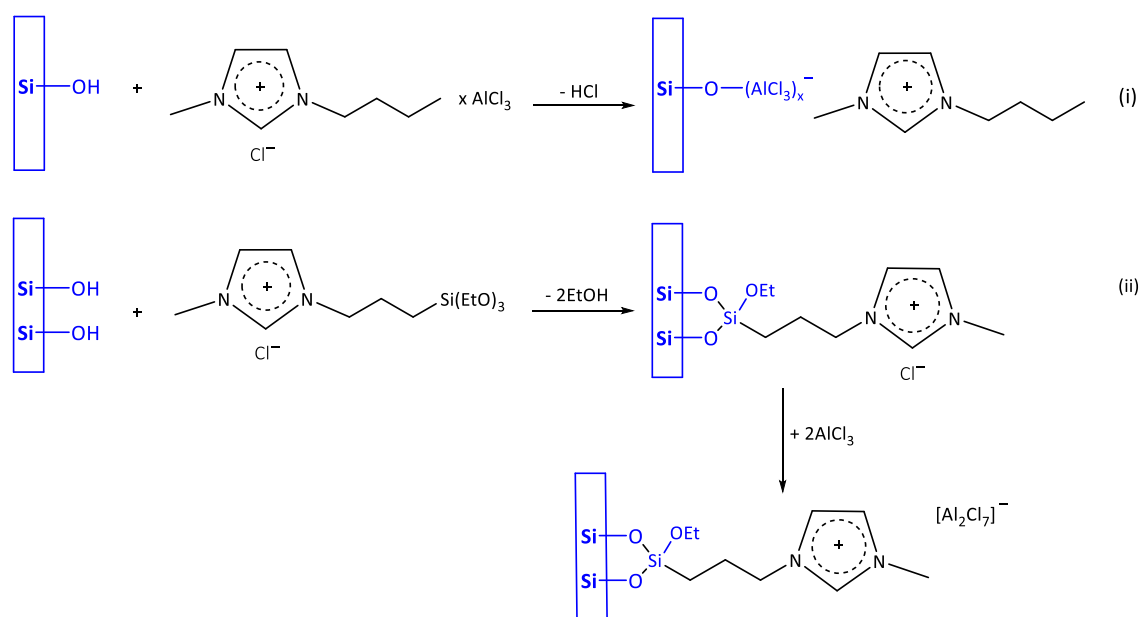


**Figure 3.2:** Immobilisation of a chloroaluminate(III) ionic liquid via (i) the anion or (ii) the cation (grafting)<sup>10</sup>

Covalent grafting involves the use of functionalized ionic liquids and a number of synthetic steps are required and the applicability of such protocols is not feasible for inert surfaces.<sup>7</sup> The most straightforward synthetic protocol for SILPs involves the physisorption of an ionic liquid by incipient wetness impregnation. Identifying the optimum method for achieving an even dispersion of the ionic

liquid onto the support can be challenging.<sup>8,12</sup> The ionic liquid is dissolved in a dry, low-boiling organic solvent prior to the addition of the porous solid support. Vigorous stirring is required so that a homogeneous distribution of the IL/catalyst onto the support is attained. The dispersion of the ionic liquid is followed by the slow removal of the volatile co-solvent by evaporation under vacuum, yielding the SILP catalyst. The growing interest in SILP technologies led to the investigation of optimum scalable production protocols.<sup>13</sup> Rotary evaporation of the added solvent is limited to small batch production protocols (< 200 g) whereas freeze-drying can only be applied to kilogram scale production. A recent study proposed fluidised-bed spray coating as a scalable method for the reproducible dispersion of ionic liquids onto a porous support.<sup>13</sup> The fluidisation of the parent support was achieved using a high-velocity, temperature-controlled gas flow (air, N<sub>2</sub> or Ar) (Figure 3.3 (i)), followed by spraying the IL/catalyst mixture through a nozzle at adjustable spraying volumes and pressures so that the thickness of the IL layer ( $s_{IL}$ ) was controlled (Figure 3.3 (ii)).

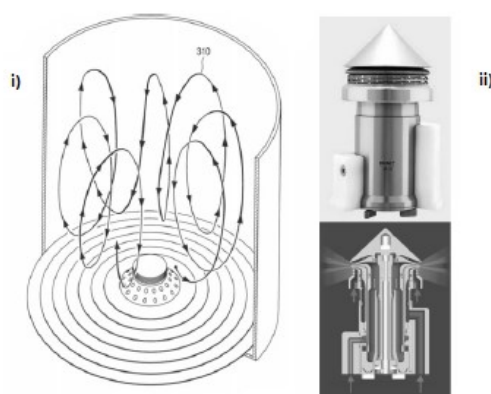


**Figure 3.3:** Illustration of the production of SILP materials production by spray coating in a fluidised-bed reactor<sup>13</sup>

The coating of the support by an ionic liquid is expected to decrease the available surface area and pore volume. The thickness of the ionic liquid layer ( $s_{IL}$ ) is approximately equal to the ratio of the ionic liquid volume to the initial surface area of the parent support.<sup>3</sup> For example, the simulated coating of porous silica with [C<sub>2</sub>C<sub>1</sub>im][NTf<sub>2</sub>] showed that most of the mesopores (2 – 20 nm) were filled by capillary forces at  $\alpha_{IL} > 30$  %.<sup>3</sup> The thickness of the ionic liquid monolayer (0.6 nm) corresponded to the theoretically-calculated dimensions of the corresponding pair of ions ([C<sub>2</sub>C<sub>1</sub>im][NTf<sub>2</sub>]).

### 3.1.2 Selected examples of applications of Supported Ionic Liquid Phases; Acidic SILPs

The use of mineral acids in acid-catalysed reactions typically leads to low selectivity and large amounts of acidic waste whereas solid acids exhibit a reduced catalytic activity, requiring extreme reaction conditions that eventually lead to catalyst deactivation. The use of Brønsted or Lewis acidic ionic liquids (**Chapter 2**) has been attempted in many reaction applications<sup>14,15</sup> due to the potential for fine-tuning their acidity via modifications of their chemical structure. However, the high viscosity of most ionic liquids makes their handling and large-scale application challenging whereas catalytic reactions become limited by diffusion processes. SILP-based catalysis allows the efficient utilisation of the ionic liquid, eliminating mass transport issues arising from the high viscosity of the medium. This is critical when ionic liquids are used as catalysts or solvents in liquid-liquid extraction processes where poor mass transfer rates lead to extended contact time requirements. There are two main types of SILP-based catalytic processes: slurry-phase and gas-phase where the SILP catalyst is suspended in the reaction mixture.<sup>5,8</sup> For example, the gas-phase hydroformylation of 1-butene (0.6 - 2.4 bar) has been tested with a silica gel-based (100 Å) SILP catalyst prepared from [C<sub>4</sub>C<sub>1</sub>im][n-C<sub>8</sub>H<sub>17</sub>OSO<sub>3</sub>] ( $\alpha_{IL} = 10\%$ ) and low loadings of Rh-based catalytic complexes (0.1 – 0.9 ww%).<sup>16</sup> The first application of SILP-catalysed hydroformylation was reported for the production of heptanal from 1-hexene, using a surface modified silica gel with covalently anchored [C<sub>4</sub>C<sub>1</sub>im][PF<sub>6</sub>] or [C<sub>4</sub>C<sub>1</sub>im][PF<sub>6</sub>].<sup>17</sup> The activity of the SILP catalyst was three times higher compared with other conventional biphasic systems due to the large surface area of the dispersed Rh-catalyst.<sup>17</sup> The first systematic study of alkene hydrogenation reactions catalysed by SILPs was also reported in 2002 for a [C<sub>4</sub>C<sub>1</sub>im][PF<sub>6</sub>]/Rh-based mixture that was dispersed on silica gel ( $\epsilon_{IL} = 25\%$ ).<sup>18</sup> SILPs proved to be more active towards the hydrogenation of alkenes, in comparison with the bulk ionic liquid due to an enhanced concentration of the active rhodium species that were dispersed onto the high surface area support. Palladium catalyst complexes, immobilised in a thin film of a silica gel-supported Brønsted acid IL, have been used in hydroamination reactions between aniline and styrene.<sup>19</sup> The combination of Lewis acidic (Pd<sup>2+</sup>) and strong Brønsted acidic sites provided highly active bi-functional catalysts. The coordination of styrene to Pd<sup>2+</sup> via the double bond was suggested to enhance the subsequent nucleophilic attack of the lone pair of electrons located on the aniline nitrogen atom. SILP materials have also been successfully applied in continuous gas-phase desulfurisation. For example, 1,3-dialkylimidazolium chlorometallate ionic liquids ([C<sub>n</sub>C<sub>1</sub>im]Cl·MCl<sub>x</sub>, (n = 4, 8, 12), MCl<sub>x</sub>=SnCl<sub>2</sub>, ZnCl<sub>2</sub>, 0.33 < X<sub>SnCl<sub>2</sub></sub> < 0.62) were employed for the preparation of SILP catalysts that were tested for the extraction of *n*-butyl mercaptan from *n*-heptane.<sup>5</sup> The ionic liquid was loaded onto an alumina support and the best performance was identified for [C<sub>12</sub>C<sub>1</sub>im]Cl·SnCl<sub>2</sub> (X<sub>SnCl<sub>2</sub></sub> = 0.5) at  $\alpha_{IL} = 20\text{ vol}\%$ .<sup>5</sup> Immobilised [C<sub>4</sub>C<sub>1</sub>im]Cl·AlCl<sub>3</sub> on mesoporous silica gel has also been investigated for the alkylation of benzene, toluene, naphthalene and phenol in batch, continuous liquid-phase as well as continuous gas-phase

reactors.<sup>6</sup> The catalytic performance of the supported Lewis acid IL was improved when compared with H-beta zeolites and unsupported ionic liquids due to better dispersion of the catalyst onto a high surface area support.<sup>6</sup> Lewis acidic SILP catalysts with a varying degree of pore filling ( $\alpha_{IL} = 10\% - 30\%$ ) have also been examined as catalysts for slurry-phase Friedel-Crafts alkylations.<sup>8</sup> Increasing  $\alpha_{IL}$  led to an enhancement of the Lewis acidity but there was a critical value for optimum performance with minimum IL leaching. Overall, continuous gas-phase processes are ideal for SILP catalysis, reducing the risk of catalyst leaching.<sup>4</sup> Liquid-phase or slurry-phase reactions require careful considerations regarding the polarity the reaction media in order to avoid leaching of the SILP components.

### 3.1.3 Ionic liquids and continuous flow processes; SILP applications

The first IL-based, continuous flow process was developed by Eastman Chemical Company (1998), using continuous stirred tank reactors (CSTR).<sup>20</sup> In this process, long-chain tetraalkylphosphonium salts ( $[P_{88818}]I$ ), containing a Lewis acid, were used as the catalytic phase for the isomerisation of 3,4-epoxybut-1-ene to 2,5-dihydrofuran, coupled with the recycling of the ionic liquid. This process provided great benefits by replacing a homogeneous catalyst that was comprised of corrosive HI or HBr and a transition metal catalyst dissolved in high-boiling solvents. The Dimersol process is another example where 1,3-dialkylimidazolium chloroaluminates(III) were used for stabilising a Ni-catalyst whilst dissolving an alkene that was converted into branched hexenes and octenes.<sup>21</sup> A liquid-liquid biphasic system was designed and the reaction was performed in a CSTR, followed by a phase separator with great improvements in preventing the leaching of the catalyst.

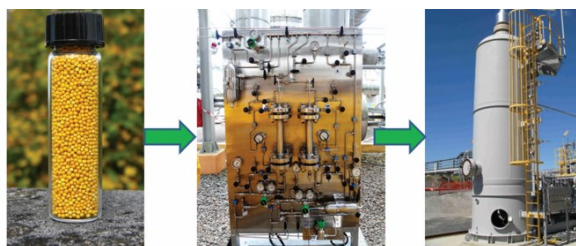


**Figure 3.4:** The transition from the lab-scale preparation of chlorocuprate(II) SILPs through to a pilot-scale production, using 100 cm<sup>3</sup> of SILPs, and finally the large-scale mercury removal where 20 m<sup>3</sup> of SILP was applied.<sup>22</sup>

SILPs are excellent catalysts in gas-phase reaction applications such as continuous-flow-operated fixed-bed processing.<sup>2</sup> The first commercial application of SILPs was reported by Petronas for the removal of mercury from natural gas in fixed-bed scrubbers (Figure 3.4).<sup>22</sup> The efficient removal of mercury from gaseous refinery streams is crucial for environmental and safety reasons as well as for preventing the corrosion of the equipment in gas processing plants. The reactive capture of mercury by



chlorocuprate(II) SILPs, containing  $[\text{CuCl}_4]^{2-}$  and  $[\text{Cu}_2\text{Cl}_6]^{2-}$ , provided a lifetime of up to three times that of commercial technologies such as sulfur-impregnated activated carbon. A small-scale application example, where acidic SILPs have also been used in a multi-stage fixed bed reactor, involved the gas phase Friedel–Crafts isopropylation of toluene and cumene.<sup>23</sup> Both the Lewis acidity and the loading of the IL had a great impact on the reaction metrics. Moderate loadings ( $\alpha_{\text{IL}} = 20\%$ ) showed excellent performance for more than 210 h time-on-stream with a reported selectivity to the mono-alkylated product of more than 95 % (Figure 3.5).<sup>23</sup>

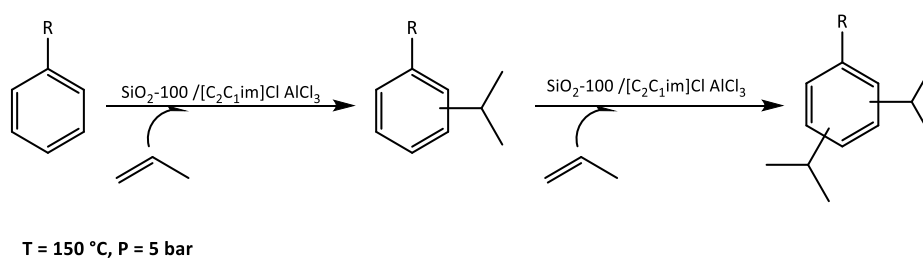


**Figure 3.5:** Continuous flow isopropylation of toluene and cumene catalysed by  $[\text{C}_2\text{C}_1\text{im}]\text{Cl}\cdot\text{AlCl}_3/\text{SiO}_2$  ( $\alpha_{\text{IL}} = 0.1 - 0.3$ ).<sup>23</sup>

A SILP-catalysed hydroformylation process has also been applied to the production of *n*-pentanal from a mixture of 1-butene (1.5 %), 2-butene (28.5 %) and *n*-butane (70 %), promoted by a Rh-based catalyst immobilised in the IL (Figure 3.6).<sup>24</sup> A high conversion of butenes ( $\leq 81\%$ ) and a great *n*-pentanal selectivity (92 %) were achieved for a residence time of 155 s and a 500 h time-on-stream.<sup>24</sup>

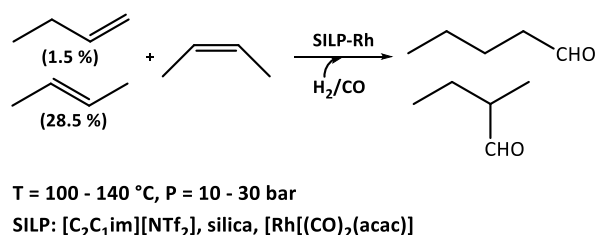


**Figure 3.6:** Continuous flow, gas-phase hydroformylation catalysed by  $[\text{C}_2\text{C}_1\text{im}][\text{NTf}_2]\text{-Rh}[(\text{CO})_2(\text{acac})]/\text{SiO}_2$  ( $\epsilon_{\text{IL}} = 0.15$ ).<sup>24</sup>

A fixed-bed reactor set-up has also been used for the synthesis of amines in a cascade reaction involving the hydroformylation of an alkene, followed by reductive amination (Figure 3.7).<sup>25</sup> The polarity and basicity of the ionic liquid, as well as the properties of the support, impacted on the reaction metrics. Silica gel (100 Å) showed the highest ethylene conversion rates (yield: 51 %) and a moderate *N,N*-diethylpropan-1-amine yield of 35 %. The long-term stability of the SILP catalyst was significantly high, with a time-on-stream of more than 18 days and a total turnover number of 115,000.

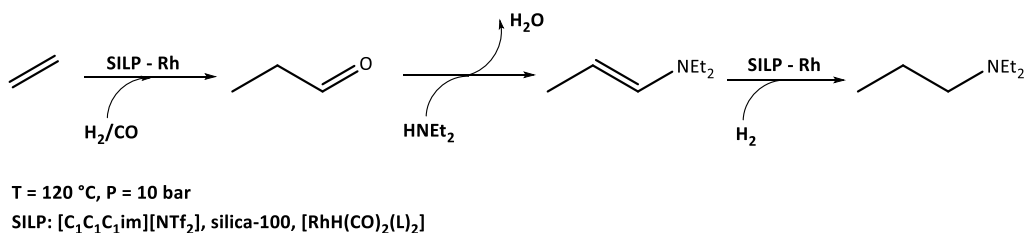


**Figure 3.7:** Continuous gas-phase hydroaminomethylation of ethylene, catalysed by  $[\text{C}_1\text{C}_1\text{C}_1\text{im}][\text{NTf}_2]\text{-}[\text{RhH}(\text{CO})_2(\text{L})_2]/\text{SiO}_2$  ( $\alpha_{\text{IL}} = 0.1$ ). The hydroformylation of ethylene is followed by a reaction with diethylamine to form *N,N*-diethylpropan-1-amine (DEPA) through an enamine intermediate.<sup>25</sup>

Cationic nickel complexes, immobilized in  $[\text{C}_2\text{C}_1\text{im}][\text{FAP}]$ -based SILPs ( $\text{SiO}_2\text{-100 } \text{\AA}$ ;  $\alpha_{\text{IL}} = 0.3, 0.6$  or  $0.9$ ), have been tested as catalysts for the tandem dimerization/isomerization of ethylene to 2-butene to produce propylene (Figure 3.8).<sup>26,27</sup> The introduction of  $[\text{FAP}]^-$ , and thus the replacement of fluorine by hydrophobic perfluoroalkyl-groups, is considered to be a successful way to increase the hydrolytic stability of fluorophosphate-based anions.<sup>28</sup> Performing the reaction in a fixed-bed reactor suffered from the formation of hot spots across the bed due to the exothermic nature of the dimerization step, leading to the deactivation of the nickel catalyst. Decreasing the reaction temperature to  $19\text{ }^{\circ}\text{C}$  led to an improved catalyst lifetime with 120 h time on stream ( $\text{TON} > 53300\text{ mol}_{\text{butene}}\text{mol}_{\text{Ni}}^{-1}$ ), although the condensation of products in the pores of the SILP became prominent at lower temperatures.<sup>26</sup> Diluting the SILP with an inert material or increasing the inert gas content did not significantly reduce the formation of hot spots in the fixed-bed reactor.<sup>26,27</sup>

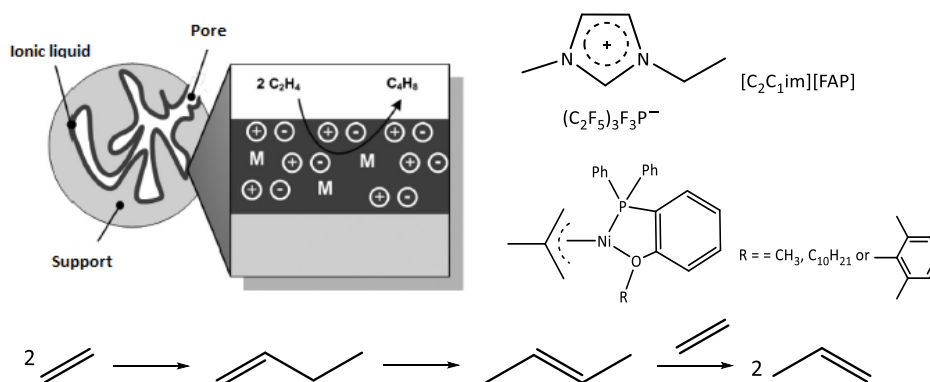


**Figure 3.8:** Schematic representation of the SILP/Ni-catalysed ( $\alpha_{\text{IL}} = 0.3 - 0.9$ ) ethylene to propylene reaction via the formation of 1-butene, the subsequent isomerization of 1-butene and the metathesis of 2-butene with ethylene.<sup>26,27</sup>

The first ever application of SILPs in a fluidised bed reactor was attempted to improve the removal of heat from the aforementioned Ni-based SILPs, in gas phase experiments, prolonging the catalyst stability.<sup>27</sup> The tested pressures of high purity ethene ( $< 15\text{ ppb O}_2$ ) ranged from 17 to 136 mbar at 292

K - 362 K by using low loadings of SILP material (0.2 – 1 g) in a glass reactor with an inner diameter of 14 mm ( $P_{\text{reaction}} = 1 \text{ bar}$ ) (Figure 3.9). The gas stream was analysed online, at the outlet of the fluidised bed reactor, by gas chromatography. Plotting the turnover number [TON ( $\text{mol}_{\text{butane}} \text{mol}_{\text{Ni}}^{-1}$ )] over the time-on-stream [TOS (h)] for the dimerization of ethene in a fluidised bed reactor over a fixed bed reactor demonstrated an improved stability of the SILP catalyst. When applied in a fluidised bed, the TON values exceeded those for the experiments performed in a fixed bed by a factor of two. A maximum activity was identified for  $\alpha_{\text{IL}} = 0.3$  yielding a  $\text{TOF}_{\text{max}}$  of  $913 \text{ mol}_{\text{butane}} \text{mol}_{\text{Ni}}^{-1} \text{h}^{-1}$  in comparison with 714 and 640  $\text{mol}_{\text{butane}} \text{mol}_{\text{Ni}}^{-1} \text{h}^{-1}$  for  $\alpha_{\text{IL}} = 0.6$  and  $\alpha_{\text{IL}} = 0.9$  respectively.

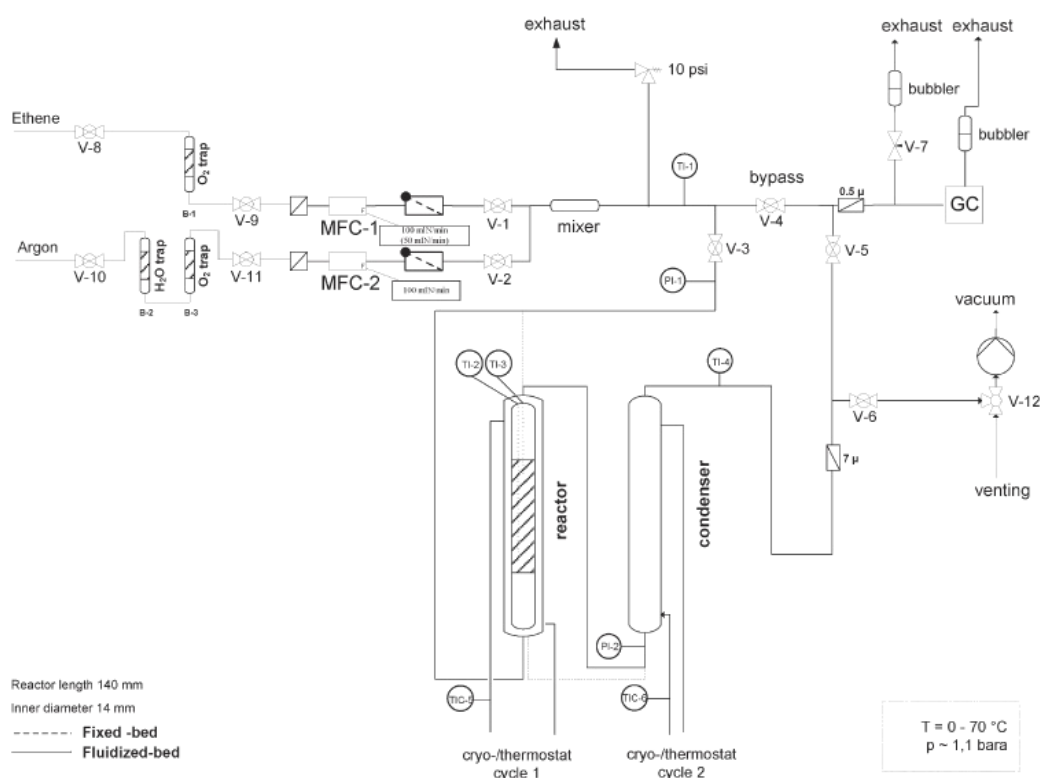


**Figure 3.9:** Experimental set-up for the SILPs-catalysed dimerization of ethene in a fluidised bed or a fixed bed reactor.<sup>27</sup> The flow rates of purified ethene/Ar were adjusted by mass flow controllers and the gas stream was analysed online via GC.

## 3.2 Results & Discussion

### 3.2.1 Preparation of Lewis acidic supported ionic liquids (SILP) - $[\text{C}_4\text{C}_{1\text{im}}]\text{Cl}\cdot\text{ZnCl}_2$ , $X_{\text{ZnCl}_2} = 0.67$

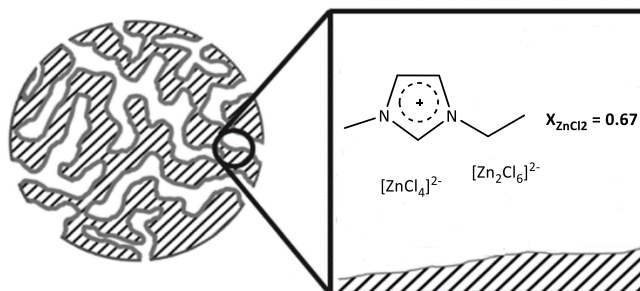


**Figure 3.10:** Schematic representation of the SILP catalyst particle containing  $[\text{C}_4\text{C}_{1\text{im}}]\text{Cl}\cdot\text{ZnCl}_2$ ,  $X_{\text{ZnCl}_2} = 0.67$

$[\text{C}_4\text{C}_{1\text{im}}]\text{Cl}\cdot\text{ZnCl}_2$ ,  $X_{\text{ZnCl}_2} = 0.67$  was chosen as an active catalyst towards the recyclization of 2,5-DMF to 2,5-DMT due to the promising results obtained in the small-scale liquid-liquid reactions (**Chapter 2**). The development and application of Lewis acidic chlorozincates(II) to produce SILP catalysts was therefore investigated (Figure 3.10). The main aim was to improve on the mass transfer and diffusion properties of the catalytic system with an increased interface in comparison with the highly viscous bulk ionic liquid. Dispersing the ionic liquid onto a high surface area support brings the additional benefit of improving the economics of the studied process by reducing the volume of the IL that is employed. Furthermore, ionic liquids can now be studied in continuous flow processes by using a fluidised reactor. Amorphous, mesoporous silica gel was chosen as the support due to its high surface area, porosity and low cost. The synthesis of the SILP catalysts was accomplished by physisorption over chemisorption given that the former is a simple and fast approach for immobilising the ionic liquid onto the porous support. Weak interactions such as van der Waals and hydrogen bonding forces are expected to dominate the interactions between the ionic liquid and the surface of the inorganic support.<sup>3</sup> The thermal treatment/calcination of silica gel samples with different surface characteristics (pore size: 60 Å & 150 Å) was performed at high temperatures (150 – 600 °C) for the removal of the adsorbed water and the hydroxyl groups from the silica surface. The SILP samples were subsequently prepared by incipient wetness impregnation from solutions of the ionic liquid in dry methanol, applying different loadings of ionic liquid. After removal of the co-solvent under reduced pressure, solid materials were obtained with ionic liquid loadings ( $\epsilon_{\text{IL}}$ ) up to 100 % ( $n_{\text{IL}} = 0.3 - 3.2 \text{ mmol g}^{-1}$ ). A thorough description of the synthetic protocols and the exact SILP compositions is provided in the experimental **Section 3.3.1**.

### 3.2.2 Surface area and pore structure analysis of Supported Ionic Liquid phases by gas adsorption

The control over the pore size and the surface properties of a catalyst is often critical for fine-tuning the metrics of a reaction.<sup>27,29</sup> Plotting the volume of an adsorbed gas ( $V_a$ ) against pressure is the first step for attempting a preliminary surface area and pore structure analysis of a solid by investigating the shape of the adsorption/desorption isotherms (**Appendix**, Figure 3.41).<sup>30</sup> The pressure is expressed as the relative pressure ( $P/P_0$ ), the actual pressure divided by the vapour pressure of the gas at the experimental temperature. The quantity of gas is expressed as volume at standard temperature and pressure conditions (0 °C, 760 torr). Enhanced adsorption occurs in micropores; hence the isotherm of a microporous solid will contain a curve with a sharp rise, followed by a nearly horizontal section and a smaller rise as the saturation point is approached and bulk condensation occurs. Filling of the micropores occurs at lower pressures than the relative pressures required for the capillary condensation and evaporation in mesopores.<sup>31</sup> Precise measurements at quite low pressures are required and thus only high vacuum manifolds are applicable for a thorough analysis of a microporous structure. The adsorption curve of a porous solid contains a rise at intermediate relative pressures, showing a wide hysteresis loop, typical of mesoporous ( $d > 2$  nm) and macroporous ( $d > 50$  nm) materials.<sup>30</sup> The presence of a hysteresis loop indicates differences between the mechanisms of bulk condensation in the pores and the evaporation within the pores. Van Der Waals forces induce physisorption whereas they are also responsible for surface tension and the condensation of liquids. The application of both Langmuir and BET (Brunauer, Emmett and Teller) theories for the calculation of pore volume and surface areas are discussed in the following paragraphs. Nonetheless, the Langmuir theory (**3.1**) is more applicable to chemisorption as it accounts to the formation of one molecular layer on an inelastic solid surface.<sup>32</sup>

$$\frac{P}{V_a} = \frac{1}{V_m b} + \frac{P}{V_m} \quad (3.1)$$

Plotting  $P/V_a$  against  $P$  provides a straight line and thus  $b$  and  $V_m$  can be calculated from the slope and intercept of the regression line.  $V_m$  is the volume of the gas adsorbed when the surface of the solid is covered with a monomolecular layer and  $b$  is an empirical constant. The specific surface area ( $s$ ) of the material is then calculated from  $V_m$  values (**3.2**).

$$s \text{ (m}^2 \text{ g}^{-1}\text{)} = \frac{V_m \sigma N_A}{m V_0} \quad (3.2)$$

Here,  $\sigma$  is the area occupied by a single adsorbed gas molecule,  $N_A$  is the Avogadro constant,  $m$  is the mass of the solid material and  $V_o$  is the molar volume of the gas. In the case of  $N_2$  being used as the adsorptive gas, (3.2) is transformed into (3.3), accounting for a  $\sigma$  value equivalent to  $16.2 \cdot 10^{-20} \text{ m}^2$ .<sup>33</sup>

$$s \text{ (m}^2\text{/g)} = \frac{4.35 V_m}{m} \quad (3.3)$$

BET (Brunauer, Emmett and Teller) theory advanced the Langmuir theory towards the concept of multilayer adsorption.<sup>34</sup> The BET model accounts for an infinite number of layers and a uniform surface coverage, in the absence of sites where preferential adsorption takes place (3.4). All adsorption sites are considered as equally energetic, not accounting for interactions amongst adsorbate molecules.

$$\frac{P}{V_a(P_o-P)} = \frac{1}{V_m C} + \frac{(C-1)}{V_m C} \left( \frac{P}{P_o} \right) \quad (3.4)$$

Plotting  $P/(V_a(P_o-P))$  as a function of the relative pressure, results into a straight line with the intercept being equivalent to  $1/V_m C$  and the slope becoming  $(C-1)/V_m C$ . A straight line is usually obtained for  $P/P_o$  values from 0.05 up to 0.30 where a monolayer is formed.<sup>33</sup> Here,  $C$  is a constant that is determined by the heat of adsorption and liquefaction of the adsorptive gas.<sup>34</sup> Determining the volume of the monolayer allows the calculation of the surface area of the solid by using the area occupied by a single molecule of nitrogen whilst assuming for a close packing onto the surface (3.3). The adsorbed quantities of gas can be normalised by the equivalent value of the monolayer, resulting to the following fractions:  $V_a/V_m$  or  $n_a/n_m$ . The thickness of the adsorbed layer can be determined by multiplying the fraction of monolayer capacity ( $V_a/V_m$ ) by the thickness of the monolayer for nitrogen ( $3.54 \text{ \AA}$ ). Plotting  $V_a$  against the statistical thickness ( $t$ ) yields the  $t$ -plot where a characteristic upwards shift occurs upon capillary condensation in mesoporous solids.<sup>35</sup>

$$\ln\left(\frac{P^*}{P_o}\right) = - \left( \frac{2\gamma v \cos\theta}{RT r_m} \right) \quad (3.5)$$

The pore size distributions of porous materials can be estimated by using a method developed by Barrett, Joyner and Halender (BJH).<sup>36</sup> The calculation of the pore size distribution is accomplished by measuring the change in volume of the adsorbed gas upon a gradual decrease of the relative pressure ( $P/P_o$ ) from 0.995 to 0.05. The quantity of the gas desorbing in each step correlates with the volume of the pores emptying. A cylindrical geometry is assumed for the pore volume calculations whereas the

Kelvin equation is applied for estimating the pore size distributions (3.5). The Kelvin equation describes the capillary condensation in small capillaries and pores at pressures below the saturated vapour pressure ( $P_o$ ). It can therefore be used to estimate the pore radius ( $r_m$ ) at which condensation can occur at a given relative pressure.  $P^*$  is the critical condensation pressure,  $\gamma$  corresponds to the liquid surface tension,  $v$  is the molar volume of the condensed gas,  $\theta$  represents the values of the contact angle between the solid and the condensed adsorptive and  $r_m$  is the mean radius of the liquid meniscus. The pore radius of cylindrical pores is calculated as the sum of  $r_m$  and the thickness of the adsorbed multilayer ( $t$ ) that is separately calculated by the Halsey equation (3.6).<sup>37</sup>

$$t = 3.54 \left[ \frac{-5.00}{\ln(P/P_o)} \right] \quad (3.6)$$

The surface area ( $\text{m}^2 \text{g}^{-1}$ , BET), pore volume ( $\text{cm}^3 \text{g}^{-1}$ ) and pore size distribution (nm, BJH) measurements were completed for the parent supports and the acidic SILP catalysts prior to their application as bed materials. The available surface area of the calcined support has an impact on the thickness of the ionic liquid layer ( $s_{il}$ ) and the performance of the SILP catalyst.<sup>2,3</sup> The catalysts, based on  $[\text{C}_4\text{C}_1\text{im}]\text{Cl}\cdot\text{ZnCl}_2$  ( $X_{\text{ZnCl}_2} = 0.67$ ), were dried under reduced pressure to remove any residual water or co-solvent that could interfere with the accurate analysis of the surface properties. The samples were loaded into the penetrometer in a glovebox, under inert atmosphere, and then cooled to 77.35 K by immersing the sample tube in a bath of liquid nitrogen. The  $\text{N}_2$  adsorption/desorption was performed by measuring the volume of the adsorbed gas as the pressure over the sample increased from atmospheric to the saturation vapour pressure. The desorption isothermal was obtained by a stepwise decrease of the pressure until atmospheric pressure was reached over the sample.

### 3.2.2.1 $[\text{C}_4\text{C}_1\text{im}]\text{Cl}\cdot\text{ZnCl}_2$ ( $X_{\text{ZnCl}_2} = 0.67$ )-based SILPs; characterisation by gas adsorption

The  $\text{N}_2$  adsorption/desorption isotherms for a selection of SILP materials, used as catalysts in gas-phase thiophene synthesis and their respective inorganic supports are presented in Figure 3.11. The Figures show the relative pressure ( $P/P_o$ ) as a function of the volume of nitrogen adsorbed at STP ( $V_a$ ). Three well-distinguished regions of the isotherm are present: (i) monolayer and multilayer adsorption, (ii) capillary condensation and (iii) multilayer adsorption on the outer surface of the silica particles. Firstly, gas molecules form a monolayer on the surface of the particles. Further increasing the relative gas pressure ( $P/P_o$ ) leads to the formation of more than one layer of  $\text{N}_2$  molecules on the surface of the adsorbent (multilayer adsorption). As the pressure increases further, gas condenses in the pores until all pores are filled at a specific saturation point. Pore condensation occurs at a pressure that is lower

than the bulk saturated vapour pressure. Capillary condensation is characteristic to mesoporous materials<sup>31</sup> and it is accompanied by hysteresis. Subsequently, the relative pressure decreases so that the condensed gas evaporates (desorption branch). Both supports yielded materials with Type IV isotherms, bearing a hysteresis loop that is typical of mesoporous solids ( $2 \text{ nm} < D_p < 50 \text{ nm}$ ). H1 and H2 hysteresis loops were observed, suggesting ordered porous materials with cylindrical pores open at both ends and disordered/interconnected porous material respectively.<sup>31</sup>

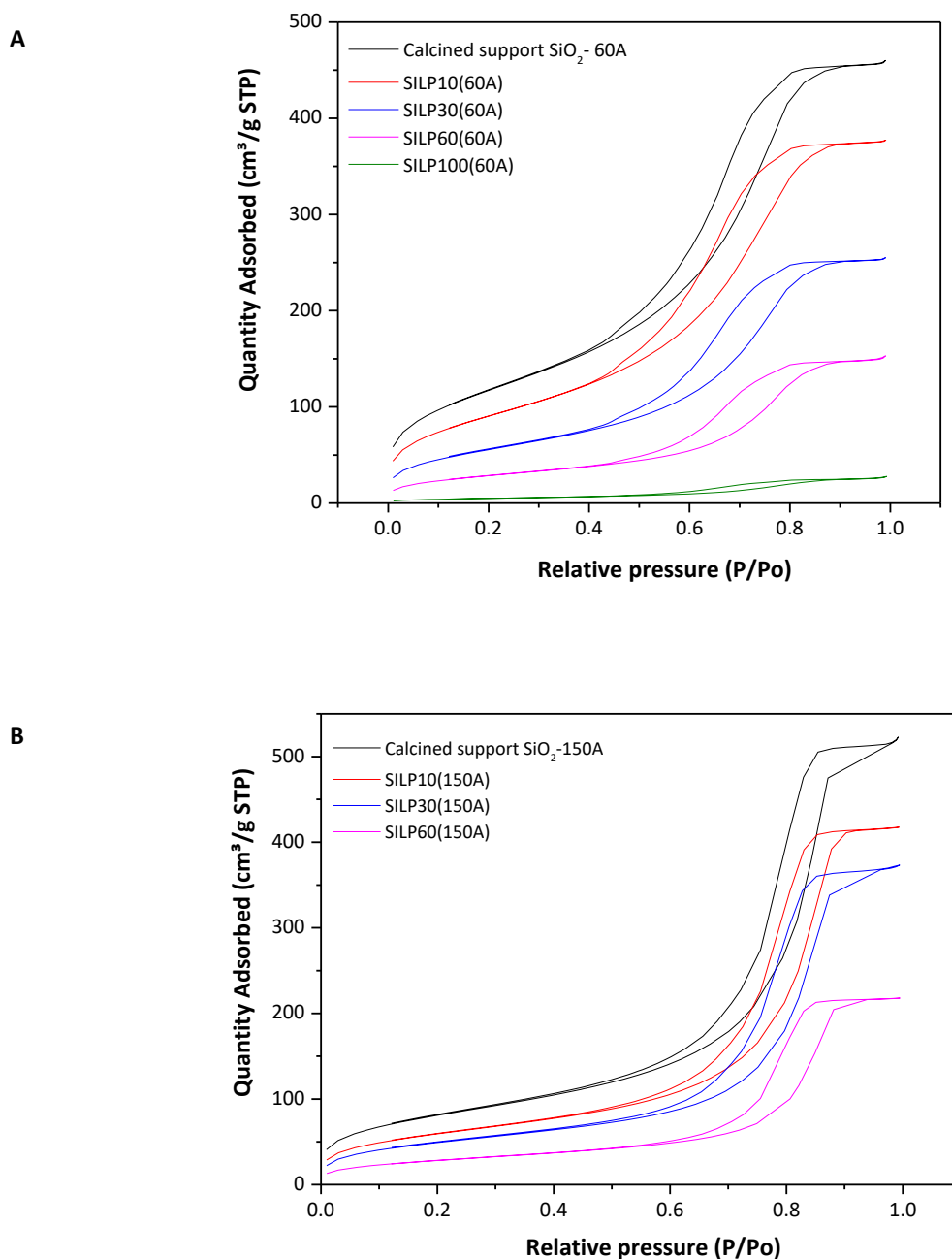


**Figure 3.11:** Adsorption/desorption isotherms of a)  $\text{SiO}_2$ -60 Å-based and b)  $\text{SiO}_2$ -150 Å-based SILP catalysts, both impregnated with increasing amounts of  $[\text{C}_4\text{C}_1\text{im}]\text{Cl}\cdot\text{ZnCl}_2$  ( $X_{\text{ZnCl}_2} = 0.67$ ). ( $\epsilon_{\text{IL}} = 10 - 100 \%$ ).



Figure 3.11 (A) illustrates the N<sub>2</sub>-sorption isotherms of SILPs based on [C<sub>4</sub>C<sub>1</sub>im]Cl·ZnCl<sub>2</sub> (X<sub>ZnCl<sub>2</sub></sub> = 0.67) immobilised on SiO<sub>2</sub> - 60 Å with varying IL loadings (ε<sub>IL</sub> = 10 – 100 %). The parent support exhibited a characteristic H2 hysteresis. The respective isotherms of SILP catalysts with ionic liquids confined in SiO<sub>2</sub> - 150 Å and the parent support itself can be classified as type IV, featuring a type H1 hysteresis loop [Figure 3.11 (B)]. The capillary condensation point of the 150 Å silica gel-based catalysts was also shifted to higher relative pressures in comparison with the silica gel – 60 Å-based SILPs (ca. P/P<sub>o</sub> = 0.60 vs. P/P<sub>o</sub> = 0.40), suggesting a relationship between the pore radius and the relative pressure at which capillary condensation takes place.<sup>31</sup>

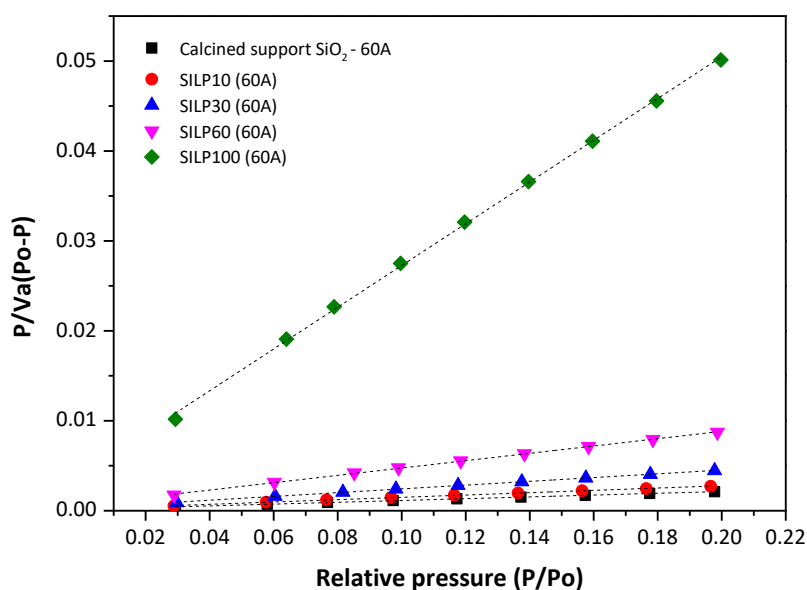


**Figure 3.12:** Characteristic BET surface area plot; SiO<sub>2</sub>-60 Å-based SILPs with variable loadings of [C<sub>4</sub>C<sub>1</sub>im]Cl·ZnCl<sub>2</sub> (X<sub>ZnCl<sub>2</sub></sub> = 0.67) (ε<sub>IL</sub> = 10 – 100 %).

The surface area ( $A_{\text{BET}}$ , cm<sup>3</sup> g<sup>-1</sup>) and the  $C_{\text{BET}}$  factor were calculated using the linearized BET equation (3.4) at  $0.04 < P/P_o < 0.20$ .  $P/(V_a(P_o-P))$  was plotted as a function of the relative pressure to approximate the  $V_m$  and  $C_{\text{BET}}$  values from the intercept and the slope of the fitted lines (Figure 3.12). The pore volume was determined from the adsorption branch of the isotherm approximately at the 0.99 P/P<sub>o</sub> signal point. The N<sub>2</sub>-sorption isotherms indicated that increasing the loading of the physisorbed ionic liquid results to the rapid reduction of the surface area and pore volume, as confirmed by the respective estimated values (Table 3.1). Moreover, the  $C_{\text{BET}}$  values were significantly shifted upon increasing the loading of the ionic liquid, potentially due to modified interactions<sup>32</sup> between N<sub>2</sub> and the surface of the tested sample in the presence of the IL. Consequently, the surface area values ( $A_{\text{BET}}$ ) are expected to be moderately overestimated due to the decreasing values of  $C_{\text{BET}}$  (3.3 - 3.4). The calcined silica gel support (60 Å) exhibited an average pore volume of 0.70 cm<sup>3</sup> g<sup>-1</sup> and a surface area of 427 m<sup>2</sup> g<sup>-1</sup>. The

impregnation of the porous material with increasing loadings of  $[C_4C_1im]Cl \cdot ZnCl_2$  ( $X_{ZnCl_2} = 0.67$ ) resulted to a reduction of both the  $V_{pore}$  and  $A_{BET}$ , accompanied by an increase in the mean pore diameter (Table 3.1& 3.2). Coating  $SiO_2-60 \text{ \AA}$  with  $0.32 \text{ mmol g}^{-1}$  ( $\epsilon_{IL} = 10 \%$ ),  $0.96 \text{ mmol g}^{-1}$  ( $\epsilon_{IL} = 30 \%$ ),  $1.92 \text{ mmol g}^{-1}$  ( $\epsilon_{IL} = 60 \%$ ) and  $3.20 \text{ mmol g}^{-1}$  ( $\epsilon_{IL} = 100 \%$ ) led to the reduction of the surface area ( $A_{BET}$ ) by approximately 23 %, 50 %, 74 % and 96 %, respectively. The pore volume was also decreased by up to almost 94 % upon reaching an  $\epsilon_{IL}$  value of 100 % (Table 3.1). The unmodified  $150 \text{ \AA}$  silica support showed a smaller  $A_{BET}$  of  $369 \text{ m}^2 \text{ g}^{-1}$  and a larger single point pore volume of  $0.99 \text{ cm}^3 \text{ g}^{-1}$  in comparison with  $SiO_2-60 \text{ \AA}$ . Similarly, to the  $60 \text{ \AA}$   $SiO_2$ -based materials, a consistent decrease in the surface area and porosity occurred upon coating  $SiO_2-150 \text{ \AA}$  with  $[C_4C_1im]Cl \cdot ZnCl_2$  ( $X_{ZnCl_2} = 0.67$ ) (Table 3.1). Plotting the surface area and pore volume values as a function of the IL loading ( $n_{IL}$ ) yielded a polynomial trendline ( $R^2 > 0.99$ ) for both supports, indicating a constant loss of pore volume and surface area with increasing amounts of ionic liquid (**Appendix**, Figure 3.43).

**Table 3.1:** Surface characteristics of uncoated  $SiO_2-60 \text{ \AA}$ ,  $SiO_2-150 \text{ \AA}$  and silica gel-based SILPs with varying loadings ( $\epsilon_{IL} = 10 - 100 \%$ ) of  $[C_4C_1im]Cl \cdot ZnCl_2$  ( $X_{ZnCl_2} = 0.67$ ); BET theory calculations.

Sample	$\epsilon_{IL}^a$ (%)	$n_{IL}^b$ ( $\text{mmol g}^{-1}$ )	$C_{BET}^c$	$V_m^d$ ( $\text{cm}^3/\text{g}$ )	$A_{BET}^e$ ( $\text{m}^2/\text{g}$ )	$\Delta(\%)A_{BET}$	$V_{pore}^f$ ( $\text{cm}^3/\text{g}$ )	$\Delta(\%)V_{pore}$
$SiO_2$ (60A)	0	0	74.4	98.2	427	Ref.	0.70	Ref.
SILP10 (60A)	10 %	0.32	66.8	76.2	332	- 23 %	0.58	- 18 %
SILP30 (60A)	30 %	0.96	64.0	47.0	204	- 50 %	0.40	- 43 %
SILP60 (60A)	60 %	1.92	61.9	24.1	105	- 74 %	0.23	- 68 %
SILP100 (60A)	100 %	3.20	58.3	4.3	18	- 96 %	0.04	- 94 %
$SiO_2$ (150A)	0 %	0	81.9	84.8	369	Ref.	0.99	Ref.
SILP10 (150A)	10 %	0.32	72.6	50.0	218	- 41 %	0.64	- 35 %
SILP30 (150A)	30 %	0.96	65.9	41.6	181	- 50 %	0.57	- 43 %
SILP60 (150A)	60 %	1.92	61.8	24.0	105	- 72 %	0.34	- 66 %

a: ionic liquid loading (ww%), b: molar loading, c: C constant (BET theory), d: volume of the gas monolayer (BET), e: surface area (BET), f: single point total pore volume at  $P/P_0$  ca. 0.99 (BET).

At  $\epsilon_{IL}$  values greater than 60 %, a steady decrease in both pore volume ( $V_{pore}$ ) and surface area ( $A_{BET}$ ) is observed whereas small changes occur on the average pore diameter. Applying the Gurvitsch rule,<sup>38</sup> the average pore diameter ( $D_p$ ) was calculated by assuming that the volume of the gas condensing within the pores, near the saturation vapour pressure, is equivalent to the volume of the pores, accounting for a cylindrical geometry. A gradual increase in the average pore diameter was estimated by applying the total pore volume that was approximated by both BET and BJH theories (Table 3.2). Additionally, plotting

the average adsorption BJH pore diameter ( $4V/A$ , nm) against  $n_{IL}$  ( $\text{mmol g}^{-1}$ ) resulted to a linear or a polynomial fitting ( $R^2 > 0.9$ ) for the  $\text{SiO}_2$ -60 Å-based and  $\text{SiO}_2$ -150 Å-based SILP catalysts respectively. A reduction of the pore volume with incrementally increasing amounts of  $[\text{C}_4\text{C}_1\text{im}]\text{Cl}\cdot\text{ZnCl}_2$  ( $X_{\text{ZnCl}_2} = 0.67$ ) and the increase in the average diameter of the pores indicated that the smaller pores must be filled first. However, it must be noted that the reduction of the  $C_{\text{BET}}$  values for both supports, 60 Å and 150 Å, is reflected in the calculations of the surface area ( $A_{\text{BET}}$ ). Consequently, any interactions between  $\text{N}_2$  and the surface of the material may result into an overestimation of  $D_p$ .

**Table 3.2:** Average pore diameter calculations for uncoated  $\text{SiO}_2$ -60 Å,  $\text{SiO}_2$ -150 Å and silica gel-based SILPs with varying loadings ( $\epsilon_{\text{IL}} = 10 - 100$  %) of  $[\text{C}_4\text{C}_1\text{im}]\text{Cl}\cdot\text{ZnCl}_2$  ( $X_{\text{ZnCl}_2} = 0.67$ ); BET and BJH theories.

Sample	$\epsilon_{\text{IL}}^a$ (%)	$n_{\text{IL}}^b$ ( $\text{mmol g}^{-1}$ )	$D_p^c$ ( $4V/A$ by BET)* (nm)	$D_p^d$	$D_p^e$
				Adsorption ( $4V/A$ by BJH)* (nm)	Desorption ( $4V/A$ by BJH)* (nm)
<b>SiO<sub>2</sub> (60A)</b>	0	0	6.6	5.5	5.1
<b>SILP10 (60A)</b>	10	0.32	7.0	5.6	5.0
<b>SILP30 (60A)</b>	30	0.96	7.7	5.9	5.2
<b>SILP60 (60A)</b>	60	1.92	8.8	7.0	5.8
<b>SILP100 (60A)</b>	100	3.20	8.7	7.4	6.2
<b>SiO<sub>2</sub> (150A)</b>	0	0	10.8	9.3	8.2
<b>SILP10 (150A)</b>	10	0.3	11.8	9.5	8.1
<b>SILP30 (150A)</b>	30	0.96	12.6	10.1	8.3
<b>SILP60 (150A)</b>	60	1.92	12.9	10.4	8.6

\* $4V/A$ ; V: total pore volume, A: BET surface area (cylindrical pores), a: ionic liquid loading (ww%), b: molar loading, c: pore diameter calculated by the volume as defined by the BET theory, d & e: BJH adsorption and desorption average pore diameter ( $4V/A$ ) determinations

\*\* Cumulative pore area [ $\text{m}^2 \text{g}^{-1}$ ] (BJH; 1.7 – 300 nm):  $\text{SiO}_2$ -60 Å-based SILPs i) 525 ( $\epsilon_{\text{IL}} = 0$  %), ii) 426 ( $\epsilon_{\text{IL}} = 10$  %) iii) 266 ( $\epsilon_{\text{IL}} = 30$  %) iii) 137 ( $\epsilon_{\text{IL}} = 60$  %) iv) 24 ( $\epsilon_{\text{IL}} = 100$  %).  $\text{SiO}_2$ -150 Å-based SILPs i) 421 ( $\epsilon_{\text{IL}} = 0$  %), ii) 272 ( $\epsilon_{\text{IL}} = 10$  %) iii) 228 ( $\epsilon_{\text{IL}} = 30$  %) iii) 131 ( $\epsilon_{\text{IL}} = 60$  %).

A broad pore diameter distribution is observed for both supports with maxima at approximately 7.24 nm and 14.53 nm for  $\text{SiO}_2$  60 Å and 150 Å respectively (Figure 3.13). The BJH pore size distributions ( $dV/d\log D_p$ ) for the mesoporous region appear to narrow on increasing the ionic liquid loading, indicating that smaller mesopores are filled first and thus narrower pore size distributions are obtained.<sup>39,40</sup> Nevertheless, BJH-pore-size distributions in the small mesopore to large micropore region should be interpreted with caution because the Kelvin equation (3.5) is reliable only for pores with pore diameters greater than 2 nm.<sup>33,40</sup> A similar narrowing trend is observed in the pore area distributions ( $dA/d\log D_p$ ) as a function of the loading of the ionic liquid (Appendix, Figure 3.42) for both supports, confirming the theory behind the pore-filling mechanism of the studied SILP materials.

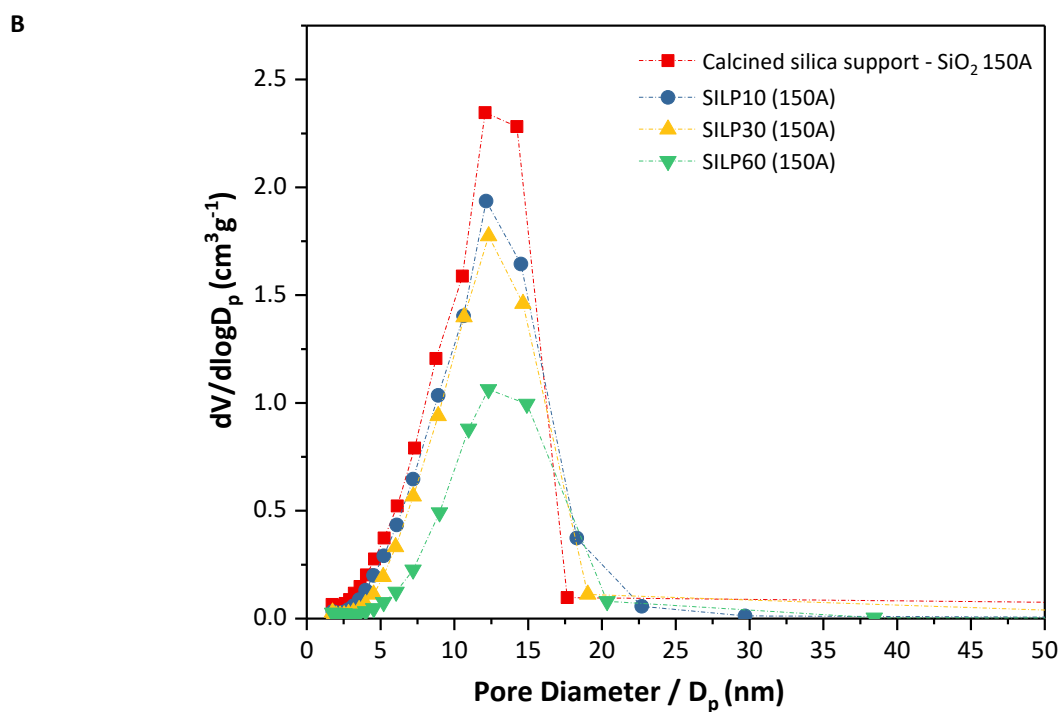
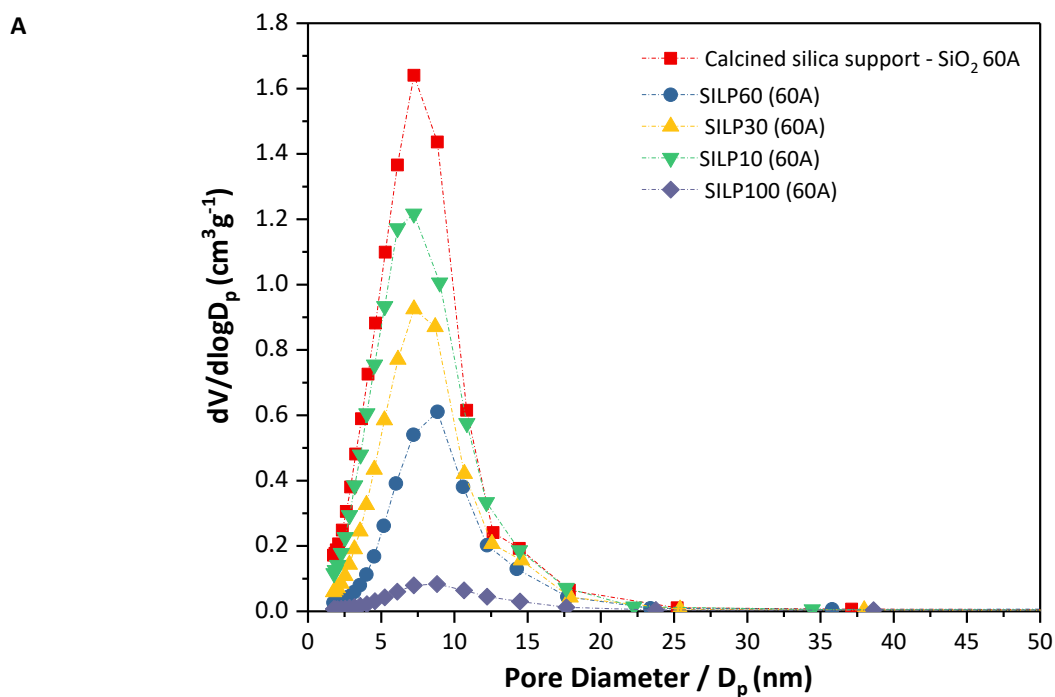


**Figure 3.13:** Pore diameter distribution for 1.7 - 50 nm (mesoporous region) as determined by BJH  $\text{N}_2$  adsorption analysis for a)  $\text{SiO}_2$  60 Å-based SILP catalysts with varying loadings of  $[\text{C}_4\text{C}_1\text{im}]\text{Cl}\cdot\text{ZnCl}_2$  ( $X_{\text{ZnCl}_2} = 0.67$ ) – ( $\epsilon_{\text{IL}} = 10 - 100$  %) and b)  $\text{SiO}_2$  150 Å-based SILP catalysts ( $\epsilon_{\text{IL}} = 10 - 60$  %).

### 3.2.3 Solid-state NMR spectroscopy investigations on Supported Ionic Liquid Phases (SILPs). Pore filling and the orientation of ionic liquids at the solid-liquid interface.

Solid-state NMR spectroscopy (ssNMR) was used to investigate the interactions between the Lewis acidic composition of  $[\text{C}_4\text{C}_{1\text{im}}]\text{Cl}\cdot\text{ZnCl}_2$  ( $X_{\text{ZnCl}_2} = 0.67$ ) and mesoporous silica gel as a function of the loading of the ionic liquid ( $\epsilon_{\text{IL}}$ ). ssNMR spectroscopy can be applied to non-crystalline materials, allowing for the determination of local molecular environments. Orientation-dependent interactions are not averaged to zero in solids in comparison with solutions or liquid samples. The Hamiltonian for an NMR signal is described by equation (3.7) where  $H_z$  is the Zeeman interaction,  $H_D$  is the dipolar interaction,  $H_J$  is equivalent to the scalar coupling,  $H_{\text{CS}}$  represents chemical shift interactions and  $H_Q$  quantifies the quadrupolar interactions.  $H_D$ ,  $H_{\text{CS}}$  and  $H_Q$  have an angular dependence, becoming significant in the solid state where molecular motion is restricted and therefore line broadening occurs. The dipolar and chemical shift interactions have an angular dependence of  $3 \cos^2\theta - 1$  where  $\theta$  is the angle between the external magnetic field and the local field around the nucleus of interest.<sup>41</sup>

$$H = H_z + H_D + H_{\text{CS}} + H_Q + H_J \quad (3.7)$$

Magic angle spinning (MAS) can be used to average out the chemical shift anisotropy and obtain spectra with a good resolution. The sample is placed in a rotor and it is mechanically rotated at a high frequency about an axis oriented at the magic angle of  $\theta = 54.74^\circ$  with respect to the static magnetic field ( $B_0$ ) to suppress the chemical shift broadening ( $3 \cos^2\theta - 1 = 0$ ) (Figure 3.14).<sup>41</sup>

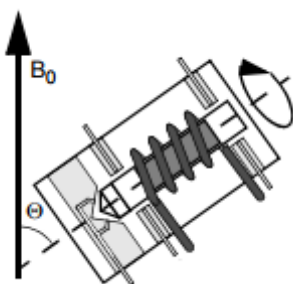


**Figure 3.14:** Schematic representation of Magic Angle Spinning (MAS). The spinning axis of the sample is at an angle of  $54.74^\circ$  with respect to the static magnetic field  $B_0$ .

Overall, most studies that have investigated the interface between solids and ionic liquids mainly involved non-porous substrates and the formation of macroscopic, thick films of ILs on their surface. Sum-frequency vibrational spectroscopy (SFVS)-based experiments revealed the orientation of the imidazolium ring at the IL/ $\text{SiO}_2$  interface with the cation being tilted away from the surface at varying

angles.<sup>42</sup> The impact of the anion, in regards to the cation orientation at the silica surface, has also been identified for  $[C_4C_1im]^+$ -based ILs, bearing  $[BF_4]^-$  or  $[PF_6]^-$ , via SFVS.<sup>43</sup> Molecular dynamics (MD) simulations of imidazolium-based ILs interacting with silica have also shown that the orientation of the cation is highly dependent on the anion.<sup>44</sup> Additionally, it was suggested that silica surfaces, with a high density of silanols (Si-OH), are characterised by a large degree of H-bonding interactions between the Si-OH groups and the anion.<sup>44</sup> The presence of water molecules affects the density of surface silanols, promoting the anion interactions with the support via hydrogen-bonding.<sup>42,44</sup> Atomic force microscopy (AFM)-based studies have also been deployed to study IL/solid interfaces, suggesting the three-dimensional growth of nano-droplets instead of layers on silicate supports for  $[NTf_2]^-$ -based ionic liquids.<sup>45</sup> MD studies on silica-capped or silica nano-confined 1,3-dialkylimidazolium ILs have also shown that the cation is found close to the surface of the support due to electrostatic interactions, albeit the preferred orientation of the imidazolium ring and the alkyl chain were debatable.<sup>46,47</sup> MD studies have also suggested a dependence of the relative ratio of adsorbed and bulk layers on both the pore size of the support and the loading of the nanoconfined ionic liquid.<sup>46,48</sup>

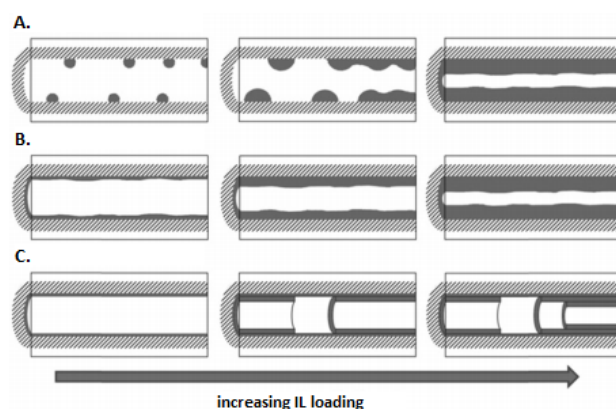


**Figure 3.15:** Schematic representation of the pore filling mode for ionic liquids confined in MCM-41 or amorphous silica (MB): A)  $[C_6C_1im][NTf_2]$ , B)  $[C_6C_1im][OTf]$  and C)  $[C_6C_1im][OAc]$ .<sup>40</sup>

The properties of ionic liquids, supported on ordered and non-ordered mesoporous silica upon incipient wetness impregnation ( $\epsilon_{IL} = 5 - 85 \%$ ), have also been recently investigated; challenging the oversimplified model of the consistent formation of an IL layer with a homogeneous thickness.<sup>40</sup> Both the support and the anion of the ionic liquid had an impact on the surface coverage, as indicated by nitrogen sorption, mercury intrusion and  $^{129}Xe$  NMR spectroscopy experiments.<sup>40</sup>  $[C_6C_1im][OTf]$  was found to be successively evenly distributed on the surface of MCM-41 whilst  $[C_6C_1im][OAc]$  showed an heterogeneous coverage due to stronger ion-ion interactions (Figure 3.15). The very hydrophobic  $[C_6C_1im][NTf_2]$  exhibited the formation of drops/aggregates at low  $\epsilon_{IL}$  values whereas a layer surface

coverage was elucidated at higher loadings (Figure 3.15).<sup>40</sup> When the same ionic liquids were confined in disordered silica, the narrowing in the pore diameter distribution indicated that the smaller mesopores were filled first, as indicated by N<sub>2</sub>-sorption experiments (Figure 3.16). Interestingly, the pore filling for SILPs that were based on SBA-15, with a microporosity of 0.11 cm<sup>3</sup> g<sup>-1</sup>, followed a pore filling mode where the successive filling of mesopores starting once the micropores were filled.<sup>40</sup>

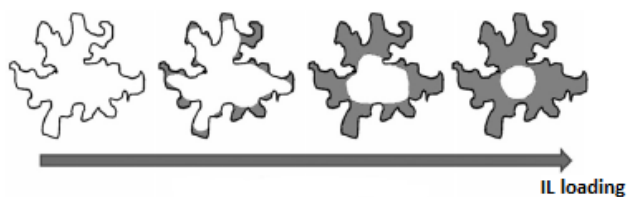


**Figure 3.16:** Schematic representation of the pore filling mode for ionic liquids confined in amorphous silica (MB).<sup>40</sup>

A relatively small number of studies has been published on using static and/or MAS NMR spectroscopy for investigating interactions within supported ionic liquid phases. One of the first examples involved [C<sub>4</sub>C<sub>1</sub>im]Cl·AlCl<sub>3</sub>/SiO<sub>2</sub> (X<sub>AlCl<sub>3</sub></sub> = 0.60) where the interactions between silica and the chlorometallate ionic liquid were studied using <sup>29</sup>Si and <sup>27</sup>Al MAS NMR spectroscopy.<sup>6,9</sup> Based on <sup>27</sup>Al MAS NMR spectroscopy, the anionic dimers of [Al<sub>2</sub>Cl<sub>7</sub>]<sup>-</sup> were covalently bound to the support through the M-OH groups of the latter. Additionally, both FT-IR and <sup>29</sup>Si CP MAS NMR spectroscopy indicated the disappearance of the hydroxyl groups on the surface of the supports upon the incipient wetness impregnation of the ionic liquid onto SiO<sub>2</sub> (ε<sub>IL</sub> = 13 – 35 %). ssNMR has also been used as a characterization tool for [C<sub>2</sub>C<sub>1</sub>im][NTf<sub>2</sub>] and [C<sub>4</sub>C<sub>1</sub>im][NTf<sub>2</sub>] ILs that were immobilized on silica gel (SiO<sub>2</sub>-100 Å) with IL loadings up to 40 vol%.<sup>39</sup> <sup>1</sup>H MAS NMR spectroscopy was applied there in order to understand the underlying pore filling mechanisms as a function of α<sub>IL</sub>.<sup>39</sup> The NMR signals assigned to the -CH<sub>2</sub> protons, adjacent to the imidazolium ring, and the hydrogen-bonded silanol protons were affected the most, with the latter signals increasing in intensity upon reducing the α<sub>IL</sub> from 40 vol% to 10 vol%. The formation of a hydrogen-bonding network between the ions of [C<sub>4</sub>C<sub>1</sub>im][PF<sub>6</sub>] (ε<sub>IL</sub> = 20 %) and the silanol groups of amorphous silica gel has also been suggested via <sup>1</sup>H and <sup>19</sup>F MAS NMR spectroscopy.<sup>49</sup> The inorganic support appeared to have a great effect on the phase behaviour of the supported IL. For example, [C<sub>4</sub>C<sub>1</sub>im][PF<sub>6</sub>] behaved almost as in the liquid phase in silica gel-based SILPs, albeit with a restricted mobility, as indicated by the line width of the ssNMR resonances.<sup>50</sup> Additionally, it was suggested that the contact between [C<sub>4</sub>C<sub>1</sub>im][PF<sub>6</sub>] and silica gel occurred via hydrogen-bonding through the aromatic protons of the cation whereas it was the α-protons that participated in interactions between the IL and a negatively charged clay surface.<sup>50</sup> Relaxation-time measurements can also provide additional insights

regarding the dynamics of the confined ionic liquids.  $^1\text{H}$  MAS NMR spectroscopy and temperature-dependent relaxation time measurements have been carried out for the first time in ionic liquids confined in monolithic silica matrices.<sup>51</sup> An increase in the spin-lattice relaxation times ( $T_1$ ) as a function of temperature was observed for the bulk liquid whereas the confined IL exhibited a relaxation time minimum at 270 K and an increase of  $T_1$  upon further decreasing the temperature.<sup>51</sup> This phenomenon was attributed to a melting point depression for the ionogel, similar to what has been demonstrated for mesoporous silica-based SILPs via temperature-resolved  $^2\text{H}$  and  $^{19}\text{F}$  solid-state NMR spectroscopy.<sup>52</sup> NMR relaxation measurements for  $^1\text{H}$  spin-lattice ( $T_1$ ) and spin-spin ( $T_2$ ) relaxation times have been used for studying the decrease in the dynamic properties of  $[\text{C}_4\text{C}_1\text{im}][\text{NTf}_2]$  when confined in mesoporous silica at varying loading fractions.<sup>53</sup> Dielectric relaxation studies have also shown that the size of nanopores governs the dynamics of the IL confined into them, studying the confinement of  $[\text{C}_4\text{C}_1\text{im}][\text{PF}_6]$  in mesoporous silica gel ( $\epsilon_{\text{IL}} = 26 - 65\%$ ).<sup>54</sup> More specifically, two dielectric relaxation peaks were identified, attributed to the IL bound on the pore wall surface and the molecules found in the central zone of the nanopores with the latter exhibiting a bulk-like dynamic behaviour.<sup>54</sup>

### 3.2.3.1 $[\text{C}_4\text{C}_1\text{im}]\text{Cl}\cdot\text{ZnCl}_2$ ( $X_{\text{ZnCl}_2} = 0.67$ )-based SILPs, IL - silica gel (60 Å and 150 Å) support interactions.

The investigation of the SILP catalysts, prepared upon the physisorption of  $[\text{C}_4\text{C}_1\text{im}]\text{Cl}\cdot\text{ZnCl}_2$  ( $X_{\text{ZnCl}_2} = 0.67$ ) onto  $\text{SiO}_2$ -60 Å ( $\epsilon_{\text{IL}} = 10 - 100\%$ ) or  $\text{SiO}_2$ -150 Å ( $\epsilon_{\text{IL}} = 10 - 60\%$ ), was completed by both static and MAS solid state NMR spectroscopy. The static spectra of the  $\text{SiO}_2$ -60 Å-based SILPs are illustrated in Figure 3.17.  $^1\text{H}$  NMR static spectra in solids are dominated by dipole-dipole coupling between protons as their chemical shift anisotropy (CSA) is small. These line shapes can be narrowed by rapid molecular motion on the NMR timescale. A broad component was present in the spectrum of the parent support as well as all the spectra of the SILP samples. Additionally, there is an apparent increase in the spectral resolution and a clear change in the peak shape upon increasing the loading of the ionic liquid. A narrowing of the peaks is observed upon increasing  $\epsilon_{\text{IL}}$ . Consequently, transitioning towards a state of lower viscosity is observed at higher loadings, albeit the dynamics of bulk IL are not attained. This was confirmed upon the analysis of the full width at half maximum (FWHM, Hz) of the static  $^1\text{H}$  NMR spectra of the SILP materials. FWHM rapidly decreased upon filling the pores of the support, reaching a plateau at  $\epsilon_{\text{IL}} = 60\%$  (Figure 3.18). A similar dependence of FWHM on the composition of SILPs was also observed for the  $\text{SiO}_2$ -150 Å-supported ionic liquids (**Appendix**, Figure 3.44). However, the measured FWHM (Hz) of the  $\text{SiO}_2$ -60 Å-based SILP at  $\epsilon_{\text{IL}} = 10\%$  was higher (11243 Hz) in comparison with the respective value of SILP10(150A) (10066 Hz). It is therefore deduced that the nanoconfinement of the IL within smaller pores results into a lower viscosity at  $\epsilon_{\text{IL}} = 10\%$ . Additionally, it was detected that reaching  $\epsilon_{\text{IL}} = 60\%$  on



SiO<sub>2</sub>-60 Å (FWHM: 5888 Hz) resulted into approaching the dynamics of the bulk IL (FWHM: 5654 Hz) in contrast to SILP60(150A) (FWHM: 6251 Hz).

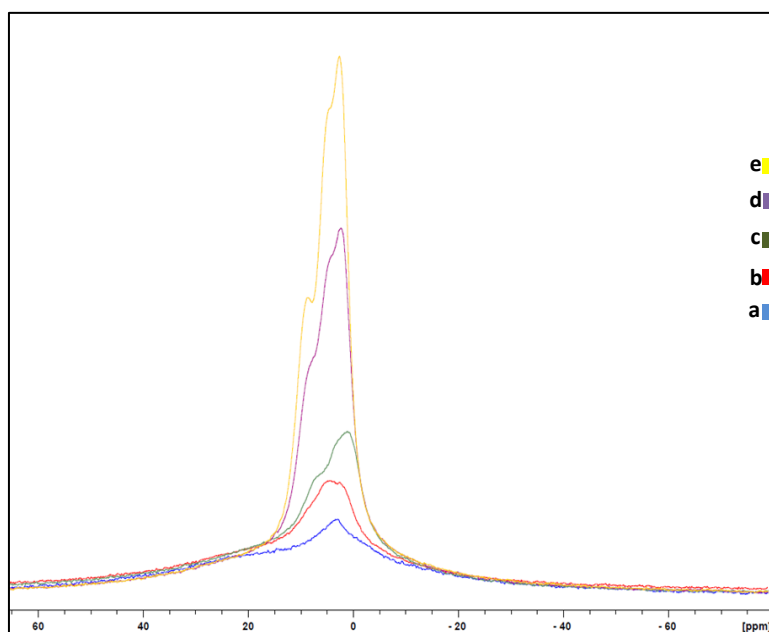


**Figure 3.17:** Static <sup>1</sup>H NMR spectra of SiO<sub>2</sub>-60 Å-based SILPs as a function of  $\epsilon_{IL}$ ; [C<sub>4</sub>C<sub>1</sub>im]Cl·ZnCl<sub>2</sub> ( $X_{ZnCl_2} = 0.67$ )  
a) Parent support (SiO<sub>2</sub>-60 Å), b)  $\epsilon_{IL} = 10\%$ , c)  $\epsilon_{IL} = 30\%$ , d)  $\epsilon_{IL} = 60\%$  and d)  $\epsilon_{IL} = 100\%$

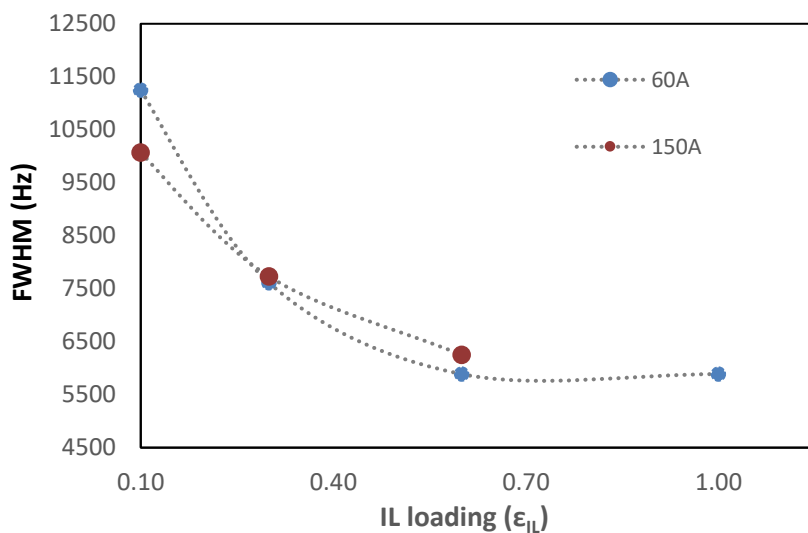


**Figure 3.18:** Composition dependence of the full width at half maximum (FWHM, Hz) of the static <sup>1</sup>H NMR spectra of SiO<sub>2</sub>-60 Å- and SiO<sub>2</sub>-150 Å-based SILPs as a function of  $\epsilon_{IL}$  ([C<sub>4</sub>C<sub>1</sub>im]Cl·ZnCl<sub>2</sub> ( $X_{ZnCl_2} = 0.67$ )). *The fitted curves serve as a visual guide.*

<sup>1</sup>H MAS NMR spectroscopy studies have previously shown that water exhibits strong hydrogen-bonding interactions with silanol groups, with different water phases forming in mesoporous silica-based materials.<sup>55,56</sup> Free silanols have a distinct <sup>1</sup>H signal in comparison with hydrogen-bonded Si-OH groups, similarly to free and hydrogen-bonded water.<sup>39,55</sup> Assigning the resonances to free silanols, hydrogen-

bonded silanols, free H<sub>2</sub>O and hydrogen-bonded H<sub>2</sub>O, with absolute certainty, can be challenging. However, the nature of the surface silanol groups can be elucidated. Studying the <sup>1</sup>H NMR spectra and the T<sub>1</sub> (spin-lattice) relaxation times of silica gel samples, at different stages of hydration, has been previously attempted in order to study surface silanols.<sup>57</sup> It was found that two silanol peaks were present, even upon the evacuation of silica gel at 200 °C.<sup>57</sup> A sharp peak at 1.7 ppm was assigned to isolated silanols whereas a broad peak at 3.0 ppm was attributed to hydrogen-bonded Si-OH moieties with the latter becoming eliminated by thermal dehydration at 500 °C.<sup>57</sup>

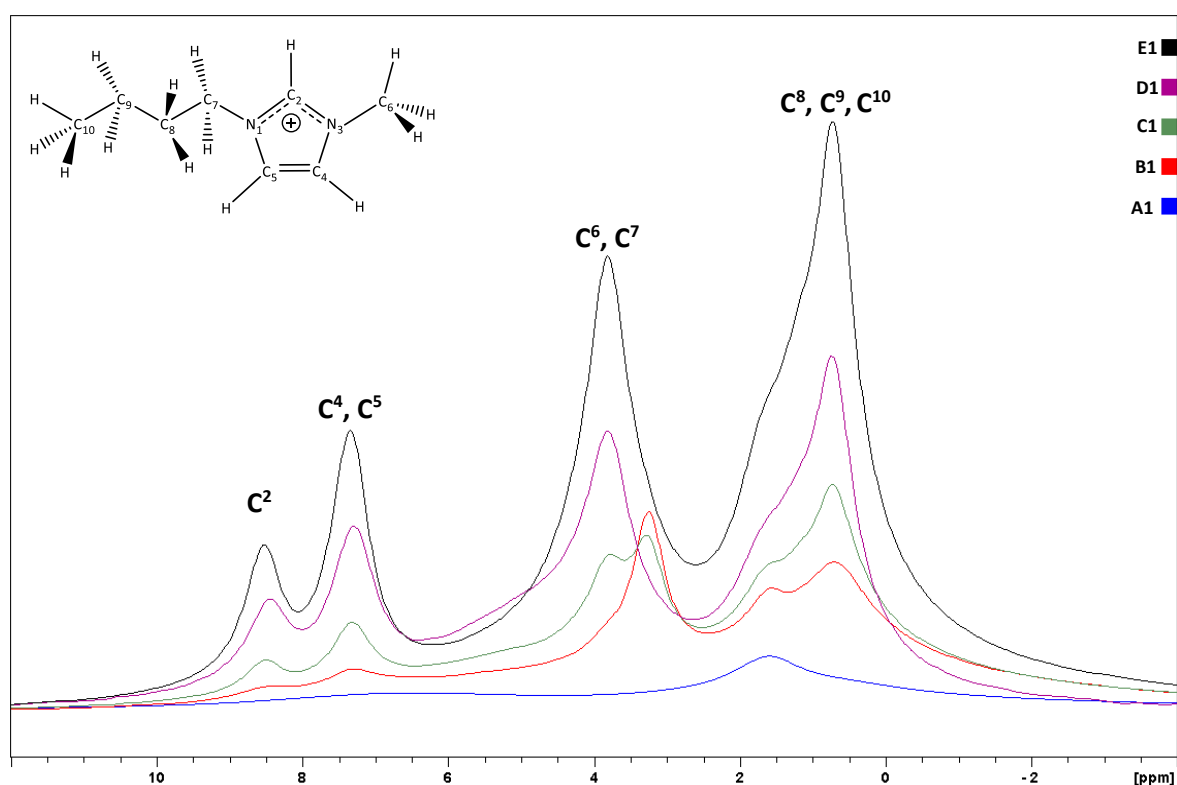


**Figure 3.19:** <sup>1</sup>H MAS NMR spectra of SiO<sub>2</sub>-60 Å-based SILPs with variable loadings of [C<sub>4</sub>C<sub>1</sub>im]Cl·ZnCl<sub>2</sub> (X<sub>ZnCl<sub>2</sub></sub> = 0.67) Ionic liquid loading (ε<sub>IL</sub>): A1: 0 %, B1: 10 %, C1: 30 %, D1: 60 % and E1: 100 %

In this work, the <sup>1</sup>H MAS NMR spectra of both calcined parent supports, SiO<sub>2</sub>-60 Å and SiO<sub>2</sub>-150 Å, contained a sharp peak at 1.7 ppm whereas a broad resonance, with a maximum at 6.8 ppm was observed as well (Figure 3.19 & **Appendix**/Figure 3.45). The sharp peak at δ < 1 ppm was assigned to isolated silanols whereas the broad peak at δ > 5 ppm was assigned to hydrogen-bonded Si-OH moieties. In addition to screening the parent supports, SILP catalysts, with varying IL loadings were also tested by <sup>1</sup>H MAS NMR spectroscopy, yielding relatively well-resolved signals for the ionic liquid ([C<sub>4</sub>C<sub>1</sub>im]Cl·ZnCl<sub>2</sub>, X<sub>ZnCl<sub>2</sub></sub> = 0.67) (Figure 3.19). Interestingly, a new peak was observed at 3.3 ppm for both ε<sub>IL</sub> = 10 % and ε<sub>IL</sub> = 30 %. A broad shoulder, rather than a sharp peak, was also observed for the SiO<sub>2</sub>-60 Å-based SILPs at ε<sub>IL</sub> ≥ 60 %. Similar trends were observed for the SILP materials that were prepared from calcined SiO<sub>2</sub>-

150 Å ( $\epsilon_{IL} = 10\% - 60\%$ ) with a new peak arising at  $\delta = 3.3$  ppm. However, the peak corresponding to hydrogen-bonded silanols was the most prominent for  $\epsilon_{IL} = 10\%$  and a broad shoulder appeared at  $\epsilon_{IL} \geq 30\%$  (**Appendix**, Figure 3.45). Overall, there was no indication of changes in the chemical shift of the protons of the imidazolium cation across the tested SILP catalysts, suggesting that the IL might exist as islands/aggregates upon filling the pores of silica gel with  $[C_4C_{1im}]Cl \cdot ZnCl_2$  ( $X_{ZnCl_2} = 0.67$ ). It is proposed that the observed IL/support interactions may occur by intermolecular hydrogen-bonding between the surface silanols and the anionic species,  $[ZnCl_4]^{2-}$  and  $[Zn_2Cl_6]^{2-}$ . Nonetheless, the anion-pore wall interactions will have to be investigated further to confirm this hypothesis. The proposed interactions are expected to affect the polarity of the Si-OH bonds by removing electron density from the silanol moiety upon the nanoconfinement of the IL. As a result, it was observed that the Si-OH protons were shifted downfield ( $\delta = 3.3$  ppm) with respect to those of those in the isolated silanols ( $\delta = 1.7$  ppm).

The measurement of the spin-lattice ( $T_1$ ) relaxation time for  $^1H$ , has been attempted for the studied Lewis acidic SILPs as a function of  $\epsilon_{IL}$ . The  $T_1$  relaxation time corresponds to the decay constant for the recovery of the component of the nuclear spin magnetization vector parallel to the external magnetic field ( $M_z$ ) to its thermal equilibrium value.<sup>58</sup> In thermodynamical equilibrium, the nuclear magnetization is parallel to the external field ( $B_0$ ). When the nuclear magnetic moments are rotated into the x-y plane by a  $\pi/2$  pulse, a state that is very different to equilibrium is produced. The magnetization reverts to the initial equilibrium via relaxational processes with a characteristic relaxation time. Energy exchange, between the nuclear spins and their environment, occurs with the longitudinal relaxation ( $M_z$ ). In this work, the measurement of the  $T_1$  relaxation times was performed by using the standard inversion recovery pulse sequence (3.9).<sup>58</sup> The decay of  $M_z$  is given by the Bloch equation (3.8) and the integration for the inverse recovery ( $M_z = -M_0$ ) at  $t = 0$  s yields (3.9).

$$\frac{dM_z}{dt} = \frac{M_0 - M_z}{T_1} \quad (3.8)$$

$$M_z(t) = M_0 \left( 1 - 2e^{-\frac{t}{T_1}} \right) \quad (3.9)$$

The spin system is initially excited to a state different to equilibrium and the nuclear magnetization parallel to the external field ( $M_z$ ) is monitored. The excitation is accomplished by an inversion pulse ( $180^\circ$ ) along the z-axis ( $t = 0$  s,  $M_z = -M_0$ ).<sup>58</sup> After a time delay ( $\tau$ ) from the initial pulse, a  $\pi/2$  pulse is applied to rotate the magnetization into the x-y plane (Figure 3.20). The magnetization recovery curves are obtained for a set of time delays and the  $T_1$  relaxation time is estimated by an experimental fit to

$M_z(t)$  (nonlinear regression). When multiple  $T_1$  times are fitted for one sample, the contribution of each component to the relaxation behaviour can be estimated as well. Any factor which slows molecular motion is expected to shorten the spin-lattice relaxation time ( $T_1$ ).

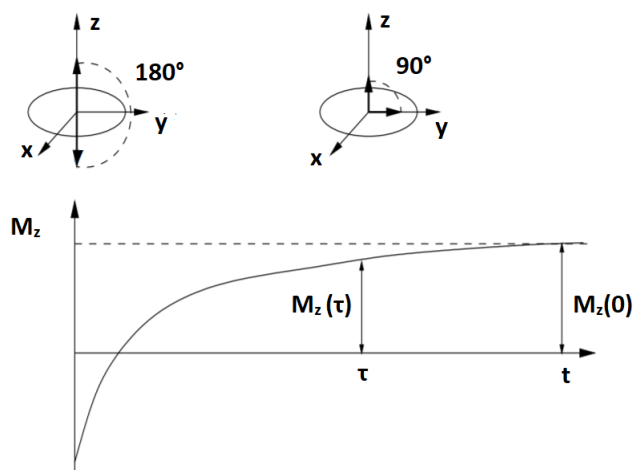


**Figure 3.20:** Schematic representation of the Inversion recovery pulse sequence

The MAS NMR analysis (Figure 3.19, **Appendix**/Figure 3.45) for determining the  $^1\text{H}$   $T_1$  values across the cation of the nanoconfined  $[\text{C}_4\text{C}_{1\text{im}}]\text{Cl}\cdot\text{ZnCl}_2$  ( $X_{\text{ZnCl}_2} = 0.67$ ) had a few limitations. An interference of the support was observed for all SILPs in regards with the peaks found near those of the isolated Si-OH groups or the hydrogen-bonded silanols. Consequently, four peaks were taken into consideration for calculating the  $^1\text{H}$   $T_1$  values across the imidazolium cation: (1)  $\text{C}^2$ , (2)  $\text{C}^4/\text{C}^5$ , (3)  $\text{C}^6/\text{C}^7$  and (4)  $\text{C}^8/\text{C}^9/\text{C}^{10}$ , corresponding to different groups of protons (Figure 3.19). A single-component fitting function was applied for the  $\text{SiO}_2$ -60 Å-based SILPs with  $\epsilon_{\text{IL}} = 60\%$  or  $100\%$ . However, poor fitting was obtained when one component was considered for the SILPs with lower loadings of IL:  $\epsilon_{\text{IL}} = 10\%$  or  $30\%$ . As a result, the contribution of two components was accounted for the  $T_1$  estimations of these SILP materials. The same approach applied for the  $\text{SiO}_2$ -150 Å-based SILPs, albeit a two-components fitting was necessary only for the SILP material at  $\epsilon_{\text{IL}} = 10\%$ . When two  $^1\text{H}$   $T_1$  relaxation times were fitted for these samples, the accuracy of the experimental fitting improved with the residual sum square (RSS) values increasing by one or two orders of magnitude (**Appendix**, Table 3.11). The component with a  $^1\text{H}$   $T_1$  value of approximately 1.2 s was consistent in each peak and it was assigned to residual moisture. The second component, with a smaller  $^1\text{H}$   $T_1$  value ( $\approx 0.2$  s), was finally used for comparing the  $^1\text{H}$   $T_1$  relaxation times across the cation of  $[\text{C}_4\text{C}_{1\text{im}}]\text{Cl}\cdot\text{ZnCl}_2$  ( $X_{\text{ZnCl}_2} = 0.67$ ) when confined in  $\text{SiO}_2$ -60 Å ( $\epsilon_{\text{IL}} = 10\%$  &  $30\%$ ) or  $\text{SiO}_2$ -150 Å ( $\epsilon_{\text{IL}} = 10\%$ ).

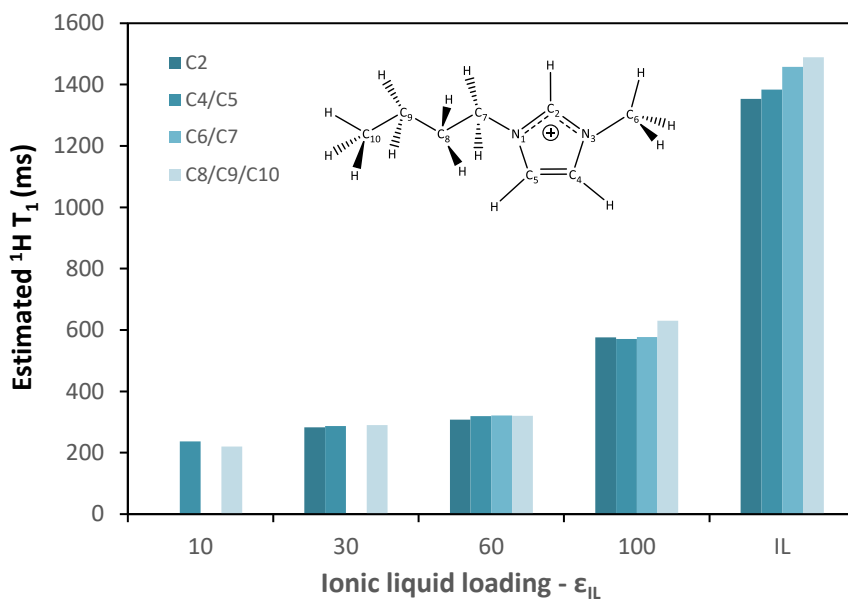


**Figure 3.21:** Estimated  $^1\text{H}$   $T_1$  (s) relaxation times across the imidazolium cation ( $\text{C}^2 - \text{C}^{10}$ ) for the  $\text{SiO}_2$ -60 Å-based SILP catalysts as a function of composition/ $\epsilon_{\text{IL}}$  ( $[\text{C}_4\text{C}_1\text{im}]\text{Cl}\cdot\text{ZnCl}_2$  ( $X_{\text{ZnCl}_2} = 0.67$ ))

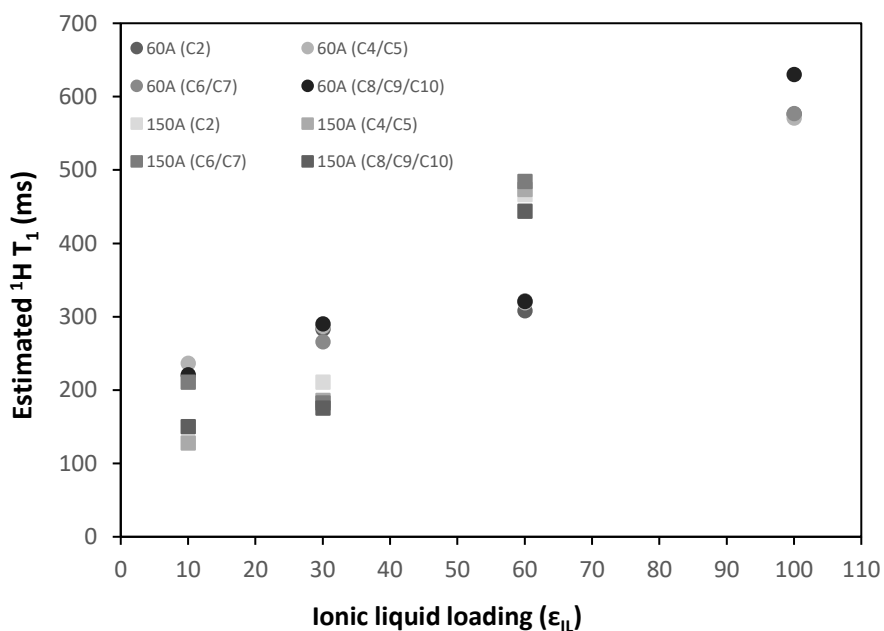


**Figure 3.22:** Comparison of the estimated  $^1\text{H}$   $T_1$  relaxation times across the imidazolium cation for the Lewis acidic,  $\text{SiO}_2$ -60 Å-based SILPs as a function of composition/ $\epsilon_{\text{IL}}$  ( $[\text{C}_4\text{C}_1\text{im}]\text{Cl}\cdot\text{ZnCl}_2$  ( $X_{\text{ZnCl}_2} = 0.67$ )).

It can be deduced that there is a consistent increase of the  $T_1$  values across the cation as a function of  $\epsilon_{\text{IL}}$  and a small increase in the mobility of the butyl chain can be inferred for all cases, including the neat ionic liquid (Figure 3.21). Combining these data with those obtained from static spectra (FWHM), it can

be suggested that the dynamics of the ionic liquid are affected by pore wall/IL interactions that become more prominent at lower loadings. The comparison (Figure 3.22) of the  $^1\text{H}$   $T_1$  relaxation times across the imidazolium cation of  $[\text{C}_4\text{C}_{1\text{im}}]\text{Cl}\cdot\text{ZnCl}_2$  ( $X_{\text{ZnCl}_2} = 0.67$ ) was also examined for when the ionic liquid was physisorbed on calcined  $\text{SiO}_2$ -60 Å or  $\text{SiO}_2$ -150 Å (**Appendix**, Figure 3.46). It can be observed that lower  $T_1$  values were obtained for the hydrogen nuclei when the ionic liquid was confined in the larger pore size-support at  $\epsilon_{\text{IL}} = 10\%$  and  $\epsilon_{\text{IL}} = 30\%$ , indicating differences in the pore-filling mode when compared to the nanoconfinement of the IL in  $\text{SiO}_2$ -60 Å. Additionally, a more remarkable change of the  $^1\text{H}$   $T_1$  value was found when the loading of the ionic liquid increased from 30 % to 60 % in comparison to the observed when the IL was supported on  $\text{SiO}_2$ -60 Å. Taking into consideration the pore area distributions (BJH) for both types of SILPs (**Appendix**, Figure 3.42), it becomes apparent that there is a larger difference in the pore area distribution of the  $\text{SiO}_2$ -150 Å-based SILP catalysts when the IL loading was increased from 30 % to 60 % in comparison to what has been estimated for the respective  $\text{SiO}_2$ -60 Å-based SILPs. This could potentially explain any differences or similarities in the pore wall (silanols)/IL interactions as reflected at the  $^1\text{H}$   $T_1$  relaxation times of the ionic liquid.

### 3.2.4 Lewis acidic [C<sub>4</sub>C<sub>1</sub>im]Cl·ZnCl<sub>2</sub> (X<sub>ZnCl<sub>2</sub></sub> = 0.67)-based SILPs; Thermal stability

The effect of the chemical structure of ionic liquids on their short-term and long-term stability has been extensively studied (Chapter 2, Section 2.3.3 & 2.3.6). However, there is a limited number of studies focusing on the impact of nanoconfinement on the thermal stability of ionic liquids. [C<sub>4</sub>C<sub>1</sub>im][PF<sub>6</sub>]-based SILPs have previously exhibited a decreased thermal stability ( $T_d = 258$  °C) in comparison with the bulk IL ( $T_d = 304$  °C) upon its confinement in silica ( $D_p = 2 - 6$  nm) by ultra-high vacuum ( $1 \times 10^{-5}$  Pa).<sup>59</sup> A two-step thermal decomposition was observed for [C<sub>4</sub>C<sub>1</sub>im][PF<sub>6</sub>]/SiO<sub>2</sub> in contrast to the neat ionic liquid, suggesting an interaction between the IL and the pore walls of the support.<sup>59</sup> The choice of anion determines the effect of confinement on the thermal stability of the neat IL. For example, the thermal stability of the confined [C<sub>6</sub>C<sub>1</sub>im][OTf] was similar to the bulk IL, without an impact of the type of the support (ordered vs. non-ordered mesoporous silica).<sup>40</sup> However, the stability of the confined [C<sub>6</sub>C<sub>1</sub>im][NTf<sub>2</sub>] was found to decrease for all silica supports, by a maximum of 45 K.<sup>40</sup> In the presence of more nucleophilic anions, such as [OAc]<sup>-</sup>, the thermal stability increased, when confined in silica, by a maximum of 60 K.<sup>40</sup> It was speculated that strong hydrogen-bonding interactions between [OAc]<sup>-</sup> and the surface of the support prevented the decomposition of the imidazolium cation in the absence of available evidence to prove the silica–anion interactions.<sup>40</sup>

Early research studies investigated the influence of inorganic impurities on the thermal stability of 1,3-dialkylimidazolium ILs.<sup>60</sup> An acceleration of the isothermal weight loss was observed upon the addition of amorphous silica or  $\alpha$ -Al<sub>2</sub>O<sub>3</sub>, indicating the catalytic activity of metal oxides on thermal decomposition.<sup>60</sup> The effect of the support itself on the thermal stability of SILPs has also been reported for [C<sub>4</sub>C<sub>1</sub>im][PF<sub>6</sub>], when immobilized on amorphous silica or  $\gamma$ -Al<sub>2</sub>O<sub>3</sub> ( $\epsilon_{IL} = 37$  %), suggesting differences in the strength of IL/support interactions.<sup>49</sup> The  $T_{peak}$  for the thermal decomposition of [C<sub>4</sub>C<sub>1</sub>im][PF<sub>6</sub>]/SiO<sub>2</sub> was much lower (315 °C) in comparison with those of the neat IL and [C<sub>4</sub>C<sub>1</sub>im][PF<sub>6</sub>]/Al<sub>2</sub>O<sub>3</sub> with  $T_{peak}$  values of 425 °C and 434 °C, respectively.<sup>49</sup> The impregnation of different supports, such as Al<sub>2</sub>O<sub>3</sub>, SiO<sub>2</sub> and TiO<sub>2</sub>, with [C<sub>8</sub>C<sub>1</sub>im][PF<sub>6</sub>] ( $\epsilon_{IL} = 5 - 60$  %) has shown that the most thermally stable SILPs were prepared from non-polar supports.<sup>61</sup> A dependence of the thermal stability of [C<sub>4</sub>C<sub>1</sub>im]<sup>+</sup>-based SILPs on both the IL/metal-oxide and interionic interactions has also been demonstrated with the former becoming a dominant factor upon decreasing the surface acidity.<sup>62,63</sup> Nevertheless, the addition of electron-donating groups on the cation or a Lewis basic anion affects the IL/metal-oxide interactions to give the opposite effect and thermal stability limits increase upon decreasing the surface acidity.<sup>64</sup> Reduced interionic interactions resulted in the expected increase in the thermal stability of both bulk 1,3-dialkylimidazolium ILs and the respective Al<sub>2</sub>O<sub>3</sub>-based SILPs, with the negative influence of the metal oxide on thermal stability of SILPs being prominent once more.<sup>63</sup> For example, a dramatic decrease of

the  $T_{\text{onset}}$  was observed for  $[\text{C}_4\text{C}_{1\text{im}}][\text{NTf}_2]$  upon physisorption onto  $\gamma\text{-Al}_2\text{O}_3$ , dropping from 421 °C to 303 °C at  $\epsilon_{\text{IL}} = 16.7$  %. More recently, the detailed investigation of the interactions between  $[\text{C}_4\text{C}_{1\text{im}}][\text{BF}_4]$  and high surface area metal oxides of a varying surface acidity ( $\text{SiO}_2$ ,  $\text{TiO}_2$ ,  $\text{Fe}_2\text{O}_3$ ,  $\text{ZnO}$ ,  $\gamma\text{-Al}_2\text{O}_3$ ,  $\text{CeO}_2$ ,  $\text{MgO}$ , and  $\text{La}_2\text{O}_3$ ) has also been accomplished.<sup>65</sup> In the presence of an acidic metal oxide such as  $\text{SiO}_2$ , the cation/metal oxide surface interactions were more apparent in comparison with more basic supports where both the cation and anion had significant interactions with the surface of the inorganic support.<sup>65</sup> Additionally, it was confirmed that metal oxides catalyse the thermal decomposition of an ionic liquid, as observed by the decrease in the activation energy upon decreasing surface acidity of the metal oxides.<sup>65</sup>

**Table 3.3:** Comparison of the  $T_{\text{onset}}$  and  $T_{\text{peak}}$  values for  $\text{SiO}_2\text{-60 \AA}$ -based chlorozincate(II) SILPs.

Sample	$\epsilon_{\text{IL}} / \%$	$T_{\text{onset}} / ^\circ\text{C}$	$T_{\text{peak}} / ^\circ\text{C}$
$[\text{C}_4\text{C}_{1\text{im}}]\text{Cl}\cdot\text{ZnCl}_2, X_{\text{ZnCl}_2} = 0.67$	NA	431	476
SILP10(60A)	10	340	368 <sup>a</sup>
SILP30(60A)	30	370	403 <sup>b</sup>
SILP60(60A)	60	365	400

a, b: a second  $T_{\text{peak}}$  is indicated at temperatures  $> 450$  °C or  $> 500$  °C for  $\epsilon_{\text{IL}} = 10$  % and 30 % respectively

In this work,  $[\text{C}_4\text{C}_{1\text{im}}]\text{Cl}\cdot\text{ZnCl}_2$  ( $X_{\text{ZnCl}_2} = 0.67$ )/ $\text{SiO}_2$ -based SILPs ( $\epsilon_{\text{IL}} = 10$  -60 %) were assessed for their short-term thermal stability by determining their onset decomposition temperature ( $T_{\text{onset}}$ ), under comparable experimental conditions (**Section 3.3**). The  $T_{\text{onset}}$  was extrapolated as the intersection of the baseline and the tangent of the weight dependence on the temperature curve as decomposition occurs (Figure 3.23A, **Appendix**/Figure 3.47). The derivative curves were also used to determine the first derivative peak temperatures ( $T_{\text{peak}}$ ) at which maximum decomposition occurs (Figure 3.23B, **Appendix**/Figure 3.47). The comparison of the  $T_{\text{peak}}$  values of the bulk ionic liquid and the ones of the SILPs aimed to show the net effect of the IL/support interactions on the thermal stability of the ionic liquid. The thermal stability of the bulk chlorozincate(II) ionic liquid was decreased at all loadings with a maximum of approximately 100 °C ( $\epsilon_{\text{IL}} = 10$  %), indicating that silica gel ( $\text{SiO}_2\text{-60 \AA}$ ) catalysed the thermal decomposition of the IL in a significant way (Table 3.3). The  $T_{\text{peak}}$  values as well as the  $T_{\text{onset}}$  values of an IL loading corresponding to 30 % and 60 % did not appear to be significantly different to each other but they were still dramatically decreased over the values corresponding to the bulk ionic liquid (Table 3.3). Additionally, the DTG curves of the SILPs display shoulders or second minima at temperatures greater than 450 °C; hence a two-step thermal decomposition might be indicated. There was no clear peak arising for  $\epsilon_{\text{IL}} = 60$  % but the appearance of a shoulder at  $T = 450$  -500 °C could be still observed. Similar



trends were observed for the SiO<sub>2</sub>-150 Å-based supported SILPs, albeit with an improved thermal stability of the SILP catalyst with a loading of 60 % when compared with the lower loadings of 10 % or 30 % that show a very similar thermal stability profile.

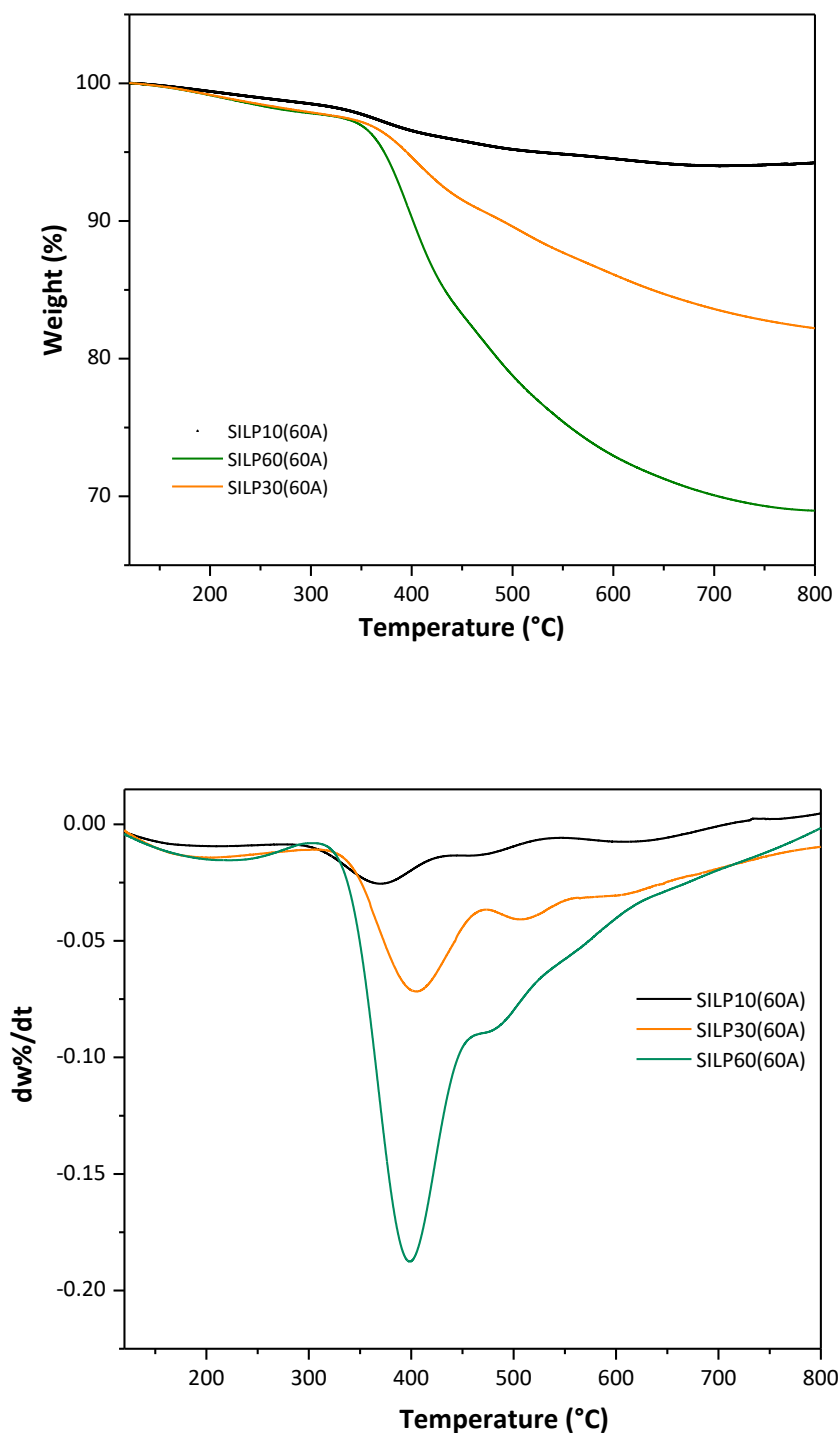


**Figure 3.23:** a) Temperature-ramped (TG) and b) derivative (DTG) curves for SiO<sub>2</sub>-60 Å-based SILPs with variable loadings of [C<sub>4</sub>C<sub>1</sub>im]Cl·ZnCl<sub>2</sub> (X<sub>ZnCl<sub>2</sub></sub> = 0.67) - (ε<sub>IL</sub> = 10 % - 60 %)

### 3.2.5 Study of the fluidisation behaviour of $[C_4C_{1im}]Cl \cdot ZnCl_2$ ( $X_{ZnCl_2} = 0.67$ )/ $SiO_2$ 60 Å-based SILPs

Studying the fluidisation behaviour of the SILP catalysts and approximating their theoretical minimum fluidisation velocity ( $u_{mf}$ ) was accomplished prior to the design and operation of a spouted bed reactor as a modified fluidised bed reactor. The minimum fluidisation point indicates the borderline between a fixed bed and a fluidised bed.<sup>66</sup> A stationary bed can transit to the “fluidised” state by an upwards stream of gas upon reaching gas flow rates that are larger than the minimum fluidisation value ( $V_{mf}$ ).<sup>66</sup> The minimum fluidisation point can be determined by measuring the pressure drop ( $\Delta P$ ) across the bed as a function of the gas flow rate. The heat transfer properties of a fluidised bed reactor are a particularly advantageous feature, with the heat transfer rates being five to ten times greater than those achieved in a packed bed reactor.<sup>67</sup> Increasing the volumetric flow rates or the superficial velocity ( $u$ ) of the gas beyond the minimum fluidisation values,  $V_{mf}$  and  $u_{mf}$  respectively, gas bubbles begin to evolve (Figure 3.24). As the gas velocity increases further, entrainment of solids in the fluidising gas takes place. An increasing amount of solid particles are carried out of the bed and the well-defined surface of the bed disappears.<sup>66,67</sup>

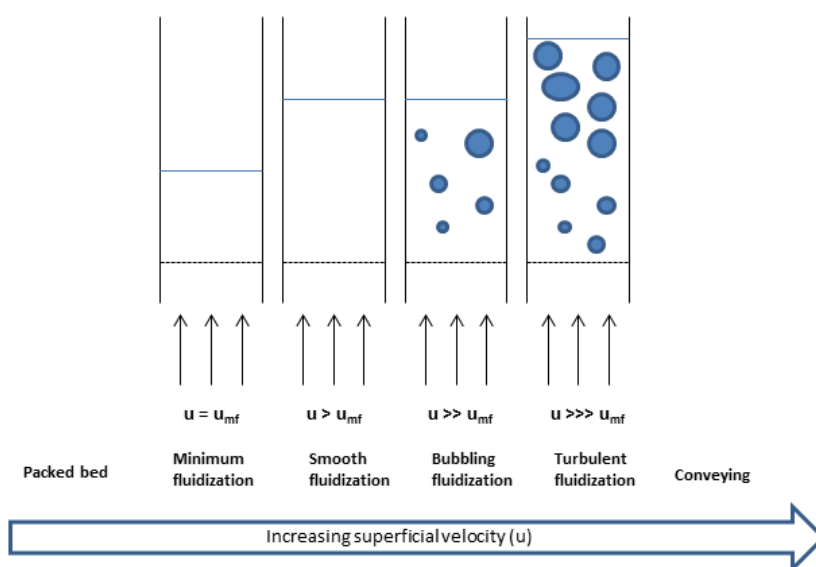


**Figure 3.24:** Fluidisation behaviour as a function of gas velocity ( $u$ )

In 1973, Geldart provided criteria based on which the fluidisation behaviour of solids is classified into four groups, based on the particle properties.<sup>68</sup> Particles in the Geldart Group A are aeratable, forming a homogeneous fluidised bed (smooth fluidisation). Group A materials have relatively small particle sizes ( $30 \mu m < d_p < 125 \mu m$ ) and densities (ca.  $1.4 \text{ g/cm}^3$ ). Group B solids tend to have larger particle sizes ( $40 \mu m < d_p < 500 \mu m$ ) and densities greater than  $1.4 \text{ g/cm}^3$ . In contrast to Group A materials, Group B solids form bubbles at superficial velocities that are not much greater than  $u_{mf}$ . Group C particles are usually

powders with a very small particle size ( $d_p < 30 \mu\text{m}$ ). They tend to form channels composed of fast-moving gas bubbles by-passing the bed; hence fluidisation is hardly feasible. Finally, Group D powders contain large and/or dense particles. They also form bubbles just above the fluidisation point but slugging and the formation of gas channels is observed.<sup>67,68</sup>

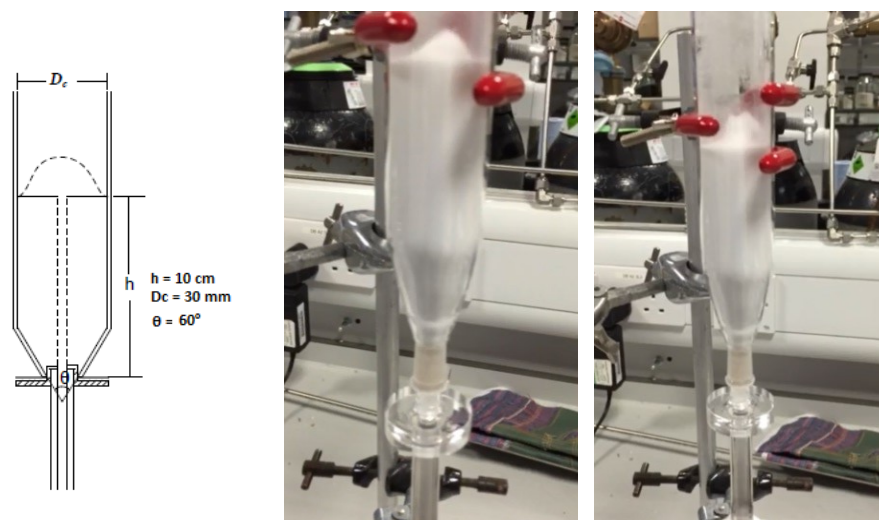


**Figure 3.25:** a) Schematic diagram of the spouted bed reactor configuration and b) cold modelling fluidisation experiments with 20 g silica gel inorganic support ( $\text{SiO}_2$ -60 Å) at ambient temperature ( $(\text{N}_2, \text{rt}, V = 0.5 \text{ L min}^{-1})$ ).

Firstly, cold modelling experiments were performed by visually inspecting the calcined support ( $\text{SiO}_2$ -60 Å) and a SILP catalyst ( $[\text{C}_4\text{C}_{1\text{im}}]\text{Cl}\cdot\text{ZnCl}_2$ ;  $X_{\text{ZnCl}_2} = 0.67$ ,  $\epsilon_{\text{IL}} = 30 \%$ ) as bed materials. The fluidisation experiments were performed in a spouted fluidised bed configuration ( $\text{N}_2, \text{rt}, V = 0.5 \text{ L min}^{-1}$ ). A spouted bed is composed of a central core, the “*spout*”, the surrounding annular region, known as the “*annulus*”, and finally the “*fountain*” that is found on the top part of the bed (Figure 3.25).<sup>69</sup> The quartz assembly consisted of a 120 mm inlet spout tube with an internal diameter of 6 mm and a column ( $D_c = 30 \text{ mm}$ ) with an inverted cone-shaped base, eliminating dead spaces at the bottom of the reactor. Both parts were connected via a standard B10 quartz connection (Soham Scientific, UK). The gas inlet tube was designed to protrude above the base of the quartz liner by 3.6 mm, improving the bed stability and allowing for a maximum bed height.<sup>70</sup> The angle of the base ( $\theta_c$ ) affects the stability of the bed by directing the solid particles towards the spout jet. A literature-based  $\theta_c$  value of  $60^\circ$  was chosen for improving the bed circulation.<sup>71</sup> During the cold testing ( $\text{N}_2, \text{rt}, V = 0.5 \text{ L min}^{-1}$ ) of both the parent support and the SILP catalyst, it was observed that there was an effective mixing of the particles and a very good circulation of the bed that went through pulsating and oscillating cycles under which the fountain at the top of the bed expanded and collapsed in a continuous mode (Figure 3.25).

Subsequently, the fluidisation behaviour of the bed was tested at elevated temperatures (250 °C, N<sub>2</sub>) after the addition of heating tapes. The experimental set-up included a pressure sensor (0 - 6 bar) and a gas flow meter. Both instruments were calibrated and used for the correlation between pressure (mbar) and gas flow rate (V<sub>N<sub>2</sub></sub> / L min<sup>-1</sup>), approximating the V<sub>mf</sub> requirements. The temperature was monitored at different distances from the gas inlet by using three thermocouples (TC Direct) to observe the effect of V<sub>N<sub>2</sub></sub> (L min<sup>-1</sup>) on the thermal distribution across the bed. The temperature of the top (x<sub>1</sub> = 10 cm), middle (x<sub>2</sub> = 5 cm) and bottom (x<sub>3</sub> = 2 cm) parts of the bed was monitored. Calcined SiO<sub>2</sub>-60 Å and SILPs, bearing two loadings of [C<sub>4</sub>C<sub>1</sub>im]Cl·ZnCl<sub>2</sub> (X<sub>ZnCl<sub>2</sub></sub> = 0.67, ε<sub>IL</sub> = 30 % & 60 %), were tested. A sample mass of 20 g resulted to a bed of 10 cm. The quartz line was pre-heated at 150 °C before and after the addition of the sample to remove any residual moisture. The fluidisation testing was performed at 250 °C, testing for gas flow rates between 0.1 L min<sup>-1</sup> and 1 L min<sup>-1</sup>.

**Table 3.4:** Fluidisation testing of SiO<sub>2</sub> 60 Å (250 °C, h<sub>bed</sub> = 10 cm); P (mbar) and T (°C) as a function of V<sub>N<sub>2</sub></sub> (L min<sup>-1</sup>).

V <sub>N<sub>2</sub></sub> (L min <sup>-1</sup> )	P (mbar) <sup>b</sup>	T <sub>1</sub> / °C (x <sub>1</sub> = 2 cm) <sup>a</sup>	T <sub>2</sub> / °C (x <sub>2</sub> = 5 cm) <sup>a</sup>	T <sub>3</sub> / °C (x <sub>3</sub> = 10cm) <sup>a</sup>	ΔT / °C (T <sub>3</sub> - T <sub>1</sub> ) <sup>c</sup>
0.5	14.5 – 19.9	198	193	178	20
0.4	17.2 – 19.9	203	198	181	22
0.3	14.5 – 19.9	212	205	183	29
0.2	14.5 – 22.6	226	212	179	47
<b>0.03</b>	<b>28.0 – 33.7</b>			<b>static bed</b>	

a: distance from the gas inlet, b: the pressure was fluctuating and the P-range (mbar) is reported, c: temperature gradient across the bed

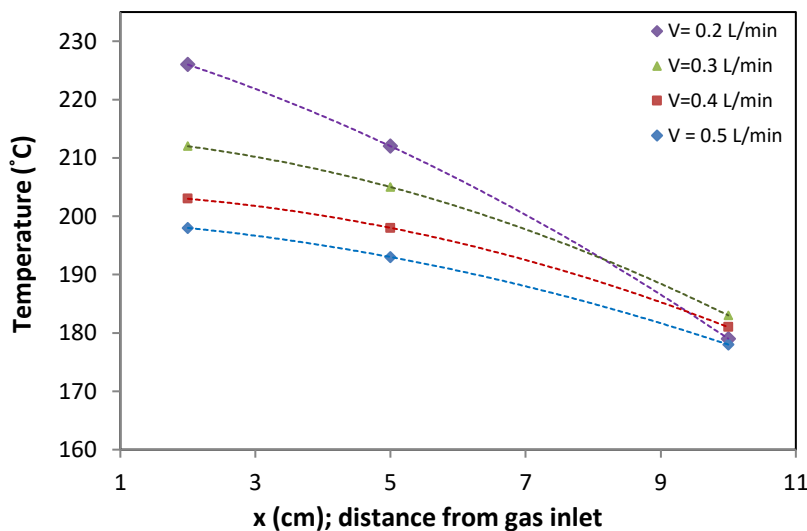


**Figure 3.26:** Temperature gradient across the bed as a function of V<sub>N<sub>2</sub></sub> (L min<sup>-1</sup>) – (SiO<sub>2</sub> 60 Å, 250 °C, h<sub>bed</sub> = 10 cm). The fitted curves serve as a visual guide.

Nitrogen flow rates as low as 0.2 L min<sup>-1</sup> were sufficient for the homogeneous fluidisation of the inorganic support (SiO<sub>2</sub>-60 Å) (Table 3.4). Reducing the flow rate to values lower than 0.1 L min<sup>-1</sup> resulted into a static bed. The gradual increase of the flow rate from 0.2 L min<sup>-1</sup> to 0.5 L min<sup>-1</sup> affected the temperature profile near the gas inlet (T<sub>1</sub>) and the temperature gradient across the bed was reduced (Figure 3.26).

**Table 3.5:** Fluidisation testing of SILP10(60A) ([C<sub>4</sub>C<sub>1</sub>im]Cl·ZnCl<sub>2</sub>, X<sub>ZnCl<sub>2</sub></sub> = 0.67, ε<sub>IL</sub> = 30 %) - (250 °C, h<sub>bed</sub> = 10 cm); P (mbar) and T (°C) as a function of V<sub>N<sub>2</sub></sub> (L min<sup>-1</sup>).

V <sub>N<sub>2</sub></sub> (L min <sup>-1</sup> )	P (mbar) <sup>b</sup>	T <sub>1</sub> / °C (x <sub>1</sub> = 2 cm) <sup>a</sup>	T <sub>2</sub> / °C (x <sub>2</sub> = 5 cm) <sup>a</sup>	T <sub>3</sub> / °C (x <sub>3</sub> = 10cm) <sup>a</sup>	ΔT / °C (T <sub>3</sub> - T <sub>1</sub> ) <sup>c</sup>
<b>0.7</b>	14.5 - 22.6	245	239	232	13
<b>0.6</b>	14.5 - 22.6	245	238	230	16
<b>0.5</b>	14.5 - 22.6	245	239	225	19
<b>0.4</b>	14.5 - 22.6	246	240	217	29
<b>0.3</b>	<b>borderline/spouting</b>				

a: distance from the gas inlet, b: the pressure was fluctuating and the P-range (mbar) is reported, c: temperature gradient across the bed

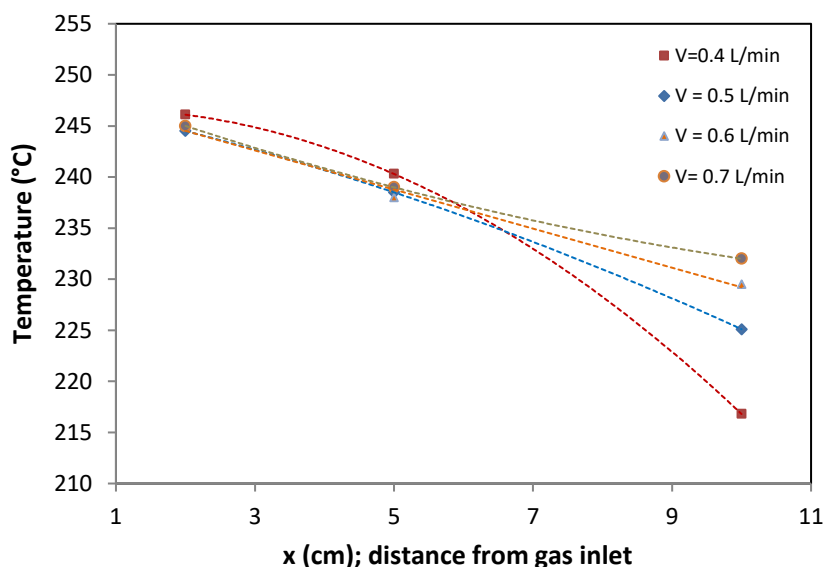


**Figure 3.27:** Temperature gradient across the bed as a function of V<sub>N<sub>2</sub></sub> (L min<sup>-1</sup>) – (SILP30 (60A), 250 °C, h<sub>bed</sub> = 10 cm)  
The fitted curves serve as a visual guide.

In consecutive experiments, the change in the fluidisation properties of the SILP-catalysts was studied (Table 3.5 - 3.6). Coating calcined silica gel with [C<sub>4</sub>C<sub>1</sub>im]Cl·ZnCl<sub>2</sub> (X<sub>ZnCl<sub>2</sub></sub> = 0.67, ε<sub>IL</sub> = 30%) had an effect on the V<sub>mf</sub> (L min<sup>-1</sup>) requirements for detecting bed fluidisation. The V<sub>N<sub>2</sub></sub> (L min<sup>-1</sup>) requirements for achieving smooth fluidisation increased from 0.2 L min<sup>-1</sup> for SiO<sub>2</sub> - 60 Å to a minimum of 0.4 L min<sup>-1</sup> for SILP30 (60A) with spouting and non-optimum bed circulation occurring at lower flow gas flow rates. Additionally, the temperature gradient across the bed was reduced as the gas flow rate was increased

from 0.4 L min<sup>-1</sup> to 0.7 L min<sup>-1</sup> given that the thermocouple was subsumed into the bed more as the bed expanded (Figure 3.27).

**Table 3.6:** Fluidisation testing of SILP60(60A) ([C<sub>4</sub>C<sub>1</sub>im]Cl-ZnCl<sub>2</sub>, X<sub>ZnCl<sub>2</sub></sub> = 0.67, ε<sub>IL</sub> = 60 %) - (250 °C, h<sub>bed</sub> = 10 cm); P (mbar) and T (°C) as a function of V<sub>N<sub>2</sub></sub> (L min<sup>-1</sup>).

V <sub>N<sub>2</sub></sub> (L min <sup>-1</sup> )	P (mbar) <sup>b</sup>	T <sub>1</sub> / °C (x <sub>1</sub> = 2 cm) <sup>a</sup>	T <sub>2</sub> / °C (x <sub>2</sub> = 5 cm) <sup>a</sup>	T <sub>3</sub> / °C (x <sub>3</sub> = 10cm) <sup>a</sup>	ΔT / °C (T <sub>3</sub> - T <sub>1</sub> ) <sup>c</sup>
1.0	14.5-22.6	243	242	227	17
0.8	11.8-25.3	243	241	217	26
0.7	14.5-22.6	245	243	211	34
0.6	9.1-25.3	246	244	206	40
0.5			<b>borderline/spouting</b>		

a: distance from the gas inlet, b: the pressure was fluctuating and the P-range (mbar) is reported, c: temperature gradient across the bed

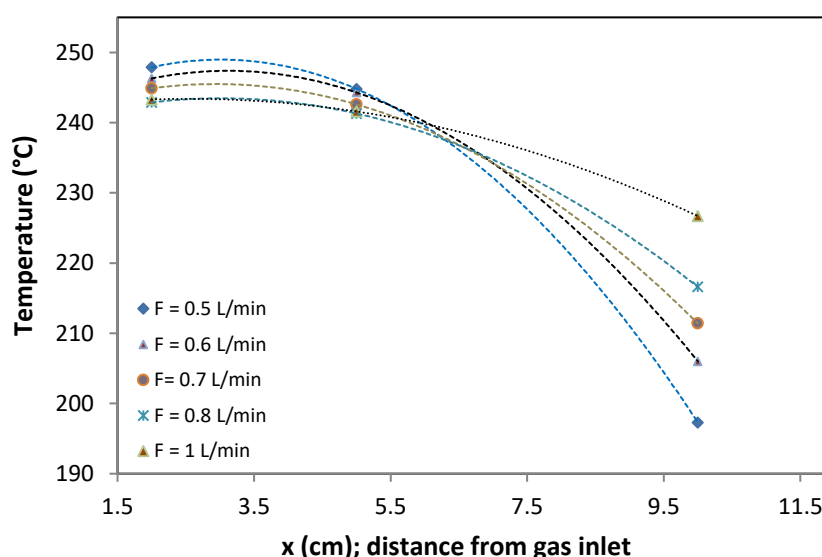


**Figure 3.28:** Temperature gradient across the bed as a function of V<sub>N<sub>2</sub></sub> (L min<sup>-1</sup>) – (SILP60 (60A), 250 °C, h<sub>bed</sub> = 10 cm)  
The fitted curves serve as a visual guide.

Finally, a higher loading of ionic liquid was tested (ε<sub>IL</sub> = 60 %). The results indicated that an increased gas flow rate was required for achieving minimum fluidisation as well as for improving the heat transfer properties across the bed (Figure 3.28, Table 3.6). A minimum of 0.6 L min<sup>-1</sup> of nitrogen was required to avoid spouting whereas increasing the flow rate up to 1 L min<sup>-1</sup> improved the homogeneous mixing of the bed, reducing the temperature differences across the bed. In conclusion, the cold modelling and visual inspection results indicated that a higher ionic liquid loading (ε<sub>IL</sub>) influenced the overall pressure drop and the volumetric gas flow rate (V<sub>mf</sub> / L min<sup>-1</sup>) requirements for minimum fluidisation. In addition to the effect on the minimum requirements for homogeneous fluidisation, increasing the gas flow rate to 1 L min<sup>-1</sup> resulted into significant improvements regarding the temperature gradient across the bed.

Consequently, the monotonic increase in temperature at  $x_3 = 10$  cm with increasing the gas flowrate indicates that the bed is becoming more homogenous.

The theoretical calculation of the minimum fluidisation velocity ( $u_{mf}$ ) was also attempted, focusing on the SiO<sub>2</sub>-60 Å-based SILPs ( $\epsilon_1 = 10 - 60$  %) at  $P_{abs} = 2$  bar and T ranging from 120 °C to 250 °C, given the reaction conditions at which SILPs were later tested as bed material/catalyst (**Section 3.2.7**). The minimum fluidisation velocity was not experimentally measured because the system was designed for high pressure operation with H<sub>2</sub>S and was therefore sealed, with the minimum possible number of sampling ports. The Reynold's number for solid particles at minimum fluidisation conditions ( $Re_{mf}$ ) was therefore calculated based on a literature procedure for predicting the minimum fluidisation velocity.<sup>72</sup> The Archimedes number (Ar) was first calculated by **(3.11)**, where  $D_p$  is the diameter of the particles,  $\rho_p$  (kg/m<sup>3</sup>) is the bulk particle density,  $\rho_f$  (kg/m<sup>3</sup>) and  $\mu_f$  (kg/m s) are the density and the viscosity of the fluid/gas, respectively. The minimum fluidisation velocity ( $u_{mf}$ ) was calculated from the estimated values of  $Re_{mf}$  [**(3.10) & (3.12)**].

$$Re_{mf} = [(33.7)^2 + 0.0408Ar]^{1/2} - 33.7 \quad (3.10)$$

$$Ar = [D_p^3 \rho_f (\rho_p - \rho_f) g] / \mu_f^2 \quad (3.11)$$

$$u_{mf} = \mu_f Re_{mf} / d_p \rho_f \quad (3.12)$$

The viscosity ( $\mu_f$ ) and density ( $\rho_f$ ) values of N<sub>2</sub>, as a function of temperature and pressure, were obtained from the NIST Chemistry Webbook (**Appendix**, Figure 3.49). The values of skeletal density ( $\rho_{skel}$ ) and particle size ( $D_p$ ) were experimentally determined (**Section 3.3**). The skeletal density corresponds to the ratio of the mass of the solid to its volume, excluding the pores and voids spaces between particles in the bulk sample. The bulk density ( $\rho_p$ ) was calculated from the porosity values ( $\phi$ ) and the skeletal density ( $\rho_{skel}$ ) of each sample [**(3.13 & 3.14)**].

$$\phi = V_{pore} / (V_{pore} + V_s) \quad (3.13)$$

$$\rho_{bulk} = \rho_{skel}(1-\phi) \quad (3.14)$$

The porosity ( $\phi$ ) is the ratio of the pore volume ( $V_{pore}$ ) to the total volume of the solid ( $V_s$ ) including the pore space **(3.13)** The pore volume ( $V_{pore}$ ) was determined as the cumulative pore volume (BJH) for pores up to 300 nm. The volume of the particle ( $V_s$ ) was calculated from the skeletal density ( $\rho_{skel}$ ).

The experimentally-measured mean particle size ( $\chi_{50}$ ) of the SiO<sub>2</sub> 60 Å-based materials ranged between 113 µm and 128 µm with the skeletal density ( $\rho_{\text{skel}}$ ) decreasing by ca. 12 % upon augmenting the loading of the IL up to 60 %. The calculated  $\rho_{\text{bulk}}$  increased from 0.88 g cm<sup>-3</sup> for the parent support to 1.40 g cm<sup>-3</sup> for the SILP with a loading ( $\epsilon_{\text{IL}}$ ) of 60 %.

**Table 3.7:** Theoretical  $u_{\text{mf}}$  (cm s<sup>-1</sup>) ( $P_{\text{abs}} = 2$  bar,  $T = 120 - 250$  °C) of [C<sub>4</sub>C<sub>1</sub>im]Cl·ZnCl<sub>2</sub> ( $X_{\text{ZnCl}_2} = 0.67$ )/SiO<sub>2</sub> 60 Å - based SILPs

$\epsilon_{\text{IL}}$ (%)	$V_{\text{pore}}^{\text{a}}$ (cm <sup>3</sup> g <sup>-1</sup> )	$\rho_{\text{skel}}^{\text{b}}$ (g cm <sup>-3</sup> )	$\phi^{\text{c}}$	$\chi_{50}^{\text{c}}$ (µm)	$\rho_{\text{bulk}}^{\text{d}}$ (g cm <sup>-3</sup> )	$u_{\text{mf,calc}}^{\text{e}}$ (cm s <sup>-1</sup> ) [250 °C]	$u_{\text{mf,calc}}^{\text{g}}$ (cm s <sup>-1</sup> ) [200 °C]	$u_{\text{mf,calc}}^{\text{h}}$ (cm s <sup>-1</sup> ) [120 °C]
0	0.70	2.33	0.62	128	0.88	0.249	0.267	0.306
10	0.59	2.21	0.56	117	0.97	0.250	0.268	0.307
30	0.40	2.11	0.46	105	1.14	0.263	0.282	0.323
60	0.23	2.05	0.32	113	1.40	0.348	0.373	0.427

a: pore volume (BJH), b: skeletal density, c: porosity, d: mean particle size., e: bulk density, e, g, h: minimum fluidisation velocity, f: gas flow rate requirements for minimum fluidisation (rt), estimated from  $V_{\text{hot}}$  (L min<sup>-1</sup>)

The particle properties as well as the theoretical values of  $u_{\text{mf}}$  for the parent support (SiO<sub>2</sub>-60 Å) and the Lewis acidic, SiO<sub>2</sub>-60 Å-based SILPs ( $\epsilon_{\text{IL}} = 10 - 60$  %) are summarised in Table 3.7. The minimum fluidisation velocity was estimated at three different temperatures (120 °C, 200 °C and 250 °C), as described in equations (3.10) – (3.14). A gradual increase in the minimum fluidisation velocity ( $u_{\text{mf}}$ ) was estimated when the temperature is dropped from 250 °C to 120 °C. Additionally, the values of  $u_{\text{mf}}$  were estimated to increase as a function of  $\epsilon_{\text{IL}}$  at all temperatures. For example,  $u_{\text{mf}}$  increases from 0.267 cm s<sup>-1</sup> for  $\epsilon_{\text{IL}} = 0$  % to 0.373 cm s<sup>-1</sup> for  $\epsilon_{\text{IL}} = 60$  % (200 °C,  $P_{\text{abs}} = 2$  bar). Accounting for the area of the reactor (7.07 x 10<sup>-4</sup> m<sup>2</sup>), given a diameter of 30 mm, and the constant experimental gas flow rate of 33 ml s<sup>-1</sup> (298 K) (Table 3.8), the superficial velocity ( $u$ ) at the inlet is approximated at 0.074 m s<sup>-1</sup> (200 °C) by dividing the volumetric flow rate at temperature (200 °C) to the area of the reactor. Applying the average bulk density of the solid particles (1169 kg m<sup>3</sup>) and particle diameter (112 µm) across the tested SILPs/bed material (Table 3.7), an average terminal velocity of 0.316 m s<sup>-1</sup> (200 °C, 2 bar) was estimated by using Stoke's law for a sphere falling in a fluid;  $R$  corresponds to the average radius of the particle (m) and  $g$  (m s<sup>-1</sup>) is the gravitational acceleration. Therefore, the terminal velocity is estimated to be much higher than the superficial velocity under the same experimental conditions and a large operation window is predicted without a high risk of entrainment.

$$u = \frac{2}{9} \frac{(\rho_p - \rho_f)}{\mu} g R^2 \quad (3.15)$$



### 3.2.6 Experimental apparatus design

All catalytic experiments were performed in a continuous gas-phase reactor that was built in-house. The assembly was an upgraded version of a pre-existing spouted-bed reactor to study the synthesis of bio-derived thiophenes with Lewis acidic SILPs (Figure 3.29). The design was modified to allow testing the gas phase reaction where liquid reactants were delivered in the vapour phase, reacting with a second gaseous component, and products were separated upon condensation. Any existing infrastructure (main reactor body, heating section/copper electrodes and control unit) is referenced across the text, accordingly. A detailed description of the components of the experimental apparatus is provided in the following sections. A standard operating protocol was developed for testing the SILP catalysts as a bed material for the synthesis of bio-derived 2,5-dimethylthiophene (Section 3.2.7).

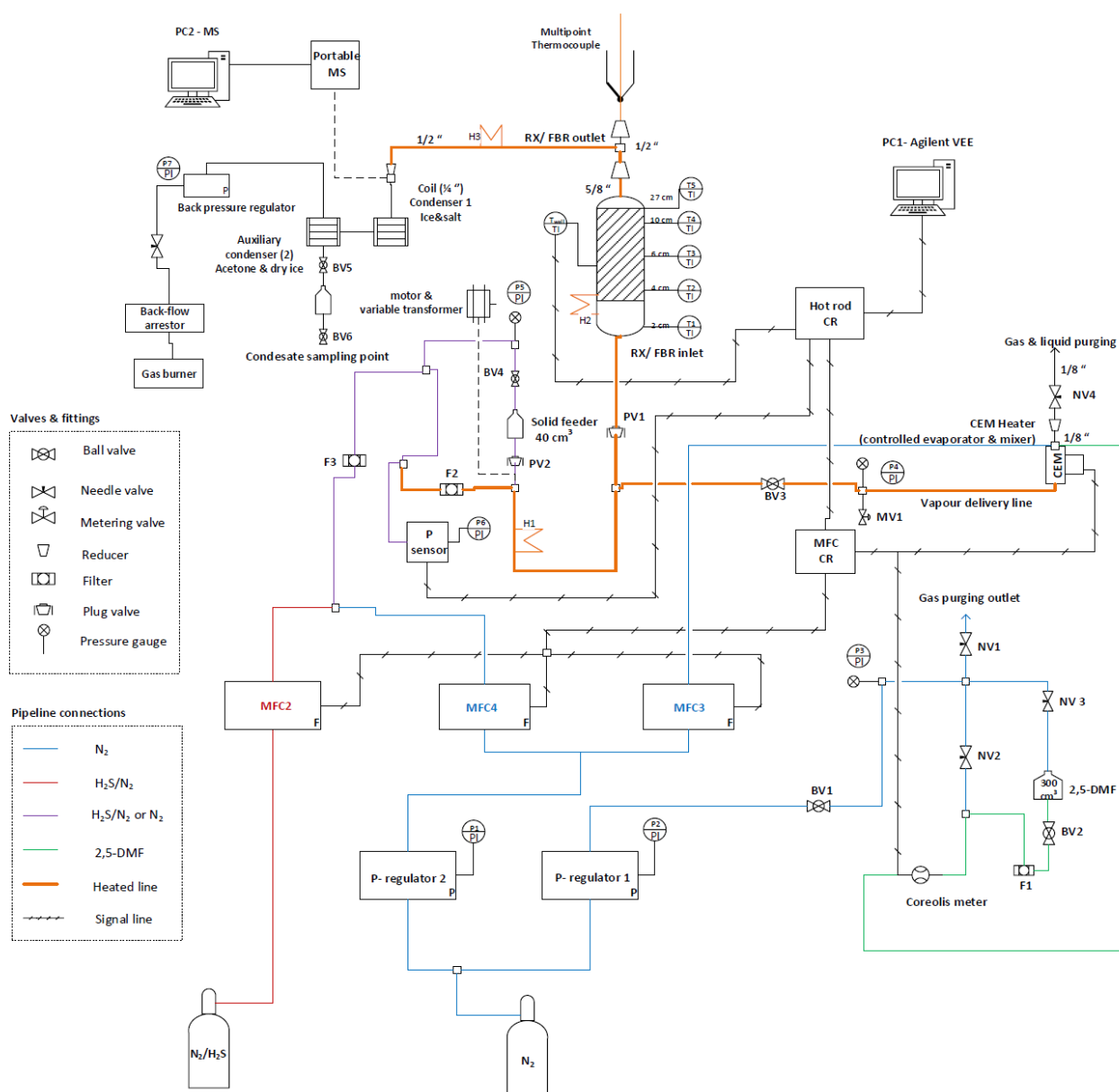


Figure 3.29: Process flow diagram for the gas-phase synthesis of bio-derived thiophenes in a spouted-bed reactor

### 3.2.6.1 Main reactor body description

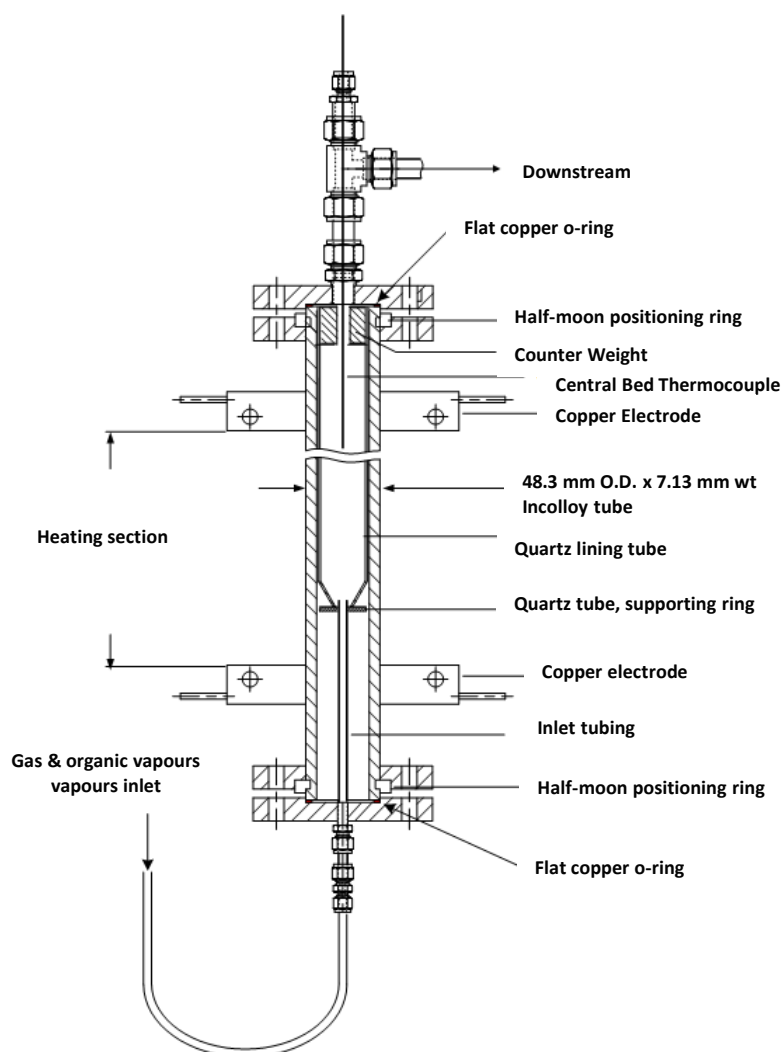


Figure 3.30: Schematic diagram of the main reactor body

The outer shell of the reactor body (wt: 7.13 mm) was made of Incoloy® Alloy 800HT, a nickel-iron-chromium alloy with a high creep-rupture strength, even at high-temperature applications (Figure 3.30).<sup>73</sup> In this work, the temperature did not exceed 250 °C. Top and bottom flanges, made of AISI 316 stainless steel, were connected to the reactor body via pairs of half-moon positioning rings that were found in machined grooves at both ends of the reactor.<sup>73</sup> Additional outer flanges were attached onto the inner flanges by using stainless steel M10 bolts.<sup>73</sup> Moreover, a flat copper-based O-ring was placed between each pair of the flanges to provide a sealed connection. The connection of the reactor to the rest of the experimental set-up was enabled by the addition of 5/8-inch and 5/16-inch fittings that were bored through and welded into the flanges at the top and bottom ends of the reactor, respectively. The internal part of the reactor ( $D_c = 30$  mm), as described in **Section 3.2.5**, was designed as a spouted bed where the gas was introduced through a single nozzle at the centre of the conical base which sat on the

top of a support ring (Figure 3.31). This design has also been previously successfully tested as a mechanically and chemically stable quartz liner to assess the effect of H<sub>2</sub>S on chemical looping combustion in a laboratory scale spouted bed reactor.<sup>73</sup>

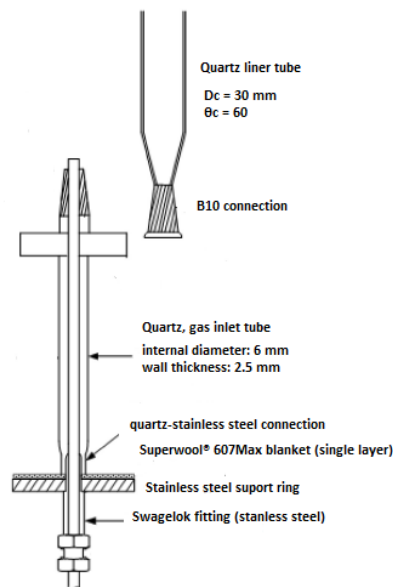


Figure 3.31: Reactor internals; quartz-liner set-up<sup>73</sup>

A 120 mm quartz tube was connected to the main column whereas a quartz ring (D = 32.5mm) provided support and mechanical strength on the quartz assembly. One layer of Superwool® 607Max blanket was placed between the quartz liner and the stainless-steel support ring, in addition to a counter weight on top of the quartz line, for proper sealing of the spouted bed configuration.

### 3.2.6.2 Temperature, pressure and gas flow control – equipment description

The heating section of the reactor was located between two sets of copper electrodes that were attached to the outside of the main reactor body. The electrical power, required to heat the external reactor wall, was supplied by a transformer (2.5 V, 1600 A) through insulated copper cables.<sup>73</sup> The copper cables, connecting the electrodes and the transformer, were cooled by a continuous flow of water passing through 1/8-inch soft copper tubing that was wrapped around the cables. A type K thermocouple was positioned in the middle of the heating section, monitoring the temperature of the reactor wall. The ¼-inch pipework, connecting the bottom part of the CEM heater (**Section 3.2.6.3**) and the inlet of the reactor as well as the connections between the outlet of the reactor and the liquid sampling system (**Section 3.2.6.6**), were heated externally by electrical heating tapes that were connected to two separate heating controllers. A custom-made multipoint thermocouple was used for

measuring and controlling the temperature at five points from the gas inlet of the main reactor body: 2, 4, 6, 10 and 27 cm. The total height of the bed under fluidisation was approximately 10 cm ( $h_{\text{bed}}$ ) and therefore the temperature gradient across the bed was monitored by using the multipoint thermocouple whereas the data obtained at 27 cm allowed for recording the temperature near the outlet of the reactor. All heated sections were insulated by applying three layers of Superwool® 607Max blanket to reduce any heat losses to the environment.

N<sub>2</sub> and gas mixtures of N<sub>2</sub>/H<sub>2</sub>S (1 – 5 % H<sub>2</sub>S) were supplied from pressurised gas cylinders, connected to the base of the reactor assembly. A single-stage regulator was used to control the pressure of N<sub>2</sub> applied to the 2,5-DMF-containing tank (**Section 3.2.6.3**). An additional single-stage pressure regulator was placed before the PID mass flow controllers (mfc). The three mfc were supported on a frame at the bottom of the experimental apparatus, controlling the flow rate of the reactive H<sub>2</sub>S/N<sub>2</sub> mixture, the carrier gas (CEM heater) as well as the flow rate of the make-up gas. An in-line filter was also installed downstream of the mfc that were connected to the inlet of the main reactor body. Pressure gauges were placed at both ends of the reactor to monitor any pressure drop, whereas a back-pressure regulator was used to pressurise the reactor upon the addition of the SILP-based bed.

### **3.2.6.3 Vapour delivery system (2,5-dimethylfuran (2,5-DMF)/N<sub>2</sub>)**

2,5-DMF (bp<sub>760</sub>: 94 °C) was introduced into the reactor in the vapour phase, as a mixture with N<sub>2</sub>. The vapour delivery system delivered controlled amounts of 2,5-DMF (0.12 – 0.15 g min<sup>-1</sup>) that reacted with H<sub>2</sub>S, in a continuous mode, inside the spouted bed reactor. A double-ended stainless-steel cylinder (300 cm<sup>3</sup>) was loaded with 2,5-DMF (200 cm<sup>3</sup>). It was equipped with a needle valve and a ball valve at the top and bottom ends, respectively. The sample cylinder was pressurised by opening the needle valve that was connected to a N<sub>2</sub> cylinder. A pressure gauge was used to monitor the pressure and a needle valve was added as a relief valve. Opening the ball valve, positioned between the lower end of the cylinder and a Coriolis flowmeter, allowed the injection of 2,5-DMF to the mini CORI-FLOW. An in-line particle filter was connected to the ball valve of the sample cylinder, preventing the contamination of the Coriolis meter. The complete system included a CEM heater. The CEM was a combination of a mixing valve, a heating device and a liquid meter with control function, applied in both atmospheric and pressurised processes. The flow rate of 2,5-DMF was controlled to the setpoint value by a control valve and a carrier-gas mixing valve. The flow rate of the carrier gas (N<sub>2</sub>) was controlled by a separate mass flow controller (**Section 3.2.6.2**). The gas/liquid mixture was transferred to the integrated evaporator with N<sub>2</sub> stimulating the evaporation whilst acting as a mixing component to transport the vapours of

2,5-DMF to the reactor. The temperature of the heat exchanger was regulated by a controller that was part of the readout and control unit.

#### **3.2.6.4 Solid SILP catalyst feeding assembly**

The solid feeder was connected to the base of the reactor via a u-shaped ¼-inch tubing-connection, supplying one batch of the SILP catalyst that was fluidized upon the addition of controlled quantities of N<sub>2</sub>. The double-ended stainless-steel cylinder (40 cm<sup>3</sup>, Swagelok®) was equipped with a ball valve and a plug valve at the top and bottom ends, respectively, allowing for the system to be isolated when the SILP catalyst was not supplied to the reactor. The plug valve of sample cylinder was connected to a rotary valve that was attached to variable speed motor. The motor was activated by connecting it to a bench power supply (6 – 10 V). A minimum nitrogen flow of 15 ml s<sup>-1</sup> was necessary to efficiently direct the solid SILP particles to the reactor preventing the blockage of the rotary valve.

#### **3.2.6.5 Process control and data collection**

A control unit was originally designed by the Department of Electronics in collaboration with the Fennell group (Chemical Engineering).<sup>73</sup> In this work, it mainly offered online data acquisition and the temperature control of the reactor assembly. A proportional temperature controller was a key component of the control unit. It was composed of a switch capacitor, a solid-state relay and a variable transformer. The variable transformer was connected in series with the load circuit to control the power that was supplied for heating the external wall of the reactor. The power output, distributed to the load circuit, could be finetuned by adjusting the resistance of the variable transformer. A multipoint thermocouple and a type K thermocouple, measuring the temperature across the bed and the T<sub>wall</sub>, were connected to the control unit. The signals from all thermocouples were logged by a USB-TC input module and were further processed in a program written in Agilent VEE™ 9.0. A USB data acquisition interface (DAQ) was used to obtain an analogue output signal upon converting the control function that was generated by the software. The output signal was processed in a series of signal converters before being transmitted to the switch capacitor and then used as a control signal for the solid-state relay. The solid-state relay could then switch on and off according to the power requirements that were calculated by the process control program. The control program allowed the automation of the PID temperature control but also the real-time adjustment of the gas and liquid flow rates. The mass flow controllers (mfcs), the Coriolis flowmeter and the CEM heater were connected to the computer via a field bus (FLOW-BUS, Bronkhorst). The FLOW-BUS offered the digital communication between the devices whilst allowing for host-control by the process control program (RS232/USB connection). Five temperature

values across the bed, the  $T_{\text{wall}}$ , the temperature of the CEM heater (vapour delivery system) as well as the PID parameters were displayed in real-time. A quadrupole mass spectrometer (Aston Analytical, QMS 422/200), measuring the concentration of unreacted 2,5-DMF and  $\text{H}_2\text{S}$ , was also connected downstream but these data were logged to a separate computer. The peak intensity signals from the portable mass spectrometer were processed in its own software (Quadstar 32-bit), and saved in a separate file.

### 3.2.6.6 Liquid sampling system (LSS) development – Gas/liquid separation

The gas stream at the outlet of the reactor contained a mixture of  $\text{N}_2$  together with unreacted  $\text{H}_2\text{S}$  as well as a mixture of vapours of hydrocarbons such as 2,5-dimethylfuran (2,5-DMF) and 2,5-dimethylthiophene (2,5-DMT). Smaller amounts of 2,5-hexanedione (25-hxd), water and other unknown by-products were also expected to be generated during the continuous reaction process. The gas stream was directed from the reactor outlet to a series of cooling traps. The condensation of the organic vapours, whilst preventing the re-entrainment of the condensed liquid products by the gaseous stream, was a key challenge. Several prototypes were developed before defining an experimental LSS set-up that could allow for an optimised gas/liquid separation. Some of characteristic examples as well as the detailed description of the final LSS experimental set-up, a two-stage vapour trap, are summarized in **Section 3.3.4**. Before using the LSS set-up for the investigation of the synthesis of bio-derived thiophenes in the fluidised bed reactor, the low-temperature vapour trap was tested in the absence of the bed to confirm the maximum recovery of 2,5-DMF. It was found that an average of 86 % ( $\pm 3$  %) of 2,5-DMF could be recovered, accounting for the total input of 2,5-DMF under the tested conditions. The experiments were performed at experimental conditions, similar to the reaction conditions:  $T_{\text{CEM}} = 85$  °C,  $T_{\text{reactor}} = 200$  °C,  $F_{\text{N}_2, \text{total}} = 33$  ml  $\text{s}^{-1}$ ,  $F_{2,5\text{-DMF}} = 0.20$  g  $\text{min}^{-1}$ ,  $t = 30$  min. Achieving 100 % recovery of 2,5-DMF was very difficult given the constant flow of gas during the experiments. All experiments were finally conducted with this LSS set-up, followed by the offline analysis of the collected samples by Gas chromatography/ Mass spectroscopy (GC(MS)).

### 3.2.7 Study of the gas-phase recyclization of 2,5-dimethylfuran (2,5-DMF) to form 2,5-dimethylthiophene (2,5-DMT), catalysed by Lewis acidic chlorozincate(II) SILPs.

#### 3.2.7.1 Preliminary testing (blanks); H<sub>2</sub>S/bed interactions and 2,5-DMF recovery

The gas-phase recyclization of 2,5-dimethylfuran (2,5-DMF) to 2,5-dimethylthiophene (2,5-DMT) was performed in a spouted-bed reactor (Section 3.2.6) by applying Lewis acidic SILPs ( $[\text{C}_4\text{C}_{1\text{im}}]\text{Cl}\cdot\text{ZnCl}_2$  ( $X_{\text{ZnCl}_2} = 0.67$ )) as the bed material. Prior to testing any of the SILPs as a catalyst, preliminary testing was conducted to study any interactions between H<sub>2</sub>S and the reactor components or the parent support of the SILP materials. Two alloys were in contact with H<sub>2</sub>S: AS316 stainless-steel (Cr: 16 – 18 %, Ni: 10 – 14 %) and Incoloy®800HT (Cr: 19 – 23 %, Ni: 30 – 35 %) (Section 3.2.6.1). The corrosion of alloys and metals by H<sub>2</sub>S is known at high temperatures ( $\geq 500$  °C), with a good resistance for high chromium (12 – 20 %) steels and a negative contribution of nickel.<sup>74</sup> The temperatures that were later applied in this work did not exceed 250 °C.

During the preliminary testing stage, a gas analyser (ABB AO2020) was temporarily connected to the outlet of the rig, detecting the amount of H<sub>2</sub>S in the exhaust gaseous stream ( $[\text{H}_2\text{S}]_{\text{output}}$ ). A calibration curve was established, correlating the concentration of H<sub>2</sub>S (ppm) with the signal of the UV-analyser by using H<sub>2</sub>S/N<sub>2</sub> (1 % H<sub>2</sub>S, SIP Analytical Ltd) and N<sub>2</sub> as the make-up gas. The maximum concentration of H<sub>2</sub>S that could be accurately detected did not exceed 6006 ppm. This concentration, corresponding to  $F_{\text{H}_2\text{S}_1\%/N_2} = 15 \text{ ml s}^{-1}$  and  $F_{N_2} = 10 \text{ ml s}^{-1}$  at 1 bar, was first tested in the absence of a bed material at room temperature and 200 °C ( $T_{\text{wall}}$ ). No drop was detected in the concentration of H<sub>2</sub>S at both room temperature and 200 °C ( $t = 15$  min), albeit the  $[\text{H}_2\text{S}]_{\text{input}}$  value was reached with slower kinetics when coolant was added at the two-stage vapour trap assembly. Using the same experimental conditions, calcined SiO<sub>2</sub> 60 Å or SiO<sub>2</sub> 150 Å (20 g) was tested in the presence of H<sub>2</sub>S ( $[\text{H}_2\text{S}]_{\text{input}} = 6006$  ppm). A negligible reduction in the  $[\text{H}_2\text{S}]_{\text{output}}$  ( $< -0.5$  %), given the error of the UV-analyser ( $\pm 0.5$  %), was observed. A concentration of 5984 ppm and 5993 ppm was detected at the outlet of the rig for SiO<sub>2</sub> 60 Å or SiO<sub>2</sub> 150 Å, respectively. A significant drop was observed in the  $[\text{H}_2\text{S}]_{\text{output}}$  value when the parent support (SiO<sub>2</sub> 60 Å) was replaced by one of the Lewis acidic SILPs ( $\epsilon_{\text{IL}} = 60$  %). After a slow increase of the  $[\text{H}_2\text{S}]_{\text{output}}$ , the concentration finally equilibrated at 4000 ppm ( $\sim -30$  % vs.  $[\text{H}_2\text{S}]_{\text{input}}$ ), indicating possible interactions between the Lewis acidic IL and H<sub>2</sub>S. A recent review presented a comprehensive summary on the gas solubility in ILs, suggesting a good solubility of H<sub>2</sub>S.<sup>75</sup> The following order: SO<sub>2</sub>  $\approx$  H<sub>2</sub>S > CO<sub>2</sub> > C<sub>2</sub>H<sub>4</sub> > C<sub>2</sub>H<sub>6</sub> > CH<sub>4</sub> > O<sub>2</sub> > N<sub>2</sub> > H<sub>2</sub> corresponded to a decreasing gas solubility in ILs. The solubility of H<sub>2</sub>S in imidazolium-based ILs increases by decreasing the temperature whereas the effect of the anion remains debatable.<sup>75</sup>

During the development of the low-temperature vapour trap (**Section 3.2.6.6**), it was found that an average of 86 % ( $\pm 3$  %) of 2,5-DMF could be recovered in the absence of the bed ( $T_{\text{CEM}} = 85$  °C,  $T_{\text{reactor}} = 200$  °C,  $F_{\text{N}_2, \text{total}} = 33$  ml s<sup>-1</sup>,  $F_{2,5\text{-DMF}} = 0.20$  g min<sup>-1</sup>,  $t = 30$  min). The recovery of 2,5-DMF was also tested, under the same experimental conditions, when 20 g of calcined SiO<sub>2</sub> 60 Å or one of the Lewis acidic SILPs ( $\epsilon_{\text{IL}} = 30$  %) was added as the bed material. Similar recovery values to what was found for the empty reactor were obtained after 30 min of continuous processing. More specifically, 84 % and 82 % of 2,5-DMF was condensed and recovered in the presence of SiO<sub>2</sub> 60 Å and the SILP catalyst; hence only a small contribution of the nanoconfined IL layer could be suggested. However, stronger interactions between the desired product, 2,5-DMT, and the nanoconfined Lewis acidic chlorozincate(II) IL could not be excluded. Aromatic compounds are in general substantially more soluble in ILs in comparison with aliphatic compounds. For example, chloroferrate(III) ILs have exhibited a high extraction efficiency of S-containing aromatic compounds from model oils with a contribution of [FeCl<sub>4</sub>]<sup>-</sup> and [Fe<sub>2</sub>Cl<sub>7</sub>]<sup>-</sup>.<sup>76</sup> The  $\pi$ -complexation between Fe<sup>3+</sup> ([Ar]3d<sup>5</sup>) and the S-containing aromatic compounds enhances the extraction and solubility of sulfur species.<sup>77</sup> It has been conclusively shown that the cation of the IL greatly affects the solubility of aromatic compounds, potentially due to the interaction between two  $\pi$  systems ( $\pi$ -stacking). Non-acidic imidazolium-based ILs have shown high absorption capacity of heterocyclic compounds, such as 2-methylthiophene.<sup>78</sup> However, the regeneration of these ILs has been previously attempted in batch processing (liquid-phase), instead of continuous gas processing. Direct distillation or a combination of distillation/re-extraction with non-polar solvents for higher boiling compounds ( $\text{bp}_{760} > 200$  °C) had to be applied before the ionic liquid could be recycled and reused.<sup>77,78</sup>



### 3.2.7.2 Gas-phase recyclization of 2,5-DMF to 2,5-DMT; summary of attempted reactions

A summary of the key reactions performed in the spouted-bed reactor is provided in Table 3.8. Most experiments were completed with SiO<sub>2</sub>-60 Å-based SILP catalysts, mainly varying the loading ( $\epsilon_{IL}$ ) of the IL ([C<sub>4</sub>C<sub>1</sub>im]Cl-ZnCl<sub>2</sub> ( $X_{ZnCl_2} = 0.67$ )) and the H<sub>2</sub>S/2,5-DMF molar ratio. The reactions were initially tested at 200 °C to prevent the condensation of 2,5-DMF, or any of the products/by-products, on the SILP material or upon contact with any surface of the rig. However, lower (120 °C) and higher temperatures (250 °C) were eventually tested to examine the effect of temperature on the desorption of organic compounds interacting with the SILP catalyst or the formation of by-products. A total gas flow rate of 33 ml s<sup>-1</sup> (1.98 L min<sup>-1</sup>) was applied at all studied reactions, providing an optimised temperature gradient across the bed and homogeneous fluidisation. An example of the consistent temperature profile across the bed is illustrated in Figure 3.32, showing a maximum  $\Delta T$  of 10 °C. The experimental protocol that was applied to all experiments, is provided in **Section 3.3.5**.

**Table 3.8:** Summary of the gas-phase experiments examining the synthesis of 2,5-DMT in the spouted bed reactor

Entry	SiO <sub>2</sub> Pore size (Å)	T <sub>bed</sub> (°C) h <sub>bed</sub> = 10 cm T <sub>1</sub> @ 6 cm	$\epsilon_{IL}$ (%)	F <sub>H<sub>2</sub>S/N<sub>2</sub></sub> (ml s <sup>-1</sup> )	F <sub>N<sub>2</sub></sub> (ml s <sup>-1</sup> )	F <sub>2,5-DMF</sub> (g min <sup>-1</sup> )	F <sub>H<sub>2</sub>S</sub> (mol s <sup>-1</sup> )	F <sub>2,5-DMF</sub> (mol s <sup>-1</sup> )
R01	60	200	30	15	10	0.15	6.7E-06	2.6E-05
				(H <sub>2</sub> S, 1%)				
R02			30					
R03			60					
R04	60	200	60	25	0	0.12	2.1E-05	2.1E-05
				(H <sub>2</sub> S, 2%)				
R05			30					
R06			0					
R07			10					
R08	60	200						
R09	60	250						
R10	60	120	30	25	0	0.12	5.2E-05	2.1E-05
R11	60	120		(H <sub>2</sub> S, 5%)				
R12	150	120						

\*CEM heater carrier gas:  $F_{CEM/N_2} = 8$  ml s<sup>-1</sup>; Total gas flow rate =  $F_{H_2S/N_2} + F_{N_2} + F_{CEM/N_2} = 33$  ml s<sup>-1</sup> where  $F_{N_2}$  corresponds to the make-up gas

\*\*T<sub>TOP</sub>: Heating tape applied at the outlet of the reactor, T<sub>BOTTOM</sub>: Heating tapes applied at the reactor inlet and at the bottom of the CEM heater; T<sub>TOP</sub> = T<sub>BOTTOM</sub> = 130 °C, T<sub>CEM</sub> = 85 °C, T<sub>wall</sub> = T<sub>set(6 cm)</sub> + 20 °C

\*\*\*20 g of the SILP catalyst/bed material were used in all experiments (h<sub>bed</sub> = 20 cm), t<sub>reaction</sub> = 30 min

\*\*\*\*Neat ionic liquid supported on silica gel by physisorption/incipient wetness impregnation: [C<sub>4</sub>C<sub>1</sub>im]Cl\*ZnCl<sub>2</sub>, X<sub>ZnCl<sub>2</sub></sub> = 0.67

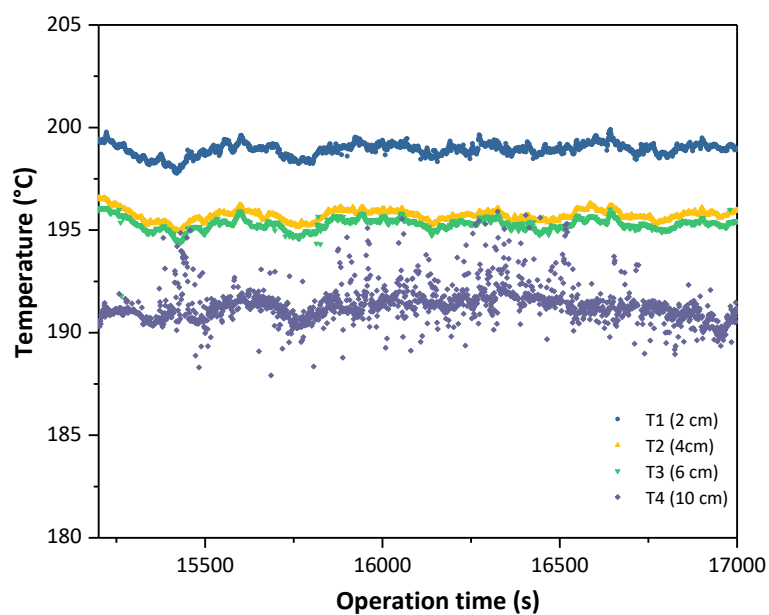


Figure 3.32: Characteristic example of the temperature gradient across the SILP-based bed ( $h_{\text{bed}} = 10 \text{ cm}$ ); **R01**

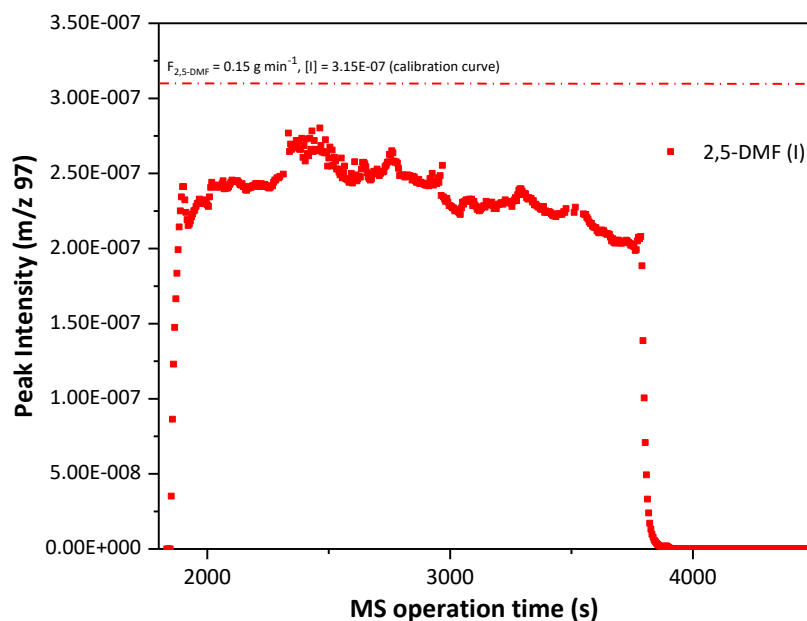
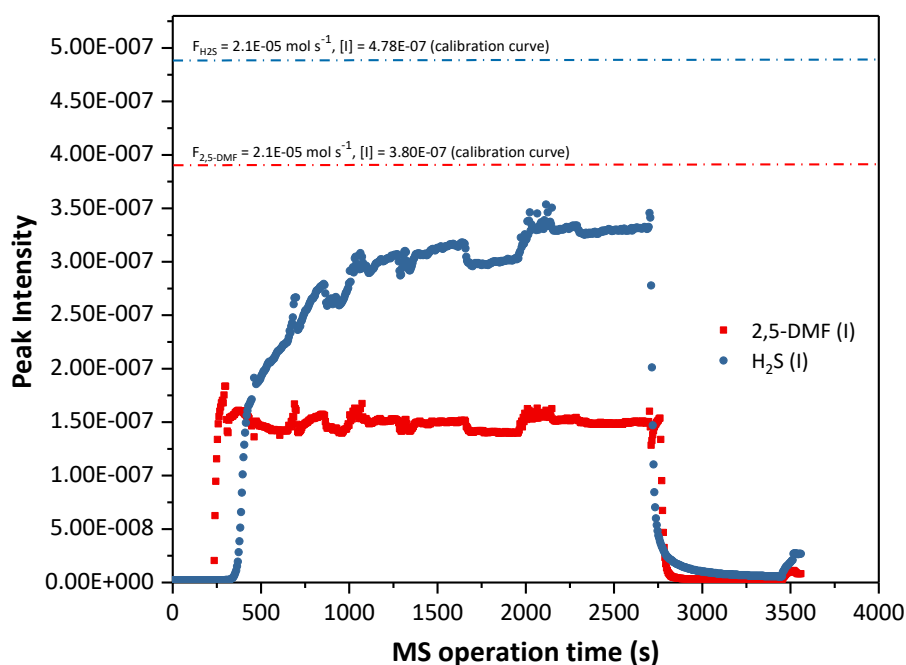


Figure 3.33: Online Mass spectrometry data (**R01**); evolution of the peak intensity corresponding to 2,5-DMF ( $m/z$ : 96)

The first reaction (**R01**) was attempted in the presence of a diluted mixture of  $\text{H}_2\text{S}$  in  $\text{N}_2$ , resulting into an excess of 2,5-DMF over  $\text{H}_2\text{S}$  (Table 3.8). A  $\text{SiO}_2$ -60 Å-based SILP catalyst with  $\epsilon_{\text{IL}}$  equivalent to 30 % was used as the bed material. Prior to the reaction, a calibration curve was established for 2,5-DMF,

correlating the peak intensity at  $m/z$  96 with the molar concentration by attaching a quadrupole mass analyser at the outlet or the rig (online analysis). During the experiment, a consistent reduction in peak intensity ( $m/z$  96) was observed in comparison with the expected intensity for the setpoint  $F_{2,5\text{-DMF}}$  ( $\text{mol s}^{-1}$ ) value that was established from the pre-reaction calibration curve (Figure 3.33). This could indicate an interaction of 2,5-DMF and SILP-based bed or the actual chemical conversion of 2,5-DMF. A total reduction of approximately 28 % was estimated by the evolution of the peak intensity values. However, the online MS data might have to be used with caution. The intensity value drop could indicate 2,5-DMF/IL or 2,5-DMF/SILP interactions but a variation in peak intensity due to the instrument cannot be excluded. At the end of the gas phase reaction, the condensed product mixture was isolated at the bottom of the two-stage trap with a LSS recovery efficiency of 82 %, accounting for the input of 2,5-DMF during the reaction. Traces of 2,5-DMT (< 1 %) were confirmed by analysing the condensate with  $^1\text{H}$  NMR spectroscopy, indicating a low conversion of 2,5-DMF to the desired product. The condensed sample was also submitted for GC(EI) analysis. The presence of 2,5-DMT but also the ring-opening product of 2,5-DMF, 2,5-hexanedione, was confirmed in combination with other unknown by-products (**Appendix**, Figure 3.53). A low molar concentration of  $\text{H}_2\text{S}$  over 2,5-DMF was considered as a key driver for the conversion of 2,5-DMF to other by-products in the presence of the Lewis acidic ionic liquid whilst a small yield of 2,5-DMT was attained.



**Figure 3.34:** Online Mass spectrometry data (R02); evolution of the peak intensity corresponding to 2,5-DMF ( $m/z$ : 96) and  $\text{H}_2\text{S}$  ( $m/z$ : 34)

Maintaining the reaction conditions and using the same Lewis acidic SILP catalyst ( $\epsilon_{IL} = 30\%$ ), experiment **R02** was performed by using a higher molar concentration of  $H_2S$  so that a 1:1 molar ratio was obtained between 2,5-DMF and  $H_2S$ . For **R02**, online calibration curves were established for both 2,5-DMF and  $H_2S$ . The regression equations were used in an attempt to correlate the peak intensities at  $m/z$  96 and  $m/z$  34 with the molar concentration of 2,5-DMF and  $H_2S$ , respectively. A consistent and significant reduction of the peak intensity, corresponding to 2,5-DMF, was also observed during the reaction **R02** (Figure 3.34). A drop of 78 % was estimated for 2,5-DMF, accounting for the expected intensity for the setpoint  $F_{2,5-DMF}$  ( $\text{mol s}^{-1}$ ) as established from the calibration curve. A slower response was observed for  $H_2S$ , in regards with the MS peak intensity. Considering the  $F_{H_2S}$  ( $\text{mol s}^{-1}$ ) setpoint value, a drop of approximately 32 % was estimated at the end of the experiment ( $t = 30$  min). The condensate sample from **R02** was also tested by GC(EI), confirming the conversion of 2,5-DMF into both 2,5-DMT and 2,5-hexanedione whereas the presence of other unknown by-products peaks ( $t > 5$  min) were also present in this chromatograph (**Appendix**, Figure 3.54).

The first experiments confirmed the feasibility towards the recyclization of 2,5-DMF to 2,5-DMT, catalysed by Lewis acidic SILPs. Interestingly, 2,5-hexanedione and other by-products were also detected in the reaction mixture. The formation of 2,5-hexanedione as the reaction intermediate and/or by-product has already been shown in the preliminary small-scale reactions (**Chapter 2**). Additionally, a few challenges were recognised at this stage. Firstly, the online MS data could not be used for the calculation of the direct conversion of 2,5-DMF given the uncertainty on how any fluctuations on the signal between the calibration stage and the actual experiment could affect the accuracy of the concentration calculations. The qualitative assessment of the isolated condensate samples was feasible by GC(EI) (**Section 3.5.9 & 3.5.10**) but the quantitative assessment was finally achieved by developing a protocol based on GC(FID) (**Section 3.3 & 3.5.11**). Calibration curves were first established for mixtures of standards (2,5-DMF, 2,5-DMT and 2,5-hexanedione), correlating the concentration of each compound with the area under the peak corresponding to each compound ( $R^2 > 0.99$ ) (**Appendix**, Section 3.5.11). Additionally, the adsorption of any products within the IL layer could not be excluded and thus the estimation of the total conversion of 2,5-DMF would be very difficult. Isolating the SILP catalyst at the end of each reaction, followed by Soxhlet extraction was attempted and most of these extraction samples were also tested by GC(EI) (**Appendix**, Figure 3.55) indicating that there was indeed no complete desorption of the products from the SILP catalyst during the experiment. Peaks corresponding to 2,5-DMF, 2,5-DMT, 2,5-hexanedione and other by-products were found at the GC(EI) chromatograph of the Soxhlet extraction samples. However, the high dilution of these samples, upon the Soxhlet extraction processing, did not allow for an accurate determination of the concentration of

these compounds by the GC(FID). Consequently, the reported isolated yield values (Table 3.9), refer to the composition of the samples that were collected from the vapours trap assembly (LSS). The LSS recovery values were larger than 70 % for most experiments, considering the mass input of 2,5-DMF. More specifically, relatively high recovery values were observed for the experiments performed at 200 °C (72 – 89 %) in regards with the total mass input of 2,5-DMF. A reduction in the mass of the condensate was observed when the temperature was elevated at 250 °C, suggesting the formation of less volatile products. Reducing the temperature to 120 °C also led to lower recovery values (62 % - 68 %).

**Table 3.9:** Summary of the composition of the isolated product mixtures; gas-phase synthesis of bio-derived 2,5-DMT

Entry	T (°C)	$\epsilon_{IL}$ <sup>3</sup>	H <sub>2</sub> S/2,5-DMF (molar ratio)	LSS recovery values <sup>1</sup>		% in product mixture (condensate) GC(FID) <sup>2</sup>			
				[2,5-DMF] <sub>input</sub> [g]	Condensed Sample % [2,5-DMF] <sub>input</sub>	2,5-DMF (%)	2,5-DMT (%)	2,5-hxd (%)	
R01	200	30 %	0.26	4.1	82	88.3	1.2	2.1	
R02		30 %		4.8	85	87.4	2.6	2.5	
R03		60 %		4.2	75	82.0	2.8	3.0	
R04		60 %		4.3	72	79.0	2.5	2.8	
R05		30 %		4.4	78	84.9	3.1	2.7	
R06		0 %		4.1	89	96.2	ND	ND	
R07		10 %		4.2	85	91.3	1.4	2.2	
R08	200	30 % [60 Å] [150 Å]	2.5	4.5	77	82.3	10.6	3.6	
R09	250			4.5	58	67.4	3.2	4.3	
R10	120			4.4	64	79.2	5.6	2.6	
R11	120			4.3	68	81	5.8	1.9	
R12	120			30 %	4.5	62	78	4.9	3.1

1: LSS recovery values refers to the amount of condensate (g) that was recovered from the two-stage trap (LSS), connected at the outlet of the reactor, over the total input of 2,5-DMF (value from Agilent VEE interphase program).

2: The experimental conditions for GC(FID) and the calibration curves of the standards (2,5-DMF, 2,5-DMT and 2,5-hxd) are summarized in the Experimental section and the Appendix, respectively.

3: SILPs where the IL has been physisorbed on SiO<sub>2</sub>-60Å, unless stated otherwise

For the reactions tested at 200 °C, an increase on the concentration of the isolated 2,5-DMT was noted when the concentration of H<sub>2</sub>S was increased to an equimolar amount in regards with the concentration of 2,5-DMF. Increasing the loading of the ionic liquid appeared to have an impact on isolated yield of 2,5-DMF and thus promoting the formation of less volatile by-products is also possible. Additionally, increasing the loading from  $\epsilon_{IL}$  = 30 % to  $\epsilon_{IL}$  = 60 % did not result to any major differences in the isolated

concentration of 2,5-DMT but the entrapment of 2,5-DMT in the IL multilayer could not be excluded as well. Testing the reaction between 2,5-DMF and H<sub>2</sub>S in the presence of the calcined parent support did not yield any detectable amounts of 2,5-hexanedione or 2,5-DMT, confirming the catalytic effect of the ionic liquid for the recyclization of 2,5-DMF into 2,5-DMT. Comparing the results for R07 ( $\epsilon_{IL} = 10\%$ ) and R02 – R05 ( $\epsilon_{IL} = 30\% - 60\%$ ), it is deduced that a lower conversion of 2,5-DMF occurred at a lower loading of the ionic liquid. It has been shown that low loadings of ionic liquid in the SILP materials result to increased pore wall/IL interactions (**Section 3.2.3.1 & 3.2.4**) and therefore an impact on the performance of the catalyst is expected. Using SiO<sub>2</sub>-60 Å-based SILP catalyst with  $\epsilon_{IL}$  equivalent to 30% but increasing the H<sub>2</sub>S/2,5-DMF molar ratio to 2.5 (**R08**) gave the highest isolated yield for 2,5-DMT (Table 3.9), indicating the crucial effect of the molar concentration of H<sub>2</sub>S on the recyclization of 2,5-DMF to 2,5-DMT. Using the SiO<sub>2</sub>-150 Å-based SILP catalyst ( $\epsilon_{IL} = 30\%$ ) was attempted to study any differences in catalytic performance but also to attempt improvements in regards with the entrapment of products/by-products in the SILP catalyst with a larger average pore size. However, lower yields were attained for 2,5-DMT, comparing the compositions of the condensates from R11 and R12, albeit an enhanced presence of 2,5-hexanedione is confirmed in the condensate. Testing at high temperatures (**R09**) indicates that converting 2,5-DMF to less volatile by-products may have taken promoted instead of the desired recyclization whereas there was a reduction in the LSS recovery values instead of improvement.

### 3.7.2.3 Summary and outlook for future work

The gas phase recyclization of bio-derived 2,5-dimethylfuran (2,5-DMF) into its thiophene analogue was attempted in a continuous process ( $P_{abs} = 2$  bar, 120 °C – 250 °C) in the presence of gaseous mixtures of H<sub>2</sub>S (1 – 5 % H<sub>2</sub>S, H<sub>2</sub>S/N<sub>2</sub>). The reaction was catalysed by Lewis acidic Supported Ionic Liquids ([C<sub>4</sub>C<sub>1</sub>im]Cl·ZnCl<sub>2</sub>,  $X_{ZnCl_2} = 0.67$ ), also used as the bed material with homogeneous fluidization and excellent temperature gradient across the bed. A spouted-bed reactor was adapted for testing the reaction, achieving a bed loading of 20 g ( $h_{bed} = 10$  cm) with a total gas flow rate of 33 ml s<sup>-1</sup>. 2,5-DMF was introduced into the reactor in the vapour phase whereas optimizations in the design of the two-stage liquid sampling system had to be made to allow for a maximum recovery that was greater than 80%. To the best of our knowledge, this is the first time that supported ionic liquids have been tested, in this scale, in a pressurized fluidized bed reactor with reactants and products to be maintained in the vapour phase in the presence of flammable H<sub>2</sub>S. The requirements of an excellent liquid/gas separation at the outlet of the reactor presented a new challenge whilst the SILP catalysts were tested under a continuous gas flow.

The scouting study provided several conclusions with the preliminary experiments demonstrating significant promise. It was deduced that the addition a Lewis acidic SILP catalyst promotes the recyclization of 2,5-DMF to 2,5-DMT with 2,5-hexanedione forming as one of the main intermediates. The reaction appeared to be highly impacted by the molar concentration of H<sub>2</sub>S. A large excess of H<sub>2</sub>S over the furanic substrate (2,5-DMF) might therefore be required to improve the reaction yields. Increasing the concentration of H<sub>2</sub>S (mixture: H<sub>2</sub>S/N<sub>2</sub>, 5 % H<sub>2</sub>S) at levels higher than those applied (Table 3.9) was not feasible in this work due to safety concerns, given the toxicity and flammability of H<sub>2</sub>S. However, it will be worthwhile to experimentally determine the residence time distribution (RTD) for this chemical reactor. Assuming the absence of dead or stagnant zones within the reactor, the average residence time of the reactive gaseous stream is roughly estimated from the total volume of the bed ( $h_{\text{bed}} = 10 \text{ cm}$ ,  $D_c = 30 \text{ mm}$ ) and the gas flow rate (33 ml/s):  $\tau = 2.14 \text{ s}$ . Finetuning the short residence time via adjustments of the assembly design, and/or other factors such as the gas flow rate and the bed height is also recommended for optimizing the 2,5-DMF conversion to the desired product.

An interaction, between the ionic liquid and the organic compounds formed during the reaction, was suspected, making the complete products isolation and mass balance problematic. Using Soxhlet extraction to close the mass balance and quantify products entrapment was unsuccessful as the samples were too diluted to be able to quantify their composition by GC(FID). Elemental analysis could be suggested as an alternative way for calculating the amount of product(s) strongly interacting with the SILP catalyst. It is also suggested that such a gas-phase reaction might be more beneficial in a set-up where the application of vacuum could be accomplished at the end of each experiment to isolate all products and regenerate the SILP catalyst *in situ*. Testing both higher and lower temperatures, herein, did not provide improvements in the recovery of the products with the former promoting side-reactions in the presence of the acidic catalyst. Modifications on the pore size of the support did not provide major improvements in the separation of the reaction products or the reaction metrics. Further work is therefore advised in regards with changing the structure of the IL, using cations and anions with a lower affinity to the heterocyclic compounds, as an additional way for controlling IL/product interactions.

### 3.3 Experimental

Mesoporous silica gel samples [60 Å (70-230 mesh) and 150 Å (100-200 mesh)] were purchased from Alfa Aesar. The materials that were used for the synthesis of the neat chlorozincate(II) ionic liquids ( $X_{\text{ZnCl}_2} = 0.67$ ) are summarised in the **Chapter 2 (Section 2.4)**. Dry methanol and diethyl ether were purchased from Sigma-Aldrich and were used without any further purification. 2,5-dimethylfuran (2,5-DMF; 99%), 2,5-hexanedione (2,5-hxd; 98%) and 2,5-dimethylthiophene (2,5-DMT, 98+%) were obtained by Sigma-Aldrich and Alfa Aesar. A 6.8 L cylinder containing a mixture of  $\text{N}_2/\text{H}_2\text{S}$  (1 – 5%  $\text{H}_2\text{S}$ ) was purchased from SIP Analytical Ltd. Additionally, a two-stage, regulator (0-10 bar), suitable for the  $\text{H}_2\text{S}$  mixtures, was obtained from BJ Industries Ltd. All experiments were performed under air-free conditions; hence the synthesis as well as any handling of the SILP catalysts were accomplished by using standard Schlenk line techniques or they were performed in a glovebox (MBraun, Labstar).

A Malvern Mastersizer 2000 laser diffraction particle size analyser was used for particle size analysis for determining the particle size of both the SILP catalysts and the parent inorganic support. Distilled water was applied as the dispersion solvent with a mixing speed of 3200 rpm. Three experimental repeats were performed for every sample and the average particle size values are reported. The skeletal/absolute density of the particles was measured via helium adsorption analysis (Micrometrics, Accupyc 1330). The  $\text{N}_2$ -adsorption/desorption isotherms were obtained using a three-station automated gas adsorption analyser (Micrometrics, Tristar 3000). All samples were previously dried under vacuum ( $3.8 \times 10^{-1}$  mbar, 60 °C) and handled in a glovebox to avoid any exposure to moisture before the parafilm-sealed samples were used for performing the measurement of the surface properties. The BET (Brunauer, Emmett and Teller) surface area and BJH (Barrett-Joyner-Halenda) pore size distributions were reported for the mesoporous region ( $D_p = 2 - 50$  nm) and small macropores up to ca. 300 nm in diameter. For most BET samples, at least two internal replicates were analysed (< 500 mg) and the average  $A_{\text{BET}}$ ,  $C_{\text{BET}}$  and  $V_{\text{pore}}$  values are reported. All solid-state  $^1\text{H}$  NMR spectra were recorded in a Bruker 600 MHz, employing a 2.5 mm MAS zirconia rotor. More specifically, the  $^1\text{H}$  NMR spectra (32 scans) were recorded at room temperature with a 14.5 kHz spinning speed, using a single-pulse excitation with a  $\pi/2$  pulse length of 4.5  $\mu\text{s}$  and a recycle delay of 5 s. The thermal stability of the SILP catalysts (5 – 10 mg) was studied with a thermogravimetric analyser (TGA, TA Instruments: Q5000) under  $\text{N}_2$  ( $V = 150$  ml  $\text{min}^{-1}$ ). The temperature-ramped testing (dynamic scans) was completed between 30 °C and 800 °C at a rate of 10 °C  $\text{min}^{-1}$  after heating the samples up to 120 °C to remove any residual moisture (10 °C  $\text{min}^{-1}$ ,  $t_{\text{isothermal}} = 1$  min). Platinum-HT pans were used for the thermogravimetric analysis so that the sample holder was not compromised at higher temperatures.



The spouted bed reactor configuration was constructed from stainless steel 316 tubing and Swagelok® tube fittings. A type K, multipoint thermocouple (¼-inch BSPT process entry & ¼-inch BSPP thermowell entry) was obtained from TC direct to measure and control the temperature across the bed. Type K thermocouples (TC direct) were also used to monitor the temperature of the reactor wall in addition to the temperature of the heated pipework connecting the vapour delivery system to the inlet of the reactor or the section between the reactor outlet and the liquid sampling system (LSS). The external heating was accomplished by using electrical heating tapes (rated to 760 °C, 627W, 120V) by RS components. Any heating section of the experimental set-up was insulated by Superwool® 607Max blanket. Mass flow controllers (Bronkhorst High-Tech B.V.), with gas flow rates ranging from a maximum of 125 ml s<sup>-1</sup> to 200 ml s<sup>-1</sup>, were used to control and monitor the flow rate of the gas mixtures that were introduced into the reactor. A controlled evaporator mixer (CEM) and a Coriolis meter (mini CORI-FLOW) were also obtained from Bronkhorst to realise the mass flow control of vapour/gas mixtures. A process control program was written in-house in Agilent VEE 9.0, allowing the automation of the PID temperature control in addition to controlling the flow rates of H<sub>2</sub>S/N<sub>2</sub> and 2,5-DMF. The control unit was originally designed by the Department of Electronics in collaboration with the Fennell group (Department of Chemical Engineering, Imperial College London).<sup>73</sup> The online analysis of unreacted 2,5-DMF and H<sub>2</sub>S was accomplished by using a quadrupole Mass spectrometer QMS 422/200 (Aston Analytical). Two calibrated wearable detectors were activated during the experiments when H<sub>2</sub>S/N<sub>2</sub> mixtures were used (BW-Gas alert microclip G2S sensors). The offline analysis of the condensed samples was completed by Gas Chromatography/ Mass spectroscopy (GC/MS) in collaboration with Dr. Lisa Haigh (Department of Chemistry, Imperial College London). More specifically, a Micromass Autospec Premier/Agilent HP6890 GC was set up, operating in electron impact (EI) mode. The retention times, obtained by testing a mixture of standards, (2,5-DMF, 2,5-DMT, 2,5-hxd) are summarized in **Section 3.5.5(6)**. For the GC(EI) experiments, a ZB-5MS column (30 m x 0.25 mm x 0.25 µm) was applied. The carrier gas flow was set at 1 ml min<sup>-1</sup> (Helium) with an isocratic at 50 °C for 5 mins, followed by temperature ramping to 200 °C (50 °C/min). The GC(FID) experiments (quantitative analysis) were completed with a Thermo Scientific Trace GC Ultra/ DSQII that was set-up with a DB-5MS UI column (30 m x 0.25 mm x 0.25 µm) (Department of Chemical Engineering, Imperial College London). The tested product mixtures (40 µl) were diluted in 1 ml of diethyl ether. The injection volume was 1 µl with the flow mode in split control (50 ml min<sup>-1</sup>, 50 split ratio). The oven temperature was initially held at 50 °C for 1 min. Hereafter, the temperature was increased with a gradient of 10 °C min<sup>-1</sup> until the temperature reached to 200 °C (hold: 5 min). Other settings were as follows: 200 °C FID temperature, 200 °C base, 220 °C SSL temperature, flame (Air: 350 ml min<sup>-1</sup>, H<sub>2</sub>: 35 ml min<sup>-1</sup>, make up gas: 30 ml min<sup>-1</sup>).

### 3.3.1 Synthesis of Lewis acidic, silica-supported ILs ( $[\text{C}_4\text{C}_1\text{im}]\text{Cl}\cdot\text{ZnCl}_2$ , $X_{\text{ZnCl}_2} = 0.67$ )

Amorphous, mesoporous silica gel (60 Å or 150 Å) was calcined in a muffle oven (Nabertherm P330) prior to its use as a support material. The inorganic support was heated up from room temperature to 150 °C, at a heating rate of 4 °C min<sup>-1</sup>. The temperature was kept constant at 150 °C for partial dihydroxylation before reaching 600 °C (4 °C min<sup>-1</sup>). Before cooling down the material to room temperature, the temperature of 600 °C was maintained for 12 h to slowly remove both physisorbed and chemisorbed water. The thermally pretreated support was evacuated overnight ( $3.8 \times 10^{-1}$  mbar, 60 °C) and eventually stored under nitrogen in a glovebox (MB-Labstar) before mixing with the IL/co-solvent solution (Figure 3.35).

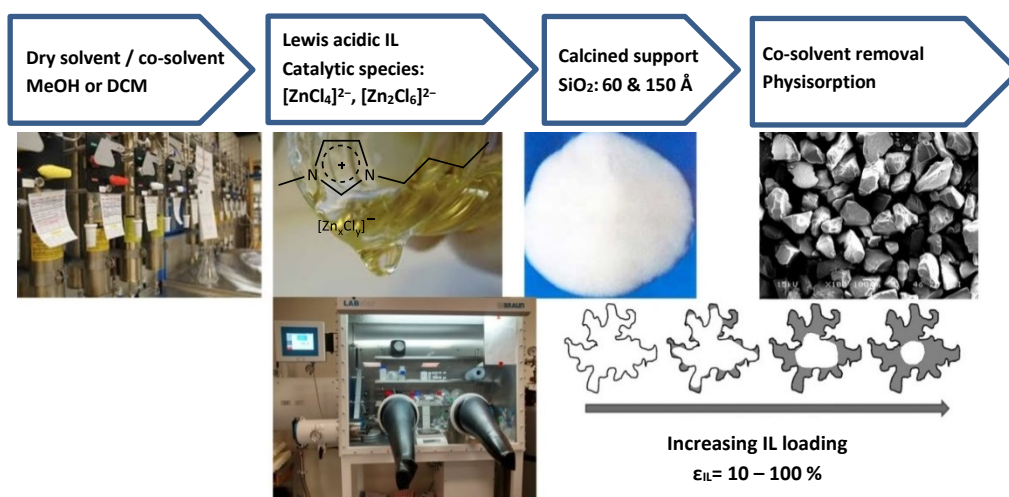


**Figure 3.35:** Schematic representation of the SILP synthesis protocol and the pore filling mode for ILs confined in silica gel.

$[\text{C}_4\text{C}_1\text{im}]\text{Cl}$  (**Chapter 2; 2.4.1.1**) and anhydrous  $\text{ZnCl}_2$  were dried under vacuum prior to the synthesis of the hygroscopic hallometallate ionic liquid ( $X_{\text{ZnCl}_2} = 0.67$ ) (**Chapter 2; 2.4.1.2**). The neat ionic liquid was used for the preparation of Lewis acidic supported ionic liquids (SILP) via physisorption onto the surface of the calcined silica gel (60 Å or 150 Å). The ionic liquid was dissolved in a suitable co-solvent prior to mixing with the inorganic support to improve the dispersion and impregnation of the viscous IL. An excess of dry methanol, with regards to the volume of the ionic liquid (ca. 10:1), was used for the dissolution of the ionic liquid (500 rpm, 1 h). Subsequently, the calcined support was added to the solution and the resulting IL/MeOH suspension was vigorously stirred at room temperature (1000 rpm, 2 h). The solvent was evaporated under mild vacuum, by rotary evaporation, to produce a thin layer of IL (320 mbar, 60 °C). All SILP samples finally were dried under vacuum ( $3.8 \times 10^{-1}$  mbar, 60 °C, 12 h) so that any residual moisture and solvent were removed, affording a free-flowing powder. SILP batches

(ca. 40 g) with three ionic liquid loadings ( $\epsilon_{IL}$ ) were prepared for each support:  $\epsilon_{IL}$  = 10 %, 30 % and 60 %. The loading and pore filling degree values were estimated from (3.16) and (3.17).<sup>3</sup> The density of the neat IL was extrapolated<sup>79</sup> as  $\rho_{298K} = 1.432 \text{ g cm}^{-3}$  with an approximate molecular weight of  $M_w = 310.96 \text{ g mol}^{-1}$  and these values were used for calculating the volume of the bulk IL.

$$\alpha_{IL} \text{ (vol \%)} = \frac{V_{IL}}{V_{\text{pore, total}}} \quad (3.16)$$

$$\epsilon_{IL} = \frac{m_{IL}}{m_{\text{solid}}} \quad (3.17)$$

Table 3.10 summarizes the detailed compositions of the synthesized SILPs that were produced in batches of roughly 40 g of SILP. Every SILP catalyst was examined against its physicochemical properties by several analytical methods (Section 3.2.2 – 3.2.5).

**Table 3.10:** Composition of the synthesized Lewis acidic, silica-based SILPs ( $[\text{C}_4\text{C}_1\text{im}]\text{Cl}\cdot\text{ZnCl}_2$  ( $X_{\text{ZnCl}_2} = 0.67$ )).<sup>k</sup>

Support <sup>k</sup>	$\epsilon_{IL}$ <sup>a</sup> (%)	$V_{\text{pore}}^b$ ( $\text{cm}^3\text{g}^{-1}$ )	$V_{\text{pore}}^c$ ( $\text{cm}^3$ )	$\alpha_{IL}$ <sup>d</sup> (%)	$m_{IL}$ <sup>e</sup> (g)	$m_{\text{Support}}^f$ (g)	$V_{IL}^g$ ( $\text{cm}^3$ )	$n_{IL}^h$ TOTAL (mmol)	$n_{IL}^i$ ( $\text{mmol g}^{-1}$ )
<b>SiO<sub>2</sub> (150 Å)</b>	10	0.99	35.6	7	3.6	36	2.51	11.58	0.32
	30		30.7	21	9.3	31	6.49	29.91	0.96
	60		24.8	42	15	25	10.47	48.23	1.92
<b>SiO<sub>2</sub> (60 Å)</b>	10	0.70	19.6	9.9	2.8	28	1.95	9	0.32
	30		16.1	29.8	6.9	23	4.81	22.18	0.96
	60		13.3	59.8	11.4	19	7.96	36.66	1.92
	100		14.0	99.8	20	20	13.97	64.32	3.20

a: ionic liquid loading (ww%), b: pore volume of the parent support (BET, P/P<sub>o</sub> ca. 0.99), c: total available pore volume per sample, d: pore filling degree, e: mass of the ionic liquid being mixed with the co-solvent (MeOH), f: mass of the silica gel support mixed with the co-solvent/IL solution, g: volume of the ionic liquid, accounting for  $\rho_{298K} = 1.432 \text{ g cm}^{-3}$ , h: total molar concentration of the ionic liquid impregnated into the inorganic support, i: molar ionic liquid loading per mass of support ( $n_{IL}$ ), k: 150 Å and 60 Å refer to pore size as per product specifications.

### 3.3.2 Liquid sampling system (LSS) development

The liquid sampling system (LSS) was developed to achieve the condensation and collection of unreacted 2,5-DMF as well as the reaction products/by-products, such as 2,5-dimethylthiophene, water and 2,5-hexanedione. The successful gas/liquid separation was a significant challenge. The vapours should be condensed and separated from the gas mixture whilst preventing the re-entrainment of the organic compounds in the presence of a continuous stream of nitrogen. A few of the tested configurations and the respective experimental conditions are summarised in this section. Firstly, the separation of 2,5-DMF vapours and N<sub>2</sub> was tested by-passing the main reactor body by attaching the LSS configuration directly at the outlet of the CEM heater (vapour delivery system). The N<sub>2</sub>/2,5-DMF mixtures were directed from the CEM to the condenser via a bored-through ½-inch Swagelok tee (Figure 3.36). The gas stream was first passed through ¼-inch stainless-steel tubing to the bottom of a vertical ½-inch outer tube. A coil made of 1/8-inch soft copper tubing was attached tightly on the external wall of the ½-inch tube/condenser. The “copper coil-based cooling jacket” was connected to a recirculating cooler (Julabo, F25), set at temperatures ranging from -5 °C to -10 °C, providing a continuous flow of coolant (50:50 vol%, ethylene glycol/ water) during the experiment. The outer coil acted as a heat exchanger and the gas stream was expected to cool down in contact with the inner ¼-inch tube and the internal wall of the ½-inch tube. Condensed 2,5-DMF was trapped at the bottom of the ½-inch tube and samples were collected via a custom-made PTFE port where a 10-ml gas-tight syringe (SGE), bearing a luer lock valve, was adjusted (Figure 3.36).

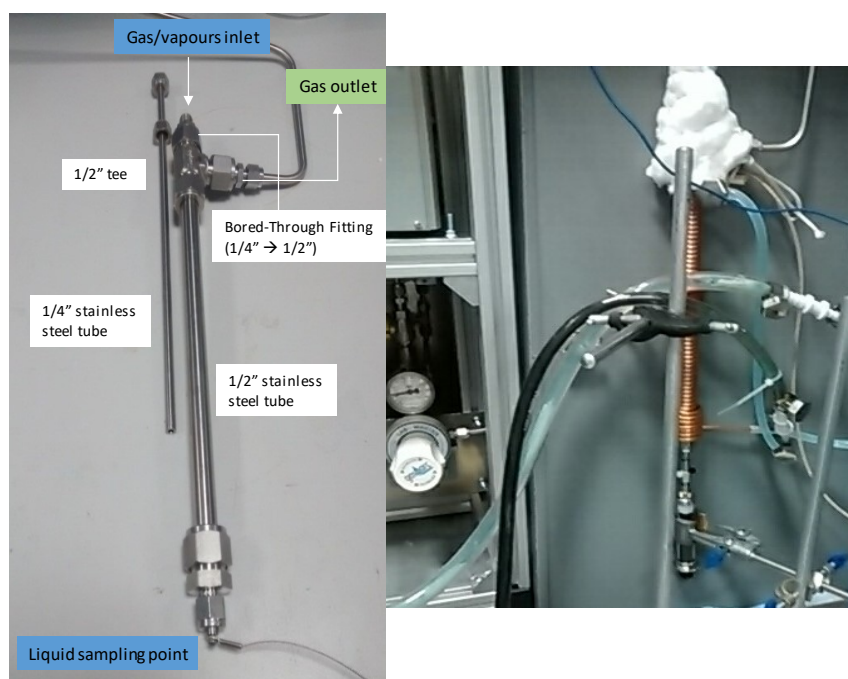
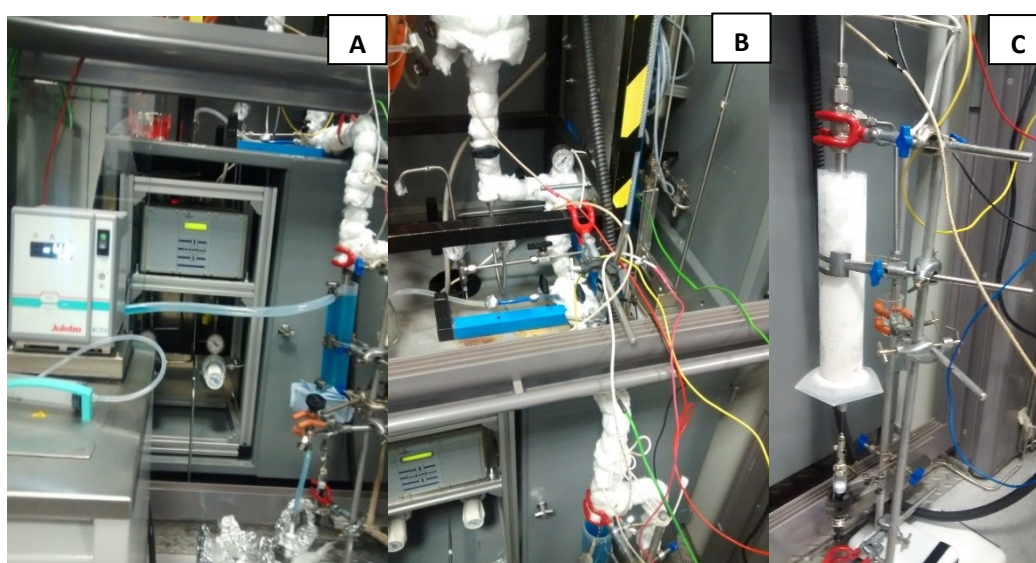


Figure 3.36: Design of the first prototype of a low-temperature vapour trap

This preliminary LSS configuration (Figure 3.37) was tested in triplicate with the flow rate of 2,5-DMF set at  $0.10 \text{ g min}^{-1}$  ( $1.74\text{E-}05 \text{ mol s}^{-1}$ ) and a  $\text{N}_2$  flow rate of  $8 \text{ ml s}^{-1}$  ( $3.23\text{E-}04 \text{ mol s}^{-1}$ ). The CEM heater was given the setpoint of  $85 \text{ }^\circ\text{C}$  whereas the connections before the condenser were heated by heating tapes ( $T_{\text{set}} = 100 \text{ }^\circ\text{C}$ ) that were insulated with a few layers of Superwool® 607Max blanket. A maximum recovery of  $46 \text{ } \%$  ( $\pm 4 \text{ } \%$ ) of 2,5-DMF was achieved by applying this set-up, considering the 2,5-DMF input ( $t = 30 \text{ min}$ ). Several factors were investigated to identify the cause of the problem and improve the mass balance profile of the LSS system. Confirming the accuracy of the Coriolis liquid flowmeter was performed first as well as a thorough leak testing of the experimental set-up. The “copper-coil”-based jacket was finally replaced due to the lack of sufficient surface area for cooling. This problem was confirmed when a temperature probe was used to monitor the temperature inside the preliminary cooling trap at different distances from the sampling point:  $x_1 = 1 \text{ cm}$ ,  $x_2 = 3 \text{ cm}$ ,  $x_3 = 12.5 \text{ cm}$  and  $x_4 = 25 \text{ cm}$ . The measurements showed a gradient of  $13 \text{ }^\circ\text{C}$  ( $\Delta T_{4,1}$ ) across the trap with a temperature of  $2 \text{ }^\circ\text{C}$  near the sampling point, even when the recirculating cooler was set at  $-10 \text{ }^\circ\text{C}$ . Modifying the cooling jacket of the vapour trap was attempted by using a plastic cylinder (500 ml) that was retrofitted as part of the cooling trap (Figure 3.37). The use of a recirculating cooler ( $-10 \text{ }^\circ\text{C}$ , 50:50 vol%, ethylene glycol/water) or a mixture of acetone/dry ice ( $-78 \text{ }^\circ\text{C}$ ) led to improvements in the recovery of 2,5-DMF. The recovery of 2,5-DMF reached a maximum of  $62 \text{ } \%$  ( $\pm 3 \text{ } \%$ ) when an acetone/dry ice mixture was used as a coolant under the same conditions to those applied with the preliminary trap trap ( $F_{2,5\text{-DMF}} = 0.10 \text{ g min}^{-1}$ ,  $t = 30 \text{ min}$ ,  $F_{\text{N}_2} = 8 \text{ ml s}^{-1}$ ,  $T_{\text{CEM}} = 85 \text{ }^\circ\text{C}$ ). It was considered that the residence time of the vapours within the condenser was not sufficient for reaching equilibrium whilst the re-entrainment of 2,5-DMF from  $\text{N}_2$  was still a challenge.



**Figure 3.37:** Modifications of the liquid sampling system (LSS) - preliminary testing, by-passing the reactor [(coolant mixtures: (A)& (B): = ethylene glycol/water, (C): dry ice/acetone

A modified LSS set-up, a two-stage vapour trap, was finally designed and constructed to be tested directly at the outlet of the reactor. The gas stream (120 °C – 250 °C), exiting the reactor, was passed through ½-inch stainless-steel tubing that was bended at 90 degrees and connected to the primary vapour trap. The first-stage trap was composed of a coil (60 mm I.D) that was constructed from 2 m of 1/4-inch stainless-steel tubing (Figure 3.38). It was cooled in the presence of a mixture of ice/salt that was in direct contact with the outer wall of the coil. The bottom part of the coil was connected to a secondary trap to ensure the efficient condensation of the organic vapours. The connection to the primary trap was such that the pressurised gaseous mixture would not be in direct contact with the condensed liquid upon entry (Figure 3.38), reducing the risk of liquid re-entrainment. The second stage vapour trap was composed of a set of ½-inch tubes that were connected to each other and to the primary trap via a ½-inch Swagelok tee. The top part of the secondary trap (O.D 1/2", length: 150 mm) was connected to ¼-inch tubing that was directed to a propane burner so that the combustible and toxic portion of the LSS outlet exhaust was burnt in the fume cupboard. The bottom part of the secondary trap (O.D 1/2", length: 70 mm) was connected to a Swagelok sample cylinder (10 cm<sup>3</sup>) that was equipped with two ball valves, allowing for its isolation at the end of each experiment. The secondary trap was submerged in an acetone/dry ice mixture which was contained in a retrofitted 1 L-measuring cylinder, accessible to top up with dry ice during operation.

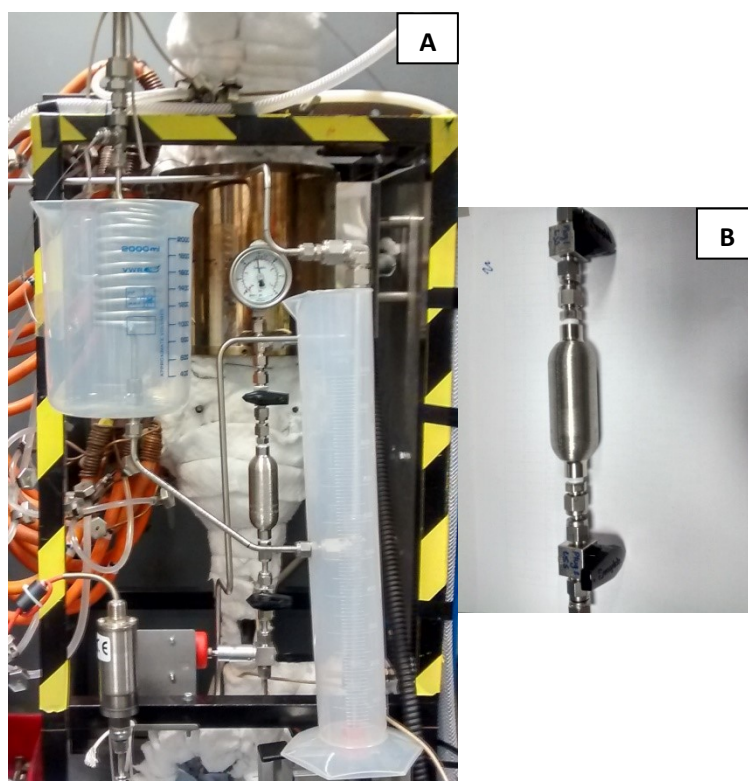


**Figure 3.38:** Final design of the two-stage liquid sampling system (A), and the detachable Swagelok sample cylinder (B).

### 3.3.3 Operating protocol for the gas-phase synthesis of bio-derived thiophenes, catalysed by Lewis acidic supported ionic liquids (SILP) in a spouted bed reactor

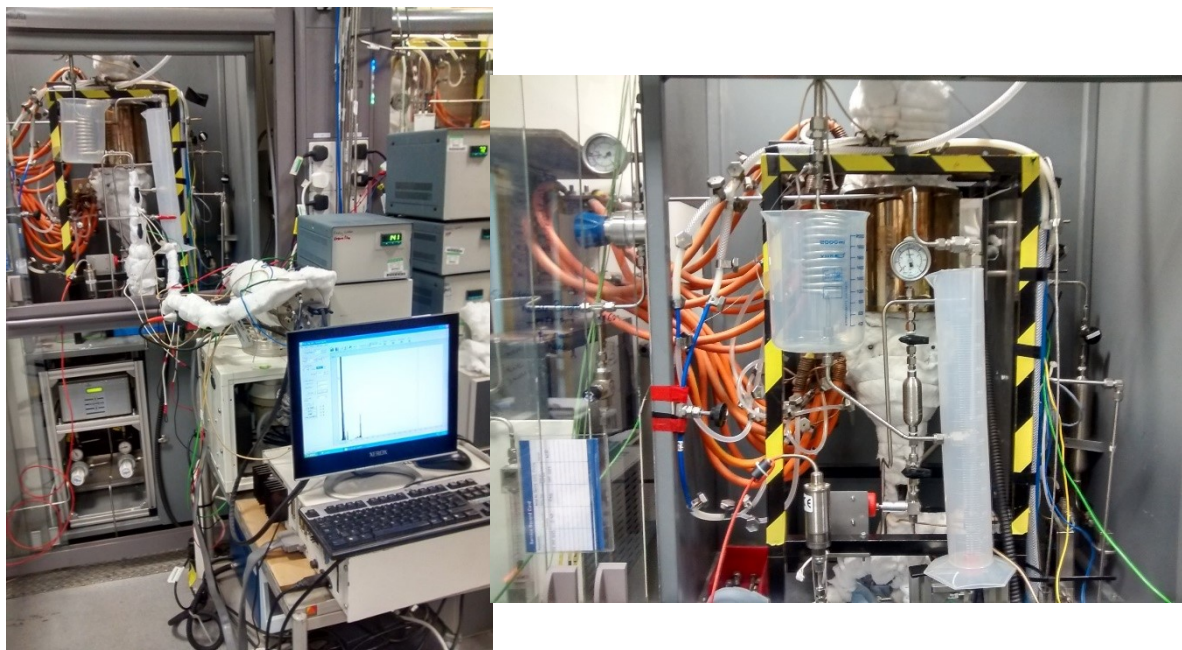


Figure 3.39: Experimental set-up for the gas-phase synthesis of bio-derived thiophenes in a spouted-bed reactor

#### 1. Preparatory steps

The reactor assembly, including the vapour delivery system and the liquid sampling configuration, were purged with acetone, followed by nitrogen, to remove any traces of solid catalyst, reactants or products prior to performing a new experiment. All fittings were tested for gas leaks by using the pressure change method. The performance of the isolated system was monitored under pressurised  $N_2$  ( $P_{abs} = 3$  bar, 10 min, rt). 2,5-dimethylfuran was filtered through silica to remove the coloured impurities and 200 cm<sup>3</sup> of 2,5-DMF were finally loaded into a Swagelok cylinder (capacity: 300 cm<sup>3</sup>) that was part of the liquid/vapor delivery system.

#### 2. Reactor heating and the calibration of the portable mass spectrometer

The Agilent VEE™-based process control program and the control unit were activated for achieving temperature, gas and liquid flow rate control. Prior to increasing the temperature of the reactor ( $T_{wall}$ ), the rig was purged with nitrogen ( $mcf_4 = 25$  ml s<sup>-1</sup>) and an additional flow of  $N_2$  was provided to the CEM heater ( $mfc_3 = 8$  ml s<sup>-1</sup>). The reactor assembly was pressurised at  $P_{gauge} = 1$  bar by using a back-pressure regulator. The 1/8-inch soft copper tubing, tightly wrapped around the cables of the heating section of the reactor body, was now cooled via the continuous flow of water, preventing the over-heating of the cables at the electrode ends. The heating of the reactor was achieved via the PID control of the  $T_{wall}$

temperature ( $T_{\text{wall}} = T_{\text{set}(6 \text{ cm})} + 20 \text{ }^{\circ}\text{C}$ ). The electrical heating tapes, attached onto the heating sections of the pipework, were also activated and controlled by two separate heating controllers ( $T_{\text{set}} = 130 \text{ }^{\circ}\text{C}$ ). The temperature of the CEM heater was set to  $85 \text{ }^{\circ}\text{C}$ . The portable mass spectrometer (MS) and the vacuum pump, directly connected to the MS, were switched on so that the right vacuum conditions were reached ( $2\text{E}-06 - 6\text{E}-06 \text{ mbar}$ ) before the emission function was enabled ( $1650 \text{ V} - 2050 \text{ V}$ ). The MS probe was connected to the outlet of the reactor, prior to the two-stage vapours trap. At this stage, the liquid sampling system configuration (LSS) was replaced by  $\frac{1}{4}$ -inch flexible tubing that directed the gas stream to a burner. The reactor remained pressurised at  $P_{\text{gauge}} = 1 \text{ bar}$  and the temperature was set at the targeted reaction temperature before a set of  $\text{H}_2\text{S}/\text{N}_2$  and 2,5-DMF flow rates were tested. A total gas flow rate of  $33 \text{ ml s}^{-1}$  was applied, including the  $\text{N}_2$  carrier gas that was applied to the vapour delivery system (mfc3), the  $\text{H}_2\text{S}/\text{N}_2$  mixture (mfc2) and the make-up gas ( $\text{N}_2/\text{mfc4}$ ). The following gas flow rates of the  $\text{H}_2\text{S}/\text{N}_2$  mixtures were tested: 5, 10, 15, 20 and  $25 \text{ ml s}^{-1}$  (mfc2). A calibration curve was established, correlating the intensity of the MS peak ( $m/z$  34) with the concentration of  $\text{H}_2\text{S}$ . The system was then purged under  $\text{N}_2$  for 15 min before a calibration curve was also generated for the second reactant of the vapour/gas phase: 2,5-DMF. The liquid flow rates of 0.20, 0.15, 0.10, 0.05 and  $0.025 \text{ g min}^{-1}$  were tested under  $\text{N}_2$  so that a correlation between the molar flow rate of 2,5-DMF and the intensity of the MS peak ( $m/z$  96) was established. The sampling line of the MS was heated up to  $100 \text{ }^{\circ}\text{C}$ , by using an electrical heating tape, preventing the condensation of 2,5-DMF within the line connecting the reactor and the portable MS. Upon the completion of the MS calibration steps, the system was purged with nitrogen for 15 min before adding the bed.

### **3. SILP catalyst/bed addition, fluidisation and purging**

A  $40 \text{ cm}^3$  Swagelok sample cylinder, part of the solid feeding system, was brought to the antechamber of a glovebox. It underwent a minimum of three evacuation/refill cycles to remove any traces of moisture before 20 g of the SILP catalyst were loaded into the cylinder. The valves of the catalyst-containing sample cylinder were closed to isolate the system which was then connected back to the solid feeding configuration. The ball valve, positioned between the bottom part of the CEM heater and the inlet of the reactor, was closed during the addition of the SILP-based bed to avoid any contamination with solid particles. The feeding process took place at atmospheric pressure at a reduced gas flow rate of nitrogen ( $\text{mfc4} = 15 \text{ ml s}^{-1}$ ). The RS motor was activated by a variable power supply (6-10 V) before opening the top and bottom valve of the cylinder, allowing for the fluidization of the bed under a flow of nitrogen. The temperature across the bed was monitored during the catalyst feeding step ( $t = -10 \text{ min}$ ) by reading the values of the multipoint thermocouple that placed inside the quartz liner. The top and bottom valves of the Swagelok cylinder were then shut off and the bed was let fluidising until the



temperature reached the targeted reaction temperature ( $T_{\text{bed}}(6 \text{ cm})$ ). The LSS configuration was not connected at this stage as any residual moisture in the SILP catalyst could lead to water freezing within the primary or the auxiliary trap, causing a significant pressure drop. After 10 - 15 min of purging with  $\text{N}_2$ , both the coil and the secondary trap were connected to the experimental set-up. An ice/salt mixture was used for cooling the coil trap whereas a dry ice/acetone mixture was used for the second-stage low-temperature vapours trap.

#### **4. Gas-phase reaction of 2,5-DMF and $\text{H}_2\text{S}$ , bio-derived 2,5-dimethylthiophene synthesis**

The sample cylinder containing  $200 \text{ cm}^3$  of 2,5-DMF was pressurised at  $P_{\text{gauge}} = 1.2 \text{ bar}$  and the valve of the CEM was loaded with 2,5-DMF and any gas bubbles were removed prior to each experiment. The setpoint of the 2,5-DMF flow rate was adjusted via the Agilent VEE process control program. The liquid flow rate was let to stabilise at the setpoint value whilst the ball valve connecting the CEM heater with the inlet of the reactor body remained shut and the metering valve near the bottom of the CEM heater remained partially open allowing for a pressure that was slightly above than 1 bar ( $P_{\text{gauge}}$ ). As soon as the setpoint value was reached, the metering valve was shut down and the ball valve connecting the CEM heater with the reactor body was opened. The flow of the  $\text{H}_2\text{S}/\text{N}_2$  mixture was initiated at a set gas flow rate and the reaction was carried out for 30 min. The vapours of any organic compounds were expected to condense in the two-stage cooling trap and they were collected in a liquid drain ( $40 \text{ cm}^3$  Swagelok cylinder) whilst any unreacted  $\text{H}_2\text{S}$  was directed from the top part of the auxiliary trap to a gas burner. During the experiment, gas sampling for online MS measurements took place, monitoring the intensity of a peak at  $96 \text{ m/z}$  and  $34 \text{ m/z}$  for  $\text{H}_2\text{S}$  and 2,5-DMF, respectively. The calibration curve equation could be used for translating the changes in the intensity of the peaks to an evolution of the concentration of reactants over time. Moreover, the temperature across the bed as well as the system pressure were monitored in real time. Upon the end of the reaction time ( $t = 30 \text{ min}$ ), the gas flow rate of  $\text{H}_2\text{S}/\text{N}_2$  was set to zero and  $25 \text{ ml s}^{-1}$  of nitrogen was used instead so that the bed kept fluidising with  $\text{H}_2\text{S}$  being purged off the system and the expectation to also remove any products or traces of reactant from the SILP catalyst. After 5 minutes of purging with nitrogen, the top valve of the liquid drain system (Swagelok sample cylinder) was closed so that the system became isolated. The condensed liquid was retrieved under pressure and it was transferred to a pre-weighed glass vial. The process was repeated until most of the condensed liquid was retrieved and the plug valve isolating the bottom part of the reactor was shut off so that the bed is dropped.

## 5. Catalyst isolation, Soxhlet extraction

The SILP catalyst/bed material (20 g) was collected at the end of every experiment and washed with diethyl ether (100 ml), aiming to the removal of any organic compounds that might have remained dissolved in the Lewis acidic ionic liquid. The solid SILPs were therefore treated with Soxhlet extraction (100 ml Et<sub>2</sub>O, 55 °C, 4 h). All samples were submitted for GC(EI) and GC(FID) offline analysis together with the neat samples that were obtained from the low-temperature vapours trap.

## 6. Offline analysis of the product mixtures

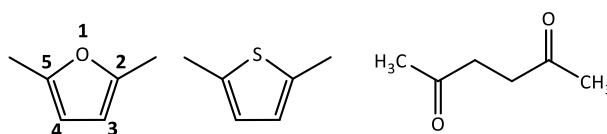


**Figure 3.40:** Chemical structure and ring numbering of 2,5-DMF, 2,5-DMT and 2,5-hexanedione: a key reaction intermediate.

The product mixtures, isolated from the LSS system for reactions R01 and R02, was analysed by <sup>1</sup>H NMR spectroscopy to verify whether there was any conversion of 2,5-DMF to 2,5-DMT and/or 2,5-hexanedione. The peaks of the reference compounds, corresponding to different proton groups, are summarized below. Moreover, a testing protocol was developed for the performing GC(EI) and GC(FID) analysis, focusing on detecting and quantifying 2,5-DMF, 2,5-DMT and 2,5-hxd (**Section 3.3**). The information relevant to testing the standards, including the GC(FID) calibration curves, can be found in the **Appendix** (Figure 3.50 – 3.52 & Figure 3.56).

### (I) 2,5-dimethylfuran (2,5-DMF)

<sup>1</sup>H NMR:  $\delta_{\text{H}}$  (400 MHz, DMSO-d<sub>6</sub>) ppm: 5.89 (2H, s, ring 2CH), 2.19 (6H, s, 2CH<sub>3</sub>).

MS (EI<sup>+</sup>) (*m/z*): 96 (100 %), (GC) retention time: 1.60 min

### (II) 2,5-dimethylthiophene (2,5-DMT)

<sup>1</sup>H NMR:  $\delta_{\text{H}}$  (400 MHz, DMSO-d<sub>6</sub>) ppm: 6.56 (2H, s, ring 2CH), 2.36 (6H, s, 2CH<sub>3</sub>).

2,5-DMT: MS (EI<sup>+</sup>) (*m/z*): 111 (100 %), retention time: 4.12 min

### (III) 2,5-hexanedione (2,5-hxd)

<sup>1</sup>H NMR:  $\delta_{\text{H}}$  (400 MHz, DMSO-d<sub>6</sub>) ppm: 2.62 (4H, s, -O=CCH<sub>2</sub>CH<sub>2</sub>C=O-), 2.10 (6H, s, 2CH<sub>3</sub>C=O-).

2,5-hxd: MS (EI<sup>+</sup>) (*m/z*): 114 (100 %), retention time: 6.20 min

### 3.4 References

- 1 C. P. Mehnert, *Chem. - A Eur. J.*, 2005, **11**, 50–56.
- 2 A. Riisager, R. Fehrmann, M. Haumann and P. Wasserscheid, *Eur. J. Inorg. Chem.*, 2006, **2006**, 695–706.
- 3 H. M. Fehrmann Rasmus, Riisager, Anders, *Supported Ionic Liquids: Fundamentals and Applications*, 2014.
- 4 C. Van Doorslaer, J. Wahlen, P. Mertens, K. Binnemans and D. De Vos, *Dalt. Trans.*, 2010, **39**, 8377.
- 5 F. Kohler, D. Roth, E. Kuhlmann, P. Wasserscheid and M. Haumann, *Green Chem.*, 2010, **12**, 979.
- 6 C. DeCastro, E. Sauvage, M. H. Valkenberg and W. F. Hölderich, *J. Catal.*, 2000, **196**, 86–94.
- 7 S. Zhang, J. Zhang, Y. Zhang and Y. Deng, *Chem. Rev.*, 2017, **117**, 6755–6833.
- 8 J. Joni, M. Haumann and P. Wasserscheid, *Adv. Synth. Catal.*, 2009, **351**, 423–431.
- 9 M. . Valkenberg, C. DeCastro and W. . Hölderich, *Appl. Catal. A Gen.*, 2001, **215**, 185–190.
- 10 M. H. Valkenberg, C. DeCastro and W. F. Hölderich, *Green Chem.*, 2002, **4**, 88–93.
- 11 J. Miao, H. Wan, Y. Shao, G. Guan and B. Xu, *J. Mol. Catal. A Chem.*, 2011, **348**, 77–82.
- 12 A. Riisager, *J. Catal.*, 2003, **219**, 452–455.
- 13 S. Werner, N. Szesni, M. Kaiser, M. Haumann and P. Wasserscheid, *Chem. Eng. Technol.*, 2012, **35**, 1962–1967.
- 14 A. S. Amarasekara, *Chem. Rev.*, 2016, **116**, 6133–6183.
- 15 J. Estager, J. D. Holbrey and M. Swadźba-Kwaśny, *Chem. Soc. Rev.*, 2014, **43**, 847–886.
- 16 M. Haumann, K. Dentler, J. Joni, A. Riisager and P. Wasserscheid, *Adv. Synth. Catal.*, 2007, **349**, 425–431.
- 17 C. P. Mehnert, R. A. Cook, N. C. Dispenziere and M. Afeworki, *J. Am. Chem. Soc.*, 2002, **124**, 12932–12933.
- 18 C. P. Mehnert, E. J. Mozeleski and R. A. Cook, *Chem. Commun.*, 2002, 3010–3011.
- 19 C. Sievers, O. Jiménez, R. Knapp, X. Lin, T. E. Müller, A. Türlér, B. Wierczinski and J. A. Lercher, *J. Mol. Catal. A Chem.*, 2008, **279**, 187–199.
- 20 US5315019, 1994.
- 21 N. V Plechkova and K. R. Seddon, *Chem Soc Rev*, 2008, **37**, 123–150.
- 22 M. Abai, M. P. Atkins, A. Hassan, J. D. Holbrey, Y. Kuah, P. Nockemann, A. A. Oliferenko, N. V. Plechkova, S. Rafeen, A. A. Rahman, R. Ramli, S. M. Shariff, K. R. Seddon, G. Srinivasan and Y. Zou, *Dalt. Trans.*, 2015, **44**, 8617–8624.
- 23 J. Joni, M. Haumann and P. Wasserscheid, *Appl. Catal. A Gen.*, 2010, **372**, 8–15.
- 24 M. Haumann, M. Jakuttis, R. Franke, A. Schönweiz and P. Wasserscheid, *ChemCatChem*, 2011, **3**, 1822–1827.
- 25 M. J. Schneider, M. Lijewski, R. Woelfel, M. Haumann and P. Wasserscheid, *Angew. Chemie Int. Ed.*, 2013, **52**, 6996–6999.
- 26 J. Scholz, V. Hager, X. Wang, F. T. U. Kohler, M. Sternberg, M. Haumann, N. Szesni, K. Meyer and P. Wasserscheid, *ChemCatChem*, 2014, **6**, 162–169.
- 27 F. T. U. Kohler, K. Gärtner, V. Hager, M. Haumann, M. Sternberg, X. Wang, N. Szesni, K. Meyer and P. Wasserscheid, *Catal. Sci. Technol.*, 2014, **4**, 936–947.

- 28 N. V. Ignat'ev, U. Welz-Biermann, A. Kucheryna, G. Bissky and H. Willner, *J. Fluor. Chem.*, 2005, **126**, 1150–1159.
- 29 L. S. Caretto and K. Nobe, *AIChE J.*, 1969, **15**, 18–24.
- 30 K. S. W. Sing, *Pure Appl. Chem.*, , DOI:10.1351/pac198557040603.
- 31 A. Grosman and C. Ortega, *Langmuir*, 2005, **21**, 10515–10521.
- 32 I. Langmuir, *J. Am. Chem. Soc.*, 1916, **38**, 2221–2295.
- 33 Paul Webb; Clyde Orr, *Analytical Methods in Fine Particle Technology*, Micromeritics Instrument Corporation, 1997.
- 34 S. Brunauer, P. H. Emmett and E. Teller, *J. Am. Chem. Soc.*, 1938, **60**, 309–319.
- 35 K. Rouquerol, Jean Rouquerol, Françoise Llewellyn, Philip Maurin, Guillaume Sing, *Adsorption by Powders and Porous Solids*, Academic Press, 2013.
- 36 E. P. Barrett, L. G. Joyner and P. P. Halenda, *J. Am. Chem. Soc.*, 1951, **73**, 373–380.
- 37 G. Halsey, *J. Chem. Phys.*, 1948, **16**, 931–937.
- 38 L. Gurvitsch, *Russ. J. Phys. Chem*, 1915, **47**, 805–827.
- 39 M. Haumann, A. Schönweiz, H. Breitzke, G. Buntkowsky, S. Werner and N. Szesni, *Chem. Eng. Technol.*, 2012, **35**, 1421–1426.
- 40 M. T. Heinze, J. C. Zill, J. Matysik, W. D. Einicke, R. Gläser and A. Stark, *Phys. Chem. Chem. Phys.*, 2014, **16**, 24359–24372.
- 41 M. J. Duer, *Introduction to Solid-State NMR Spectroscopy*, Wiley-Blackwell, 2004.
- 42 B. D. Fitchett and J. C. Conboy, *J. Phys. Chem. B*, 2004, **108**, 20255–20262.
- 43 C. Romero and S. Baldelli, *J. Phys. Chem. B*, 2006, **110**, 6213–6223.
- 44 N. Sieffert and G. Wipff, *J. Phys. Chem. C*, 2008, **112**, 19590–19603.
- 45 S. Bovio, A. Podestà, C. Lenardi and P. Milani, *J. Phys. Chem. B*, 2009, **113**, 6600–6603.
- 46 G. Ori, F. Villemot, L. Viau, A. Vioux and B. Coasne, *Mol. Phys.*, 2014, **112**, 1350–1361.
- 47 G. Kritikos, N. Vergadou and I. G. Economou, *J. Phys. Chem. C*, 2016, **120**, 1013–1024.
- 48 B. Coasne, L. Viau and A. Vioux, *J. Phys. Chem. Lett.*, 2011, **2**, 1150–1154.
- 49 L. Rodríguez-Pérez, Y. Coppel, I. Favier, E. Teuma, P. Serp and M. Gómez, *Dalt. Trans.*, 2010, **39**, 7565.
- 50 M. R. Castillo, J. M. Fraile and J. A. Mayoral, *Langmuir*, 2012, **28**, 11364–11375.
- 51 J. Le Bideau, P. Gaveau, S. Bellayer, M.-A. Néouze and A. Vioux, *Phys. Chem. Chem. Phys.*, 2007, **9**, 5419.
- 52 M. Waechtler, M. Sellin, A. Stark, D. Akcakayiran, G. Findenegg, A. Gruenberg, H. Breitzke and G. Buntkowsky, *Phys. Chem. Chem. Phys.*, 2010, **12**, 11371.
- 53 K. S. Han, X. Wang, S. Dai and E. W. Hagaman, *J. Phys. Chem. C*, 2013, **117**, 15754–15762.
- 54 M. P. Singh, Y. L. Verma, A. K. Gupta, R. K. Singh and S. Chandra, *Ionics (Kiel)*, 2014, **20**, 507–516.
- 55 B. Grünberg, T. Emmler, E. Gedat, I. Shenderovich, G. H. Findenegg, H.-H. Limbach and G. Buntkowsky, *Chem. - A Eur. J.*, 2004, **10**, 5689–5696.
- 56 G. Buntkowsky, H. Breitzke, A. Adamczyk, F. Roelofs, T. Emmler, E. Gedat, B. Grünberg, Y. Xu, H.-H. Limbach, I. Shenderovich, A. Vyalikh and G. Findenegg, *Phys. Chem. Chem. Phys.*, 2007, **9**, 4843.
- 57 C. E. Bronnimann, R. C. Zeigler and G. E. Maciel, *J. Am. Chem. Soc.*, 1988, **110**, 2023–2026.

- 58 T. C. Farrar and E. D. Becker, *Fourier Transform NMR*, Elsevier, 1971.
- 59 S. Chen, Y. Liu, H. Fu, Y. He, C. Li, W. Huang, Z. Jiang and G. Wu, *J. Phys. Chem. Lett.*, 2012, **3**, 1052–1055.
- 60 M. Kosmulski, J. Gustafsson and J. B. Rosenholm, *Thermochim. Acta*, 2004, **412**, 47–53.
- 61 J. Lemus, J. Palomar, M. A. Gilarranz and J. J. Rodriguez, *Adsorption*, 2011, **17**, 561–571.
- 62 A. Akçay, M. Babucci, V. Balci and A. Uzun, *Chem. Eng. Sci.*, 2015, **123**, 588–595.
- 63 A. Akçay, V. Balci and A. Uzun, *Thermochim. Acta*, 2014, **589**, 131–136.
- 64 M. Babucci, A. Akçay, V. Balci and A. Uzun, *Langmuir*, 2015, **31**, 9163–9176.
- 65 M. Babucci, V. Balci, A. Akçay and A. Uzun, *J. Phys. Chem. C*, 2016, **120**, 20089–20102.
- 66 J. Werther, in *Ullmann's Encyclopedia of Industrial Chemistry*, Wiley-VCH Verlag GmbH & Co. KGaA, Weinheim, Germany, 2007.
- 67 T. Cocco, R., Karri, S. B. R., Knowlton, *Chem. Eng. Prog.*, 2014, **110**, 21–29.
- 68 D. Geldart, *Powder Technol.*, 1973, **7**, 285–292.
- 69 J. R. Epstein, Norman, Grace, *Spouted and Spout-Fluid Beds. Fundamentals and Applications*, Cambridge University Press, 2010.
- 70 F. Manurung, Univeristy of New South Wales, 1965.
- 71 K. B. Mathur and N. Epstein, 1974, pp. 111–191.
- 72 C. Y. Wen and Y. H. Yu, *AIChE J.*, 1966, **12**, 610–612.
- 73 Z. Zhang, Imperial College London, 2014.
- 74 L. . White, A, Marek, *Ind. Eng. Chem. Res.*
- 75 Z. Lei, C. Dai and B. Chen, *Chem. Rev.*, 2014, **114**, 1289–1326.
- 76 N. H. Ko, J. S. Lee, E. S. Huh, H. Lee, K. D. Jung, H. S. Kim and M. Cheong, *Energy & Fuels*, 2008, **22**, 1687–1690.
- 77 P. S. Kulkarni and C. A. M. Afonso, *Green Chem.*, 2010, **12**, 1139.
- 78 S. Zhang and Z. Conrad Zhang, *Green Chem.*, 2002, **4**, 376–379.
- 79 Q.-G. Zhang and Y. Wei, *J. Chem. Thermodyn.*, 2008, **40**, 640–644.

### 3.5 Appendix

#### 3.5.1 IUPAC classification of N<sub>2</sub>-physisorption isotherms

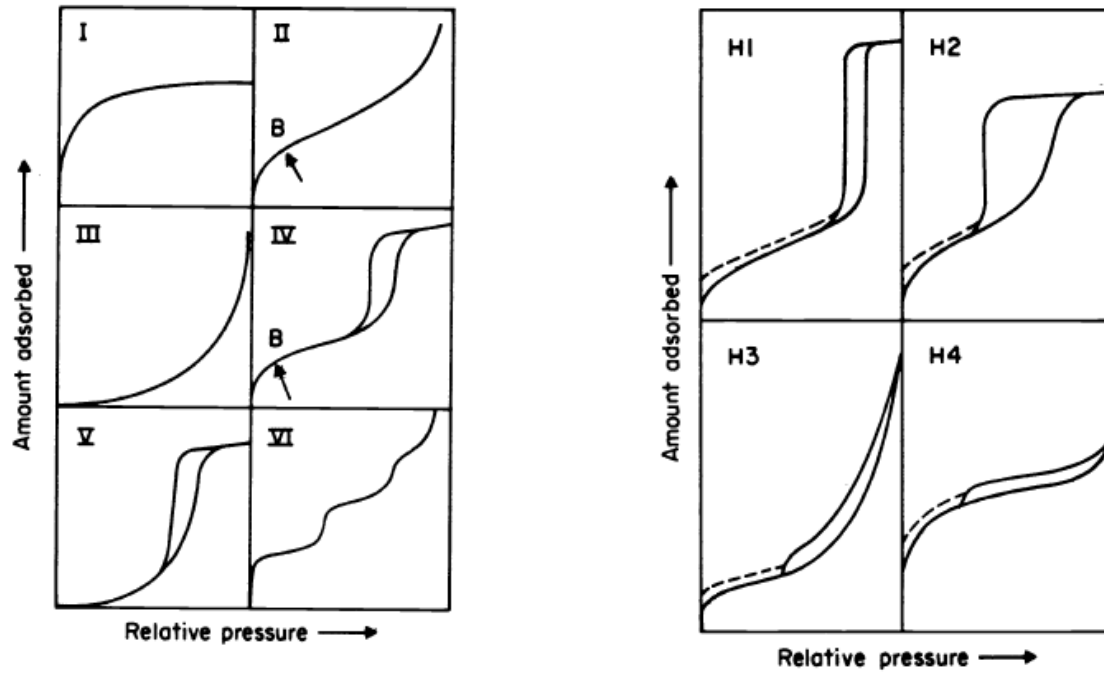


**Figure 3.41:** Physisorption isotherms and hysteresis loops; IUPAC classification; **Type I:** characteristic for microporous materials; **Type II and IV:** indicative of either non-porous materials or materials with very large pores; **Types III and V:** characteristic of conditions where the adsorptive molecules have a greater affinity to one another than they do for the solid; **Type VI:** indicative of a non-porous material and a rarely uniform surface.<sup>30</sup>

### 3.5.2 Pore area distribution graphs of SiO<sub>2</sub>-150 Å-based SILPs as a function of $\epsilon_{IL}$ – BJH theory

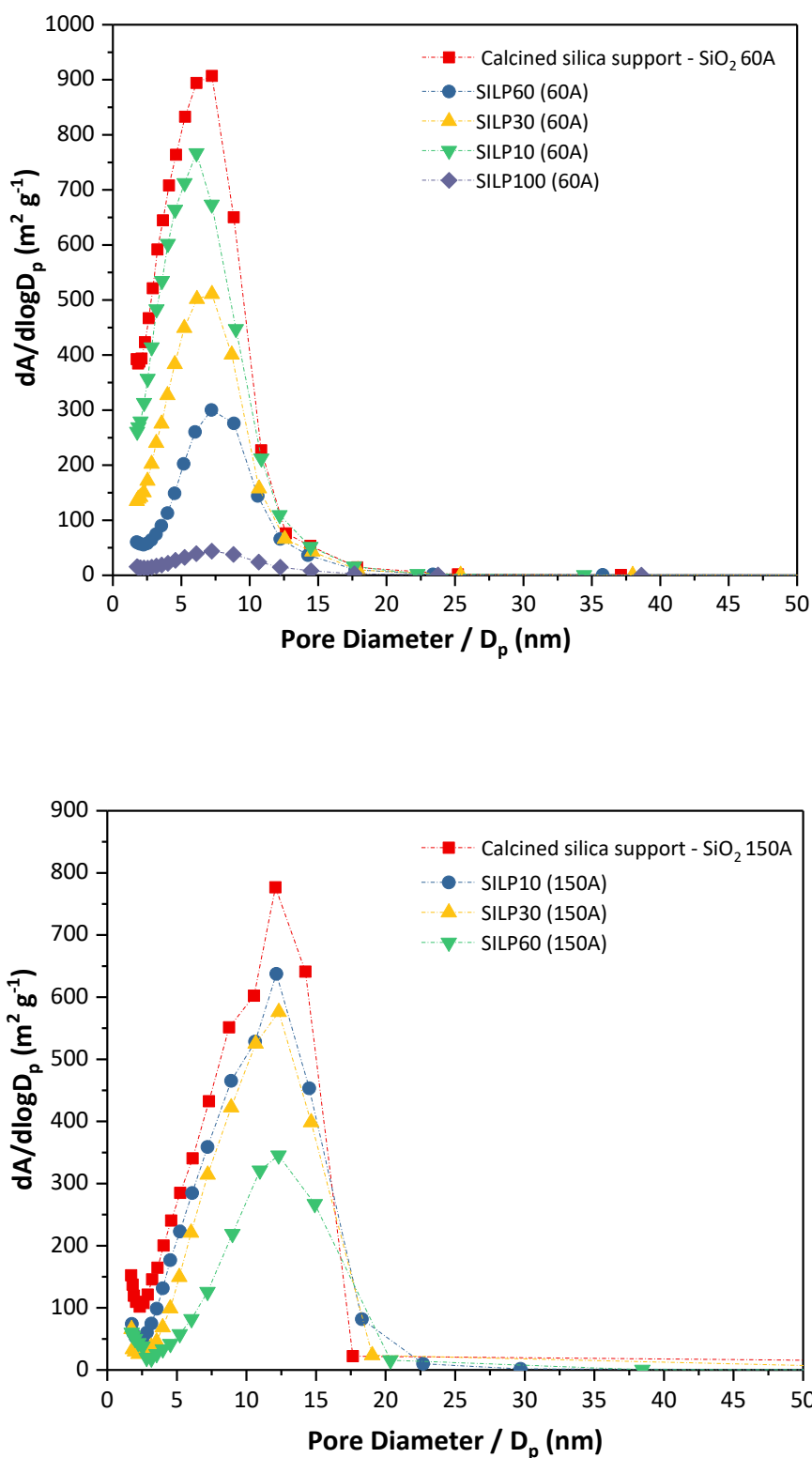


**Figure 3.42:** Pore area distribution for 1.7 - 50 nm (mesoporous region) as determined by BJH N<sub>2</sub> adsorption analysis for a) SiO<sub>2</sub> 60 Å-based SILPs with varying loadings of [C<sub>4</sub>C<sub>1</sub>im]Cl-ZnCl<sub>2</sub> ( $X_{ZnCl_2} = 0.67$ ) – ( $\epsilon_{IL} = 10 - 100\%$ ) and b) SiO<sub>2</sub> 150 Å-based SILPs with varying loadings of [C<sub>4</sub>C<sub>1</sub>im]Cl-ZnCl<sub>2</sub> ( $X_{ZnCl_2} = 0.67$ ) – ( $\epsilon_{IL} = 10 - 60\%$ ).

3.5.3 Effect of  $n_{IL}$  ( $\text{mmol g}^{-1}$ ) on the surface characteristics of Lewis acidic SILPs with varying amounts of  $[\text{C}_4\text{C}_1\text{im}]\text{Cl}\cdot\text{ZnCl}_2$  ( $X_{\text{ZnCl}_2} = 0.67$ )

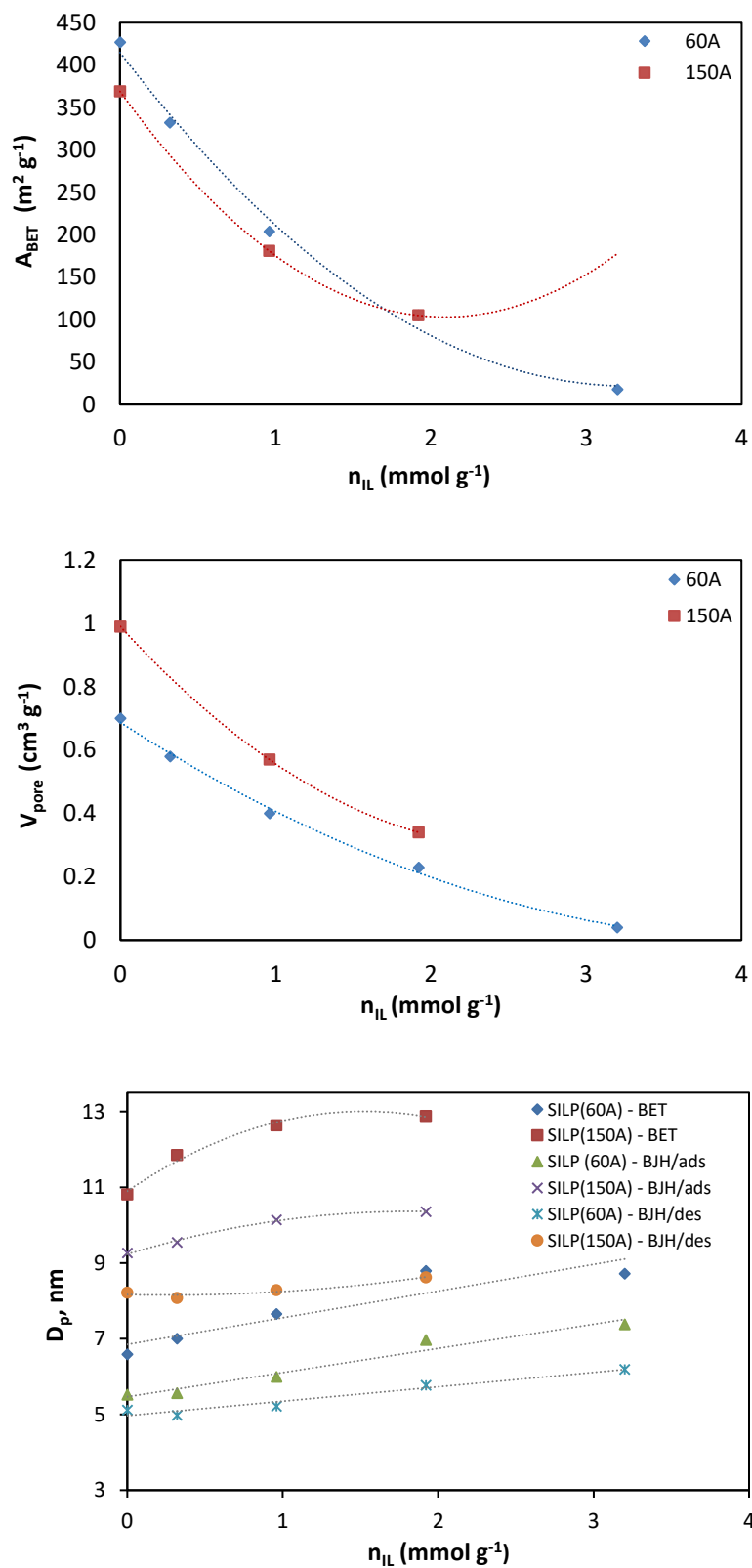


Figure 3.43: Effect of the ionic loading ( $n_{IL}$  /  $\text{mmol g}^{-1}$ ) on the surface characteristics of  $[\text{C}_4\text{C}_1\text{im}]\text{Cl}\cdot\text{ZnCl}_2$  ( $X_{\text{ZnCl}_2} = 0.67$ ) - based SILPs: i) surface area ( $A_{\text{BET}}$ ;  $\text{m}^2 \text{g}^{-1}$ ), single point adsorption total pore volume ( $V_{\text{pore}}$ ;  $\text{cm}^3 \text{g}^{-1}$ ) and average pore size ( $D_p$ , nm).



3.5.4 Static and  $^1\text{H}$  MAS ssNMR spectra of  $\text{SiO}_2$ -150 Å-based SILPs as a function of composition;  $[\text{C}_4\text{C}_{1\text{im}}]\text{Cl}\cdot\text{ZnCl}_2$  ( $X_{\text{ZnCl}_2} = 0.67$ )

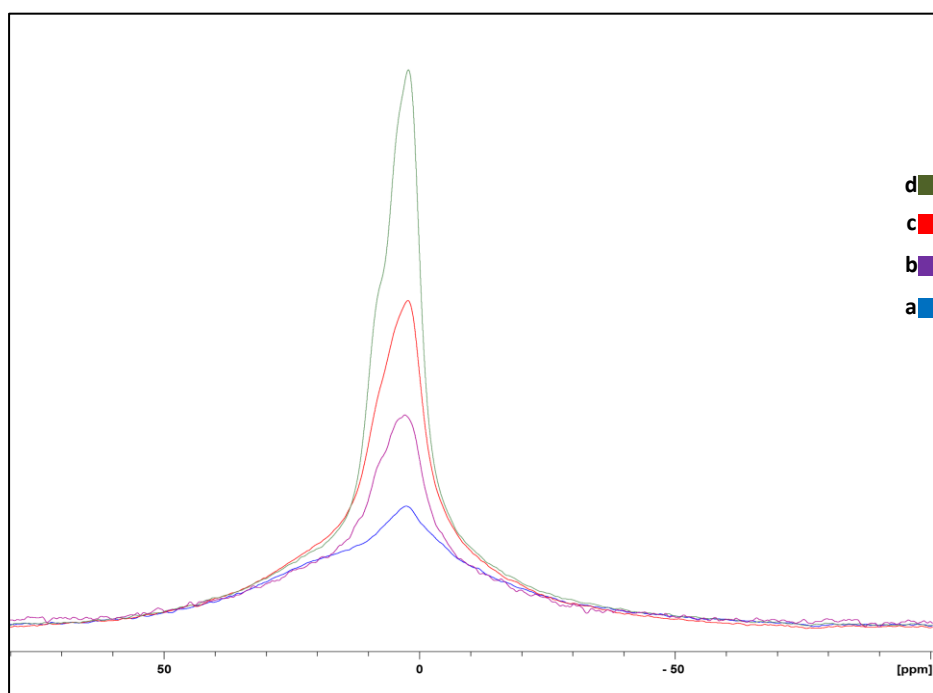


Figure 3.44: Static  $^1\text{H}$  NMR spectra of  $\text{SiO}_2$ -150 Å-based SILPs as a function of  $\epsilon_{\text{IL}}$ ;  $[\text{C}_4\text{C}_{1\text{im}}]\text{Cl}\cdot\text{ZnCl}_2$  ( $X_{\text{ZnCl}_2} = 0.67$ )  
 a) Parent support ( $\text{SiO}_2$ -150 Å), b)  $\epsilon_{\text{IL}} = 10\%$ , c)  $\epsilon_{\text{IL}} = 30\%$  and d)  $\epsilon_{\text{IL}} = 60\%$

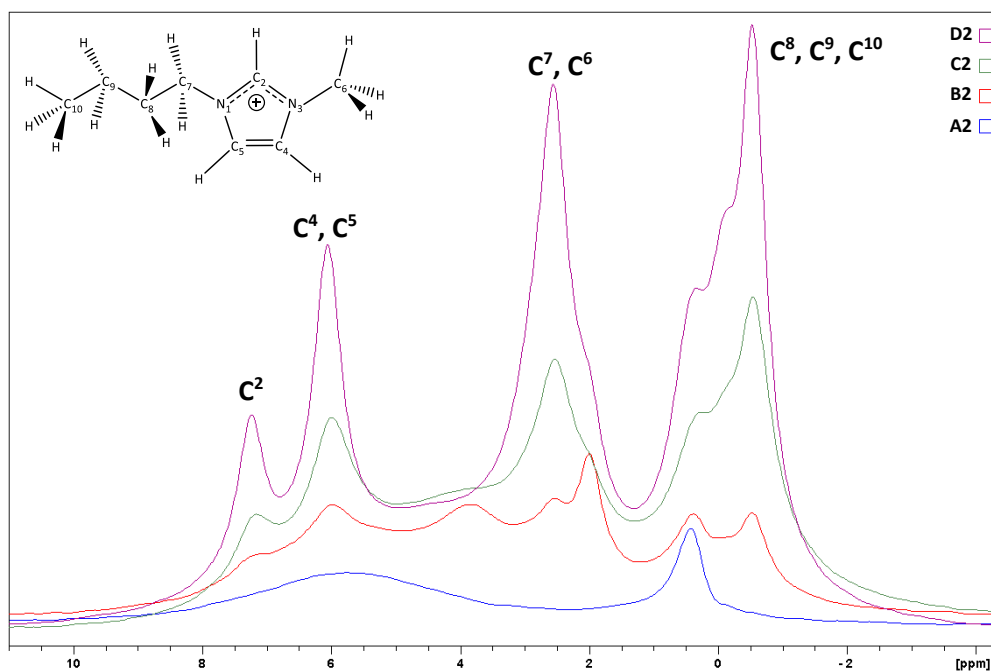
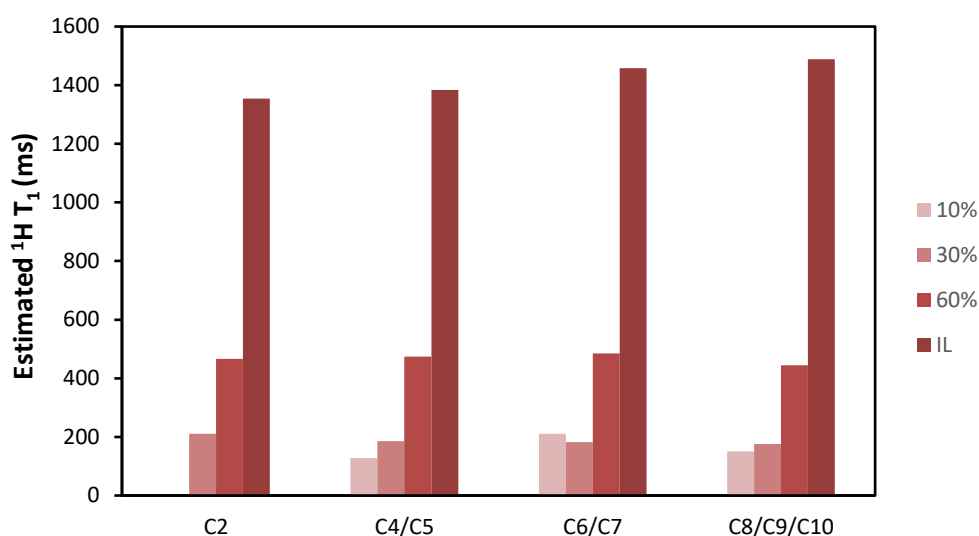


Figure 3.45:  $^1\text{H}$  MAS NMR spectra of  $\text{SiO}_2$ -150 Å-based SILPs with variable loadings of  $[\text{C}_4\text{C}_{1\text{im}}]\text{Cl}\cdot\text{ZnCl}_2$  ( $X_{\text{ZnCl}_2} = 0.67$ )  
 Ionic liquid loading ( $\epsilon_{\text{IL}}$ ): A2: 0%, B2: 10%, C2: 30% and D2: 60%

**3.5.5  $T_1$  relaxation time calculations for  $\text{SiO}_2$ -150 Å-based SILPs as a function of composition;  $[\text{C}_4\text{C}_1\text{im}]\text{Cl}\cdot\text{ZnCl}_2$  ( $X_{\text{ZnCl}_2} = 0.67$ ) – Inversion recovery pulse sequence**



**Figure 3.46:** Estimated  $^1\text{H}$   $T_1$  relaxation times across the imidazolium cation for  $\text{SiO}_2$ -150 Å-based SILP catalysts as a function of  $\epsilon_{\text{IL}}$  (10 % – 60 %) - (IL:  $[\text{C}_4\text{C}_1\text{im}]\text{Cl}\cdot\text{ZnCl}_2$  ( $X_{\text{ZnCl}_2} = 0.67$ )).

**Table 3.11:** Inversion recovery pulse sequence –  $^1\text{H}$   $T_1$  estimation; RSS for the regression with 1 or 2 components for the  $\text{SiO}_2$ -150 Å-based SILP catalyst at  $\epsilon_{\text{IL}} = 10\%$  and the  $\text{SiO}_2$ -60 Å-based SILPs at  $\epsilon_{\text{IL}} = 10\%$  or  $30\%$  ( $[\text{C}_4\text{C}_1\text{im}]\text{Cl}\cdot\text{ZnCl}_2$  ( $X_{\text{ZnCl}_2} = 0.67$ )).

Sample	Peak C <sup>4</sup> /C <sup>5</sup>		Peak C <sup>6</sup> /C <sup>7</sup>		Peak C <sup>8</sup> /C <sup>9</sup> /C <sup>10</sup>	
	1 component	2 components	1 component	2 components	1 component	2 components
SILP10 (60A)	3.13E-004	4.69E-005	1.95E-003	1.95E-004	6.92E-005	2.45E-005
SILP30 (60A)	7.26E-004	4.92E-005	3.71E-003	1.49E-004	1.33E-002	1.92E-004
SILP10 (150)	6.27E-004	9.69E-005	6.27E-004	1.30E-004	7.60E-004	1.03E-004

### 3.5.6 Thermal stability of SiO<sub>2</sub>-150 Å-based SILPs as a function of $\epsilon_{IL}$ ([C<sub>4</sub>C<sub>1</sub>im]Cl·ZnCl<sub>2</sub> (X<sub>ZnCl<sub>2</sub></sub> = 0.67)) Dynamic Scans

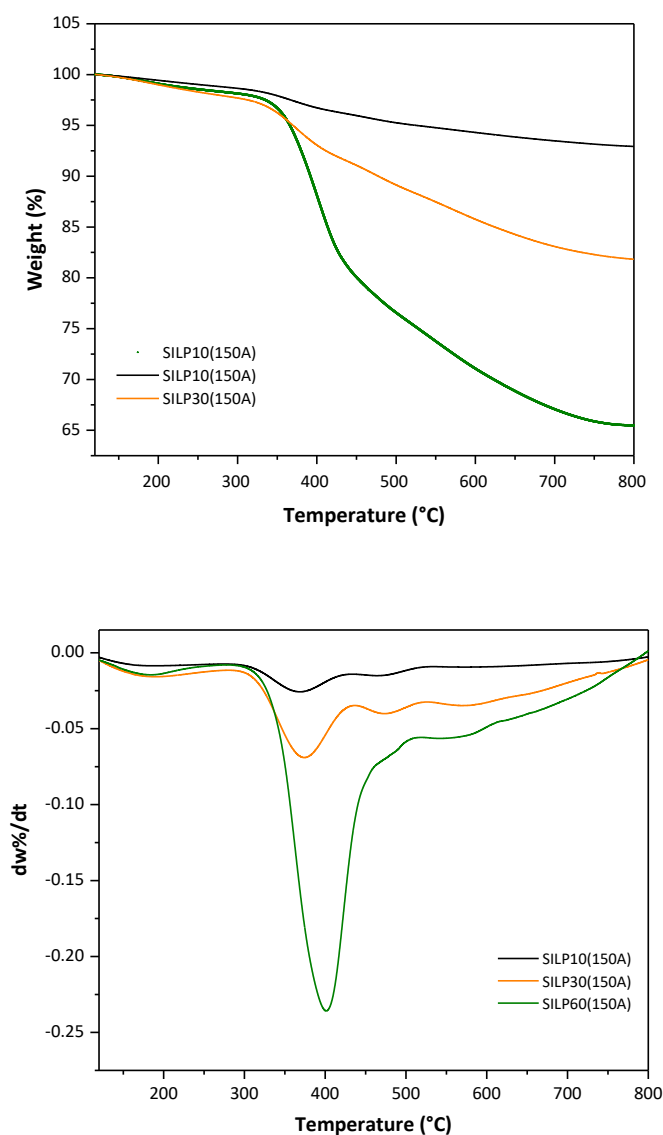


**Figure 3.47:** a) Temperature-ramped (TG) and b) derivative (DTG) curves for SiO<sub>2</sub>-150 Å-based SILPs with variable loadings of [C<sub>4</sub>C<sub>1</sub>im]Cl·ZnCl<sub>2</sub> (X<sub>ZnCl<sub>2</sub></sub> = 0.67) - ( $\epsilon_{IL}$  = 10 % - 60 %)

**Table 3.12:** Comparison of the  $T_{onset}$  and  $T_{peak}$  values for SiO<sub>2</sub>-150 Å-based chlorozincate(II) SILPs.

Sample	$\epsilon_{IL}$ / %	$T_{onset}$ / °C	$T_{peak}$ / °C
[C <sub>4</sub> C <sub>1</sub> im]Cl·ZnCl <sub>2</sub> , X <sub>ZnCl<sub>2</sub></sub> = 0.67	NA	431	476
SILP10(150A)	10	335	365 <sup>d</sup>
SILP30(150A)	30	330	375 <sup>e</sup>
SILP60(150A)	60	395	406

a, b: a second  $T_{peak}$  is indicated at temperatures > 450 °C for both  $\epsilon_{IL}$  = 10 % and 30 %

### 3.5.7 Thermal stability of the bulk ionic liquid: ([C<sub>4</sub>C<sub>1</sub>im]Cl·ZnCl<sub>2</sub> (X<sub>ZnCl<sub>2</sub></sub> = 0.67))

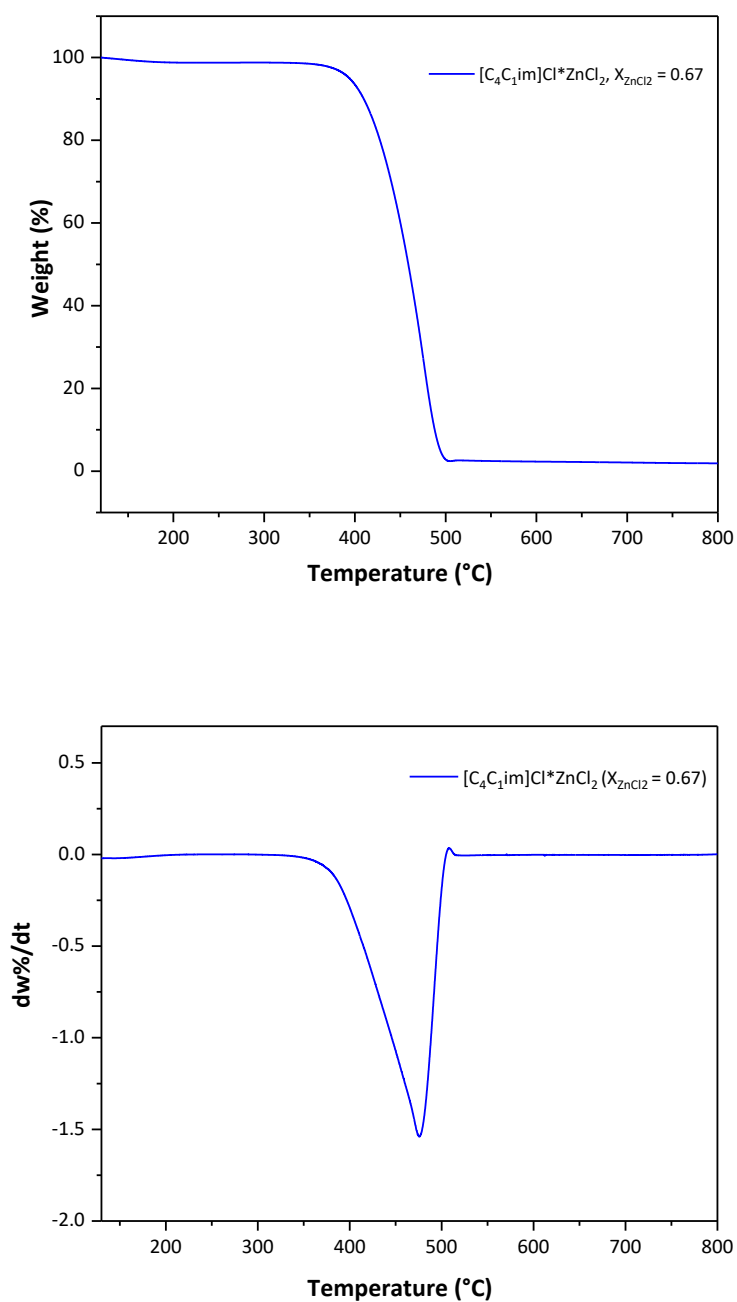


**Figure 3.48:** a) Temperature-ramped (TG) and b) derivative (DTG) curves of the bulk [C<sub>4</sub>C<sub>1</sub>im]Cl·ZnCl<sub>2</sub> (X<sub>ZnCl<sub>2</sub></sub> = 0.67)  
[T<sub>onset</sub> = 431 °C, T<sub>peak</sub> = 476 °C]

3.5.8 Nitrogen density and viscosity correlations with T and P; NIST Chemistry webbook data

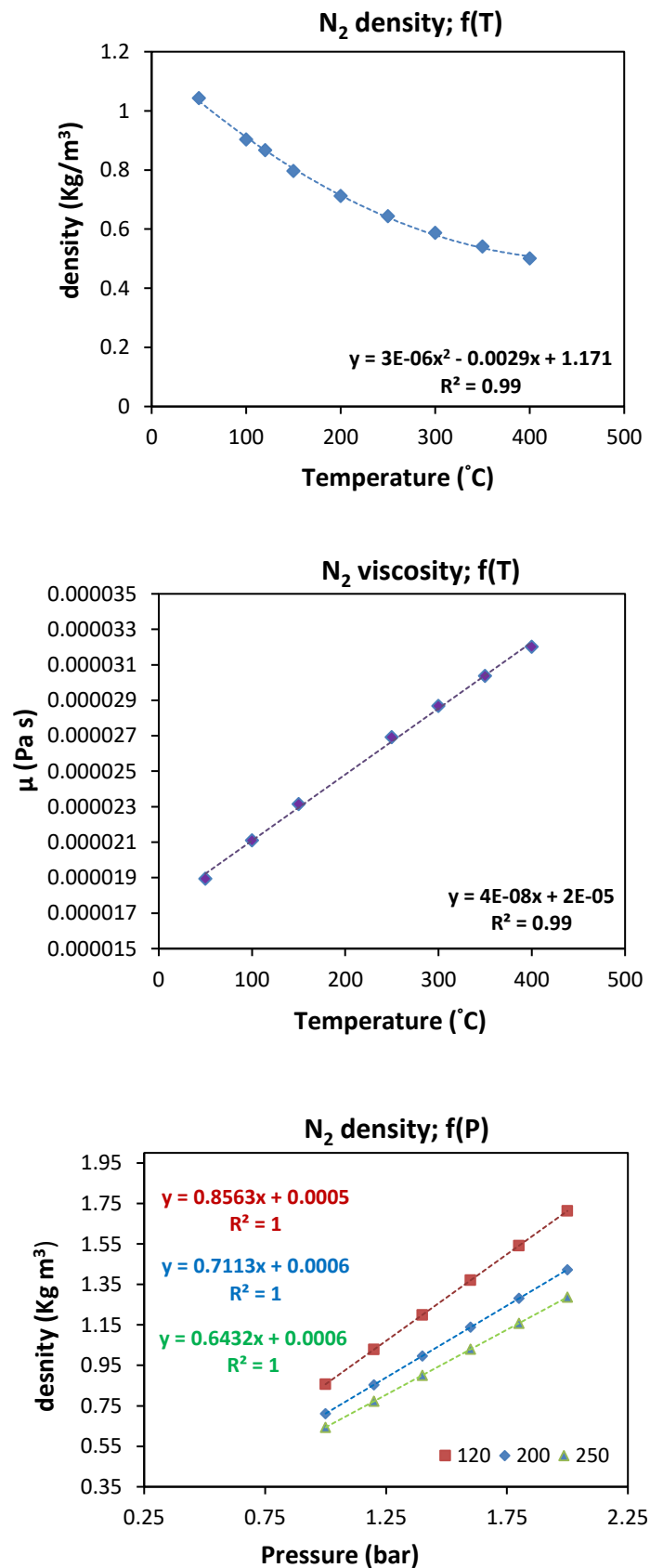


Figure 3.49: NIST Chemistry Webbook data for N<sub>2</sub> as a function of T or P: a) density (Kg/m<sup>3</sup>) and b) viscosity (Pa s)

### 3.5.9 Standards GC(EI) – Mass spectra (2,5-DMF, 2,5-DMT, 2,5-hxd)

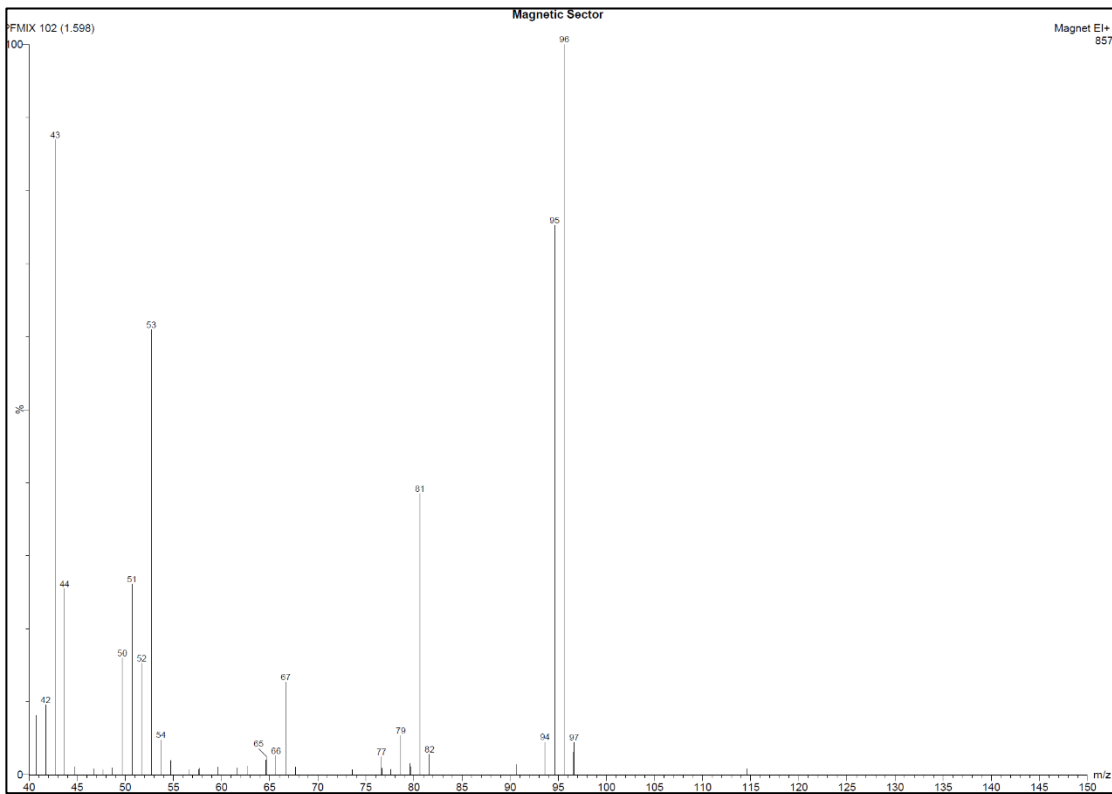


Figure 3.50: GC(EI) spectrum – 2,5-dimethylfuran (2,5-DMF) standard

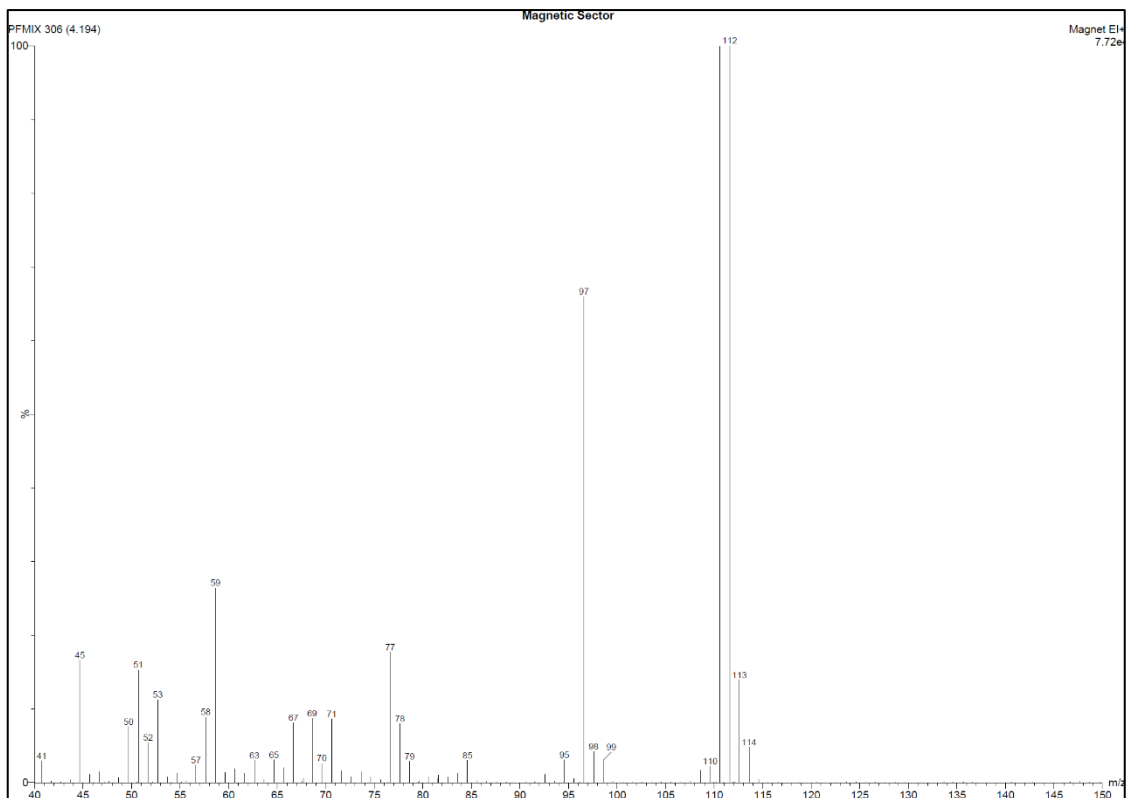


Figure 3.51: GC(EI) spectrum – 2,5-dimethylthiophene (2,5-DMT) standard

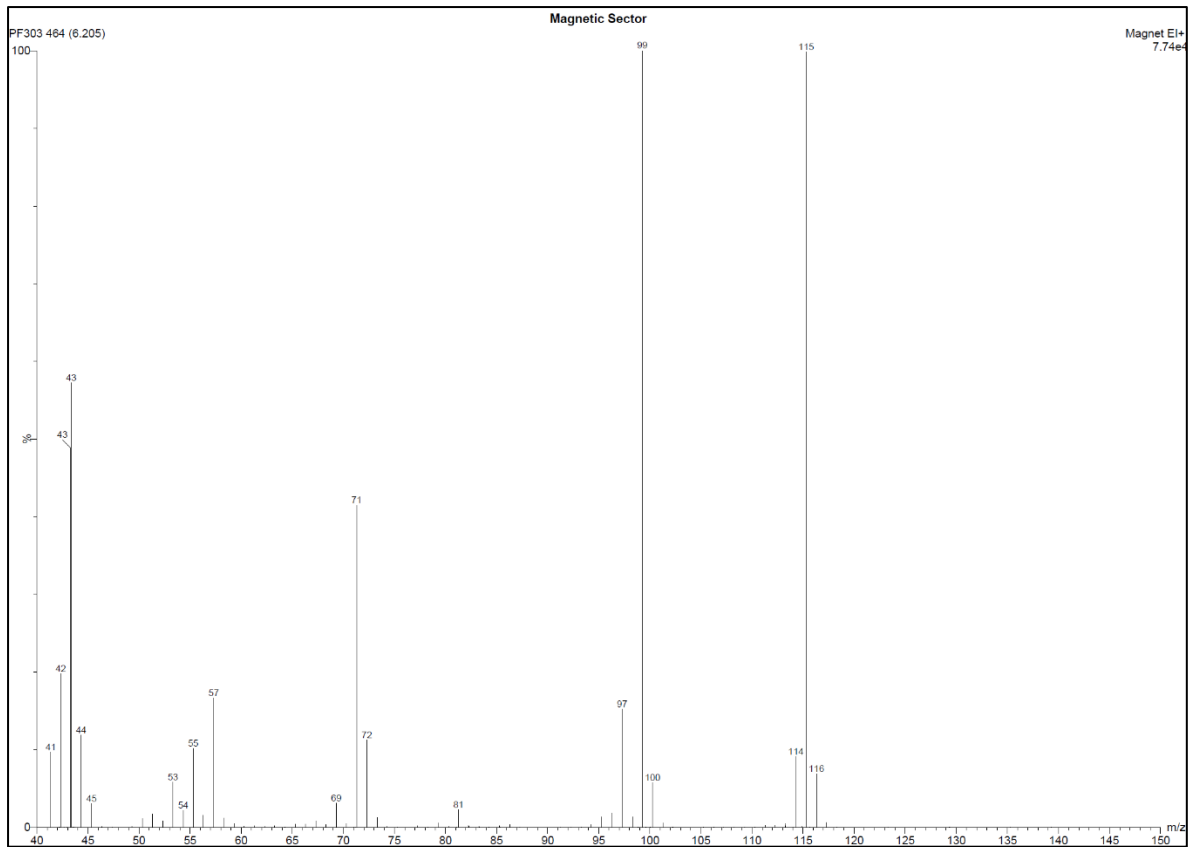
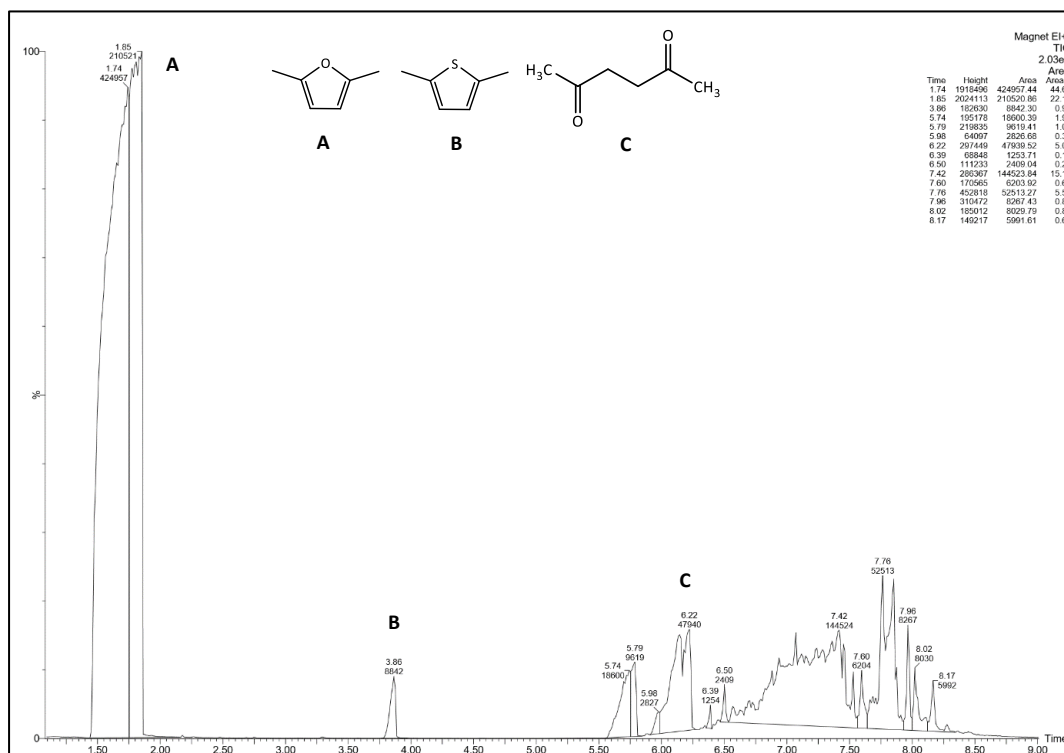
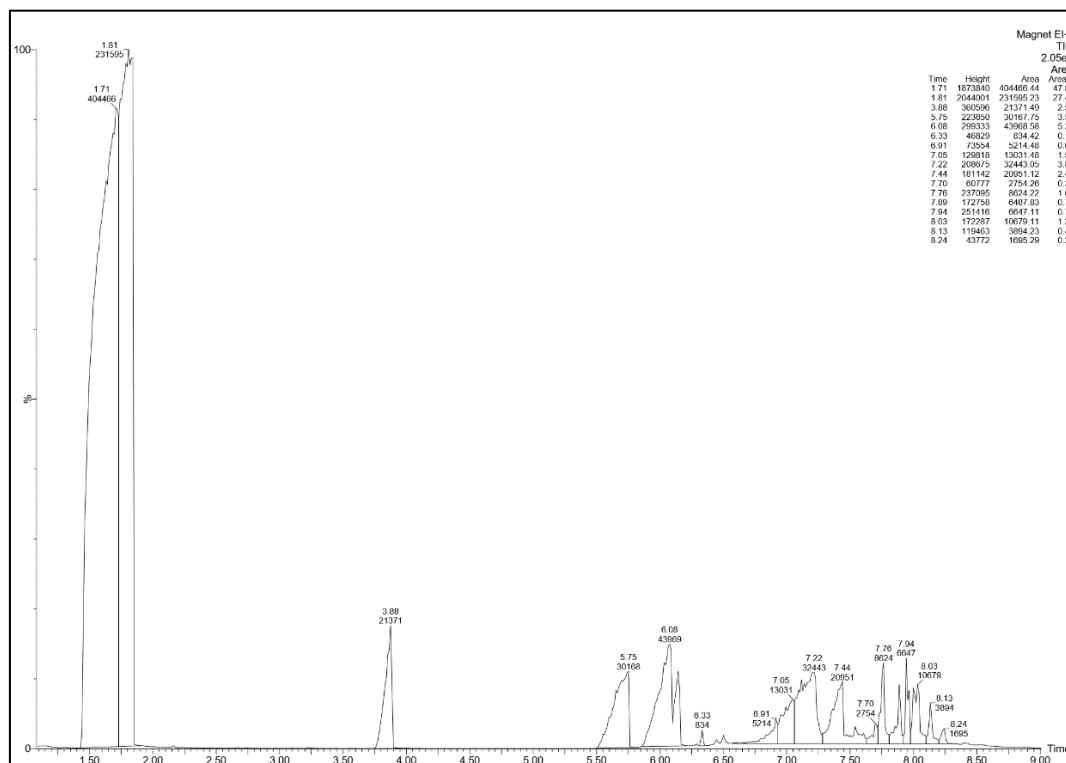


Figure 3.52: GC(EI) spectrum – 2,5-hexanedione (2,5-hxd) standard

### 3.5.10 Sample GC chromatographs; study of the gas-phase synthesis of 2,5-DMT, catalysed by Lewis acidic chlorozincate(II) SILPs.



**Figure 3.53:** GC(EI) analysis (R01)  
[200 °C, SILP30(60A), H<sub>2</sub>S (6.7E-06 mol s<sup>-1</sup>)/2,5-DMF (2.6E-05 mol s<sup>-1</sup>)]



**Figure 3.54:** GC(EI) analysis (R02)  
[200 °C, SILP30(60A), H<sub>2</sub>S (2.1E-05 mol s<sup>-1</sup>)/2,5-DMF (2.1E-05 mol s<sup>-1</sup>)]



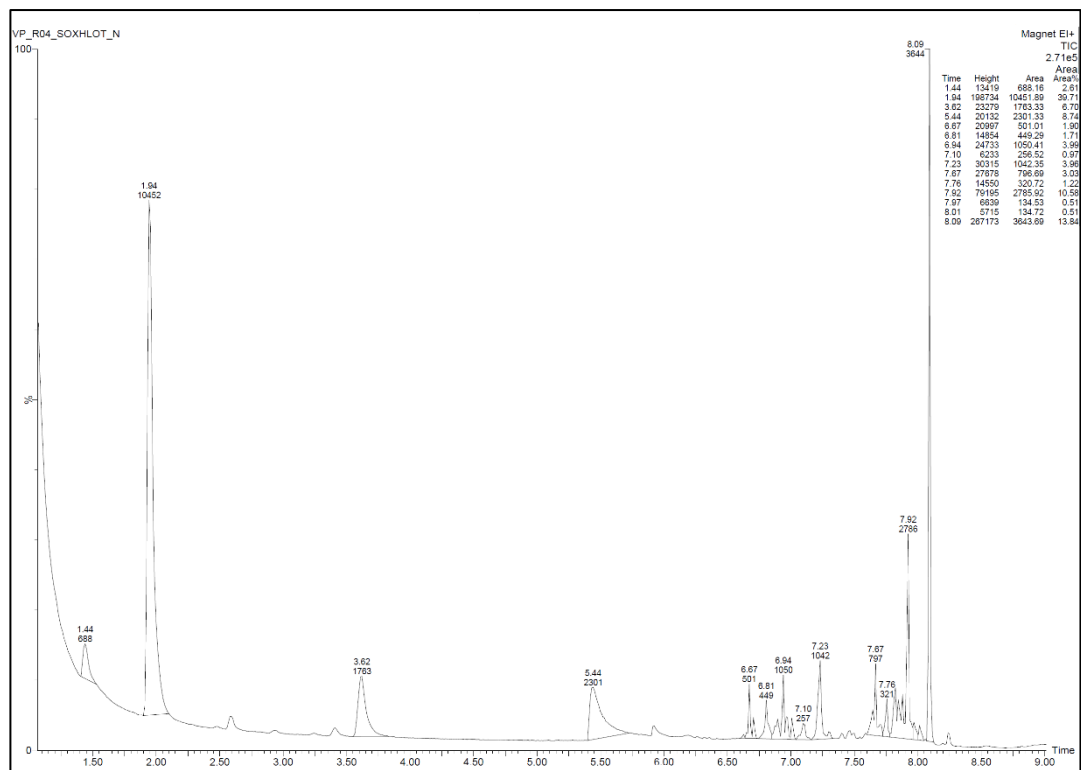


**Figure 3.55: GC(EI) analysis (R04/Soxhlet sample)**  
 [200 °C, SILP60(60A), H<sub>2</sub>S (2.17E-05 mol s<sup>-1</sup>)/2,5-DMF (2.1E-05 mol s<sup>-1</sup>)]

### 3.5.11 Calibration curves (2,5-DMF, 2,5-DMT, 2,5-hxd) – Quantitative analysis GC(FID)

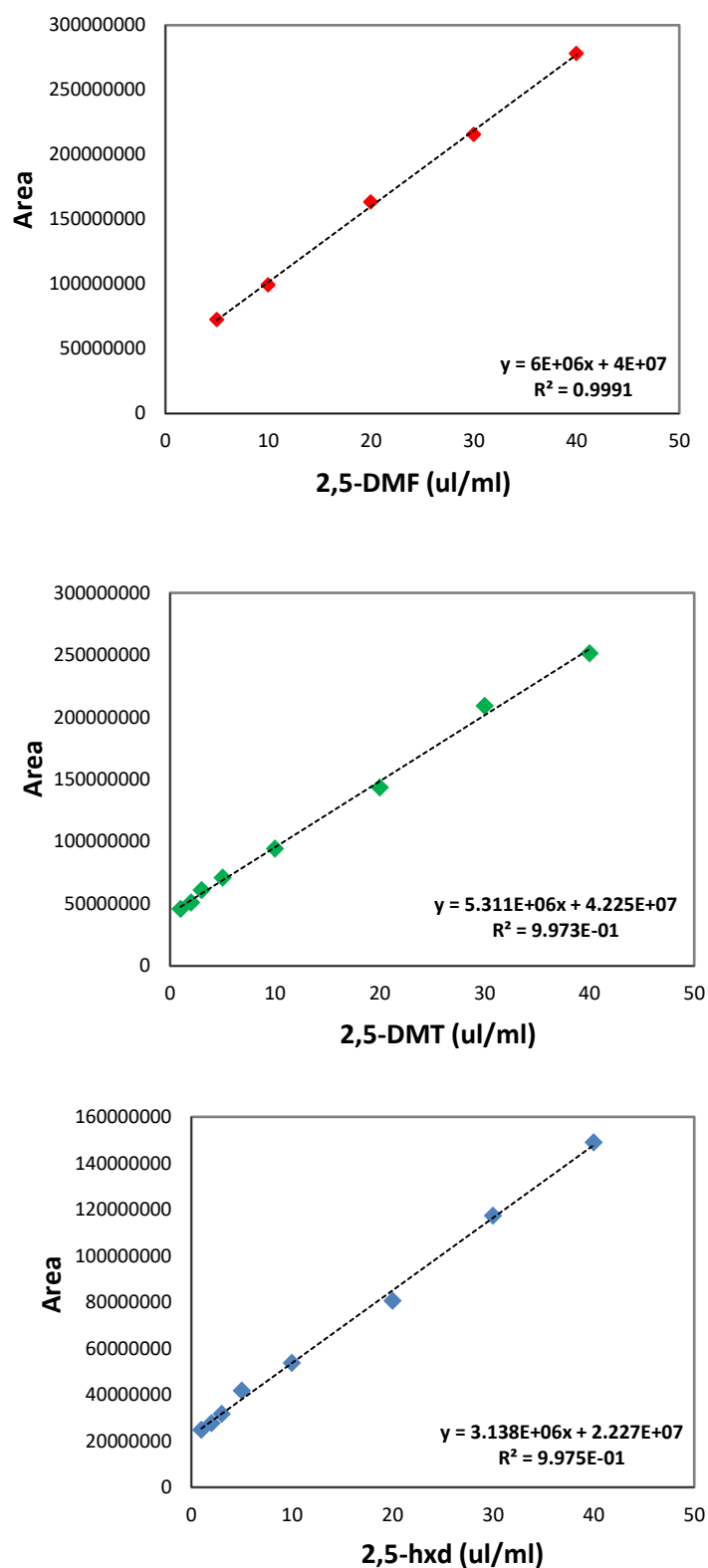


Figure 3.56: GC(FID) calibration curves: i) 2,5-DMF (1.82 min), ii) 2,5-DMT (3.82 min) and iii) 2,5-hxd (6.20 min)

## CHAPTER 4

### Ionic liquids for the synthesis of bio-derived 3,6-dimethylphthalic anhydride

#### 4.1 Introduction

The application of 2,5-dimethylfuran (2,5-DMF) as a platform chemical to produce bio-based aromatics has been summarized in **Chapter 1**, including the synthesis of phthalic anhydride (PA) analogues from furanics towards the production of renewable polyesters and polycarbonates.<sup>1,2</sup> More specifically, the synthesis of bio-derived 3,6-dimethylphthalic anhydride (3,6-DMPA) is a tandem reaction: a cycloaddition of 2,5-DMF to MA, followed by the acid-catalysed dehydrative aromatization of the cycloadduct intermediate (Figure 4.1).<sup>3,4</sup>

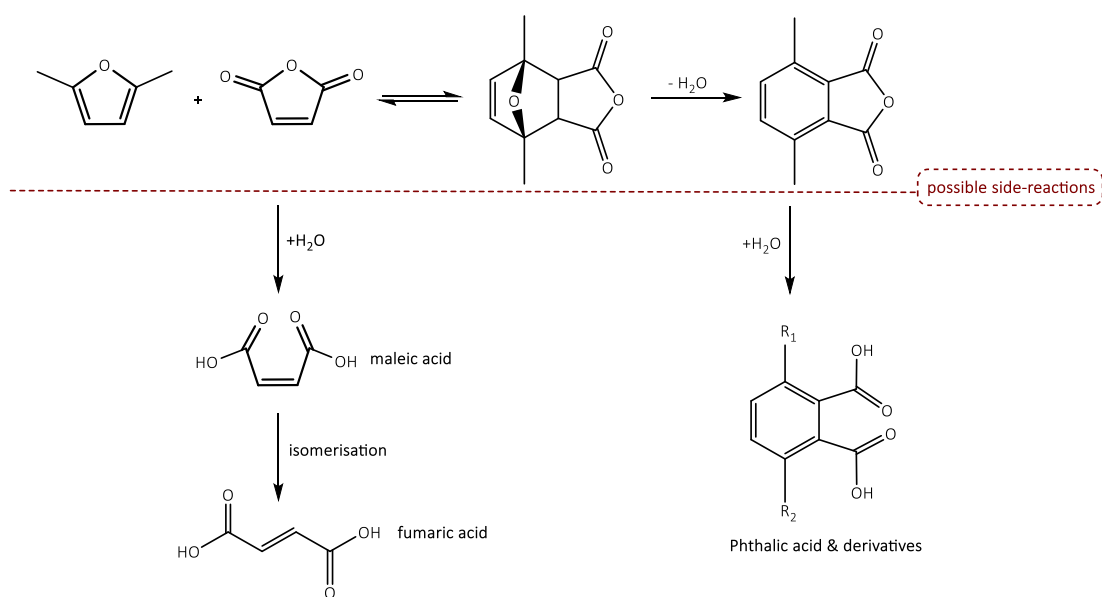


**Figure 4.1:** Synthesis of bio-derived 3,6-dimethylphthalic anhydride (3,6-DMPA) from 2,5-DMF and maleic anhydride (MA), followed by dehydrative aromatization.

The competition between the retro-D-A reaction and the desired dehydrative aromatisation step has been highlighted as a key risk for the reaction between furanics and MA.<sup>4</sup> The formation of phthalic acid derivatives, fumaric acid and maleic acid presents another significant problem, driven by the acid-catalysed hydrolysis of phthalic anhydride and maleic anhydride (Figure 4.1).<sup>4</sup> Moreover, the literature review (**Chapter 1**) revealed that the synthesis of 3,6-DMPA from 2,5-DMF and MA requires different reaction conditions for each step of the Diels-Alder/dehydration reaction scheme. Brønsted acidity

promotes the dehydration of the cycloadduct intermediate whereas Lewis acid catalysis reduces the activation energy of the cycloaddition. Optimising the selectivity towards 3,6-DMPA, especially under Brønsted acidic conditions remains challenging. Low-temperature conditions suppress the retro-Diels-Alder reactions and the decomposition of the starting materials. However, high temperatures promote the dehydrative aromatization but also the formation of side-products.

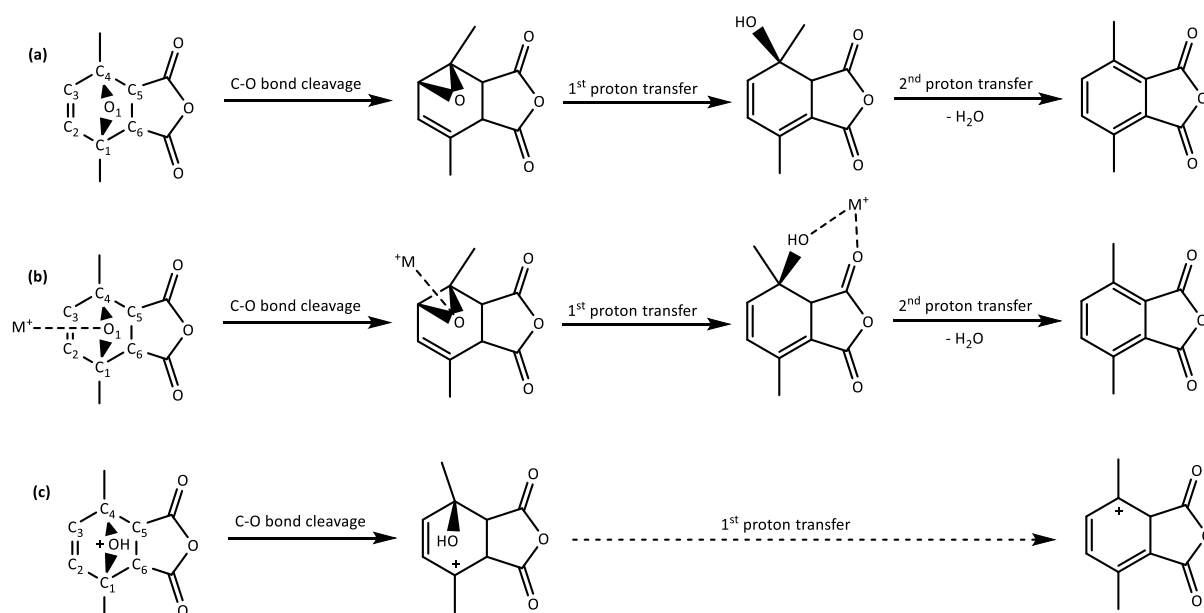


**Figure 4.2:** MA + 2,5-DMF cycloadduct dehydration mechanisms: (a) uncatalyzed; (b) Lewis acid catalysed and (c) Brønsted acid catalysed (gas phase).<sup>5</sup>

Recent DFT calculations have been published, exploring the solvent effects of the acid-catalysed cycloaddition between 2,5-DMF and MA.<sup>6</sup> It was deduced that a Lewis acidic catalyst interacts with MA, lowering the  $\text{HOMO}_{\text{DMF}}\text{-LUMO}_{\text{MA}}$  gap of the reactive species whereas a Brønsted acid binds to the carbonyl oxygen of MA so that the reaction mechanism changes from concerted to stepwise.<sup>6</sup> Additionally, it was estimated that the activation barrier of both Lewis acid ( $\text{Na}^+\text{-MA}$ ) and Brønsted acid-catalysed ( $\text{H}^+\text{-MA}$ ) pathways increases with increasing solvent polarity, whereas the  $\text{H}^+\text{-DMF}$  path is estimated not to be feasible due to a very large activation energy in all studied solvent environments.<sup>6</sup> A high activation barrier value (68.7 kcal/mol) has been calculated for the dehydration of the cycloadduct between 2,5-DMF and MA, in the absence of an added catalyst, without any significantly positive solvent effect.<sup>5</sup> A similar mechanism was estimated for both the Lewis acid-catalysed and the uncatalyzed pathway, albeit with a significantly lower activation barrier for the former (Figure 4.2). The cleavage of the  $\text{C}_1\text{-O}_1$  bond precedes the proton transfer from  $\text{C}_6$  to  $\text{O}_1$  with a concomitant  $\text{C}_3\text{-O}_1$  bond

cleavage, whereas the final step of the dehydrative aromatisation involves a second proton transfer from C<sub>5</sub> to O<sub>1</sub>, followed by water elimination (Figure 4.2; (b)).<sup>5</sup> NBO analysis indicated that the addition of a Lewis acid results in interactions between the metal and O<sub>1</sub>, modifying the electron density of O<sub>1</sub> and consequently the strength of the adjacent bonds.<sup>5</sup> However, gas phase calculations indicate that the Lewis acid-catalysed dehydration can be less effective due to the strong binding of 3,6-DMPA to the metal cation.<sup>5</sup> The dehydration in the presence of a Brønsted acid catalyst proceeds via a modified mechanism with the cycloadduct being protonated prior to the C<sub>1</sub>-O<sub>1</sub> bond cleavage (Figure 4.2; (c)). The final proton transfer from C<sub>6</sub> to O<sub>1</sub> is combined with water elimination and the Brønsted acid-catalysed pathway has been calculated to have a substantially lower activation barrier (13.8 kcal/mol) (Figure 4.2; (b)). The addition of solvents introduced a positive effect by reducing the energy barriers for the dehydration reaction but high temperatures were still required for the Lewis acid-catalysed reaction and Brønsted acid catalysis appears as the most effective strategy for the dehydrative aromatisation, affording 3,6-DMPA.<sup>5</sup> Combining the conclusions from both theoretical studies,<sup>5,6</sup> it could be suggested that a single Brønsted acidic catalyst could be effective in catalysing both the cycloaddition and the dehydration step in the conversion of MA and 2,5-DMF to 3,6-DMPA. Nonetheless, a thorough study on the kinetics of the complex reaction and a careful catalyst design are required for controlling the Brønsted acid-catalysed side-reactions.<sup>3,4</sup>

The synthesis of 3,6-dimethylphthalic anhydride (3,6-DMPA) requires strategies of multiple synthetic steps, providing good yields for the cycloaddition but low to moderate yields for the dehydrative aromatization of the isolated intermediate. The design of optimised catalysts that could promote the direct synthesis of 3,6-DMPA from 2,5-DMF and MA becomes of significant importance. In this work, ionic liquids and binary systems of ionic liquids and Brønsted acids were tested for the tandem Diels-Alder/dehydrative aromatization reaction between 2,5-DMF and MA. This work was completed in collaboration with Ms. Kai Ni Teh (**Section 4.2.1**) and Ms. Linqian Li (**Section 4.2.3**) who performed these experiments as part of the “MRes in Green Chemistry” programme (Department of Chemistry, Imperial College London) with the author of this PhD thesis being responsible for performing the first experiments together with the students to establish the reaction protocols, the experimental design, as well as the data analysis/critical assessment of all data presented herein.

## 4.2 Results & Discussion

### 4.2.1 Diels-Alder cycloaddition between 2,5-dimethylfuran (2,5-DMF) and maleic anhydride (MA)

A Diels-Alder reaction is a stereospecific  $[4\pi+2\pi]$  cycloaddition between a conjugated diene and a substituted alkene or alkyne (dienophile). The reaction is completed via a transition state where two thermodynamically stable single bonds and one double bond are formed simultaneously, yielding six-membered cyclic molecules. A form of selectivity arises when substituted dienophiles are used; two different isomers, *endo* and *exo*, can be formed. The symmetry in the *endo* product promotes interactions between the p-orbitals of the dienophile substituents and the newly formed double bond, stabilising the *endo* product. However, steric interactions can also determine the stereoselectivity and thus different substituents can ultimately lead to *exo* over *endo* selectivity.<sup>7</sup> The Frontier Molecular Orbital (FMO) theory is applied for predicting the impact of substituents on the reaction metrics of cycloadditions. For normal electron-demand reactions, the interactions between the electrons in the HOMO orbital of the diene and the LUMO of the dienophile determine the overall reactivity. Introducing electron-withdrawing (EWG) groups on the dienophile reduces the energy of its LUMO whereas the presence of electron-donating (EDG) groups in the diene increases the energy of the electrons found in the diene-HOMO orbital. Therefore, the reactivity is enhanced upon the reduction of the HOMO-LUMO energy gap. The impact of the reaction solvents on the rate and selectivity has been well-established.<sup>8,9</sup> Hydrogen bonding solvent-solute interactions, solvent polarity as well as solvophobic effects promote Diels-Alder reactions. Moreover, the addition of an electron withdrawing Lewis-acid catalyst lowers the energy of the LUMO of the substrate, usually the dienophile, to which it is coordinated.<sup>10</sup> Ionic liquids have been used as D-A solvents and catalysts due to their tuneable acidity, dipolarity and hydrogen-bond donor ability.<sup>8</sup> Chloroaluminates(III) were reported for the first time as solvents and catalysts for the cycloaddition between cyclopentadiene and methyl acrylate.<sup>11</sup> An acidic composition of  $[\text{C}_2\text{C}_1\text{im}]\text{Cl}/\text{AlCl}_3$  gave a reaction rate that was 10 and 560 times faster than in water and 1-chlorobutane, respectively. The acidity of the complex anions and the enhanced hydrogen bonding interactions between the cation and the dienophile or the transition state gave the overall improvement in the reaction metrics. In the context of this project, ionic liquids with hydrogen-bond donor properties were tested for the activation of maleic anhydride. The moisture-stable  $[\text{C}_4\text{C}_1\text{im}][\text{NTf}_2]$  was selected because of its hydrogen bond donor properties due to the weakly coordinating anion and the acidic protons of the imidazolium cation. The Kamlet-Taft  $\beta$  parameter, describing the ability of the anion to form hydrogen bonds, has been previously measured for a number of ILs together with the dipolarity/polarizability scales  $\pi^*$  and hydrogen bond acidity ( $\alpha$ ).<sup>12</sup> The  $\beta$  value for  $[\text{C}_4\text{C}_1\text{im}]^+$ -based ILs decreased in the following order:  $[\text{OTf}]^- > [\text{BF}_4]^- > [\text{NTf}_2]^- > [\text{PF}_6]^-$ .<sup>12</sup> A low  $\beta$ -value for  $[\text{C}_4\text{C}_1\text{im}][\text{NTf}_2]$

indicates that the anion will not compete with the cycloadduct on forming of a hydrogen-bonding network with the cation. Ionic liquids form hydrogen bond interactions of varying strengths depending on the type of cation and anion present within the ion pair. Representative Kamlet-Taft values of both organic solvents and ILs are summarized in Table 4.1.

**Table 4.1:** Literature Kamlet-Taft parameters ( $\alpha$ ,  $\beta$  and  $\pi^*$ ) for sample organic solvents and imidazolium-based ionic liquids

Solvent	$\alpha$	$\beta$	$\pi^*$
Dichloromethane <sup>13</sup>	0.30	0.00	0.82
Diethyl ether <sup>13</sup>	0.00	0.47	0.27
Water <sup>13</sup>	1.17	0.47	1.09
[C <sub>4</sub> C <sub>1</sub> im][NTf <sub>2</sub> ] <sup>12</sup>	0.61	0.23	0.99
[C <sub>8</sub> C <sub>1</sub> im][NTf <sub>2</sub> ] <sup>12</sup>	0.60	0.29	0.96
[HC <sub>4</sub> im][HSO <sub>4</sub> ] <sup>14</sup>	1.12	1.42	0.58
[HC <sub>1</sub> im][CH <sub>3</sub> COO] <sup>14</sup>	0.51	0.85	1.03

The cycloaddition of 2,5-DMF to MA is expected to be a normal electron demand Diels-Alder reaction. The presence of EDG and EWG groups in 2,5-DMF and MA, respectively, should lower the HOMO-LUMO gap and improve the reaction rates. This reaction has been reported to show a high *exo* selectivity.<sup>4</sup> Before proceeding with testing the direct synthesis of 3,6-DMPA in ionic liquids-based catalytic systems, the performance of neat [C<sub>4</sub>C<sub>1</sub>im][NTf<sub>2</sub>] was compared over conventional organic solvents for the cycloaddition between 2,5-DMF and MA. An equimolar (1:1) concentration of both reactants was used for the cycloaddition reactions that were performed at room temperature. The reaction progress was monitored by <sup>1</sup>H NMR spectroscopy at fixed time intervals and the conversion of MA (%) was calculated. More specifically, the conversion (%) was calculated by the integration of the peak of the cycloadduct at 6.40 ppm and the one corresponding to the protons of MA at 7.48 ppm. The thorough analysis of the <sup>1</sup>H spectra indicated that there were two distinct sets of proton peaks corresponding to both the *endo* (6.49 ppm, 3.69 ppm, 1.66 ppm) and the *exo* (6.40 ppm, 3.32 ppm, 1.58 ppm) cycloadducts. However, a high *exo/endo* selectivity was confirmed for both the organic solvents and ionic liquid-based systems, ranging from 75:25 to 90:10 for both the ILs and the conventional solvents. The use of acetonitrile and dichloromethane led to minimal differences in the conversion (%) of MA to 3,6-DMPA (Table 4.2). A reduced performance of diethyl ether was observed when it was tested up to a reaction time of one hour (rt), reaching 59 % in comparison with a 70 % conversion for the other two organic solvents. However, extending the reaction time to 24 h led to a conversion of 84 % for the cycloadditions that

were performed in diethyl ether. The use of [C<sub>4</sub>C<sub>1</sub>im][NTf<sub>2</sub>] (Table 4.2, Entry 4) led to a high conversion within 1 h of reaction time, similar to the performance of organic solvents (CH<sub>3</sub>CN and DCM). Interestingly, after 24 h, there was a plateau in performance and there was no further improvement in the conversion of MA towards the synthesis of 3,6-DMPA. A conversion (%) drop was observed after 48 h, confirming the instability of the Diels-Alder cycloadduct that most probably undergoes the retro Diels-Alder reaction. Ionic liquids are known to be solvents of a high viscosity that could potentially affect the rate of Diels-Alder reactions.<sup>15</sup> Binary systems of [C<sub>4</sub>C<sub>1</sub>im][NTf<sub>2</sub>] and DCM were therefore tested to reduce the viscosity of the media. The addition of 20 or 40 v/v % of DCM led to improved kinetics and higher conversions were reached faster when compared to the neat IL (Table 4.2, Entries 4 – 6) with negligible differences between the two tested loadings of the co-solvent.

**Table 4.2:** Diels-Alder cycloaddition of 2,5-DMF and MA, using ionic liquids or organic solvents

Entry	Solvent	conversion (%)					
		0.25 h	0.5 h	1 h	2 h	24 h	48 h
1	Acetonitrile (CH <sub>3</sub> CN)	61	64	71	/	/	/
2	Dichloromethane (DCM)	58	62	77	/	/	/
3	Diethyl ether (Et <sub>2</sub> O)	34	50	59	/	84	/
4	[C <sub>4</sub> C <sub>1</sub> im][NTf <sub>2</sub> ]	/	/	68	80	79	59
5	[C <sub>4</sub> C <sub>1</sub> im][NTf <sub>2</sub> ] / DCM (20 v/v %)	56	64	79	/	/	/
6	[C <sub>4</sub> C <sub>1</sub> im][NTf <sub>2</sub> ] / DCM (40 v/v %)	57	65	78	/	/	/

\*The reactions were run in duplicates and the reported values correspond to an average value (%), 2,5-DMF/MA (1:1), rt

Overall, the reaction between the highly activated diene, 2,5-DMF, and the reactive dienophile, MA, afforded very good yields in both organic solvents and [C<sub>4</sub>C<sub>1</sub>im][NTf<sub>2</sub>]. Consequently, addressing the challenge of optimising the reaction conditions for succeeding the tandem Diels-Alder/ dehydrative aromatization was investigated further. Before testing the direct synthesis of 3,6-DMPA from 2,5-DMF and MA, the dehydration of the cycloadduct was investigated in IL-based systems (**Section 4.2.2**).



#### 4.2.2 Dehydrative aromatization of the cycloadduct intermediate: 1,7-dimethyl-4,10-dioxatricyclo[5.2.1.0<sup>2,6</sup>]dec-8-ene-3,5-dione

The dehydrative aromatization of the isolated cycloadduct intermediate was first performed by using Brønsted acidic ionic liquids, bearing  $[\text{HSO}_4]^-$ . The reactions were tested at room temperature or at elevated temperatures (40 °C and 80 °C). Successful dehydration reactions have been previously reported in imidazolium-based ionic liquids with  $[\text{HSO}_4]^-$  anions, at temperatures ranging from 40 °C to 120 °C.<sup>16,17</sup> Herein, the application of  $[\text{C}_4\text{C}_1\text{im}][\text{HSO}_4]$  or  $[\text{HC}_4\text{im}][\text{HSO}_4]$  did not yield any 3,6-DMPA when the isolated cycloadduct was used as the reaction substrate at rt, 40 °C or 80 °C (24 h). It must be noted that the retro Diels-Alder reaction was found to be a main problem at 40 °C or 80 °C, even after 1 h of reaction time. It was therefore decided to reduce the temperature to 0 °C and attempt a series of dehydrative aromatisation reactions of the cycloadduct by using neat  $[\text{HSO}_4]^-$ -based ILs as well as binary mixtures of these ionic liquids with concentrated  $\text{H}_2\text{SO}_4$  (Table 4.3).

Binary mixtures of acids with Brønsted acidic ionic liquids present advantages such as prolonged catalyst lifetime and enhanced catalytic activity. Using  $\text{H}_2\text{SO}_4/[\text{cation}][\text{HSO}_4]$  systems has already been reported.<sup>18</sup> The Brønsted acidic ILs were then used as additives for the Friedel–Crafts alkylation of benzene with 1-decene, resulting in improvement in the product yield.<sup>18</sup> Combining neutral or acidic imidazolium-based ILs with sulfuric acid ( $\text{H}_2\text{SO}_4$ ) or triflic acid ( $\text{CF}_3\text{SO}_3\text{H}$ ) has also shown a superior performance in C4-alkylation reactions over the neat ILs or the Brønsted acids themselves.<sup>19</sup> The recyclability of the IL/acid mixtures was highlighted as a key benefit against the pure acids in combination with a tuneable acidity and the opportunity of optimising the solubility of the reactants.<sup>19</sup> The Hammett acidity functions ( $H_0$ ) quantitatively measure the acid strength of the non-aqueous or highly concentrated Brønsted acids. The acid strength is defined as the extent to which the acid protonates a base of known basicity. Recent studies have reported the  $H_0$  values for  $[\text{HC}_2\text{im}][\text{HSO}_4]/\text{H}_2\text{SO}_4$  systems<sup>20</sup> as well as combinations of ionic liquids ( $[\text{C}_4\text{C}_1\text{im}][\text{HSO}_4]$ ,  $[\text{C}_4\text{C}_1\text{im}][\text{TfO}]$ , and  $[\text{C}_4\text{C}_1\text{im}][\text{TFA}]$ ) with  $\text{H}_2\text{SO}_4$  or triflic acid.<sup>21</sup> Both the loading of the acid and the type of the anionic species controlled the acidity of the medium, essential feature for improving the conversion and selectivity of acid-catalysed reactions.<sup>21,22</sup> It has been found that the acidity of IL/acid systems with the general formula  $[\text{C}_n\text{C}_1\text{im}][\text{A}]/\text{HA}$  are characterized by the formation of an anionic cluster  $([\text{A}(\text{HA})_x]^-)$ .<sup>23,24</sup> Hydrogen-bonded clusters,  $[(\text{HSO}_4)(\text{H}_2\text{SO}_4)_x]^-$ , dependant on the molar ratio of sulfuric acid ( $X_{\text{H}_2\text{SO}_4}$ ), are formed upon mixing  $\text{H}_2\text{SO}_4$  with protic ionic liquids.<sup>23</sup> Varying  $X_{\text{H}_2\text{SO}_4}$  leads to varying the acidity but also the miscibility of the reaction substrates, affecting the kinetics of the reaction.<sup>23</sup>

In this work, it was confirmed that even when the reaction temperature was reduced to 0 °C, the neat ionic liquids, [HC<sub>4</sub>im][HSO<sub>4</sub>] and [TEA][HSO<sub>4</sub>], (Table 4.3, Entry 1 & 4), did not catalyse the conversion of the cycloadduct to 3,6-DMPA. The Hammett acidity constant ( $H_0$ ) for [HC<sub>4</sub>im][HSO<sub>4</sub>] has been estimated at 1.73.<sup>25</sup> When concentrated H<sub>2</sub>SO<sub>4</sub> was added to [HC<sub>4</sub>im][HSO<sub>4</sub>] (Table 4.3, Entry 2 & 3), leading to an increase in acidity, the formation of 3,6-DMPA was observed and quantified by <sup>1</sup>H NMR spectroscopy where the ionic liquid was used as the internal standard. The addition of 92 mol % of H<sub>2</sub>SO<sub>4</sub> was required for achieving moderate yields of 3,6-DMPA (24 %) with the estimated acidity of the reaction medium ( $H_0$ ) approximating the one of concentrated sulfuric acid. The binary systems of [TEA][HSO<sub>4</sub>] and concentrated H<sub>2</sub>SO<sub>4</sub> (Table 4.3, Entry 5 & 6) gave lower yields of 3,6-DMPA upon the addition of 92 mol % of H<sub>2</sub>SO<sub>4</sub> (15 %), indicating a lower acidity of the reaction medium.

**Table 4.3:** Dehydrative aromatisation of ,7- dimethyl-4,10-dioxa-tricyclo[5.2.1.0<sub>2,6</sub>]dec-8-ene-3,5-dione, using binary IL/H<sub>2</sub>SO<sub>4</sub> systems combinations of ionic liquids and H<sub>2</sub>SO<sub>4</sub>.(0 °C)

Entry	Solvent	IL (v/v %)	H <sub>2</sub> SO <sub>4</sub> (mol%)	H <sub>0</sub> <sup>d</sup>	3,6-DMPA (% yield)
1	[HC <sub>4</sub> im][HSO <sub>4</sub> ]	100	0	1.7	ND <sup>c</sup>
2	[HC <sub>4</sub> im][HSO <sub>4</sub> ]	40	81	-8.7	5
3	[HC <sub>4</sub> im][HSO <sub>4</sub> ]	20	92	-10.1	24
4	[TEA][HSO <sub>4</sub> ] <sup>a</sup>	100	0	NA <sup>b</sup>	ND <sup>c</sup>
5	[TEA][HSO <sub>4</sub> ] <sup>a</sup>	40	81	NA <sup>b</sup>	ND <sup>c</sup>
6	[TEA][HSO <sub>4</sub> ] <sup>a</sup>	20	92	NA <sup>b</sup>	15

a: Triethylammonium sulfate, b: NA = data are not available, c: NR = 3,6-DMPA was not detected

d: H<sub>0</sub> value estimated from literature data.<sup>25</sup>

Binary acid/IL systems were explored further for the direct synthesis of 3,6-DMPA from 2,5-DMF and MA. Varying loadings of a very strong acid, trifluoromethanesulfonic acid (TFA, CF<sub>3</sub>SO<sub>3</sub>H), were tested in combination with [C<sub>4</sub>C<sub>1</sub>im][NTf<sub>2</sub>] and compared against similar loadings of H<sub>2</sub>SO<sub>4</sub>. The ionic liquid, [C<sub>4</sub>C<sub>1</sub>im][NTf<sub>2</sub>], was used as a solvent given its excellent performance in promoting the cycloaddition reaction between 2,5-DMF and MA (**Section 4.2.1**) as well as its hydrophobicity and low viscosity<sup>26</sup>, when compared to other ionic liquids. TFA has a pK<sub>a</sub> of -13.6 and a H<sub>0</sub> value of -14.1.<sup>27</sup> Moreover, it is thermally stable and resistant to oxidative and reductive cleavage.<sup>28</sup>

### 4.2.3 Direct synthesis of 3,6-DMPA in binary acidic systems

The synthesis of 3,6-dimethylphthalic anhydride (3,6-DMPA) from maleic anhydride (MA) and 2,5-dimethylfuran (2,5-DMF), without the isolation and purification of the cycloadduct intermediate, was finally performed. Binary IL/acid systems, [C<sub>4</sub>C<sub>1</sub>im][NTf<sub>2</sub>]/TFA and [C<sub>4</sub>C<sub>1</sub>im][NTf<sub>2</sub>]/H<sub>2</sub>SO<sub>4</sub>, were tested as dual catalysts. Various TFA (5 – 40 mol%) and H<sub>2</sub>SO<sub>4</sub> loadings (20 – 40 mol%) and different reaction temperatures (-8 °C – rt) were tested. The molar ratio of MA to 2,5-DMF was kept constant at 1:1. Some experiments were tested in duplicates or triplicates to confirm their repeatability. A summary of the attempted reactions, including the yields of 3,6-DMPA and key by-products (24 h timepoint) is provided in Table 4.4.

**Table 4.4:** Summary of the key reactions towards the direct 3,6-DMPA synthesis in [C<sub>4</sub>C<sub>1</sub>im][NTf<sub>2</sub>]/TFA, [C<sub>4</sub>C<sub>1</sub>im][NTf<sub>2</sub>]/H<sub>2</sub>SO<sub>4</sub> and [C<sub>4</sub>C<sub>1</sub>im-SO<sub>3</sub>H][NTf<sub>2</sub>] (24 h, MA: 2,5-DMF: 1:1)

Entry	Solvent	Catalyst	mol [%]	T [°C]	MA conversion [%]	D-A <sup>1</sup> yield [%]	3,6-DMPA yield [%]	Maleic acid yield [%]	Fumaric acid yield [%]
1					81		9	9	15
2					71		14	13	14
3	[C <sub>4</sub> C <sub>1</sub> im][NTf <sub>2</sub> ]	TFA	20	RT	74		14	12	18
4					72		10	8	11
avg. 1-4					75(±4)		12(±2)	11(±2)	14(±2)
5					62	3	11	3	1
6	[C <sub>4</sub> C <sub>1</sub> im][NTf <sub>2</sub> ]	TFA	20	0	61	5	9	3	
avg. 5-6					61.5±0.5	4(±1)	10(±1)	3(±0)	0.5(±0.5)
7	[C <sub>4</sub> C <sub>1</sub> im][NTf <sub>2</sub> ]	TFA	20	-8	50	10	5		
8			5		64	11	6	2	2
10			10		65	6	8	5	6
12			30		83		9	8	14
13	[C <sub>4</sub> C <sub>1</sub> im][NTf <sub>2</sub> ]	TFA	40	RT	77		10	7	15
14			40		76		8	8	12
avg. 13-14			40		76.5±(0.5)		9(±1)	7.5±(0.5)	13(±2)
16			20		62	28	2	2	2
17	[C <sub>4</sub> C <sub>1</sub> im][NTf <sub>2</sub> ]	H <sub>2</sub> SO <sub>4</sub>	30	RT	60	5.4	4	6	7
18			40		64		4	16	11

1: D-A: cycloadduct intermediate

#### 4.2.3.1 3,6-DMPA synthesis in $[\text{C}_4\text{C}_1\text{im}][\text{NTf}_2]/\text{TFA}$ (20 mol%); preliminary observations

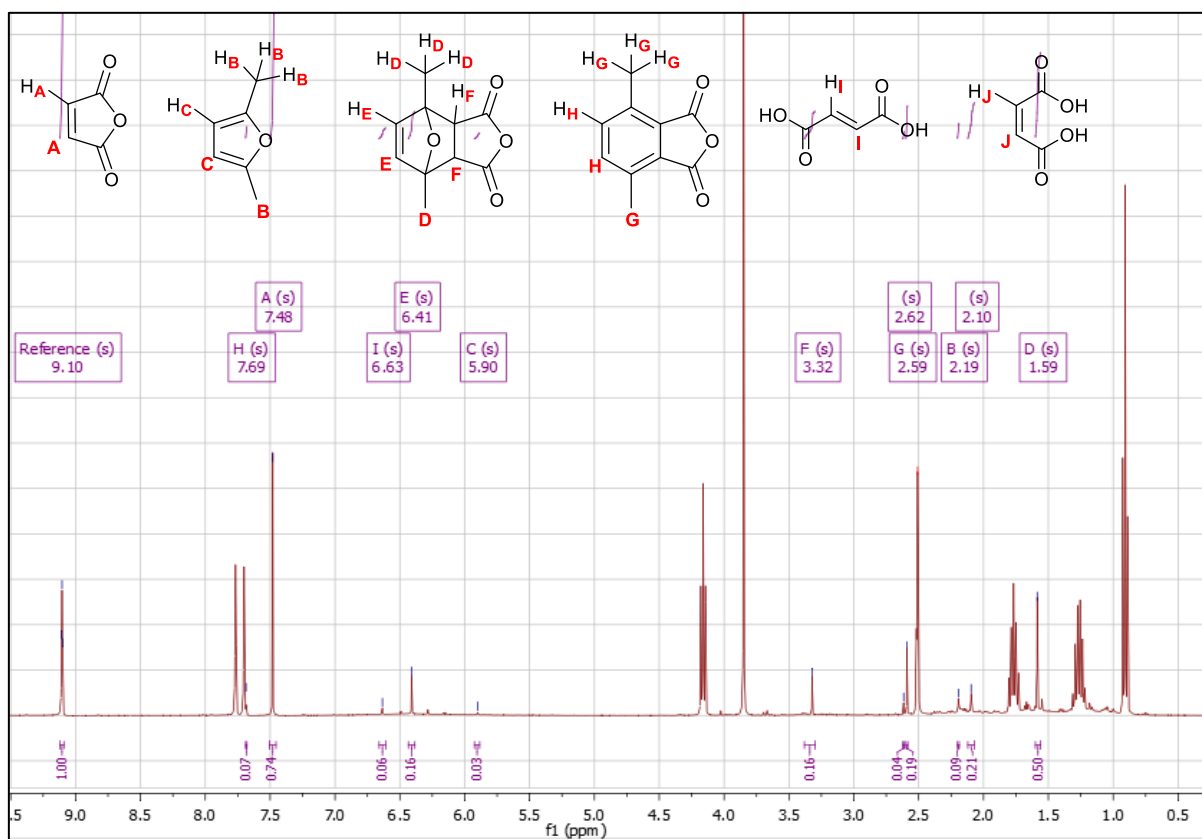


Figure 4.3:  $^1\text{H}$  NMR spectrum of the crude reaction mixture; ( $[\text{C}_4\text{C}_1\text{im}][\text{NTf}_2]/20$  mol% TFA, RT, 30 min).

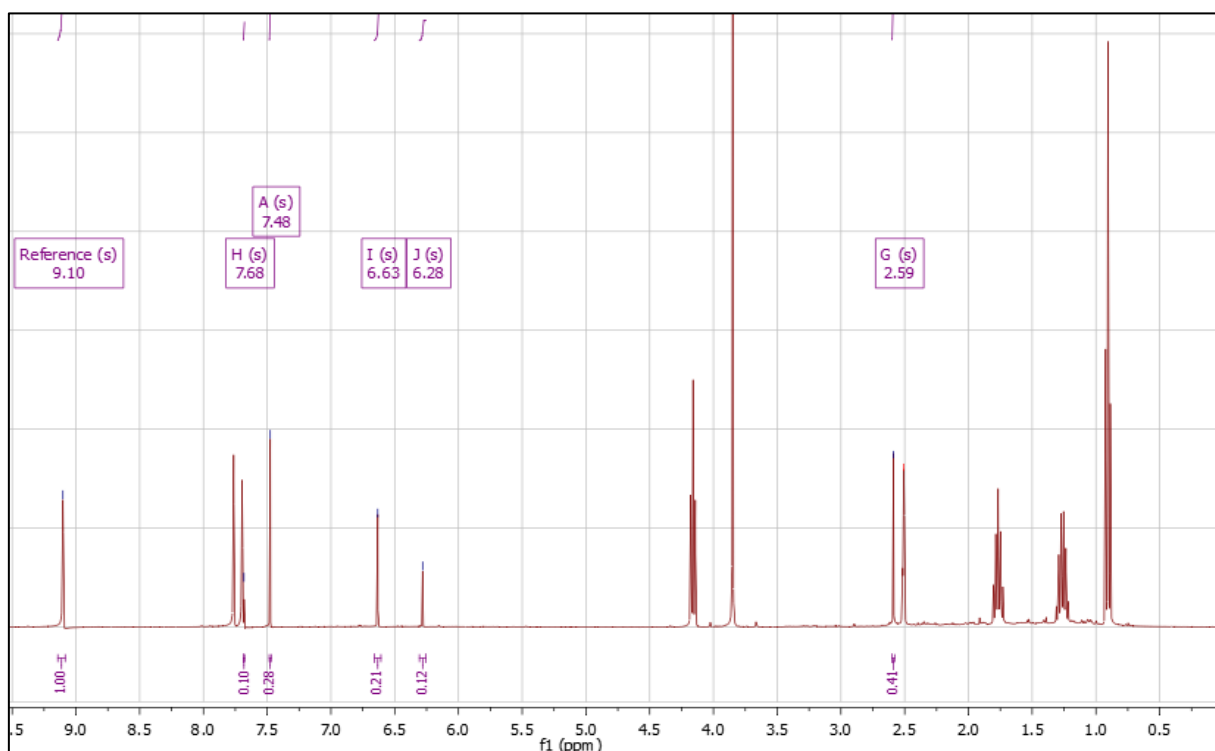


Figure 4.4:  $^1\text{H}$  NMR spectrum of the crude reaction mixture; ( $[\text{C}_4\text{C}_1\text{im}][\text{NTf}_2]/20$  mol% TFA, RT, 24 h).

The preliminary experiments were performed by using a 20 mol% loading of TFA together with  $[\text{C}_4\text{C}_1\text{im}][\text{NTf}_2]$ , testing the reaction between 2,5-DMF and MA at room temperature. Cycloadduct formation was observed by  $^1\text{H}$  NMR spectroscopy after 30 min of reaction time (Figure 4.3). The peaks corresponding to the cycloadduct were also observed at later timepoints when the reaction was tested at lower temperatures: 0 °C and –8 °C. The formation of 3,6-DMPA was also observed after only 30 min of reaction time (Figure 4.3). However, the strongly acidic reaction medium promoted the formation of by-products as well. A small peak at  $\delta = 6.63$  ppm (Figure 4.3, **H<sub>i</sub>**) was assigned to fumaric acid which is a known product of the isomerization of maleic acid, following the acid-catalysed hydrolysis of maleic anhydride.<sup>29</sup> Two peaks, corresponding to unknown products, were detected at 2.10 ppm and 2.62 ppm (30 min, rt) (Figure 4.3). Nonetheless, they disappear when the reaction was let to progress for longer (24 h, rt / Figure 4.4). More cycloadduct was formed and then converted into 3,6-DMPA whereas fumaric acid and the maleic acid were also detected after 24 h if reaction time (Figure 4.4). The investigation of the temperature and catalyst loading effect is described in the following sections, focusing on the  $[\text{C}_4\text{C}_1\text{im}][\text{NTf}_2]/\text{TFA}$ -based catalyst systems.

#### 4.2.3.2 3,6-DMPA synthesis; reaction metrics calculations

The reported MA conversion and the yield of products and by-products correspond to the values at 24 h of reaction time (Table 4.4), unless stated otherwise. The  $\text{C}^2$ -proton peak of  $[\text{C}_4\text{C}_1\text{im}]^+$  ( $\delta = 9.1$  ppm) was used as a reference peak for the conversion calculations due to the absence of any interference with any of the product peaks (Figure 4.3 & Figure 4.4). The area under the  $\text{C}^2$ -proton peak was therefore integrated and the concentration for each component was calculated based on the known molar concentration of the chemically stable ionic liquid. The peaks with chemical shifts at 7.48 ppm, 6.41 ppm, 2.59 ppm, 6.63 ppm and 6.28 ppm were used for calculating the conversion of MA and the yield of the cycloadduct, 3,6-DMPA, fumaric acid and maleic acid respectively. The standard deviation for results obtained from the experiments, carried out under same reaction conditions, was estimated to be less than 2 % for most cases (Table 4.4). The formation of other side-products, such as acid-catalysed polymerisation products, is also suggested by the MA-conversion values (%) (Table 4.4).

#### 4.2.3.3 The direct synthesis of 3,6-DMPA in $[C_4C_{1im}][NTf_2]/TFA$ (20 mol%); reaction temperature

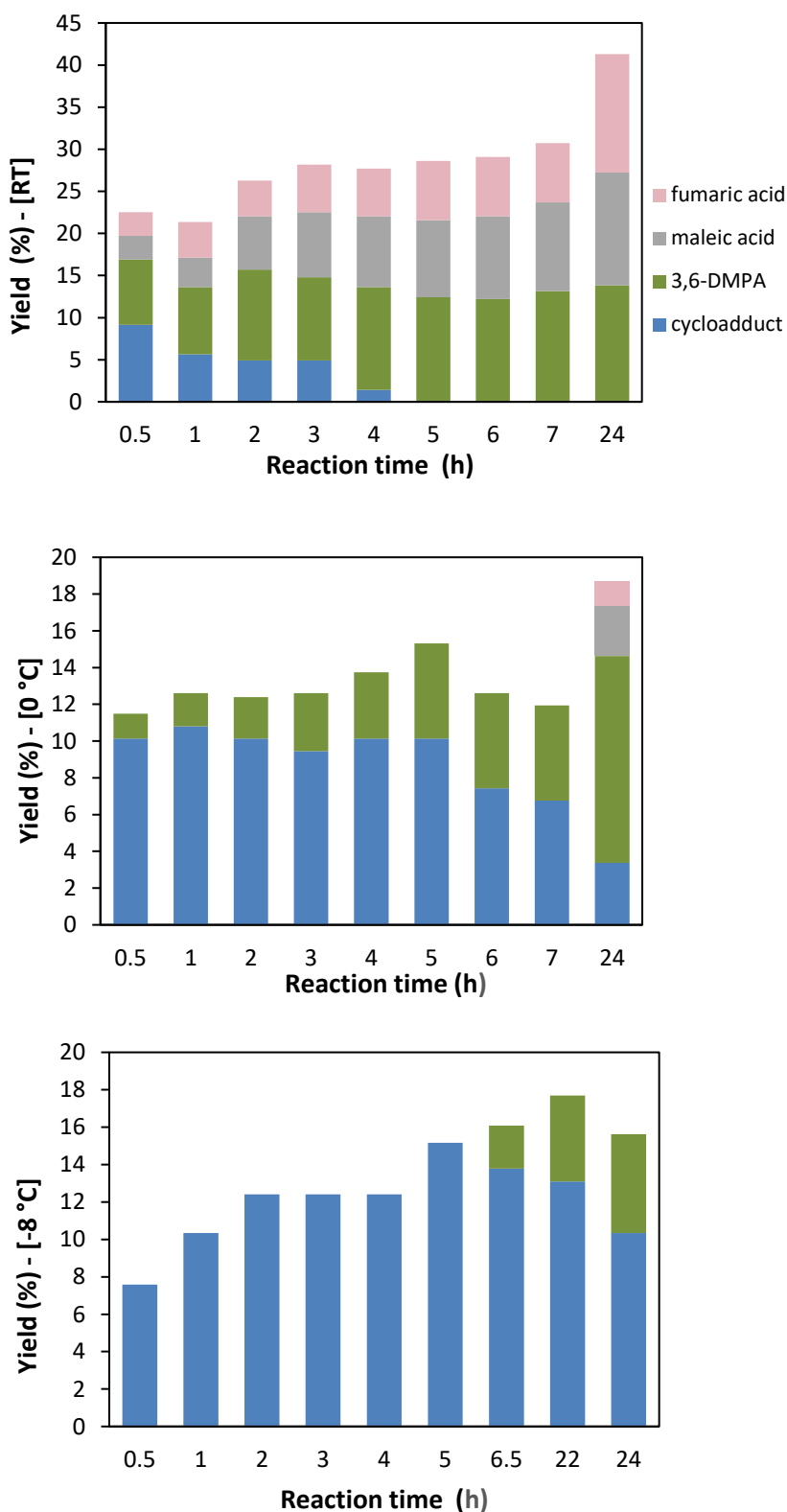


Figure 4.5: The effect of temperature (rt, 0 °C, -8 °C) on 3,6-DMPA synthesis from 2,5-DMF and MA ( $[C_4C_{1im}][NTf_2]/TFA$  (20 mol%))

The binary system of  $[\text{C}_4\text{C}_1\text{im}][\text{NTf}_2]/20 \text{ mol\% TFA}$  was tested for the direct conversion of 2,5-DMF and MA to 3,6-DMPA at different reaction temperatures (RT, 0 °C, -8 °C). The yield of 3,6-DMPA, maleic acid and fumaric acid was monitored as described in **Section 4.2.3.2**. After 24 h, a decrease in the yield of 3,6-DMPA was detected upon lowering the reaction temperature from room temperature to -8 °C (Table 4.4, Figure 4.5). The yield of 3,6-DMPA decreased from 12 % at room temperature to 10 % at 0 °C and finally a yield of 5 % was reached when the temperature was dropped to -8 °C (24 h). Furthermore, the conversion of MA as well as the yield of fumaric acid and maleic acid were also negatively affected by decreasing the temperature (Table 4.4, Figure 4.5), potentially due to slower reaction kinetics at lower temperatures. However, the effect of decreasing the viscosity of the IL-based medium on the conversion rates cannot be excluded. The yield of maleic acid was 11 % at room temperature but it was reduced to 3 % at 0 °C (24 h). Only traces of fumaric acid (0.5 %, 24 h) were found when the temperature was dropped to 0 °C in contrast to a yield of approximately 14 % at room temperature (24 h, Table 4.4). An increasing concentration of the cycloadduct is consistent before its slow conversion to 3,6-DMPA at 0 and -8 °C (Figure 4.5). Interestingly, no side-products were detected when  $[\text{C}_4\text{C}_1\text{im}][\text{NTf}_2]/\text{TFA}$  (20 mol%) was tested at -8 °C. As a result, the selectivity towards the formation of 3,6-DMPA over maleic acid and fumaric acid was largely increased going from 32 % at rt to 75 % at 0 °C and 100 % at -8 °C (Figure 4.5), indicating the suppression of fumaric acid and maleic acid formation at lower temperatures. However, the low conversion values for MA at such low temperatures even after 24 h of reaction time may be a concern for larger-scale applications.

#### **4.2.3.4 The direct synthesis of 3,6-DMPA in $[\text{C}_4\text{C}_1\text{im}][\text{NTf}_2]/\text{TFA}$ ; TFA loading effect (rt)**

Different TFA loadings (mol%), ranging from 5 mol% to 40 mol%, were investigated in the presence of  $[\text{C}_4\text{C}_1\text{im}][\text{NTf}_2]$  at room temperature (Entry 8 – 14, Table 4.4). Lower loadings of TFA in the binary mixtures of  $[\text{C}_4\text{C}_1\text{im}][\text{NTf}_2]/\text{TFA}$  led to lower 3,6-DMPA yields after 24 h (rt) with a yield of 6 % for 3,6-DMPA at 5 mol% TFA, increasing to 12 % for a catalyst loading of 20 mol%. Nevertheless, increasing the TFA loading further led to reduced 3,6-DMPA yields with an estimated value of 9 % at 40 mol% TFA whilst promoting the formation of maleic acid and fumaric acid (Table 4.4, Figure 4.6). The increasing MA conversion (Table 4.4) at higher TFA loadings and the combined yields of 3,6-DMPA, maleic acid and fumaric acid indicate that higher catalyst loadings may promoted other acid-catalysed reactions as well. Both temperature and catalyst loading affected the conversion of maleic anhydride to 3,6-DMPA and side-products. It was shown that when reaction temperature decreases the MA conversion decreases as well (**Section 4.2.2.3**). However, the selectivity for 3,6-DMPA increased, which might be attributed to the differing activation energies of product and side-products formation. In terms of the effect of

catalyst loading, the higher the TFA loading, the faster the reaction proceeds (Figure 4.6). However, very high TFA loadings do not enhance the 3,6-DMPA formation in contrast to the formation of other by-products.  $[C_4C_{1im}][NTf_2]/TFA$  (20 mol %) was therefore identified as the optimum catalytic system, under the tested conditions.

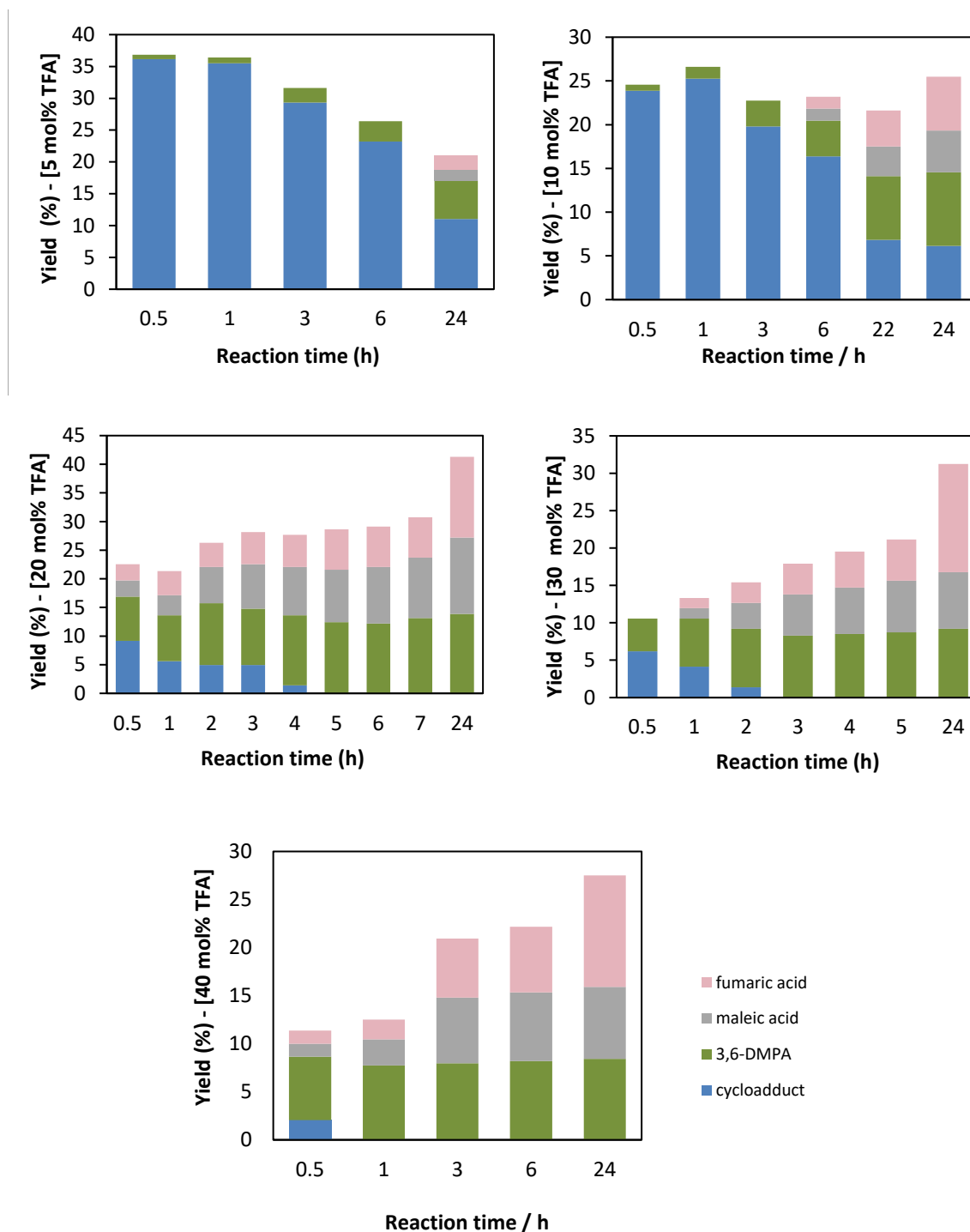


Figure 4.6: The effect of TFA loading (mol%) on 3,6-DMPA synthesis from 2,5-DMF and MA ( $[C_4C_{1im}][NTf_2]/TFA$  (room temperature))



The reaction was also attempted at 0 °C for lower and higher loadings (%mol) of TFA in to confirm whether the selectivity towards the formation of 3,6-DMPA could be optimised further (Table 4.5). However, lower loadings mainly promoted the cycloaddition reaction whereas higher loadings promoted the formation of unknown by-products as well as mainly maleic acid even when the temperature was reduced to 0 °C.

**Table 4.5:** The effect of TFA loading (mol%) on 3,6-DMPA synthesis from 2,5-DMF and MA ([C<sub>4</sub>C<sub>1</sub>im][NTf<sub>2</sub>]/TFA (0 °C, 24 h))

Solvent	Catalyst	mol [%]	T [°C]	MA conversion [%]	D-A <sup>1</sup> yield [%]	3,6-DMPA yield [%]	Maleic acid yield [%]	Fumaric acid yield [%]
[C <sub>4</sub> C <sub>1</sub> im][NTf <sub>2</sub> ]	TFA	5	0	65	38		1	
		10		58	31	2	1	1
		20		61	5	9	3	0.5
		30		57	5	6	4	2
		40		100		2	24	

#### 4.2.3.5 The direct synthesis of 3,6-DMPA synthesis in [C<sub>4</sub>C<sub>1</sub>im][NTf<sub>2</sub>]/H<sub>2</sub>SO<sub>4</sub> (rt)

Additional experiments were carried out by using concentrated H<sub>2</sub>SO<sub>4</sub> as an added catalyst in binary IL/acid systems for the direct synthesis of 3,6-DMPA from 2,5-DMF and MA. Sulfuric acid is a less strong Brønsted acid catalyst ( $H_0 = -12$ )<sup>30</sup> when compared to TFA ( $H_0 = -14.2$ )<sup>31</sup>. The experiments were still performed by using [C<sub>4</sub>C<sub>1</sub>im][NTf<sub>2</sub>] as a solvent/co-catalyst and H<sub>2</sub>SO<sub>4</sub> loadings between 20 mol% and 40 mol% were investigated at room temperature. The formation of 3,6-DMPA was less promoted when H<sub>2</sub>SO<sub>4</sub> was used instead of TFA at all catalyst loadings (Figure 4.6 – 4.8, Table 4.4). After 24 h of reaction time, a yield of only 2 % -4 % was obtained for 3,6-DMPA without any significant differences across the different loadings of H<sub>2</sub>SO<sub>4</sub> (Table 4.4, Figure 4.7/4.8). Interestingly, the formation of maleic acid and fumaric acid seems to be promoted with as estimated yield of 16 % for maleic acid and 11 % for fumaric acid (24h, 40 mol% H<sub>2</sub>SO<sub>4</sub>, Table 4.4). Higher loadings of H<sub>2</sub>SO<sub>4</sub> translated into the enhanced formation of both maleic acid and fumaric acid (Table 4.4). The overall reduced acidity of the reaction medium and possibly the formation of different anionic clusters in [C<sub>4</sub>C<sub>1</sub>im][NTf<sub>2</sub>]/H<sub>2</sub>SO<sub>4</sub> over [C<sub>4</sub>C<sub>1</sub>im][NTf<sub>2</sub>]/TFA may explain the reduction in the yields of 3,6-DMPA with observed slower kinetics for the dehydrative aromatisation of the cycloadduct (Figure 4.7 , 4.8). The formation of the cycloadduct intermediated appeared to be still promoted in [C<sub>4</sub>C<sub>1</sub>im][NTf<sub>2</sub>], resulting in more than 28 % of MA being converted into the cycloadduct intermediate (20 mol% H<sub>2</sub>SO<sub>4</sub>, RT, 24 h). A reduction in the cycloadduct yield between 6 h and 24 h of reaction time and the rise of fumaric and maleic acid indicate the retro-D-A reaction

taking place, followed by the acid-catalysed conversion of MA into by-products (Figure 4.7, 4.8). No cycloadduct was spectroscopically detected in  $[C_4C_{1im}][NTf_2]/20\text{ mol\% TFA}$  acidic system after 24 h of reaction time (Table 4.4). It is suggested that the dehydration reaction of the intermediate proceeds via slower rates when  $H_2SO_4$  was applied as the catalyst, promoting mainly the formation of side-products.

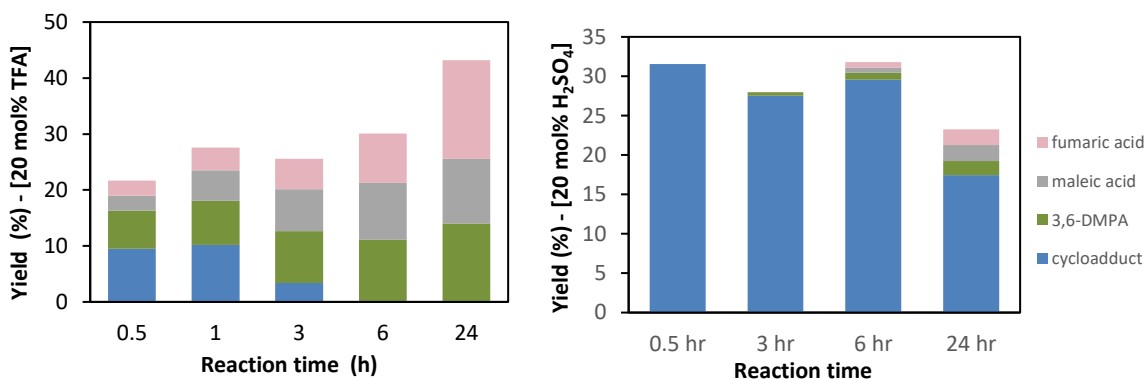


**Figure 4.7:** The effect of acidity on 3,6-DMPA synthesis in  $[C_4C_{1im}][NTf_2]/20\text{ mol\% TFA}$  (left),  $H_2SO_4$  (right), RT, 24 h.

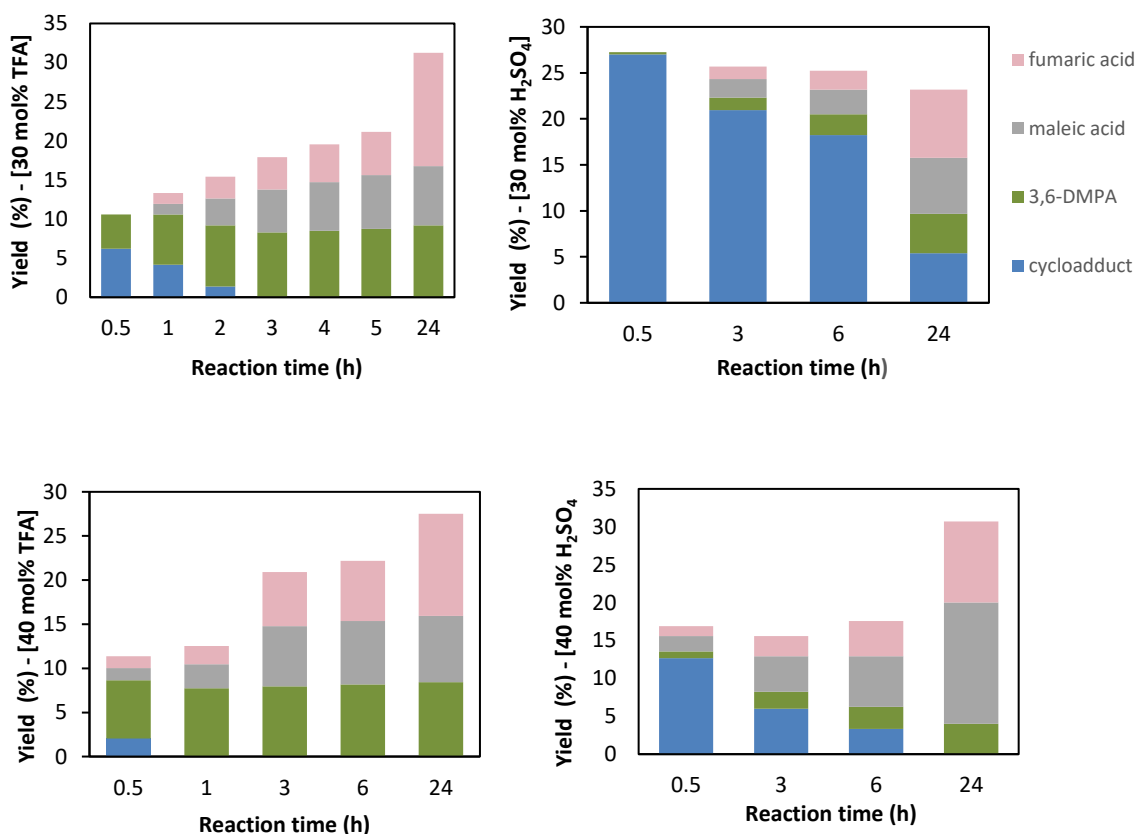


**Figure 4.8:** Direct 3,6-DMPA synthesis from 2,5-DMF and MA in  $[C_4C_{1im}][NTf_2]/H_2SO_4$  ( $H_2SO_4$ : 30 mol% & 40 mol%) in comparison with  $[C_4C_{1im}][NTf_2]/TFA$  (TFA: 30 mol% & 40 mol%)

#### 4.2.3.6 Summary and outlook for future work

The novel direct synthesis of 3,6-DMPA from 2,5-DMF and MA was achieved in acidic media based on  $[C_4C_{1im}][NTf_2]$  and trifluoromethane sulphonic acid (TFA) with a superior performance of TFA over  $H_2SO_4$ . Combining strong Brønsted acids with ILs is known to provide the benefit of more facile catalyst recycling whereas a synergistic catalytic effect is possible, mainly due to interactions between the anionic species of the IL and the Brønsted acid. 3,6-DMPA, was formed in low to moderate yields, not exceeding 14 % after 24 h of reaction time (20 mol% TFA, rt), albeit with a positive effect of lowering the temperature to  $-8\text{ }^\circ\text{C}$  in regards with improving the selectivity towards 3,6-DMPA. Implementing higher catalyst loadings (30 mol% or 40 mol%) led to promoting side reactions at room temperature and  $0\text{ }^\circ\text{C}$ . Apart from 3,6-DMPA, maleic acid and fumaric acid were formed as side products and unidentified by-products were attributed to polymerisation under the tested acidic conditions.

It becomes apparent that there is a complex network of reactions taking place upon directly reacting 2,5-DMF and MA under acidic conditions. Maleic acid participates as a dienophile but also as a reactant towards the formation of maleic acid and fumaric acid whereas both the cycloadduct and 3,6-DMPA may also participate in other side reactions. There is a still work to be completed to gain a thorough insight on the different mechanistic pathways and realise the full potential of using the binary IL/acid systems. It is recommended to conduct quantum chemical studies to establish the reaction mechanism and establish the exact energy requirements for the different reaction pathways. Moreover, additional experiments should be undertaken in order to quantify the Hammett acidity of the tested systems as given that an optimum acidity/catalytic performance was identified for  $[C_4C_{1im}][NTf_2]/20\text{ mol}\%$ . Finally, finetuning the reaction conditions by testing IL/acid systems with varying acidity (e.g.  $C_4C_{1im}[NTf_2]/HNTf_2$ ,  $[C_4C_{1im}][HSO_4]/HNTf_2$ ,  $[C_4C_{1im}][HSO_4]/TFA$ ) and viscosity profiles at both room temperature and lower temperatures is highly recommended for achieving optimum 3,6-DMPA selectivity without compromising on the reaction kinetics.

### 4.3 Experimental

All reagents were purchased from Sigma-Aldrich, Fluorochem, VWR International and Alfa Aesar. The reactions were performed under N<sub>2</sub>. 2,5-dimethylfuran (99 %) was dried over CaCl<sub>2</sub> (rt) and it was purified via atmospheric distillation under N<sub>2</sub> before use. All organic solvents were used dry (H<sub>2</sub>O, < 5 ppm). Concentrated sulfuric acid, 95 v/v % H<sub>2</sub>SO<sub>4</sub> (Sigma-Aldrich), was used as received. The synthesized ionic liquids, maleic anhydride (MA), trifluoromethane sulphonic acid (TFA) and lithium bis(trifluoromethyl-sulfonyl)imide (LiNTf<sub>2</sub>) were kept in a glovebox (H<sub>2</sub>O, O<sub>2</sub> < 0.5 ppm). The ionic liquids [HC<sub>4</sub>im][HSO<sub>4</sub>] and [C<sub>4</sub>C<sub>1</sub>IM][HSO<sub>4</sub>] were previously synthesised by members of the group. These ionic liquids were dried under vacuum (40 °C, 2 mbar, 24 h) and their purity was confirmed by <sup>1</sup>H and <sup>13</sup>C NMR spectroscopy. The low water content of the ILs was monitored by Karl-Fischer titration (< 20 ppm). Karl Fischer titration was performed on a SCHOTT Instruments Titroline KF Trace. The <sup>1</sup>H and <sup>13</sup>C NMR spectra were recorded on a Bruker AV-400 spectrometer (400 and 101 MHz, respectively) in DMSO-d<sub>6</sub>. <sup>1</sup>H NMR spectroscopy, using peaks of the IL used as the internal standard (δ = 9.2 ppm), was performed to investigate how the reaction proceeded over time. LSIMS (20 - 2500 Da) mass spectrometry, in both positive and negative mode, were performed by Dr. Lisa Haigh on a Micromass Autospec Premier mass spectrometer (Department of Chemistry, Imperial College London).

#### 4.3.1 Synthesis of 1-butyl-3-methylimidazolium bis(trifluoromethanesulfonyl)imide ([C<sub>4</sub>C<sub>1</sub>im][NTf<sub>2</sub>])

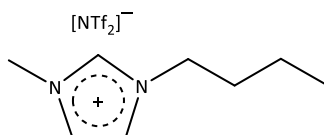


**Figure 4.9:** Chemical structure of 1-butyl-3-methylimidazolium bis(trifluoromethanesulfonyl)imide ([C<sub>4</sub>C<sub>1</sub>im][NTf<sub>2</sub>])

In a 1L two-neck flask, Li[N(SO<sub>2</sub>CF<sub>3</sub>)<sub>2</sub>] (86 g, 0.299 mol, 1.03 eq.) was added to a solution of [C<sub>4</sub>C<sub>1</sub>im]Cl (50.64 g, 0.289 mol, 1 eq.) in CH<sub>2</sub>Cl<sub>2</sub> (180 ml). Both Li[N(SO<sub>2</sub>CF<sub>3</sub>)<sub>2</sub>] and [C<sub>4</sub>C<sub>1</sub>im]Cl have been pre-weighed in a dry glovebox given that they are hygroscopic materials. The resulting suspension was stirred vigorously under nitrogen (48 h, rt). The reaction mixture was added into a separating funnel and the residual salt was washed with dichloromethane (2 x 10 ml) and the combined organic extracts were washed with water (20 x 30 ml) until the aqueous phase was halide free as indicated by AgNO<sub>3</sub> test.

Residual solvent and water were removed under vacuum (35 °C, 24h) until a colourless viscous liquid was obtained (117.22 g, 0.280 mol, 96 %).

$^1\text{H}$  NMR (400 MHz, DMSO- $d_6$ ) ppm: 9.11 (1H, s,  $\text{N}_2\text{CH}$ ), 7.77 and 7.70 (2H, m, 2 $\text{NCH}$ ), 4.16 (2H, t,  $^3J_{\text{HH}} = 7.2$  Hz,  $\text{NCH}_2(\text{CH}_2)_2\text{CH}_3$ ), 3.85 (3H, s,  $\text{NCH}_3$ ), 1.77 (2H, quintet,  $^3J_{\text{HH}} = 7.2$  Hz,  $\text{NCH}_2\text{CH}_2\text{CH}_2\text{CH}_3$ ), 1.28 (2H, sextet,  $^3J_{\text{HH}} = 7.6$  Hz,  $\text{NCH}_2\text{CH}_2\text{CH}_2\text{CH}_3$ ) and 0.91 (3H, t,  $^3J_{\text{HH}} = 7.2$  Hz,  $\text{N}(\text{CH}_2)_3\text{CH}_3$ ).

$^{13}\text{C}$  NMR (100 MHz, DMSO- $d_6$ )/ppm: 136.96 (s,  $\text{N}_2\text{CH}$ ), 124.04 and 122.69 (s, 2 $\text{NCH}$ ), 118.35 (q,  $^1J_{\text{CF}} = 321.8$  Hz,  $[\text{N}(\text{SO}_2\text{CF}_3)_2]^-$ ), 48.99 (s,  $\text{NCH}_2(\text{CH}_2)_2\text{CH}_3$ ), 36.14 (s,  $\text{NCH}_3$ ), 31.79 (s,  $\text{NCH}_2\text{CH}_2\text{CH}_2\text{CH}_3$ ), 19.20 (s,  $\text{N}(\text{CH}_2)_2\text{CH}_2\text{CH}_3$ ) and 13.59 (s,  $\text{N}(\text{CH}_2)_3\text{CH}_3$ ).

MS (FAB $^+$ )  $m/z$ : 142 ( $[\text{C}_4\text{C}_1\text{im}]^+$ , 100 %), (FAB $^-$ )  $m/z$ : 280 ( $[\text{NTf}_2]^-$ , 100%).

#### 4.3.2 General protocol for the reaction between 2,5-dimethylfuran (2,5-DMF) and maleic anhydride (MA); synthesis of 1,7- dimethyl-4,10-dioxo-tricyclo[5.2.1.0 $^{2,6}$ ]dec-8-ene-3,5-dione

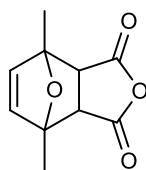


**Figure 4.10:** Chemical structure of 1,7- dimethyl-4,10-dioxo-tricyclo[5.2.1.0 $^{2,6}$ ]dec-8-ene-3,5-dione

Maleic anhydride (MA) (4.90 g, 50 mmol, 1 eq) was added to a two-necked round bottom flask, fitted with a stopcock adapter, in the glovebox ( $\text{N}_2$ ). Dry solvent (5 ml) or a co-solvent or the ionic liquid, was added to MA. 2,5-dimethylfuran (2,5-DMF) (5.3 mL, 50 mmol, 1 eq) was added drop-wise to the IL/MA mixture. The reaction mixture was then stirred at rt and the reaction progress was followed via  $^1\text{H}$  NMR spectroscopy at different time intervals. The crude reaction mixture, the solid was isolated by vacuum filtration and washed with dry diethyl ether  $\text{Et}_2\text{O}$ .

$^1\text{H}$  NMR:  $\delta$  (400 MHz, DMSO- $d_6$ ) ppm: 6.41 (s, 2H,  $\text{HC}=\text{CH}$ ), 3.32 (s, 2H,  $\text{O}=\text{C}-\text{CH}-\text{CH}-\text{C}=\text{O}$ ), 1.59 (s, 6H,  $\text{H}_3\text{C}-\text{COC}-\text{CH}_3$ )

#### 4.3.3 General protocol for the dehydrative aromatization of 1,7-dimethyl-4,10-dioxatricyclo[5.2.1.0<sup>2,6</sup>]dec-8-ene-3,5-dione by using binary IL/H<sub>2</sub>SO<sub>4</sub> mixtures.

Concentrated sulfuric acid (95 v/v % H<sub>2</sub>SO<sub>4</sub>) was added to the ionic liquid that was cooled at 0 °C and a homogeneous solution was obtained. The cycloadduct (100 mg) was added in small portions and mixed with the IL/acid mixture. The reaction mixture was then stirred at 0 °C for 1 h and finally poured over crushed ice. The solid was collected via vacuum filtration and washed with cold water.

#### 4.3.4 General protocol for the direct synthesis of 3,6-DMPA in [C<sub>4</sub>C<sub>1</sub>im][NTf<sub>2</sub>]/TFA mixtures.

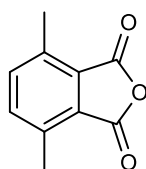


Figure 4.11: Chemical structure of 3,6-dimethylphthalic anhydride

To a two-neck round bottom flask, 0.49 g of MA was added to 2 mL of [C<sub>4</sub>C<sub>1</sub>im][NTf<sub>2</sub>] and 150 mg (20 mol%), or other loadings of TFA, were added in the glovebox. After the maleic anhydride was dissolved, 0.48 g of 2,5-dimethylfuran, 2,5-DMF was added under nitrogen. A colour shift to red was observed, immediately after the addition of 2,5-DMF. The flask was covered with aluminium foil in order to prevent exposure to light. <sup>1</sup>H NMR spectroscopy was used to monitor the reaction progress. Samples were taken for analysis at different time intervals, such as 30 min, 1, 2, 3, 5, 24 h and 72 h.

The same protocol was applied when H<sub>2</sub>SO<sub>4</sub> was used as a catalyst instead of TFA.

<sup>1</sup>H NMR: δ (400 MHz, DMSO-d<sub>6</sub>) ppm: 7.69 (s, 2H, CH), 2.59 (s, 6H, CH<sub>3</sub>)

<sup>13</sup>C NMR: δ (101 MHz, DMSO-d<sub>6</sub>) ppm: 163.78 (C=O), 138.17 and 137.22 (C-2/4), 128.82 (C-3), 17.27 (CH<sub>3</sub>)

IR (cm<sup>-1</sup>): 1755.54 and 1501.77 (aromatic C=C bending), 883.7 and 845.93 (C-H bending)

LSI Mass Spectrometry (EI<sup>+</sup>, 5.61 eV): 104, 120, 132, 148, 176 m/z

#### 4.4 References

- 1 S. Giarola, C. Romain, C. K. Williams, J. P. Hallett and N. Shah, *Chem. Eng. Res. Des.*, 2016, **107**, 181–194.
- 2 C. R. Dias, M. F. Portela and G. C. Bond, *J. Catal.*, 1995, **157**, 353–358.
- 3 S. Thiyagarajan, H. C. Genuino, M. Śliwa, J. C. van der Waal, E. de Jong, J. van Haveren, B. M. Weckhuysen, P. C. A. Bruijninx and D. S. van Es, *ChemSusChem*, 2015, **8**, 3052–3056.
- 4 E. Mahmoud, D. A. Watson and R. F. Lobo, *Green Chem.*, 2014, **16**, 167–175.
- 5 T. Salavati-fard, S. Caratzoulas and D. J. Doren, *Chem. Phys.*, 2017, **485–486**, 118–124.
- 6 T. Salavati-fard, S. Caratzoulas and D. J. Doren, *J. Phys. Chem. A*, 2015, **119**, 9834–9843.
- 7 R. Gleiter and M. C. Bohm, *Pure Appl. Chem.*, , DOI:10.1351/pac198855020237.
- 8 C. Chiappe, M. Malvaldi and C. S. Pomelli, *Green Chem.*, 2010, **12**, 1330.
- 9 A. Wittkopp and P. R. Schreiner, in *PATAI'S Chemistry of Functional Groups*, John Wiley & Sons, Ltd, Chichester, UK, 2009.
- 10 V. D. Kiselev and A. I. Konovalov, *Russ. Chem. Rev.*, 1989, **58**, 230–249.
- 11 C. W. Lee, *Tetrahedron Lett.*, 1999, **40**, 2461–2464.
- 12 M. A. Ab Rani, A. Brant, L. Crowhurst, A. Dolan, M. Lui, N. H. Hassan, J. P. Hallett, P. A. Hunt, H. Niedermeyer, J. M. Perez-Arlandis, M. Schrems, T. Welton and R. Wilding, *Phys. Chem. Chem. Phys.*, 2011, **13**, 16831.
- 13 M. J. Kamlet, J. L. M. Abboud, M. H. Abraham and R. W. Taft, *J. Org. Chem.*, 1983, **48**, 2877–2887.
- 14 S. K. Shukla, N. D. Khupse and A. Kumar, *Phys. Chem. Chem. Phys.*, 2012, **14**, 2754.
- 15 N. D. Khupse and A. Kumar, *J. Phys. Chem. A*, 2011, **115**, 10211–10217.
- 16 S. Lima, M. M. Antunes, M. Pillinger and A. A. Valente, *ChemCatChem*, 2011, **3**, 1686–1706.
- 17 S. Eminov, J. D. E. T. Wilton-Ely and J. P. Hallett, *ACS Sustain. Chem. Eng.*, 2014, **2**, 978–981.
- 18 P. Wasserscheid, M. Sesing and W. Korth, *Green Chem.*, 2002, **4**, 134–138.
- 19 S. Tang, A. M. Scurto and B. Subramaniam, *J. Catal.*, 2009, **268**, 243–250.
- 20 J. Gräsvik, J. P. Hallett, T. Q. To and T. Welton, *Chem. Commun.*, 2014, **50**, 7258–7261.
- 21 S. Zhang, T. Zhang and S. Tang, *J. Chem. Eng. Data*, 2016, **61**, 2088–2097.
- 22 A. Wang, G. Zhao, F. Liu, L. Ullah, S. Zhang and A. Zheng, *Ind. Eng. Chem. Res.*, 2016, **55**, 8271–8280.
- 23 K. Matuszek, A. Chrobok, F. Coleman, K. R. Seddon and M. Swadźba-Kwaśny, *Green Chem.*, 2014, **16**, 3463–3471.
- 24 J. A. McCune, P. He, M. Petkovic, F. Coleman, J. Estager, J. D. Holbrey, K. R. Seddon and M. Swadźba-Kwaśny, *Phys. Chem. Chem. Phys.*, 2014, **16**, 23233–23243.

- 25 J. Grøsvik, J. P. Hallett, T. Q. To and T. Welton, *Chem. Commun.*, 2014, **50**, 7258.
- 26 J. G. Huddleston, A. E. Visser, W. M. Reichert, H. D. Willauer, G. a. Broker and R. D. Rogers, *Green Chem.*, 2001, **3**, 156–164.
- 27 S. Liu, W. Zhu, L. Shi, H. Liu, Y. Liu, Y. Ni, L. Li, H. Zhou, S. Xu and Z. Liu, *RSC Adv.*, 2014, **4**, 40999–41002.
- 28 R. D. Howells and J. D. Mc Cown, *Chem. Rev.*, 1977, **77**, 69–92.
- 29 T. Felthouse, J. Burnett, B. Horrell, M. Mommey and Y.-J. Kuo, *Kirk-Othmer Encycl. Ind. Chem.*, 1933, **15**, 1–49.
- 30 K. N. Pelletreau and G. Muller-Parker, *Mar. Biol.*, 2002, **141**, 1–9.
- 31 I. L. Aleksander Trummal, Lauri Lipping, Ivari Kaljurand, Ilmar A. Koppel, *J. Phys. Chem. A*, 2016, **120**, 3663–3669.